TIME-RESOLVED X-RAY ABSORPTION SPECTROSCOPY OF TRANSITION METAL COMPLEXES

THÈSE N^{O} 3673 (2006)

PRÉSENTÉE LE 3 NOVEMBRE 2006

À LA FACULTÉ DES SCIENCES DE BASE

Laboratoire de spectroscopie ultrarapide

SECTION DE PHYSIQUE

ÉCOLE POLYTECHNIQUE FÉDÉRALE DE LAUSANNE

POUR L'OBTENTION DU GRADE DE DOCTEUR ÈS SCIENCES

PAR

Wojciech GAWELDA

Magister in physics, Adam Mickiewicz University, Poznan, Pologne
de nationalité polonaise

acceptée sur proposition du jury:

Prof. R. Schaller, président du jury
Prof. M. Chergui, Prof. C. Bressler, directeurs de thèse
Dr M. Benfatto, rapporteur
Prof. V. Sundström, rapporteur
Prof. F. van der Veen, rapporteur

ÉCOLE POLYTECHNIQUE
FÉDÉRALE DE LAUSANNE

Lausanne, EPFL
2006

Kochanym Rodzicom i Ana Belén

Time-Resolved X-Ray Absorption Spectroscopy of Transition Metal Complexes

Ph.D Thesis

Wojciech Gawelda
Laboratoire de Spectroscopie Ultrarapide
Institut des Sciences et Ingénierie Chimiques
Faculté des Sciences de Base - EPFL-BSP CH-1015 Dorigny-Lausanne

Abstract

Electronic structure changes are at the origin of the making, breaking and transformation of bonds. These changes can be visualized by measuring the geometric structure in "real-time" during the course of a chemical reaction, a biological function or a physical process. Time-resolved X-ray Absorption Spectroscopy (XAS) delivers information about both the electronic (via XANES) and geometric (via EXAFS) transient structural changes, when interfaced with an ultrafast laser in a pump-probe scheme. Moreover, XAS offers unique flexibility, since it is both element-selective and it can be applied to any kind of disordered or ordered systems.

In this thesis, we successfully investigated the excited state electronic and geometric structures of two different transition metal complexes. In both cases, for the first time, their excited state molecular geometries were characterized "on the fly", without any *a priori* assumptions about its excited state structure. More importantly, it has been shown that time-resolved XAS is the only method capable of delivering the transient molecular structures of their short-lived excited states.

First, we investigated ruthenium(II)-tris(2,2'-bipyridine), $[Ru^{II}(bpy)_3]^{2+}$. This molecule has served as a prototype and a model system of intramolecular electron and energy transfer reactions, due to its unique excited state properties. Our studies focused on the energy and structural relaxation process of the short-lived excited states of this molecule. By using the combined ultrafast laser and x-ray spectroscopies, we have determined various relaxation pathways of its excited states down to 15 fs lifetimes. The geometrical distortion of its lowest-lying excited state (^{3}MLCT state) has also been determined by picosecond XAS, delivering a Ru-N bond contraction of $\sim$ -0.04 Å.

Second, our study focused on iron(II)-tris(2,2'-bipyridine) $[Fe^{II}(bpy)_3]^{2+}$. This class of compounds is being extensively studied in relation to the phenomenon of spin crossover, where a spin transition takes place, involving the low-spin (LS) ground state and the high-spin (HS) excited state. Here, we have characterized its excited states by means of both ultrafast optical and x-ray spectroscopy.

The optical studies have revealed several new aspects concerning the relaxation pathways of its charge transfer and ligand-field states, including their corresponding lifetimes. The structural analysis has determined the geometric distortions taking place in the lowest-lying excited HS state of $[Fe^{II}(bpy)_3]^{2+}$. The extracted Fe-N bond elongation of 0.2 Å agrees well with previously predicted values and it is for the first time that the room-temperature solvated structure of the HS short-lived excited state of a ferrous transition metal is obtained.

KEYWORDS: *X-ray Absorption Spectroscopy, Transition Metal Complexes, Electron Transfer Reaction, Spin Crossover, Time-resolved spectroscopy, Femtosecond Laser Pulses, Picosecond X-ray Pulses, Synchrotron Radiation, Pump-Probe Spectroscopy*

Spectroscopie d'Absorption X Résolue en Temps de Complexes de Métaux de Transition

Thèse de Doctorat

Wojciech Gawelda
Laboratoire de Spectroscopie Ultrarapide
Institut des Sciences et Ingénierie Chimiques
Faculté des Sciences de Base - EPFL-BSP CH-1015 Lausanne

Résumé

Le changement de structure électronique est à l'origine de la formation, rupture et transformation des liaisons moléculaires. Celles-ci peuvent être visualisées par la mesure de la structure géométrique en "temps-réel", lors du processus chimique. La Spectroscopie d'Absorption X Résolue en Temps fournit des informations en les changements de structure électroniques (via XANES) et géométriques (via EXAFS), dans une experience en géométrie pompe-sonde avec un laser ultrarapide. De plus, la spectroscopie d'absorption X (XAS) est unique, puisqu'elle est selective à l'élément chimique choisi, et elle est applicable à tout type de systèmes désordonnés ou ordonnés.

Dans la présente thèse, nous avons effectué des recherches sur les changements structuraux dans les états excités de deux différents complexes de métaux de transition.

La première partie de la thèse se consacre à l'étude du complexe de Ru(II)-tris(2,2'-bipyridine), $[Ru^{II}(bpy)_3]^{2+}$. Cette molécule a servi comme prototype et comme un système modèle des réactions de transfert intramoléculaire d'électron et d'énergie, en raison des propriétés exceptionnelles de les états excités. À travers l'utilisation combinée de la spectroscopie laser ultrarapide et des impulsions des rayons X, nous avons déterminé différentés voies de relaxation des états excitées, des les premières 15 femtoseconds. Nous avons aussi déterminé la distorsion géométrique de son état excité le moins énergétique (^{3}MLCT) et la contraction de la liason moléculaire Ru-N (-0.04±0.02 Å), resultant du transfert d'électron.

La deuxième partie de notre étude est axée sur l'analyse du composé Fe(II)–tris(2,2'-bipyridine), $[Fe^{II}(bpy)_3]^{2+}$. Les études de ce type de molécule ont été activement poursuivies en relation au phénomène de "spin crossover", dans lequel la transition a lieu entre l'état fondamental de spin et l'état excitée de haut-spin . Nous avons caractérisé ses états excitées au moyen de la spectroscopie ultrarapide optique et des rayons X. Les études optiques ont indiqué plusieurs nouveaux aspects des voies possibles de relaxation de ses états MLCT et LF, et ont permis de déterminer leurs temps de vies correspondants. L'analyse structurale a permit de déterminer les déformations géométriques ayant lieu dans l'état excitée de spin haut.

L'élongation de la liason moléculaire Fe-N (0.2 Å) est en bon accord avec les valeurs predités par la théorie. Notre résultat represente la première mesure de la structure de ce complex dans l'état excitée en solution à température ambiante.

En conclusion, ceux-ci sont les premières études pour ces deux molécules où leurs geometries moléculaires des états excitée ont été caractérisés dynamiquement en "temps réel" (dans le domaine temporal ultrarapide), sans aucun prétention *a priori* au sujet de la structure des ces états excités.

MOT-CLÉS: *Spectroscopie d'Absorption X, Les Complexes de Métaux de Transition, Les Réactions de Transfert de l'Électron, Spin Crossover, Spectoscopie Résolue en Temps, Impulsions de Laser des Femtoseconds, Impulsions des Rayons X des Picoseconds, Radiation de Synchrotron, Spectroscopie Pompe-Sonde*

Contents

Chapter 1

Introduction

The ever-since dream of mankind is to visualize the microscopic atomic world that constitutes the rich variety of macroscopic forms of Nature. Therefore, a tremendous effort has been made over the past centuries of Science in order to fulfill this desire. The major progress in structural studies has become possible with the advent of x-rays. Since its discovery by Wilhelm Conrad Röntgen (1895) [1], multiple structure-sensitive techniques have been established and applied to extract the microscopic structures underlying everything the human perception is blind to.

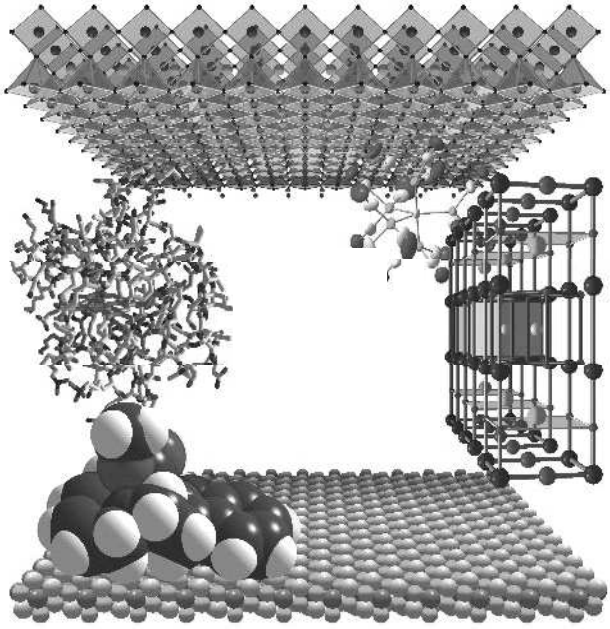

Figure 1.1: The atoms can be arranged into a vast variety of more complex and sophisticated structures, such as molecules, macro biomolecules (e.g. proteins), crystal lattices, surfaces, etc.

The knowledge of structure is vital and fundamental to our full understanding of Nature. It is therefore why it plays such an important role in many branches of Science, like Biology, Chemistry and Physics. What brings all these sciences together is a desire to determine, as accurately as possible, the atomic coordinates and solve the structures of their systems of interest, whether it is a relatively small molecule in solvent environment or a complicated bio-macromolecule like a protein structure (Fig. 1.1). As Nobel Prize Laureate, Francis Crick, has motivated it *"if you want to understand function, study structure"*[1] [1, 2]. The function in Biology is inherently bound to the underlying structures. No function can be understood without the prior knowledge of its structure. However, the function should be rather seen as a sequence of events taking place over some time and exhibiting structural changes during the ongoing process. Therefore, in order to understand the function, one should rather study the *time-dependent (transient) structures*. Ultimately, transient structure envision, not only where the atoms are, but also how they move during an occurring dynamical process, e.g. an ongoing chemical reaction. Watching atoms on the time scale of their motion would allow a better understanding of chemical reaction pathways on a molecular level. It would allow monitoring molecules at various stages of their vibrational distortion and observe short-lived reaction intermediates with intermediate unstable geometries that govern the outcome of chemical reaction.

From an experimental point of view, it is a challenging task to determine precisely where the atoms are within a given structure. One of the most commonly used structure-sensitive probes is x-radiation, which is used in the scope of this thesis, in particular, *X-ray Absorption Spectroscopy* (XAS), rather than diffraction techniques. Since the discovery of x-rays, it has been observed that x-rays were absorbed more strongly by some materials than others. It was not until the 1970's, and the pioneering work by Sayers *et al.* [3], that x-ray absorption spectra began to be interpreted quantitatively in the atomic level structural analysis. Since the absorption of x-rays is influenced by the nearest environment surrounding the absorber (typically within several atomic diameters) and is an unique signature of a given element, the x-ray absorption spectroscopy has become a powerful structural technique to probe the electronic and structural properties of a large class of systems, ranging from solid-state materials to proteins [4]. A detailed discussion of the characteristic features found in the x-ray spectra (the so called fine structure [4–11]) will be presented in Sections 3.1.1 and 3.1.2 of this thesis. In addition, a comprehensive overview of both theoretical and experimental concepts underlying the XAS can be found in Chapter 3.

One of the objectives of this thesis, is the extension of steady-state XAS spectroscopy into the time domain, on which the atomic motions take place. Molecular vibrations typically take place on femtosecond (1 fs = $1{\cdot}10^{-15}$ s) to picosecond (1 ps = $1{\cdot}10^{-12}$ s) time scales. So far the only tools, capable of monitoring sequences of events in "real time" on such ultrashort time scales,

[1] Francis Crick, Nobel Prize Laureate in Medicine, one of the discoverers of the double-helix structure of DNA molecule.

have been ultrafast optical spectroscopies. The implementation of femtosecond laser spectroscopies for the study of molecular phenomena and, in particular, of chemical reactions has given birth to the field of *Femtochemistry* [12–14]. Most commonly the ultrafast dynamics is measured via the so called *pump-probe* scheme, in which a first ultrashort pump laser triggers a reaction (at time t=0), and a second probe laser pulse records snapshots of the molecular system, as it undergoes structural changes (Section 2.5). In the spectral range accessible with ultrafast laser spectroscopy (UV-IR), the spectroscopic observables (optical transition energies and intensities) can be translated into structures, only in very few cases, e.g. for small diatomic molecules [15–19]. This was clear from the beginning of femtosecond spectroscopy and it led to a number of alternative and complementary proposals, where the optical probes were exchanged with ultrashort pulses of electrons [20–26] or x-rays [27–45] (Section 2.5.1). It is then when the ultimate dream of every chemist has become true; watching atoms move during the bond making and breaking is becoming real.

Similarly to femtosecond optical spectroscopy, ultrafast XAS [27, 35, 36, 43–54] is based on the pump-probe scheme, where a femtosecond laser pulse excites the system under investigation, and a time-delayed x-ray pulse measures the local structure around the absorber. But the power of ultrafast XAS stems from the fact that both transient electronic and geometric structural changes are monitored as a function of time delay between both pulses. Because ultrafast XAS relies on an intense and tunable source of ultrashort x-radiation, at present, the choice of pulsed x-ray sources is rather limited. Synchrotron radiation storage rings are capable of delivering intense and spatially-confined beams of pulsed x-rays and provide unprecedented photon beam stability (down to the shot-noise limit). In addition, they are fully tunable over broad energy ranges, required by XAS. Unfortunately, the synchrotron-generated x-ray pulses are inherently limited in their pulse widths to ca. 50-100 ps. Nevertheless, these pulsed x-rays offer the best compromise between the tunability, stability and intensity requirements imposed by ultrafast XAS experiments (Section 3.4). In addition, over the past years, one novel approach was proposed [55–57], which allows substantial pulse width reduction, down to hundreds of fs, however, at the expense of the photon flux. On the other hand, laser-generated x-ray pulses (originating from laser-produced plasmas in either metallic or liquid targets [58–66]) derive their temporal characteristics from the initial laser pulse, and can thus yield ultrashort bursts of x-radiation. However, these sources provide a fully divergent beam (due to the isotropic x-ray emission from plasmas), which accompanied with a lack of suitable focusing optic results in a rather low average flux in an actual experiment. In addition, their tunability is limited compared to synchrotron radiation. A short review of various structure-sensitive techniques using either x-rays or electrons will be given in Section 2.5.1.

Ultrafast time-resolved x-ray absorption spectroscopy [27, 52] is a very young research field and it still requires continuous efforts and improvements. Research based on time-resolved XAS in an optical-pump-x-ray-probe scheme has first been implemented at synchrotron radiation sources. Mills *et al.* [67], who used a 20 Hz repetition rate Nd:YAG laser to photolyze carbonmonomyoglobin (MbCO) and monitor the photolysis product with time-resolved XAS around the Fe K absorption edge. Other studies were carried out on different types of photolyzed systems in liquids, by Thiel *et al.* [68], Clozza emphet al. [69], Chance *et al.* [70] and Chen emphet al. [47]. Time-resolved XAS has also been used to characterize the changes in ablated particles [71], doped glasses [72], and solid-state material samples [73], upon laser irradiation. All of these studies were limited to the nanosecond or even longer time scales. Chen *et al.* [43] managed to obtain 14-ns snapshots of an excited Nickel-tetraphenyl-porphyrin complex and determine the change of electronic and molecular structure using both XANES and EXAFS. Only very recently, they carried out the sub-nanosecond measurement of structural dynamics of an excited copper(I)-diimine complex [45]. Yet, in none of the aforementioned experiments, the transient difference absorption scheme proposed by Bressler and co-workers [27,74–76] was explored. It is very recently that Saes *et al.* [50] reported on the first time-resolved XANES studies of a ruthenium(II)-trisbipyridine complex in water solution reaching the sub-100 picosecond pulse-limited time resolution. Also, Gawelda *et al.* [35,36] has reported the extended analysis of both XANES and EXAFS of the same molecule. In both cases, the transient difference x-ray absorption spectra were recorded for each incident laser pulse [27]. In the above context, this thesis can be regarded as a required intermediate step towards the aim of establishing ultrafast XAS as a routine technique. It contributes to the field of time-resolved x-ray absorption spectroscopy in solvated systems using the picosecond hard x-ray pulses. The extensive description of the experimental apparatus used during the measurements, which contribute to this thesis will be presented in Chapter 4 and Appendix B.

In this thesis, we studied two representative transition metal compounds, namely ruthenium(II)-tris(2-2'-bipyridine), $[Ru^{II}(bpy)_3]^{2+}$, and iron(II)-tris(2-2'-bipyridine), $[Fe^{II}(bpy)_3]^{2+}$. Although, at first glance, these two molecules seem nearly identical, their photochemistry is very distinct and the photoinduced structural dynamics leads to completely different transient molecular structures. Details on the photochemical and photophysical properties of transition metal complexes, and of these two molecules in particular, including the description of their ground state electronic properties, optical spectra and photochemical cycles is given in Chapter 2. The results of Chapters 5 and 6 include the application of the above sketched time-resolved scheme in studying the photoinduced intramolecular electron transfer reactions [77–80] in solvated transition metal complexes.

In the case of $[Ru^{II}[bpy)_3]^{2+}$, Chapter 5 presents the results on the transient geometric changes resulting from an electron transfer reaction involving both the metal and ligand orbitals. It also includes a systematic study of the energy relaxation pathways in photoexcited $[Ru^{II}[bpy)_3]^{2+}$ upon high-intensity fs laser excitation [81]. In these studies (Section 5.1), we identify several transient photoproducts and measure their relative concentrations and lifetimes, down to ca.15 fs in case of the shortest-lived excited state [82]. The unprecedented measurement sensitivity (see Chapter 4 for technical details) achieved in the time-resolved x-ray experiments (Section 5.2) allow for detecting minute structural distortions upon photoexcitation, originating from the presence of the electron on the ligand system and the resulting electrostatic interaction between the (more) positively charged Ru ion and the reduced ligand. Although $[Ru^{II}[bpy)_3]^{2+}$ is probably one of the most widely studied coordination chemistry compounds, it is the first time that such a change is experimentally detected.

The second case study, $[Fe^{II}[bpy)_3]^{2+}$, although bares many similarities with $[Ru^{II}[bpy)_3]^{2+}$ (Fig. 2.11), delivers a completely different photochemistry, due to the laser-triggered spin crossover transition (not occurring in $[Ru^{II}[bpy)_3]^{2+}$), which has profound influence on the subsequent structural dynamics of its excited states. In Chapter 6, both ultrafast optical and x-ray results are discussed. The femtosecond broadband transient absorption studies (Section 6.1) deliver new results on the possible relaxation pathways originating from the photoinduced spin cross over transition. Several new aspects concerning some earlier hypotheses will be presented. For the picosecond-resolved XAS experiments (Section 6.2), we implemented a novel dual-mode detection scheme, based on simultaneous monitoring of both x-ray fluorescence and transmission signals, and carry out the structural analysis of the transient x-ray spectra. These represent a milestone contribution to a wide range of potentially attractive studies on various spin crossover complexes, which can be fully characterized, in terms of their excited state geometries, "on the fly", without *a priori* knowledge about the excited state structure, or the necessity to slow down the excited state relaxation rates by means of temperature or chemical tailoring, which would alter the sample from its room temperature environment.

Finally, the conclusions of this thesis will be drawn and both near-term and long-term perspectives for this young research field will be presented.

Chapter 2

Transition Metal Complexes

This chapter introduces the most important aspects of transition metal complex photochemistry and photophysics, stressing the manifold of different excited states encountered in this class of compounds and the involvement of the d electrons in forming bonds with ligand molecules. In the scope of this thesis, two particular transition metal complexes will be discussed in more detail, namely $[Ru^{II}(bpy)_3]^{2+}$ and $[Fe^{II}(bpy)_3]^{2+}$. In both cases, we will introduce and discuss their steady-state optical absorption spectra in relation to their energy level diagrams. Each photochemical cycle, following laser excitation, will be presented as well. In both complexes, the photophysical mechanisms, which are involved in the photochemical reactions, have strong influence on the transient molecular structure of their excited states and we will discuss these issues as well. Finally, the general motivation for studying the excited state structural dynamics will be given in relation to both $[Ru^{II}(bpy)_3]^{2+}$ and $[Fe^{II}(bpy)_3]^{2+}$, and a brief review of structure-sensitive pump-probe spectroscopy will be outlined at the end of this Chapter.

2.1 Introductory Remarks

Transition metal complexes [83] represent an important class of coordination chemistry compounds [84] and have been extensively studied as molecular model systems for complex interactions involving electronic, spin and structural degrees of freedom in catalysis, material synthesis, photochemistry and biology. In most cases these molecules consist of a number of transition metal ions (usually cations) surrounded and bonded to another group of organic molecules (neutral or anionic non-metal species) called *ligands* [84]. Table 2.1 lists the most commonly encountered oxidation states of transition metal complexes.

	III	IV	V	VI	VII	VIII	IX	X	XI	XII
4	Sc 3+	Ti 3-4+	V 2-5+	Cr 2-4+,6+	Mn 2-4+,6-7+	Fe 2-3+	Co 2-3+	Ni 2+	Cu 1-2+	Zn 2+
5	Y 3+	Zr 4+	Nb 3-5+	Mo 2-6+	Tc 2-7+	Ru 2-8+	Rh 1+,3+	Pd 2+, 4+	Ag 1+	Cd 2+
6	La 3+	Hf 4+	Ta 3-5+	W 2-6+	Re 2-7+	Os 3-8+	Ir 1+,3+	Pt 2+,4+	Au 1+,3+	Hg 1-2+

Table 2.1: Groups 3-12 in the periodic table form the so-called *d-block*, which embraces all transition metal atoms. The first row assigns the corresponding group of the periodic table (e.g. III-XII), and the first column indicates its period (4-6). Here the most commonly found oxidation states of these metals are listed below each element.

In case of Fe (a first-row transition metal), the most commonly encountered oxidation states are 2+ and 3+, whereas Ru (a second-row metal) can have many different oxidation states ranging from 2+ up to 8+. Transition metal ions usually form complexes with a well-defined number of ligands. The number of ligand atoms, which form bonds with the transition metal ion is often referred to as the *coordination number*, usually ranging from 4 to 6. The 4-coordinated complexes typically have a tetrahedral (T_d) or square-planar symmetry, whereas most of the 6-coordinated complexes exhibit an octahedral (O_h) symmetry. However, various distortions, e.g. trigonal distortion (D_3 symmetry), can be found as well. In Fig. 2.1, a representative example of a transition metal complex (slightly distorted O_h symmetry) is shown.

Here a single metal ion (central sphere) is embedded into a rather complex ligand system consisting of N, C and H atoms. In this particular example, the ligand system is formed by three identical molecules, each called *bipyridine* (hereafter abbreviated with *bpy*), thus the entire ligand system is thus referred to as *tris-bipyridine* or $(\text{bpy})_3$. Ligands can be attached to the metal ion through a single atom (*monodentate*) or two (and more) atoms (*bidentate*, *tridentate* etc.).

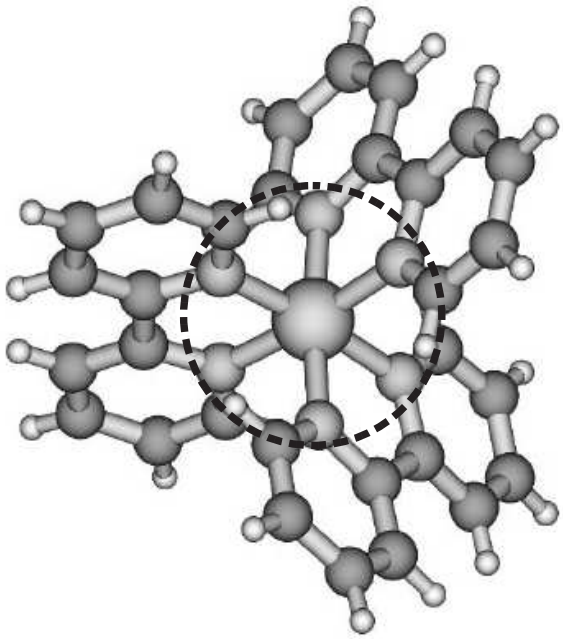

Figure 2.1: Molecular structure of a $M(bpy)_3$ (where M=Fe^{2+}, Ru^{2+} etc.) transition metal compound bonded to a tris-bipyridine ligand system (bpy_3). The six nearest neighboring N atoms are indicated by the dashed circle. Further-lying C and H atoms are represented by dark grey and light grey spheres respectively.

Polydentate ligands are usually referred to as *chelating* ligands. In the example depicted in Fig. 2.1, the bpy ligand attaches to the metal cation, via 2 N atoms, and thus it belongs to a group of bidentate (chelating) ligands. Examples of transition metal ions that can be associated with the molecule shown in Fig. 2.1 are Fe^{2+}, Ru^{2+}, Os^{2+}, Cr^{3+} ions, where the superscripts refer to the ionic valence state of the metal atom. On the other hand, the valency of a transition metal ion in a molecular complex form is usually denoted by a capital Latin number, e.g. Ru^{II} or Fe^{II}, and this nomenclature will be used throughout this thesis. In the following Chapters 5 and 6, the experimental results of the time-resolved optical and x-ray spectroscopies carried out on aqueous solutions of both $[Ru^{II}(bpy)_3]^{2+}$ and $[Fe^{II}(bpy)_3]^{2+}$ will be presented and discussed.

2.2 Photochemistry of Transition Metal Complexes

Chemical reactivity depends mainly on the excited state properties of a given molecular system and is relevant to all photochemical processes regardless of the origin and nature of the photoactive species. Here we are mainly concerned with transition metal complexes, which introduces several new types of of excited states (and thus chemical reactivity patterns), which are unique to their photochemistry and photophysics [85–87]. First of all, most of the

photochemical reactions in transition metal complexes can be triggered with visible light, since their excitation energies are usually lower than for most organic molecules. The visible excitation usually accesses the available low-energy charge transfer states of mixed metal and ligand character, the so called *Metal-to-Ligand Charge Transfer* (MLCT) states [88]. These states provide a rather unique gateway, through which the optical excitation energy can be very efficiently transferred into molecular excitation energy triggering a variety of possible relaxation processes involving electronic, magnetic and structural dynamics.

The photoinduced dynamics of transition metal complexes involves many different types of excited states, which may differ in their localization within the molecule, orbital parentage, energy, dynamics and thus chemical reactivity [89]. Also, the characteristic timescales of the involved dynamical processes may span over many orders of magnitude, ranging from tens of femtoseconds (1 fs = 10^{-15} s), i.e. intersystem crossing processes in $[Ru^{II}(bpy)_3]^{2+}$ [82] and $[Fe^{II}(bpy)_3]^{2+}$ as discussed in Chapters 5 and 6, up to many microseconds (1 μs = 10^{-6} s). In addition, the density of available excited states is much higher than in case of organic molecules, which means that several different excited states may be populated within the same narrow energy range. This, in turn, leads to an enhanced interaction between them, which makes the photochemical cycle rather complex with competing relaxation and reactivity pathways [86]. Many transition metal complexes are redox-active already in their electronic ground state configuration [90]. Their corresponding *electron transfer* (ET) reactions can involve either an increase of the oxidation state of the metal (MLCT reactions) or that of the ligand (*Ligand-to-Metal Charge Transfer*, LMCT, reactions). This redox activity is often preserved in the excited states as well [91]. Therefore, many of these complexes undergo photoinitiated ET (either intramolecular or intermolecular) [92], which may occur within the metal orbitals, ligand orbitals or within both simultaneously.

In case of a solvated aqueous $[Ru^{II}(bpy)_3]^{2+}$ complex (see Chapter 5), the photoexcitation with a visible photon brings the system in its excited MLCT state, involving intramolecular ET from the Ru^{2+} ion to the bpy ligand system and thus oxidizing Ru to its trivalent form (i.e. Ru^{2+}). The resulting excited states are long-lived and of charge transfer character. On the other hand, in a nearly identical complex, where the central Ru^{2+} ion is exchanged with Fe^{2+} ion (preserving the same molecular symmetry as depicted in Fig 2.1), the resulting energy landscape is completely different. While photoexcitation in the visible range accesses the MLCT states again, in contrast to $[Ru^{II}(bpy)_3]^{2+}$ complex, the MLCT states of aqueous $[Fe^{II}(bpy)_3]^{2+}$ (see Chapter 6) are extremely short-lived, as they cross efficiently to lower-lying *metal-centered* (MC) states of mainly metal character [91], resulting in an ultrafast electron back transfer. The ET reaction involves an oxidation state change of the metal ion, however, in case of the Fe complex, the electron is transferred back to the metal orbitals on an ultrafast timescale before it undergoes a subsequent spin transition within the manifold of MC (also knows as *Ligand-Field*, LF) states [93]. The results presented in both Chapters 5 and 6 involve such an

intramolecular ET reaction. The intriguing and interesting differences lie in the subsequent electronic and structural dynamics initiated during this reaction and their characteristic timescales.

2.2.1 The Role of *d* Electrons in Transition Metal Complexes

Perhaps one of the most characteristic features, which distinguish the transition metals from the main group metals (I-II) is the presence of unpaired d electrons, which are those involved in molecular bonding, and which determine the complex chemistry of transition metal compounds [94]. Furthermore, the inclusion of ligands (in a complex molecule) lowers the spherical symmetry of the transition metal ion and breaks the energetic degeneracy of the atomic d levels, which affects both the spin state and the molecular symmetry of the complex ground state configuration [83].

A representative picture of the 5 atomic d orbitals is illustrated in Fig. 2.2. It shows the electron density associated with these orbitals in a Cartesian coordinate system, where the transition metal atom is placed at the origin, (x,y,z)=(0,0,0). Three of the five orbitals (d_{xy}, d_{yz}, d_{zx}) are degenerate and are oriented between Cartesian axes. The remaining two orbitals (d_{z^2}) and $d_{x^2-y^2}$), on the other hand, point along axes.

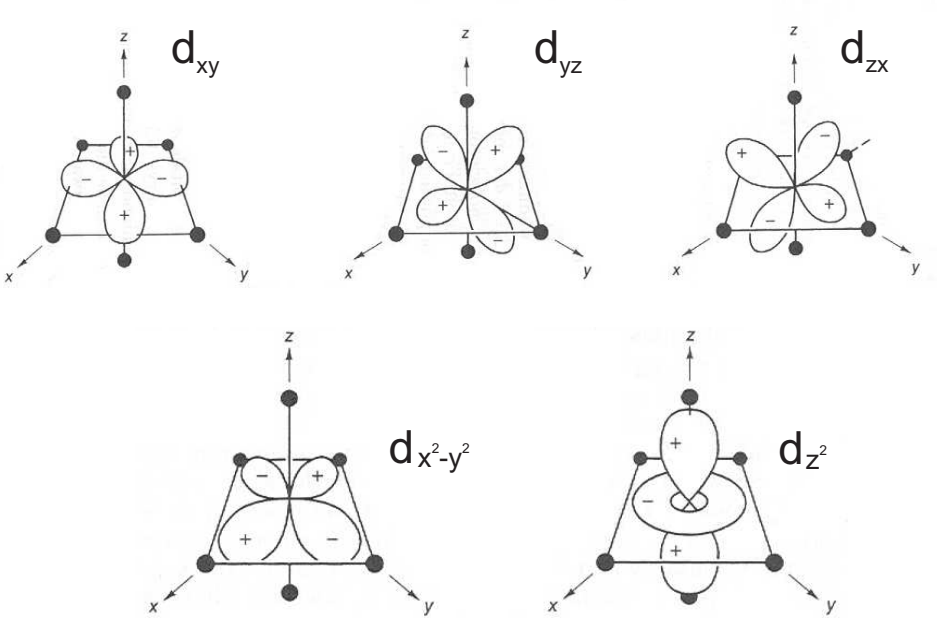

Figure 2.2: Transition metal d orbitals occur in 5 different forms as shown here. Each of these d orbitals can accommodate 2 electrons, thus a total of 10 electrons can occupied in the d states. The orbitals d_{xy}, d_{yz} and d_{zx} are degenerate and are responsible for molecular bonding in T_d symmetry, whereas d_{z^2}) and $d_{x^2-y^2}$ are forming bonds in O_h symmetry. Figure taken from Ref. [84]

In a single ion complex, the two most commonly found ion-ligand bond

geometries are of tetrahedral and octahedral symmetries [84], which is obvious when inspecting the geometries of the involved d orbitals (Fig. 2.2). In these cases, the ligand σ-bonding orbitals are directed either along Cartesian axes (in octahedral coordination O_h, see Fig. 2.3)using d_{z^2}) and $d_{x^2-y^2}$ orbitals, or in-between axes (in tetrahedral coordination T_d) using d_{xy}, d_{yz}, and d_{zx} orbitals.

Fig. 2.3 shows an example of σ-bonding between the metal and ligands orbitals in an octahedral complex.

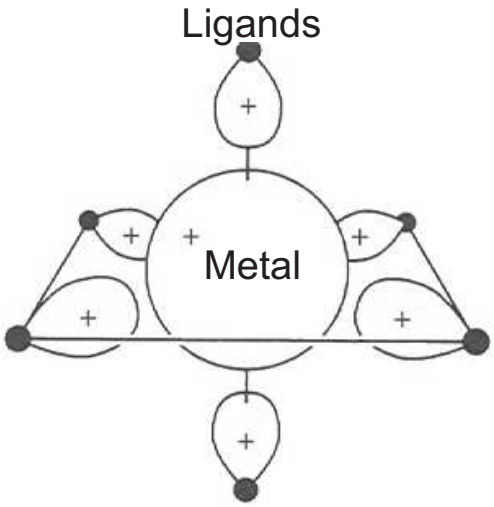

Figure 2.3: σ bonds in O_h symmetry are formed between the transition metal ion and the surrounding ligands. ing. The involved ligand orbitals share one lone pair (2 electrons) each with the metal orbitals. Figure taken from Ref. [84]

As mentioned above, the ligands break the spherical symmetry of the bare metal ion, thus lifting the degeneracy of its d energy levels. A simplified physical picture of this splitting may be rationalized by considering both metal and ligand orbitals as electron clouds. If both ligand and metal orbitals are oriented along a given Cartesian axis, there will be an increased repulsion between them due to the increased spatial overlap between both clouds, which increases the energies of the split energy levels. However, for a metal orbital that is aligned in-between the axes, the energetic cost will be much less due to reduced orbital overlap with the ligand orbitals. This in turn will lower the energy of the split d-levels. Therefore, the energetic ordering of the split d-orbitals reflects their spatial orientation with respect to the σ-bonding orbitals of the ligands.

There are two commonly used approaches to describe the bonding of the transition metal complexes, namely the *ligand-field* (LF) (also known as *crystal-field*, CF) theory [83, 95] and the *molecular orbital* (MO) theory [96]. Here, we limit ourselves to the ligand-field description, which suffices to explain their basic physical properties. This theory implies an electrostatic approach, where we treat the ligands as negative point charges in the vicinity of the d-electrons of the transition metal ion [83]. The action of the ligands is treated,

within perturbation theory, as an external electrostatic perturbation term, which has to be added to the total Hamiltonian describing the entire molecule, i.e. $H_{complex}$=H_{atom}+H_{ligand}, which distorts the spherical symmetry of the ionic metal d-levels and causes the energetic splitting between them. The symmetry of the ligands determines the degeneracy and relative energies of the ligand-field split ionic d-levels.

An illustrative example in case of O_h ligand symmetry is shown in Fig. 2.4. Here, the energy splitting of the d-levels groups the five d-orbitals into 2 bands, namely t_{2g} and e_g (Fig. 2.2).

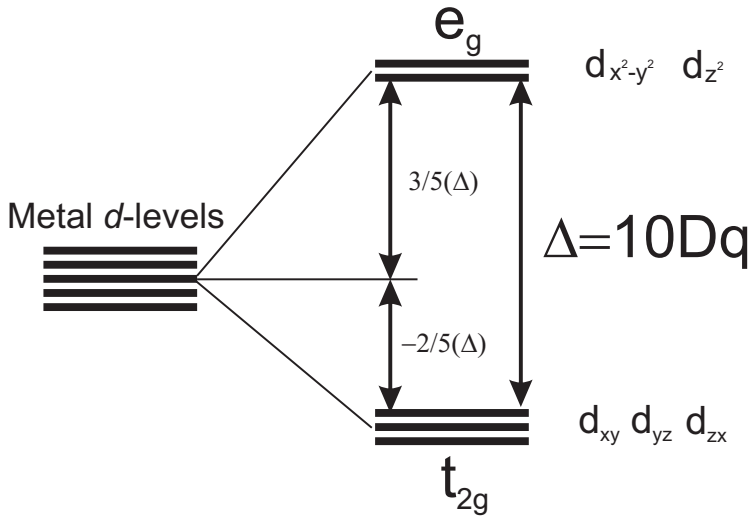

Figure 2.4: The energies of the d-orbitals in an octahedral crystal field. The electrostatic perturbation induced by the ligands causes the energy splitting Δ of the initially spherically symmetric metal levels, while the relative mean energy (as compared to the unperturbed free atom energy) remains unchanged.

The d-orbitals that are oriented in-between the Cartesian axes in Fig. 2.2 (i.e. d_{xy}, d_{yz}, d_{zx}) are those, which constitute the t_{2g} band. The e_g band contains the d-orbitals, which are directed along the Cartesian axes (i.e. $d_{x^2-y^2}$ and d_{z^2}). The parameter Δ, which describes the energetic gap between t_{2g} and e_g bands, is called the *ligand-field splitting*, also denoted as 10Dq. The effect of the crystal-field splitting on the relative energies of the metal d-levels can be described as follows: first, the strong repulsion of ligand electrons and metal electrons causes the initial destabilization of the d-levels. The splitting into t_{2g} and e_g bands stems from the rearrangement of the ligand electron pairs towards bonding directions. Finally, the electrostatic attraction between the ligand electron pairs and positive metal ion lowers the relative energies of the crystal-split d-levels (see t_{2g} band in Fig. 2.4), although the mean energy remains unchanged.

The electrons of the d-shell populate the reorganized electronic states based on energetic considerations, affecting the spin state. The orbitals are filled according to *Hund's Rule* [84], which implies that each orbital within the same band (t_{2g} or e_g in Fig. 2.4) will be occupied with an electron of parallel spin orientation before an electron of opposing spin occupies an orbital. There-

fore, the resulting total spin of a molecule, in equilibrium, will be determined by the filling of the split d-orbitals. At this point, we can further mention that there exists a competition between *spin-pairing energy* E_{sp} (energy required to bring two electrons of opposed spins to an orbital) and the ligand-field splitting energy 10Dq (energy separating t_{2g} and e_g levels) [97]. When $E_{sp} \geq$ 10Dq, all of the d-orbitals from Fig. 2.2 can be filled with electrons (the so called *weak-field* case). However, when 10Dq $> E_{sp}$ (*strong-field* case), only the lower-energy states (i.e. those who belong to t_{2g} band) will be filled with electrons, according to Hund's Rule, and thus will yield a drastically different spin state configuration.

It is important to remark that both ground and excited state geometric structures of a transition metal complex will strongly depend on the electronic configuration. The metal-ligand bond length and strength is reflected by the occupation of bonding and anti-bonding orbitals. In O_h symmetry, the ligand σ-orbitals will donate 2 electrons each to form a bond with a metal ion. In addition, the complex bonding may be further stabilized by the so called π-*backbonding* [84], which originates from the electron density backdonation to the ligand via the mixing (interaction) of metal d-orbitals and ligand π^*-orbitals (see Section 2.3 for more details). In general terms (and in agreement with Fig. 2.4), we can say that the empty metallic s- and p-orbitals and the occupied ligand donor orbitals will contribute together in forming strongly *bonding* orbitals. Their energies lie below the ligand-field split d-levels. At higher energies, strongly *antibonding* orbitals are found. Finally, the ligand-field split d-orbitals will form the so called *nonbonding* orbitals, mainly attributed to the t_{2g} band in Fig. 2.2, and weaker antibonding orbitals at higher energies assigned to the e_g band. Depending on the ligand-field strength (weak-field vs. strong-field cases), their relative electron occupation numbers may change and thus their corresponding electronic, spin and geometric structures will be affected. In Sections 2.3 and 2.4, we will discuss in detail the resulting energy splitting of the $4d$ and the $3d$ metal orbitals in a distorted O_h symmetry for $Ru(bpy)_3$ and $Fe(bpy)_3$ complexes. In case of $Ru(bpy)_3$, removal of one d-electron (upon photoexcitation to a ligand π^* orbital) from fully occupied t_{2g} band of the ground state results in a slightly increased 10Dq [35], and affects the Ru-ligand bond distance in the excited state structure. On the other hand, in $Fe(bpy)_3$, the photoexcitation induces a spin transition, which changes the relative occupation of the t_{2g} and e_g bands and thus modulates the electron density of the antibonding orbitals [97]. Here, the resulting excited state structure will experience a substantial Fe-ligand bond elongation due to the increased occupancy in the antibonding orbital of the high-spin state.

2.3 Ru(II)-tris-bipyridine

This Section introduces one of the transition metal complexes studied in this thesis, namely ruthenium-(trisbipyridine), $[Ru^{II}(bpy)_3]^{2+}$. This molecule has been one of the most widely investigated coordination chemistry compounds since the discovery of its visible luminescence by J.P. Paris et al. [98] in the late 1950's. Since then, most of the ground and excited state properties of this complex have been studied by means of different spectroscopic methods [86,87,91]. The unique properties of $[Ru^{II}(bpy)_3]^{2+}$ stem from its extraordinary photosensitivity combined with its redox properties in the excited state [90], which make it an extremely efficient photocatalyst in many molecular assemblies, where either electron or energy transfer reactions are involved. Therefore, it has served as a paradigm and a model system of *intramolecular electron transfer* (IET) reactions [92]. Due to the aforementioned manifold of properties, this molecule has been exploited in many different fields, ranging from biochemistry [99] to photosensitization in semiconductors [100]. $[Ru^{II}(bpy)_3]^{2+}$ is also considered as the core member of a family of transition metal-based devices for solar energy conversion [101, 102].

In the scope of this thesis, the most relevant ground and excited state properties of this molecule can be experimentally best described by means of optical and x-ray spectroscopies, both in static and time-resolved domains. In the following paragraphs, we will briefly outline some of the characteristic features, which describe the steady-state optical absorption spectra of $[Ru^{II}(bpy)_3]^{2+}$ complex and will be further presented and discussed in Chapter 5. Their relation to the energy-level scheme of this molecule will be discussed as well. This will also serve as input information, when interpreting the time-resolved optical (Section 5.1) and x-ray (Section 5.2) transient absorption spectra. In addition, the molecular and electronic structure of ground state $[Ru^{II}(bpy)_3]^{2+}$ will be introduced.

2.3.1 Ground State Structure

The ground state molecular structure of $[Ru^{II}(bpy)_3]^{2+}$ complex, in its crystalline form is well known by means of x-ray diffraction [103, 104]. The molecular symmetry of $[Ru^{II}(bpy)_3]^{2+}$ is that of a trigonally distorted octahedron (D_3 symmetry) and is illustrated in Fig. 2.5.

The central Ru atoms is surrounded by the three bpy ligands, which bind via the nitrogen atoms. The six nitrogen atoms have a uniform bond distance of 2.056Å [103,105] from the central atom. The N-Ru-N angle within the same bipyridine ligand amounts to 78.7°, which corresponds to a small distortion from octahedral symmetry, where this angle equals to 90°. The smaller N-Ru-N angle originates from a steric constraint introduced by the bipyridine molecule. The bridging C=C bond between the two pyridyl rings (constituting one bpy ligand) is too short and there is too little angular flexibility to allow both N atoms to be accommodated under the optimum angle of 90°. The

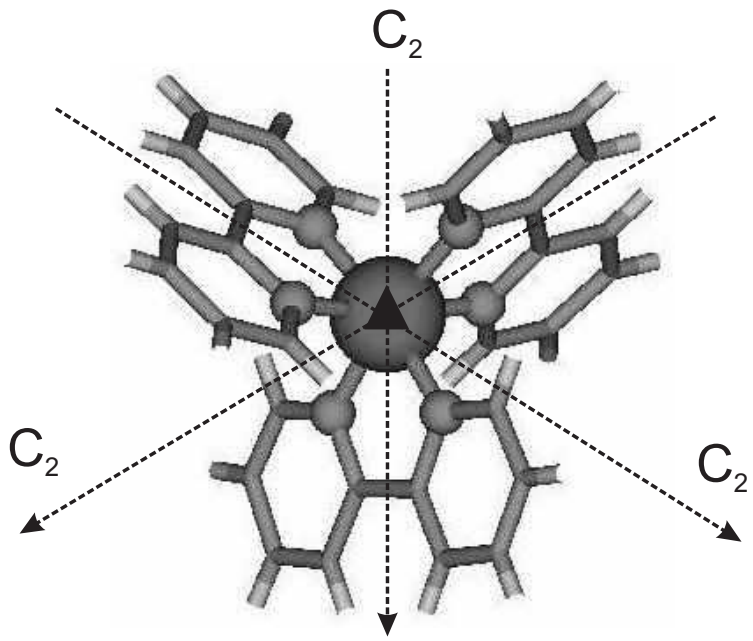

Figure 2.5: The molecular structure of $[Ru^{II}(bpy)_3]^{2+}$ complex. The central Ru ion is surrounded by 3 bidentate bpy ligands, which form bonds with Ru via 2 N atoms (each ligand). The triangle at the Ru atom position indicates the C_3 axis, which is towards the reader.

molecular symmetry possesses one three-fold rotation axis C_3 (which points orthogonally to the plane of view in Fig. 2.5) and three two-fold rotation axes C_2, which are perpendicular to C_3 axis. The symmetry of solvated $[Ru(bpy)_3]^{2+}$ was reported to have the D_3 as well [106].

2.3.2 Molecular Orbital Scheme

As we mentioned before, in order to obtain the molecular orbital scheme of $[Ru^{II}(bpy)_3]^{2+}$, we will consider an isolated Ru atom (spherical symmetry), with 6 N atoms attached to it, in an octahedral symmetry. This is illustrated in Fig. 2.6.

In the first step, the O_h symmetry splits the $4d$-states into t_{2g} and e_g bands, as already mentioned in Section 2.2.1 and shown in Fig. 2.4. The t_{2g} orbital is threefold degenerate, whereas the e_g orbital is twofold degenerate in O_h symmetry [107]. The index g indicates inversion symmetry.

The six nitrogen atoms of the three bipyridine ligands are σ-donors, contributing two electrons each to the metal-ligand bond. The complex is stabilized by π-back bonding, that stems from a partial back transfer of electron charge from the ligand via the interaction with metal d-orbitals and ligand π^*-orbitals.

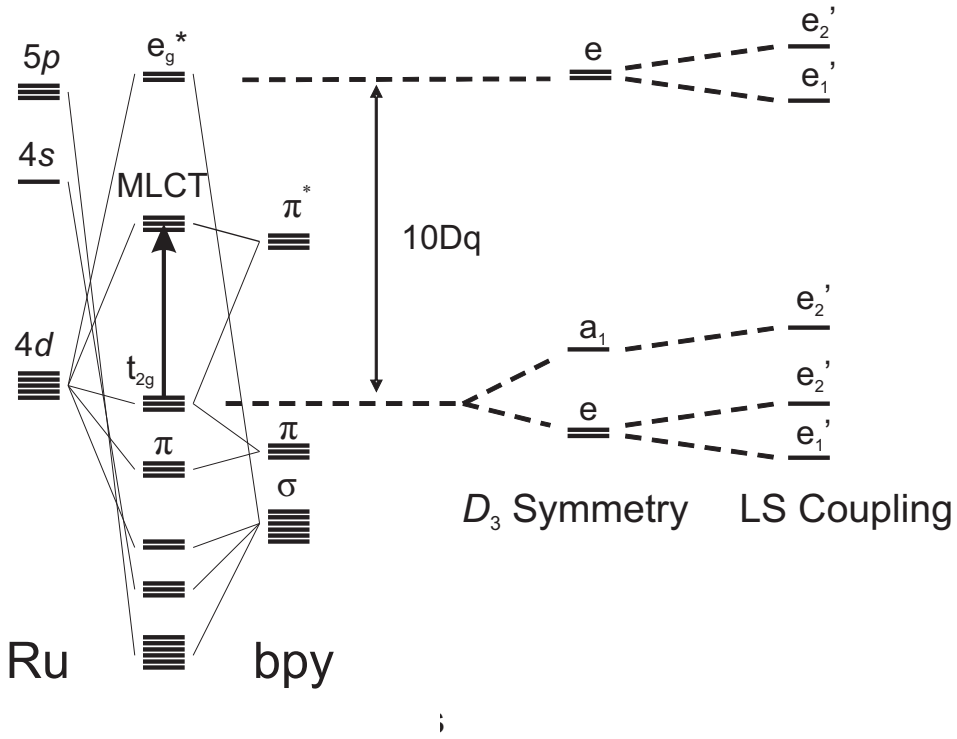

Figure 2.6: The energy level scheme of $[Ru^{II}(bpy)_3]^{2+}$. The ligand-field splitting 10Dq acts on the Ru d-orbitals given by the O_h symmetry in the first approximation. The additional trigonal distortion imposed by the D_3 symmetry further splits the t_{2g} and e_g states into a_1 and e (doubly degenerate) representations. Finally, the $4d$ spin-orbit coupling (LS coupling) lifts the degeneracy of the e states

As we see in Fig. 2.6, the additional trigonal distortion (D_3 symmetry) further splits t_{2g} and e_g levels into doubly degenerate e and a_1 levels. Finally, the addition of $4d$ spin-orbit coupling (LS coupling) splits further these levels further into e_1' and e_2' orbitals [108, 109]. The arrow included in Fig. 2.6 indicates the lowest energetic transition from the ground state t_{2g} level to the MLCT manifold (note that the latter originates from both $4d$ metal and ligand π^* orbitals). This transition is the one, which we excite in the photochemical cycle of $Ru(bpy)_3$ (see below and Chapter 5).

2.3.3 Optical Spectroscopy

The steady-state optical absorption and emission spectra of aqueous $[Ru^{II}(bpy)_3]^{2+}$ in the ultraviolet (UV) to near-infrared (IR) range is plotted in Fig. 2.7.

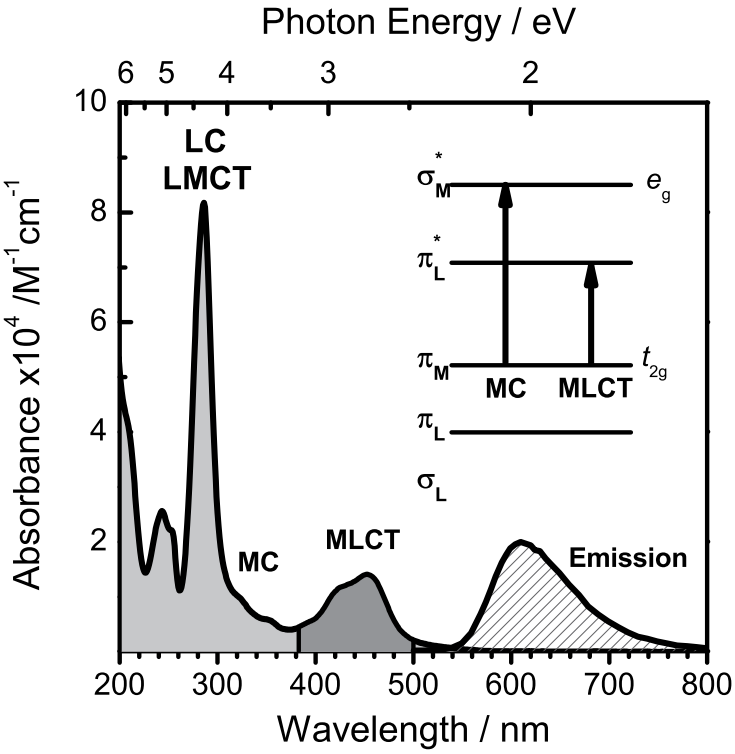

Figure 2.7: Steady-state UV-IR absorption spectrum of aqueous $[Ru^{II}(bpy)_3]^{2+}$ complex. The most significant absorption bands are assigned to various transitions involving either ligand or metal charge transfer states and forbidden metal-centered states (MC) are indicated (see text for more details). The inset indicates two possible transitions involving the MLCT and MC states and labels the involved molecular orbitals.

It is characterized by a series of main absorption bands, which are classified according to Ref. [91, 110] (Table 2.2).

Band	Assignment	Wavelength /nm	Absorbance $/M^{-1}cm^{-1}$
LC	Ligand-Centered	200-300	5-8×10^4
LMCT	Ligand-to-Metal Charge Transfer	220-260	1.5-2.6×10^4
MC	Metal-Centered	300-360	0.6-2×10^4
MLCT	Metal-to-Ligand Charge Transfer	380-520	0.5-1.5×10^4
Emission	MLCT	620 nm	-

Table 2.2: The main absorption bands of $[Ru^{II}(bpy)_3]^{2+}$ (Fig. 2.7) can be assigned to four different transitions involving either metal (MC) or ligand (LC) orbitals or both at the same time (LMCT and MLCT) [91]. The emission band in the VIS originates from the lowest MLCT state (^{3}MLCT)

The broad absorption band centered at 450 nm (MLCT) corresponds to a transition from one of the $4d$-orbitals of Ru^{2+} ion to the ligand π^*-orbitals. During this transition the electron is removed from the *highest occupied molecular orbital* (HOMO), which is the t_{2g} metal orbital in this case, and excited into the lowest unoccupied molecular orbital (LUMO) of the ligand π^* orbital (see the inset of Fig. 2.7). As a result, the transition metal ion changes its oxidation state to Ru^{3+}. The UV range (200-300 nm) is dominated by strong transitions involving ligand orbitals (π and π^* orbitals). They can be grouped into *ligand-centered* (LC, <300 nm and ≥260 nm) and *ligand-to-metal charge transfer* (LMCT, 220-260 nm) transitions. In case of LMCT transition the absorption in the π orbital and the antibonding metal d-orbitals are involved. According to Ref.[], the 300-360 nm can be assigned to the metal-centered (MC) states [91], which strongly overlaps with the metal-to-ligand charge transfer (MLCT) states. Therefore, the MC absorbtion bands are buried below the strong background absorption of the MLCT states (which in general have larger absorption cross sections than MC states) [110]. Upon photoexcitation in the region 380-490 nm (MLCT band in Fig. 2.7), the long-lived triplet ^{3}MLCT state is formed, which exhibits visible luminescence centered at 620 nm, as shown in Fig. 2.7.

2.3.4 Photochemical Cycle of Ru(II)-tris-bipyridine

The photochemical cycle of $[Ru^{II}(bpy)_3]^{2+}$ can be sketched by a simple 3-level scheme as illustrated in Fig. 2.8.

Light excitation of a metal-centered valence electron from its singlet ground state (^{1}GS) (originating from the ligand-field split $4d$ level, as indicated in Fig. 2.6) into the lowest-energy absorption band (400-500 nm) leads to the formation of a Franck-Condon singlet Metal-to-Ligand Charge Transfer (^{1}MLCT) state, and localization of the electron on one of the bipyridine ligands [88, 111, 112], which undergoes intersystem crossing to a long-lived triplet

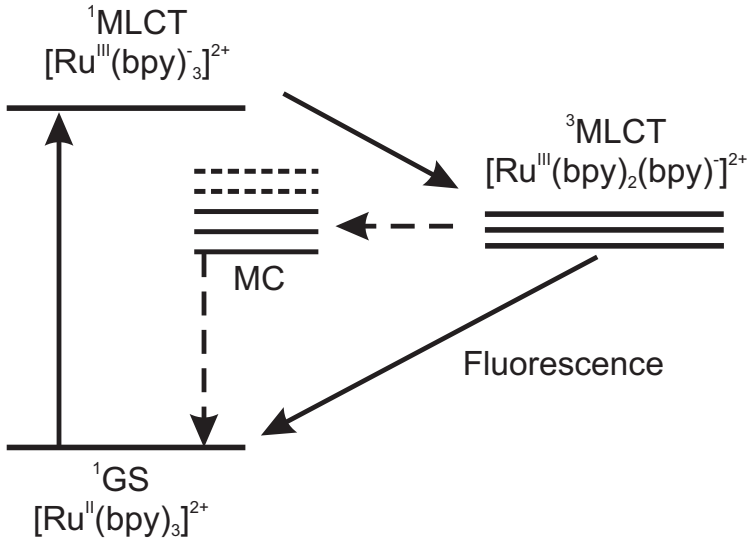

Figure 2.8: Photochemical cycle of $[Ru^{II}(bpy)_3]^{2+}$ in a simplified energy level scheme. Absorption of visible light removes a metal-centered (MC) $4d$ electron in its ^{1}GS into the ^{1}MLCT) state, where it undergoes ultrafast intersystem crossing into the ^{3}MLCT state, localized onto the bipyridine ligand system. The ^{3}MLCT state decays nonradiatively via the high vibrational levels of the MC ground state and via excited states, and radiatively with a fluorescence lifetime of ∼600 ns at room temperature.

state (^{3}MLCT) in ∼15 fs [82]:

$$[Ru^{II}(bpy)_3]^{2+}(^1GS) \xrightarrow{\hbar\omega} [Ru^{III}(bpy)_3^{-1/3}]^{2+}(^1MLCT) \quad (2.1)$$

$$\longrightarrow [Ru^{III}(bpy)^{-1}(bpy)_2]^{2+}(^3MLCT) \quad (2.2)$$

At room temperature and in aqueous solutions the emission of the ^{3}MLCT state exhibits a measured lifetime of about 600 ns [113] due to efficient (95%) nonradiative quenching to high vibrational levels of the ground state and to the triplet *metal-centered* (MC) states (Fig. 2.8).

2.3.5 Structural Implications of Intramolecular Electron Transfer

The photoinduced electronic changes (change of oxidation state, localization of the electron on the bipyridine ligand system) should have consequences on the molecular structure. The localization of the electron on one bpy ligand changes the ground state D_3 symmetry to C_2 symmetry in the ^{3}MLCT state [112], at least from the electronic point of view and probably, the structural one also. Both the increased electrostatic interaction and polarization between the Ru^{III} atom and the bpy^- and bpy ligands, as well as the reduced π-backbonding, due to the increased oxidation state of the Ru atom, should lead to a modification of the Ru-N bond distances [114]. The first two effects tend to contract the Ru-ligand bonds, whereas the reduction of the π-backbonding, in general, elongates the metal-ligand bond lengths. So, in this case, the $4d$-electron

transfer to the ligand triggers a rather complex structural change, where counteracting mechanisms affect the molecular bond between the Ru ion and the bpy ligands. In addition, the presence of the electron on the ligand system, whether it is delocalized over a single or two bpy ligands, also implies structural changes among the interatomic distances of the ligand constituents (C and N atoms). These were monitored by means of IR and Raman [115–117] spectroscopies, where the characteristic vibrations of the reduced bpy ligand were studied and compared to the parent, isolated bpy molecule, and thus yielding the structural distortions in C-C, C=C and N-C bonds of the bpy ligand upon electron transfer. Unfortunately, the characteristic low-frequency vibrations of the Ru-N bonds (ca. 350 cm^{-1}) [117] are difficult to access with Raman spectroscopies and therefore no observations on the possible structural distortion of the σ-bonds between the Ru-ion and N were reported so far.

The interplay between electronic and geometric changes is of prime importance in elementary charge transfer processes . From a fundamental point of view, structural information is valuable in order to get insight into the photocycle itself and the non-adiabatic dynamics therein taking place. This may be exploited to design new transition-metal based compounds for optimum reductive-oxidative functions with applications in solar cells [101]. Structural information is of special interest in the development of molecular-based materials, capable of performing efficient intermolecular charge transfer, by means of a control of the spatial arrangement of their constituents [118, 119]. In several such arrangements strong electronic coupling between the excited species and its surrounding environment makes the electron transfer adiabatic [86]. Hence, the rate is governed by the nuclear dynamics, as the activation energy depends to a great extent on the reorganization energy of the reacting species after the electron transfer, which involves stretching or contraction of metal-ligand bonds.

Despite the fundamental and practical importance of metal-polypyridine (and in particular Ru-) complexes and the numerous studies that were undertaken on these systems [85, 86, 88, 90, 102, 110–113, 120, 121], surprisingly few studies have addressed the issue of the structural changes occurring upon photoexcitation. Static and time-resolved resonance Raman studies have been carried out on $[Ru^{II}(bpy)_3]^{2+}$ to measure the structural changes in the ^{3}MLCT photoproduct [115, 116, 122, 123], but these have mainly concentrated on the bond changes within the bpy^- ligand. In only one work has an estimate of the Ru-N bond change been given (0.048Å), namely for the $[Ru^{II}(NH_3)_4(bpy)]^{2+}$ complex, using a time-dependent treatment of the pre-resonance Raman spectrum [122].

While static crystallographic studies on $[Ru^{II}(bpy)_3]^{2+}$ and chemically-stabilized $[Ru^{III}(bpy)_3]^{3+}$ show no difference in the Ru-N distance between both compounds [124], similar studies on $[Ru^{II}(NH_3)_6]^{2+}$ and $[Ru^{III}(NH_3)_6]^{3+}$ point to a bond contraction of ca. -0.04Å for the trivalent Ru center [114], which was attributed to polarization effects due to the increased charge of the central Ru ion [114, 124]. However, both results cannot be directly linked with photoexcited Ru-polypyridine complexes (in particular, $[Ru^{II}(bpy)_3]^{2+}$), as the

photocycle of the latter (see Fig. 2.8) implies an additional change of charge and spin along with the reduction of the ligand.

In Chapter 5, we will present both the ultrafast optical and x-ray spectroscopic results, which show that both energy and structural relaxation processes that accompany the photoinduced IET reaction will affect the molecular structure of the excited ^{3}MLCT state and will result in bond length change for the Ru-N molecular bonds. In this thesis, we have applied a time-resolved x-ray absorption spectroscopy, for the first time, to monitor the photoinduced geometric changes in the vicinity of the Ru central ion within the solvated aqueous $[Ru(bpy)_3]^{2+}$) complex.

2.4 Fe(II)-tris-bipyridine

The ferrous (Fe^{2+}) metal complexes, including heme molecules and photosensitizers, exhibit strongly coupled electronic, magnetic and structural dynamics [125]. The study of this class of compounds is being actively pursued for their potential applications in magnetic data storage and as basis for photoswitchable molecular devices [126]. In biology, ferrous metal complexes play an important role in the binding of ligands in heme protein [127]. In particular, they have been extensively studied in relation to the phenomenon of spin crossover (SCO) [128, 129], where a transition from a low spin (LS) ground state with a maximum number of paired up electrons in the t_{2g} band to a high spin (HS) excited state, with the unpaired electrons entering the e_g band of the *d*-orbitals, can be induced by means of temperature and light excitation [130–140], while the reverse transformation can be induced by pressure [141–147] (more details description of the SCO phenomenon is included in Section 2.4.5).

Iron(II)(2,2')-tris-bipyridine, $[Fe^{II}(bpy)_3]^{2+}$, belongs to the class of ferrous metal complexes, which possess a LS ground state configuration. The energetics (Section 2.4.3) and ultrafast photochemistry [148] (Section 2.4.2) of $[Fe^{II}(bpy)_3]^{2+}$ are representative of the whole family of ferrous LS compounds and, like most other SCO compounds, its optical absorption spectrum exhibits the characteristic and intense MLCT absorption, which relaxes after the SCO into the HS state [149].

In Sections 2.4.3 and 2.4.6, the structural implication related to the SCO transition will be pointed out and discussed. The novelty of the time-resolved x-ray absorption results described in Section 6.2 stems from the fact that it is the first time the HS state structure of a solvated transition metal complex was measured in "real-time" without either any *a priori* assumptions about its HS state structure. (on contrary to the results presented in Ref. [48]) or the necessity of low-temperature trapping the excited state HS population (see Section 2.4.5 for details on the so called LIESST phenomenon).

2.4.1 Low-Spin Structure

The ground state molecular structure of LS crystals of $[Fe^{II}(bpy)_3]^{2+}\times(PF_6)_2$ has been determined by x-ray diffraction [150]. Similar to the aforementioned case of $[Ru^{II}(bpy)_3]^{2+}$, the ground state symmetry is D_3 as depicted in Fig. 2.5. Here, the central Fe atom is again surrounded by a nearest shell of 3 pairs of N atoms, each pair originating from the same bpy ligand. The 6 nitrogen atoms have a uniform bond distance of 1.97-1.98Å from the central atom. The N-Fe-N angle within the same bipyridine ligand amounts to 81.6 °, which reflects the action of the trigonal distortion (imposed by D_3 symmetry) onto the octahedral 90 ° angle (e.g. in $[Ru^{II}(bpy)_3]^{2+}$ molecule this angle was smaller,78.9 °, which reflects the increased size of the Ru atom) . The DFT calculations have shown that the symmetry of the solvated $[Fe(bpy)_3]^{2+}$ complex is also D_3 [151] (Fig. 2.5. In the same study, no solvent dependence was observed for LS geometries neither in H_2O nor Et(OH). However, the optimized calculations for the HS form of the same complex have suggested a possible angular distortion of the N-Fe-N in the excited state. A calculated angular change of ca. -6 ° (with respect to the LS state value of 81.6 °) has been obtained [151].

2.4.2 Optical Spectroscopy of SCO compounds

The steady-state optical absorption spectrum of aqueous $[Fe^{II}(bpy)_3]^{2+}$ in the UV-NIR range contains 3 main absorption bands [152–154], which are depicted in Fig. 2.9 and summarized in Table 2.3.

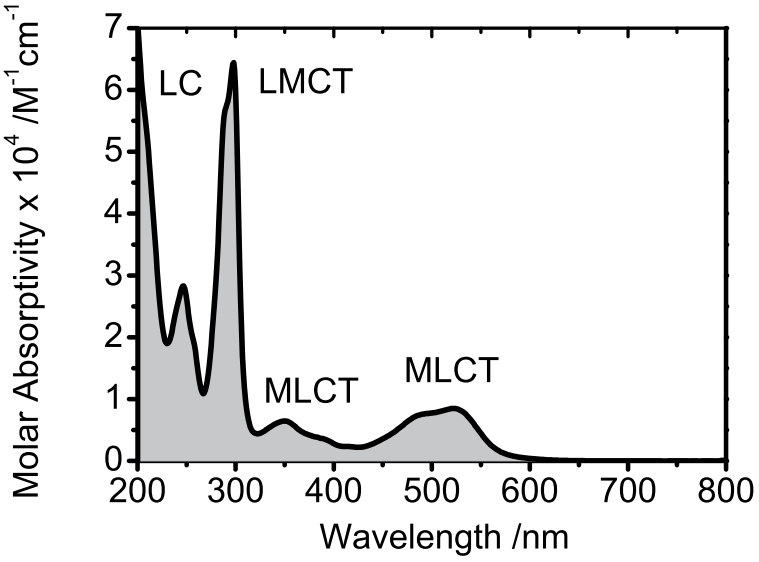

Figure 2.9: Static UV-NIR absorption spectrum of aqueous $[Fe^{II}(bpy)_3]^{2+}$ complex. The main absorption bands are assigned to originate from ligand-centered transitions (LC) involving the bpy orbitals and the metal-to-ligand charge transfer (MLCT) transitions, where the ligand π^*-orbitals mixed with metal $3d$-orbitals are involved [153].

Band	Assignment	Wavelength /nm	Absorbance /$M^{-1}cm^{-1}$
LC	$\pi \rightarrow \pi^*$	200-320	5-8$\times 10^4$
MLCT	$d \rightarrow \pi^*(\chi)$	320-400	6-7$\times 10^4$
MLCT	$d \rightarrow \pi^*(\psi)$	450-590	3-8$\times 10^4$

Table 2.3: The summary of the 3 main absorption bands found in the steady-state spectrum of aqueous $[Fe^{II}(bpy)_3]^{2+}$ complex as illustrated above in Fig. 2.9.

As seen in Fig. 2.9, the UV part of the spectrum is dominated, similarly to the absorption spectrum of $[Ru^{II}(bpy)_3]^{2+}$ in Fig. 2.7, by ligand-centered (LC) transitions among π- and π^*-orbitals of the bipyridine ligands. The assignment of the lower lying bands has been extensively discussed in the literature. According to Refs. [153, 154], the 350 and 520 nm bands can be assigned to metal-to-ligand charge transfer (MLCT) transitions involving $3d$-orbitals of the metal and π^*-orbitals of the bpy. Here, as indicated in Table 2.3, we can distinguish between the two lowest-lying unoccupied π^*-orbitals, namely $\pi^*(\psi)$ (520 nm band) and $\pi^*(\chi)$ (350 nm band), where ψ and χ refer to the symmetric and antisymmetric wavefunctions associated with these orbitals. As discussed in [153], these 2 orbitals can be distinguished by their symmetry with respect to the mirror plane, which bisects the C=C double bond of the 2 pirydyl rings within one bpy ligand (see Fig. 2.5). The normal coordinate modes describing these two orbitals has been characterized using the resonance Raman spectroscopy as a function of the excitation wavelength (in the 350-532 nm wavelength range).

In contrast to $[Ru^{II}(bpy)_3]^{2+}$ (Fig. 2.7), there is no visible emission observed. This results from the decreased ligand-field strength, 10 Dq, which is sufficiently large to result in a low-spin ground state, however, is not too far away from the crossover point in the *Tanabe-Sugano* diagram [84, 108] (see Fig. 2.10). Here, the electronic energy E/B has been plotted as a function of the ligand-field splitting 10Dq/B, where in both cases B is a constant related to the so called *Racah* parameter C [97, 108], which indicates the magnitude of the interelectronic repulsion between different levels in the gaseous ions that have the highest multiplicity. Therefore, in the Tanabe-Sugano diagram, the Racah parameter allows one to express the energy difference between the levels of the highest spin multiplicity in terms of some integer, n, that is ΔE=nB. In Fig. 2.10, the C parameter equals to C=4.41B [108]. Electronic configurations on both ordinate axes have been labeled according to group-theory considerations. The vertical lines indicate the energetic ordering in the electronic ground states of both $[Fe^{II}(bpy)_3]^{2+}$ and $[Ru^{II}(bpy)_3]^{2+}$ compounds.

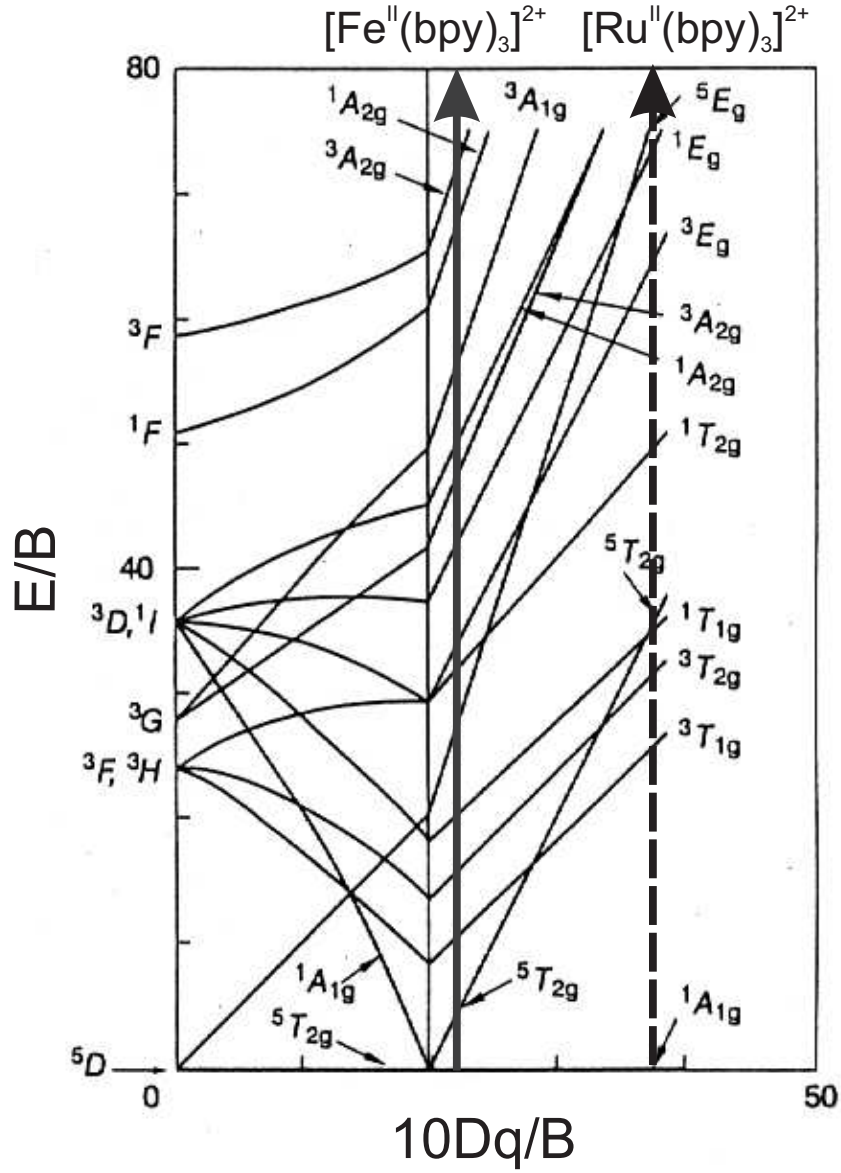

Figure 2.10: Tanabe-Sugano diagram for a transition metal ion with electronic d^6 configuration in O_h symmetry, showing the energy of the excited ligand-field states, in units of the Racah parameter of electron-electron repulsion B, relative to the respective ground state, versus the ligand-field strength 10Dq also in units of B [108].

Fig. 2.10 aids in assigning the possible d-d (metal-centered) transitions in octahedral symmetry. As we move from left to right along the abscissa axis, the ligand-field spitting 10Dq increases from its free ionic value towards the strong-field case (the distinction between weak-field and strong-field was explained in Section 2.2.1 of this Chapter). In case of $[Ru^{II}(bpy)_3]^{2+}$, 10Dq is much larger than E_{sp} (spin-pairing energy) and we observe no SCO transition, within the metal states, in this complex. It also explains the absence of low-energy d-d transitions in the VIS part of the spectrum in Fig. 2.9. The lowest-lying MC transitions in $[Ru^{II}(bpy)_3]^{2+}$ are found in the UV region (300-360 nm as summarized in Table 2.2 and Fig. 2.7). Therefore the lowest-lying excited state of this molecule is solely dominated by the long-lived ^{3}MLCT state, which is

also responsible for its visible emission (Fig. 2.7).

On the other hand, $[Fe^{II}(bpy)_3]^{2+}$ finds itself relatively close to the spin transition region in the Tanabe-Sugano diagram (Fig. 2.10). In this region, E_{sp} becomes larger than 10Dq. The resulting reorganization of the lowest-lying electronic and spin state leads from the $^1A_{1g}$ ground state to the $^5T_{2g}$ high spin state. In addition, and in contrast to the $[Ru^{II}(bpy)_3]^{2+}$ optical absorption spectrum, there is a number of low-lying singlet, triplet and quintet *ligand-field* (LF, also referred to as MC states) states, which are responsible for extremely rapid and non-radiative decay from the MLCT manifold down to the lowest-lying HS state ($^5T_{2g}$) [93].

A qualitative comparison between the energy level schemes of $[Ru^{II}(bpy)_3]^{2+}$ (see Sections 2.3.2 and 2.7) and $[Fe^{II}(bpy)_3]^{2+}$ is displayed in Fig. 2.11.

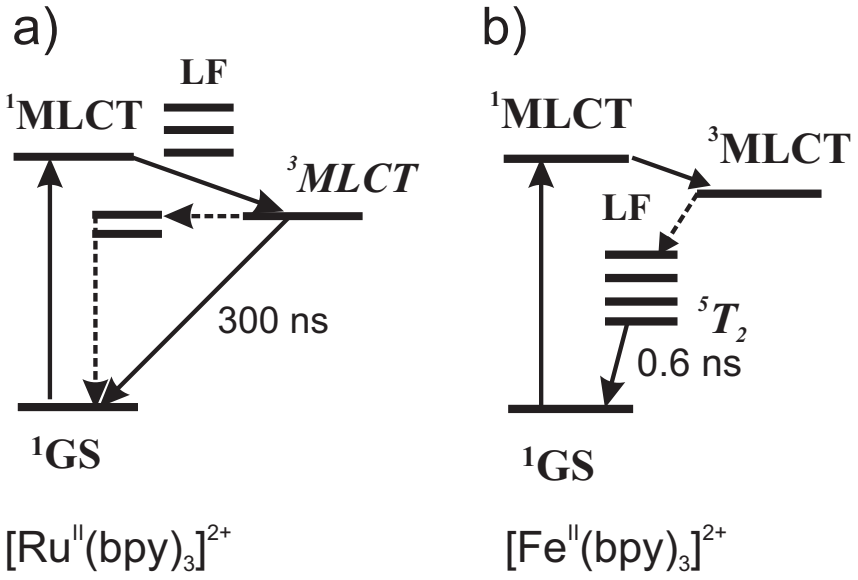

Figure 2.11: The energy level schemes of $[Ru^{II}(bpy)_3]^{2+}$ (a) and $[Fe^{II}(bpy)_3]^{2+}$ (b) are depicted indicating qualitatively the changes in relative energies of their MLCT and LF state. These changes are the main reasons of the differences relaxation mechanisms observed in their photochemical cycles (for details see Sections 2.8 and 2.13) and their characteristic timescales

Here the effect of the reduced ligand-field strength for $[Fe^{II}(bpy)_3]^{2+}$ causes the LF states to lower their energies below the MLCT states. It also explains the absence of the luminescence in $[Fe^{II}(bpy)_3]^{2+}$ complex. The LF states (also known as the *d-d* or MC states) underlie the entire visible spectrum of $[Fe^{II}(bpy)_3]^{2+}$ as shown in Fig. 2.9. They are characterized by low transition intensities (and thus low absorption cross sections) due to their orbital-forbidden character. We notice that the HOMO orbital of $[Fe^{II}(bpy)_3]^{2+}$ has T_{2g} symmetry (and we label its wavefunction as Ψ_{HOMO}), whereas the LUMO is of E_g symmetry (Ψ_{LUMO}). According to the selection rules for electric dipole transitions [155]:

$$\langle \Psi_{LUMO} | e \cdot \overrightarrow{r} | \Psi_{HOMO} \rangle = e \int \Psi^*_{LUMO} \overrightarrow{r} \Psi_{HOMO} d\overrightarrow{r} \tag{2.3}$$

Since $\overrightarrow{r}$ changes sign by inversion, all the contributions from r to the integral in Eq. 2.3 will cancel, unless $\Psi^*_{LUMO}\Psi_{HOMO}$ also changes sign, i.e. the product of the two wavefunctions has odd (*ungerade*, u) parity. If its parity is even (*gerade*, g) the resulting dipole matrix element given in Eq. 2.3 will be zero. In case of HOMO and LUMO orbitals of $[Fe^{II}(bpy)_3]^{2+}$, and since the electric dipole operator belongs to T_{1u} representation, the resulting product of $E_g \times T_{1u} \times T_{2g}$ changes sign [107] (i.e. g×u×g=u) and it yields asymmetric representation, which does not contain A_{1g} representation, which is the electronic ground state of $[Fe^{II}(bpy)_3]^{2+}$ complex in O_h symmetry. Therefore the orbital selection rule is violated for the promotion of t_{2g} electrons to e_g orbitals in octahedral ligand field [84]. In consequence, the *d*-*d* transitions are very weak ($\varepsilon \sim 10^{-2}$-10^2 $M^{-1}cm^{-1}$) and they are called *Laporte* (or orbitally) forbidden transitions [156]. In Simply speaking, one can state that only those transitions, which involve mixed gerade and ungerade ground and excited states will be Laporte allowed in O_h symmetry. Further details concerning the possible relaxation pathways upon the photoexcitation into one of MLCT bands in Fig. 2.9 will be discussed in the following Sections.

2.4.3 Energy Level Scheme of Fe(II)-tris-bipyridine

The energy level scheme of octahedral (and nearly octahedral) ferrous (Fe^{2+}) complexes is schematically drawn in Fig. 2.12.

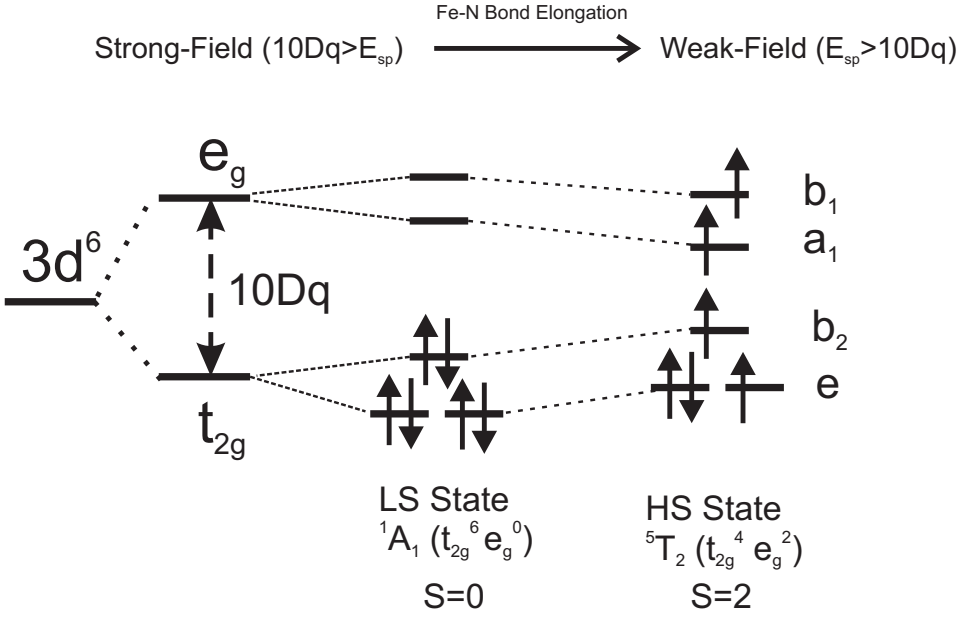

Figure 2.12: Schematic energy level diagram for $3d^6$ electronic configuration of the LS ground state $[Fe(bpy)_3]^{2+}$ in a distorted octahedral field. The horizontal arrow at the top of the graph indicates the direction of the decreased ligand-field splitting, 10 Dq, which enables the spin transition and changes the electronic configuration of the t_{2g} and the e_g bands.

Identical to ruthenium-trisbipyridine (see diagram in Fig. 2.6), $[Fe^{II}(bpy)_3]^{2+}$ has six d electrons in its ground state configuration, all of which occupy the lower ligand field-split t_{2g} band. In a perfectly octahedral symmetry, as previously described in Section 2.2.1, the $3d$-orbitals of the Fe ion split into two subsets of states, accommodating d_{xy}, d_{yz} and d_{zx} orbitals into the t_{2g} band and the remaining $d_{x^2-y^2}$ and d_{z^2} orbitals within the e_g subset (see Fig. 2.4). Similarly, the ligand-field strength 10Dq in this complex is large enough, so that the ground state symmetry is again (as in case of $[Ru^{II}(bpy)_3]^{2+}$) of $^1A_1$ (t_{2g}^6) symmetry. As can be seen in Fig. 2.12, the action of the octahedral field splits both t_{2g} and e_g states into singly degenerate a_1 and b_1 states and one doubly degenerate e state [135]. In this electronic configuration, the ground state spin is zero, and therefore it is called the low-spin (LS) state. Upon further reduction of 10Dq, which characterizes the spin transition, the electron distribution among t_{2g} and e_g states changes and the unpaired electron enters the empty b_1 and a_1 states of the e_g band, leaving another 2 unpaired electron in b_2 and e states of the t_{2g} manifold (and thus the total spin increases to S=2). The HS excited state has the electronic configuration $^5T_2(t_{2g}^4e_g^2)$. This transition can be found in the Tanabe-Sugano diagram (Fig. 2.10) as we move upwards to the left of the abscissa axis. In addition, as it was discussed in Section 2.2.1, the O_h-split e_g molecular orbitals are antibonding in nature, which affects the Fe-ligand bond distance (as already indicated by the horizontal arrow at the top of Fig. 2.12). The relation between the crystal-fild splitting 10Dq in both LS and HS states can be established via [157]:

$$\frac{10Dq^{LS}}{10Dq^{HS}} = \left(\frac{r_{HS}}{r_{LS}}\right)^n \tag{2.4}$$

where n=5-6 [97] and $r_{HS} > r_{LS}$=1.98Å. Eq. 2.4 establishes a direct link between the metal-ligand bond length changes as a function of the ligand-field strength, as illustrated Fig. 2.10. Further structural implications related to the spin transtion will be discussed in more details in Section 2.4.6 of this Chapter.

2.4.4 Relaxation Dynamics upon Spin Transition

The ultrafast photochemistry of light-induced SCO has been characterized by conventional and ultrafast laser techniques over the past decades in a wide class of compounds [87–89,93,113,125,148,149,152,158–167]. In general, these studies delivered a consistent picture of the photochemical cycle, which describes the relaxation pathways in these complexes upon the MLCT photoexcitation in agreement with the one shown in Fig. 2.13. Here, the photochemical cycle of room temperature aqueous $[Fe(bpy)_3]^{2+}$ complex is illustrated. Here the photoexcitation with visible light (e.g. 400 nm, which corresponds to 3.1 eV) is indicated with a vertical arrow. As discussed in Section 2.4.2 (Fig. 2.9), laser irradiation into the visible MLCT absorption band of the LS ground state $[Fe(bpy)_3]^{2+}$ brings the system into its singlet ^{1}MLCT state.

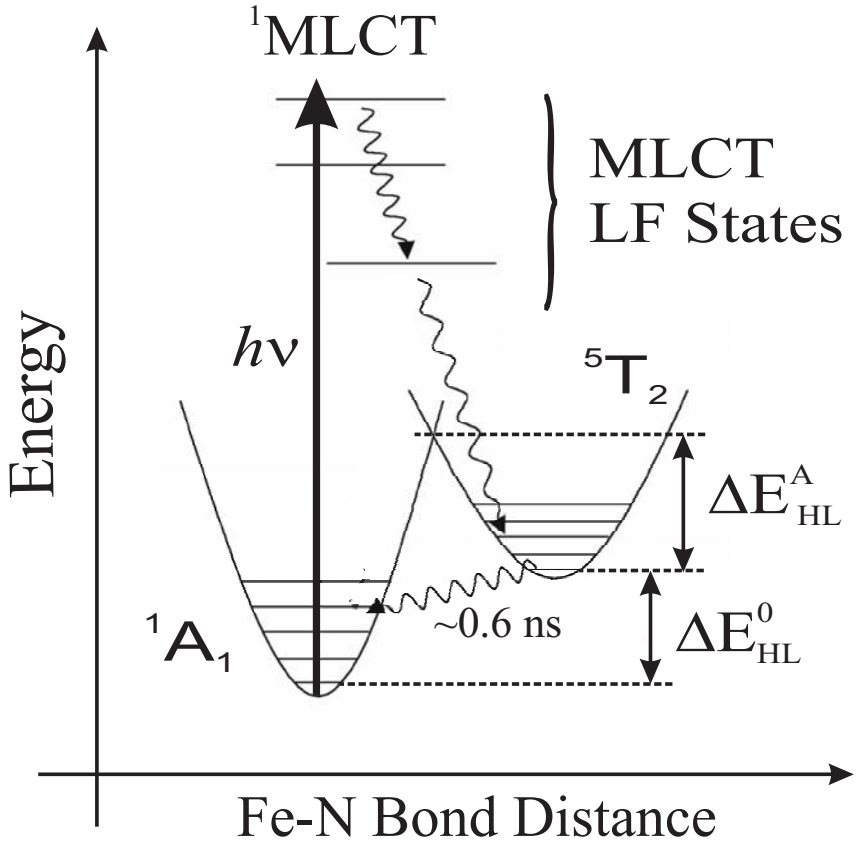

Figure 2.13: Photochemical cycle of $Fe(bpy)_3$ involving the previously discussed energy level scheme (see Section 2.4.3). Laser pulse excitation brings the LS molecule into its ^{1}MLCT state, from which it cascades over MLCT and LF states of different spin multiplicities into the lowest-lying HS $^5T_2$ state. At room temperature and in aqueous solutions, it relaxes nonradiatively back to the ground state within ~0.6 ns

Shortly after (see results presented in Section 6.1), a cascade of intersystem crossing events takes place involving both the triplet ^{3}MLCT states and LF manifolds of different spin multiplicities. In Fig. 2.13 we omitted the spin multiplicities of the intermediate states. Finally, the lowest-lying quintet (S=2) HS state $^5T_2$ is reached in <1 ps [93, 161]with almost unit quantum yield [163]. This state relaxes nonradiatively to the LS ground state in <700 ps in case of aqueous $Fe(bpy)_3$ at room temperature [148, 149]. At cryogenic temperatures and embedded into a solid matrix, the HS state lifetime increases many orders of magnitude up to ~150 μs [168].

2.4.5 Spin Crossover Phenomenon

As mentioned above, $[Fe^{II}(bpy)_3]^{2+}$ belongs to a class of ferrous metal complexes, which exhibit the SCO transition between the LS ground state and the HS excited state [128, 129]. Metal complexes, which have a sufficiently low zero-point energy difference ΔE^0_{HL} (see Fig. 2.13) between LS and HS states, e.g. of the order of 100-1000 cm^{-1}, undergo the SCO in thermal or pressure-induced transition.

The thermal spin transition is entropy-driven and occurs from the LS state populated at low temperatures to an almost fully converted population of the HS at elevated temperatures. The temperature, at which the fraction of complexes in the HS state reaches γ_{HS}=0.5, is generally referred to as the transition temperature $T_{1/2}$, and is a measure for the difference in zero-point energy ΔE^0_{HL} (see Fig. 2.13) between the two states. In dilute systems, like liquids and doped crystalline systems, the thermal transition is gradual and corresponds to the Boltzmann distribution between the vibronic manifolds of both the LS and HS states. The reaction coordinate for the SCO process is best described by a single normal mode, that is, the totally symmetric breathing mode along metal-ligand bonds [151]. Therefore, in Fig. 2.13, we can exchange the configuration coordinate axis Q with Fe-N bond distance, which is mainly affected during the spin transition.

Due to the transfer of two electrons to the antibonding e_g orbitals of the HS state and concurrent loss of π-backbonding from the t_{2g} orbitals, the Fe-N bond distance is substantially elongated with respect to the LS value. In case of $[Fe^{II}(bpy)_3]^{2+}$, due to increased ΔE^0_{HL}, ∼2500-5000 cm^{-1} [151], no thermally-induced population of the HS state can be established below 520 K. Nevertheless, the spin crossover can still be optically triggered so that a substantial fraction of the HS state population is trapped (this phenomenon is known as *Light-Induced Excited Spin State Trapping*, LIESST) [130,133]. This can be achieved by using laser excitation into either MLCT) or LF absorption bands (Fig. 2.9), which characterize the optical absorption spectrum of these complexes.

2.4.6 Structural Dynamics of the SCO Transition

The most commonly model used to explain the HS→LS relaxation in SCO complexes, including Fe(II) compounds, is based on the radiationless *nonadiabatic multiphonon relaxation*, as proposed by Buhks *et al.* [169] for first-row (see Table 2) transition metal ions.

In the following theoretical description, we will often refer to the one-dimensional potential wells associated with the LS and HS states as sketched in Fig. 2.13. Here the reaction coordinate Q is best-described by a single normal mode, namely the totally symmetric "breathing" mode, which mainly involves the metal-ligand bond stretch (and that is why in Fig. 2.13 the Fe-N distance is assigned to the abscissa axis). In this one-configuration coordinate model, the horizontal displacement between HS and LS potentials, ΔQ_{HL} is given by $\Delta Q_{HL} = \sqrt{6}\Delta R_{HL}$ [151,168]. Assuming the average value of ΔR_{HL} ≈0.2 Å, which has been determined for an extensive variety of SCO complexes [170–172] (including the results presented in Chapter 6), ΔQ_{HL} ≈0.5 Å.

In the scope of this thesis, our interest concerns on the HS→LS relaxation, which determines the excited state HS lifetime. This relaxation process, in the classical picture, implies that a molecule trapped in the HS potential (as in Fig. 2.13) would have to acquire enough thermal energy to pass over the top of the energy barrier between both potentials ΔE^{A}_{HL} (Fig. 2.13). The quantum mechanical description allows an additional mechanism to take place, namely the tunneling process between the vibrational states of both potential wells. Assuming the HS→LS relaxation involving spontaneous, nonradiative transition from a given vibrational level k of the HS state to a vibrational level l of the LS state, the transition probability W_{kl} can be derived from Fermi's Golden Rule [173, 174] (see also Eq. 3.5 in Section 3.2):

$$W_{kl} = \frac{2\pi}{\hbar^2\omega}\beta^2_{HL}|\langle\chi_l|\chi_k\rangle|^2\delta(E_l - E_k) \tag{2.5}$$

Here $\beta_{HL} = \langle\Phi_{LS}|H_{S-O}|\Phi_{HS}\rangle$ is the electronic coupling matrix given by the second-order spin-orbit coupling (S-O), $\hbar\omega$ is the vibrational energy of the active vibrational mode, $\delta(E_l - E_k)$ ensures the energy conservation and the matrix element $|\langle\chi_l|\chi_k\rangle|^2$ is the so called *Franck-Condon overlap factor*, which accounts for the overlap of the vibrational wavefunctions of both spin states. For complexes, where the total electronic spin changes by ΔS=2, β_{HL} takes on a value of ca. 150 cm^{-1} [169]. The so called *reduced energy gap* $n = \Delta E^0_{HL}/\hbar\omega$ is a dimensionless measure of the vertical displacement of both potential wells in Fig. 2.13 [168]. In this context, the Franck-Condon factor $|\langle\chi_l|\chi_k\rangle|^2$ depends on both ΔQ_{HL} (horizontal displacement) and ΔE^0_{HL} (vertical displacement) of LS and HS potential wells. The theory of nonadiabatic multiphonon relaxation implies the following relation for the tunneling probability [130, 175]:

$$k_{HL}(T) = \frac{2\pi}{\hbar^2\omega}\beta^2_{HL}F_n(T) \tag{2.6}$$

where $F_n(T)$ is the thermally averaged Franck-Condon factor given by [175]:

$$F_n(T) = \frac{\sum_k |\langle\chi_{k+n}|\chi_k\rangle|^2 e^{\frac{-k\hbar\omega}{k_BT}}}{\sum_k e^{\frac{-k\hbar\omega}{k_BT}}} \tag{2.7}$$

where k_B is the Boltzmann constant. At low temperatures ($T \to 0$), the rate constant in Eq. 2.6 reduces, given that only the lowest vibrational level ($\nu = 0$)of the HS state is populated:

$$k_{HL}(T) = \frac{2\pi}{\hbar^2\omega}\beta^2_{HL}|\langle\chi_n|\chi_0\rangle|^2 \tag{2.8}$$

For a harmonic approximation involving potentials with equal force constants, the Franck-Condon factors reduce to [176]:

$$|\langle\chi_l|\chi_k\rangle|^2 = \frac{S^n e^{-S}}{n!} \tag{2.9}$$

where $S \propto \Delta Q_{HL}^2/\hbar\omega$ is the so called *Huang-Rhys factor* [176] describing the dimensionless horizontal displacement of the involved potential wells from Fig. 2.13 and n is the aforementioned reduced gap related to the vertical separation of these potentials.

Therefore, at low temperatures ($\leq$50 K), one can regard the HS→LS relaxation as a temperature-independent process with its relaxation rate constant $k_{HL}(T)$ being essentially governed by a pure tunneling process [130, 166] (Eq. 2.8). In this case, the electronic energy of the HS state is spontaneously converted into vibrational energy in the LS state and the HS→LS transition takes place. As the temperature increases, the HS→LS relaxation becomes thermally-activated and an additional energy barrier has to be overcome. The classical energy barrier E^A can be described via [177, 178]:

$$E^A = \frac{1}{4}\hbar\omega S\Big(1 - \frac{n}{S}\Big)^2 \tag{2.10}$$

However, at finite temperatures, it has been reported that the measured effective activation energy E_{eff}^A is always smaller than the classical limit in Eq. 2.10 [130]. Hence, it was proposed that in the thermally-activated region, the spin transition should be treated as a tunneling process from thermally populated levels of the HS potential [130], characterized by large Franck-Condon factors with the corresponding LS vibrational levels. It was then proposed to define E_{eff}^A via [179]:

$$E_{eff}^A = -\frac{ln(k_{HL})}{1/kBT} \tag{2.11}$$

The effective energy barrier, as defined above, is indeed temperature-dependent; particularly in the region between low-temperature tunneling and high-temperature region, it increases abruptly from essentially 0 to up as much as 2000 cm^{-1} [151] for a given complex. In agreement with Eq. 2.10, E_{eff}^A changes linearly (decreases) with increasing ΔE_{HL}^0. In the high-temperature limit, where n≪S, both quantities, defined in Eq. 2.10 and Eq. 2.11, merge into [176]:

$$E^A = \frac{\hbar\omega S}{4} - \frac{\hbar\omega n}{2} \tag{2.12}$$

The above presented theoretical concepts all point towards unusually large structural changes, between both spin states, characterizing this class of transition metal compounds. The experimental verification of these theoretical concepts has been presented in various structure-related studies in many SCO complexes using different spectroscopic techniques. In case of ferrous compounds, previous structural studies on temperature or light-induced SCO transition, under steady-state conditions, have been carried out by means of x-ray crystallography [171, 180–182] and x-ray absorption spectroscopy [134–139, 141, 144, 145, 183–187], all delivering an elongation of the Fe-N bond length by

ca. 0.2-0.24 Å, with respect to the LS ground state. All these cases exploited the LIESST phenomenon, which allowed efficient trapping of a substantial fraction of the HS state population at cryogenic temperature in a crystal sample (due to the largely decreased $k_{HL}(T \rightarrow 0$, and thus an increased HS state lifetime), and thus obtaining its structure. Only very recently, Fe K-edge steady-state XAFS of the solvated LS $[Fe(tren(py)_3)](PF_6)_2$ and its HS analogue $[Fe(tren(6\text{-}Me\text{-}py)_3)](PF_6)_2$, were combined to interpret the picosecond transient spectra of the solvated photoexcited $[Fe(tren(py)_3)](PF_6)_2$ ns-lived complex [48], showing a very good agreement with the anticipated result for the HS complex.

The results presented in Section 6.2 contain the first picosecond-resolved spectra of the Fe K-edge absorption of $[Fe(bpy)_3]^{2+}$ in H_2O at room temperature. Compared to previous x-ray studies on SCO complexes, both static and time-resolved, the results presented in this thesis (Chapter 6) bring new developments in several aspects that are:

- for the first time, the transient molecular structure of a short lived photoinduced HS intermediate is recorded in "real-time" (no LIESST effect involved), with 100 ps hard x-ray pulses.
- the structural parameters of the HS state are extracted directly from a fit of the experimental transient absorption spectra, without prior assumptions about its structure.
- both the geometric and electronic changes are extracted from the transient difference X-ray Absorption Near Edge Structure (XANES) features and the consistency of our results is supported by the fitting of the Extended X-ray Absorption Fine Structure (EXAFS) features. The results obtained in Chapter 6 are in a very good agreement with the structural results of the HS state geometry in a variety of Fe(II) SCO complexes [171].

Therefore, the dynamical measurements of the photoinduced spin-transition and its description are crucial not only for our fundamental understanding of this intramolecular process, but also may profit in designing new molecules with longer-lived HS states. Another application in ultrafast molecular magnetism may offer a new route for novel data processing and storage materials at the nanoscale [126, 188].

2.5 Excited State Structural Dynamics

The structure-related aspects of the excited state dynamics of transition metal complexes make the energy and structural relaxation studies of these compounds very interesting and challenging. One especially novel aspect concerns the experimental methodology applied in this thesis. Ultrafast X-Ray Absorption Spectroscopy [27] offers a unique structure-sensitive tool to probe the underlying nuclear dynamics in this class of coordination chemistry compounds. Among many other spectroscopic techniques, it is the only one, which allows observations in "real-time" of the molecular structural dynamics of the involved excited states (see the discussion in Section 2.5.1).The ultrafast optical spectroscopy can deliver the most relevant timescales of the relaxation pathways involved in the photoinduced processes. Nevertheless, the spectroscopic observables available in these experiments cannot be directly easily translated into the structural parameters.

As shown in Fig. 2.13, the reaction coordinate, which governs the spin transition in $Fe(bpy)_3$ complex, is mainly involving the symmetric elongation of the Fe-N bonds. The transient optical spectra recorded in our optical measurements (see Section 6.1 of Chapter 6), by no means, can be directly linked to this coordinate and thus inhibit direct interpretation of the molecular structures involved in the process. We can, however, infer the involved species and determine the characteristic timescales, on which they occur.

Similarly, the electron transfer reaction monitored upon the visible photoexcitation of $Ru(bpy)_3$ complex is usually described in terms of the reaction coordinates, involving combinations of complicated molecular vibrations, often including the solute-solvent interactions. In a standard chemist's view of this class of reactions, the fundamental understanding of the electron transfer dynamics requires an a priori knowledge acquired from either steady-state spectroscopy or quantum mechanical calculations (or both) in order to disentangle the complex dynamics occurring on the multidimensional potential energy landscape. Deriving the structural information from experimentally accessible observables is nearly impossible. On the other hand, our approach offers a direct link to the underlying reaction coordinates and the underlying nuclear motion. Time-resolved x-ray spectroscopy complements the optical dynamics picture with structural information. In this way, we are able to deliver a complete picture of the underlying structural dynamics and support it with the transient snapshots of the involved molecular structures on the picosecond time scale. The results presented in Chapter 5 show how the excited state structure responds to the electron transfer reaction in terms of the metal-ligand bonding and its electronic configuration.

In the following Section, a brief overview of pump-probe spectroscopy will be given and its extension to structure-sensitive configuration will be outlined. Extensive discussion of the involved experimental boundary conditions and requirements is followed in Chapter 3 and 4.

2.5.1 Structure-Sensitive Pump-Probe Spectroscopy

With the advent of femtosecond lasers, it became possible to carry out physical observations on time scales that are comparable (or even shorter) than a nuclear oscillation period in molecular systems. It therefore became feasible to record molecules at various stages of their vibrational distortion corresponding to well-defined, although non-equilibrium, molecular geometries [**?**, 189, 190]. Such transient structure are usually the intermediates between reactant and product states, involved in a given photochemical reaction. Given the time resolution of fs lasers, these unstable transition states could now be followed in "real-time" [12, 14, 191], meaning with the temporal resolution corresponding to the timescales, on which they occur. The experimental fulfillment of these possibilities requires not only the adequate temporal resolution, but also implies that the excitation mechanism initiating the molecular motion should be coherent in phase, so that it leads to the transient structures [192]. The typical and most commonly used approach for recording such motion is based on *pump-probe* scheme sketched Fig. 2.14.

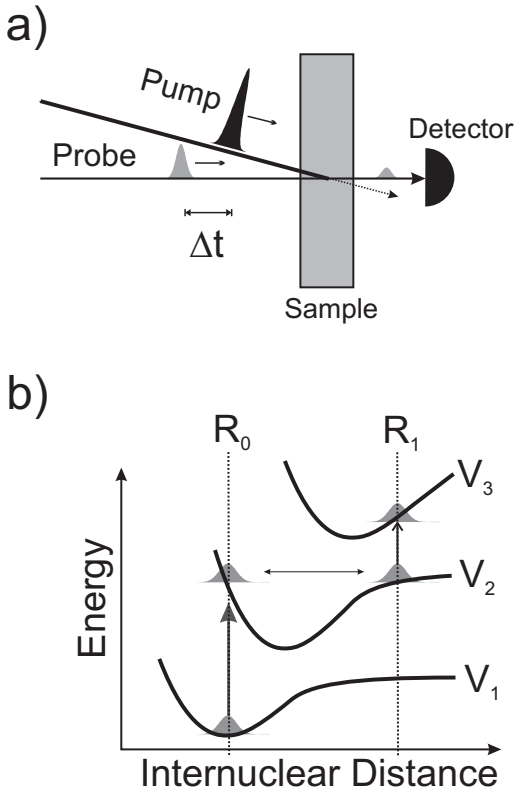

Figure 2.14: a) Pump-probe spectroscopy allows monitoring both spectral and temporal evolutions of a given sample by recording the photoinduced changes, initiated with the pump pulse, as a function of a time delay $\Delta\tau$ between the pump and probe pulses. b) Schematic picture of a potential energy diagram of a molecular system. The effect of the pump pulse is indicated by the vertical arrow, which excites the system from its ground state configuration V_1 at R_0 to its first excited state V_2. The probe pulse monitors the temporal evolution of the excited state by inducing a second transition from V_2 to V_3. By tuning the energy (wavelength) of the probe pulse, a particular configuration R_1 of the excited state V_2 is chosen and recorded as a function of the time delay between both pulses.

The pump-probe spectroscopy involves a relatively simple scheme, where two (or more) ultrashort pulses of light are synchronized to each other with a controllable time delay, denoted as Δt in Fig. 2.14a. Absorption of the first pulse, called the pump pulse, brings a molecular system from its ground state potential V_1 to the first Franck-Condon excited state potential V_2 (Fig. 2.14b). If the pump pulse duration is short enough (i.e.shorter than the characteristic oscillation period of the molecule in the excited state V_2), then a coherent superposition of vibrational levels (a so-called *wavepacket*) is created [13], which is localized in space at the ground state equilibrium configuration at time t=0. The wavepacket will undergo oscillations at a frequency, characteristic of the vibrational level spacings of the potential V_2, if the latter is bound, and its time evolution will reflect the evolution of the ensemble of coherently excited molecules, which evolve in phase. The observation of this motion is fulfilled by using a second ultrashort laser pulse (called the probe pulse in Fig. 2.14a) that monitors the ensemble excited by the pump pulse at a given time delay Δt. The probe pulse induces a transition between V_2 and a higher lying state V_3. The choice of the probe wavelength will select the probed configuration of the later as can be seen in Fig. 2.14b. Therefore, by tuning the wavelength of the probe pulse, one accesses different molecular configurations of the excited state. The spatial width of the probed window in real space, which is provided by the probe pulse, will depend on its spectral width and on the slope of the potential difference between V_2 and V_3. Each time the wavepacket enters the probe window, a signal is detected, which can be the excited state probe pulse absorption, an induced fluorescence signal from V_3 or an ion signal (if V3 is an ion potential).

It is important to remark here that the probed configuration is preselected by the probe pulse wavelength and the actual probed window will strongly depend on the spectral characteristics of the probe pulse and the energetics of the involved potentials. Therefore, the structural dynamics can extracted from spectroscopic observables only if the knowledge of the energetics of the molecular system is provided. Over past decades, pump-probe spectroscopy has proven its powerful capabilities in observing molecular motion in real-time ranging from bound states of small diatomic molecules [15–19], liquids [193, 194], solids [195–198] to biological molecules [199–202].

As long as relatively small molecular systems are concerned, establishing the relation between the probe wavelength and the probed molecular configuration is feasible (i.e. simple diatomic and some triatomic molecules. As the studied system grows in size and thus in complexity, this relationship in no more unambiguous and severely hinders the photoexcited structural dynamics underlying the involved photochemical mechanisms. In this case, the spectroscopic observables (see Fig. 2.14b) given by the transition energies and intensities are insufficient to extract the involved molecular motion. Certain unambiguities can be overcome by combining (if available) steady-state spectroscopy and quantum chemical calculations in order to disentangle the observed ultrafast dynamics recorded in a pump-probe experiment. However, further translating of these observables into structural parameters (i.e. nu-

clear coordinates) becomes a very difficult (if possible at all) task.

In order to overcome these limitations, novel *structure-sensitive* pump-probe techniques have emerged in the last decade, as a complementary tool to overcome the structural limits of the optical ones. Naturally, one demands a technique, which is capable of providing equally short temporal window to probe an ultrafast process, while gaining the structural sensitivity, preferably down to the atomic spatial resolution. Structural techniques such as x-ray diffraction, electron diffraction and x-ray absorption spectroscopy (XAS) are well-established and, in principle, are capable of delivering the demanded structural information provided sufficiently short and intense pulses of x-rays or electrons can be produced.

The majority of time-resolved structural studies have been carried out with ultrashort pulses of x-rays or electrons, either using diffraction techniques or x-ray spectroscopies. In analogy to Fig. 2.14a, a pump-probe experiment involving either x-rays [27–45] or electrons [20–26] is conceptually the same as in case of visible light pulses. Therefore, one could easily imagine an experimental configuration, in which the probe pulse, synchronized to a visible pump ultrashort pulse, would be either an ultrafast x-ray or electron pulse. The essential difference here originates from the mismatch between the pump and probe wavelength, which implies careful optimization of the experiment [36, 74–76](see the discussion in Section 3.4 of Chapter 3).

In the scope of this thesis, x-ray spectroscopic techniques are of primary interest. However, it is worth mentioning that a tremendous effort and progress have been achieved over the past years in implementing the ultrashort bursts of both x-ray pulses and electrons in diffraction techniques. It has culminated with the demonstration of the feasibility of ultrafast electron diffraction, where transient structures of gaseous molecules have been determined with picosecond temporal resolution [20–26]. The success of electron diffraction partially stems from high scattering cross sections of electrons, which is five orders of magnitude larger than that for x-rays, however, its extension to condensed phase systems would be a major challenge due to the low penetration depth of electrons in matter. On the other hand, x-ray photons offer the advantage of high penetration depth in matter. Therefore, x-ray diffraction offers the advantage to study systems in bulk media. In addition, it probes the long-range ordering within the medium and provides relatively strong signals due to the coherent nature of the diffraction process. Yet, it requires well-defined atomic ordering (i.e. crystal structure) within the studied system, otherwise the diffraction condition imposed by the Bragg law cannot be fulfilled efficiently, i.e. $2d \sin\Theta = \lambda$, where d denotes the crystal plane spacing, λ stands for the x-ray wavelength and Θ is the angle of incidence between the x-ray beam and the considered atomic plane. Nevertheless, ultrafast x-ray diffraction has been successfully applied to a variety of systems, including metallic and semiconducting crystals [30, 31, 31, 203–205], molecular crystals [206–209], and even liquids (in the so called diffused scattering experiments [210])

On contrary to diffraction, XAS techniques do not require any long-range order within the probed system. As pointed out in details in Chapter 3, XAS allows structural studies in a variety of condensed phase system, including liquids, disordered solids, amorphous or glassy materials etc [4,10]. The extension of XAS techniques into the ultrafast temporal domain has been a tedious and challenging task over the past years. The first implementation of x-ray absorption spectroscopy in a pump-probe type experiment was on photobiological reactions, namely the dissociation of the CO ligand from carboxymyoglobine and its recombination over time-scales of micro- to milliseconds [67, 211, 212]. In these experiments, a Nd-YAG laser synchronized to the x-ray pulses from a synchrotron source served s the pump source, whereas the x-ray pulses probed the iron K-edge, hereby monitoring an edge shift for the photolyzed species to lower energies and a change in the pre-edge transition (1s→3d). In later studies, Chen *et al.* successfully extended the x-ray absorption spectroscopy to the nanosecond regime. In their study, the photodissociation of NiTPP-L_2 (NiTPP = nickel tetraphenylporphyrin; L= piperidine) was probed with 14 ns pulsed synchrotron x-rays [43] Several successful experiments have been carried out since then on various systems, including liquid-phase coordination chemistry compounds [35, 45, 48, 50, 213], amorphous solids [51, 54], biological systems [69, 70] and semiconductors [53], with improved temporal resolution, often down to the x-ray pulse limit [35, 50]. In addition, several theoretical works extending the static XAS schemes into the time-resolved domain have been reported [28]. The results reported in Chapters 5 and 6 include the application of the aforementioned time-resolved scheme in studying the photoinduced chemical process in solvated transition metal complexes. Here, we were mainly concerned with the effect of the intramolecular electron transfer reactions on the transient molecular structure. In both cases, we have achieved high quality results, which allowed to retrieve the photoinduced structural changes occurring in these systems on 50-100 ps timescales.

Chapter 3

X-ray Absorption Spectroscopy - Theory and Experiment

The following Chapter introduces the basic concepts lying behind the theoretical description and experimental realization of the X-ray Absorption Spectroscopy (XAS). Here, a brief description of the physical phenomena involved in XAS will be given, followed by a short review of the more mathematically rigorous theoretical models, including the so called Full Multiple Scattering (FMS) theory. Several examples of the computational codes used in calculating the XAS spectra will be given in relation to the previously discussed theoretical framework and highlighting the different approaches in simulation the x-ray absorption spectra. Subsequently, basic concepts of the experimental XAS detection will be explained for both the transmission and fluorescence yield measurements, followed by their extension into the time-resolved XAS detection. The principle of a laser-pump x-ray-probe experiment will be outlined, including a discussion of the most important boundary conditions set by the experiment.

3.1 Introduction to X-ray Absorption Spectroscopy

X-ray Absorption Spectroscopy (XAS) measures the probability as a function of photon energy that an x-ray photon incident upon a sample will be absorbed by that sample. In the experiment, the energy of the incident beam of photons is changed monotonically in discrete steps, while a signal proportional to the absorption cross section is measured [4, 6]. The outcome of such XAS experiment delivers the characteristic x-ray absorption spectrum (Fig. 3.1), where the variation of the absorption coefficient shows several general features [11]:

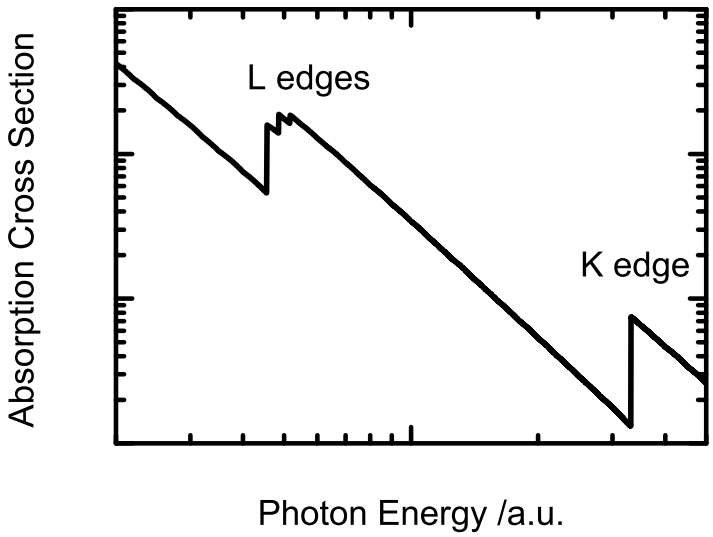

Figure 3.1: Variation of the atomic x-ray absorption coefficient as a function of the photon energy. The characteristic saw-tooth-like features with a sudden increase of the absorption at certain energies represent the absorption edges

1. An overall decrease in x-ray absorption with increasing energy. This feature is illustrative of the well-known quantum-mechanical phenomenon of x-ray absorption by atoms [173].

2. The presence of saw-tooth-like features with a sharp rise at discrete energies, called absorption edges. The energetic positions of these features are unique for a given absorbing element. They occur near the ionization energy of inner shell electrons and contain spectral features due to bound-bound and bound-continuum transitions.

3. When increasing the energy above an absorption edge, an oscillatory fine structure appears for molecules and solids that modulate the otherwise smooth absorption profile, typically by a few percent of the absorption edge jump. This feature, which is absent for single atoms in the gas

phase (and in Fig. 3.1), contains precise structural information such as interatomic distances and coordination numbers.

The absorption edges are related to the transitions from a particular atomic core-orbital to the free continuum (ionization of core orbitals, Fig. 3.2), but also include transitions to unoccupied bound levels just below the ionization limit.

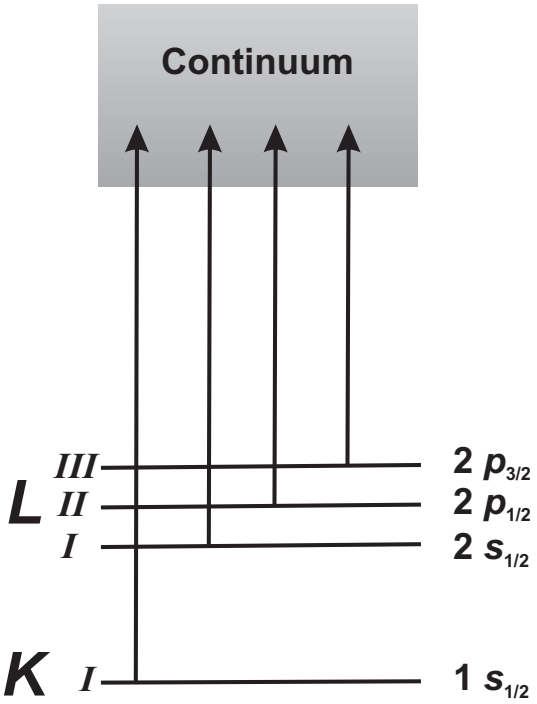

Figure 3.2: Transitions resulting from the absorption of an x-ray photon by the deep-core electron. The ionized photoelectron can be excited to either higher-lying unoccupied state or into the continuum. Here the transitions are shown for all possible 1s and 2p core excitations, i.e. K and L absorption edges

The nomenclature for x-ray absorption features reflects the core orbital, from which the absorption originates. In Fig. 3.2, the two innermost core orbitals are shown namely the K and L shells and the characteristic transitions to the continuum states are indicated. For example, K edges refer to transitions from the innermost n=1 electron orbital (thus the K edge involves 1s electron), whereas L edges refer to the n=2 absorbing electrons (L_1 to $2s$, L_2 to $2p_{1/2}$, and L_3 to $2p_{3/2}$ orbitals), to the corresponding higher-lying bound core shells and continuum states. The transitions are always referred to unoccupied states, i.e., to states with an electron above the Fermi energy E_f, leaving behind a core hole, and absorption features may appear just below the edge, which correspond to transitions to bound unoccupied levels just below the ionization limit. Above the ionization limit, the excited electron is considered as a photoelectron, and depending on its kinetic energy, it can propagate more or less freely through the material. The photoelectron propagation can be approximated by a spherical wave with a kinetic energy E_{kin} given by $E_{kin} = \hbar\omega - E_B$, where $\hbar\omega$ defines the incident x-ray photon energy and E_B refers to the binding

energy. The photoelectron wave vector can then be calculated via [214, 215]:

$$k = \frac{2\pi}{\hbar}\sqrt{2m_e(\hbar\omega - E_B)} \tag{3.1}$$

When zooming into the vicinity of one of the absorption edges shown in Fig. 3.1, a fine structure of the spectrum can be seen (Fig. 3.3). The XAS spectrum is typically divided into two regions, the x-ray absorption near edge structure (XANES) and the extended x-ray absorption fine structure (EXAFS) [4, 8]. The transition energy between these two regions lies typically around a few tens of eV above the absorption edge, but this distinction is somewhat arbitrary and the two regions generally overlap. In Fig. 3.3, the K-edge XAS spectrum of a solvated Fe complex (i.e. $[Fe^{II}(bpy)_3]^{2+}$) is shown.

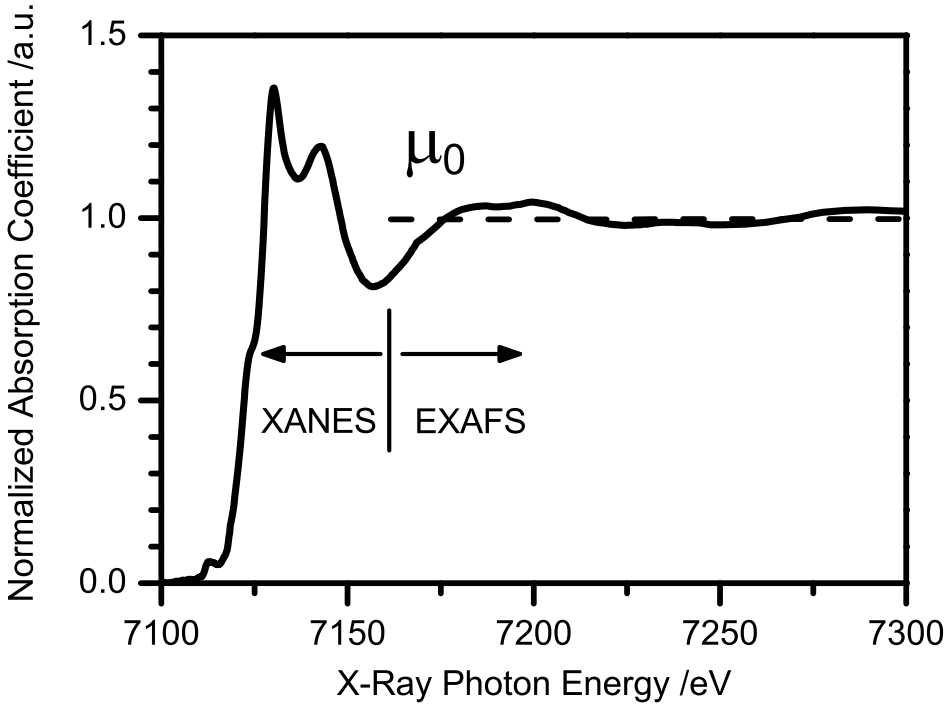

Figure 3.3: The K-edge x-ray absorption spectrum of a solvated transition metal complex (e.g. $[Fe^{II}(bpy)_3]^{2+}$). Here the division into the two characteristic spectral regions, namely XANES and EXAFS, is indicated with a vertical line at ~ 7160 eV. The horizontal dashed line marks the atomic-background intensity μ_0 used in the normalization of XAS spectra (the total edge jump equals 1).

3.1.1 XANES Spectrum

The XANES part of the XAS spectrum depicted in Fig. 3.3 can be defined as the initial ca. 20-50 eV above the absorption edge (ca. 7125 eV). It contains information about both the electronic and the molecular structure of the system of interest [8, 10]. Indeed, it has been shown that XANES is in part determined by the geometrical arrangements of the atoms in a local cluster around the x-ray absorber in biological systems [216], on surfaces [217] and in both solid and liquid samples [218]. This originates from the complicated electron scattering geometries found at these energies and is referred to as the multiple scattering (MS) of the excited photoelectron. Note that at low energies above the absorption edge, the photoelectron wavelength λ_e, related to its kinetic energy (and thus its momentum k) via de Broglie's relation [173]:

$$\lambda_e = \frac{h}{m_e \nu} = \frac{2\pi}{k} = \frac{\hbar}{\sqrt{2m_e(\hbar\omega - E_B)}} \tag{3.2}$$

is thus much larger than at higher energies in the so called EXAFS region [5] (see below in Section 3.1.2). It implies that the photoelectron can scatter off nearly all atoms present in the molecular cluster in complicated geometrical arrangements. As the λ_e decreases (at higher photoelectron's E_{kin} in the EXAFS range), the single scattering (SS) events between selected pairs of atoms dominate the process, although the MS is still present and should be accounted for in the proper description of EXAFS. In Fig. 3.4 , the electron scattering is sketched for an outgoing and backscattered photoelectron wave in case of both SS and MS geometries.

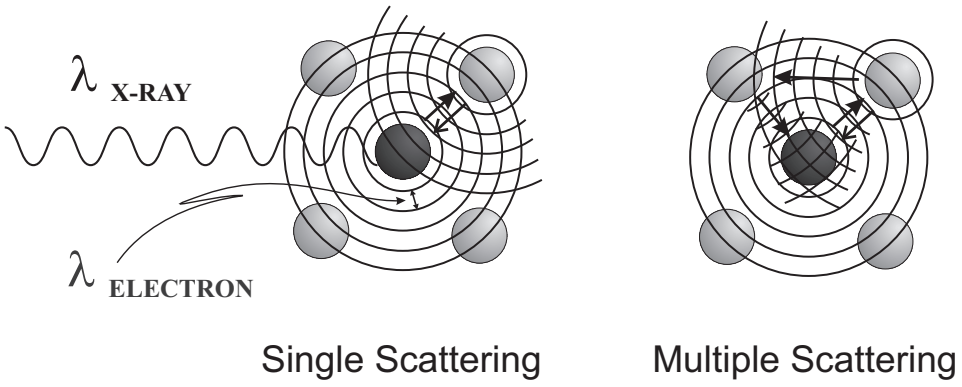

Figure 3.4: Photoelectron wave scattering in the case of EXAFS (*single scattering* and XANES (*multiple scattering*). The interference between the outgoing and the backscattered waves reflects the local geometric arrangement of the nearest neighbor atoms (grey spheres) around the absorber (black sphere).

The absorption resonances encountered in the XANES region, in particular in the first 10 eV energy range above the absorption threshold (which often lies just below the ionization threshold of a given shell), have a physical origin, which is different for different classes of materials. It is dominated by the transitions to bound valence states or quasibound states (so-called *shape resonances* in molecules), core excitons in ionic crystals, unoccupied local elec-

tronic states in metals and insulators, etc. These are the states that bind the systems together in molecules and solids and determine their electronic structure. Therefore a careful analysis of this energy range in XAS spectra delivers valuable information about the electronic landscape of the unoccupied valence shells in molecules (which are those that determine the chemical reactivity) and unoccupied density of states in solids [219]. In addition, the energies and intensities of the transitions to these states will reflect the valency of the involved ions, which may change for different molecular symmetries or local bonding around the absorber (see the example of chemical shift in case of $[Fe^{II}(bpy)_3]^{2+}$ complex presented in Section 6.2 of Chapter 6) and upon the charge transfer reactions (i.e. oxidation state induced shift due to photoinduced electron transfer in $[Ru^{II}(bpy)_3]^{2+}$ [35,50], (see Section 5.2 of Chapter 5) and therefore can be monitored in the XANES spectra.

It has been shown for several molecular and crystalline systems that the effective charge of the atom can by measured by means of so called *valence shift* of the core level binding energy [220–223]. Due to a non-zero overlap of the core levels with valence shells, ionization threshold and low-energy MS resonances, the change of the charge state of the absorber will affect the observed transition energies and intensities in the XANES spectra. The quantitative analysis of these effects is rather complicated as the corresponding XANES absorption features are in addition strongly influenced by the nature of the local surroundings (i.e. ligands system and their bondings), giving rise to the so called *chemical shift* [9, 224, 225]

Furthermore, since the XANES transitions are subject to the same selection rules as optical transitions, the partial relaxation of these rules yields the information about the local symmetry around the absorber, which may manifest itself in the XANES region by the enhancement of formally-forbidden transitions (see example of L_2 edge spectra of $[Ru^{II}(bpy)_3]^{2+}$ complex discussed in Chapter 5 or the pre-edge features in $[Fe^{II}(bpy)_3]^{2+}$ spectrum as presented in Chapter 6). At higher energies (just above the ionization limit), the XANES spectra are largely dominated by the aforementioned MS events [9, 226, 227]. The shape of XANES spectra concerning the number of MS resonances and their relative intensities is rather similar for each type of molecular symmetry [9,226,228]. Therefore, XANES features are considered to be very sensitive to small changes of the local molecular geometry [229] and surroundings of the absorber and can even couple with nuclear motion [230, 231]. In several studies, it has been reported that the local geometry of a molecule can easily be recognized by the shape of its XANES spectrum, and the corresponding energies of the MS features were found to be strongly correlated to the interatomic distances [232–234]. Furthermore, the spectra of K edges are very different from those of $L_{2,3}$ edges (see Fig. 3.2), since K shells release p-electrons and L_2 and L_3 shells release s and/or d electrons.

3.1.2 EXAFS Spectrum

The EXAFS region covers the high-energy continuum above the ionization threshold (above 7175 eV for the spectrum shown in Fig. 3.3). It is dominated by an oscillatory pattern on the XAS spectra, which can be related to the photoelectron SS events with the neighboring atoms [5]. In this regime, the photoelectron states can approximated with spherical waves.

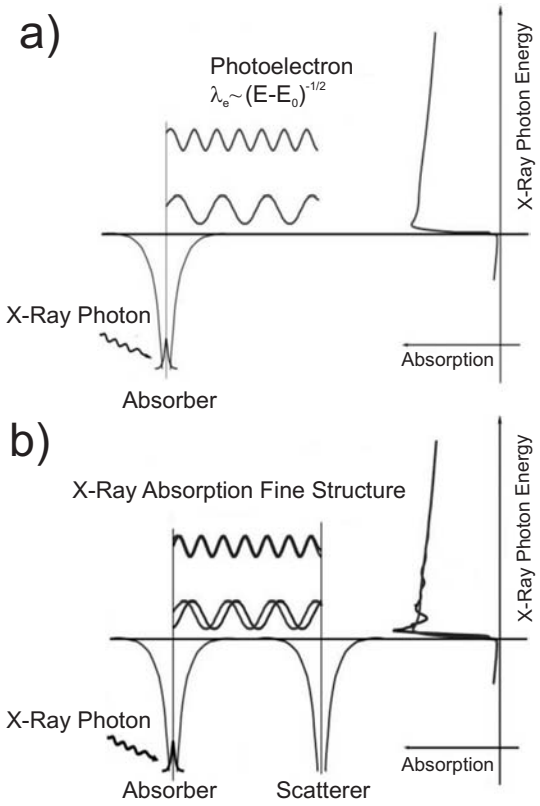

Figure 3.5: The photoelectron scattering off the neighboring atoms causes the characteristic oscillatory pattern (the so called X-ray Absorption Fine Structure) in the EXAFS region of the x-ray absorption spectra (b). In the absence of the surrounding atoms(a)the absorption coefficient reflects only the atomic-background absorption (gas-phase spectrum) of the isolated absorber atom. Figure taken from [235]

The oscillatory structure is due to the interference between the outgoing photoelectron wave and the wave scattered back at neighboring atoms (see Fig. 3.5a and b). Therefore, it does not exist in the case of the isolated atom (Fig. 3.5a). The oscillatory pattern superimposed onto the gas-phase (or atomic-like) background absorption spectrum is referred to as the x-ray absorption fine structure (XAFS) and it includes both the XANES and EXAFS regions. As the photoelectron wavelength λ_e decreases with increasing photoelectron kinetic energy, at sufficiently high energies the electron scattering is such that the only significant contributions to the final state wave function in the vicinity of the absorbing atom comes from paths in which the electron is scattered only once (SS events, Fig. 3.4), since MS probabilities decrease stronger with increasing energy [5,7]. The photoelectron spherical wave

emitted from the core-excited absorber is damped out rapidly due to inelastic effects caused by the extended valence orbitals of the nearby-lying atoms, and can be approximated by its mean-free path λ. This limits the probed spatial region and ensures that MS effects beyond simple backscattering can be ignored. The fact that multiple-scattering events can be neglected allows the analysis of the data by a simple Fourier transformation [3]. For this purpose one has to generate a normalized XAS spectrum (normalized to the absorption edge jump $\Delta\mu_0(E)$ under consideration), which is defined as the normalized oscillatory part of $\mu(E)$ (the absorption coefficient), i.e., the EXAFS, via:

$$\chi(E) = \frac{\mu(E) - \mu_0(E)}{\Delta\mu_0(E)} \tag{3.3}$$

where $\mu_0(E)$ corresponds to the atomic-like background underlying the XAFS pattern and $\Delta\mu_0(E)$ being the normalization factor corresponding to the absorption edge jump (a step-function-like sudden increase of the net absorption coefficient at the ionization threshold). At this point, it is convenient to switch from the energy space to photoelectron wavevector space, so called *k-space*, in order to describe the interference effects in electron scattering. Using Eq. 3.1 and/or 3.3, we can parameterize the EXAFS function $\chi(k)$ as follows:

$$\chi(k) = \sum_i S_0^2 N_i \frac{|f_i(k)|}{kR_i^2} \sin(2kR_i + 2\delta_c + \phi) e^{-2\sigma_i^2 k^2} e^{-2R_i/\lambda(k)}, \tag{3.4}$$

which is the a standard EXAFS description proposed by D. Sayers et al. in Ref. [3]. The structural parameters, for which the subscript i refers to the group of N_i atoms with identical properties, e.g., bond distance and chemical species, are (a) the interatomic distances R_i, (b) the coordination number (or number of equivalent scatterers) N_i, and (c) the temperature-dependent root mean square fluctuations in bond length σ_i^2, which should also include effects due to structural disorder. Furthermore, $f_i(k) = |f_i(k)|e^{i\phi(k)}$ stands for the backscattering amplitude, δ_c is the central-atom partial-wave phase shift of the final state, $\lambda(k)$ is the energy-dependent photoelectron mean free path (not to be confused with photoelectron's de Broglie wavelength λ_e), and S_0^2 is the overall amplitude reduction factor. Although the original EXAFS formula was derived to account for SS events from neighboring atomic shells only, the same phenomenological description can be used to represent the contribution from N_i equivalent MS contributions of total path length 2R [11,185]. In relation to the structural analysis, the EXAFS description provided by Eq. 3.4 includes all the most relevant and essential parameters required for fitting the local atomic structure around the absorbing atom from the measured EXAFS [236, 237]. The dependence of the oscillatory structure on interatomic distance and energy is described by the $\sin(2kR)$ term.

Fig. 3.6 shows this oscillatory part for an example of two nearest-neighbor distances $R_1 < R_2$.

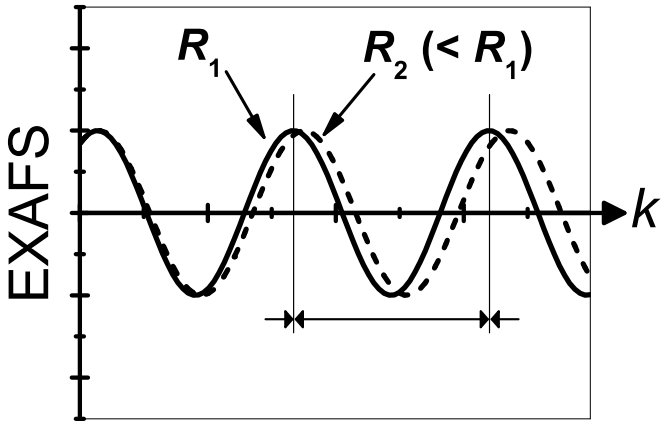

Figure 3.6: The characteristic oscillations of the EXAFS function χ(k) (obtained via Eq. 3.4) in photoelectron wave vector space (k-space) are the measure of the interatomic bond distance between the absorber an the nearest neighbors R_1. The observed shifts of χ(k) will reflect the bond length changes as shown here in the case of bond contraction $R_2 < R_1$.

It is clear that $\chi(k)$ oscillations gradually shift in k-space (and thus energy space) with respect to both distances, which can be directly linked to different interatomic distances from R_1 to R_2 ($\leq R_1$) and such shifts are often observed in XAS spectra of two distinct chemical species (i.e. the ground and excited states of a complex) as discussed in case of $[Ru^{II}(bpy)_3]^{2+}$ and $[Fe^{II}(bpy)_3]^{2+}$ in Chapters 5 and 6, respectively. The decay of the photoelectron wave due to the mean free path and finite lifetime (including the ultrashort core-hole lifetime) of the electron is captured by the exponential term $e^{-2R_i/\lambda(k)}$. This factor is largely responsible for the relatively short range probed in an EXAFS experiment (up to a few tens of angstroms at most). The strength of the reflected interfering waves depends on the type and number of neighboring atoms and is governed by the backscattering amplitude $|f_i(k)|$ and hence is primarily responsible for the intensity of the EXAFS signal. Other factors, namely, the spherical-wave factors $(1/kR_2)$ and mean-free path terms, appear secondary but are important for a quantitative description of the EXAFS amplitude. The phase factor $\phi = \arg f(k)$ reflects the quantum mechanical wavelike nature of the backscattering process. A somewhat larger contribution to the overall phase is given by the phase shift $2\delta_c$ at the position of the absorbing atom, since the photoelectron encounters the potential created by this atom twice. These phase shifts account for the difference between the measured and geometrical interatomic distances, which is typically a few tenths of an angstrom and must be corrected by either a theoretical or an experimental reference standard. Another exponential term, $e^{-2\sigma_i^2 k^2}$, present in Eq. 3.4, accounts for the Debye-Waller (DW) broadening to a good approximation, is partly due to thermal effects, which cause the atoms to fluctuate around their

equilibrium atomic positions. This small jitter in their positions smears out the otherwise sharp interference pattern of the rapidly varying $\sin(2kR)$ term with increasing k. The effects of structural disorder are similar and they give an additive contribution to σ_i^2. In the case of asymmetric distribution of distances within a scattering shell (large anharmonicity), a cumulant expansion of the EXAFS equation may include the higher orders of σ_i^2 within the DW factor (i.e. σ_i^4 etc.) and the total phase of the EXAFS function [4]. In any case, the DW effect seems more pronounced at shorter photoelectron wavelengths, and hence it terminates the EXAFS at sufficiently large energy beyond $k \sim 1/\sigma$, which is typically around 10 $\mathrm{\AA}^{-1}$. Finally, S_0^2 is a many-body effect due to the relaxation of the system in response to the creation of the core hole [238]. It is usually approximated by a constant, which phenomenologically accounts for inelastic losses upon the creation of the photoelectron. The origin of such losses is related to multiple electronic excitations of other electrons in the surroundings of the absorber. A photoelectron (thus with excess of kinetic energy) can excite some passive electrons in the valence shells to either a higher-lying bound state (*shake-up* process) or to continuum state (*shake-off* process) [4]. In consequence, the loss of the kinetic energy in the excitation process will shift the phase of the corresponding EXAFS oscillation and may result in an altered interference condition, which in turn affects the measured EXAFS amplitude.

3.1.3 EXAFS Analysis

The most powerful application of Eq. 3.4 comes from the fact that it allows to express the complicated oscillatory pattern found in the XAS spectra in terms of a sum of damped sine waves with their characteristic periods, which are related to the different interatomic distances via the $\sin(2kR_i)$ term [4, 185, 214, 239]. Soon after Eq. 3.4 was proposed, it was found out that a Fourier transform of the EXAFS spectrum $\chi(k)$ (with respect to k) will deliver a corresponding frequency spectrum of the oscillatory part, where the characteristic frequencies will correspond to the interatomic bond distances between the absorber and the surrounding atomic shells [236]. Therefore, the Fourier spectrum delivers a pseudo radial distribution function (RDF) of the first nearest neighbor distances [240]. The general procedure applied in the EXAFS analysis is schematically plotted in Fig. 3.7.

The initial step requires an additional weighting of the raw $\chi(k)$ EXAFS function by k_n (where n typically ranges from 1-3) in order to account to stronger damping of the EXAFS oscillations at higher k values. The truncated and weighted $k_n \times \chi(k)$ accompanied by a convolution with a special window function, which selects the k-range to be used in the analysis, e.g. it suppresses the high frequency noise pattern at higher k-values). The subsequent Fourier transformation (FT) delivers the above mentioned Fourier spectrum in R-space with the specific interatomic distances. At this point, the convolution with another window function allows selective analysis of a given shell of the RDF by truncating the FT spectrum and its inverse FT (FT^{-1}) delivers the corresponding EXAFS function with only those contributions, which

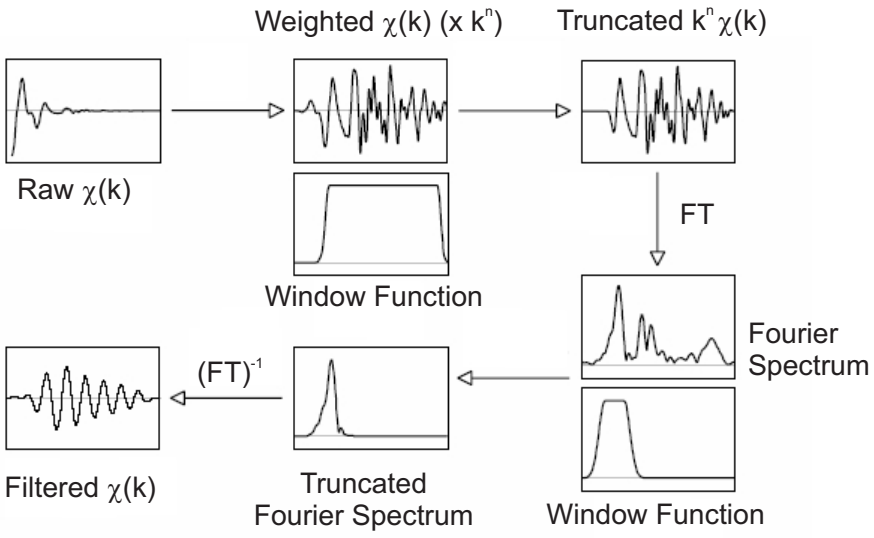

Figure 3.7: Generic scheme showing the consecutive steps of a standard EXAFS $\chi(k)$ data treatment procedure, including the their weighting, windowing, conversion in the conjugate R-space (via Fourier transformation) and the EXAFS filtering (see the text for more details).

correspond to the analyzed shell (the so called filtered $\chi(k)$). In Chapters 5 and 6, the above described analysis was applied to the first peak in the RDFs of the EXAFS spectra of aqueous $[Ru^{II}(bpy)_3]^{2+}$ and $[Fe^{II}(bpy)_3]^{2+}$ complexes respectively.

In the first case, the limited k-range of the $\chi(k)$ data (due to a naturally limited energy separation between L_3 and L_2 edges of Ru, ca. 150 eV, which translates into ca. 6 $Å^{-1}$), hindered 3 atomic shells underneath the first Fourier peak and as the consequence three scattering contributions were need in order to fit the R-space data. In the later case of Fe complex, the range of the data in k-space allowed to separate the Fe-N shell (these measurements were doe at K-edge of Fe) from the nearest Fe-C shells and thus with only one SS contribution the corresponding first peak in the Fourier spectrum was fitted. In both cases, prior to actual fitting. we have followed the standard EXAFS analysis procedure, as schematically sketched in Fig. 3.7. The specific details concerning these analyses are described in Section 5.2 ($[Ru^{II}(bpy)_3]^{2+}$) and Section 6.3.2 ($[Fe^{II}(bpy)_3]^{2+}$).

3.1.4 Conclusions

In the scope of the scattering theory, we can conclude that at high energies the scattering of excited electrons is weak, such that the only significant contributions to the final state wave function in the vicinity of the absorbing atom come from paths in which the electron is scattered only once (EXAFS). However, when lowering the photoelectron energy into the XANES region, MS becomes more and more dominant. It appears from the above that because MS is sensitive to multiatomic correlations, it delivers information not only on the radial distances of the surrounding atoms but also on their orientations relative

to one another, including bond angles. In comparison, EXAFS mainly delivers the pair correlation function (i.e. RDF) and the mean displacement. In summary, direct structural information can be extracted from XANES, which, like EXAFS, is due to scattering of the photoexcited electron by neighboring atoms. However, while for EXAFS the theory is straightforward and easy to handle, XANES requires more elaborate theories beyond one-electron theories. Furthermore, multielectronic interactions complicate matters and their theoretical treatment is specific for each class of atom and requires introducing spin-orbit effects, crystal-field effects, and multiplet effects that originate from two-electron Coulomb and exchange interaction between electrons from different orbitals. These, combined with the overlapping contributions that occur in the XANES, have delayed its use as a structural technique compared to EXAFS. Up to date, it is mainly used to deduce the electronic structure of various systems. Only very recently, the first quantitative treatment of the XANES spectra, within the so called full MS theory (for more details see the following sections), has delivered the structural details on a comparable level to the EXAFS analysis.

To summarize, XAS offers the following advantages as a spectroscopic technique for the analysis of geometric structures:

- It can be implemented in any type of media: gases, liquids, and solids (amorphous or ordered)
- It is highly selective, since one can interrogate one type of atom specifically, e.g., the central atom of a given solute inside a bath of solvent species by simply tuning into its characteristic absorption edge.
- It probes mainly the local structure around the atom of interest, which is fine for ultrafast processes, since short time scales correspond to short distance scales, i.e., on the femtosecond time scale the evolving chemical reaction affects only nearest neighboring atoms.
- It delivers both electronic and structural information. This is essential in chemistry, as it is the electronic structure changes that drive the nuclear dynamics (at least in a Born-Oppenheimer regime).
- The precision of structural determination by EXAFS is on the order of 10^{-2}-10^{-3} Å, which is excellent for observing the transient structures of reaction intermediates.

All these advantages are particularly attractive for the study of dynamical processes in chemistry, biology, and material science and call for the extension of XAS to the ultrashort time domain.

3.2 Basic Principles of Multiple Scattering Theory

The multiple scattering (MS) theory, in general terms, describes the transport of particles interacting with a host medium through various processes of scattering, absorption and emission, the first-mentioned being the most important and significant one. In the particular case of the XAS phenomenon [11, 241–243], the MS theory describes the propagation and the scattering events that a photoexcited deep-core electron undergoes, once it is ionized from the absorbing atom and gains sufficient kinetic energy to propagate outwards from the atom. The presence of the surrounding atoms (including their electronic clouds) causes the photoelectron to move on "bent" trajectories and to scatter backwards onto the absorber and thus a quantum interference effect of both the outgoing and returning waves occurs. In plain words, one can think of an XAS experiment results as of an interferogram of the atomic environment around the absorber.

3.2.1 Understanding XAS Phenomenon within MS Theory

The mathematical description of the XAS phenomenon is rather involved, therefore it will be limited here to its most fundamental aspects [11, 241, 242]. As mentioned above, the x-ray absorption process involves the photoionization of a deep core electron, creating a core-hole state, and the excitation of the photoelectron to either higher-lying unoccupied states (below the ionization limit) or continuum states above the ionization threshold. In a one-electron picture, within a dipole approximation, XAS measures the dipole-mediated transition of a deep core electron $|i\rangle$ of the absorbing atom into an unoccupied final state $|f\rangle$. The probability for such a transition is described by Fermi's Golden Rule:

$$\mu(E) \propto \sum_{f}^{E_f > E_F} |\langle f|\hat{\varepsilon}\cdot\vec{r}|i\rangle|^2 \delta(E - E_f) \tag{3.5}$$

where $\hat{\varepsilon}\cdot\vec{r}$ is the dipole operator for the incident electromagnetic wave interacting with the atom and the summation extends over all the energies above the Fermi energy E_F. The deep core initial state $|i\rangle$ is usually the $1s$ (K-edges), $2s$ or $2p$ state (L-edges), although transitions from higher lying core levels (N, M, etc.) are also regularly measured. The XAS description is based on the accurate representation of the quantum interference of these two states using Eq. 3.5. In addition, the integral included in Eq. 3.5 applies to a product of electron wavefunctions, where the initial state can be approximated, to a good extent, as an extremely localized state around the absorber nucleus (and thus the dipole approximation is well-justified), whereas the final state contains a mixture of outgoing and back-scattered electron waves. Therefore, the absorption coefficient $\mu(E)$ in Eq. 3.5 will be mainly affected by the interference

pattern at the center of the absorbing atom. One can distinguish two general strategies to solve Eq. 3.5. The first one consists of an accurate representation of both the initial core state $|i\rangle$, the presence of a deep-core hole, and the final state $|f\rangle$, followed by an explicit evaluation of the integral implied by the Fermi's Golden Rule. This strategy, in general terms, is the approach taken by *molecular orbital* (MO) theory [95, 96].

The second approach uses the MS theory to rewrite Eq. 3.5 in terms of Green's function [11, 244]. In this case, we consider a flat interstitial potential V_{int} due to the system of ions and electrons in a given system (region II in Fig. 3.8a). The ions are the scattering sites of potential δV. The total Hamiltonian of such a system can be expressed as $H = H_0 + V_{int} + \delta V$. The scattering atomic potentials H_0 are approximated with spherically symmetric Coulomb-type potentials embedded within the interstitial potential V_{int} (region I in Fig. 3.8a). This approximation is called *muffin-tin* (MT) potential approximation. Within the MT approximation, the electron wavefunction can be expressed by spherical harmonics within the MT potential with additional radially-dependent part, which extends into the V_{int} region. The outer region (region III in Fig. 3.8a) sets the specific boundary conditions onto the electron wavefunction acting within the cluster sketched in Fig. 3.8a.

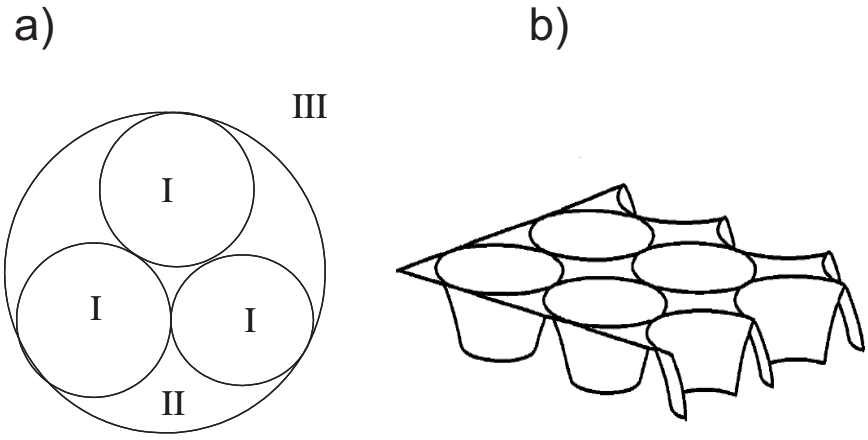

Figure 3.8: Schematic representation of the muffin-tin potentials. In (a) the top-view of a MT potential energy surface is shown, indicating the three characteristic regions used in their construction. The region I describes the atomic potentials, embedded into a flat interstitial region II and surrounded by the outer region III, which provides the suitable boundary conditions for the photoelectron wavefunction. In (b), a 3D sketch of the MT potential energy landscape is displayed. The effect of the flat interstices is clearly visible. Taken from Ref. [11]

In Fig. 3.8b, a two-dimensional drawing of the potential energy landscape within the MT approximation is illustrated. Here, only the regions I and II of Fig. 3.8b are depicted in order to highlight the truncation (approximation) effect of the flat interstitial potential V_{int} superimposed onto the spherically-symmetric atomic potentials. Using the total Hamiltonian H, the one-particle Green's function can be written as $\mathbb{G}(E) = 1/(E - H + i\zeta)$ (where ζ is the net lifetime of the core-hole state including the effects of both intrinsic and extrinsic losses) [11]. The Eq. 3.5 can be then rewritten, using the operator

form of this Green's function, $\sum_f |f\rangle\mathbb{G}(E)\langle f|$ [241], as:

$$\mu(E) \propto \frac{1}{\pi} Im\langle i|\hat{\varepsilon}^* \cdot \vec{r}\mathbb{G}(E)\hat{\varepsilon} \cdot \vec{r}|i\rangle|\Theta(E - E_f) \tag{3.6}$$

where $\Theta(E - E_f)$ is the Heaviside step function to assure that the absorption cross section is non-zero only above the Fermi energy E_F. In this representation, $\mathbb{G}(E)$, is the full one-electron propagator in the presence of the scattering potential. At this point, the MS expansion can be derived by expanding the Green's function to a Dyson series,$\mathbb{G} = G^0 + G^0TG^0 + ...$, where G^0 is the free-electron propagator, $\mathbb{G}(E) = 1/(E - H_0 + i\zeta)$ and $T = V + V\mathbb{G}T$ is the full atomic scattering matrix [245, 246]. The T-matrix can be expressed in terms of the single site scattering matrices t by:

$$T = t + tG^0t + tG^0tG^0t + ... \tag{3.7}$$

The Dyson equation is then solved using Eq. 3.7, which is recognized as the Taylor expansion:

$$\mathbb{G} = G^0 + G^0tG^0 + G^0tG^0tG^0 + ... \tag{3.8}$$

$$\mathbb{G} = (1 - G^0t)^{-1}G^0 \tag{3.9}$$

The MS fine structure can then be obtained by taking an appropriate trace over the matrix $\mathbb{G}$, which includes all those elements of $\mathbb{G}$ corresponding to the absorbing atom and the angular momentum of the photoelectron final state.

3.2.2 Theoretical Calculation of XAS Spectra

The MS equations included in the preceding section are the starting point for understanding how modern theoretical computer codes used in XAS calculations operate. In the scope of this thesis, a brief description of two MS codes will be given, namely FEFF and MXAN codes. Both programs allow computing the XAS spectra within the MT approximation used in MS theory and in addition the MXAN code can be used to fit the experimental spectra given the initial structure of the atomic cluster and experimental data are provided. In both cases, these codes use the one-electron picture within the dipole approximation and calculate the x-ray absorption cross section by both direct and explicit inversion of the $(1 - G^0t)$ matrix in Eq. 3.9 (the XANES region, for which the so called *full multiple scattering* FMS applies) or by further expansion of Eq. 3.8 as a sum over the most relevant scattering paths, which is then used as the basis for EXAFS analysis and fitting [247].

At the end of this section a brief description of another code used throughout this thesis will be given, namely the atomic multiplet code. This code goes beyond the one-particle picture and included many-electron effects like multiplet and charge transfer effects etc. due to the strong overlap between the

core and valence wavefunctions. It can be very efficiently used to calculate the pre-edge features of the XAS spectra (only the bound-bound transitions can be reproduced by the multiplet code) and it fails to simulate the higher energy XANES or EXAFS resonances due to the fact it does not imply any of the aforementioned scattering models.

Full Multiple Scattering vs. Path Expansion Approach

Before the difference between the FMS and path expansion approaches will be given, we will try to interpret and relate the MS equations to the XAS phenomenon, as qualitatively described above. Each of the major terms in the preceding equations 3.8 and 3.9 can be given a physical meaning, which may help understanding the below details. Upon absorption of an x-ray photon, the photoelectron propagates outwards the absorber atom as a spherical wave. This is schematically depicted in Fig. 3.4a, which shows a outwardly propagating and backscattered portion of the final state photoelectron wavefunction in the vicinity of neighboring atoms around the absorber.

The $\mathbb{G}$ propagator describes all possible ways that the photoelectron can scatter from one or more of the surrounding atoms before coming back to the core-hole state [244]. Of course in a real experiment, we always measure the ensemble average of all absorbing atoms in a steady-state picture. The core-hole lifetime is on the order of 10^{-15}s, and is much smaller for high Z elements [248]. Therefore the XAS process is inherently ultrafast for a single absorber atom. In an ensemble, this effect on the XAS spectra is the core-hole broadening $\Delta E \sim \hbar/\tau_{core}$ of the measured resonances on the order of a few eVs (again it increases for high Z elements). The G^0 term describes how an electron propagates between two points in space (as shown in Fig. 3.8 a) and the matrix t is responsible for the electron scattering of a single neighboring atom. Therefore we can interpret the additive contribution, which appear in Eq. 3.8 as different orders of electron scattering events that the photoelectron of interest undergoes, while propagating outwards from the absorber (Fig. 3.4a). For example, the two terms included in Eq. 3.8, describe single scattering events, G^0tG^0, and $G^0tG^0tG^0$ describes all the paths the photoelectron can take by passing by exactly two surrounding atoms [249].

Some representative examples of possible MS scattering paths are depicted in Fig. 3.9. In Fig. 3.9a, an arbitrary atomic lattice is shown with the absorber atom (red circle) being at the origin of the possible scattering pathways, which enter into Eq. 3.8. The first three orders in the above-mentioned equation describe the scattering paths, which involve: 2 atoms (*single scattering*, 3.9b (i)), 3 atoms (*double scattering*, 3.9b (ii)) and 4 atoms (*triple scattering*, 3.9b (iii) and (iv)).

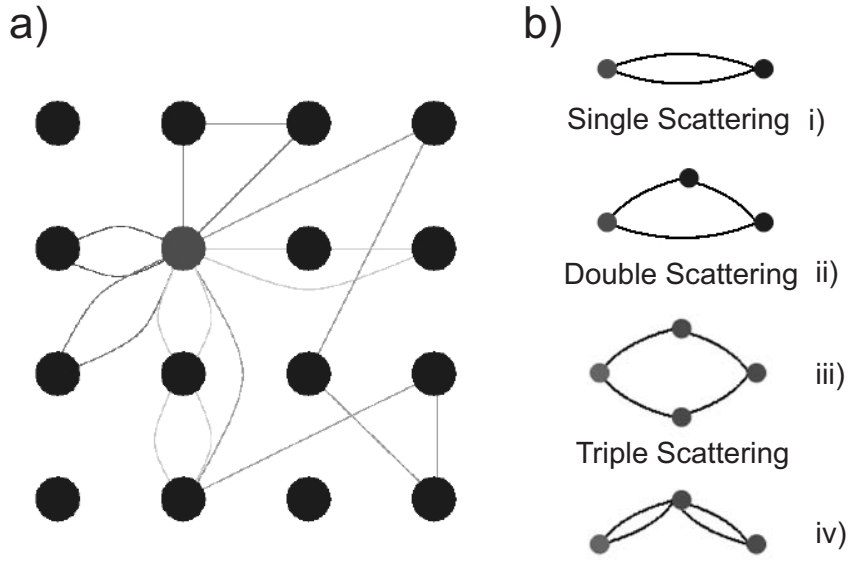

Figure 3.9: (a) Multiple scattering in an arbitrary lattice of atoms is shown here. The scattering geometries may involve not only the nearest-lying neighbors, but also atoms situated relatively far away from the absorber (light grey circle). In (b) several possible scattering paths are sketched involving: i) only one pair of atoms (single scattering), ii) only three atoms (double scattering) and iii) involving four atoms or iv) three atoms, but in four consecutive scattering event (triple scattering) [249]

Higher terms of the Dyson equation will include the MS scattering events involving 3, 4 and even more atoms. Each of these terms can be further expanded as a sum over every possible path of that order, i.e. G^0tG^0 can be expressed as the sum over all single scattering events and $G^0tG^0tG^0$ can be written as a sum of all existing double scattering paths. Therefore Eq. 3.8 can be rewritten as follows [241]:

$$\mathbb{G} = G_c + \sum_{i\neq 0} G_c t_i G_c + \sum_{\substack{i,j\neg 0 \\ i\neq j}} G_c t_i G^0_{i,j} t_j G_c + \sum_{\substack{i,k\neg 0 \\ i\neq j \\ j\neq k}} G_c t_i G^0_{i,j} t_j G^0_{j,k} t_k G_c + ... \quad (3.10)$$

where G_c is the propagator between the central atom and some neighboring atom and $G^0_{i,j}$ is the propagator between atoms i and j. The summations included in Eq. 3.10 ensure that no terms describing the propagation of the electron from an atom back to itself is are used more than once. The electron

propagation between different atoms within the cluster is referred to as a scattering path, which always begins and ends at the central atom as indicated by the G_c propagators.

With Eq. 3.10 it is clear that $\mathbb{G} = (1-G^0t)^{-1}G^0$ (see Eq. 3.9), contains all possible orders of scattering events. Explicitly inverting the matrix $(1 - G^0t)$ and multiplying it by the G^0 matrix is called the FMS approach [11, 250], which is computationally very expensive and usually required only in the low-energy (XANES) region. The path expansion approach used mainly in the EXAFS region, allows selecting the most intense (and thus relevant) scattering contributions from the overall sum of paths as described in Eq. 3.10. Especially in the high-energy region of the spectrum where single scattering events largely dominate over the MS events, this approach is applied in quantitative fitting of the Fourier-transformed EXAFS function as shown in Fig. 3.7 and applied to the analysis of the results presented in Chapters 4 and 5.

FEFF

FEFF is an *ab initio* real-space MS code [251], which delivers the theoretical backscattering amplitudes and phases used during the fit procedure of the EXAFS data. The FEFF code uses the Rehr-Albers method [244], which includes a separable representation of the Green's function propagators to overcome certain computation difficulties of the MS theory. Assuming that the absorption cross section can be factorized into terms describing the atomic background absorption modulated by the XAS, one obtains:

$$\mu(E) = \mu_0(E)[1 + \chi_\ell] = \mu_0(E)[1 + \sum_\ell \chi_\ell] \tag{3.11}$$

where $\chi_\ell = \sum_\Gamma \chi_\ell^\Gamma$ expresses the XAS modulation as a sum over Γ paths and ℓ refers to the photoelectron angular momentum (only the dipole-allowed final states are probed by the photoelectron, which are also referred to as ℓ-projected density of unoccupied states). Rehr *et al.* have shown that the MS expansion, as shown in Eq. 3.11, can be expressed in an alternative way, and they obtained [244]:

$$\chi_\ell^\Gamma = S_0^2 Im\frac{exp[i(\rho_1 + \rho_2 + ...\rho_{N+2}\delta_1)]}{\rho_1\rho_2...\rho_N} \cdot exp[-2\sigma_\Gamma^2 p^2/2] \times TrM_\ell F^N ...F^2F^1 \tag{3.12}$$

where $\rho = kr_n$ (the index n refers to n^{th} leg in the scattering path), F^N are the scattering matrices at the atomic site N, S_0^2 is the amplitude reduction factor (discussed before), p refers to the photoelectron momentum, σ_Γ^2 describes the mean-square variation in total path length (similar to DW factors) and M_ℓ is the termination matrix for the final state of angular momentum ℓ.

The above Eq. 3.12 can be also written in a more conventional notation as:

$$\chi^{\Gamma}(k) = \sum_{\Gamma} \frac{S_0^2}{kR^2} |f_{eff}^{\Gamma}(k,R)| sin(2kR + \phi^{\Gamma}(k) + 2\delta_1(k)) \cdot e^{-2\sigma_{\Gamma}^2 k^2} \cdot e^{-2R/\lambda(k)} \quad (3.13)$$

where $f_{eff}(k,R)$, which refers to the effective scattering amplitude (thus the acronym FEFF), and the remaining variables are those that were proposed by Sayers et. [3] in their empirical single-scattering formula (see Eq. 3.4)the "EXAFS" equation, but with the effective scattering amplitude and phases ($f_{eff}(k,R)$ differing from the original scattering amplitude by including its additional dependence on R). The original EXAFS equation did not include the curved-wave corrections introduced by Rehr *et al.* [244] (the R dependence reflects the spherical character of the photoelectron wavefunction as opposed to the initial plane-wave approximation used in the early EXAFS description). The latest version of the code, version 8.2 [252], can be also used to perform XANES calculation using the FMS theory as described in the preceding section.

The power of FEFF lies in the relative simplicity of the required input from the user. The calculation of the x-ray absorption cross section is based on an atomic cluster specified by a particular set of Cartesian coordinates describing the (x,y,z) positions of all the atoms involved in the cluster, including the central absorber atom in (0,0,0). The scattering potentials are then calculated self-consistently based on the MT approximation [11], using as input this geometrical structure and properly overlapped according to the Norman criterion. The charge densities are then superimposed and spherically averaged within the MT potentials and the interstitial region. The electron wavefunction is then integrated radially at each energy to obtain the scattering phases for each atom. Finally, using the T-matrix formalism and Green's function propagators [241, 244], the scattering effective amplitudes are calculated and via Fermi's Golden Rule the absorption cross sections are calculated to deliver the theoretical XAS spectrum.

MXAN

In contrast to FEFF, the MXAN code [253, 254] uses only the FMS approach and thus is limited to calculate only the initial XANES energy region of a XAS spectrum (up to 200 eV above the absorption edge [229]). However, the uniqueness and novelty of MXAN comes from the fact that it can be used for a quantitative structural analysis of the low-energy portion of a XAS spectrum by performing a geometrical fit of the analyzed structure [255]. The FMS formalism used in the MXAN procedure is analogous to what has been described before and further details can be found in a various references.

The novel extension of MXAN code, which describes the MXAN analysis using both the static and difference XAS spectra of the photoexcited aqueous $[Ru^{II}(bpy)_3]^{2+}$ complex [256], is a part of my thesis work and the results obtained are presented in Appendix A[1].

Here we only mention briefly the most relevant features of MXAN as compared to FEFF and standard path expansion approach used in the structural analysis of XAS spectra. The quantitative analysis of the XAS spectra using the MXAN code is based on the comparison between the experimental data and several theoretical iterations performed by varying selected structural parameters starting from a well defined initial geometrical configuration around the absorber (given by the set of Cartesian coordinates defining the atomic cluster used in the calculation). The optimization in parameter space is achieved by minimization of the square residual function [253, 254]:

$$\mathbb{R}^2 = n\frac{\sum_{i=1}^{m}[(y_i^{th} - y_i^{exp})\varepsilon_i^{-1}]^2}{\sum_{i=1}^{m} w_i} \tag{3.14}$$

where n is the number of independent parameters, m is the number of data points, y^{th} and y^{exp} are the theoretical and experimental values of absorption respectively, ε_i is the individual error in the experimental data set, and w_i is a statistical weight. For $w_i = 1$, the square residual function $\mathbb{R}^2$ becomes the statistical χ^2 function. Here, a constant experimental error equal to 0.6% of the main jump for the whole experimental data set was assumed. Theoretical calculations of the scattering amplitudes and phases are performed within the FMS approach, i.e. the inverse of the scattering path operator was computed exactly, avoiding any *a priori* selection of the relevant MS paths, and using the MT approximation for the shape of the potential [257]. The MT radii are chosen according to the Norman criterion with a specific percentage of overlap, and the potential is recalculated at each step of the minimization procedure, keeping the overlap factor fixed. The exchange and correlation part of the potential is calculated in the framework of the Hedin-Lundqvist (HL) scheme. In order to avoid overdamping of the spectrum at low energies, caused by the use of the full complex HL potential, MXAN uses a phenomenological approach to calculate the inelastic losses. It is based on the convolution of the theoretical spectrum, calculated by using only the real part of the HL potential, with a suitable Lorentzian function with an energy-dependent width given by $\Gamma = \Gamma_c + \Gamma(E)$. The constant part Γ_c accounts for contributions of the core hole lifetime and the experimental resolution, while the energy dependent term $\Gamma(E)$ represents both intrinsic and extrinsic inelastic processes [255, 258]. $\Gamma(E)$ is zero below the onset energy E_s, and begins to increase from a value A_s, following the universal functional form of the mean free path in a solid. This method introduces three non-structural parameters that are derived during the fit on the basis of a Monte Carlo search, at each step of the computation.

The real advantages of using *MXAN* include in energy space fitting of the low-energy XAS spectra (avoiding systematic errors due to EXAFS function

[1]Benfatto et al. J. Phys. Chem. B, 2006

truncation in the windowing procedure and during the Fourier transformation) for both K and L edges, the FMS approach reproduces very well MS resonances in the close vicinity to the absorption edge. It can be used to fit directly the transient difference spectra measured during a time-resolved XAS experiment (see the discussion in the attached article and Chapter 5) and extract correlations between the excitation yield and the optimized bond distance change. In addition, some of the non-structural parameters, like chemical shift, can be modeled and quantified during the MXAN fitting procedure, which yields additional electronic information about the investigated system.

TT-Multiplets

Applying one-electron codes (where one-electron refers to the one-electron core excitation) to describe the $1s$ core excitation (thus around K edges) usually yields excellent agreement with the measured data. However, it breaks down for the case of higher-lying edges, i.e. $L_{2,3}$ edges [259]. This discrepancy is caused by the increasing overlap of the core wave function with the valence wave functions, which is negligible in case of most $1s$ initial state holes. In the final state of an x-ray absorption process, one finds a core hole state, for example a $2p^5$ configuration. When one studies a system with a partly filled $3d$-band, (i.e. Fe complexes) or $4d$-band, ($[Ru^{II}(bpy)_3]^{2+}$), the $2p$ hole and the $3d(4d)$ holes will have radial wave functions that overlap significantly [260,261]. This wave function overlap is an atomic *multiplet effect* that can be very large [95]. It creates final states that are found to strongly couple to the deep-core $2p$ wave function. This effect is well known in atomic physics and actually plays a crucial role in the calculation of atomic spectra. *Theo Thole* (TT) multiplet code [262–264] used in the interpretation of $[Ru^{II}(bpy)_3]^{2+}$ results (Chapter 4) and is based on the total Hamiltonian H_{total} of the complex compound, consisting of the atomic Hamiltonian H_{atom} of the absorber atom, to which an electrostatic crystal field Hamiltonian $H_{crystal}$ is added as a perturbation [95]:

$$H_{total} = H_{atom} + H_{crystal} \tag{3.15}$$

The atomic Hamiltonian contains terms due to the kinetic energy of the electrons, their Coulomb interaction with the nucleus of charge +Z, their mutual electrostatic repulsion and the spin-orbit interaction of each electron. The potential due to the ligand field is treated as a perturbation to the atomic case and this is written as a superposition of spherical harmonics [108]. Using the $[Ru^{II}(bpy)_3]^{2+}$ complex as an example [35], the parameters, which enter the multiplet calculations of the XANES line shapes at the L edges, are: i) the spin-orbit splitting of the $2p$ core shell, ii) the spin-orbit splitting of the $4d$ electrons, iii) the correlations within the $4d$ valence band electrons, which are factorized via the F^2 and F^4 Slater integrals for the initial and final states (see Section 5.2 for details).

The starting point in this analysis is the calculation of the energy levels of the initial-state $2p^6 4d^N$ ($2p^6 4d^{N-1}$ for the excited state complex) multiplet

and the final-state $2p^5 4d^{N+1}$ ($2p^5 4d^N$, excited state, respectively) multiplet in a spherical (atomic) symmetry. The crystal field effects are then stepwise included, projecting the atomic multiplets onto the octahedral symmetry (O_h), then the trigonal (D_3) symmetry and including the spin-orbit interaction (ζLS) [109]. Finally, the dipole selection rules for the ground state of the initial-state multiplet to all final states in the x-ray absorption process are applied and convoluted with the lifetime and monochromator widths respectively. Further details and the simulated line shapes can be found in the Chapter 5.

3.3 Experimental Framework-XAS Detection

As mentioned in Section 3.1, XAS delivers the x-ray absorption cross section as a function of incident x-ray photon energy. Experimentally, this type of measurement can be realized in several different ways, each with its own advantages and disadvantages. In the following section, the two most commonly XAS detection modes will be discussed namely the transmission and fluorescence yield modes [6, 237]. Both techniques have been implemented in the experimental setup described in Chapter 4 and used in the measurements that delivered the results presented in Chapters 5 (transmission mode only) and 6 (both transmission and fluorescence modes). In this section, the static x-ray transmission and fluorescence detection will be explained and in subsequent paragraphs their implementation into a time-resolved XAS setup will be given.

3.3.1 X-ray Transmission Mode

The most straightforward and widely used method to measure the x-ray absorption coefficient of a given sample is in x-ray transmission mode. In this case, the observable, detected in the experiment, is the transmitted intensity of the x-ray beam I_t, which is then normalized to the incident beam intensity I_0. The x-ray absorption coefficient $\mu(E)$ can be derived according to the *Lambert-Beer* (L-B) law as via:

$$I_t = I_0 e^{-\mu(E)d} \tag{3.16}$$

where I_0 is the incident x-ray intensity, $\mu(E)$ is the linear absorption cross-section in the units of [cm^{-1}] and d the sample thickness [cm]. According to Eq. 3.16, we can then define the measured absorption signal in the following way:

$$\mu(E) = \ln\left(\frac{I_0}{I_t}\right) \tag{3.17}$$

In a transmission experiment one thus measures the transmission through a sample of a given thickness. Of course, it requires that both I_0 and I_t are simultaneously detected before and after the sample so that $\mu(E)$ can be calculated using Eq. 3.17. In principle, $\mu(E)$ refers to the total absorption coefficient of the sample, which includes not only the absorber atom (the selected atom,

whose absorption one wants to measure) but all the other atoms as well, which may come from the solvent molecules, counterions, residual lattice atoms, in which the absorber is embedded, next to coherent inelastic Compton scattering. In case of liquid samples containing $[Ru^{II}(bpy)_3]^{2+}$ and $[Fe^{II}(bpy)_3]^{2+}$ (results presented in Chapters 5 and 6 respectively), these contributions include the solute $\mu_A(E)$ absorption coefficient (the atom of interest), the solvent absorption $\mu_{sol}(E)$, and the molecular environment, in which the solute is embedded $\mu_{rest}(E) = \mu_{lig}(E) + \mu_{CI}(E)$ (ligands $\mu_{lig}(E)$ and counterions $\mu_{CI}(E)$).

Experimentally, a transmission measurement is most commonly performed by using an x-ray monochromator, which selects a given wavelength of the x-ray beam λ (within the monochromator bandwidth $\Delta\lambda$) and both the transmitted I_t and incident I_0 intensities are measured for several wavelengths. The full XAS spectrum is then recorded by sequentially stepping the monochromator through the desired wavelength (energy) range. In our experiments, we used a step-scanning double-crystal x-ray monochromator, which allows transmission measurements with a monochromatic x-ray beam with $\Delta E/E$=$1.5 \cdot 10^{-5}$. The experimental scheme used in our transmission measurements is shown in Fig. 3.10a.

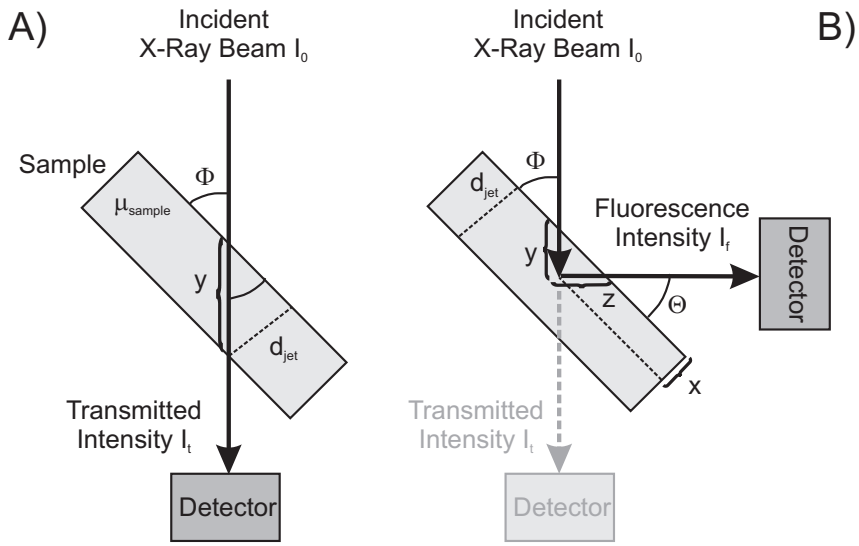

Figure 3.10: The two most commonly used experimental configurations for measuring XAS spectra include the transmission (a) and the fluorescence yield (b) modes. Here the exact geometrical arrangement used in the experiments presented in Chapter 6 is shown. The dual-mode detection allows measuring both the transmission and fluorescence signal simultaneously. The geometrical factors play an important role, especially for the x-ray fluorescence measurements (b), whereas they have no significant influence on the transmission signal (a), apart from the change of sample thickness (see text for details).

In this particular geometry, the sample (liquid jet) of total thickness d_{jet} was oriented at $\phi = 45°$ with respect to the incident x-ray beam, although in principle, one would prefer a normal incidence geometry. However, in our setup (see Chapter 4) the simultaneous detection of both transmission and fluorescence yields favors this arrangement, which minimizes the elastic scattering background recorded on the fluorescence detector (Fig. 3.10b). At this point, considering the transmitted beam intensity, the angular orientation of the sample will only affect the effective thickness that the x-ray beam traverses and thus $y = d_{jet}/sin\phi > d_{jet}$.

3.3.2 X-ray Fluorescence Mode

In some cases, it is advantageous to measure $\mu(E)$ by monitoring processes that are proportional to the absorption coefficient. X-ray fluorescence is one of these methods [265–270] next to, e.g., the total (Auger) electron yield. Detecting XAS using these techniques is particularly useful when the XAS signal of interest contributes only a small fraction of the total absorption (or when the sample transmission is very large) [271]. Isolating the useful contribution from the background in transmission measurement implies then the subtraction of two nearly identical signals (see Eq. 3.16), which requires very accurate data.

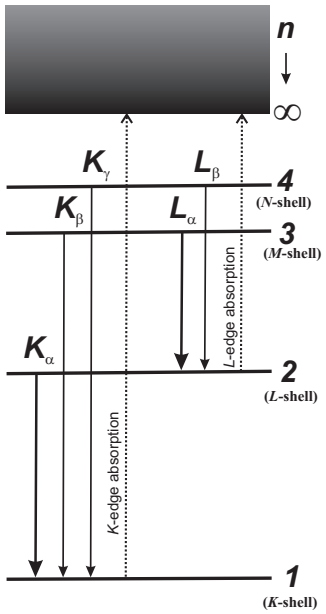

Figure 3.11: X-ray emission lines (solid arrows) originating from the K- and L-shell electron excitation (dashed arrows). The standard nomenclature used for labeling the consecutive emission lines is shown.

In the x-ray fluorescence process, a high-energy photon is emitted due to the recombination process between the core hole created upon the x-ray photo absorption and the electrons occupying the (nearest) higher lying shells, which have the largest orbital overlap and are dipole-allowed. The possible transitions are labeled according to the nomenclature as illustrated in Figure 3.11. In this

picture, a K-shell excitation is followed by spontaneous emissions from the $n \geq 2$ shells to n=1, as well as subsequent emissions from $n \geq 3$ to n=2, which occur in a cascade. An L-shell excitation induces transitions from $n \geq 3$ shells, and from $n \geq 4$ to n=3, and so on. In our case, the K-edge excitation of Fe atom is followed by dominant K_α emissions from L_3 ($K_{\alpha 1}$) and L_2 ($K_{\alpha 2}$) edges at 6405 eV and 6392 eV, with relative efficiencies of 60% and 30%, respectively. However, the core-hole recombination process can also induce the emission of an Auger electron. Both Auger and x-ray fluorescence emissions are competing processes and their relative strengths have been found to depend on the atomic number of the absorber [4]. For light elements, the Auger process is more probable whereas x-ray emission becomes more prominent for heavy elements.

For the same element, the fluorescence process is more probable for K-shell excitations than for higher lying shells, e.g. in case of Fe atom, the K-shell emission probability is 0.32 as compared to the L-shell emission probability, which is only 0.015. respectively [272]. The fluorescence and Auger signals are due to the absorbing atom only, and in a proper (geometrical) arrangement they can be considered background-free techniques (apart from the elastically and Compton scattered photons, both of which are at higher energies than the corresponding emission lines). The experimental setup for x-ray fluorescence detection used in our measurements is shown in Fig. 3.10b. In this case, a detector is placed very close to the sample, which is oriented at $\phi = \theta = 45^\circ$ with respect to the incident x-ray beam and the outcoming fluorescence photon, in order to cover a maximum fraction of the emitted isotropic fluorescence.

As mentioned above, the advantage of transmission mode originates from the direct and straightforward interpretation of the measured signal, via the Lambert-Beer law (Eq. 3.16, in terms of the absorption coefficient $\mu(E)$. In case of fluorescence mode, the measured signal I_f is merely proportional to the absorption coefficient $\mu(E)$, and needs to be corrected for the fluorescence quantum efficiency and geometrical factors. As depicted in Fig. 3.10b, the fluorescence yield at the point of absorption is proportional to the x-ray intensity I at that point and the fluorescence efficiency ϵ_A. The incident intensity I at a depth y will be equal to:

$$I = I_0 e^{-\mu(E)y} \tag{3.18}$$

The fluorescence photon produced following absorption will then have to escape from the sample and reach the detector. Therefore the measured fluorescence flux at position y within the sample is given by:

$$I_f = I_0 \mu_A(E) \epsilon_A \cdot e^{-\mu(E)y} \cdot e^{-\mu(E_f)z} \tag{3.19}$$

where $\mu_A(E)$ is the absorption coefficient due to a given core excitation of the absorbing atom, e.g. K-excitation of Fe atom, $\mu(E)$ is the total absorption coefficient including the solvent, ligand atoms and counterions found in the sample, ϵ_A stands for the fluorescence yield efficiency per unit solid angle, E is the incident beam energy and E_f is the line emission energy (fluorescence photon energy). In the following we will treat the case of aqueous $Fe(bpy)_3$ as an example, measured at the Fe K edge. We have E_f=6405 eV, which accounts

for 60% [272] of the detected emission ($K_{\alpha 1}$) and the absorption coefficient at $K_{\alpha 1}$ and $K_{\alpha 2}$ energies for $[Fe(bpy)_3]^{2+}$ in H_2O are nearly identical. Eq. 3.19 applies to particular y and z depths within the sample (Fig. 3.10b), so in order to calculate the fluorescence signal for the entire sample thickness we must integrate:

$$dI_f = I_0 \mu_A(E) \epsilon_A \cdot e^{-(\mu_T y + \mu_f z)} dy \tag{3.20}$$

Here the explicit energy dependencies were omitted, but we respect the total absorption coefficient $\mu_T \equiv \mu(E)$ and the absorption coefficient at the dominant emission energy $\mu_f \equiv \mu(E_f)$. In addition, z and y variables are dependent via: $ysin\phi = zsin\theta = x$ (Fig. 3.10b), and via substitution one obtains:

$$dI_f = I_0 \mu_A(E) \epsilon_A \cdot e^{-(\frac{\mu_T}{sin\phi} + \frac{\mu_f}{sin\theta})x} dx \tag{3.21}$$

Hence, the integrated fluorescence flux is then obtained by integration over the entire jet thickness d:

$$I_f = I_0 \mu_A(E) \epsilon_A \frac{1}{sin\phi} \int_0^d e^{-(\frac{\mu_T}{sin\phi} + \frac{\mu_f}{sin\theta})x} dx \tag{3.22}$$

$$= \frac{I_0 \mu_A(E) \epsilon_A}{\mu_T + g\mu_f} \{1 - exp[-(\frac{\mu_T}{sin\phi} + \frac{\mu_f}{sin\theta})d]\} \tag{3.23}$$

where $g = sin\phi / sin\theta$. This above-written equation describes the integrated fluorescence flux at the direction given by the angle $\theta = 45°$ in case of the setup shown in Fig. 3.10b. At this point, strict analysis would require another integration over the entire detector's solid angle, however, for geometries where $\phi + \theta = 90°$ (as it is here), the maximum error in g factor was found to be on the order of ca. 7% [273]. Therefore, we can finally write the fluorescence intensity in our geometry as:

$$I_f = \frac{I_0 \mu_A(E) \epsilon_A}{\mu_T + \mu_f} \{1 - exp[-(\mu_T + \mu_f)d']\} \tag{3.24}$$

where $g = 1$, $sin\phi \equiv \sin\theta = sin45°$ and d'=d/sin(45°). The fluorescence intensity is thus directly proportional to the absorption coefficient of the absorber, but in addition, the geometrical factors and the quantum efficiency are now included. One important remark should be made here concerning the absorption coefficient $\mu_A(E)$. It takes into account the central atom contribution to the total absorption, due to the given core-hole creation process. For practical reasons, it can be regarded as $\mu_A(E_{below}) = 0$ at energies below the absorption edge and $\mu_A(E_{above}) = \mu_A(E) - \mu_0(E)$, where $\mu_0(E)$ is the slowly varying part that is not related to the edge of interest. Although $\mu_0(E)$ is implicitly energy-dependent, it can be approximated, to a good extent, with its value just below the absorption edge, so that $\mu_A(E_{above}) = \mu_A(E) - \mu_0(E_{below})$. Eq. 3.24 is usually further approximated in two different cases: a) the *thick-sample* [266,267] and b) the *thin-sample* [271] limits.

In the first case, one assumes that the sample thickness is much larger compared to the absorption length. The fulfillment of this condition implies

that $(\mu_T + \mu_f)d' >> 1$, and thus $e^{-(\mu_T+\mu_f)d'} << 1$. Hence, the fluorescence flux coming out of a thick sample can be re-written as:

$$I_f \approx I_0 \epsilon_A \frac{\mu_A}{\mu_T + \mu_f} \tag{3.25}$$

If, in addition, the element of interest is dilute, then the XAS contribution to the overall absorption from the denominator can be neglected and the detected (I_f/I_0) will be practically equal to $\mu_A(E)$.

In the second case, for the thin-sample limit, both the sample thickness and the absorption lengths are small, so that the argument of the exponential term becomes $(\mu_T + \mu_f)d' \leq 1$ and therefore $exp[-(\mu_T + \mu_f)d'] \approx 1$. We can then Taylor-expand the exponential term to first-order, so that $e^{-(\mu_T+\mu_f)d'} \approx 1 - (\mu_T + \mu_f)d'$ and thus Eq. 3.24 reduces to:

$$I_f \approx I_0 \epsilon_A \frac{\mu_A}{\mu_T + \mu_f}[(\mu_T + \mu_f)d'] \approx I_0 \epsilon_A \mu_A(E) d' \tag{3.26}$$

As can be seen in both cases, the resulting x-ray fluorescence can be directly related to the changes in the absorption coefficient of the central absorbing atom and thus it should yield quantitatively the same XAS spectrum, as recorded in x-ray transmission [269]. In the further parts of this section, the extension of the above treated x-ray transmission and x-ray fluorescence signals to transient signals recorded in a time-resolved experiment will be given. Therefore, we remark that in case of $[Fe^{II}(bpy)_3]^{2+}$ (Chapter 6) the results were recorded in both transmission and fluorescence modes simultaneously. The fluorescence signal was analyzed according to the thin-sample limit (Eq. 3.26). Using the absorption coefficients, as presented in Table C.5 in Appendix C, we can estimate that $(\mu_T + \mu_f)d' = 0.0675$ and therefore $e^{-(\mu_T+\mu_f)d'} = 0.935 \approx 1$, which fulfills the thin-sample limit conditions.

3.4 Extension to Time-Resolved Experiments

Extending XAS experiments to the time domain implies the demonstration of its conceptual and practical feasibility. In the scope of this thesis, these mainly concern the optimization of the transient XAS signals one anticipates with present day and future sources of ultrashort x-ray pulses for a particular sample studied. In the following sections, a discussion of sample optimization and experimental boundaries set by a time-resolved XAS experiment will be discussed. In addition, definitions of time-resolved (transient) transmission and fluorescence signals will be given. A numerical example of a feasibility study performed for $[Fe^{II}(bpy)_3]^{2+}$ molecule studied in Chapter 6 will be presented in Appendix E.

3.4.1 Experimental Boundary Conditions

Time-resolved XAS experiments with picosecond time resolution make use of ultrashort excitation and probe pulses. Photoexcitation may be achieved by an ultrashort, (femtosecond) laser pulse derived from a commercial fs amplified laser system. These lasers are currently available with 1-5 W of average output power, which is roughly constant for all pulse repetition rates, e.g., at a repetition rate of 1 kHz the pulse energy at 800 nm lies between 0.5 and 5 mJ, which translates to about $2{\cdot}10^{15}$-$2{\cdot}10^{16}$ laser photons per pulse available for sample excitation. The weakest link is therefore given by the rather low x-ray pulse intensity, which typically contains 10^4 - 10^6 photons per pulse (and 0.1-0.015% bandwidth) at 3^{rd} generation synchrotron radiation beamlines. This boundary condition necessitates an optimization of the sample to minimize the number of x-ray photons required to measure a given x-ray absorption cross section with the highest possible accuracy (thus maximizing the signal-to-noise ratio S/N), so that we can monitor small changes due to the photoexcitation process [36, 74–76]. In the following discussion, we will limit our consideration only to samples in liquid phase, which are the ones investigated in this thesis.

Another strong discrepancy lies between the optical and x-ray absorption cross-sections in matter. Optical absorption bands have cross-sections in the order of 10^{-17} to 10^{-15} cm^2. On contrary, x-ray absorption cross-sections are typically 2 to 4 orders of magnitudes smaller; therefore the interaction of the sample with the x-ray probe-pulse is weak, yielding small x-ray signal changes. In addition, the sample optimization implies a compromise between the concentration of the solute and the background absorption due to the solvent. Neglecting the photoexcitation process for the moment, in general, increasing the solute concentration c and decreasing the sample thickness d optimizes the conditions for measuring time-resolved XAS, until we decreased the solute-only transmission to ca. 10.5 % (or ca. 0.98 OD). Thus, we can determine the optimum concentration of a given solute, if we fix the sample thickness *d*.

Next, we consider the x-ray spot size, which influences the laser excitation requirements. At typical 3^{rd} generation bend magnet beamlines (e.g. beamline BL 5.3.1 at the ALS), we have x-ray foci in the 100-300 μm diameter range. The divergence of the x-ray beam is inherent to the source properties and limits the brilliance of the beam. Therefore, modern synchrotrons like the SLS offer additional special optics, e.g. KB focusing mirrors [274], may significantly reduce the x-ray focal size down to 1-10 μm range, at the expense of the x-ray flux (in general). For sample concentrations in 10-100 mM range (assuming their optical cross section are in 10^{-17}-10^{-16} cm^2 range), this translates into ca. $5{\cdot}10^{14}$ and $5{\cdot}10^{15}$ molecules in the probed volume. In order to achieve a reasonable photoinduced signal we should excite as many solute molecules as possible, which requires on the order of 10^{15} laser photons per pulse, or ca. 0.25 mJ of pulse energy (e.g., at 800 nm). In other words, one should aim to increase the laser pulse intensity, until full excitation is achieved, or until the high-intensity pump conditions begin to stimulate (nonlinear) absorption

processes, which do not belong to the investigated photochemical reaction. As long as we are in the linear regime of the pump process, it is always better to increase the laser pulse intensity and sacrifice the repetition rate of the laser system. For the aforementioned examples, this argument motivates the use of a 1 kHz femtosecond laser rather than a multi-MHz system, which has orders of magnitude less pulse energy.

On the other hand, modern 3^{rd} generation synchrotron beamlines, e.g. microXAS beamline at the SLS, are far more brilliant than the bend magnet endstations and provide a photon beam of much better optical quality (less divergence). Therefore, using an optical layout as implemented at the microXAS beamline (intermediate focusing), one may achieve focal sizes below 5 μm diameter or even less. This opens new possibilities to exchange the powerful amplified 1 kHz lasers with rather compact multi-MHz laser oscillators and laser diode-based systems. In combination with smaller focal areas probed in the experiment, one can establish a compromise where an excitation yield will actually be the same as in case of low repetition rate, high pulse energy pumping. If we assume a microfocusing beamline with $10\mu m$ spot size and $100\mu m$ jet thickness, the number of probed solute species would decrease to ca. 10^{11} for 25 mM concentration. Therefore we would only need this amount of laser photons to probe the excitation volume. It translates into ca. 25-50 nJ of pulse energy at 800nm and 400nm respectively. These pulse energies lie in the range of commercially available laser systems with much higher repetition rates. It will be shown below, however, that the S/N increases linearly with the fraction of excited state species (or with the laser pulse intensity in the linear regime), while it increases only with $\sqrt{N}$ of the number of accumulated x-ray photons N [75], and thus with the repetition rate of the measurement.

The above-mentioned estimates already sketch out the basic requirements for designing the sample and choosing the femtosecond laser for a given x-ray source. However, the ideal conditions should be calculated considering the interplay between several involved parameters, such as the optical excitation and the x-ray cross-sections (including those of the excited state as well), the available number of exciting laser photons, the background absorption (mainly in the x-ray domain) induced by solvent molecules and background species (e.g., counter ions) and the sample thickness *d*. The results of such calculations will then yield a suitable sample design, which accommodates the boundary conditions, e.g., for a liquid jet sample, thicknesses below d=100 μm are inconvenient (though possible), while larger thicknesses can be considered, when required by the limited solubility and when the proportionally increasing background absorption permits this.

3.4.2 Laser-Pump X-ray-Probe Experiment

In a time-resolved XAS experiment, the laser-pump-x-ray-probe scheme is implemented, where a femtosecond laser pulse starts a chemical reaction and a delayed x-ray pulse probes the photoinduced changes in a system. In full analogy to a laser-only experiment, by scanning the time delay between pump and probe pulses one can observe the time evolution of the transient chemical species. The detected transient XAS signals will contain all the photoinduced changes between the laser-unpumped ground state spectrum and the laser-pumped excited state spectrum. The dual-mode detection (combined transmission and fluorescence yields) urges a proper definition of the transient spectra recorded in both modes and their comparison.

Transient Transmission Signal

The transmitted x-ray intensity can be defined as a function of the amount of excited species, thus modifying the Lambert-Beer law with respect to the photoexcitation yield $f(n_{sam})$, where n_{sam} is the sample concentration (in units of particles/mm^3). In the following analysis, a fixed sample thickness d=const will be used. The main adjustable parameter is n_{sam}, which in turn affects the amount of excited-state species, $f(n_{sam}) \cdot n_{sam}$, in the laser-excited volume, averaged over the sample thickness d. Below, we will estimate the photoexcitation yield $f(n_{sam})$ as a function of sample concentration using the linear L-B law, taking into account the number of incident laser photons per pulse, N_0^{ph}, and the optical absorption cross section, σ_{opt}. Given the low x-ray flux available in these experiments, the x-ray probing process is linear. Using the L-B law, already defined in Eq. 3.16, and expressing the transmitted x-ray intensity I_t as a function of the fraction of excited state species $f(n_{sam})$ (assuming $f(n_{sam}) = 0$ for the ground state), one obtains [75, 76]:

$$I_t = I_0 \cdot e^{-(1-f)n_{sam}\sigma_{gr}d} \cdot e^{-fn_{sam}\sigma_{ex}d} \cdot e^{-n_{sam}\sigma_{rest}d} \cdot e^{-n_{sol}\sigma_{sol}d} \tag{3.27}$$

where n_{sol} and n_{sam} are the solvent and sample concentrations, respectively, σ_{sol} is the x-ray absorption cross section of the solvent molecule, σ_{gr} and σ_{ex} are the x-ray absorption cross sections of the ground state (unpumped) and excited state (pumped) absorbing atom at a given x-ray energy, respectively. σ_{rest} accounts for the x-ray absorption of all residual atoms present in the molecule, i.e., the 3 bpy ligands (mainly N and C atoms) next to Cl^- counterions. We notice that Eq. 3.27 and 3.16 are identical given that the absorption coefficient $\mu(E) \equiv n \cdot \sigma = N_A \cdot c \cdot \sigma$, where σ denotes the absorption cross section (in the units of mm^2) and N_A is the Avogadro number ($6.02214 \cdot 10^{23}$ particles/M).

Setting $\Delta\sigma_{ex} = \sigma_{ex} - \sigma_{gr}$ and $\sigma_{total} = \sigma_{gr} + \sigma_{rest}$, we can re-write Eq. 3.27 as follows:

$$I_t = I_0 \cdot e^{-n_{sam}\sigma_{total}d} \cdot e^{-fn_{sam}\Delta\sigma_{ex}d} \cdot e^{-n_{sol}\sigma_{sol}d} \tag{3.28}$$

Here, the transmitted x-ray intensity is described as a function of the optical pump process and we notice the $e^{-fn_{sam}\Delta\sigma_{ex}d}$ term, which defines the contribution due the excited state created upon optical excitation with excitation yield

given by f. Therefore, the transient pump-probe signal S_{tr} in transmission will be defined as the logarithmic ratio of the unpumped x-ray transmission to the laser-pumped one, which is equal to the transient absorption T_{tr} of the photoexcited sample [75]:

$$S_{tr} \equiv T_{tr} = \ln(\frac{I_t^{up}}{I_t^p}) = f \cdot n_{sam} \cdot \Delta\sigma_{ex} \cdot d \tag{3.29}$$

Transient Fluorescence Signal

In a similar way, we can define the transient pump-probe signal recorded in fluorescence yield detection mode as:

$$S_{fl} \equiv T_{fl} = \frac{I_f^p - I_f^{up}}{I_0} \tag{3.30}$$

By using the Eq. 3.26, we then obtain:

$$T_{fl} = \varepsilon_A[\mu_A^p(E) - \mu_A^{up}(E)]d' \tag{3.31}$$

The substitution of $\mu_A^p(E) \equiv \mu_A^p = [n_{sam}(1-f)\sigma_{gr} + f n_{sam}\sigma_{ex}]$ and $\mu_A^{up}(E) \equiv \mu_A^{up} = n_{sam}\sigma_{gr}$ and using the same definition for the $\Delta\sigma_{ex} = \sigma_{ex} - \sigma_{gr}$, delivers the final expression for the transient absorption signal detected in the fluorescence mode as:

$$T_{fl} = \varepsilon_A \cdot f \cdot n_{sam} \cdot \Delta\sigma_{ex} \cdot d = \varepsilon_A^{-1} \cdot T_{tr}, \tag{3.32}$$

which establishes the relation between the transient signals measured in transmission T_{tr} and fluorescence T_{fl} modes. Both of these signals are identical apart from the constant factor ε_A^{-1}. This result confirms that the dual-detection mode delivers identical transient absorption spectra under both circumstances. Therefore, provided a proper normalization of both signals (as discussed in Chapter 6) is applied, they can be averaged together to deliver the final transient absorption spectrum (see Fig. 6.22) used in the structural analysis of the excited HS state of aqueous $[Fe(bpy)_3]^{2+}$ complex.

Signal-to-Noise Ratio

During the experiment, the measured intensities of both transmission and fluorescence signals corresponding to the excited and the ground state sample are determined by the number of x-ray photons recorded on their detectors. In order to achieve a high *signal-to-noise* (S/N) ratio, one has to accumulate for many thousands of pump-probe shots. Provided most of electronic noise is suppressed, especially low-frequency (e.g. 50 Hz) noise, the only prominent noise contribution present in the experiment will originate from the inherent shot noise of the x-ray beam (probe pulse). This one can be described by distribution function, which obeys Poisson statistics [275] of the transmitted pulse intensity, as discussed in details in Section 4.9.2 in Chapter 4. Applying

the error propagation formula [275] to Eq. 3.29 and Eq. 3.30 yields pump-probe signals, S_{tr} and S_{fl} and shot-noise determined noise contributions N_{tr} and N_{fl}, respectively, as follows:

$$N_{tr} = \sqrt{\frac{1}{I_t^p} + \frac{1}{I_t^{up}}} \tag{3.33}$$

$$N_{fl} = \frac{1}{I_0}\sqrt{I_f^p + I_f^{up}} \tag{3.34}$$

In both above equations, we have assumed that the only significant noise contribution to both pumped and unpumped intensities stems from the shot noise. In other words, once the error propagation formula is derived for Eqs 3.29 and 3.30, the standard deviation for both pumped and unpumped spectra can be substituted via:

$$\Delta I_{tr,fl}^{p,up} = \sqrt{I_{tr,fl}^{p,up}} \tag{3.35}$$

In case of transmission measurement, the ratio between Eqs. 3.29 and 3.33 defines the S/N ratio, which one aims to maximize in the experiment. Mathematically, we find the optimum experimental conditions, e.g., the optimum sample concentration n_{sam} for a fixed sample thickness d, by finding the extreme value in:

$$\frac{\partial}{\partial n_{sam}}(\frac{S}{N}) = 0 \tag{3.36}$$

In a steady-state XAS measurement, in order to measure the EXAFS of a given molecule with the highest precision and using the lowest x-ray photon flux possible, one would choose a concentration, for which the transmission above the selected absorption edge of the entire molecule is exactly 10.89%, as mentioned in preceding Section. That is, this value includes the transmission through all atoms that make up the molecule (and for ionic samples also the counterions). The solvent contribution will also decrease the total transmission below this value and reduces the overall S/N ratio, although it will not affect the optimum sample concentration, as derived from Eq. 3.36.

Laser Excitation Process

The optimum sample concentration is only one of the parameters, which enter into the global optimization considerations. By finding the optimum concentration, we can estimate the number of solute molecules within the probed volume (defined by the jet thickness and the x-ray robe focal spot size). However, the optimized pump-probe signal will also depend on the laser excitation beam properties (i.e. intensity, focal size, repetition rate) and the optical cross section σ_{opt} of the probed sample at the excitation wavelength. Among the most crucial parameters, we find the excitation (photolysis) yield f(t), which depends on many parameters, including the number of laser photons for the excitation process itself. For example, if the incident laser flux contains less photons/pulse than particles in the optimized probed volume of the sample, then the optimum concentration should be considered smaller. The excitation

yield f(n_{sam}, N_0^{ph}, σ_{opt},t), at time instance t, in one-photon absorption process (neglecting solvent and excited state absorptions at the excitation wavelength), can be calculated according to [75, 76]:

$$f(n_{sam}, N_0^{ph}, \sigma_{opt}, t) = \frac{N_0^{ph}}{n_{sam} V_{ex}^{laser}} (1 - e^{-n_{sam}\sigma_{opt} d}) \tag{3.37}$$

where the fraction of the excited state species is averaged over a constant sample thickness d, assuming the incident laser photon flux is equal to N_0^{ph}, the excitation volume covered by the laser beam $V_{ex}^{laser} = Fd$ (where F defines the focal area of the laser beam) and σ_{opt} is the optical cross section of the sample at the excitation wavelength λ_{ex} of the laser.

Ideally, F should have the size on the order of the x-ray probe focus, and typical foci diameters are in the 100-300 μm range. The recent development at the SLS microXAS beamline provided the additional focusing mirror for the hard x-ray beam (the KB mirrors), which allow focusing down to the several μm range (standard x-ray focus should not exceed a few tens of microns at the moment). This, in principle, allows decreasing F by a more than a factor of 10, if we could focus the laser beam down to several tens of μm as well. In a typical experiment shown in this thesis, a liquid jet was used with d in the range of 100-300 μm. Assuming an ideal photoexcitation process (f=1), the best sample concentration has been already estimated via Eq. 3.36 and thus quantified the best possible S/N under realistic probe conditions (e.g., the x-ray photon flux). This already helps in selecting possible XAS experiments under presently available pump and probe conditions. However, both Eqs. 3.29 and 3.32 contain a product of f and $\Delta\sigma_{ex}$, which governs the S/N ratio.

While the validity of Eq. 3.37 is based on a strictly linear excitation process, it will generally deliver high-intensity pump conditions, where the presence of nonlinear absorption processes in both the sample and the solvent cannot be neglected. As a consequence, the photoexcitation yield may become considerably smaller than calculated via Eq. 3.37. Therefore, it is necessary to determine the amount of excited-state species in a separate all-optical measurement (see Chapter 5 and 6 for $[Ru(bpy)_3]^{2+}$ and $[Fe(bpy)_3]^{2+}$), and these results have to be used in the model calculation for determining the feasibility of a given time-resolved XAS experiment.

Chapter 4

Experimental Methods

This Chapter presents the experimental setup used for carrying out the time-resolved x-ray absorption experiments at the microXAS beamline of the Swiss Light Source, Villigen, Switzerland. The obtained results are presented in Chapter 6. In addition, Appendix B includes the description of the earlier version of the setup, implemented at the beamline BL 5.3.1. [276] of the Advanced Light source in Berkeley, USA, which was exploited in order to record the results from Chapter 5.

In the following Sections, we describe the synchrotron x-ray source, the laser source, the beamline endstation, the data acquisition and timing schemes applied in order to provide reliable and controllable synchronization between both x-ray and laser pulses at the sample site. In all case, the differences between both setups will be remarked. All these above mentioned elements form a part of the picosecond x-ray absorption spectroscopy apparatus used in this thesis. In addition, we discuss the signal detection and photon statistics issues. At the end, a detailed description of the optical time-resolved setups is provided. These were used in the femtosecond transient absorption experiments on aqueous solutions of both $[Ru^{II}(bpy)_3]^{2+}$ (Chapter 5) and $[Fe^{II}(bpy)_3]^{2+}$ (Chapter 6)

4.1 Synchrotron X-ray Source

Synchrotron Radiation (SR) is the name of the electromagnetic field emitted by relativistic, accelerated charged particles (in our case the electrons), which move on closed curved trajectories, so called orbits, in the presence of static magnetic fields inside of a circular structure known as a *synchrotron* [277]. The experiments presented in Chapters 5 and 6 were performed at 2 different synchrotron sources namely at the *Advanced Light Source* (ALS) in Berkeley, USA and at the *Swiss Light Source* (SLS) in Villigen, Switzerland. A schematic drawing of a modern synchrotron storage ring is depicted in Fig. 4.1.

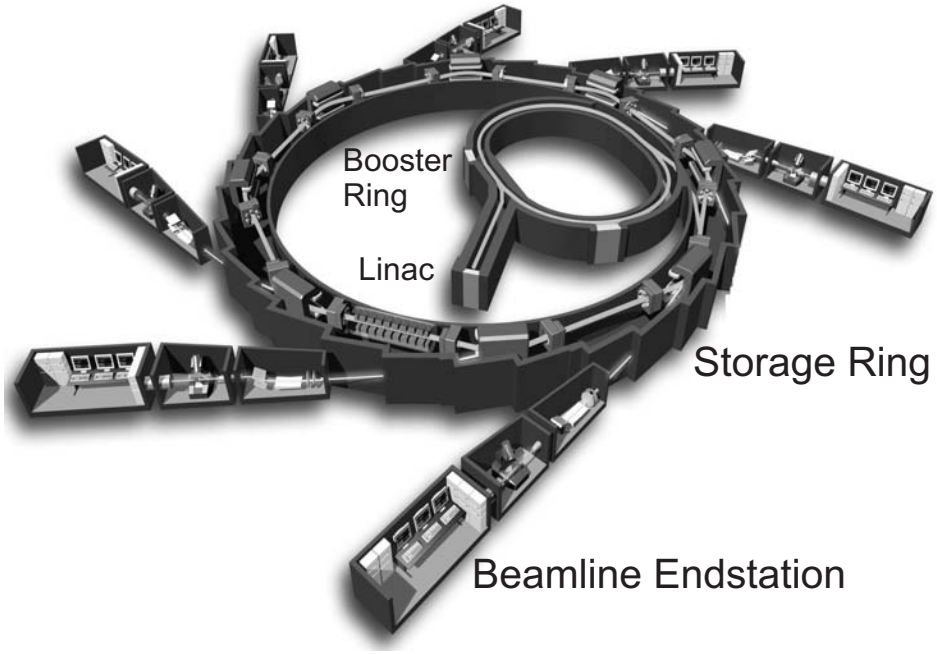

Figure 4.1: Generic scheme of a modern synchrotron storage ring [278]. The key elements of the machine are shown, including the linac, booster and storage rings and the experimental beamline endstations.

It shows all conceptually most relevant elements of the machine. Although the technical design details implemented at the ALS and the SLS are different, the basic operation scheme remains unchanged for both sources [279]. The electrons are produced in the electron gun, which injects them into the linear accelerator (the so called *linac*, see Fig. 4.1), which is located inside of the actual storage ring. The acceleration in the linac, provides an electron beam of 50 MeV (at the ALS) and 100 MeV (at the SLS). The pre-accelerated electrons enter a *booster ring* (Fig. 4.1), which is circular in shape with a small linear acceleration section, capable of increasing the electron energy up to the final value, e.g. 1.9 GeV and 2.4 GeV at the ALS and SLS, respectively. This part of the synchrotron is the reason for naming it "synchrotron", derived historically from "synchrotron cyclotron", because the magnetic fields need to be synchronously increased with the increasing electron beam energy, due to the relativistic mass increase (which decreases e/m_e). Finally, the GeV electron

beam is injected into the *storage ring* (Fig. 4.1), where it can circulate for many hours, generating the desired SR, which in turn is used at several *beamline endstations* Fig. 4.1 simultaneously. In order to suppress the energy losses of the electrons due to collisions with residual gas molecules, the storage ring is kept under ultrahigh vacuum. An additional "cleaning" of the storage ring vacuum is provided by leaving a ca. 100 ns section of the storage ring fill empty. During this gap, residual gas ions experience a ca. 1 MHz radio frequency field (RF), which effectively removes them from the electron orbit. Furthermore, the RF cavity provides the electron beam with the energy lost due to radiation at each round trip of the electron beam. In addition, scattering losses accumulate and the stored current decreases accordingly, which requires a new electron injection that adds new electrons to the remaining stored electron beam. The injection is commonly realized in two different ways; either the entire beam is restored inside of the storage ring every few hours (ca. 8 h at the ALS) or a small portion of electrons is injected every few minutes and thus the stored current remains essentially unchanged during the operation (the so called *top-up* mode at the SLS).

The electron beam circulates inside the storage ring on a well-defined circular orbit, which is maintained by magnetic field forces. These forces are provided by a complex magnetic lattice around the storage ring, which also ensures a well focused electron beam, especially within the insertion devices. The circular trajectory is formed with the so called *bending magnets* (also called *bend magnets*), which exert an additional transverse acceleration onto the electrons and cause them to radiate the electromagnetic field. The first synchrotron storage rings were built using bending magnets as the main source of SR, are grouped as the 2^{nd} generation SR sources (ALS)[1]. The modern developments in SR research pushed towards the next generation of accelerators called the 3^{rd} generation SR sources (SLS). These machines have their storage rings based on a different lattice geometry, where extended straight sections are inserted in-between the bending magnets. The SR is produced by a periodic acceleration within so called *insertion device* (ID) magnets (*wigglers*, *undulators* and *wavelength shifters*) located in the straight sections [277, 279]. The electrons are periodically "wiggled" by magnetic fields and the radiation is emitted at the wavelength of its periodic motion in the insertion device[2]. The resulting SR, coming from either bending magnets or insertion devices, is extracted at the beamline endstations, which provide a user interface between the storage ring and the experimental hutch, were the measurements are carried out. Our experiments were performed at two different synchrotrons, where we have both used the bend magnet (ALS) and the undulator (SLS) devices to extract the hard x-ray radiation for our measurements.

[1]The so called 1^{st} *generation* storage rings were built for high energy experiments, and the first SR users were using them in parasitic mode.

[2]This wavelength, after Lorentz transformation of the magnetic period inside of the insertion device (typically a few cm), contracts many orders of magnitude in the reference frame of the relativistic electron beam (electron speed is nearly that of the light).

4.2 Bend Magnet and Undulator Radiation

4.2.1 Bend Magnet

The relativistic electrons circulating on a closed orbit within the storage ring and experiencing the transverse acceleration will emit the electromagnetic field, which will appear to the observer in the laboratory frame as if all emitted in the general direction of motion. This forward collimation is particularly pronounced for charged particles traveling with a speed close to the speed of light. In this case, most of the electromagnetic field will be confined within a small cone with a vertical divergence angle (typically between 0.1-1 mrad), $\theta_V \propto \frac{1}{\gamma^2}$, where γ is the particle energy in units of its rest energy ($m_e c^2$) [279].

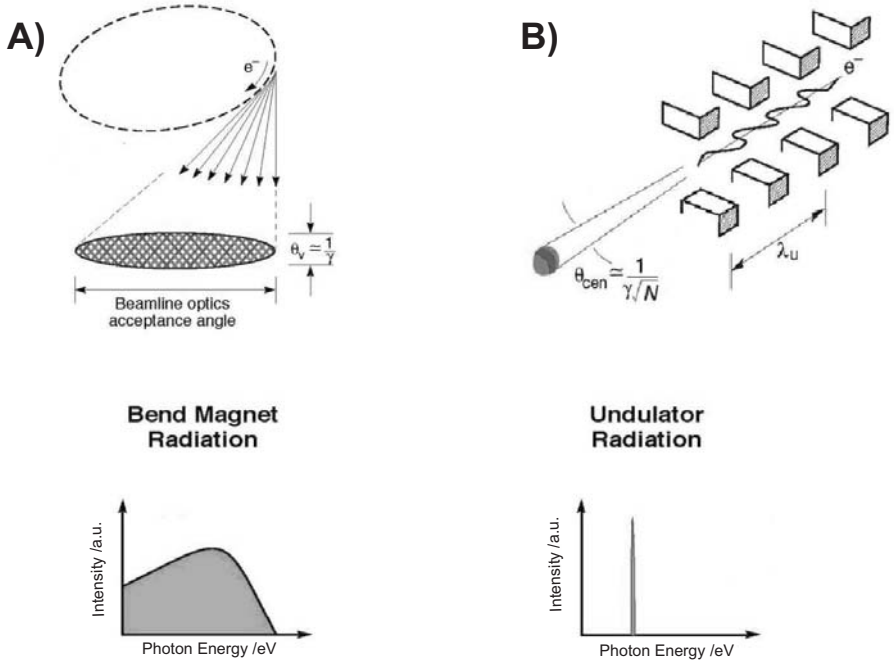

Figure 4.2: The characteristic features of (a) the bend magnet SR as opposed to (b) undulator SR are displayed. Both the spatial and spectral properties of the resulting synchrotron radiation are highlighted [280]. More quantitative description of both cases can be found in the below text.

The SR will be emitted tangentially to the orbit and remain well collimated in the nondeflecting, vertical, plane (see Fig. 4.3). The horizontal divergence θ_V is usually a few times larger and defines a small fraction of the circular path of the electron that can be seen in the laboratory frame and described as a distorted sinusoidal motion. The corresponding spectrum of a typical bend magnet is very broad and continuous and the spectral intensity varies little over an extended wavelength range, while it drops off exponentially at photon energies higher than so called *critical photon energy* $E_{cr} \propto B\gamma^2$, where B denotes magnetic field strength (Fig. 4.2a). The storage ring geometry is defined by the bend magnets, therefore it is impossible to change the magnetic field strength easily and the critical photon energy remains fixed for a given

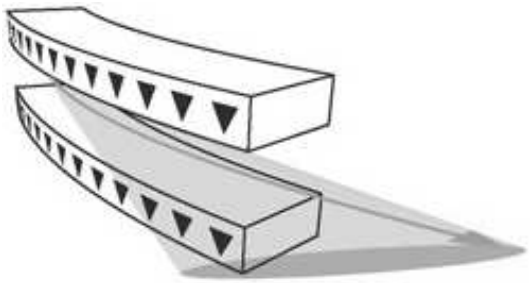

Figure 4.3: A schematic drawing of a bending magnet. At each deflection of the electron path a beam of SR is produced. The effect is similar to the sweeping of a search light from a lighthouse. Figure taken from [281]

magnet.

The experiments presented in Chapter IV were performed at the ALS bend magnet beamline 5.3.1., which is operated at 1.27 Tesla magnetic field and E_{cr}=3 keV. For x-ray photon energies in the close vicinity to E_{cr}, the bend magnet emits radiation, which is confined within an angular range close to $1/\gamma$, and thus sets the vertical divergence θ_V to approximately 0.3 mrad.

4.2.2 Undulator

In this section, we will briefly point out the main differences between the SR derived from the undulator, mostly found at 3^{rd} generation storage rings like the SLS, as compared to a bend magnet source. A schematic picture of an undulator is depicted in Fig.Fig. 4.2b. It consists of a period of magnetic poles with characteristic wavelength λ_U, where the vertical magnetic field varies sinusoidally along the undulator axis. The electrons passing through such a field will also undergo sinusoidal motion in the horizontal plane of the insertion device. An important parameter describing the electron motion within a periodic magnetic field of an insertion device is called the deflection parameter K given by [279]:

$$K = \frac{eB_0\lambda_U}{2\pi m_e c} = 0.934 \times \lambda_U[cm] \times B_0[T] \tag{4.1}$$

The maximum angular deflection of electron motion, in terms of K, is equal to $\delta = K/\gamma$ and therefore we can distinguish two types of insertion devices depending on the deflection parameter strength. For $K \leq 1$, the radiation from adjacent periods will interfere coherently, because the angular deflection of the electrons lie within the nominal $1/\gamma$ radiation cone and the magnetic structure is called *an undulator*. The resulting undulator spectrum (Fig. 4.4b). It consists of sharp peaks at harmonics of the fundamental wavelength (n=1) and is given by:

$$E_n[keV] = 0.95 \times \frac{2nE^2[GeV]}{\lambda_U[cm] \times \left(1 + \frac{K^2}{2}\right)} \tag{4.2}$$

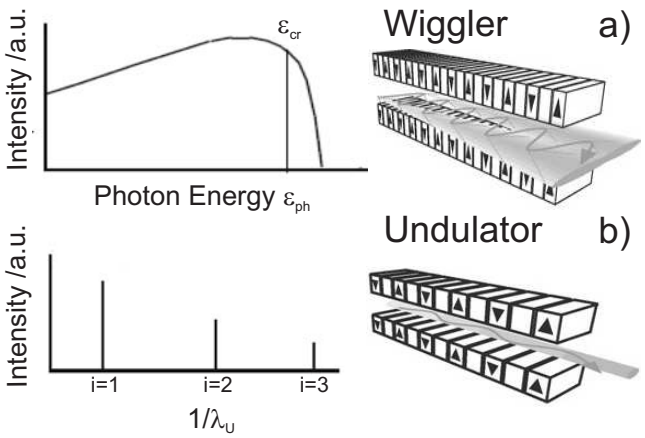

Figure 4.4: A qualitative comparison between (a) a wiggler and (b) an undulator insertion devices is sketched. In (a) at the peak of each harmonics (case (b)), a beam of SR is emitted. These beams reinforce each other and appear as a broad spectrum of incoherent synchrotron light, when viewed in the horizontal plane ahead of the wiggler. On the contrary, in (b) the undulator magnetic poles produce less deflection of the electron beam, which results in a narrow beam of coherent synchrotron light, with certain frequencies amplified by up to $1{\cdot}10^4$ times, as compared to a wiggler. Figure taken from [281]

The fundamental wavelength, and its harmonics, wavelength can be shifted in energy by varying the magnetic field of the insertion device (by changing the ga between the magnetic poles) providing a fully tunable source over an extended spectral range. In case of $K \gg 1$, the interference effects are less important and a periodic undulator motion becomes distorted due to increased relativistic effects generating higher harmonics of the single wavelength undulator radiation. The radiation from different parts of the electron trajectory adds up incoherently and the resulting spectrum merges all produced harmonics of the fundamental wavelength into a broad and continuous distribution similar to a bend magnet spectrum, however, now the intensity is n-fold increased (as compared to the bend magnet radiated intensity). This kind of magnetic structure is referred to as a *wiggler* (Fig. 4.4a).

Both wiggler and undulator radiation can be rationalized using the same physical phenomenon. Once the electron beam enters the periodic series of magnets within either of these devices, the electrons are forced to wiggle around the straight path as the feel the periodic magnetic field inside of it. As a result, a very high flux of x-rays can be achieved along either the wiggler or undulator beamline. The only difference is the deflection parameter K. In case of the undulator, the electron "wiggling" (deflection) is much weaker and the synchrotron light continues to illuminate the undulator beamline continuously. The result is a longer pulse of light rather than a series of short bursts (wiggler). Given the absence of short burst of light, the resulting radiation bandwidth is smaller, thus the undulator emission is not spread in a broad band, like in case of a wiggler (see Fig 4.4a, but concentrated into harmonics (compare in Fig 4.4b) , producing high levels of flux and brightness.

The undulators reveal another link between synchrotron light and the relativity. Apparently, the emitted undulator wavelength is not equal to the magnet array period (typically a few centimeters), rather it is a factor of 2-3×10^7 smaller, as given by typical x-ray wavelength range. The explanation may be given considering the electrons are moving across the magnetic array of an undulator or a wiggler at velocity close to the speed of light $\nu_e \approx c$. In this case, the relativity causes the electrons, traveling along its axis, to "see" the undulator squeezed along its length, due to the relativistic *Lorentz contraction* effect [277]. Quantitatively, the Lorentz contraction effectively shortens the undulator length L and period N by $1/\gamma$, so that the electron travels across the contracted undulator $L/N\gamma$. Furthermore, the emitted wavelength is affected by the same relativistic *Doppler effect*, due to electron motion during the radiation emission. The wiggling electrons inside of the undulator will emit the SR at the wavelength equal to its contracted period $\sim /N\gamma$. The Doppler effect causes a further wavelength reduction seen in the laboratory frame (e.g. at the beamline endstation where the SR is observed) by a factor $\approx 2\gamma$. Thus, the relativistic effects (combined Lorentz and Doppler effects) effectively reduce the wavelength of the emitted SR to $\lambda_U \approx L/2N\gamma^2$, and transforms the rather large undulator period into the x-ray wavelength range [282].

4.3 Temporal Structure of the Storage Ring

Due to the RF accelerating field present in the RF cavity, all synchrotron light sources are inherently pulsed sources and the filling pattern of a storage ring defines the temporal structure of the x-rays. The RF of the storage ring (at both the ALS and SLS the RF signal is 500 MHz) creates a sequence of potential wells (so called *buckets*), along the orbit, which can be filled with electrons. The number of available buckets varies at different light sources as a function of its circumference. The ALS storage ring has 328 buckets (T=656 ns), whereas the SLS offers 480 buckets (T=960 ns). In both cases, T refers to the round-trip time of the storage ring. The injected electrons that are trapped inside those buckets form the so called *electron bunches* within a well-defined spatial length (this length can be directly translated into pulse duration; ALS: ca. 70 ps and SLS: ca. 100 ps). The adjacent electron bunches are separated from each other by ca. 2 ns. Therefore the radiated x-rays are limited in their pulse widths to the spatial length of the electron bucket and at most present synchrotrons it results in 50-100 ps at full-width half maximum (FWHM).

Figure 4.5a shows a typical filling pattern used in this work at the SLS and the resulting temporal structure of radiated x-rays recorded at the sample position with fast photodiode is shown in Fig. 4.5b and c. The filling pattern at the ALS is essentially the same; the only differences come from a different number of available buckets, the length of the empty section and the total current stored in the ring.

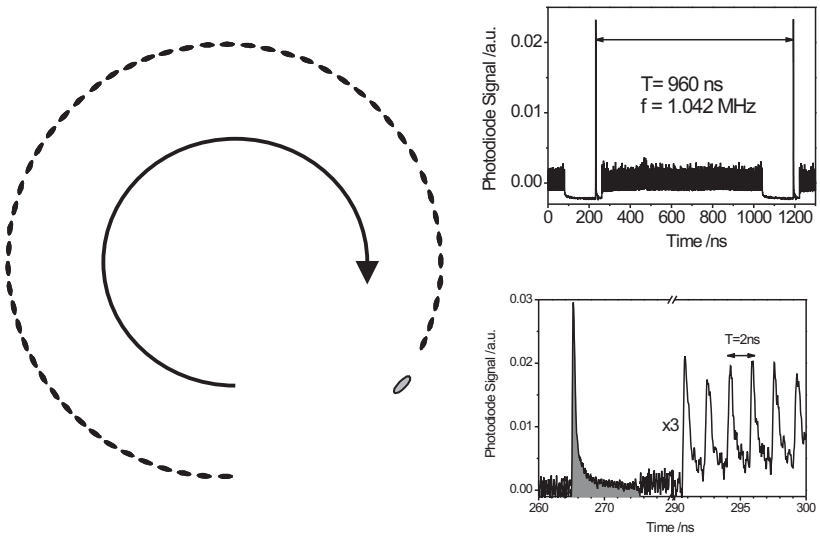

Figure 4.5: (a) A typical filling pattern of a modern 3rd generation synchrotron, e.g. the ALS or the SLS, is shown. (b) The resulting time structure of the emitted hard x-rays will be determined by the particular electron bunch filling of the storage ring (here the SLS filling pattern is presented). (c) The zoomed region within the empty gap, where a single electron bunch is located and emits a single x-ray pulse used in the experiments presented in Chapters 5 and 6

The majority of the electrons are injected into 390 adjacent buckets forming so called *hybrid pulse* (or *multibunch pulse*) of a total duration of ca. 800 ns. Subsequent 90 buckets are left empty in order to provide sufficient time for degassing the storage ring from ion residuals, which are formed inside of the storage ring. Within this gap (see 180 ns gap in Fig. 4.5b), a single electron bunch can be injected in order to provide a single x-ray pulse of ca. 50-100 ps pulse duration, which is the actual x-ray source used in our time-resolved x-ray absorption experiments. In Fig. 4.5c, a zoom into the gap showing a single x-ray pulse and a few adjacent buckets of the hybrid pulse. It can be clearly seen that the temporal spacing between them is ca. 2 ns. The rise time of the single pulse is convoluted with the photodiode temporal response, which was ca. 280 ps in this measurement. The total current stored in the ring amounts to 350 mA, with ca. 0.9 mA per bucket (ca. 6×10^9 electrons/bucket). The current stored in the single bunch within the gap is usually 3-4 times larger, although increasing its value affects the temporal characteristics of the x-rays (pulse broadening due to a more densely packed bucket). In Fig. 4.5c, the ratio between the single pulse and hybrid pulse intensities is slightly over 4, which means the single bunch current was ca. 4 mA. A detailed comparison between the ALS and SLS storage rings is presented in Table 4.1.

Relevant Parameters	ALS	SLS
Circumference /m	197	288
RF signal /MHz	500	500
Ring Round-Trip Time /ns	658	960
Electron Beam Energy /GeV	1.9	2.4
Electron Beam Current /mA	400	350 (present)
Electron Beam Lifetime /hours	6 at 400mA	"top-up"
Number of Buckets	328	480
Filled Buckets	276 buckets	390 buckets
Gap Width /ns	ca. 100	180
Current /mA	1.4	0.9
Bunch Spacing /ns	2	2
Single Bunch Length /ps	70	100

Table 4.1: The comparison between the most relevant storage ring parameters of the Advanced Light Source and the Swiss Light Source synchrotrons, including the electron beam properties and the resulting temporal structure of the emitted synchrotron radiation

4.4 Beamline Endstation

The time-resolved x-ray absorption experiments reported in this thesis were collected at two different beamlines endstations, the beamline BL 5.3.1 of the ALS and the microXAS beamline of the SLS. For some experiments, additional static x-ray absorption measurements were performed at LUCIA beamline of the SLS and the KMC-1 beamline at the BESSY synchrotron in Berlin, Germany. However, these results will not be shown here. A detailed description including all most relevant beamline components used in our measurements at the ALS has been already published in Review of Scientific Instruments[3] (see the text included in Appendix B). The following Section will focus on the description of microXAS beamline at the SLS, but point to the main differences between the two time-resolved beamlines, including the advantages and drawbacks of an undulator-based beamline with respect to a bend magnet source.

4.4.1 microXAS (Swiss Light Source)

The microXAS beamline is located in a long straight section (5L) at the SLS hosting two insertion devices (ID); a wiggler (so the called *modulator* in Fig. 4.7) and an undulator (the so called *radiator*, Figs. 4.7 and 4.6). The principal ID is an in-vacuum undulator, which serves as the radiation source and provides high-brightness hard x-rays in the energy range between 4-20 keV that covers most of the K- and L absorption edges of transition metals, lanthanides and actinides.

[3]M.Saes et al., *Rev.Sci.Instrum.*,75(2004) 24-30

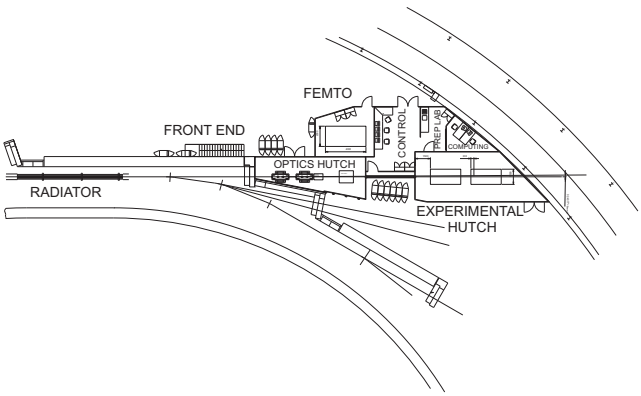

Figure 4.6: The 5L straight section of the Swiss Light Source storage ring is shown. It indicated the beamline endstation facilities, including the optics hutch, laser hutch and the experimental hutch. It also shows one of the IDs (the radiator) installed at 5L straight section. The modulator wiggler is installed further up in the 5L section and is not displayed here [283].

The optical concept of the beamline is optimized regarding *microfocusing* down to sub-micron ($<1\times1$ μm^2) spot size using a monochromatic hard x-ray beam with an energy resolution $\Delta E/E < 10^{-4}$. The beam characteristics fulfill all the necessities required for optimized XAS measurements such as spatial stability, high photon flux and flux density, high energy resolution, and minimized contamination by higher energy radiation (harmonics). Next to high-resolution x-ray absorption spectroscopy, additional experimental capabilities include, among others, micro-diffraction and micro-imaging. As a fascinating add-on, the microXAS beamline serves as the extraction path for the fs-sliced x-ray pulses (FEMTO project [284–286]). Within this project, a new technique to produce hard x-ray pulses of ca. 100 fs duration is implemented. This is the reason why the first ID (modulator, not shown in Fig. 4.6) was placed in the same straight section of the ring. The wiggler-based modulator serves as a source of laser-sliced electron bunches, which radiate femtosecond hard x-rays in the undulator-based radiator (Fig. 4.6). The basic principle of electron bunch slicing was laid out by Zholents *et al.* [287] and experimentally demonstrated by Schoenlein *et al.* [56]. A mini-gap, in-vacuum undulator serves as radiation source for the beamline. The position of the electron beam inside of the ID eventually defines the spectral characteristics of the photon beam, in terms of the horizontal and vertical beam divergence and thus its brilliance. While in the vertical dimension the source point coincidences with the midpoint of the insertion device, the horizontal virtual source point is located downstream of the radiator. At lower energies, the spatial extension of the photon source is to a considerable degree determined by the diffraction limit. A summary of the fundamental parameters of both beamlines where our experiments were performed is provided in Table 4.2 and the schematic of the layout of the microXAS beamline is depicted in Fig. 4.6 and 4.7.

Characteristics	BL 5.3.1 (ALS)	microXAS (SLS)
Insertion Device	Bend Magnet	In-vacuum Undulator
Energy Range	1.8-12 keV	5-20 keV
Photon Flux	5×10^{11} ph/s/0.015%BW (400mA)	2×10^{12} ph/s/0.015%BW (350mA)
Monochromator (Fixed Exit)	Double-crystal: Si(111) Ge(111) InSb(111) White beam	Double-Crystal: Si(111) Si(220) Ge(111) Pink beam
Energy Resolution	0.08% (at 5 keV)	0.02%
X-Ray Focal Size	100×300 μm^2	$1\times1\mu$m^2
Polarization	Horizontal	Horizontal
Beam Divergence ($\theta_H \times \theta_V$)	3×0.33mrad^2	$100\times250\mu$rad^2

Table 4.2: The comparison between the x-ray beam properties at BL 5.3.1 and microXAS beamlines of the Advanced Light Source and the Swiss Light Source synchrotrons respectively.

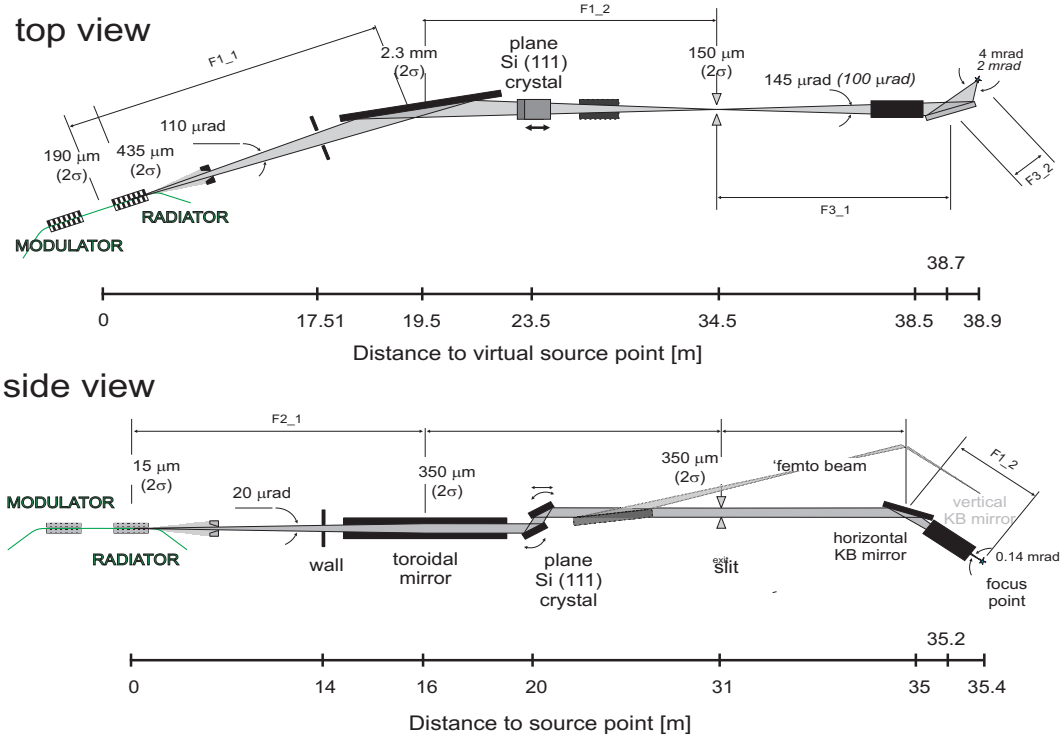

Figure 4.7: The layout of the microXAS beamline, including all main beamline components at their relative distance from the center of the undulator (radiator) as seen from the top view (top picture) and from the side (bottom picture) [288].

The calculated spectral brightness of the microXAS beamline is shown in Fig. 4.8. The grey-shaded region indicates the energy gap of the undulator between the 1st and 3^{rd} harmonics.

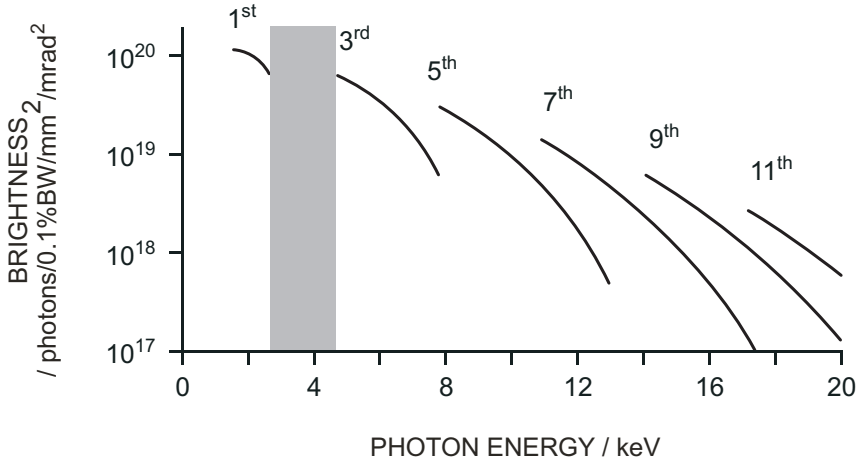

Figure 4.8: The calculated brightness curve of the microXAS beamline in the 2-20 keV energy range. The shaded area between the 1st and the 3rd harmonic indicated the energy gap, where the SR is unavailable. The radiation safety components filter this part of the flux curve in order to prevent radiation damage of some of the beamline components [289].

The spectral brightness of different odd harmonics is shown while scanning the ID gap. The front-end section includes all the SLS standard radiation safety equipment as well as an aperture system and slit systems, which reduce bremsstrahlung and the total radiation power. Eventually, these apertures define the divergance of the photon beam to 250×100 μrad^2. The first optical element, a *focusing mirror*, is located at a distance of ca. 16 m from the center of the undulator. It is a Rh(Rhodium)-coated torroidal mirror, operated in grazing-incidence mode, dynamically bent, and capable of producing a horizontal 1.3:1 image of the source, while simultaneously collimating the beam in the vertical direction. Operating in grazing-angle incidence mode, this mirror refocuses the beam horizontally at a distance of ca. 31 m from the undulator, which is subsequently imaged down to the micron-scale with additional set of focusing mirrors (see further text for details). At this intermediate focus point, adjustable slits are located which are used to redefine the source size mechanically. Given its length of 1 m and an angle of incidence of 3.5 mrad, the mirror accepts 180 μrad in the horizontal direction. This value corresponds to $\sim3.3\sigma$ of the monochromatic undulator beam. In the vertical direction, the full aperture is accepted. Another important beamline component is the *x-ray monochromator*, which is located in between the mirror and its horizontal focus point (at ca. 31 m from the source). This cryogenic-cooled fixed-exit device is equipped with two sets of monochromator crystals, Si(111) and Si(220). Concerning energy resolution, due to a vertical collimation applied, the transmitted bandwidth is mainly determined by the natural limits given by the Darwin width of the monochromator crystals used. Consequently, the energy resolution $\Delta E/E$ for a Si(111) crystal amounts to ca. 1.4×10^{-4} (0.014 % energy bandwidth BW), while for Si(220) crystals yields $\Delta E/E$ of $\sim0.6\times10^{-4}$.

Contamination by higher order harmonics is expected to be in the order of $\sim 10^{-4}$.

At the horizontal focal point the beam passes an additional slit system before entering the *Kirkpatrick-Baez* (KB) mirror system [274]. The KB mirrors are a pair of Si-crystal mirrors with the dynamical bending This strategy has several advantages as compared to direct focusing allowing an increased fraction of the beam to match the acceptance angle of the KB mirrors. The size of the source at this intermediate focus and the beam divergence will define the beam size in the experimental station and will set the limits on the KB systems characteristics. It appears that in this configuration, the working distance of these mirrors has to be shorter than 15cm, which limits the mirror length to about 10 cm. In this configuration, the first, vertically focusing mirror yields a demagnification (focusing) of 44:1, while the horizontal focus mirror demagnifies by 28:1. Adding the horizontal focusing provided by the first torroidal mirror of 1.3, the total horizontal demagnification increases up to ca 36:1. This means that for a source size of 195×14 μm^2, the final (calculated) image size of $\sim$5.0×0.3 μm^2 can be achieved. However, due to mirror surface imperfections and aberrations, the real image can be expected to be broadened to about 5.5×0.9 μm^2. In principle, using a two-step focusing strategy allows to focus the x-ray beam below this value down to a final spot size of 1×1 μm^2, or even less. However, the optimum photon flux density is reached at a beam size of $\sim$6×1 μm^2 and any further reduction in spot size will result in a corresponding reduction of the total photon flux.

The experimental station (hutch) is equipped with 2 optical tables where various experimental setups can be arranged. The time-resolved XAS setup is schematically drawn in Figure 4.9.

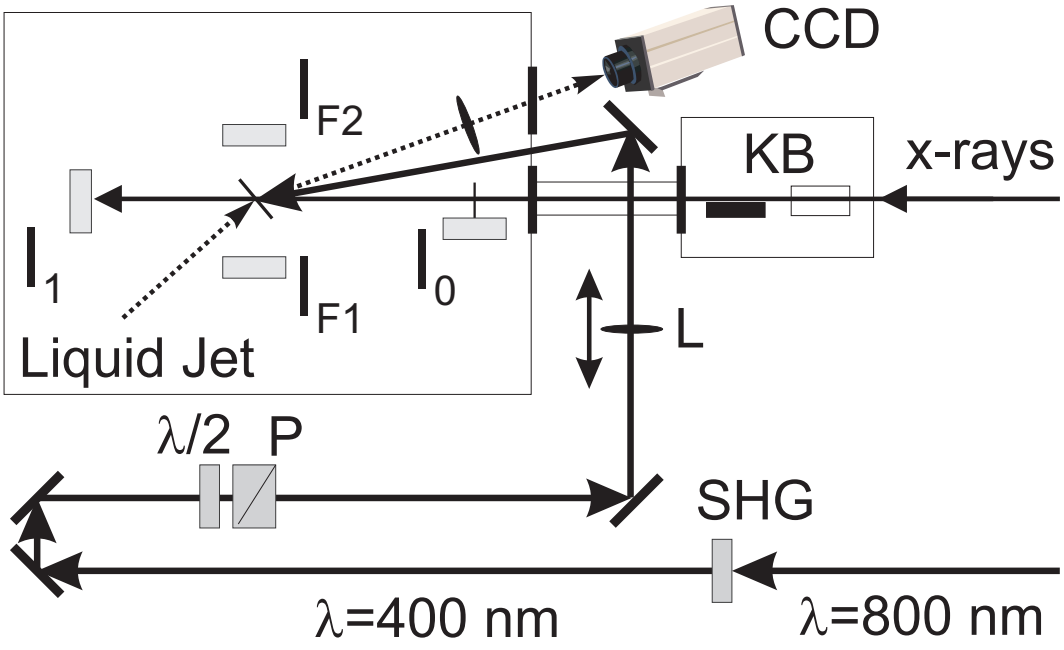

Figure 4.9: The experimental apparatus used in the dual-mode XAS detection at the microXAS beamline.

The sample chamber is placed one of the tables and connected to the beamline vacuum tube via a thin, 50 μm, Be (Beryllium) windows. Its purpose is to separate the beamline ultrahigh vacuum from the chamber, which is either kept at atmospheric pressure or purged with He (Helium) gas in order to minimize the air transmission loses at lower x-ray photon energies. In front of the chamber, the KB mirror system is placed. Inside of the experimental chamber, an x-y motorized stage is located, which serves as the sample holder mount. In principle the sample holder can be adjusted for mounting any type of samples. In the studies presented here, only liquid samples were concerned and therefore we have used a free-flowing jet made of a sapphire nozzle, which produces a thin and homogenous sheet of liquid close to the nozzle exit. The thickness of the jet is determined by the nozzle width, which can be varied between 100-500 μm. The advantages of using a free-flowing jet are the absence of any entrance windows as in case of flow cells (made of either quartz or glass) or x-ray capillaries and the possibility to use high laser intensities without the danger of damaging the entrance windows. The sample solution is flown in the jet by means of a gear pump, which provides a sufficiently fast speed of ca. 5 m/s and refreshes the solution for each incoming laser shot (at the repetition rate of 1 kHz). Both the x-ray and laser beam are spatially and temporally overlapped on the jet surface using the apparatus described in the following sections (see Fig 4.9. In this configuration, both steady-state and time-resolved XAS spectra can be detected simultaneously. The steady-state spectra are recorded in the absence of the laser beam on the sample, whereas the pump-probe signals originate from laser-excited sample. The details of the pump-probe spectroscopy and both x-ray transmission and fluorescence yield transient signals are defined and explained in the Chapter 3.

There are several detectors inside of the experimental chamber. The x-ray sensitive detectors are the *avalanche photodiodes* (APD) next to some additional photodiodes used in measurements of the focal size of both beams and their relative timing at the sample site. The technical details of all these components will be given in the subsequent Sections of this Chapter.

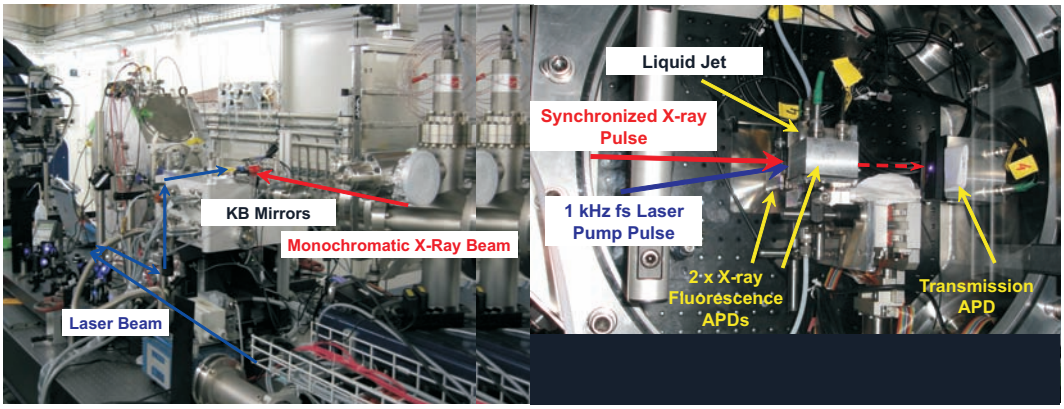

Figure 4.10: The up-stream view of the experimental setup from Fig. 4.9 (left-hand side photo) and the inside of the experimental chamber (right-hand side photo), as seen from the storage ring side of the experimental hutch.

In Fig. 4.10, a picture of the interior of the experimental chamber is shown, indicating the sample position, the direction of the incoming laser and x-ray beams and the APD detectors used in both x-ray transmission and fluorescence measurements. On the left-hand side of Fig. 4.10, the experimental setup is depicted looking from the incoming x-ray beam perspective (downstream the beamline), showing all the major aforementioned components found in the experimental hutch. The chamber flanges provide sufficient number of both signal (BNC) and high voltage bias (SHV) connectors The APD signals are pre-amplified using low-noise fast current amplifiers (FEMTO DHPCA-100) and fed into the read-out electronics (i.e. Gated Integrators). The data acquisition scheme and laser-x-ray synchronization strategy are also both described in more details in the subsequent sections of this Chapter.

4.5 Laser Source

In this section, we will describe the femtosecond laser system installed at the microXAS beamline, which provides both the pump (excitation) source for any kind of time-resolved experiment and it also serves as an electron-bunch slicing laser implemented to provide ultrashort x-ray pulses. In Fig. 4.11, a block diagram of the laser system is shown. In the following a brief description of all important parts of both phases will be included and synchronization and timing issues explained.

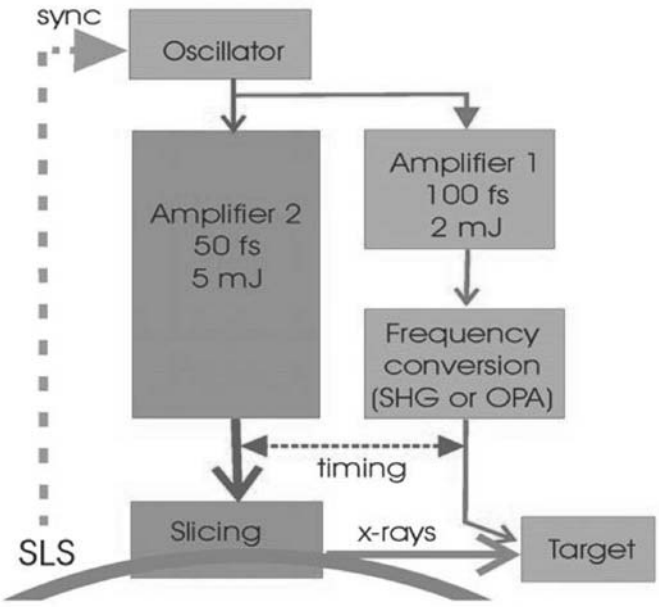

Figure 4.11: Main components of the femtosecond laser system installed in the laser hutch of the microXAS/FEMTO facility [285, 286].

4.5.1 1 kHz Amplified Laser System

The most important part of the entire femtosecond laser system is the laser oscillator. It is this component, which not only provides the seed pulses to the subsequent amplifiers but also is phase-locked to the storage ring radio frequency (500 MHz) and thus it allows synchronizing the laser pulse to a single selected x-ray pulse. The *Femtosource* laser oscillator is a Ti-sapphire based Kerr-lens mode-locked system (*Femtolaser*) pumped by a 5 W, 532 nm, CW diode Verdi laser (*Coherent*). It provides an average power of 400mW of laser light at 800 nm wavelength with a repetition rate is 100 MHz. Each output pulse is of ca. 20 fs pulse duration and ca. 4 nJ pulse energy. In order to increase the low pulse energy provided at the oscillator output, it is further seeded into the subsequent laser amplifier. The Amplifier I (see Fig. 4.11) is a commercial two-stage amplification system (*Spectra Physics*), which allows amplifying the pulses up to 2 mJ pulse energy at the same wavelength. In consequence, the output pulse is temporally broadened to ca. 120 fs and the repetition rate is decreased to 1kHz. The amplifier is based on the so called *regenerative amplification* scheme. First, the seed pulse is temporally stretched to ca. 200 ps to avoid high peak intensities on the optics inside the amplifier. Then the stretched pulses enter the intracavity of the regenerative amplifier. By switching the in-coupling Pockel's cells, the seed pulse may be trapped inside the cavity for ca. 10 round trips, each time passing through an active medium and gaining in energy. A Ti: sapphire rod, placed inside the intracavity and pumped externally by a 10 W, 527 nm, 1 kHz Nd:YLF laser (*Evolution, Spectra Physics*). During the entire amplification process inside the regenerative cavity, the seed pulse increases its pulse energy to ca. 1 mJ. Once the optimum gain is achieved, a second, out-coupling, Pockel's cell extracts (by means of polarization) the amplified pulse outside the intracavity and it enters into the second stage amplifier. Here the pulse undergoes additional 2 passes through another Ti: sapphire crystal. After compression, we obtain ca. 2 mJ, 120 fs, 800 nm laser pulses at a repetition rate of 1 kHz.

4.6 Synchronization and Data Acquisition

4.6.1 Laser Oscillator Phase-Locking

The oscillator is equipped with synchronization electronics (*Femtolock Unit*), which allows phase-locking of the oscillator frequency (100 MHz) to a Master clock signal, which is the storage ring frequency of 500 MHz with a nominal jitter on the order of less tha 1 ps. The oscillator timing, with respect to the single x-ray pulse, is a key factor in order to keep the overall synchronization of both sources. Its accuracy defines the minimum timing jitter between laser and x-ray pulses on the sample and allows a full control over the relative time delay between both of them. The general synchronization scheme is sketched in Fig. 4.12. The reference frequency is provided by the 500 MHz RF signal

(blue signal in Fig. 4.12) of the storage ring repetition rate, which defines the bunch spacing (2 ns) inside the storage ring. The laser oscillator operates at 1/5 of this frequency, which is 100 MHz (red signal in Fig. 4.12). The synchronization is achieved by locking the oscillator frequency to the storage ring and maintains a constant phase difference between both of them. A small portion of the oscillator output beam is collected by a fast photodiode. This 100 MHz oscillator signal is properly filtered (a band pass filter selects its 5^{th} harmonic) and fed into an *RF mixer*. An additional input of the mixer is the RF signal of the storage ring. The output of the mixer provides both the sum- and the difference-frequencies of both inputs. The high frequency part (sum-frequency) of this signal is eliminated through a low-pass filter and the difference signal defines the phase error signal, which is used to adjust the laser oscillator cavity length.

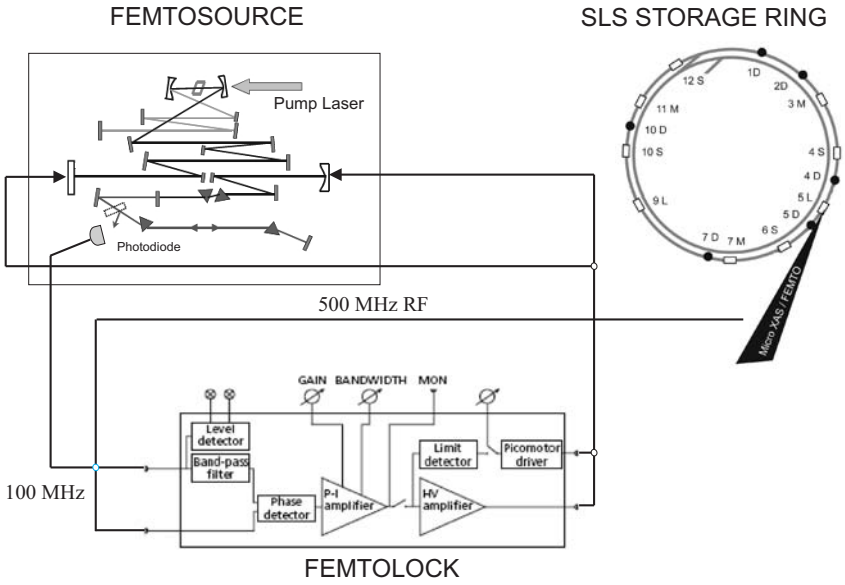

Figure 4.12: A schematic diagram showing the synchronization scheme of the laser oscillator (*Femtosource*) to the radio frequency of the SLS storage ring. The phase-locking of both the 100 MHz oscillator frequency to the 500 MHz strorage ring frequency is provided by the timing electronics (*Femtolock*), including the phase shifter.

This adjustment is done two-fold: the phase error function generates a high voltage bias, which drives either a piezo crystal or a picomotor driver, both mounted on cavity end mirrors (in Fig. 4.12 the end mirrors are those to which the bias voltage (arrows) is connected). By adjusting the cavity length, one modulates the frequency ν of the pulse train via $\nu = c/2L$, where c stands for the speed of light. The oscillator is said to be *phase-locked*, once the phase difference signal is stable. Any further small fluctuations, i.e. few tens of μm, can be compensated by continuous adjustments of the cavity length by means of a piezo crystal. In case of thermal drifts, the cavity expansion and/or contraction may exceed the micrometer range of the piezo crystal and the picomotor driver corrects the cavity length by translating the corresponding end mirror. The crucial point here is the precision, to which one may stabilize the mixer output signal. This will define the temporal jitter of both light

sources and thus will set the limit on the jitter between the pump and probe pulses used in the actual experiments. The jitter of the mixer output at the ALS was measured and estimated to ca. 5 ps by relating the noise of the phase difference signal to the non-phase-locked mixer output. Given the x-ray pulse width of about 70 ps, this jitter was not affecting the precision of the pump-probe measurements at the ALS. The jitter of the phase-locked oscillator at the SLS has not been measured experimentally so far. The synchronization strategy is basically identical, although the *Femtolock* phase-locker has been specified to provide a phase jitter of less than a few hundreds of fs (definitely < 1 ps). Typical values reported for the jitter between a laser oscillator and a synchrotron or free-electron laser (FEL) source using similar synchronization techniques are on the order of 1 ps or less.

4.6.2 Laser Amplifier Synchronization

Once the oscillator is synchronized to the storage ring, we need to ensure that the selected oscillator pulse will be seeded into the amplifier. Fig. 4.13 illustrates the synchronization of the amplifier system. The laser amplifier requires a 1 kHz trigger,which is synchronized to a particular electron bunch in the storage ring and synchronized, from which we extract a single x-ray pulse. The round-trip time $T_{round-trip}$ of this single bunch at the SLS has a period of 960 ns (1.04 MHz). Therefore we can use this signal to generate all subsequent triggers required to synchronize the laser amplifier and the data acquisition instruments.

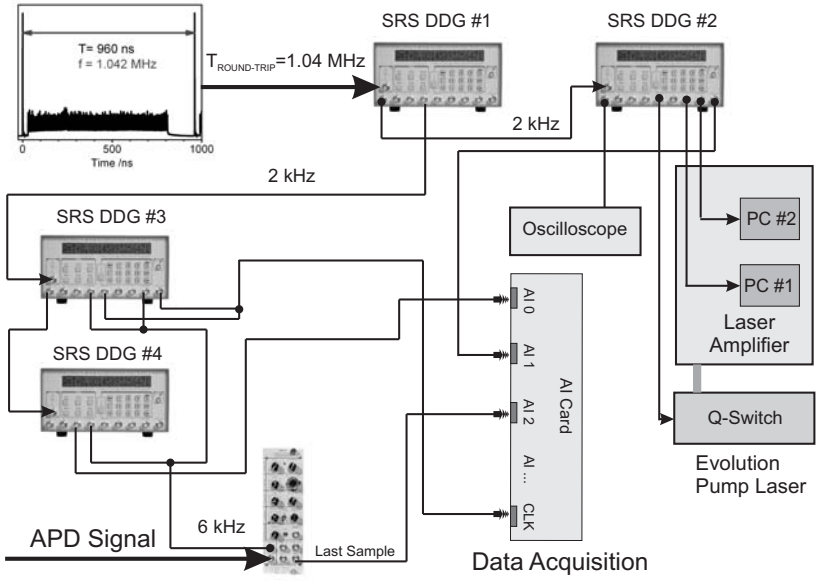

Figure 4.13: A block diagram showing the overall synchronization and data acquisition strategies implemented at the microXAS beamline in order to conduct the time-resolved x-ray experiments using the single x-ray pulse, as shown in Fig. 4.5 (see the text below for details)

First, the 1.04 MHz signal is fed into Digital Delay Generator (*Stanford Research Systems*), labeled DDG#1 in Fig. 4.13, which divides it down to desired synchronized 2 kHz signal. This signal is used to trigger the remaining delay generators and defines the repetition rate of single x-ray pulse intensities (twice the laser frequency). The DDG#2 provides the synchronized trigger for the laser amplifier and thus ensures that the selected oscillator pulse, synchronized to the RF storage ring frequency (500 MHz), will be further amplified. The output of DDG#2 unit provides 3 trigger signals delayed with respect to each other at 1kHz. These signals control both the Q-Switch of the amplifier pump laser (see Evolution laser in Fig. 4.13) and the two Pockel's cells of the amplifier (labeled as PC1 and PC2 in Fig. 4.13). The in-coupling (PC1) and out-coupling (PC2) Pockel's cells define the time window, in which the oscillator seed pulse is amplified inside of the amplifier cavity (synchronized to the Q-switched pump pulse). An additional channel of DDG#2 produces a marker signal for the Analog Input (AI) Card, which indicates the presence of the amplified laser pulse used in the experiment (Laser ON marker, which sorts the laser-pumped and unpumped spectra recorded during the measurement). With the synchronization scheme described above, one can easily change the time delay between x-ray and laser pulses in steps of 10 ns (the period of the oscillator pulse train) by simply amplifying an adjacent oscillator pulse. The time delay change adjusts the timing of both PCs and the Q-Switch at DDG#2. For smaller time delays, however, the output of the laser oscillator itself has to be modified. The phase shifter inside the *Femtolock* unit adjusts the instantaneous phase of the reference RF signal, which synchronizes the laser oscillator pulse. Subsequently, the trigger of the delay generator, which controls the Pockel's cells and the Q-switches of the pump laser, is changed accordingly.

4.6.3 Data Acquisition Scheme

The x-ray signals are measured simultaneously in transmission and fluorescence yield modes (Fig. 4.9), using the same data acquisition strategy for all detectors, as shown in Fig. 4.14. In either case, the electronic signal is the measured x-ray pulse intensity recorded on a fast APD detectors placed inside of the chamber. The output signals are then fed into several Gated Integrators (*Stanford Research Systems*, SR250), which allow to integrate the signal over a certain time window (the so called gate) set around the detected x-ray pulse intensity (as sketched in Fig. 4.14) and consequently rejectes all other signals. The output is an averaged signal over a specified number of duty cycles (triggers) supplied externally to the integrator (see Fig. 4.13)). A typical output signal of an APD is shown below in Fig. 4.14a. We can recognize the trailing (left side) and leading (right side) edges of the multibunch pulse train separated by a gap where a single x-ray pulse is located. The external synchronized trigger (DDG#4) drives the integrator at a frequency of 6 kHz.

The x-ray single pulses are recorded at 2 kHz, meaning at twice the repetition rate of the laser, which allows subtracting the adjacent pairs of x-ray pulse intensities (namely laser-pumped and unpumped pairs) and obtaining the difference intensity. In addition, we record two zero (background) signals; so called *clearing* and *real* zeros. Both zero signals account for a memory effect of the integrator (the next output contains ca. 5% of the previous signal output voltage), which means they effectively discharge the integrator capacitors. The *clearing* zero is neglected in the acquisition process, whereas the *real* zero is subtracted from the signal, thus correcting for long-term baseline drifts. Each signal has a corresponding boxcar gate, which defines the temporal interval of the integration (see Fig. 4.14a). The gate width is governed by the temporal response of the APD. Typical gate widths used with the APD detectors are in the range of 5-15 ns. The integrator gates used to detected different signals are synchronized in a sequence at 6 kHz repetition rate and the corresponding marker signals, supplied to the data acquisition card (AI card in Fig. 4.13 and 4.15), indicate, which signals should further be processed and which should be rejected (e.g. clearing zero signals are rejected).

The marker signals also help to distinguish between pumped (1 kHz) and unpumped (2 kHz) x-ray pulse intensities. Once properly marked, the AI card (analog-to-digital converter card) sorts them and digitizes them, so the further processing of the signals can be performed by a computer. As mentioned above, the measured signals from adjacent pulse intensities allow subtracting them and recording a difference signal, which contains all the laser-induced intensity changes. This strategy is a very effective way of eliminating slow voltage drifts in the detector and/or electronics. Each laser-pumped signal has a corresponding reference signal taken within a short interval of 500 μs after it and thus all signal changes, which are slower than the 2 kHz repetition rate, are naturally filtered out, especially low-frequency, e.g. 50 Hz, electronic noise.

We can summarize the data acquisition scheme with the help of Fig. 4.14. In Fig. 4.14a, the relative position of the gated integrator's gates is sketched within the same round-trip of the single x-ray pulse. The position of the x-ray pulse within the 180 ns empty gap can be adjusted, so that the additional background signals (see the clearing and real zero signals in Fig. 4.14a) can be read-out. The signal gate width is usually set to ca. 10-20 ns, which is determined by the signal pulse width corresponding to the time response of the APD detector. During the actual measurement, the background signals, I_{bck}, are recorded a few round-trips after the signal. In Fig. 4.14b, an example of a read-out sequence is shown.

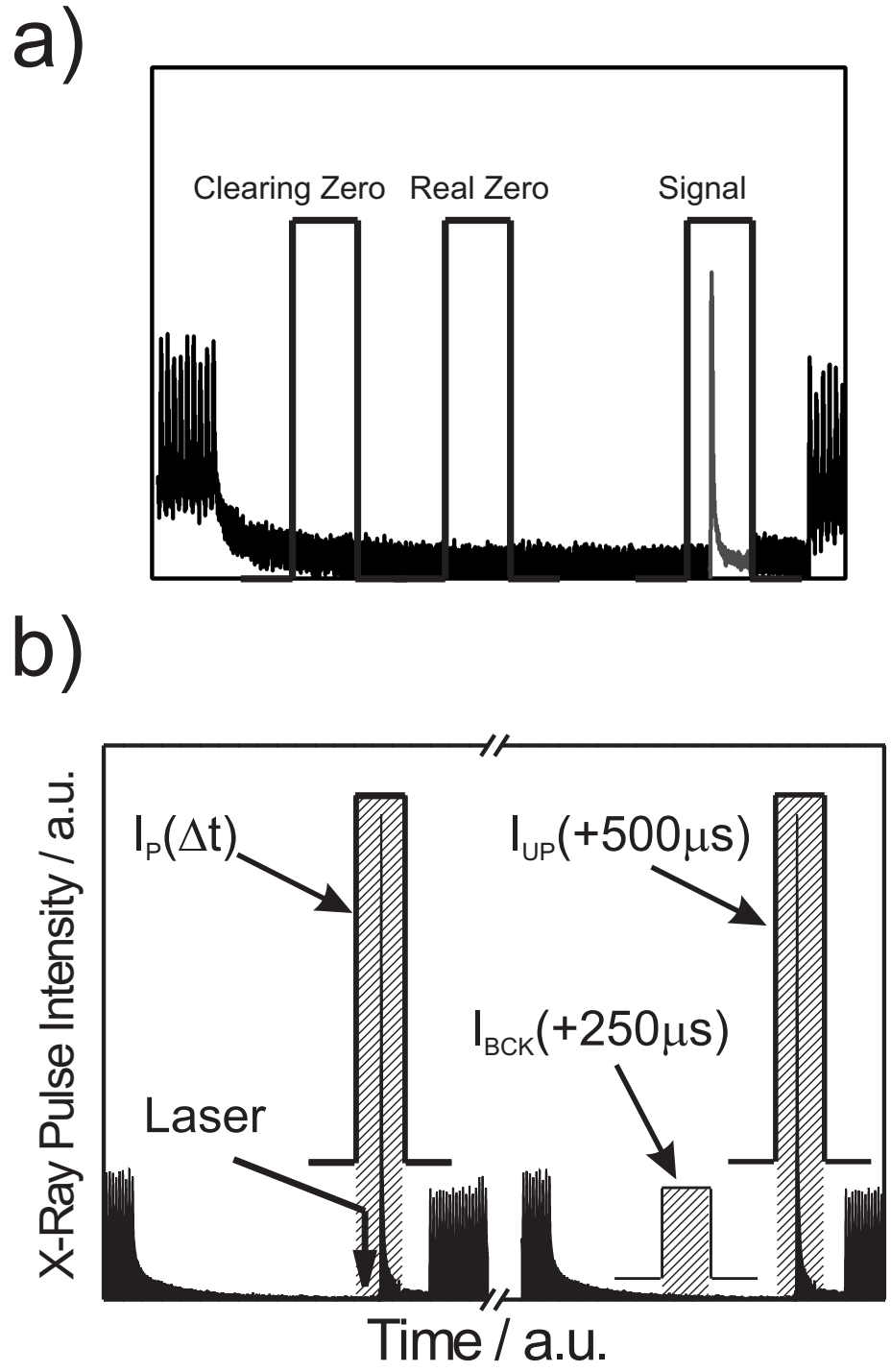

Figure 4.14: Data acquisition scheme employed at the microXAS beamline of the Swiss Light Source. In (a) the relative positions of the integrator gates are shown (although during he experiment they are displaced from each other by several round-trips). (b) A gated integrator measures sequentially the x-ray intensity at the chosen time delay Δt, the background signal ca. 250 μs later, the x-ray signal of the unexcited sample after 500 μs (each within the indicated shaded time windows), and a second background signal without x-rays (not shown, 250 μs after I_u). This acquisition scheme is repeated for several thousand times per data point.

First, the x-ray signal at time Δt after laser excitation is measured ($I_p(\Delta$ t), then a background signal without x-rays is recorded after ca. 250 μs ($I_{bck}(+250\mu s)$), which enables post-correcting baseline drifts in the gated integrator, and finally, after 0.5 ms, the unpumped x-ray signal from a fresh sample without laser excitation is recorded (I_{up}) followed by a baseline correction measurement ($I_{bck}(500\ \mu s + 250\ \mu s)$, not shown in Fig. 4.14b). The detected signals are both transmitted and fluorescent x-ray photons. The pump-probe signals in transmission, T_{tr}, and fluorescence, T_{fl}, modes are defined as the transient absorption of the photoexcited sample via (for more details refer to Eqs. 3.29 and 3.30 in Chapter 3):

$$T_{tr} = \ln\left(\frac{I^{tr}_{unpumped}}{I^{tr}_{pumped}}\right) \tag{4.3}$$

with $I^{tr}_{pumped} = Ip(\Delta t) - I_{bck}(\Delta t + 250\mu s)$ and $I^{tr}_{unpumped} = I_u(+500\mu s) - I_{bck}(500\mu s + 250\mu s)$ being both the baseline (I_{bck}) corrected photoexcited and unexcited x-ray signals, respectively. The transient fluorescence signal, T_{fl}, can be defined similarly via:

$$T_{fl} = \frac{I^{fl}_{pumped} - I^{fl}_{unpumped}}{I_0} \tag{4.4}$$

with I^{fl}_{pumed}, $I^{fl}_{unpumped}$ and I_0 being each baseline corrected as described above for transmission mode. Likewise, normalization of the unpumped spectra to the incident flux yields the static XAS signal of the sample.

The subsequent data flow is schematically depicted in Fig. 4.15. Once the Client PC (control computer) initiates the data acquisition, it sends a command to a *virtual machine environment* (VME) crate, which provides the hardware-software interface in the data acquisition scheme discussed above.

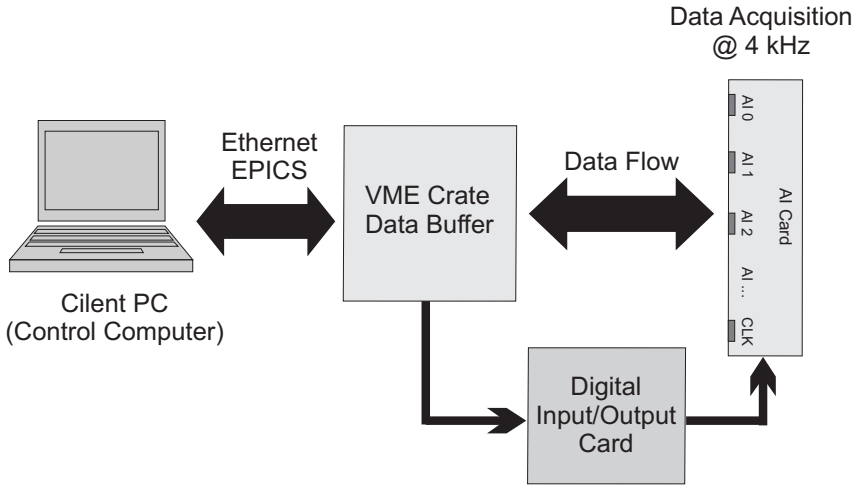

Figure 4.15: The schematic of the data flow incorporated at the microXAS beamline and used during the time-resolved x-ray experiments described here.

Next, a digital input/output card retrieves the digitized data from the AI card (see the data flow chart in Fig. 4.15) and send them to the VME crate, which also allows buffering the data before it is sent to the control computer over an ethernet connection. Subsequently the data is buffered in the VME crate (and the acquisition is terminated), the AI card is reset and ready for the new data to be recorded. At the end of the data flow chart, a computer-executed set of data acquisition programs allows the user to fully control all the devices included in the experiment. It includes all the relevant beamline instruments, experimental chamber and laser-storage ring synchronization devices (phase shifter, Pockel's cell timing etc.). Each device is represented via a variable defined in separate user interface software written in Python language. These variables can be grouped into two sets, namely independent and dependent variables. The independent variables are assigned to those devices, which are fully controllable during the experiment, like various stepper motor (sample holder, experimental table, laser mirrors etc), x-ray monochromator and laser timing. The dependent devices are those related to the data acquisition and control mostly the AI card and the single x-ray pulse current. The entire control of the SLS storage ring, including the beamline control, and data acquisition systems is provided by the EPICS environment.

4.7 Detectors

The detectors used in our experiments are *large-area avalanche photodiodes* (LAAPD). They fulfill all the characteristics of the measurements, which are: a) good sensitivity to hard x-rays, b) sufficient temporal resolution (on the order of 5-20 ns) in order to resolve a single x-ray pulse signal from the adjacent multibunch pulse sequence, c) wide dynamic range due to varying pulse intensity (linearity condition), d) compact size and large active area (especially useful for fluorescence yield detection), e) sufficient internal gain of ca. 50-100, which amplifies the small signals above the electronic noise background.

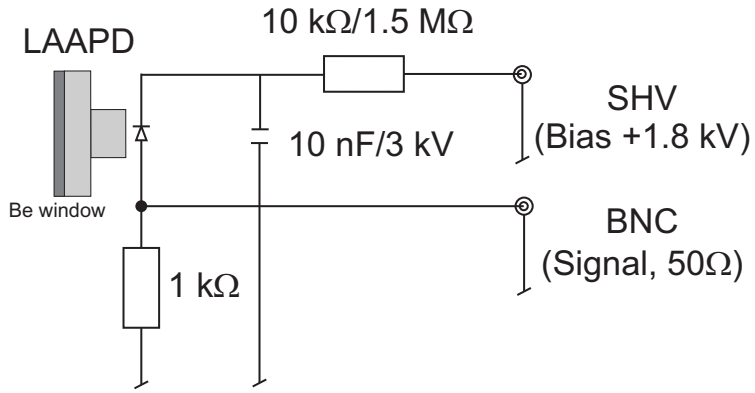

Figure 4.16: The electrical circuit of the APD detectors used in the experiments presented in Chapters 5 and 6. Depending on the detection mode (transmission or fluorescence), the different resistances and capacitances of the circuit are indicated.

The LAAPD [290–292] used here are windowless *Advanced Photonix* diodes with 16 mm (Model 630-70-75-500) and 10 mm (Model 394-70-73-500) diameter of active area. The total thickness of the si chip is of ca. 380 μm in both models. The wiring of the used APD is illustrated in Fig. 4.16. The APD is mounted in a sealed aluminum box with a 15 μm Be window, which protects the diode from the intense scatter from the laser beam. A 7 μm foil of polyimide (so called *Kapton* tape) covers the beryllium window as a protection against the liquid spray produced in the jet upon intense laser irradiation (sample evaporation forms the liquid spray in the close vicinity to the jet).

The basic operation of an APD can be explained with the help of Fig. 4.17. In Fig. 4.17a, a *reach-through* APD is shown, whereas Fig. 4.17b) depicts a *beveled-edge* APD structure.

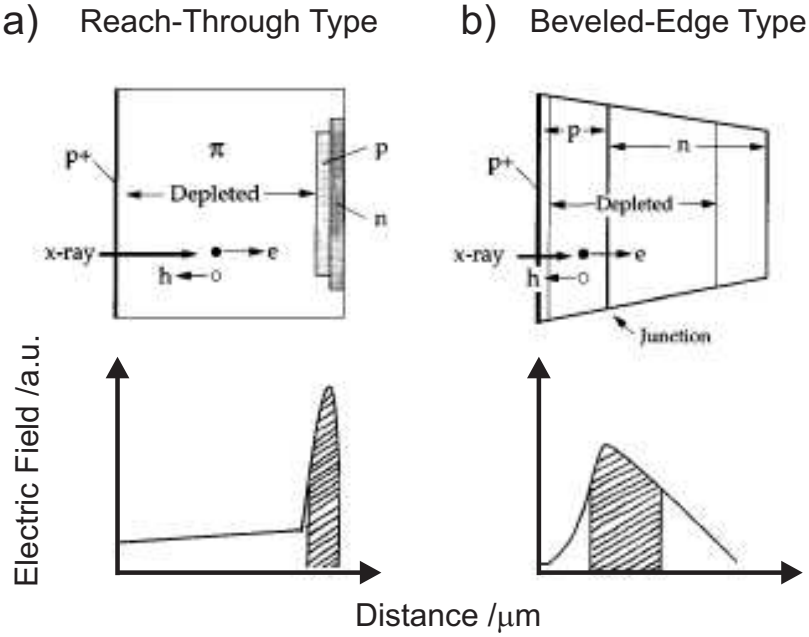

Figure 4.17: In (a) a reach-through APD operation principle is sketched, whereas (b) displays the driving mechanism in case of beveled-type APD. At the bottom of both (a) and (b), their corresponding electric field profiles inside the active area are plotted as a function of the active area thickness [293].

In either case, the doping of the semiconductor structure consists of $p+$, p, n and $n+$ layers and the depletion region divides into two parts: a low-field drift region and high-field gain region. The electric field profiles, which characterize both reach-through and beveled-edge APD devices are shown underneath their structures in Fig. 4.17 [293]. The principal mechanism of an APD operation combines the benefits of both a conventional PIN photodiode and a photomultiplier tube (PMT), in that an APD can be regarded as a silicon photodiode with an internal gain. The absorption of an incoming photon creates an electron-hole (e-h) pair in the depletion region (see the depleted region in both APD types in Figs. 4.17a and b). In case of Si, the energy required for single e-h pairs to be created is 3.6 eV. A high reverse bias voltage supplied to an APD (up to 2 kV in case of Advanced Photonix APDs), creates

a strong internal field, which accelerates the electrons through Si layers and produces secondary e-h pairs by impact ionization. The resulting *avalanche process* produces gain factors in electron yield up to a few hundred times (with respect to a single e-h pair created within the initial absorbtion event). In reach-through APDs (Fig. 4.17a), as the bias voltage is applied, the depletion region extends from the front contact down to the *p-n* junction, where the internal field is the highest and the avalanche process takes place. The effective thickness of the avalanche region extends usually to ca. 5-10 μm and thus the fraction of the penetrating photons absorbed within the gain region is usually relatively small. On contrary, in beveled-edge devices ((Fig. 4.17b), the gain region is broader because the junction lies in the low-dopant region and it is characterized by much higher gains (100-1000) then a reach-through type (typically 20-100). There are, however, several drawbacks encountered in these devices; first of all, their bias voltages are on the order of 1-2.5 kV, which makes it difficult to operate them in He atmosphere (as He gas provokes discharges at these high voltages biases); second, the extended avalanche region makes the undepleted part of the device also broader, meaning that some of e-h pairs can drift there before they reach the depleted region and feel the internal electric field. In consequence, such drifts will produce a long temporal tail in the time response of the APD, which is usually longer than the reach-through type. Eventually, the choice between either of these APDs, will depend on the requirements of the experiment. The compromise in the temporal response and a high gain will favor the beveled-edge structures. For these diodes, also the active area has been extended to several tens of millimeters in diameter, which makes them especially useful in fluorescence yield detection, where the isotropic x-ray emission has to be collected over as large solid angle as possible.

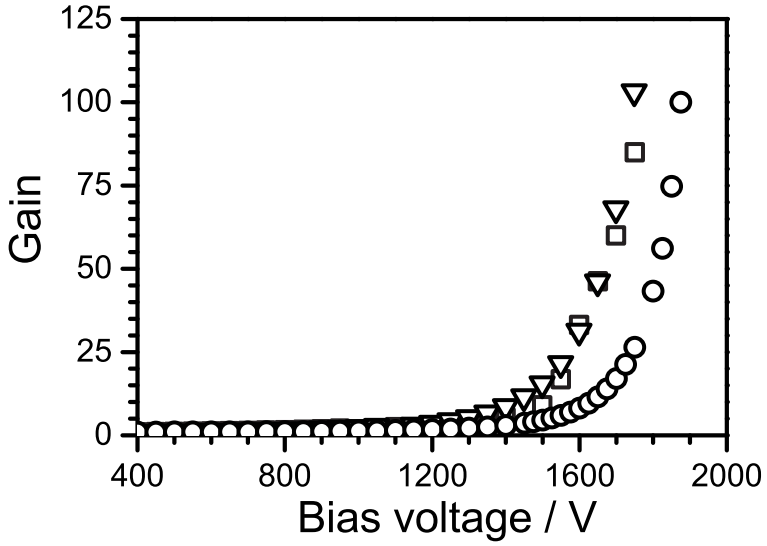

Figure 4.18: The Advanced Photonix (Model 630-70-75-500) APD gain curves recorded using visible (ca. 1.6 eV, ▽ and □) and hard x-ray (7.3 keV, ◯) photons. The detailed description and interpretation follows below in the text.

In order to estimate the gain of the detector, we measured the output of the APD as a function of bias-voltage, the so called *gain curves*. The results plotted in Fig. 4.18 are normalized to the signal at low bias (typically between 300-500 V for Advanced Photonix diodes), assigned as the unit gain. The gain curves measured using 800nm (1.55 eV) laser light pulses (ca. 120 fs) represented with □ and ▽ in Fig. 4.18. The curves were taken with 2 different laser intensities corresponding to an unfocused (e.g. ▽ in Fig. 4.18) and focused (e.g. □ in Fig. 4.18) beams. The effect of the flux density is negligible from this measurement. The gain curve measurement carried out at higher photon energies, i.e. in the x-ray range, is plotted with ◯ in Fig. 4.18. In this case, the gain curve was obtained using 7.3 keV photons coming from a single bunch at the SLS storage rings. The deviation at higher bias between both sets of gain curves may be assigned to space-charge effects induced by a higher density of electrons produced upon high energy photon illumination (x-ray pulse). Here, the internal electric field within the avalanche region is decreased by the excess of electrons and the gain changes locally so that not all the electrons will be amplified uniformly. Note that due to the local nature of the effect this need not give rise to an overall non-linear response. As long as the x-ray photons are spread over a sufficiently large area of the detector, the electron pulses produced by different x-ray absorption events are independent of each other and only affect their own local gain. Therefore, the measured signal should still be proportional to the number of the incident x-ray photons on the detector.

Finally, we have verified the linearity of the APD signal response at a constant bias voltage (i.e. kept at 1900 V in both measurements) as a function of incident x-ray pulse intensity, as illustrated in Fig. 4.19.

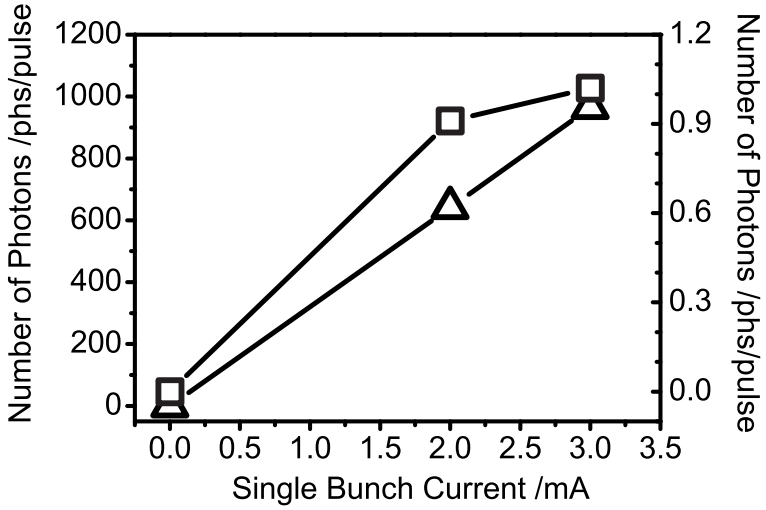

Figure 4.19: Linearity check of the APD detector response. The single x-ray intensities (in photons/pulse units) are plotted for the I_0 (□) and I_t (△) detectors as a function of the single bunch current.

These measurements were done by recording a single x-ray pulse intensities, at x-ray photon energy of 7.1 keV, on the APD as a function of the current injected into the single electron bunch of the SLS storage ring. The results presented in Fig. 4.19 correspond to the single x-ray pulse intensities recorded simultaneously on both the I_0 (□) and I_t (△) detectors, in identical configuration as shown in Fig 4.9. Next to it, we have also recorded and analyzed the single x-ray pulse height distributions corresponding to these measurements (more details in the following section), which are an efficient way of measuring the effective single pulse photon flux N_{eff}. Note the units of the ordinate axes in Fig. 4.19 are the number of x-ray photons/pulse(left/right ordinate axis corresponds to △/□ detectors respectively), which relates the measured intensities to the actual photo flux. The single bunch current and the APD signal (and therefore the single pulse flux) are found to be nearly linear with respect to each other.

4.8 Spatial and Temporal Overlap

Spatial and temporal overlap is secured in two independent steps. Initially, we align both x-ray and laser beams through a 50 μm pinhole at the sample position. At low laser intensities, we can estimate the spatial dimensions by scanning the pinhole across both beams in both vertical and horizontal directions. At higher laser intensities, the laser profile may change due to nonlinear effects it may experience either in the air or in the sample and the pinhole scans are impossible due to the permanent damage caused by the focused laser beam. To solve this, we have developed an imaging setup, which is schematically shown in Fig. 4.20.

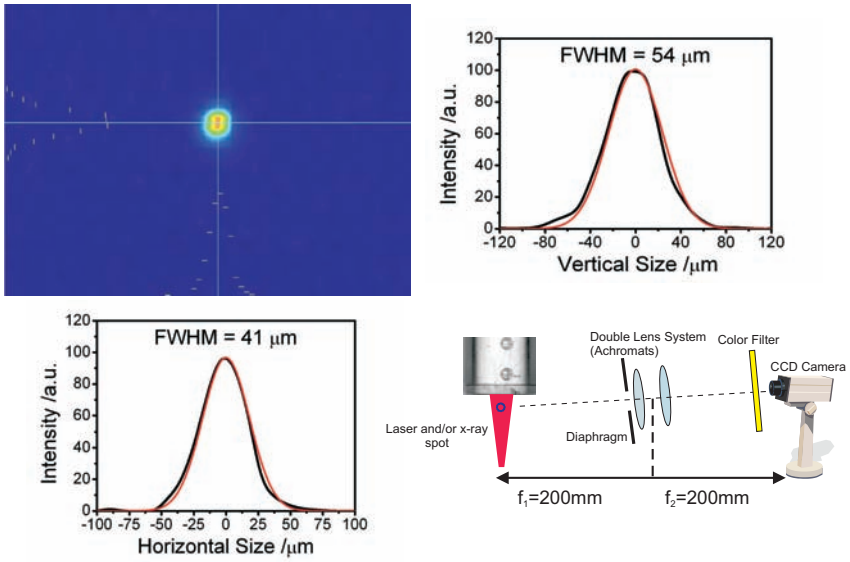

Figure 4.20: The schematic drawing of the CCD imaging setup used to measure the incident x-ray and laser beam profiles. The vertical and horizontal profiles of a representative image are shown on both side. In the bottom-right corner, the optical imaging setup is drawn.

Here the CCD image of a focused (using KB mirrors) x-ray beam spot size recorded on a fluorescent screen (see below for details) is shown. Next to it, Fig. 4.20 shows the vertical and horizontal slices taken across the image, which show the measured vertical and horizontal diameters of the beam. In the bottom-right corner of Fig. 4.20, the imaging optics used in this setup is sketched. Here, we use one of the viewports on the side of the chamber to image either the x-ray or the laser spot at the sample position by recording the visible fluorescence they induce in a fluorescing material. A 1:1 image is formed using a double lens system consisting of two identical 1-inch achromatic lenses placed at their focal distance away from the source (inside of the chamber). At corresponding focal distance away from the lens system, a CCD camera is placed, which records an image of the beam spot. An additional color filter attenuates the residual laser scatter and decreases the image intensity to avoid CCD saturation. A example of a typical x-ray beam spot measured with the above described setup is shown in Fig. 4.20 as well. It has the vertical size of 54 μm and horizontal size of 41 μm. As mentioned above, the image system was designed to produce 1:1 images, which was calibrated by imaging 1 mm distance on a ruler. The actual magnification of the setup is ca. 1:1.2, which means the x-ray spot shown in μm has a real size of ca 65μm×49μm. Furthermore, this setup can be used to spatially overlap both laser and x-ray beams as illustrated in Fig. 4.21. Here, we use a 100 μm-thick Ce-doped YAG crystal (5-10 mm diameter) mounted in a calibrated holder, which places the crystal at the center of the jet position.

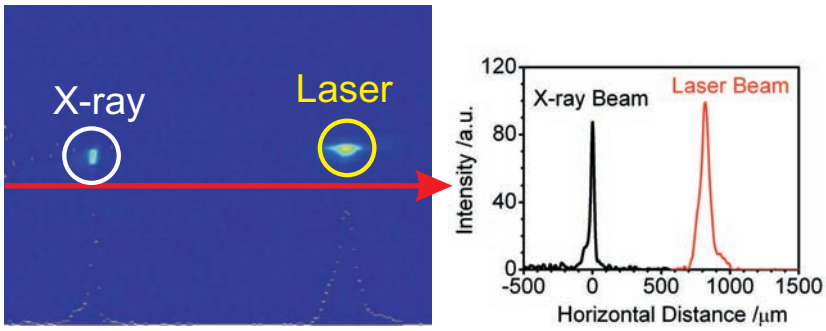

Figure 4.21: The spatial overlap of both the x-ray and laser beam can be monitored prior and during the measurements, via the imaging system depicted in Fig. 4.20. The image shown here was recorded before the laser beam was steered onto the x-ray beam by means of a motorized mirror (not shown here, see text below).

This crystal is a well-known material used in x-ray imaging, because it fluoresces in the visible upon x-ray irradiation. It also fluoresces upon visible irradiation, i.e. upon 400 nm light irradiation used here; therefore we can image both beams simultaneously once they are aligned on the crystal. Fig. 4.21 shows an image of both x-ray and laser beams aligned on the crystal surface, before steering the laser beam onto the x-ray beam to gain perfect spatial overlap. During the experiments, the laser beam can be monitored on the jet via the scattered light produced on its surface, which allows controlling the size of the excitation beam used in the experiment.

For achieving temporal overlap, we measure the initial time delay, at which the laser and x-ray pulses will arrive at the sample position, as shown in Fig. 4.22. We measure this time delay by means of a fast windowless photodiode (rise time about 250 ps) placed at the sample position (where both laser and x-ray beams spatially overlap) and recording both the laser and x-ray pulses on a 1 GHz oscilloscope. We record both x-ray and laser pulses and adjust their delay by shifting the phase shifter and changing the amplifier timing.

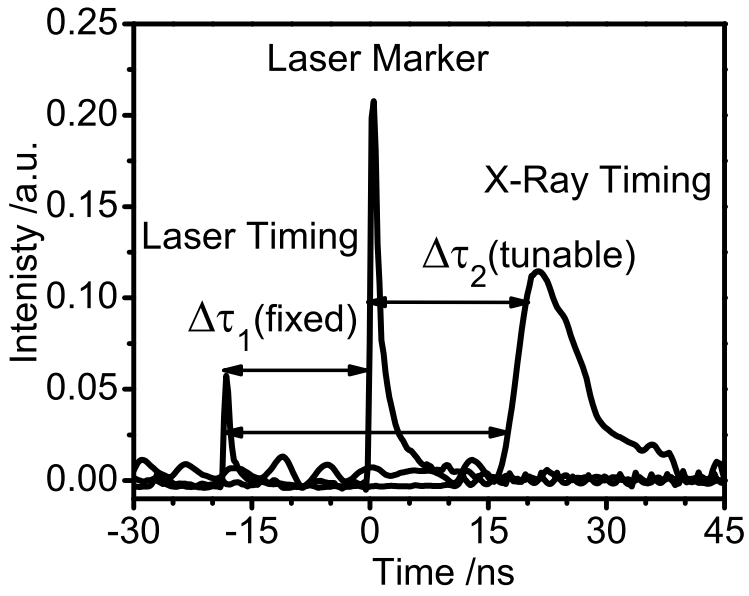

Figure 4.22: The temporal overlap strategy used in our time-resolved x-ray experiments. The relative timing of the x-ray and the laser pulses are recorded on a fast photodiode at the overlap position. By setting a marker signal (external laser signal), the relative time delays, $\Delta\tau_1$ and $\Delta\tau_2$, of the laser and x-ray pulses, respectively, can be estimated and used to monitor the laser-x-ray time delay during the measurements (details in the text)

This allows us to set the timing with a precision of ca. 200 ps by comparing the rise times of both signals. Once the time delay is determined, we set a laser marker (laser scattered light recorded on a fast photodiode inside of the laser hutch), which we use for monitoring the time delay during the measurements (see τ_1 and τ_2 delays as indicated in Fig. 4.22). Once τ_1 time delay is fixed, we can measure the time delay between the laser marker and the x-ray signal τ_2 before it enters the gated integrator. During the experiment, τ_1 remains fixed and we monitor (and adjust) τ_2, which allows setting the laser-x-ray time delay. In addition, the laser reference signal allows a quick check whether both signals remain at their initial time delays and no sudden timing change has occurred. Once the pump-probe signal is detected, precise time scans around time-zero of the measurement determine accurately the time delay between both beams.

As discussed above, the laser beam is guided into the chamber via an encoded motorized mirror. This allows scanning reproducibly the laser and x-ray alignment during the experiment. In addition, it allows recording the actual spatial profile of the pump-probe signal, which delivers the excitation profile (laser beam size at the actual intensity used in the experiment) as shown in Fig. 4.23. This is a very important information because it overcomes the difficulty in estimating the laser shape and focal size measured before at attenuated power. The 2D pump-probe scans are done in-situ without neither opening the chamber nor interfering with the laser power. An example of such a profile is shown below (Fig. 4.23).

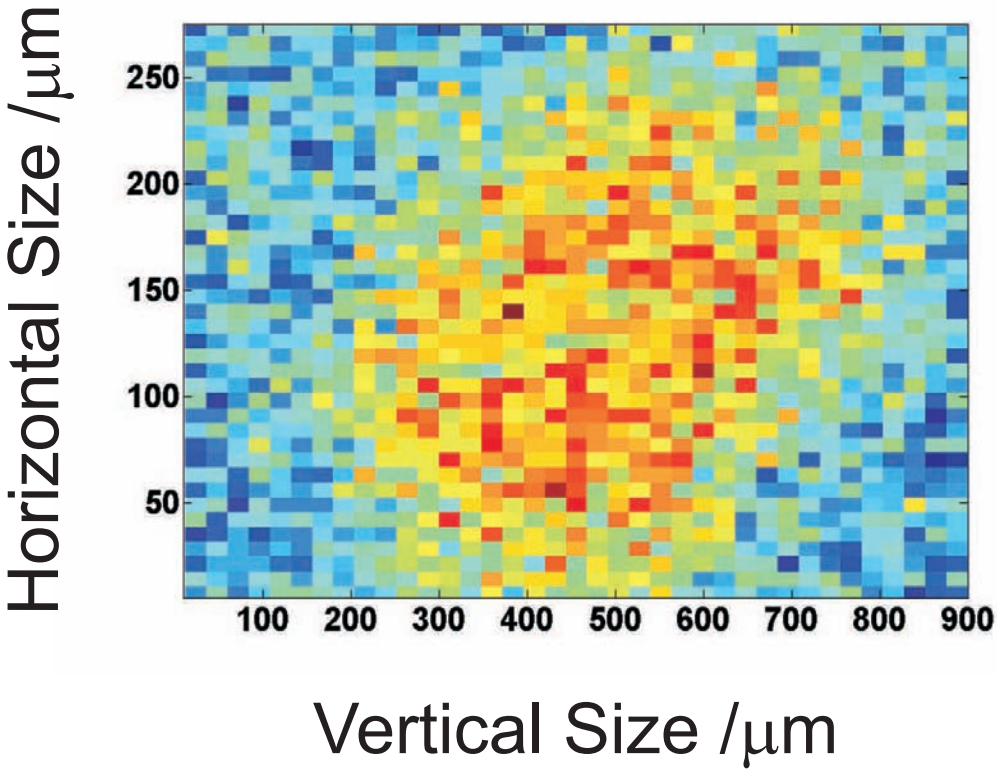

Figure 4.23: The spatial profile of the pump-probe signal measured in an aqueous solution of 25 mM of $Fe(bpy)_3$ via fluorescence yield detection. The spatial dimensions here correspond to the "true" high-intensity laser profile at the sample site.

The horizontal and vertical size corresponds to calibrated angular steps of the motorized laser mirror, which is scanned around the x-ray beam and thus measures the transient signal intensity as a function of both horizontal and vertical displacement of both beams.

4.9 X-ray Photon Flux and Statistics

One of the most important and critical aspects of the time-resolved laser-pump x-ray-probe experiments (see Chapter 3) is the x-ray photon flux used in the experiments and the detection sensitivity achieved in the present configuration. In the following we will describe the calculated flux curve of the microXAS beamline and compare it with static flux measurements. Furthermore, we will analyze the detection sensitivity in terms of photon statistics and determine the single x-ray photon flux as measured by the statistical signal height distributions during the experiments, verifying that shot-noise is the only significant source of noise in the measurement. The comparison between both flux measurements will be discussed as well.

4.9.1 microXAS Flux Curve

In order to characterize the beamline flux, we have performed measurements in the experimental hutch in various energy ranges (mainly around a few selected harmonics) taking into account all present losses due to air paths, filters and other beamline components. The experimental setup is schematically illustrated in Fig. 4.24. Here, the detectors are the ionization chambers. Additional measurements using the Si photodiodes were performed in the same arrangement, where the photodiodes were placed in front of the gas chambers so that the total air path can be assumed equal in both measurements.

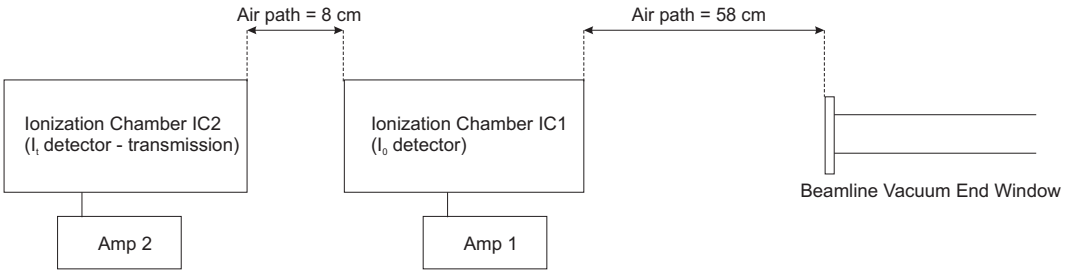

Figure 4.24: The experimental layout of the flux measurements using a pair of ionization chambers (IC_1, IC_2).

We have used 2 different types of detectors in order to perform the flux measurements: 1) *Oxford Danfysik* Ionization Chambers and 2) Si photodiodes (280 μm thickness)(not shown in Fig. 4.24). In case of both detectors we have used low-noise current amplifiers (*FEMTO DLPCA-200*), which were set to typical gain settings between 10^7-10^9 V/A. In both cases, the monochromatic x-ray beam was sent through 2 sequentially mounted ionization chambers (IC) of equal lengths of 30 cm gas path, IC_1 and IC_2, which were filled with He gas up to approximately 250 mbar at bias voltage of 1200 V. Before starting the measurements we have checked the linearity of both IC by measuring the amplified current value as a function of gradually increasing bias voltage. The results are shown in Fig. 4.25.

We have reached the plateau value of the IC current above approximately 200 V and we have not seen any further increase in the current readout thus we have set and kept the bias voltage equal to 1200 V throughout our measurements. The x-ray energy during the measurement shown in Fig. 4.25, was set to the maximum of the 3^{rd} harmonic at a constant 7.5 mm undulator gap. Using 10^7 V/A gain setting we have estimated that the total current measured on the He-filled IC was ca. 77 nA, which was below the critical current threshold at which the IC may behave nonlinear.

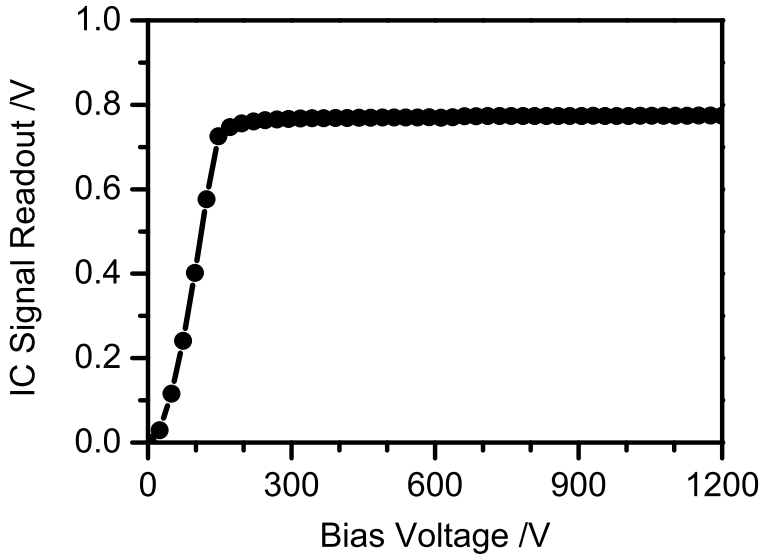

Figure 4.25: The optimized IC read-out signal as a function of the bias voltage. The flat plateau region corresponds to the optimized operation of the ion chamber. Increased bias voltage (>1200 V) brings it to the nonlinear operation (not shown here).

Once the optimum gas filling and the bias voltage were found, we have performed a series of flux measurements at 3^{rd}, 5^{th} and 7^{th} harmonic using a constant ID gap. We have not optimized the 2^{nd} monochromator crystal pitch when switching between harmonics, which has resulted in decreased flux, measured at higher energies, as discussed below. The results of flux measurements at 3 different harmonics are shown in Fig. 4.26. The black curve shows the calculated flux curve of the undulator used at the mXAS beamline assuming a gap of 7.5 mm, 400 mA storage ring current and 2.4 GeV electron beam. The flux is expressed in number of photons measured per second and per given energy bandwidth (BW) as determined by the Si(111) monochromator crystals (in principle the energy BW changes as a function of the x-ray photon energy). In addition 80% transmission of the beamline focusing mirror (M1) was assumed. These measurements were performed around the 3^{rd} (5.87 keV), 5^{th} (9.79 keV) and 7^{th} (13.73 keV) harmonics at 9 mm undulator gap at 350 mA storage ring current.

The signals measured by the ionization chambers are the ionization currents that reach chamber electrodes upon photoionization of the chamber gas.

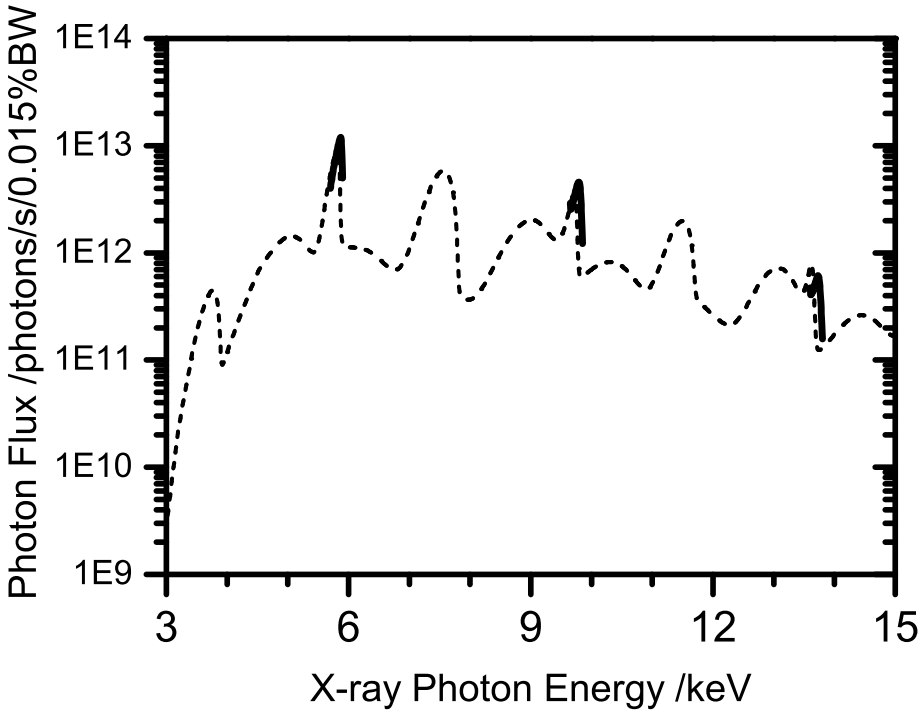

Figure 4.26: A comparison between the theoretical (dashed line) and the experimental (solid line) flux curves. The experimental data was recorded using the setup shown in Fig. 4.24 for three selected energy ranges (around 3^{rd}, 5^{th} and 7^{th} harmonic of the ID).

The electrons produced in the chamber are accelerated towards the electrode due to the high voltage bias applied to them. We can extract the photon flux by using the following equation:

$$\Phi = \frac{V_{ion}[V] \times E_{ion}[eV]}{1.6 \cdot 10^{-19}[C] \times E_{x-ray}[eV]} \times C \times G[A/V] \tag{4.5}$$

For practical reasons we use V_{ion} as the voltage signal recorded at the voltage preamplifier attached to the ion chamber. In principle, the gain factor G allows extracting the actual current inside of the chamber. Next to it, we have to estimate how many electrons will be produced upon a single x-ray photon of the energy E_{x-ray}. The E_{ion}/E_{x-ray} ratio estimates the number of electrons produced in a given gas with ionization energy E_{ion}. In case of He, we have used ca. 28 eV as the E_{ion} value although some other authors suggested values as large as 40 eV. The term C in Eq. 4.5 is a general loss term. In this particular measurement it accounts for the transmission losses through air, entrance windows and the number of x-ray photons absorber inside of the ion chamber. In the best case, one would adjust the absorptions inside of the ionization chamber detectors in Fig. 4.24, so that the IC_1 chamber would

absorb ca. 10-30% of the incident intensity and IC_2 would absorb the remaining 100% of the intensity. In order to adjust the transmitted/absorbed intensity ratio, one often uses a mixture of gases in order to fill the ion chambers. In case presented here (Fig. 4.5) have used He gas as the IC medium, which absorbs very weakly throughout the investigated energy range. The correction term C takes into account the photoelectric cross section at the given 3 energies (see the 3 harmonics measured in Fig. 4.26). The x-ray photon flux measured using the setup shown in Fig. 4.24 and calculated via Eq. 4.5 agrees very well with the calculated microXAS beamline flux curve as presented in Fig. 4.26.

4.9.2 Photon Statistics

In order to verify the detection sensitivity of our setup, we have recorded the individual output signals of the gated integrator for a certain number of triggers (number of x-ray pulses) and analyzed the pulse height distribution for single x-ray pulses. In this way, we can compare the width of the distribution function (standard deviation) at different experimental conditions in order to estimate the noise sources in our results. In fact, the careful measured noise analysis shows that our current sensitivity has reached the 90% of the shot-noise limit of the x-ray source with our setup at the ALS beamline, because the pulse height distribution analysis delivered nearly the same results as the beamline specification indicates (in terms of the incident x-ray photon flux) [36, 276]. We have performed similar measurements at the SLS microXAS beamline and data recorded in transmission are illustrated in Fig. 4.27.

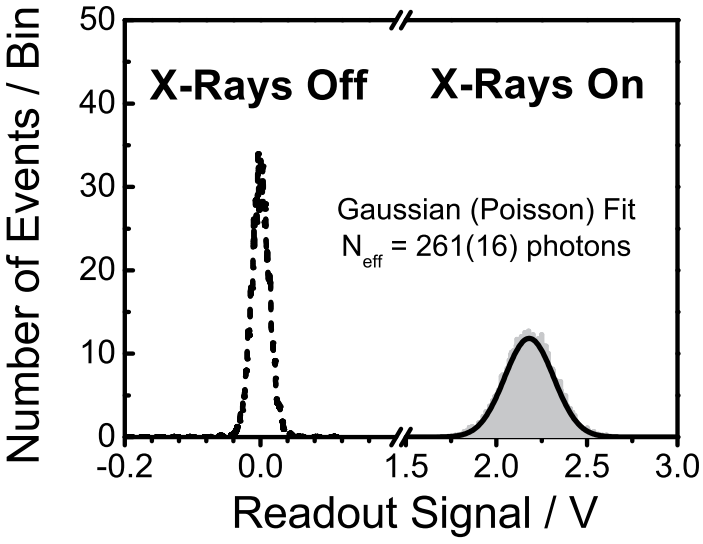

Figure 4.27: Pulse height distribution of 10^3 single x-ray pulses recorded in transmission mode without x-rays (=I_{bck}, left side) and with ca. 260 photons per pulse at 7 keV (= I_1, right side) together with the corresponding Gaussian fits. The binning was ten-fold denser for the background distribution.

It shows the single x-ray pulse height distribution of ca. 10^3 recorded x-ray pulse intensities. Here the measured width without beam (left) amounts to less than 20% of the width measured with x-rays on the APD (at this x-ray intensity). We can clearly identify the zero signal, which corresponds to no x-rays on the APD detector and its distribution peaks narrowly around the 0 V signal (see the curve on left-hand side in Fig. 4.27). As soon as we send some x-ray photons on the detector, the distribution broadens and peaks around a certain read-out signal voltage (gated integrator signal, see the right-hand side curve in Fig. 4.27) with its corresponding mean $\overline{S}$ and standard deviation σ_S values. The FWHM of the zero signal is ca. 5% of that measured with incident x-rays on the detector. From the distribution shown in Fig. 4.27, we can estimate an effective number of monochromatic x-ray photons per pulse, via the equation [36, 276]:

$$N = \left(\frac{N}{\Delta N}\right)^2 = \left(\frac{N}{\sqrt{N}}\right)^2 \geq \left(\frac{\overline{S}}{\sigma_S}\right)^2 = N_{ph}^{eff} \tag{4.6}$$

with N being the average number of photons per pulse, $N = \sqrt{N}$ being the standard deviation or shot-noise distribution of the x-ray source, $\overline{S}$ being the averaged measured signal height (in Volts), and $= \sigma_S$ being its measured standard deviation (in Volts). Of course, this relation holds only, if $= \sigma_S$ contains no other contributions, e.g., electronic noise. If there would be no electronic noise sources, then the "$\geq$" sign in Eq. 4.6 could be replaced with "=", which means that N_{eff} would yield the actual photon flux N. Nevertheless, in realistic cases, one has to include some external noise sources present in the measurement. Therefore we can derive a lower limit of the photon flux by using N_{eff}. For this particular measurement, the N_{eff}=261 photons/pulse with the standard deviation of 16 photons/pulse. This value can be compared to the beamline flux measurements presented above. Including all beamline losses, like transmission losses due to air path, beamline components (windows, filters, monochromator etc.), the delivered flux value is identical to the one derived via Eq. 4.6 from the pulse height distributions. We have compared the values shown in Fig. 4.27 with the beamline specifications, and after correcting for various additional factors, e.g., sample and air transmission, we find that both values are identical to within less than a factor of two.

Furthermore, we have also performed similar measurements in the fluorescence yield mode, where we expect to detect orders of magnitude lower photon fluxes due to solid angle limitation and the overall efficiency of the process. These results are show in Figs. 4.28 and 4.29. For fluorescence yield detection we enter the single-photon counting regime, as seen in both Figures, showing the pulse height distributions for ca. 0.6 and 3 photons per pulse.

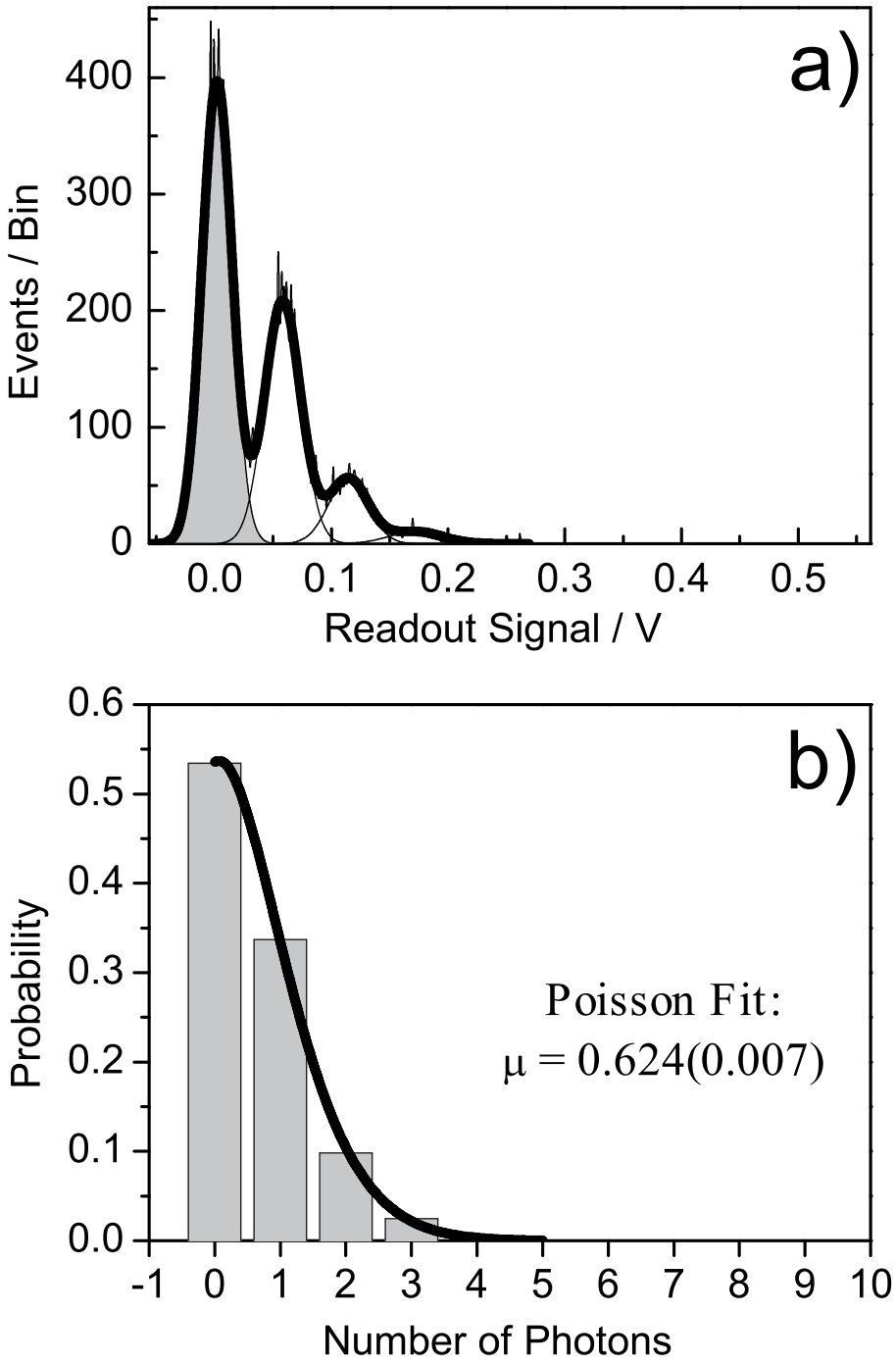

Figure 4.28: Pulse height distribution of ca. 10^4 recorded single x-pulses with the fluorescence detector. Here the fluorescence photon flux calculated via Eq. 4.6 amounts to $\overline{\mu}$=0.624 photons per pulse. The background signal without x-rays is shown as well. The lower plot shows the analysis using Poisson statistical distribution including the corresponding fit curve.

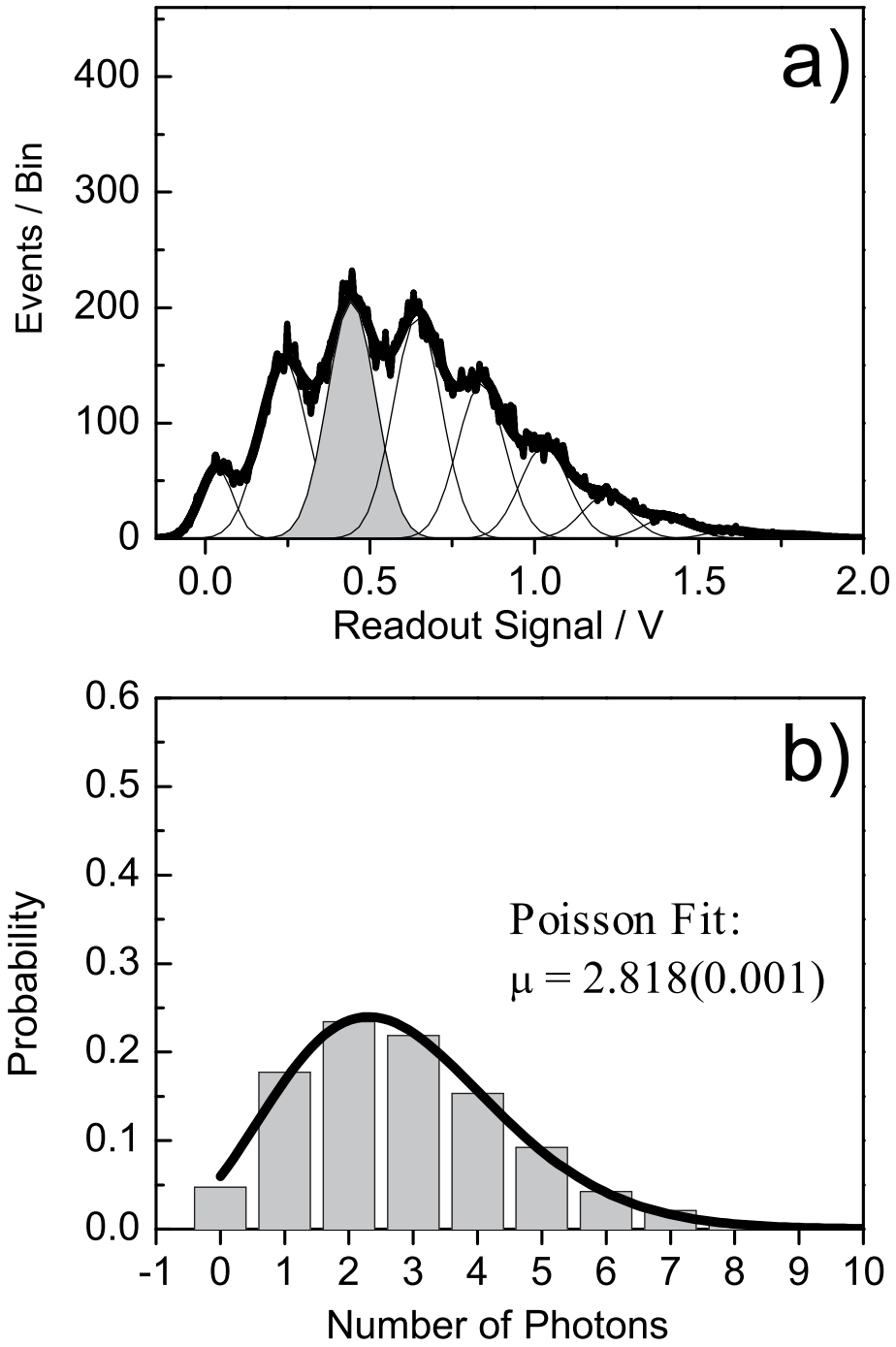

Figure 4.29: Pulse height distribution of ca. 10^4 recorded single x-pulses with the fluorescence detector. Similarly to Fig. 4.28, the fluorescence photon flux was estimated accrding to Eq. 4.6 as $\overline{\mu}$=2.82 photons per pulse. The background signal without x-rays is shown as well. The lower plot shows the analysis using Poisson statistical distribution including the corresponding fit curve.

In the first case (Fig. 4.28a), we can see the zero-signal distribution centered on the 0 V read-out voltage and then we identify subsequent 3 pulse-height distributions, separated by discrete read out voltage values (ca. 0.7 V). These are clearly N-photon event distribution, where N=1-3, originating from the fluorescence photons, which reached the detector. In this case the background signal has the same width as a single photon event. Nevertheless, we can reliably distinguish between one- and more photon events, and by fitting each event with a Gaussian-shaped function we can calculate the probability for each event.With this we can analyze the data according to the expected Poisson distribution, which is nicely confirmed (see Fig 4.28b).

In the second case (Fig. 4.29a), similarly to the distribution shown in (Fig. 4.28a), we detect the average number of photons $N_{eff} \approx 3$ and we see the effect of the distribution broadening and smearing the single-photon events. Here the photon flux was increased by a factor ca. 5 and we gradually see that the pulse height distribution merges into a Gaussian-shaped distribution centered on a mean value $\overline{S}$ with a corresponding standard deviation σ_S width. Further increase in flux (as we have shown in case of transmission measurement), would yield a pulse height distribution similar to the one shown in Fig. 4.27. The corresponding analysis using Poisson statistics and the estimated probabilities is depicted in (Fig. 4.29b). In both cases, the distributions are recorded for each data point during a spectral scan.

The fact that we can clearly distinguish between 1-, 2- and 3- photon events without any pile-up effects (similar to single-photon counting techniques), which are present in conventional *constant-fraction discrimination* (CFD) and single-photon counting methods, is very novel and promising. It allows detecting hard x-ray fluorescence with relatively small detectors covering nearly 7-10% of the solid angle. Usually in fluorescence XAS, one operates the detectors with single photon counters preceded by a CFD. This procedure ignores two- and more photon events, and can only be approximately corrected in a postcalibration measurement. The current scheme, on the other hand, always delivers accurate values and proves that although we are integrating the total intensity over a number of triggers within the gate width of the boxcar, we are still able to resolve the N-photon events without suffering from CFD penalty. Indeed, in conventional fluorescence XAS measurement the detector is usually so far away to ensure a negligible probability for 2-photon events. Sometimes this limit is compensated by recording the nonlinearity of the output signal as a function of the incident intensity in a calibration measurement. In our case, the recorded x-ray fluorescence flux is low that it naturally reaches the single-photon limit, meaning that less than a single photon is created per one absorbed x-ray photon. Although, the fluorescence flux in Fig. 4.29 is largely reduced, it remains fully consistent with the larger value of 263 photons/pulse, as recorded simultaneously in a transmission measurement (see Fig. 4.27). In addition, it allows moving the detectors rather close to the sample thus increasing its solid angle, but due to the limited energy resolution of the detector we can not distinguish between scattered and fluorescent light.

The background signal due to scattered light was reduced to <10% of the edge jump signal by placing the detectors within the direction of the x-ray polarization. Nevertheless, the intrinsic energy resolution $\Delta E/E$ of a LAAPD is relatively poor (for large active area APDs running at room temperature it is usually $\leq$10%, i.e. ca. 700 eV for a 7 keV photon). In addition, it is interesting to note that this acquisition scheme exploiting gated LAAPDs permits us to measure actual intensities for a wide range of pulse intensities. While Fig. 4.28a shows that we can reliably detect less than one photon per pulse, we have previously confirmed the linearity of APDs up to 6×10^4 photons/pulse in transmission mode (see Fig. 4.27).

To give a practical example of the detection sensitivity we have achieved with the fluorescence detection setup, we will estimate the fluorescence photon flux expected at the detector upon the x-ray fluorescence process in aqueous solution of $[Fe^{II}(bpy)_3]^{2+}$ sample, which is discussed in more details in Chapter 6. In Fig. 4.30, the Fe K-edge absorption edge of $[Fe^{II}(bpy)_3]^{2+}$ in H_2O is shown in the narrow energy range above the edge energy E_0=7122.5 eV. The plot shows the number of fluorescence photons recorded in this energy range of the absorption spectrum, as analyzed from the pulse height distributions. We have marked the photon flux recorded at ca. 7130 eV, which corresponds to the most intense XANES peak (which is approximately twice more intense than the underlying absorption edge jump). At 7130 eV, we have detected on the average ca. 1.05 photons/pulse.

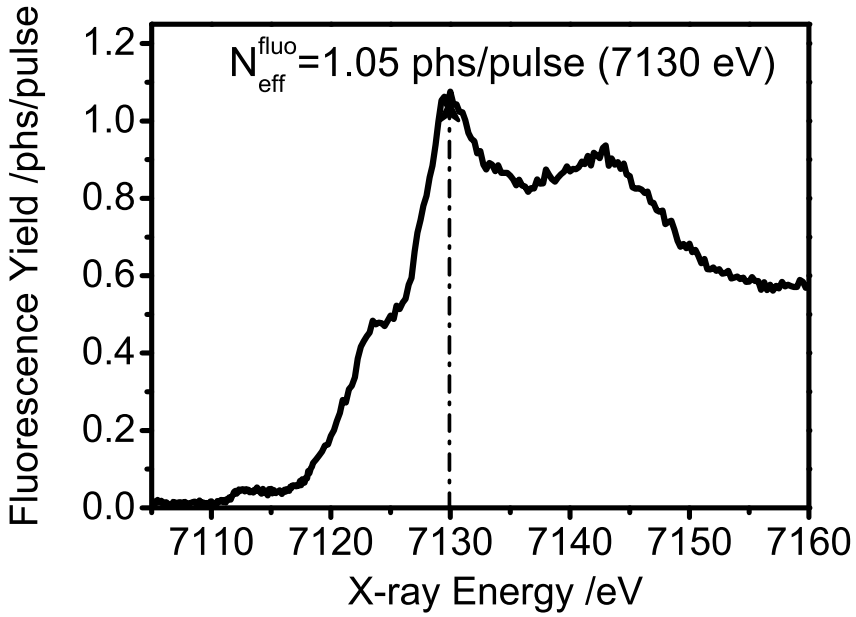

Figure 4.30: The K-edge XANES spectrum of 25mM aqueous solution of $Fe(bpy)_3$ complex measured in fluorescence mode. The detected intensity is displayed in terms of photos/pulse via Eq. 4.6. The vertical line (- · -) indicates the energy, at which the detected number of photons is compared to the estimated photon flux using Fig. 4.26.

In the following we will estimate the overall efficiency of the fluorescence process and the total losses up-stream the microXAS beamline, including the sample itself and all the beamline components. Next, we will compare the measured beamline flux (assuming the shot-noise distribution of the x-ray pulse intensity) with the value provided by theoretical flux curve (see Fig. 4.26) value around the Fe K-edge absorption. The x-ray fluorescence is an isotropic process meaning that the x-ray photons produced are emitted in the entire 4π of a solid angle. Our detector can only extract a small fraction of the solid angle, which depends on the active area of the APD and its distance from the x-ray beam on the sample. We estimated the slid angle of our 16 mm APD to be on the order of 5-7 %, using the following relation:

$$\Omega = \frac{Active\,Area}{4\pi R^2} = \frac{\pi r_{APD}^2}{4\pi R^2} \tag{4.7}$$

and assuming that R=17 mm is the distance from the APD active area to the sample jet, and r_{APD}=8 mm is the detector's active area radius. The quantum yield of the detector is assumed to be ≥ 0.8. The quantum yield for the fluorescence process at Fe K-edge (i.e. assuming it is mainly due to $K_{\alpha 1}$ emission from the L_3 edge) is ca. 30%. These 3 loss contributions yield an overall factor of 1×10^{-2}. Next to it, the absorbed fraction of incoming x-ray photons in a ca. 300 μm thick jet of 25 mM aqueous solution of $[Fe^{II}(bpy)_3]^{2+}$ is ca. 2%, according to Lambert-Beer's law (see Eq. 3.16), meaning that only this fraction of the incident photons will be absorbed and contribute to the fluorescence signal. On the other hand, we have measured a photon flux of ca. 3000 photons/pulse below the Fe K-edge of the same compound in transmission mode, which translates into ca. 60 photons that will be emitted during the fluorescence process. With the present solid-angle and detector efficiency we expect $\sim$0.6 photons/pulse to contribute to the absorption edge jump measured in fluorescence mode, which very close to 1 photon/pulse detected at the most intense XANES resonance above the actual absorption edge (about a factor of 2 less intense than the XANES feature discussed above). This gives us confidence that the photon flux estimated from the measured data is in agreement with our assumption that the experimental noise is mainly dominated by the shot-noise contribution of the x-ray photon flux.

Now, let us compare the derived photon flux to the calculated values of the microXAS endstation. The beamline is specified to deliver ca. $2\cdot10^{12}$ photons/s/0.015% BW at 7.1 keV for 350 mA of stored current and 7.5 mm gap settings (see in Fig. 4.26). At this beam current value, the camshaft current amounts to ca. 2-3 mA, which corresponds to 1.6×10^4 camshaft photons/pulse and 0.015% energy bandwidth. Taking into account the loss due to mismatch in acceptance angle of the KB mirrors and incident beam size (a factor of ca. 2.5), transmission through a 250 μm thick diamond filter placed for security reasons upstream the beamline (ca. 72 % transmission at 7.1 keV), absorption losses in ca. 300 μm thick H_2O jet (ca. 66 % transmission at 7.1 keV) and absorption in a 0.5 μm thick Cr foil used in the I_0 detector (89 % transmission), we are expecting the measure as few as ca. 3×10^3 transmitted camshaft photons/pulse.

Hence, we obtain a very good agreement between the calculated and measured flux values via pulse-height distributions. We can, therefore, make the reasonable assumption that the electronic noise is negligible in our current setup. In any case, the electronic noise is independent of the shot-noise (photon noise), so that its contribution to the total noise present in our data is minor. In addition, the data shown in Fig. 4.19 follows the square law dependence of the noise, which is a characteristic feature of the shot noise. If any other noise sources would contribute significantly to the measured signal, i.e. mechanical beamline noise or electronics noise, one would expect a clear deviation from the square law dependence. Hence, we can conclude that no additional and significant noise contribution are present in our current experimental configuration, including the overall microXAS beamline design and the data acquisition scheme.

4.10 Femtosecond Optical Pump-Probe Setup

The femtosecond (fs) transient absorption spectrometer, used in the experiments presented and discussed in Chapters 5 and 6, is based on a 1 kHz Ti:sapphire pumped regenerative amplifier system producing ∼120 fs, 0.8 mJ pulses centered at λ=800 nm. The schematic drawing of the setup is shown in Fig. 4.31. It is based on pump-probe scheme [294], where the pump pulse provides the excitation intensity required for triggering the investigated photoinduced process and the probe pulse monitors the subsequent spectro-temporal evolution of the process as a function of time delay between both pulses.

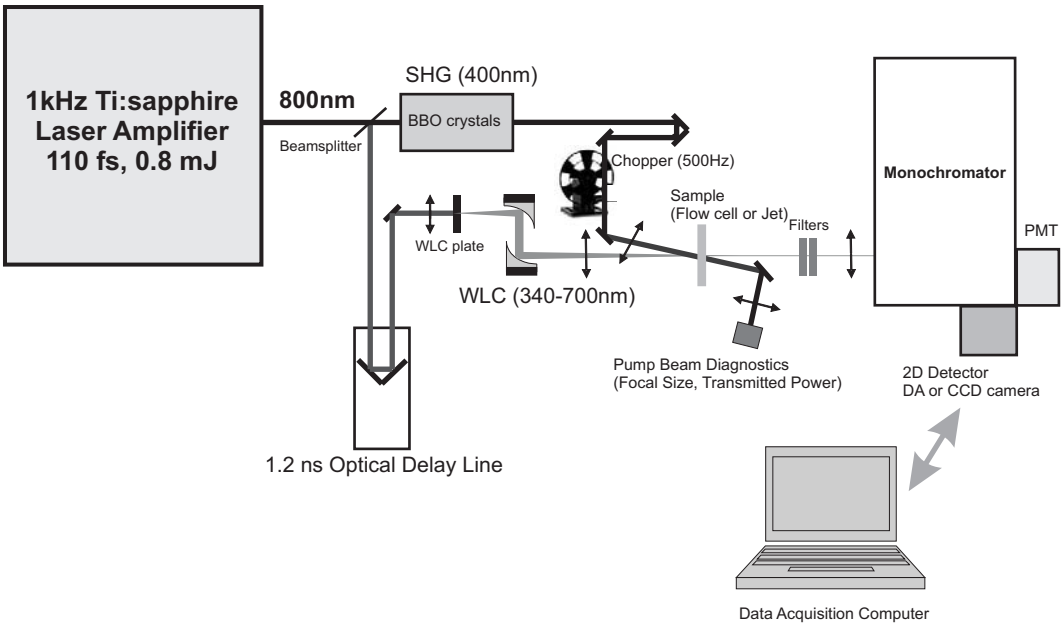

Figure 4.31: The schematic drawing of the femtosecond transient absorption setup used in the experiments (see text for details)

In case of the fs transient absorption setup illustrated in Fig. 4.31, the major part of the amplifier output light ($\sim 90\%$) is used second harmonic generation (λ_{SHG}=400 nm)process (denoted as in Fig. 4.31), which serves as the pump pulse in the experiments providing pulse energies up to ca. 100 μJ. The remaining part (10%)of the amplified output at the fundamental wavelength of 800 nm is used to generate the spectrally broad probe pulse via white-light continuum (WLC) generation process [295]. The WLC in a broad spectral range from 340-650 nm can be obtained by focusing a small part of the fundamental output into a 2 mm thick CaF_2 window. The time delay between both pump and probe pulses can be controlled by means of an optical delay line, which adjusts the optical path of the probe pulse (with respect to the pump). The optical delay line consists of a stepper-motor controlled translation stage capable of increasing the optical path lengths in 0.1μm motor steps N_{steps}. The path length can be translated into the temporal delay $\Delta\tau$ via:

$$\Delta\tau = \frac{C \times N_{steps}[\mu m]}{3.3[\frac{\mu m}{fs}]} \tag{4.8}$$

where C is a constant factor, which accounts for the retroreflection (180° reflection) of the probe beam in the optical delay line (see Fig. 4.31). In a simple case, C=2, the total optical path length change due to one motor step movement would change by a 0.2 μm (both incoming and outcoming path lengths will be affected), which corresponds to ca. 0.6 fs. The optical delay line in Fig. 4.31 allows adjusting the total optical path length up to 10 cm, which corresponds to the total time delay of ca. 600 ps (with C=2). In the experiments discussed in Chapters 5 and 6, this time delay was extended to ca. 1.2 ns by double-folding (retroreflecting the probe beam twice) the delay line and thus C=4 (in this case $N_{steps} = 1$ corresponds to ca. 1.2 fs). The 3.3 [μm/fs] constant in the denominator of Eq. 4.8 converts 1 μm path length into fs.

After the optical delay line, the probe beam is re-collimated by means of parabolic mirrors and focused on the sample by either a thin lens or another parabolic mirror. The pump beam crosses the optical chopper and is focused on the sample as well. The optical chopper divides the frequency of the pump beam down to 500 Hz (twice less than the fundamental repetition rate of the laser amplifier, see Fig. 4.31)for the reasons explained further in this Section. The full width at half maximum (FWHM) diameters of the excitation and probe beams at the sample position were measured two-fold: a) with a 50 μm pinhole placed at the sample position and b) using a CCD camera inserted into both laser beams at the same position. The probe beam diameters used in the experiments presented in Section 5.1 and Section 6.1 of Chapter 5 and 6 were fixed to 60 μm and 65 μm respectively, whereas the pump beams were fixed to 180-220 μm and 180 μm respectively.

The relative polarization of the excitation and probe electric field vectors were orthogonal to each other in the experiments on aqueous samples of $[Fe^{II}(bpy)_3]^{2+}$ (see Section 6.1 in Chapter 6), whereas in case of measurements on $[Ru^{II}(bpy)_3]^{2+}$ (Section 5.1 in Chapter 5), the polarization of the excitation and probe electric field vectors were either orthogonal or set to the magic an-

gle [296–298] (54.7°). The samples were flown in a free-flowing jet having a thickness of 100-200 μm opening, depending on the optical density of the sample. The gear pump was operated at sufficient speed (ca. 5m/s) in order to refresh the sample after each incident laser shot. In this scheme, we recorded adjacent pairs of pumped and unpumped spectra for each laser shot and after subtraction we obtained transient spectra.

Behind the sample, the probe beam was re-collimated and focused on the entrance slits of a monochromator coupled with either a 512 pixel diode array (DA) (measurements presented in Section 6.1, Chapter 6)or a charge-coupled device (CCD) camera (as in case of measurements shown in Section 6.1, Chapter 6). In both case, the monochromator grating of 150 l/mm was used in order to cover a broad spectral range between 340-650 nm of teh recorded transient absorption spectra. In the earlier version of the setup shown in Fig. 4.31, the kinetics were recorded by means of a photomultiplier tube (PMT coupled to the second exit of the monochromator. A motorized mirror mounted behind the gratings allowed to switch between the PMT and CCD detectors, so that the spectra at a given time delay could have been recorded by means so the CCD camera. The DA detector records full 2D transient spectra (both wavelengths and time), so inherently the temporal and spectral information is acquired simultaneously at 1kHz repletion rate. The spectral response and the energy calibration were measured two-fold; either by using a Hg line emission lamp or by recording a steady-state spectrum of the sample with the WLC.

The group-velocity dispersion (GVD) of the WLC was measured in a neat water jet exploiting the two-photon absorption [299] and the cross-phase modulation [300] signals around time zero . The transient absorption spectra measured at short delay times (t<10 ps) were corrected for the chirp in both measurements on $[Ru^{II}(bpy)_3]^{2+}$ and $[Fe^{II}(bpy)_3]^{2+}$.

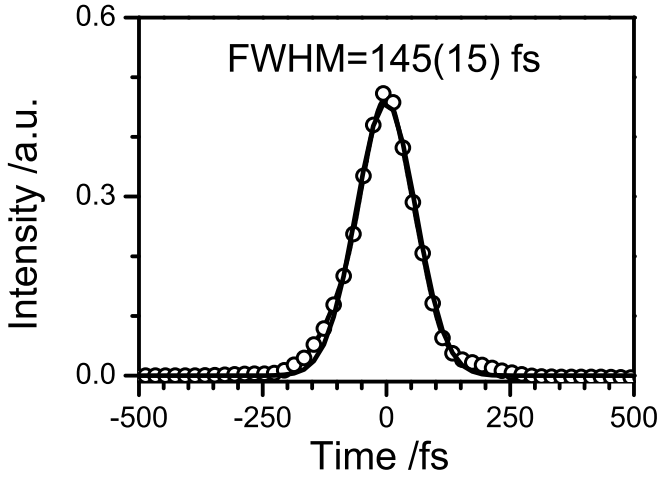

Figure 4.32: The impulsively-induced Raman line emission of H_2O solvent can be detected around 450-460 nm. Although it is an artefact, it serves as a useful measure of the cross-correlation function of both pump and probe pulses at the sample site.

In both cases, H_2O was the solvent and we observed a strong emission feature at 450-460 nm in liquid water due to the impulsively-induced Raman-active symmetric stretch mode of H_2O [300,301] (ν_1=3490 cm^{-1}) as illustrated in Fig. 4.32. Here the Raman signal measured during the measurements on aqueous samples of $[Fe^{II}(bpy)_3]^{2+}$ is shown and it delivers the cross-correlation function (instrument response function, IRF) between the pump and probe pulse, i.e. FWHM duration 140±15 fs. In the earlier version of the setup (Fig. 4.31) used in the measurements presented in Section 5.1, the recorded Raman signal (not show here) delivered a slightly broader cross-correlation function of ca. 195±15 fs at FWHM. Using the signal shown in Fig. 4.32 and assuming Gaussian-shaped pump and probe pulses of equal pulse width, one can infer the excitation (pump) pulse width at 400 nm to be equal to ca. 95±10 fs (FWHM) in case of $[Fe^{II}(bpy)_3]^{2+}$ and ca. 110-135 fs (FWHM) for the pump pulse in $[Ru^{II}(bpy)_3]^{2+}$ experiments. This approximately agrees with the autocorrelation measurements of the 800 nm beam, which delivered ca. 100-110 fs pulse widths.

Chapter 5

Energy and Structural Relaxation Dynamics of $[Ru(bpy)_3]^{2+}$

In this chapter we present the results of the experimental studies of energy and structural relaxation dynamics in an aqueous form of $[Ru^{II}(bpy)_3]^{2+}$ complex molecule. We introduce the photochemical cycle of the compound and describe the different relaxation pathways of involved photoproducts involved upon the laser-induced charge-transfer reaction involving the *Metal-to-Ligand Charge Transfer* (MLCT) states of $[Ru^{II}(bpy)_3]^{2+}$. We identify all main photoproducts and their reaction kinetics involved in the energy relaxation processes by means of femtosecond to picosecond transient absorption spectroscopy. Furthermore, we investigate the influence of the electron transfer reaction on the electronic and molecular structure of the lowest-lying MLCT state by means of picosecond time-resolved x-ray absorption spectroscopy. We demonstrate for the first time that the charge transfer reaction involving the ligand system leads to a detectable Ru-ligand bond distance decrease of ca. 0.03Å [35], which has not been possible to observe by means of time-resolved optical methods so far.

5.1 Time-Resolved Optical Studies

5.1.1 Introduction

Ruthenium(II)-tris-2,2'-bipyridine, $[Ru^{II}(bpy)_3]^{2+}$, represents a paradigm and a model system of intramolecular electron transfer reactions [82, 86, 91, 111, 113, 119, 302–307]. It is also the core member of a family of transition metal-based devices for solar energy conversion [101, 102, 302]. $[Ru^{II}(bpy)_3]^{2+}$ has been extensively studied, and most is known about its excited state properties [86, 90, 91, 120]. The photochemical cycle of $[Ru^{II}(bpy)_3]^{2+}$ can be sketched by a simple level scheme (Fig. 5.1). Light excitation of a metal-centered valence

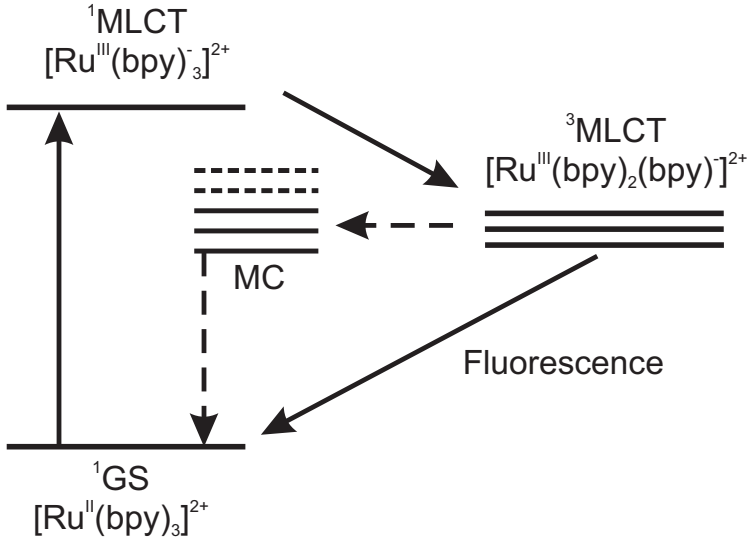

Figure 5.1: Photochemical cycle of $[Ru^{II}(bpy)_3]^{2+}$ in a simplified energy level scheme. Absorption of visible light removes a metal-centered (MC) $4d$ electron in its ^{1}GS into the (^{1}MLCT) state, where it undergoes ultrafast intersystem crossing into the ^{3}MLCT state, localized onto the bipyridine ligand system. The ^{3}MLCT state decays nonradiatively via the high vibrational levels of the MC ground state and via excited states, and radiatively with a fluorescence lifetime of ∼600 ns at room temperature [113].

electron from its singlet ground state (^{1}GS) (originating from the ligand-field split t_{2g} level, see Fig. 2.6) into the lowest-energy absorption band (400-500 nm) leads to the formation of a singlet Metal-to-Ligand Charge Transfer (^{1}MLCT) state, which undergoes intersystem crossing, with nearly unit probability [308], to a long-lived triplet state (^{3}MLCT) in ca. 15 fs [82] (see Eq. 5.1). Localization of the photoexcited MLCT electron on one (or two) of the bpy ligands is still unclear and a subject to debate, although in various studies it has been reported to localizes on a single bipyridine ligand within ca. 300 fs [111, 112].:

$$[Ru^{II}(bpy)_3]^{2+}(^1\text{GS}) \xrightarrow{\hbar\omega} [Ru^{III}(bpy)_3^{-1/3}]^{2+}(^1\text{MLCT}) \tag{5.1}$$

$$\longrightarrow [Ru^{III}(bpy)^{-1}(bpy)_2]^{2+}(^3\text{MLCT}) \tag{5.2}$$

At room temperature and in aqueous solutions the emission of the ^{3}MLCT state exhibits a measured lifetime of about 600 ns [113], due to efficient (95%) nonradiative quenching to high vibrational levels of the ground state and to the triplet *metal-centered* (MC) states (Fig. 5.1) [91, 309]. The photoinduced electronic changes (change of oxidation state, a possible localization of the electron on a single (or two) ligands) should have consequences on the transient molecular structure. The localization of the electron on one bpy ligand changes the ground state D_3 symmetry to C_2 symmetry in the ^{3}MLCT state [111], at least from the electronic point of view and probably, the structural one also. Both the increased electrostatic interaction and polarization between the Ru^{III} atom and the bpy^- and bpy ligands, as well as the reduced π-backbonding, due to the increased oxidation state of the Ru atom, should lead to a modification of the Ru-N bond distances [114]. The first two effects tend to contract the Ru-ligand bonds, whereas the reduction of the π-backbonding, in general, elongates the metal-ligand bond lengths. So, in this case, the $4d$-electron transfer to the ligand triggers a rather complex structural change, where to counteracting mechanisms affect the molecular bond between the Ru ion and the bpy ligands.

The interplay between electronic and geometric changes is of prime importance for our understanding of elementary charge transfer processes [92, 310]. From a fundamental point of view, structural information is valuable in order to get insight into the photocycle itself and the non-adiabatic dynamics therein taking place. From a practical point of view, this may help design new transition-metal based compounds with optimized reductive-oxidative functions in fabricating artificial solar cells [101, 102, 120, 121, 302, 311]. Structural information is of special interest in the development of molecular-based materials, capable of performing efficient intermolecular charge transfer, by means of a control of the spatial arrangement of their constituents [118, 119]. In several such arrangements strong electronic coupling between the excited species and its nearest neighbors makes the electron transfer adiabatic [86]. Hence, the rate is governed by the nuclear dynamics, as the activation energy depends to a great extent on the reorganization energy of the reacting species during the electron transfer, which involves the stretching or contraction of metal-ligand bonds.

5.1.2 Femtosecond Optical Transient Absorption Results[1]

In the following section, we report a femtosecond pump-probe study on the photochemistry of concentrated aqueous solutions of $[Ru^{II}(bpy)_3]^{2+}$, as a function of pump power (up to 2 TW/cm^2) with 400 nm light. The transient absorption spectra in the 345-660 nm range up to 1 ns time delay were recorded (see Section 4.10 for more details on the experimental setup) and their analysis revealed the coexistence of the following photoproducts: the triplet ^{3}MLCT (Metal-to-Ligand-Charge-Transfer) excited state, the reduced form $[Ru^{II}(bpy)_3]^{2+}$ [91], the oxidized species $[Ru^{III}(bpy)_3]^{3+}$ [91], next to the by-product of high intensities as a solvated electron e_{aq} [312, 313]. The ^{3}MLCT state is formed

within the excitation pulse and undergoes vibrational relaxation in 3-5 picoseconds, as evidenced by the shift of the ligand-centered (LC) absorption band below 400 nm.[1]

As already discussed, light absorption within the visible MLCT band of $[Ru^{II}(bpy)_3]^{2+}$ populates the ^{1}MLCT singlet excited state, which undergoes ultrafast intersystem crossing [82] with a near unit probability [314] to the long-lived (600 ns in water at room temperature [113]) triplet ^{3}MLCT excited state (Fig. 5.1). In the latter state, the transferred electron is localized on one (or two) of the bpy ligands [111, 112], giving rise to a $[Ru^{III}(bpy)^-(bpy)_2]^{2+}$ species in the following reaction sequence shown in Eq. 5.1. The dominant intramolecular decay of the ^{3}MLCT state is radiationless, involving thermally activated relaxation to optically dark metal-centered excited states (so-called triplet metal-centered ^{3}MC or *d-d* states) [91], and to high vibrational levels of the ground state. Bimolecular quenching is also important for the ^{3}MLCT state because of its long lifetime.

The reduction and oxidation potentials of the ^{3}MLCT state are large and nearly equal in magnitude (ca. 0.85 V) [91], so both oxidative and reductive quenching can occur, resulting in the formation of the reduced product $[Ru^{II}(bpy)^-(bpy)_2]^+$ (later abbreviated as $[Ru^{II}(bpy)_3]^+$) and the oxidized product $[Ru^{III}(bpy)_3]^{3+}$. With femtosecond photolysis pulses, peak intensities of $\sim 10^{28}$-10^{30} photons/cm^2/s ($\sim$0.005-0.5 TW/cm^2) are easily achievable, which lie in the range of saturation intensities for metal complexes. This may also lead to multi-photon absorption to highly-excited states, which in return exhibit new deactivation pathways, e.g., charge ejection. Furthermore, in concentrated samples and in molecular assemblies, cooperative effects [?, ?, 315] may arise, due to the high density excitation, which are still not fully understood.

Despite the impressive literature on Ru-polypyridyl complexes, few studies have dealt with the issues of high excitation intensities and large concentrations for these systems, and these were mainly done with nanosecond pulses. Milosavijvich and Thomas [303] carried out the only such study for the case of $[Ru^{II}(bpy)_3]^{2+}$ ($\leq$100 mM) adsorbed onto cellulose as well as in water solution. They observed that the ^{3}MLCT emission obeyed pseudo first-order decay when changing concentration of the ground-state complexes in the range 10-100 mM, and ascribed this to *catalyzed deactivation* of the excited complex by a neighboring ground-state complex. At large excitation energies (and in consequence, large ^{3}MLCT concentrations), the ^{3}MLCT decay followed mixed first- and second-order kinetics attributed to the presence of both ground-state quenching and triplet-triplet annihilation. It was concluded that triplet-triplet annihilation gives rise to singly charged complexes (observed by their absorption at 520 nm) via intermolecular electron transfer [303, 315, 316].

Recently, however, an energy-transfer annihilation mechanism was invoked for polypyridyne Ru(II) complexes bound to polystyrene [119]. Nanosecond laser intensity effects have been investigated in dilute aqueous solutions

[1]The results presented below were submitted to *J. Phys. Chem.* **B** 2006

by Thompson *et al.* [317] and by Goez *et al.* [312, 313]. In the latter case, no product other than ^{3}MLCT was observed, even at the highest intensities of the 532-nm excitation pulse. Upon excitation at 308 and 355 nm, the solvated electron was observed and its occurrence explained by sequential two-photon photoionization of $[Ru^{II}(bpy)_3]^{2+}$ via the ^{3}MLCT intermediate [312, 313]. It was also suggested that the same nanosecond photolysis pulse drives the excited state reduction of a ($[Ru^{III}(bpy)_3]^{3+}$) by-product by the solvent H_2O, thereby re-generating the ^{3}MLCT species. However, this interpretation is very different from that of Thompson *et al.* [317] who, following high-power 355-nm photolysis of $[Ru^{II}(bpy)_3]^{2+}$, proposed a photochemical route with formation of a long-lived complex (lifetime ca. 80 μs) with a monodentate ligand.

This brief review shows that the behavior of $[Ru^{II}(bpy)_3]^{2+}$ in concentrated solutions under high-intensity femtosecond excitation is by no means clear and, given the many potential applications of Ru-polypyridine complexes, it deserves further investigation, which we present below. In this thesis, we determine product concentrations of the light-triggered and subsequent dark reactions up to 1 ns time delay, and disentangle, in a systematic way, the ensuing processes. Previously, femtosecond laser studies [82,111,112,307] within the first picosecond revealed rich dynamics in the initially populated ^{1}MLCT and ^{3}MLCT states, and microsecond-to-millisecond studies [90,91,303,317,318] unraveled the diffusion-controlled and slower reactions involving photolysis products of this complex, but much less is known about the intermediate time scale. Our results can be embedded into a rather simple picture of known reaction products without invoking unknown dark channels or exotic reaction intermediates [317]. They also demonstrate the "robustness" of $[Ru^{II}(bpy)_3]^{2+}$ under high intensity laser excitation.

Assuming the existence of all aforementioned photoproducts, it is necessary to know the absolute absorption cross-section of the involved species, whose spectra are shown in Fig. 5.2.

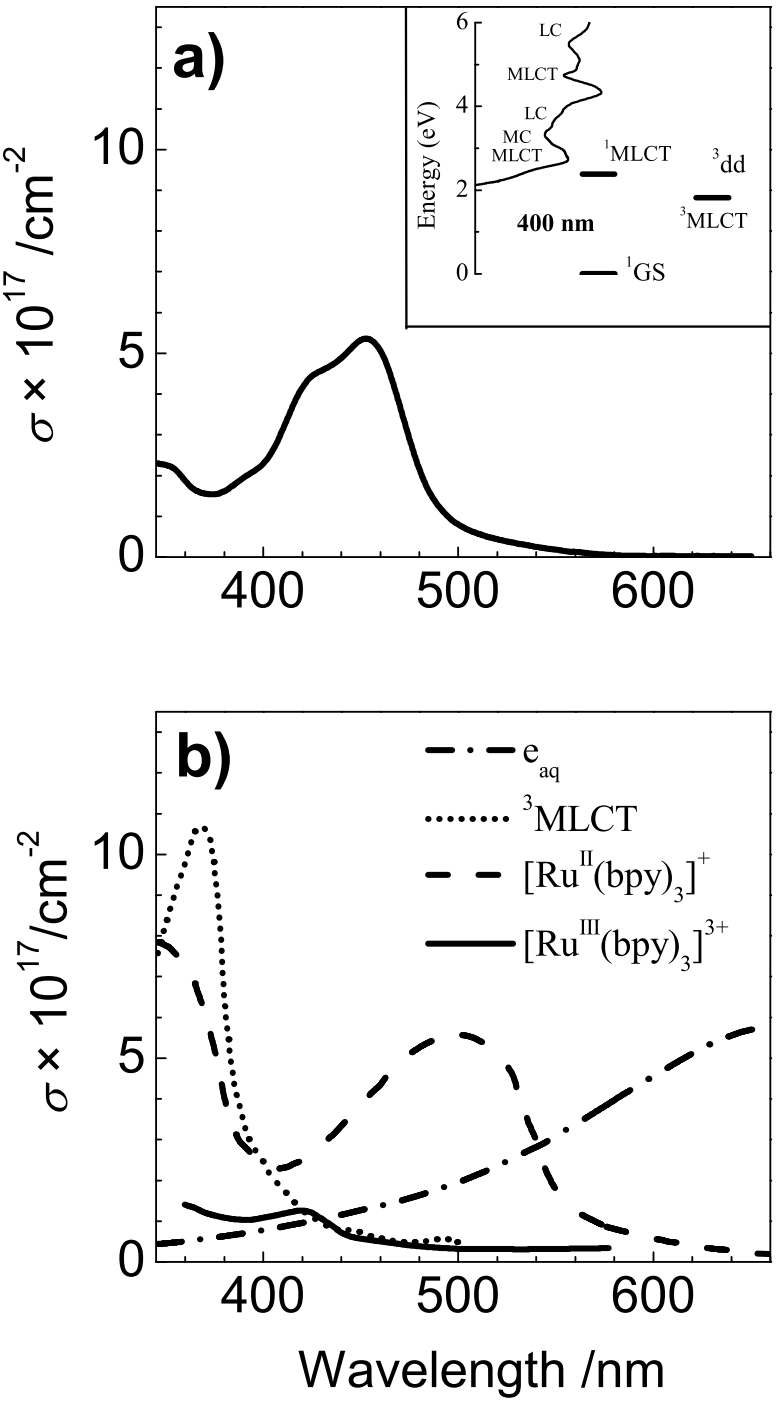

Figure 5.2: a) Absorption spectrum of aqueous $[Ru^{II}(bpy)_3]^{2+}$. The inset shows a simplified energy level diagram of the lowest excited states together with the absorption spectrum from the singlet ground state ^{1}GS. The assignment of the MC, LC and MLCT bands is adopted from Ref [91]. b) Absorption spectra of the product species involved in the photolysis of $[Ru^{II}(bpy)_3]^{2+}$ in water solutions: ^{3}MLCT state [319], $[Ru^{II}(bpy)_3]^{+}$ [320], $[Ru^{III}(bpy)_3]^{3+}$ [302], and e_{aq} [321].

As the spectrum of $[Ru^{III}(bpy)_3]^{3+}$ was reported only from 360 to 600 nm, we have set σ_{360}=1.4·10^{-17} cm^2 in the 346-360 nm interval and σ_{600}=0.35·10^{-17} cm^2 in the 600-660 nm interval. The absolute cross-section of the ^{3}MLCT state reported in the literature is somewhat contradictory. For production of only the ^{3}MLCT species at the expense of the ground state $[Ru^{II}(bpy)_3]^{2+}$ species, Eq. D.3 reduces to:

$$\Delta A_\lambda = \frac{10^{-3} N_A l}{\ln 10} \Delta c [\sigma_\lambda(^3MLCT) - \sigma_\lambda([Ru^{II}(bpy)_3]^{2+}) \tag{5.3}$$

where Δc is the (identical) concentration change of both species. Once either the absolute value of $\lambda(^3$MLCT) at a single wavelength or the concentration of the excited state species are known by means of photochemical methods [322], the transient absorption spectrum can be converted to an absolute cross-section spectrum. The λ_{368nm} values at the ^{3}MLCT absorption maximum in H_2O lie around ca. 8.5-11.0·10^{-17} cm^{-2} [113, 319, 323–331]. Here we use the spectrum reported by Ref. [319], which agrees with several of the above cited. As this spectrum was reported only for to $\lambda \leq$500 nm, we extended it to 660 nm using Eq. 5.3 and the ΔA spectrum measured for the 0.4 mM sample at low power. We obtain a roughly constant $\lambda(^3$MLCT)=0.46·10^{-17} cm^2 in this range, which reasonably agrees with the published values [325, 330]. We hereby neglect a weakly pronounced spectral dependence in the 500-660 nm range, which does not alter the fit results shown below.

Measurements in Neat Water

Since we are concerned with the behavior of $[Ru^{II}(bpy)_3]^{2+}$ under high intensity excitation, it is important to first assess the contribution of photogenerated solvated electrons from the pure water solvent. Excitation of neat H_2O with high intensity 400 nm, 135 fs pulses yields a broad absorption band, centered around 700 nm, due to solvated electrons, which are formed by three-photon ionization of water molecules [332, 333]:

$$H_2O \rightarrow H_2O^+ + e_{aq} \tag{5.4}$$

The solvated electrons exhibit practically no decay within 1 ns and their concentration shows a non-linear dependence on the excitation fluence (E_0) to the power of ca. 2.5 (not shown here). At the largest irradiance of 2.15 TW/cm^2 (E_0=0.31 J/cm^2), we observe their strongest absorption(corresponding to $\Delta c^{100ps}{}_{max}$=1.35 mM averaged over the 100 μm thick water jet). For energy fluences smaller than 0.028 J/cm^2 no measurable signal (ΔA_{660nm} <8·10^{-4}) was detected. The lack of substantial recombination on the 1 ns time scale and the nearly cubic excitation energy dependence of the e_{aq} concentration are consistent with earlier studies on water photoionization with ca. 150 fs laser pulses at a similar wavelength [332]. However, a substantial (tens of °C) heating of water was suggested for intensities > 1 TW/cm^2 based on a red shift in the electron absorption spectrum [332, 333].

The range 345-660 nm, in which the ΔA spectra were measured here (the irradiance range 1-1.9 TW/cm^2) is sufficient for the comparison. The relative ΔA amplitudes are clearly different from the experimental spectrum of photoelectrons observed 50 ps after the excitation of water with a 1.9 TW/cm^2 pulse [332,333], or from the spectrum of the thermalized hydrated electrons in 80°C water. Both the spectrum of e_{aq} at room temperature and the spectrum of the photoelectrons averaged along the path of the beam [332], agree with our spectra.

Measurements of Aqueous $[Ru^{II}(bpy)_3]^{2+}$

The photolysis wavelength 400 nm lies on the high-energy side of the broad MLCT band of $[Ru^{II}(bpy)_3]^{2+}$, which peaks at 453 nm in water (Fig. 5.2a). Figures 5.3 through 5.6 show the transient absorption spectra of aqueous $[Ru^{II}(bpy)_3]^{2+}$ (10 mM) at different pump-probe time delays and for varying pump fluences. Fig. 5.3 displays the depleted absorbance between 400 and 500 nm, the induced absorbance below 400 nm, due to the ^{3}MLCT excited state absorption, and in the wavelength region 500-660 nm, due to the solvated electron.

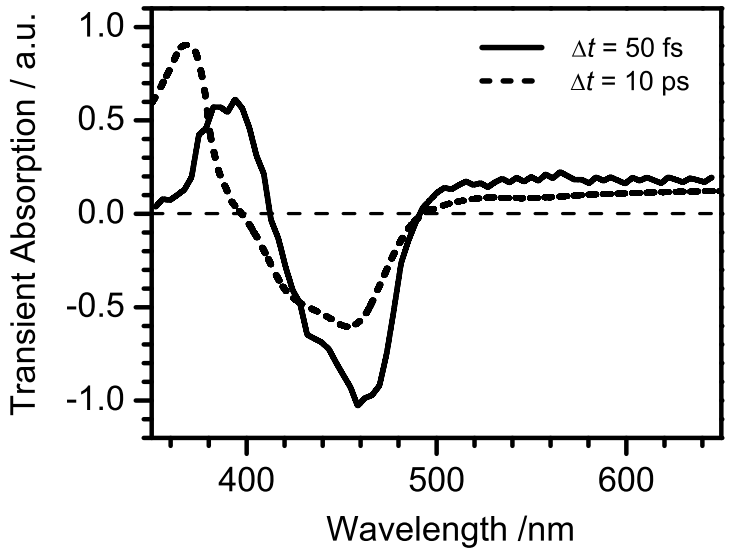

Figure 5.3: Transient absorption spectrum of aqueous $[Ru^{II}(bpy)_3]^{2+}$ 50 fs and 10 ps after photoexcitation (indicated). Both bleach and electron absorption decrease above 500nm, are probably due to ultrafast geminate recombination. Note the blue shift of $\sim$0.25 eV of the excited state absorption due to relaxation within the ^{3}MLCT manifold.

These features differ to some extent between 50 fs and 10 ps: a) the amplitudes of the bleach component and the electron absorption change, most probably due to immediate geminate recombination, which would reform the ground state complex; b) the ^{3}MLCT excited state absorption below 400 nm,

due to the Ligand-centered (LC) band, narrows and shifts to the blue, most probably due to electronic-vibrational relaxation in the triplet manifold. The ultrafast ΔA spectra (-50 fs$\leq$t$\leq$50 fs) provide further insight into the initial formation of reaction products (Figs 5.3 and 5.4a).

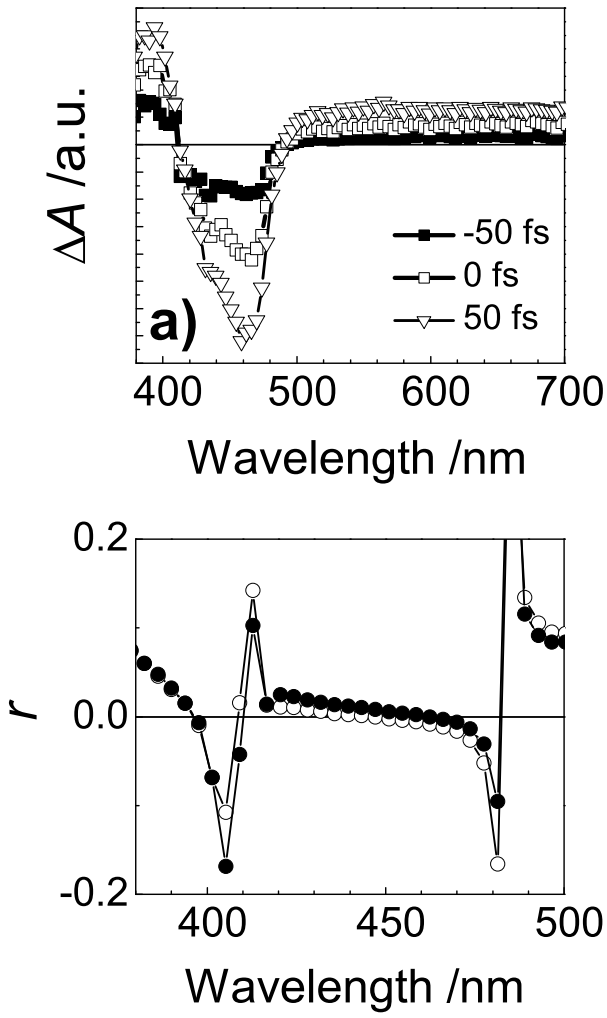

Figure 5.4: Aqueous $[Ru^{II}(bpy)_3]^{2+}$ (10 mM) excited with 400 nm photolysis pulses of 135 fs duration. a) Ultrafast transient absorption spectra at magic angle, within the photolysis pulse and incident fluence of 0.028 J/cm^2. The time delays are indicated in the plot. b) Wavelength dependence of the anisotropy at 20 ps (open circles) and 100 ps (solid circles) time delay, for E_0=0.12 J/cm^2.

Indeed, the absorption of the nascent photoelectron (above 500 nm) is already present, along with the substantial absorption from vibrationally hot ^{3}MLCT molecules. The latter can be rationalized by the extremely rapid intersystem crossing (ca. 15 fs), which in addition occurs at constant energy, as recently measured by femtosecond fluorescence up-conversion techniques [82]. The evolution of the absorption below 400 nm occur with a time constant of

3.5 ps at low E_0, increasing to 5 ps at the highest E_0 used, as measured at fixed wavelengths (not shown).

Our results differ from those of Wallin *et al.* [305, 306], who found no evolution of the band between 1-1000 ps, suggesting that the relaxation within the triplet manifold occurs in <1 ps. Comparing the short time scale ΔA spectra measured for increasing E_0 and normalized to the electron absorbance, we notice an additional absorption feature in the 510-530 nm region as early as 75 fs after excitation (Fig. 5.5a), which is also seen as a shoulder band at 510 nm at longer time delays (Fig. 5.5b). Within the first 2 ps, the electron absorbance undergoes a blue shift, which terminates at the spectrum of solvated e_{aq} observed at later times (e.g., 10 ps, Figs. 5.3 and 5.6). This shift was attributed to solvation and nonadiabatic electronic relaxation of the nascent electrons [321, 334]. At 10 ps, the absorbance at 660 nm is substantially larger than that observed in neat water under comparable excitation conditions, indicating that the majority of the solvated electrons is produced by photoionization of the solute.

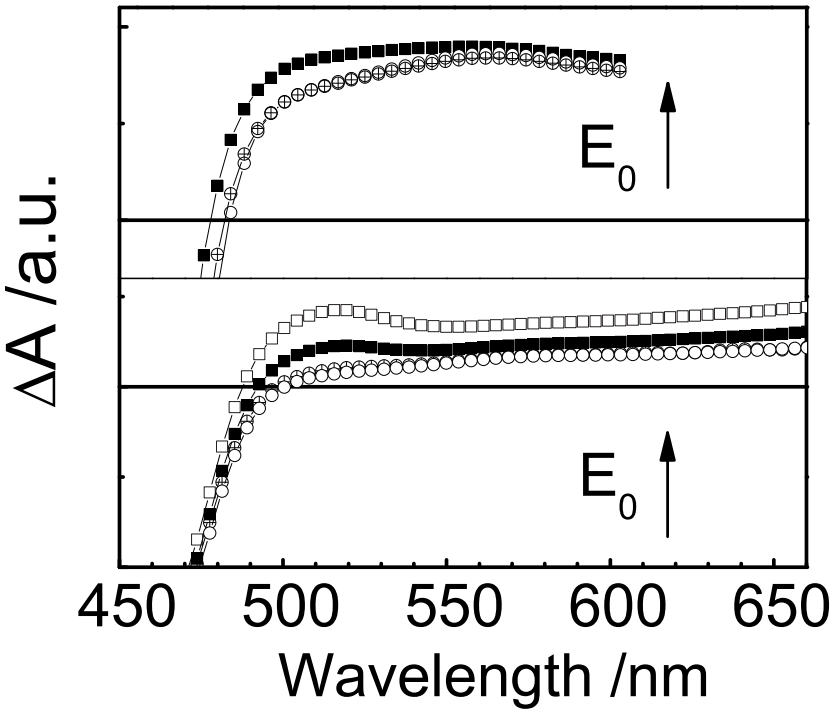

Figure 5.5: Transient absorption spectra of aqueous $[Ru^{II}(bpy)_3]^{2+}$ (10 mM) at magic angle, for different excitation energies E_0, recorded immediately one after the other with all other conditions being identical. In a), ΔA curves at 75$\pm$30 fs time delay, normalized at the ΔA_{660nm} point. In b), ΔA curves at 1 ns time delay, normalized at the ΔA_{450nm} point. The ΔA curves from top to bottom in both panels correspond to the following excitation energies E_0 (in J/cm^2): 0.15 (shown only in the panel b), 0.055 ,0.028 and 0.012

Typical ΔA spectra at longer time delays 10, 100 and 1000 ps for E_0=0.08-0.31 J/cm^2 are shown in Fig. 5.6

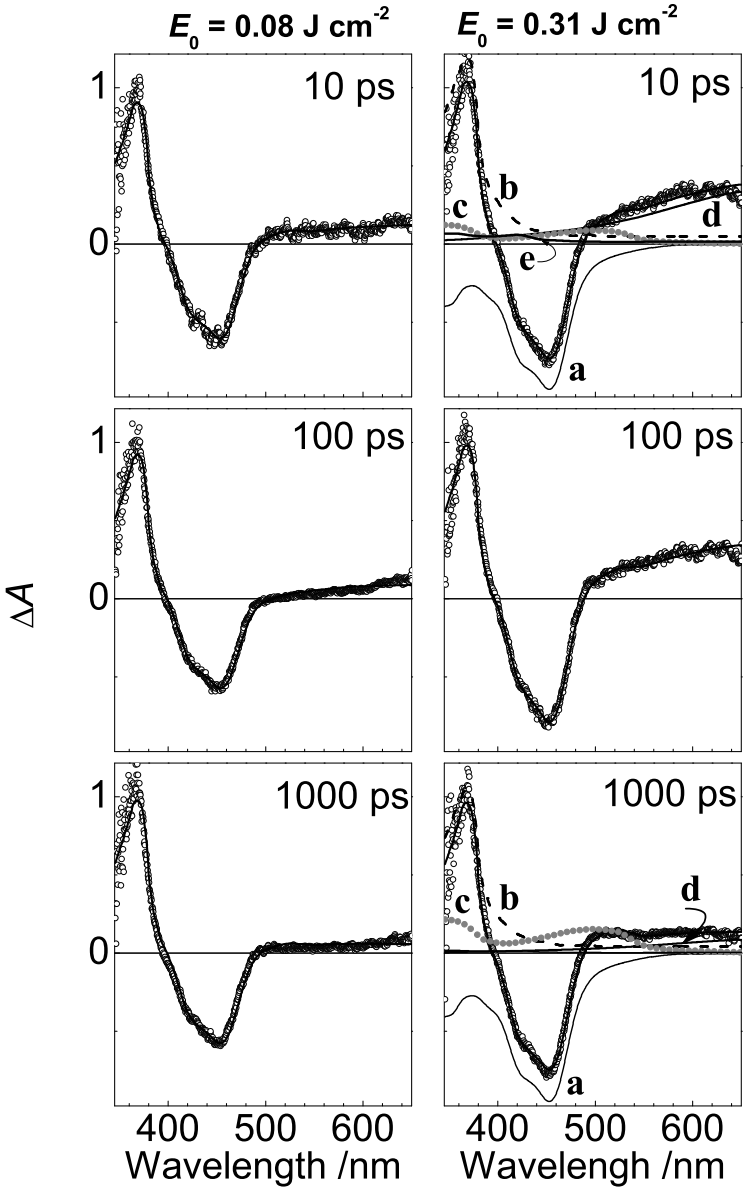

Figure 5.6: The measured transient absorption ΔA spectra (open dots) upon 400 nm photolysis of aqueous $[Ru^{II}(bpy)_3]^{2+}$ (10 mM) and their fits (shown as solid thin lines) to the steady-state absorption spectra of the involved species. Time delays are shown in the top left corners of each window. In the right panel, the individual steady-state product spectra obtained by spectral deconvolution of the measured ΔA spectra using Eq. 5.3 are shown: $[Ru^{II}(bpy)_3]^{2+}$ (a), ^{3}MLCT (b), $[Ru^{II}(bpy)_3]^{+}$ (c), e_{aq} (d), $[Ru^{III}(bpy)_3]^{3+}$ (e).

The most obvious change in the spectra between 10 and 1000 ps is the decay of the e_{aq}. As shown in Fig. 5.7a, it exhibits a 100 to 200 ps component for 0.08 and 0.38 J/cm^2, respectively, while an interesting increase of the ground-state bleach also shows up (Fig. 5.7b). This increase is larger than if it were merely caused by the decay of the overlapping absorption of solvated electrons (e.g. like in Fig. 5.3), suggesting therefore a net decrease of the ground-state $[Ru^{II}(bpy)_3]^{2+}$ population on ca. 200 ps time scale. The 510 nm absorption shoulder peak in the ΔA spectra, which was assigned to the absorption of the $[Ru^{II}(bpy)_3]^{+}$product (Fig. 5.2b) [320], also develops on the same time scale. The major, slower decay component of e_{aq} is not fully resolved on the 1 ns time scale of this experiment. Having taken into account that the decay at 660 nm (due to the solvated electron) has an offset due to the ^{3}MLCT absorption, we extract a time constant $\sim$1 ns for this slow component, which is roughly independent of excitation energy. The decrease of both ground-state bleach $[Ru^{II}(bpy)_3]^{2+}$and e_{aq} population together with the build up of the pronounced 510 nm band (thus due to the reduced species $[Ru^{II}(bpy)_3]^{+}$ is also clearly observed for the concentrated 20 mM solution. In fact, the amplitude increase of the reduced ground state from 50 ps to 1 ns could be ca. 1.5 times larger in the 20 mM solution than in the 10 mM solution at comparable initial e_{aq} concentrations (thus after ca. 50 ps). However, there is less probe transmission through the concentrated (20 mM) sample yielding less accurate spectra and consequently poorer fits of the ΔA spectra to Eq. 5.3. Therefore the yields of the product species were not systematically determined for such large solute concentrations.

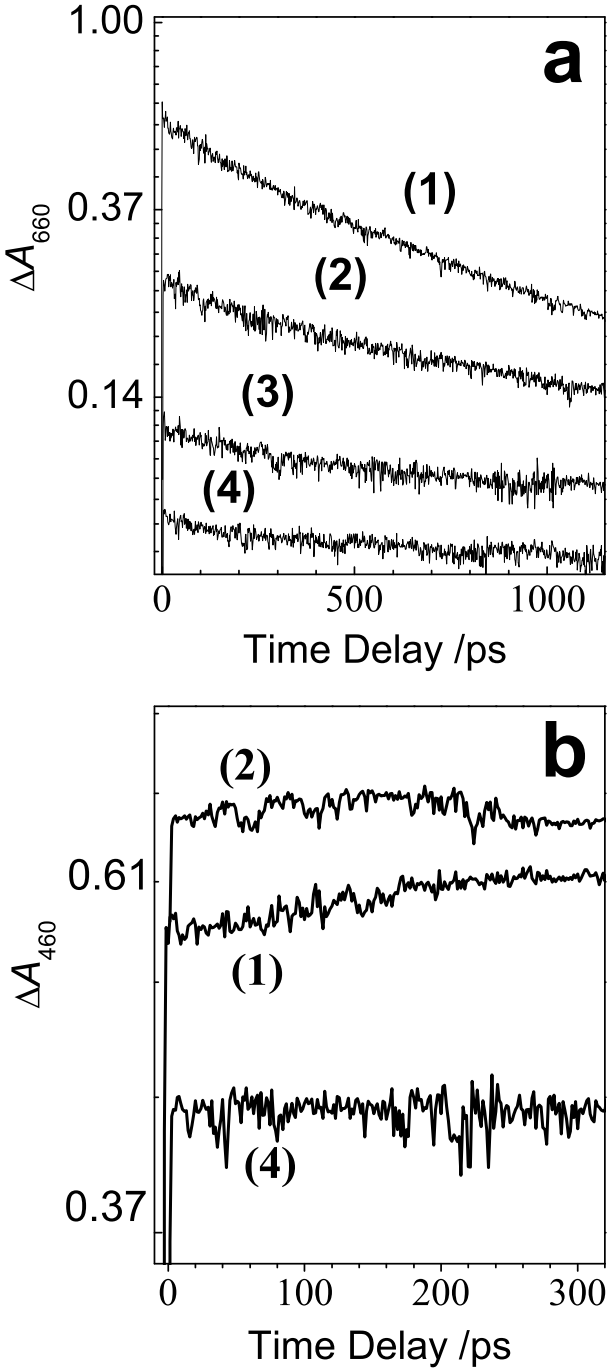

Figure 5.7: Temporal evolution of photoproducts following excitation of aqueous $[Ru^{II}(bpy)_3]^{2+}$ (10 mM) with 400 nm femtosecond laser pulses. The used excitation energies are (in J/cm^2): 0.15 (1), 0.055 (2), 0.028 (3), and 0.012(4). a): probing predominantly the solvated electron (λ=660 nm) b): probing predominantly the ground-state depletion (λ=460 nm).

Anisotropy Measurements

Rotational diffusion of metal-centered complexes similar to the ones considered in this work has often been studied in polar solvents other than water [304, 335–337]. When re-scaling the measured rotational periods according to the different viscosities of the used solvents with respect to that of water, we expect rotational diffusion times on a 100-150 ps time scale. The rotational diffusion time of $[Ru^{II}(bpy)_3]^{2+}$ (in D_2O at 33°C) has been measured to be 100 ps [338]. In addition, the localized electron in the ^{3}MLCT state can inherently hop from one ligand to another in a process called *interligand electron transfer* (ILET). An early estimate by Cooley *et al.* [337] indicates a 15 ps time constant for ILET in aqueous $[Ru^{II}(bpy)_3]^{2+}$, but more recent direct ultrafast studies of this and similar molecules suggest that it may be much faster [304–306].

Both rotational diffusion and ILET change the orientation of the molecular transition dipole moment, which is probed in these experiments, and may thus affect the population dynamics on the 10-100 ps time scale investigated in this work. Therefore, special care was taken such that neither rotational diffusion nor ILET be of any importance under our conditions. We find that neither the kinetic behavior nor the quantitative appearance of the products are noticeably affected by the relative polarization of the excitation and probe electric field vectors. Two relative orientations between the excitation and probe electric field vectors were compared: perpendicular and magic angle (54.7°) [296]. We also measured the transient absorption spectra with the parallel ($\Delta A^{\parallel}$) and perpendicular ($\Delta A^{\perp}$) relative polarizations at different excitation levels, from which we constructed the anisotropy (r) spectra using the usual expression: $r=(\Delta A^{\parallel}-\Delta A^{\perp})/(\Delta A^{\parallel}+2\Delta A^{\perp})$ [112]. The r spectra obtained at E_0=0.12 J/cm^2 reveal very small r values (r<0.05) within the absorption of 3MLCT and ground-state complexes (Fig. 5.3b). Much smaller values (r≈0) are obtained at larger E_0. The power dependence of r suggests that the anisotropy values are reduced by saturation effects [339], where the intense pump pulse excites a nearly isotropic distribution of ^{3}MLCT orientations (and of the depleted ground-state concentration discussed below).

Analysis of Transient Absorption Spectra at t≥10 ps

With the absolute σ-curves over the entire spectral range presented earlier, we use Eq. 5.3 to fit the ΔA spectra of $[Ru^{II}(bpy)_3]^{2+}$ (10 mM) measured between 10 ps and 1 ns. The use of three fit parameters, namely the concentration changes of ground-state $[Ru^{II}(bpy)_3]^{2+}$, ^{3}MLCT, and e_{aq}, yields fits of poor quality, which deviate significantly from the measured ΔA spectra around 380 nm and around 510 nm, especially at longer time delays and for larger excitation fluences. This suggests the presence of a new product species, namely $[Ru^{II}(bpy)_3]^{+}$, which absorbs both around 380 and 510 nm [320], (Fig. 5.2b). The inclusion of $[Ru^{II}(bpy)_3]^{+}$ in the fitting routine (i.e., four fit parameters) greatly improves the fits allowing us to adequately reproduce the entire ΔA curve (Fig. 5.6).

The addition of weakly absorbing $[Ru^{III}(bpy)_3]^{3+}$ to the fit improves the χ^2 values to a noticeable degree, but only for the ΔA spectra measured at 0.31 J/cm^2. The best-fit concentrations of $[Ru^{III}(bpy)_3]^{3+}$ are found to be at most 15%, on average, lower than the best-fit concentrations of e_{aq} at each time delay. The fact that both concentrations are correlated, even when not constrained by any specific relationship in the fit function, suggests that these two species are linked through a subsequent mechanism. A further increase in the number of product species is beyond the accuracy of our data and not necessary (see below). The species involved and their best-fit concentrations Δc as a function of time and incident pump fluence E_0 are summarized in Figures 5.8 and 5.9 and Table 5.1[2]

E_0 /Jcm^{-2}	Δc /mM	*Involved Species*[2]
	Time Delays /ps	
	10 100	
0.04	0.23 0.066	e_{aq}
	-3.02 -3.24	$[Ru^{II}(bpy)_3]^{2+}$
	2.98	$[Ru^{III}(bpy)^-(bpy)_2]^{2+}$
	0.0 0.028	$[Ru^{II}(bpy)_3]^{+}$
	0 0	$[Ru^{III}(bpy)_3]^{3+}$
0.08	0.53 0.083	e_{aq}
	-4.73 -4.98	$[Ru^{II}(bpy)_3]^{2+}$
	3.98	$[Ru^{III}(bpy)^-(bpy)_2]^{2+}$
	0.16 0.48	$[Ru^{II}(bpy)_3]^{+}$
	0 0	$[Ru^{III}(bpy)_3]^{3+}$
0.17	0.95 0.27	e_{aq}
	-5.90 -6.15	$[Ru^{II}(bpy)_3]^{2+}$
	4.32	$[Ru^{III}(bpy)^-(bpy)_2]^{2+}$
	0.33 0.58	$[Ru^{II}(bpy)_3]^{+}$
	0 0	$[Ru^{III}(bpy)_3]^{3+}$
0.31	2.13 0.58	e_{aq}
	-6.60 -6.15	$[Ru^{II}(bpy)_3]^{2+}$
	4.32	$[Ru^{III}(bpy)^-(bpy)_2]^{2+}$
	0.61 1.05	$[Ru^{II}(bpy)_3]^{+}$
	1.80 0.48	$[Ru^{III}(bpy)_3]^{3+}$

Table 5.1: The product species and their best-fit depleted concentrations at 10 ps and 1 ns time delays after photolysis of 10mM aqueous solution of $[Ru^{II}(bpy)_3]^{2+}$ with 135-fs laser pulses of various fluences (E_0) centered at 400 nm wavelength

[2]See Figs. 5.8 and 5.9 for the temporal behavior of the species concentrations

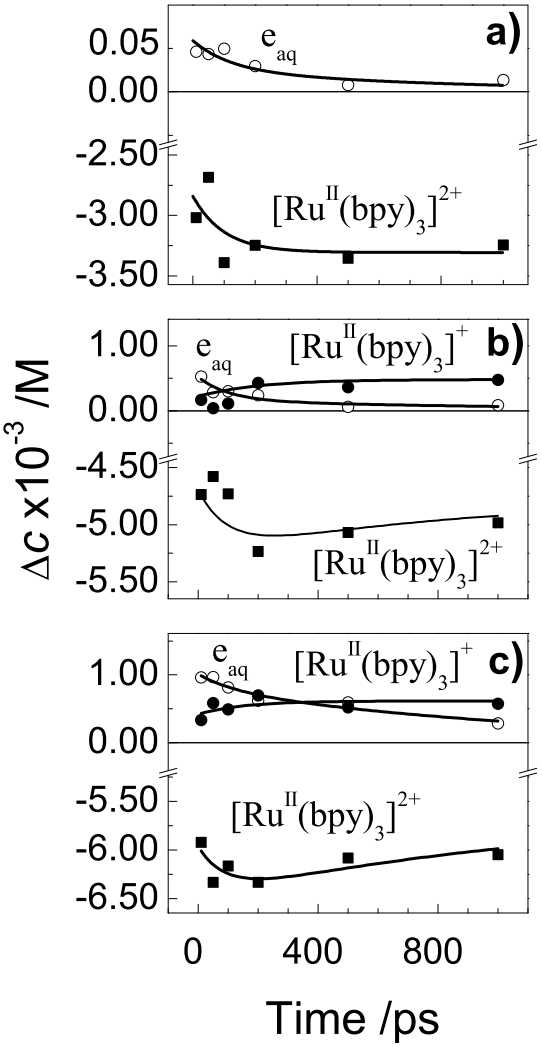

Figure 5.8: Concentrations of the depleted ground-state $[Ru^{II}(bpy)_3]^{2+}$, and of the formed products $[Ru^{II}(bpy)_3]^{+}$ and e_{aq} (symbols) determined by spectral deconvolution of the transient absorption spectra of aqueous $[Ru^{II}(bpy)_3]^{2+}$ (10 mM) using Eq. D.3. The spectra were measured at the following excitation fluence E_0 (in J/cm^2): 0.04 (a), 0.08 (b), and 0.17 (c). The double exponential fit curves (lines) to concentrations of the indicated species are given as a guide to the eye.

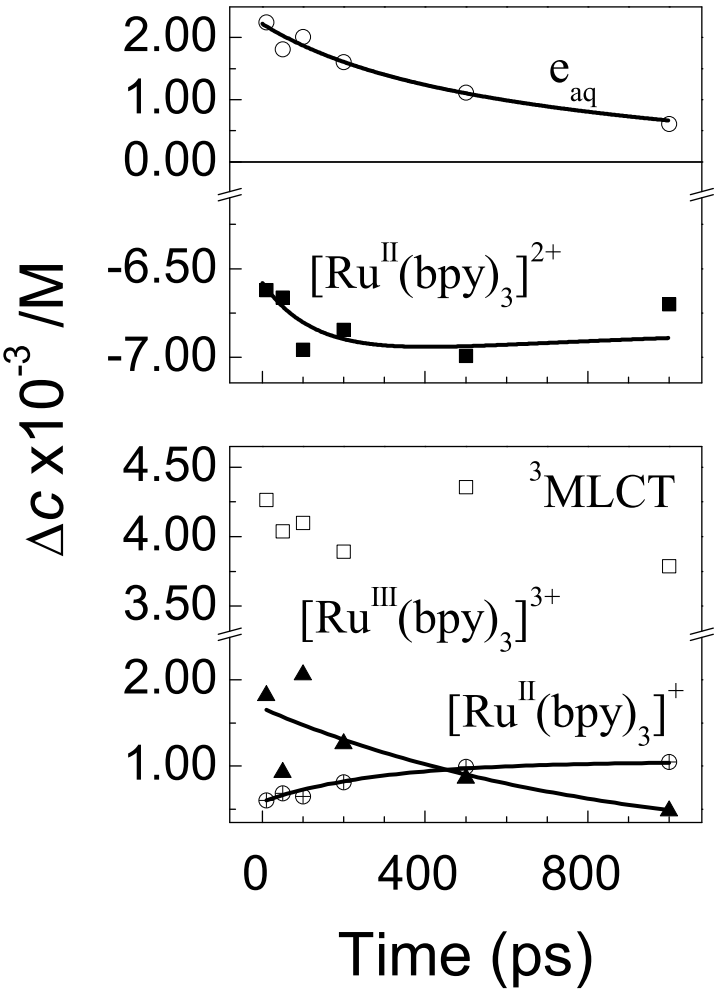

Figure 5.9: Concentrations of the depleted ground-state $[Ru^{II}(bpy)_3]^{2+}$, and of the formed products $[Ru^{II}(bpy)_3]^{+}$, $[Ru^{III}(bpy)_3]^{3+}$, and e_{aq} (symbols) determined from the transient absorption spectra of aqueous $[Ru^{II}(bpy)_3]^{2+}$ (10 mM) using spectral deconvolution with Eq. D.3. The spectra were measured at E_0=0.31 J/cm^2. The double exponential fit curves (lines) to concentrations of the indicated species are given as a guide to the eye.

Photoproduct Concentrations on 10 ps Timescale

Since the 10-ps ΔA spectra are characteristic of the fully thermalized ^{3}MLCT absorption [319], and the energetic relaxation of nascent electrons followed by their solvation is complete on a similar time scale [321, 334], the use of the equilibrated values to obtain the product concentrations from the ΔA spectra for t≥10 ps. We find that with increasing fluence E_0, the degree of depletion of both $[Ru^{II}(bpy)_3]^{2+}$ and $\Delta c(^3MLCT)$ tends to level off (Fig. 5.10a). The produced amount of e_{aq} follows a quasi-linear E_0 dependence, $\Delta c(e_{aq}) = \alpha \cdot E_0^{\beta}$ (Fig. 5.10b), where α and β are constants (i.e. β=1.17)

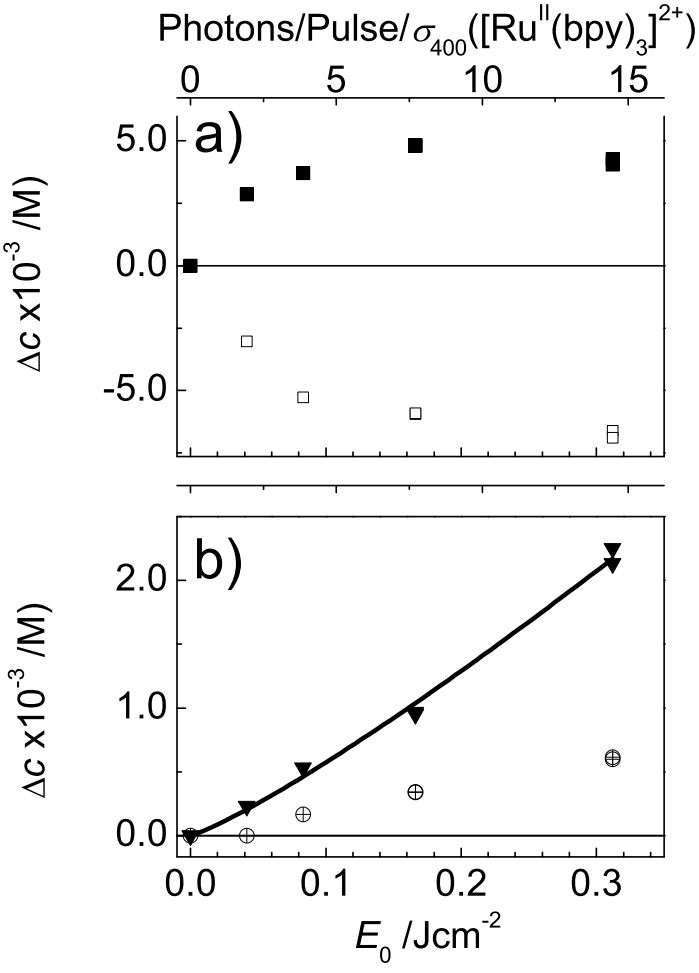

Figure 5.10: Pump fluence dependence of the photoproduct concentrations 10 ps after 400 nm photolysis of 10 mM of aqueous $[Ru^{II}(bpy)_3]^{2+}$ the top axis relates this to the number of incident photons per cross section of the reactant at 400 nm. In a) the depleted ground-state $[Ru^{II}(bpy)_3]^{2+}$ (□) and generated ^{3}MLCT (■)concentrations. In b) produced e_{aq} (▼) and $[Ru^{II}(bpy)_3]^{+}$ (⊕) concentrations. The line represents the best fit of the e_{aq} concentration to the function $\alpha \cdot E_0^{\beta}$, where β=1.17

At the highest fluence (E_0=0.31 J/cm^2), ca. 2 mM are produced in the 10 mM sample, which is 1.5 times larger than in neat water. However, the concentration of electrons produced by photoionization of water in 10 mM $[Ru^{II}(bpy)_3]^{2+}$ has to be much smaller because of the strong linear solute absorption, since its fluence corresponds to an intensity of 15 photons per MLCT cross section on the sample surface. Further evidence that the $[Ru^{II}(bpy)_3]^{2+}$ complex is the main source of solvated electrons comes from the nearly linear dependence of the e_{aq} concentration on E_0 for the 10 mM solution (while it is nearly cubic in neat water [340]). Because of this linear dependence, the relative fraction of e_{aq} produced by photoionization of the solvent H_2O is likely to be much smaller at lower excitation fluences. The presence of an appreciable, E_0-dependent amount of $[Ru^{II}(bpy)_3]^{+}$ is indicated by the fits of the 10 ps ΔA spectra. At all excitation fluences (E_0=0.04-0.31 J/cm^2) and at all delay times, a roughly balanced ratio of depleted to generated populations is found:

$$\frac{-\Delta c([Ru^{II}(bpy)_3]^{2+}}{\{\Delta c(^3MLCT) + \Delta c([Ru^{II}(bpy)_3]^{+}) + \Delta c([Ru^{III}(bpy)_3]^{3+})\}} = 1 \qquad (5.5)$$

within ca. 10% (Table 1), indicating that these species predominantly contribute to the photochemistry 10 ps after the 400 nm excitation pulse.

5.1.3 Discussion

In the following, we will discuss the origin of the different photoproducts that show up from the fits of our data:

Solvated Electron e_{aq}

The emission from the initially excited ^{1}MLCT state in water is found to be extremely short-lived (τ_{isc}=15$\pm$10 fs [82]) due to a fast intersystem crossing (ISC) to the vibrationally hot ^{3}MLCT triplet manifold. Accordingly, upon intense excitation of $[Ru^{II}(bpy)_3]^{2+}$ with a 135 fs, 400-nm pulse, the initial absorption to ^{1}MLCT can be subsequently followed by absorption of one (or more) 400 nm photon(s) of the same pulse from both the unrelaxed ^{1}MLCT and/or ^{3}MLCT states. The induced absorption at 400 nm observed on the leading edge (-50 fs) of the excitation pulse (Fig. 5.3a) is likely due to the spectral signature of the nascent ^{1}MLCT or ^{3}MLCT state. Population can build up in the ^{1}MLCT state at high femtosecond pulse intensities (I_0 $\sim$(1-4)$\cdot 10^{30}$ photons/cm^2/s), since the GS+$\hbar\omega_{400nm}$ $\rightarrow$ ^{1}MLCT first-order excitation rate constant ($(\sigma([Ru^{II}(bpy)_3]^{2+})\cdot I_0 \approx (2.5\text{-}10)\cdot 10^{13}$ s^{-1}) is comparable to ^{1}MLCT decay rate ($1/\tau_{isc}$=6.7$\cdot 10^{13}$ s^{-1}).

Given the appreciable excited state absorption at 400 nm at early times (Fig. 5.3a), the probability to absorb a second photon at early times in a (1+1) resonant excitation process (via ^{1}MLCT) is high at these fluences. At lower fluences, the ^{1}MLCT absorption contribution becomes small and the population of the nascent ^{3}MLCT state following intersystem crossing within the pump

pulse width becomes dominant. Since the ISC occurs at constant energy [82], the subsequent absorption of a 400 nm photon by the ^{3}MLCT state within the pump pulse will populate doubly excited, triplet ($^3[Ru^{III}(bpy)_2(bpy)^{-*}]^{2+}$) states, located around 6.2 eV above the ground state. Large oscillator strengths for the triplet-triplet absorption (large excited state absorption cross-section of the ^{3}MLCT state, $\sigma_{400nm}(^3\text{MLCT})=2.4\cdot10^{-17}$ cm^2, Fig. 5.2b), may offer a distinct possibility of the population build-up in the doubly-excited triplet state, maybe even with some absorption probability of a third photon. Our observation of the solvated electron 2 ps after photolysis of $[Ru^{II}(bpy)_3]^{2+}$ strongly supports the hypothesis of prompt photoionization of this complex following the occurrence of high-intensity photochemical pathways. Finally, the appearance of the oxidized species $[Ru^{III}(bpy)_3]^{3+}$ at relatively early times ($\sim$10 ps) supports the original interpretation [341] that this species is a direct product of the photoionization process.

At 10 ps, the concentration of depleted $[Ru^{II}(bpy)_3]^{2+}$ species is nearly equal to the sum of concentrations of the three identified products ^{3}MLCT, $[Ru^{II}(bpy)_3]^{+}$, $[Ru^{III}(bpy)_3]^{3+}$, next to the by-product e_{aq}, at all excitation energies used (Table 5.1). This implies that essentially all higher-lying excited states (coupled to ^{1,3}MLCT at 400 nm) have relatively short lifetimes ($\ll$10 ps). One (or more) of these states is the electron precursor state with a lifetime <2 ps. The solvated electron detected in previous UV photolysis experiments using micro- and nanosecond pulses [312, 341–344] was ascribed to 2-photon photoionization via the ^{3}MLCT intermediate, because of the fast decay rate of ^{1}MLCT. Furthermore, the absorption of a second photon within the micro- and nanosecond long pulses can occur only from the relaxed ^{3}MLCT state, because the vibrational energy relaxation rates ($>10^{11}$ s^{-1}) are much larger than the typical pump rates in these studies ($\sigma_{UV}\cdot I_0 \leq 3\cdot10^9$ s^{-1}). The lowest photon energy for which solvated electrons were observed in biphotonic nanosecond photolysis studies of $[Ru^{II}(bpy)_3]^{2+}$ is 3.5 eV (a 355 nm excitation wavelength) [312, 342]. Taking into account the ultrafast ISC and relaxation in the ^{3}MLCT state, the second photon acts on the thermalized ^{3}MLCT state located 2.12 eV [91] above the ground state. Thus, in total 3.50 eV+2.12 eV=5.62 eV represents a lower boundary for the ionization energy of $[Ru^{II}(bpy)_3]^{2+}$. Long-pulse photolysis with $\lambda \geq$400 nm ($\leq$3.1 eV) was found inefficient in the production of e_{aq} [341], (thus with 3.1 eV+2.12 eV=5.22 eV), and the ionization threshold lies therefore between 5.2-5.6 eV above the ground state.

In this work, with femtosecond 400 nm pulse excitation, the (1+1) excitation (E_{exc}=6.2 eV) through the non-thermalized ^{1}MLCT and ^{3}MLCT manifolds is in excess of these values, and is sufficient to generate electrons from the solute. For a step-wise two-photon absorption to an electron precursor state, a nearly linear increase of the concentration of e_{aq} with photolysis energy suggests saturation of one of the two involved transitions [345]. Already, the ^{1}MLCT transition is saturated [3], so that the e_{aq} may be produced by means of

[3] In the case when the pulse duration, 135 fs, is long compared to the ^{1}MLCT lifetime ($\tau_{isc} \approx$15 fs), the GS+$\hbar\omega_{400nm} \longrightarrow {}^1$MLCT transition is saturated by the intensity of the

one-(400 nm)-photon (unsaturated) absorption from the ^{1}MLCT. Eventually, for the three photon absorption, presumably the second step from ^{3}MLCT is driven into saturation relatively quickly (large $\sigma_{400nm}(^3\text{MLCT})$). At all (high) intensities used in this study, these two scenarios seem to be possible.

The Reduced Species: $[\mathbf{Ru^{II}(bpy)_3}]^+$

It may arise from a reduction mechanism involving a highly electronically excited $[Ru^{II}(bpy)_3]^{2+}$ acceptor and a nearby water molecule donor on a 100 fs time scale. Using the Rehm-Weller equation [343], the corresponding driving force is estimated to be $\Delta G_0 \approx 7.28 - E_{0-0}$. Indeed, the involved free energy is:

$$\Delta G^0 = E^0[\frac{H_2O^+}{H_2O}] - E^0[\frac{Ru^{II}(bpy)_3^{2+}}{Ru^{II}(bpy)_3^+}] - E_{0-0} + W_p - W_r \qquad (5.6)$$

where $E^0[\frac{Ru^{II}(bpy)_3^{2+}}{Ru^{II}(bpy)_3^+}]$ is the acceptor ground state reduction potential (-1.26 V in H_2O versus normal hydrogen electrode, *NHE* [91], $E^0[\frac{H_2O^+}{H_2O}]$ is the donor oxidation potential, E_{0-0} is the purely electronic excitation energy of the acceptor state, and W_p and W_r represent the work required to bring reactants and products together (neglected in strongly polar solvents following standard practice). The $E^0[\frac{H_2O^+}{H_2O}]$ value is estimated using the correlation between oxidation potentials and gas-phase ionization potentials (IP) by Miller *et al.* [346], $E_0[A^+/A]$=0.89 IP-5.51 (vs NHE). For H_2O, IP=12.96 eV [347]. Therefore, electron transfer from water to excited $[Ru^{II}(bpy)_3]^{2+}$ is energetically feasible for excitation energies larger than 7.28 eV. This is available through three 400 nm photon absorption (E_{exc}=9.3 eV), and the highly excited state(s) involved, possibly *Rydberg*-like charge-transfer-to-solvent (CTTS) excited states of large spatial extent, should be very short-lived, consistent with the ∼100 fs observation time scale.

We observed further development of reduced $[Ru^{II}(bpy)_3]^+$ on a 100-200 ps time scale. It is very likely that following the photoionization of $[Ru^{II}(bpy)_3]^{2+}$ the photoelectron is ejected away from the parent cation to a large distance R_0 with a broad distance distribution by analogy with the studies of multiphoton ionization of neat water and resonant one-photon electron detachment from mono- and polyvalent anions [345, 348, 349]. Photoelectrons with less than 1 eV excess kinetic energy (near-threshold photoionization) are thought to localize ca. 10-15 Å from the parent species on a sub-picosecond time scale [345,348,350]. For high-energy photoionization, the electrons are promoted into the water conduction band, producing delocalized [332], conduction band electrons that can migrate to a length of more than 35 Å from the original site [351]. Given the conduction band gap of

excitation pulse. The population of these two levels equalize when the saturation parameter, $\sigma_{400nm}([Ru^{II}(bpy)_3]^{2+})\cdot I_0 \cdot \tau_{isc}$, becomes much greater than unity. For the peak irradiance I_0 in the range (0.56-4.35)·10^{30} photons/cm^2/s, and σ_{400nm}=2.3·10^{-17} cm^2, the saturation parameter accepts values from 0.2 to 1.5

water and energetics of a hydrated electron [352], the ionization threshold for $[Ru^{II}(bpy)_3]^{2+}$, and the total energy in the excitation process, the two-photon photoionization of $[Ru^{II}(bpy)_3]^{2+}$ is expected to be near-threshold, whereas in the three-photon photoionization the electrons are transferred into the conduction band. The most-probable solute nearest-neighbor distance can be estimated via $R_{mp}=(2\pi\rho)^{-1/3}$, where ρ is the $[Ru^{II}(bpy)_3]^{2+}$ number density in solution. At 10 and 20 mM, R_{mp}=30 Å and 24 Å, respectively. It is reasonable to assume that some electrons are photoejected closer to adjacent $[Ru^{II}(bpy)_3]^{2+}$ cations forming solvent-separated contact pairs, and thus react via Eq. 5.7 (see below) with faster rates than observed for the bulk homogeneous diffusion kinetics. This explanation is consistent with the fact that the $\sim$1.5 $\cdot$ increase of the $[Ru^{II}(bpy)_3]^{+}$ product concentration 50 ps onwards is observed upon increasing the solute concentration from 10 mM to 20 mM. The formation of $[Ru^{II}(bpy)_3]^{+}$ on this time scale is not observed in the excited, dilute samples (0.4 mM), as expected. Therefore, the reduction observed from ten picoseconds to a few hundred picoseconds can be rationalized via the combination of the ejected electron with nearby-lying ground state molecules.

Long-Lived Photoproducts: $[Ru^{II}(bpy)_3]^{+}$

With respect to the observed concentration changes on the 1 ns time scale, we discuss the following scenarios: next to Eq. 5.1 describing the photoexcitation process and ignoring the e_{aq} photogeneration details, we have to consider the reactions:

$$^{1,3}\mathrm{MLCT} \xrightarrow{\hbar\omega} [Ru^{III}(bpy)_3]^{3+} + e_{aq} \tag{5.7}$$

$$[Ru^{II}(bpy)_3]^{2+} + e_{aq} \xrightarrow{6.7\cdot 10^{10} M^{-1}s^{-1}} [Ru^{II}(bpy)_3]^{+} \tag{5.8}$$

$$^{3}\mathrm{MLCT} + [Ru^{II}(bpy)_3]^{2+} \xrightarrow{5.1\cdot 10^{7} M^{-1}s^{-1}} 2\,[Ru^{II}(bpy)_3]^{2+} \tag{5.9}$$

$$^{3}\mathrm{MLCT} + {}^{3}\mathrm{MLCT} \xrightarrow{1.1\cdot 10^{8} M^{-1}s^{-1}} [Ru^{III}(bpy)_3]^{3+} + [Ru^{II}(bpy)_3]^{+} \tag{5.10}$$

$$e_{aq} + e_{aq} + 2\,H_2O \xrightarrow{5.5\cdot 10^{9} M^{-1}s^{-1}} H_2 + 2\,OH^{-} \tag{5.11}$$

$$[Ru^{III}(bpy)_3]^{3+} + [Ru^{II}(bpy)_3]^{+} \xrightarrow{3.4\cdot 10^{9} M^{-1}s^{-1}} 2\cdot[Ru^{II}(bpy)_3]^{2+} \tag{5.12}$$

$$[Ru^{III}(bpy)_3]^{3+} + e_{aq} \xrightarrow{5.2 \cdot 10^{10} M^{-1}s^{-1}} [Ru^{II}(bpy)_3]^{2+} \quad (5.13)$$

$$^3MLCT \quad (5.14)$$

$$"Isolated\ State" \quad (5.15)$$

Eqs. 5.9-5.12, with second-order rate constants in the range (0.05-3.4)·10^9 $M^{-1}s^{-1}$ at room temperature [303,318,346,353], should occur on a sub-microsecond to microsecond time scale (at the mM concentrations of the involved species), and are thus disregarded on the 1-ns time scale studied here. Reactions found in Eq. 5.8 [341, 354] and Eq. 5.13 [318] are comparatively fast. Second-order rate constants of 8.2·10^{10} $M^{-1}s^{-1}$ [354] and 5.6·10^{10} $M^{-1}s^{-1}$ [341] have been reported for the reduction of ground-state $[Ru^{II}(bpy)_3]^{2+}$ by e_{aq}, (Eq. 5.8).

Assuming an average ejection distance of the solvated electron around 25Å (see above), these rates correspond to a reduction time around 200 ps, as observed in this experiment. We also observe that the fast decay of e_{aq} on a ca. 200 ps time scale is concurrent with the build up of reduced $[Ru^{II}(bpy)_3]^{+}$ and with the loss of ground-state $[Ru^{II}(bpy)_3]^{2+}$, indicating the presence of reaction 5.8. Combining the published rate constant with the extended electron ejection distance, we find a nice agreement with the observed formation rate of around 200 ps. Note that the diffusion-controlled reaction 5.8 depends on temperature, but even assuming that 100% of the absorbed energy is released as heat, the maximum average temperature jump in the photolyzed volume at our highest E_0 (0.31 J/cm^2) can be estimated to be ca. 10 K; this heat release is roughly one fifteenth of that required to explain the observed kinetic behavior. Another key observation is that the slow decay of e_{aq} is concomitant with the decay of $[Ru^{III}(bpy)_3]^{3+}$ (∼800 ps), which may be assigned to recombination (back electron transfer).

We observe no evidence for a fast (2 ps < t < 200 ps) recombination. This is probably because some photoelectrons are distributed farther away from the parent cation, and because, as the electron carries away the energy in excess of the ionization threshold (5.62 eV), the larger radius geminate pairs are produced at larger excess excitation energies. The ions thermalize quickly after excitation (within a few picoseconds in polar solvents [355,356]), therefore the outcome of the recombination of $[Ru^{III}(bpy)_3]^{3+}$ and e_{aq} could be expected to be the same as for their diffusion encounter, Eq. 5.13. This encounter leads to ground state $[Ru^{II}(bpy)_3]^{2+}$ (Reaction 1.16), ^{3}MLCT (Reaction 1.17), and another, longer lived dark state ((Reaction 1.18) that does not convert to ^{3}MLCT with the corresponding yields 7, 38 and 55%, respectively [90]. Let us translate these yields into the product concentrations. For example, for E_0=0.31 J/cm^2, the concentration of e_{aq} and $[Ru^{III}(bpy)_3]^{3+}$ that recombine is ca. 1.6 mM. The "isolated" dark state would be produced in the concentration of ca. 0.88 mM for a 55% yield, which approximately corresponds to the observed shortage on the product side (ca. 1.25 mM) in the concentration balance at 1 ns.

Finally, we note that the fast decay component of $\Delta c(e_{aq})$ becomes relatively less pronounced with increased E_0, suggesting that the recombination (Eq. 5.13) becomes dominant over the reduction, Eq. 5.8. This may be attributed to the increase of the absolute number of recombination partners, and the decrease of the relative importance of Eq. 5.8 with the majority of $[Ru^{II}(bpy)_3]^{2+}$ being in the product states.

5.1.4 Conclusions

One of the aims of this study was a better characterization of the behavior of aqueous $[Ru^{II}(bpy)_3]^{2+}$ under high-intensity femtosecond laser pulses at 400 nm in time-resolved x-ray absorption spectroscopy (XAS) experiments carried out with 70 ps x-ray pulses [35, 36, 49, 50]. From the present optical studies, we find that the concentration balance between the depleted ground-state $[Ru^{II}(bpy)_3]^{2+}$ species, and only three product species formed 10 ps after the 400 nm excitation pulse, is maintained to within 10 %, even at the very high power density of 2.15 TW/cm^2 (which is similar to the one used in the time-resolved x-ray experiment [35]). In addition, the ^{3}MLCT state remains the dominant photoproduct (up to >66 %), thus supporting the analysis of the transient XAS data presented in the following Section of this Chapter.

5.2 Picosecond X-ray Absorption Spectroscopy[4]

In this section, we report a picosecond time-resolved X-ray Absorption Spectroscopy studies on the aqueous solutions of $[Ru^{II}(bpy)_3]^{2+}$. The experiments were performed using the pump-probe geometry as described in Chapter 4 and Appendix B. We have recorded $L_{2,3}$ x-ray absorption spectra of the complex in its ground and excited states, 50 ps after short pulse laser excitation. We have detected significant changes both in the XANES (X-ray Near-Edge Absorption Structure) and the EXAFS (Extended X-ray Absorption Fine Structure) regions of the excited state of $[Ru^{II}(bpy)_3]^{2+}$.

The XANES lineshapes have been quantitatively simulated using a crystal field multiplet code in trigonal symmetry. In addition, spectral changes in the EXAFS region of both ground and excited states are analyzed in order to extract structural parameters of their corresponding molecular structures. We obtain a Ru-N bond contraction by $\sim$0.03Å in the excited state complex, as compared to the ground state compound. This weak bond contraction is discussed in terms of a dominant electrostatic and polarization interaction between the oxidized Ru atom and the neutral and reduced bpy ligands, and by steric effects due to straining of the latter. In addition, the weak structural change between ground and excited ruthenium tris-bipyridine complexes implies that the rate for electron transfer processes should be high.

The complete analysis of these results and the corresponding discussion and interpretation has been already published [4] and the following part of this Chapter is a copy of the printed version of this article.

[4] *Journal of the American Chemical Society*, **128**(2006), 5001

J|A|C|S
ARTICLES
Published on Web 03/23/2006

Electronic and Molecular Structure of Photoexcited $[Ru^{II}(bpy)_3]^{2+}$ Probed by Picosecond X-ray Absorption Spectroscopy

Wojciech Gawelda,[†,‡] Melanie Johnson,[†,‡] Frank M. F. de Groot,[§] Rafael Abela,[‡] Christian Bressler,[†] and Majed Chergui*[,†]

Contribution from the Ecole Polytechnique Fédérale de Lausanne, Laboratoire de Spectroscopie Ultrarapide, Institut des Sciences et Ingénierie Chimiques, CH-1015 Lausanne-Dorigny, Switzerland, Swiss Light Source, Paul Scherrer Institut, CH-5232 Villigen PSI, Switzerland, and Department of Inorganic Chemistry and Catalysis, Utrecht University, Sorbonnelaan 16, 3584 CA Utrecht, The Netherlands

Received July 22, 2005; E-mail: majed.chergui@epfl.ch

Abstract: $L_{2,3}$ X-ray absorption spectra of aqueous $[Ru^{II}(bpy)_3]^{2+}$ have been recorded in its ground and excited states, 50 ps after short pulse laser excitation. Significant changes in both the XANES (X-ray Near-Edge Absorption Structure) and the EXAFS (Extended X-ray Absorption Fine Structure) regions of the excited state complex are detected. The XANES line shapes have been quantitatively simulated using a crystal field multiplet code in trigonal symmetry. In addition, spectral changes in the EXAFS region of both ground and excited states are analyzed in order to extract structural parameters of their corresponding molecular structures. We obtain a Ru−N bond contraction by ∼0.03 Å in the excited-state complex, as compared to the ground-state compound. This contraction results from electrostatic and polarization contributions, limited by steric constraints on the bpy ligands.

1. Introduction

Ruthenium(II)-tris-2,2′-bipyridine, ($[Ru^{II}(bpy)_3]^{2+}$), represents a paradigm[1] and a model system of intramolecular electron-transfer reactions.[2] It is also the core member of a family of transition metal-based devices for solar energy conversion.[3−7] $[Ru^{II}(bpy)_3]^{2+}$ has been extensively studied, and most is known about its excited-state properties.[1,5,8−10] The photochemical cycle of $[Ru^{II}(bpy)_3]^{2+}$ can be sketched by a simple level scheme (Figure 1). Light excitation of a metal-centered valence electron from its singlet ground state (^{1}GS) (originating from the ligand-field split 4d level) into the lowest-energy absorption band (400−500 nm) leads to the formation of a Franck−Condon singlet Metal-to-Ligand Charge Transfer (^{1}MLCT) state and localization of the electron on one of the bipyridine ligands, which undergoes intersystem crossing to a long-lived triplet state (^{3}MLCT) in less than 300 fs:[11,12]

$$[Ru^{II}(bpy)_3]^{2+}\ (^1GS) + h\nu \rightarrow [Ru^{III}(bpy^{-1/3})_3]^{2+}\ (^1MLCT) \rightarrow [Ru^{III}(bpy^{-1})(bpy)_2]^{2+}\ (^3MLCT) \quad (1)$$

At room temperature and in aqueous solutions the emission of

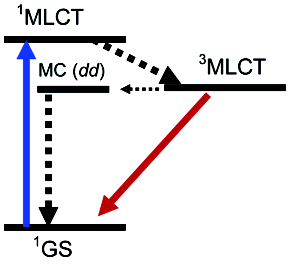

Figure 1. Photochemical cycle of $[Ru^{II}(bpy)_3]^{2+}$ in a simplified energy level scheme. Absorption of visible light removes a metal-centered (MC) 4d electron in its singlet ground state (^{1}GS) into the singlet Metal-to-Ligand Charge Transfer (^{1}MLCT) state, where it undergoes ultrafast intersystem crossing into the triplet ^{3}MLCT state, localized onto the bipyridine ligand system. The ^{3}MLCT state decays nonradiatively via the high vibrational levels of the MC ground state and via excited states[1] and radiatively with a fluorescence lifetime of ∼600 ns at room temperature.

[†] Ecole Polytechnique Fédérale de Lausanne.
[‡] Paul Scherrer Institut.
[§] Utrecht University.

(1) Juris, A.; Balzani, V.; Barigelletti, F.; Campagna, S.; Belser, P.; Von-zelewsky, A. *Coord. Chem. Rev.* **1988**, *84*, 85−277.
(2) Gray, H. B. In *Electron transfer in chemistry*; Balzani, V., Ed.; Wiley-VCH: Weinheim, 2001.
(3) Kalyanasundaram, K. *Coord. Chem. Rev.* **1982**, *46*, 159−244.
(4) Sauvage, J. P.; Collin, J. P.; Chambron, J. C.; Guillerez, S.; Coudret, C.; Balzani, V.; Barigelletti, F.; Decola, L.; Flamigni, L. *Chem. Rev.* **1994**, *94*, 993−1019.
(5) Balzani, V.; Sabbatini, N.; Scandola, F. *Chem. Rev.* **1986**, *86*, 319−337.
(6) Kalyanasundaram, K.; Gratzel, M. *Coord. Chem. Rev.* **1998**, *177*, 347−414.
(7) Kalyanasundaram, K.; Zakeeruddin, S. M.; Nazeeruddin, M. K. *Coord. Chem. Rev.* **1994**, *94*, 259−264.
(8) Balzani, V.; Juris, A.; Venturi, M.; Campagna, S.; Serroni, S. *Chem. Rev.* **1996**, *96*, 759−833.
(9) Vlcek, A. *Coord. Chem. Rev.* **1998**, *177*, 1−2.
(10) Vlcek, A. *Coord. Chem. Rev.* **2000**, *200*, 933−977.
(11) Damrauer, N. H.; Cerullo, G.; Yeh, A.; Boussie, T. R.; Shank, C. V.; McCusker, J. K. *Science* **1997**, *275*, 54−57.
(12) Yeh, A. T.; Shank, C. V.; McCusker, J. K. *Science* **2000**, *289*, 935−938.

10.1021/ja054932k CCC: $33.50

the ^{3}MLCT state exhibits a measured lifetime of about 600 ns[13] due to efficient (95%) nonradiative quenching to high vibrational levels of the ground state and to the triplet Metal-Centered (MC) states[1] (Figure 1).

The photoinduced electronic changes (change of oxidation state, localization of the electron on a ligand) should have consequences on the molecular structure. The localization of the electron on one bpy ligand changes the ground state D_3 symmetry to a C_2 symmetry in the ^{3}MLCT state, at least from the electronic point of view and, probably, the structural one also. Both the increased electrostatic interaction and polarization between the Ru^{III} atom and the bpy^- and bpy ligands, as well as the reduced π-back-bonding, due to the increased oxidation state of the Ru atom, should lead to a modification of the Ru−N bond distances.

The interplay between electronic and geometric changes is of prime importance in elementary charge-transfer processes. From a fundamental point of view, structural information is valuable in order to get insight into the photocycle itself and the nonadiabatic dynamics therein taking place. From a practical point of view, this may help design new transition-metal-based compounds for optimum reductive−oxidative functions with applications in solar cells. Structural information is of special interest in the development of molecular-based materials, capable of performing efficient intermolecular charge transfer, by means of a control of the spatial arrangement of their constituents.[14,15] In several such arrangements strong electronic coupling between the excited species and its nearest neighbors makes the electron transfer adiabatic.[10] Hence, the rate is governed by the nuclear dynamics, as the activation energy depends to a great extent on the reorganization energy of the reacting species prior to electron transfer, which involves the stretching or contraction of metal−ligand bonds.

Despite the fundamental and practical importance of metal−polypyridine (and in particular Ru-) complexes and the numerous studies that were undertaken on these systems,[13,5−11,13,16] surprisingly few studies have addressed the issue of the structural changes occurring upon photoexcitation. Static and time-resolved resonance Raman studies have been carried out on $[Ru^{II}(bpy)_3]^{2+}$ to measure the structural changes in the ^{3}MLCT photoproduct,[17−20] but these have mainly concentrated on the bond changes within the bpy^- ligand. In only one work has an estimate of the Ru−N bond change (0.048 Å) been given, namely for the $[Ru^{II}(NH_3)_4(bpy)]^{2+}$ complex, using a time-dependent treatment of the preresonance Raman spectrum.[17] However, with these optical methods it is difficult to detect the low frequency modes, which are precisely those of interest for assessing the metal−ligand bond length changes. While crystallographic studies on $[Ru^{II}(bpy)_3]^{2+}$ and $[Ru^{III}(bpy)_3]^{3+}$ showed no difference in the Ru−N distance between both compounds,[21] similar studies on $[Ru^{II}(NH_3)_6]^{2+}$ and $[Ru^{III}(NH_3)_6]^{3+}$ pointed to a bond contraction of ca. −0.04 Å for the trivalent Ru center,[22] which was attributed to polarization effects[21,22] due to the increased charge of the central Ru ion. However, these experiments are difficult to compare with photoexcited Ru−polypyridine complexes (in particular, $[Ru^{II}(bpy)_3]^{2+}$), as the photocycle of the latter implies a change of charge and spin along with the reduction of the ligand.

X-ray Absorption Spectroscopy (XAS) is a direct approach to determine the molecular structure changes and the electronic ones that underlie them. In a laser pump/X-ray probe scheme, it can thus deliver information about the transient electronic structure changes including orbital occupancy, degree of oxidation, and ligand field strength in the valence states (which are those driving chemical reactions), via XANES spectroscopy. Simultaneously, coordination numbers and bond distances around a specific atom (here, the Ru atom) can be reliably determined from the EXAFS spectroscopy.[23]

The goal of the present work is to provide a detailed analysis of the electronic and molecular structure of the ground and excited states of $[Ru^{II}(bpy)_3]^{2+}$ via static and picosecond-resolved XANES and EXAFS. The rationale behind this approach has been extensively discussed in ref 23.

So far, few successful time-resolved XAS studies have been reported (see ref 23 for a detailed review), let alone of coordination compounds in the liquid phase. Chen and co-workers investigated photoexcited NiTPP (TPP = tetraphenylporphyrin) by XANES and EXAFS, with a resolution of 14 ns, using X-ray pulses from a synchrotron,[24] and a Cu−diimine complex with 100 ps X-ray pulses.[25] These studies were aimed at understanding the coordination of solvent species to the excited complex. In a foregoing contribution, we showed that we can capture the ^{3}MLCT of $[Ru^{II}(bpy)_3]^{2+}$ by L_3-edge XANES of Ru at a time delay of 70 ps after laser excitation.[26]

In this contribution, we present the first complete picosecond resolved XANES and EXAFS study of a Ru−polypyridine compound ($[Ru^{II}(bpy)_3]^{2+}$) at both L_3- and L_2-edges of the metal atom. The experimental procedures are given in the Supporting Information and in refs 27−29. We present a detailed analysis of the XANES at both *L*-edges of Ru, based on a calculation of the transition energies and intensities of the core excitations, which provides information about the ligand field of the excited complex and about the bond distances, fully supported by our analysis of the EXAFS, and we find that the Ru−N distances actually *decrease* in the excited state. The origin of this change and its implications for electron-transfer processes are also discussed.

(13) Creutz, C.; Chou, M.; Netzel, T. L.; Okumura, M.; Sutin, N. *J. Am. Chem. Soc.* **1980**, *102*, 1309−1319.
(14) Fleming, C. N.; Maxwell, K. A.; DeSimone, J. M.; Meyer, T. J.; Papanikolas, J. M. *J. Am. Chem. Soc.* **2001**, *123*, 10336−10347.
(15) Shaw, G. B.; Papanikolas, J. M. *J. Phys. Chem. B* **2002**, *106*, 6156−6162.
(16) Calzaferri, G.; Rytz, R. *J. Phys. Chem.* **1995**, *99*, 12141−12150.
(17) Doorn, S. K.; Hupp, J. T. *J. Am. Chem. Soc.* **1989**, *111*, 4704−4712.
(18) Mallick, P. K.; Strommen, D. P.; Kincaid, J. R. *J. Am. Chem. Soc.* **1990**, *112*, 1686−1690.
(19) Strommen, D. P.; Mallick, P. K.; Danzer, G. D.; Lumpkin, R. S.; Kincaid, J. R. *J. Phys. Chem.* **1990**, *94*, 1357−1366.
(20) Baranovski, V. I.; Lubimova, O. O.; Makarov, A. A.; Sizova, O. V. *Chem. Phys. Lett.* **2002**, *361*, 196−202.
(21) Biner, M.; Bürgi, H. B.; Ludi, A.; Röhr, C. *J. Am. Chem. Soc.* **1992**, *114*, 5197−5203.
(22) Stynes, H. C.; Ibers, J. A. *Inorg. Chem.* **1971**, *10*, 2304−2308.
(23) Bressler, C.; Chergui, M. *Chem. Rev.* **2004**, *104*, 1781−1812.
(24) Chen, L. X.; Jager, W. J. H.; Jennings, G.; Gosztola, D. J.; Munkholm, A.; Hessler, J. P. *Science* **2001**, *292*, 262−264.
(25) Chen, L. X.; Jennings, G.; Liu, T.; Gosztola, D. J.; Hessler, J. P.; Scaltrito, D. V.; Meyer, G. J. *J. Am. Chem. Soc.* **2002**, *124*, 10861−10867.
(26) Saes, M.; Bressler, C.; Abela, R.; Grolimund, D.; Johnson, S. L.; Heimann, P. A.; Chergui, M. *Phys. Rev. Lett.* **2003**, *90*, 047403−047401.
(27) Saes, M. G. W.; Kaiser, M.; Tarnovsky, A.; Bressler, Ch.; Chergui, M.; Johnson, S. L.; Grolimund, D.; Abela, R. *Synchrotron Radiation News* **2003**, *16*, 12.
(28) Saes, M.; Bressler, C.; van Mourik, F.; Gawelda, W.; Kaiser, M.; Chergui, M.; Bressler, C.; Grolimund, D.; Abela, R.; Glover, T. E.; Heimann, P. A.; Schoenlein, R. W.; Johnson, S. L.; Lindenberg, A. M.; Falcone, R. W. *Rev. Sci. Instrum.* **2004**, *75*, 24−30.
(29) Gawelda, W.; Bressler, C.; Saes, M.; Kaiser, M.; Tarnovsky, A.; Grolimund, D.; Johnson, S. L.; Abela, R.; Chergui, M. *Physica Scripta* **2005**, *T115*, 102.

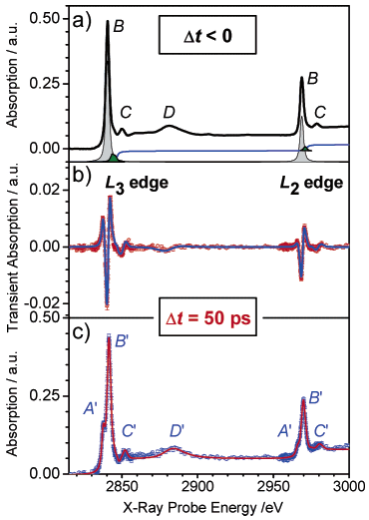

Figure 2. (a) Static absorption spectrum of aqueous $[Ru(bpy)_3]^{2+}$ in the region of the Ru L_3- and L_2-edges (solid black trace with labels) together with the fit results to features B (gray bands), higher-lying bound-bound transitions (green bands), and the edge step of the ionization continuum (solid blue curve). See text and Table 1 for details. (b) Transient difference absorption spectrum measured 50 ps after photoexcitation. The solid line results from the a global fit of the spectrum (Table 1). (c) Excited-state XAS spectrum extracted from spectra a and b using eq 2. The red trace represents the results of the fit (as in spectrum a), with the parameters given in Table 1. Note that compared to spectrum a, an additional band (A′) shows up.

2. Results

The static XAS spectrum of the ground-state complex, recorded under pump−probe conditions, is shown in Figure 2a. It exhibits bands labeled B, C, and D at both L-edges, which we assign below. Figure 2b shows the difference spectrum between the unexcited ($\Delta t < 0$) and the excited sample transmission spectra, at a time delay of 50 ps after laser excitation. Although the X-ray pulse width is 70 ps, this time delay is determined by the low jitter between laser and X-ray pulses.[29,27]

Figure 3 compares the difference absorption spectra at time delays of 50 ps and 70 ns, where the latter has been multiplied by 4.8 to match the 50 ps spectrum. This scaling is motivated by the temporal evolution of the changes observed near the B-band (see Figure S1). To within noise (see residual in Figure 3), the spectra are identical at both time delays and the essential features remain unchanged over time, in particular the weak changes in the region of the D-band. This demonstrates that the changes in the regions of the A/B features and the D-band go hand in hand. This point is of importance for the interpretation of the structural analysis, since features A/B are of electronic nature, while D is geometric (see below).

We attribute the changes observed in Figures 2b and 3 predominantly to the ^{3}MLCT photoproduct, for the following reasons:

(a) In ref 27, we showed that, for a low concentration sample (c = 10 mM), the decay kinetics of the X-ray signal at the B feature reflects that of the simultaneously recorded ^{3}MLCT phosphorescence. This is evidence that the kinetics of the X-ray

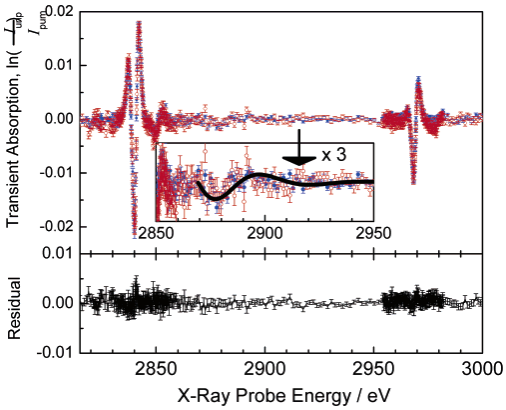

Figure 3. Comparison of the difference absorption spectra at 50 ps (red) and 70 ns (blue) time delay, with the 70 ns transient having been multiplied by 4.8 (see Figure S1). The residual difference between both transients is given below, while the inset shows a zoom of the EXAFS region (together with the transient difference EXAFS from the FEFF simulation). Note the identical signals in the region of the D feature near 2880 eV (also seen in the residual).

signal reflects that of the ^{3}MLCT state. In the present case (c = 80 mM), the laser penetration depth is 10−20 μm of the 0.1 mm liquid jet, and it therefore deposits more energy into this layer, thus heating this part of the sample with a radial distribution of temperatures along the Gaussian-shaped excitation pulse. Microscopic imaging of the phosphorescence from the center outward shows different decay traces with increasing time constants toward the outer edges of the Gaussian pump area. The phosphorescence decay curve near the center nicely matches that of the X-ray decay signal, since the tighter X-ray spot also only samples the central region of excitation. The observed temperature-dependent decay is fully in line with the temperature-dependent intramolecular quenching of aqueous $[Ru(bpy)_3]^*$ in its ^{3}MLCT state. We can therefore safely conclude that the transient X-ray signal is predominantly due to the ^{3}MLCT state.

(b) Intense laser excitation, as used in this study, leads also to the fully ionized complex $[Ru^{III}(bpy)_3]^{3+}$ and to the reduced species $[Ru^{II}(bpy)_2(bpy)^-]^{1+}$ (following recombination with photogenerated solvated electrons), along with the ^{3}MLCT state. We have quantitatively determined the concentrations of these three product species in laser-only studies (not shown here) in the 1−20 mM range (higher concentrations are optically inaccessible due to total absorption of the 0.1 mm sample) and found that, in all cases, the ^{3}MLCT state is to $>^2/_3$ the dominant product species in the 10−100 ps time range. In addition, the concentration of the ionized species $[Ru^{III}(bpy)_3]^{3+}$ decreases to below our detection sensitivity after a few nanoseconds, leaving only the reduced species and the dominant ^{3}MLCT state (now to >80%) in the laser excited solution. Therefore, we can expect that, after 70 ns, we are left with only those two species. In addition, as far as changes in the region of the D-band (which is an EXAFS feature) are concerned, we believe that $[Ru^{III}(bpy)_3]^{3+}$ does not contribute because X-ray diffraction studies of $[Ru^{II}(bpy)_3]^{2+}$ and $[Ru^{III}(bpy)_3]^{3+}$ [21] point to no structural changes (which would cause the changes in the region of the D-band) between both compounds. Last, the correspondence

Table 1. Energies (*E*) and Full Width at Half Maximum (Γ) of the Spectral Features Appearing in the XAS Spectra of the Ground State (GS) and Excited State (GS) Complex Obtained from the Fit of Figures 2a, 2c and 4[a]

		4d (t_{2g}), A		4d (e_g), B		C		D		additional transitions		IP
		E	Γ	*E*	Γ	*E*	Γ	*E*	Γ	*E*	Γ	*E*
GS	L_3			2840.5	2.7	2850.0	3.3	2881.1	16.7	2843.5	2.6	2846.8
										2845.6	2.6	
	L_2			2968.8	2.7	2978.7	4.0			2971.0	2.7	2972.2
ES	L_3	2837.6	2.5	2841.4	3.0	2852.0	3.3	2883.9	15.8	2844.4	2.6	2848.6
										2846.6	2.6	
	L_2	2966.0	2.7	2969.8	3.1	2980.6	4.3			2972.0	2.7	2974.1

[a] The ionization potential (IP) is taken as the energy at the center of the step function (see text for details). The additional transitions correspond to the weak green bands found above the B-bands in Figure 2. All units are in eV. Uncertainty 0.1 eV for L_3-edge, 0.1−0.2 eV for L_2-edge.

between the signals at the D- and B-bands (Figure 3) confirms the minor role of the oxidized complex in the X-ray difference spectra. The relative population between reduced and ^{3}MLCT species will also change considerably between 50 ps and 70 ns (favoring the reduced species at longer time delays). Since we do not observe a significant change in the difference XAS between both time delays (Figure 3) we can safely assume that we are mainly dealing with XAS changes due to the desired ^{3}MLCT product state.

Thus, all evidence points to the fact that our X-ray signal in the picosecond to the nanosecond time domain (Figures 2 to 4) is largely dominated by the ^{3}MLCT photoproduct. We therefore constructed the XAS spectrum of the photoproduct via[23]

$$T(E,t) = f(t) \cdot [A_{es}(E,t) - A_{gs}(E)] \qquad (2)$$

where $f(t)$ is the relative population of the excited complex species (^{3}MLCT) at time t, and $T(E,t)$ denotes the transient difference absorption spectrum (Figure 2b), which contains all the photoinduced changes from the ground-state complex spectrum, $A_{gs}(E)$ (Figure 2a), to the excited complex spectrum, $A_{es}(E,t)$, at the time t following photoexcitation. The time-dependent photolysis yield, $f(t)$, has an influence on the spectral shape of the excited-state XAS $A_{es}(E,t)$, and we measured it independently in laser-only transient absorption experiments under identical experimental conditions (concentration, sample geometry, pump power) and obtained $f(t) \cong 10\%$. Figure 2c shows the recovered X-ray absorption spectrum of the photo-excited species, where we distinguish bands labeled B′, C′, and D′, that are counterparts of the bands in the ground-state spectrum (hereafter primes will always be used for the excited compound spectral features), while an additional spectral feature (A′) shows up at both *L*-edges.

For a more detailed analysis of the data, we require accurate information about the individual peak positions and widths and about the energy of the ionization potential (IP). For this purpose we performed a least-squares global fit of the entire spectra in Figures 2a and 2c. We used Voigt profiles for the A′ and B/B′ features, an arctangent step function for the IP, and an asymmetric Voigt profile for both features C/C′ and D/D′ (decomposed bands not shown). In addition, thanks to our sensitivity, we identify transitions lying at higher energies, which we fitted with Voigt profiles (two for the L_3- and one for the L_2-edge), and these are seen as green bands in Figure 2a. The Lorentzian widths for all Voigt profiles and the edge step functions were fixed to the lifetime width of the L-edges of Ru, which amounts to 1.75 eV for the L_3-edge and between

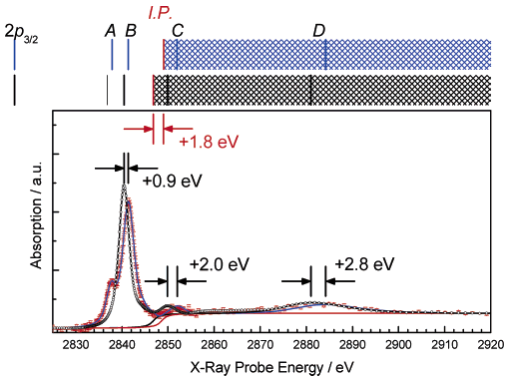

Figure 4. Ground (black dots) and excited state (red dots with errors bars) XAS spectra of $[Ru(bpy)_3]^{2+}$ at the Ru L_3-edge, together with a fit of the dominant features (solid curve through data points). The hatched areas at the top of the figure represent the ionization threshold (IP) and continuum of the ground (black) and excited complex (blue). The measured energetic positions of the various spectral features (bands and ionization edge) are indicated above the spectrum and are given in Table 1.

1.9 and 2.1 eV in the case of the L_2-edge,[30,31] while the Gaussian widths were fitted and delivered results in the 1.2−1.4 eV range, as expected from the calculated monochromator width (energy resolution) at these X-ray energies.[28] The fit results are summarized in Table 1.

In addition, Figure 4 zooms into details of the ground and excited state (time delay: 50 ps) L_3-edge absorption spectra, along with the resulting fit curves, showing the very good agreement with the experiment. The *B*′ peaks at both L_3- and L_2-edges have shifted to the blue by 0.9 eV with respect to the B peaks. This shift results from the change of oxidation state of the Ru atom, in good agreement with the difference observed between ruthenium compounds of different valencies previously reported.[32−34] It is also fully in line with the fact that an entire charge is transferred to the bpy ligand, as supported by quantum chemical calculations.[16,35] It is important to stress not only the accuracy of the fits concerning the peak positions (<0.1 eV) but also the precise determination of the oxidation-state induced shift of the ionization potential of 1.8 eV (Table 1). This is

(30) de Siervo, A.; Landers, R.; de Castro, S. G. C.; Kleiman, G. G. *J. Electron Spectrosc.* **1998**, *88*, 429−433.
(31) Ohno, M.; van Riessen, G. A. *J. Electron. Spectrosc.* **2003**, *128*, 1−31.
(32) Sham, T. K. *J. Am. Chem. Soc.* **1983**, *105*, 2269−2273.
(33) Sugiura, C.; Kitamura, M.; Muramatsu, S. *J. Chem. Phys.* **1986**, *84*, 4824−4827.
(34) Sham, T. K. *J. Chem. Phys.* **1985**, *83*, 3222−3224.
(35) Buchs, M.; Daul, C. *Chimia* **1998**, *52*, 163−166.

crucial for a precise EXAFS analysis as will be discussed in section 3.3.

3. Analysis and Discussion

3.1. Ground and Excited Compound X-ray Absorption Spectra. The spectra in Figures 2 to 4 are the first complete L_3- and L_2-edge XAFS spectra of a Ru−polypyridine complex ($[Ru^{II}(bpy)_3]^{2+}$) in its ground and its excited state, captured picoseconds onward after photoexcitation. Before discussing the photoinduced changes, we recall the origin of the bound−bound transitions. The Ru atom has a $4d^6$ configuration in the ground state of $[Ru^{II}(bpy)_3]^{2+}$, and in the presence of an octahedral crystal field the 4d orbitals transform into t_{2g} and e_g orbitals, separated in energy by the octahedral crystal field splitting energy (denoted as 10Dq [36]). Since we are dealing with a low spin compound, all 6 electrons fill up the t_{2g} orbitals, while the e_g orbitals are empty. This defines the ground state with $^1A_1$ symmetry. Note that this $^1A_1$ ground state is not affected by the trigonal distortion or by the 4d spin−orbit coupling ζLS. The L-edges arise from atomiclike electric dipole transitions (change of angular momentum $\Delta l = \pm 1$) from the $2p_{1/2}$ (L_2) and $2p_{3/2}$ (L_3) core orbitals to unoccupied orbitals of both s and d symmetry. Excitation of the 2p electron is only possible to the empty e_g states, giving rise to the B-band at both L_3- and L_2-edges. In trivalent compounds, such as $[Ru^{III}(NH_3)_6]^{3+}$, an additional A-band appears ∼3.93 eV below the B-band at the L_3 edge but not at the L_2-edge, since an electron is missing in the t_{2g} orbital.[32] The A−B splitting therefore delivers information on the ligand field splitting. Likewise, the new feature A′, seen in Figures 2c and 4, originates from the light-driven charge-transfer process (changing the central atom occupancy from $4d^6$ to $4d^5$), which creates a vacancy in the previously fully occupied t_{2g} orbital. The A′−B′ splitting amounts to 3.75 eV, which is close to the value found in purely octahedral compounds,[32] suggesting that the trigonal distortion (D_3) and the axial distortion (leading to C_2 symmetry) of the photoexcited complex are minor perturbations to the dominant O_h ligand field.

While the XAS spectra of the trivalent and octahedral compounds $[Ru^{III}(NH_3)_6]^{3+}$ and $[Ru^{III}Cl_6]^{3-}$ do not exhibit the A′(t_{2g}) feature at the L_2-edge,[32−34] it does show up at the L_2-edge of the photogenerated $[Ru^{III}(bpy)_2bpy^-]^{2+}$. To explain this difference, we have to analyze the symmetries of the $2p^64d^5$ initial and the $2p^54d^6$ final states of the X-ray transition of the laser-excited compound, in the field of the ligands. In the case of octahedral compounds, the $4d^5$ initial state has $^2T_2$ symmetry. Spin−orbit coupling is important, which implies that the double group symmetry is given by the multiplication of the spin (E′) and the orbital (T_2) symmetries. This gives the double group symmetries Γ_7 and Γ_8, where the initial state is given by Γ_7.[37] The final state is $2p^5t_{2g}^6$ with $^2T_1$ symmetry. In double group symmetry, we have $E' \otimes T_1 = \Gamma_6 + \Gamma_8$, which is split by the large 2p spin−orbit coupling. The t_{2g} peak has Γ_8 symmetry at the L_3-edge and Γ_6 symmetry at the L_2-edge. An allowed dipole transition promotes $4d^5(\Gamma_7)$ to either a Γ_7 or Γ_8 state, while the Γ_6 state is forbidden. This implies that the A′(t_{2g}) band is not visible at the L_2-edge in octahedral symmetry. Trigonal distortion will mix the two spin−orbit split states, Γ_7 and Γ_8 of the $4d^5$ ground state. From the Γ_8 ground state all symmetries are dipole allowed, which implies that the Γ_6 state (A′-band) at the L_2-edge then becomes visible.

This qualitative explanation has two implications: (a) a D_3 symmetry for the excited compound is sufficient (but not unique) to explain the new spectral feature at the L_2-edge; (b) there is a close interplay between the 4d spin−orbit interaction and the D_3 ligand field. In section 3.2, we show that other features of the spectra are also quantitatively explained restricting ourselves to D_3 symmetry for the excited compound.

Turning now to features C and D in Figures 2 and 4, these lie clearly above the ionization potential (IP), according to Table 1. This is also confirmed by the fact that we observe the C feature for $[Ru^{II}(bpy)_3]^{2+}$ at nearly the same energy above the B-band as that in $[Ru^{III}(NH_3)_6]^{3+}$.[32] We assign the C-band to a quasi bound above-ionization resonance, 3.2 eV above the IP. Such resonances can arise from multiple scattering of the low energy outgoing photoelectron with the surrounding ligand atoms. The *D* feature, far above the IP, represents an EXAFS modulation and is analyzed in section 3.3 below. Finally, Table 1 and Figure 3 show a blue shift by 1.8 eV of the excited complex IP compared to that of the ground-state complex. This is due to the fact that following the removal of one of the 4d (t_{2g}) valence electrons the $2p_{1/2,3/2}$ core levels are more strongly bound (by 1.8 eV), while both 4d(t_{2g}) and (e_g) levels are lowered in energy by 0.9 eV. This difference is expected, since the change in electronic shielding upon charge transfer to the ligand system is more pronounced for the valence electrons than for the core ones. Indeed, the larger 1.8 eV shift for the 2p core levels is still relatively small with respect to their IPs of 2846.8 and 2972.2 eV, respectively, compared to the 0.9 shift for the 4d levels with their IPs around 10 eV.[16,35,38] This also agrees with previous studies by Wong et al.,[39] in which the oxidation state dependent energies were observed for vanadium compounds with valencies varying from 0 to +5, showing larger K-edge energy than valence energy shifts in the XAS.

3.2. Analysis of the XANES Line Shapes: XANES delivers information about ligand field splittings (which themselves are determined by the Ru−N bond distances) and about the modifications of selection rules (due to the changes in molecular symmetry), so we exploit it to extract structural information about the excited-state complex. For this purpose, we have simulated the XANES line shapes using the *Theo Thole* (TT) multiplet code[40−42] (see Supporting Information for details), which is based on the total Hamiltonian of the complex compound, consisting of the atomic Hamiltonian H_{atom} for Ru, to which an electrostatic crystal field Hamiltonian $H_{crystal}$ is added as a perturbation:

$$H_{total} = H_{atom} + H_{crystal} = H_{atom} + H_{O_h} + H_{D_3} + H_{\zeta LS} \quad (3)$$

where H_{O_h} is the octahedral crystal field contribution, H_{D_3} is the trigonal distortion, and $H_{\zeta LS}$ includes the 4d spin−orbit coupling. The atomic Hamiltonian contains terms due to the kinetic energy of the electrons, their Coulomb interaction with

(36) Sugano, S.; Tanabe, Y.; Kamimura, H. *Multiplets of transition-metal ions in crystals*; Academic Press: New York, 1970.
(37) Nielson, C. W.; Koster, G. F. *Spectroscopic coefficients of the p^n, d^n, and f^n Configurations*; MIR Press: Cambridge, 1963.
(38) Rensmo, H.; Lunell, S.; Siegbahn, H. *J. Photochem. Photobiol., A* **1998**, *114*, 117−124.
(39) Wong, J.; Lytle, F. W.; Messmer, R. P.; Maylotte, D. H. *Phys. Rev. B* **1984**, *30*, 5596−5610.
(40) de Groot, F. M. F. *J. Electron Spectrosc.* **1994**, *67*, 529−622.
(41) de Groot, F. M. F.; Vogel, J. Oxford University Press: Oxford, 2004.
(42) de Groot, F. M. F. *Coord. Chem. Rev.* **2005**, *249*, 31−63.

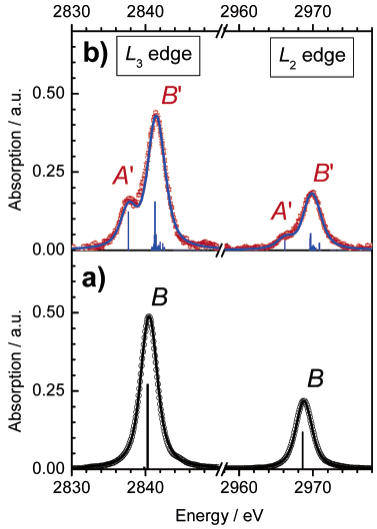

Figure 5. Experimental and simulated line shapes of the XANES L_3 and L_2 features for the ground (a) and the excited (b) complex. The calculated transition strengths for the involved energy levels are given by the stick diagram, which, after convolution with a Lorentzian (lifetime width) and Gaussian (experimental resolution), yield the solid curves. The experimental data were generated from Figure 4 after subtraction of the absorption edge and higher lying (weaker) transitions (see text). The labeled features A and B correspond to transitions to the t_{2g} and e_g levels, respectively.

the nucleus of charge +Z, their mutual electrostatic repulsion (which causes the multiplet effects), and the spin−orbit interaction of each electron.

The potential due to the ligand field is treated as a perturbation to the atomic case, and this is written as a superposition of spherical harmonics.[36] In other words, the spectra are determined by crystal field effects with splittings due to multipole 2p−4d and 4d−4d interactions, which are included in the atomic Hamiltonian. The latter are factorized in F^2 and F^4 Slater integrals, and the initial and final states are determined by the 4d−4d multipole interaction (see Table S1). Important additional interactions are caused by the core hole: the 2p core hole spin−orbit interaction splits the absorption into the L_3 and L_2 parts, and the 2p−4d multipole Coulomb and exchange interactions F^2, G^1, and G^3 (which are on the order of 1−2 eV) also modify the simulated spectrum significantly, giving rise to several spectral lines.

As mentioned above, from an electronic point of view, the excited-state structure should have a C_2 symmetry due to localization of an electron on one of the bpy ligands. The excited-state simulated XANES line shapes have been generated using the trigonal symmetry. The reasons for this choice is that the main contribution of the ligand field is the octahedral one, while the trigonal symmetry already accounts for the observation of the A′ band at the L_2-edge. Including the C_2 symmetry does not change the measured XANES of either the ground or the excited-state spectra within the (already quite high) sensitivity of the experiment.

A posteriori, the agreement between measured and the simulated XANES line shapes at both L-edges is striking (Figure 5). For this purpose, we have subtracted the IP (the edge jump)

Table 2. Ligand Field Splittings Used for the Fit of the Ground State and Excited State Complex XANES Line Shapes (Figure 5)[a]

	octahedral crystal field (10Dq)	trigonal field splitting
ground state	3.74(0.06)[b]	0.26(0.07)[c]
excited state	3.89(0.06)	0.39(0.07)

[a] All units are in eV. Uncertainties are given in brackets. [b] Reference 16. [c] Reference 59.

and the weaker higher-lying transitions from the experimental spectrum (step function and green bands in Figure 2a), to recover only the A′ and B′ features. The calculated transitions to the multiplet levels appear as sticks in Figure 5, and the simulated curve was derived after convolution with the Lorentzian and Gaussian functions reflecting the lifetime broadening and the experimental band-pass of the monochromator, respectively (see Supporting Information). The ground-state line shape was simulated using the literature values of the ligand field splittings (Table 2). The excellent agreement reflects the quality and precision of both the measurement and calculations.

For the excited complex, the octahedral and trigonal field splittings were adjusted, as these parameters influence the A′−B′ splitting and intensity ratios, at both L-edges, and the widths of the A′ and B/B′ bands. Therefore the range of possible values for these parameters is very limited, and those used for the fit in Figure 5 are also given in Table 2. Here again, the agreement between experiment and simulation is remarkable, in that without the underlying multiplet structure the full line shapes cannot be retrieved. This allows us to rationalize many detailed features of the ground and excited-state spectra:

(a) The increased line width of the B′ feature with respect to the B-band (Table 1) is due to the appearance of several transitions to new sublevels of the final states. The B-band relates to a single $2p^54d^7$ final state, while the B′-band contains more than 10 $2p^54d^6$ final states spread over ∼3 eV, as indicated by the stick diagram in Figure 5.

(b) The larger line width of the B′ feature compared to A′ (Table 1) is due to a similar reason, as the excited complex t_{2g} A′-peak consists of a single transition. A similar effect was discussed by Sham for the trivalent $[Ru^{III}(NH_3)_6]^{3+}$ compound.[34]

(c) The measured intensity ratio between the B-bands at both L-edges, as well as for both ground and excited states, is very well reproduced in the simulation. These ratios are sensitive to the strength of the crystal fields and comfort us in our simplification to use a D_3 symmetry for the excited-state complex.

(d) As mentioned above, the appearance of the A′ feature at the L_2-edge is specific to the nonoctahedral trivalent excited complex. The ratio of the A′ to B′ band intensity is smaller at the L_2- compared to the L_3-edge. Since this ratio is governed by the choice of the trigonal field splitting, the excellent agreement in Figure 5 stresses its interplay with the spin−orbit interaction of the 4d electrons (see above). As a further check of this interplay, we repeated the calculations, setting the trigonal field splitting to zero, and found that the A′-band disappears at the L_2-edge, as observed for a purely octahedral compound.[32] When setting the 4d spin−orbit constant to zero, the A′-band is present at the L_2-edge, but neither the A′−B′ intensity ratios nor the ratio of B′-bands at the two L-edges is reproduced any longer. Interestingly, our excited-state XANES line shape simulation points to an increase by ∼0.13 eV of the D_3 field

splitting, compared to the ground state (Table 2). This can be related to a shorter Ru−N bond length in the case of the excited complex, although this connection is not trivial to rationalize beyond octahedral symmetry.

(e) Finally, we also calculated the transitions lying above the B-band. They are due to charge transfer (CT) effects and to higher lying (e.g., Rydberg) states. The CT satellite peaks become visible in the X-ray absorption spectra, if the final state charge transfer differs from that of the ground state.[40]

(f) The A′−B′ energy splitting is governed by the octahedral field strength 10Dq. The ligand field splitting between the t_{2g} and e_g levels, used in our simulation (Table 2), is larger for the excited state compared to the ground state (determined by quantum chemical calculations[16]).

Using an electrostatic model, König et al.[43] showed that the octahedral ligand field splitting is inversely proportional to the 5th power of the metal−ligand distance. Thus, assuming that the change of 10Dq (which is proportional to the measured change of splitting ΔE(A′−B′) between ground and excited complex) is related to a change in the Ru−N bond length,[44]

$$\frac{10Dq^{ES}}{10Dq^{GS}} = \left(\frac{R^{GS}_{Ru-N}}{R^{ES}_{Ru-N}}\right)^5 \quad (4)$$

In ref 43, this relation was found satisfied to within 2.6% for iron complexes. We used the same expression in the present case, assuming it valid for the case of Ru complexes, and calculated the photoinduced structural change of the local environment to

$$\Delta R_{Ru-N} = R^{gs}_{Ru-N}\left[\left(\frac{\Delta E_{gs}}{\Delta E_{es}}\right)^{1/5} - 1\right] \quad (5)$$

The calculated values of ΔE_{gs} for a trigonally distorted octahedron for the ground-state complex[16,35,38] and our values determined from the multiplet calculation for the excited state (Table 2), thus, deliver a contraction of the Ru−N bond by about ∼0.02 Å in the excited state. This should however only be taken as approximate, since neither ground nor excited states are octahedral, although its dominant character justifies our approach. The suggested trend is further confirmed below by the structural analysis of the EXAFS spectrum.

3.3. Molecular Structure from the EXAFS: EXAFS is sensitive to the wave vector of the X-ray generated free photoelectron wave (thus above the IP). Feature C shifts by nearly the same amount as the IP upon oxidation of the central Ru atom. It lies at 3.2 eV above the IP and thus corresponds to a photoelectron wavelength of ca. 6.3 Å (or a photoelectron wave vector $k = 1$ Å^{-1}), which reflects the spatial dimensions of $[Ru^{II}(bpy)_3]^{2+}$. Therefore, the C band should be largely dominated by multiple scattering contributions, also originating from atoms (mostly carbon) beyond the first shell. In fact, a possible additional energy shift of this feature for the excited state lies within the experimental uncertainty, fully in line with the minor structural modifications of the complex on the order of −0.02 Å (see above) for the Ru−N distance.

The D feature, which represents a clear EXAFS modulation, is blue shifted by 1 eV (after correcting for the IP shift), pointing to a bond contraction of the Ru−N nearest-neighbor distance. Note that the energetic shift is considerably smaller than if we had taken the 2.8 eV shift observed in the raw spectra (Table 1 and Figure 3). The capability to precisely measure light-driven energetic shifts in the X-ray domain, as we do here, is a key component to quantify rather small transient structural changes. Natoli et al.[45] laid the theoretical grounds for relating the position of continuum resonances in energy space to the bond lengths within the first coordination shell. They derived a simple relationship, which correlates the energy spacing between the resonance energy E_{res} and the IP to the nearest-neighbor distances R (Ru−N bond distance in our case) via

$$(E_{res} - IP)R_{Ru-N}{}^2 = \text{const} \quad (6)$$

Modifying eq 6 using our measured values for $(E_{res} - IP)$ to calculate the ground (Δ_g) and excited state (Δ_e) energetic difference yields for the relative bond distance changes

$$\Delta R_{Ru-N} = R^{GS}_{Ru-N}\left[\left(\sqrt{\frac{\Delta_g}{\Delta_e}}\right) - 1\right] \quad (7)$$

Equation 6 was already verified[46] as a probe of the first coordination shell distance changes following the energy shifts of the main continuum resonance above the inflection point E_0.[47,48] We have modified this relation to account for the actual energy to generate a propagating photoelectron wave (thus replacing E_0 with IP). With eq 7, we obtain a contraction of the metal−ligand bond distance $\Delta R_{Ru-N} \cong -0.04$ Å, in fair agreement with the above estimate based on the XANES simulation (section 3.2).

Finally, we carried out a full calculation of the ground and excited-state EXAFS using the FEFF 8.20 code (see Supporting Information for details), to the Ru−N bond distances, which were all treated equally (i.e., in D_3 symmetry, see above). Figure 6a and 6b (Figure 6c and 6d) respectively show the ground state (excited state) experimental and optimized EXAFS spectra in q-space and their Fourier transform power spectra (transform magnitudes).

The latter power spectra represent a Pseudo Radial Distribution Function (PRDF, see Supporting Information), which is characterized by a main peak near 1.8 Å and a weaker one near 3.3 Å. The Fourier transform spectra were not phase-corrected for the central atom phase shift; therefore the actual peaks show up at R values shorter than those corresponding to nearest-neighbor atoms. The first peak corresponds to single scattering contributions by the nearest shells of N and C atoms around the Ru atom (N/N′, C2/C2′, and C6/C6′ shown in the inset of Figure 6b), while the second peak is largely due to contributions of more distant shells of atoms (C3/C3′ to C5/C5′), but it also includes complicated multiple scattering paths involving 3 or more atoms in different geometrical arrangements, including collinear multiple scattering paths (the so-called focusing

(43) König, E.; Watson, K. J. *Chem. Phys. Lett.* **1970**, *6*, 457−459.
(44) Hauser, A. *Top. Curr. Chem.* **2004**, *233*, 49−58.
(45) Natoli, C. R.; Benfatto, M.; Doniach, S. *Phys. Rev. A* **1986**, *34*, 4682−4694.
(46) Hodgson, K. O.; Hedman, B.; Penner-Hahn, J. E. *EXAFS and near edge structure III: proceedings of an international conference, Stanford, CA, July 16−20, 1984*; Springer-Verlag: Berlin; New York, 1984.
(47) Bianconi, A.; Fritsch, E.; Calas, G.; Petiau, J. *Phys. Rev. B* **1985**, *32*, 4292−4295.
(48) Lytle, F. W.; Greegor, R. B. *Phys. Rev. B* **1988**, *37*, 1550−1562.

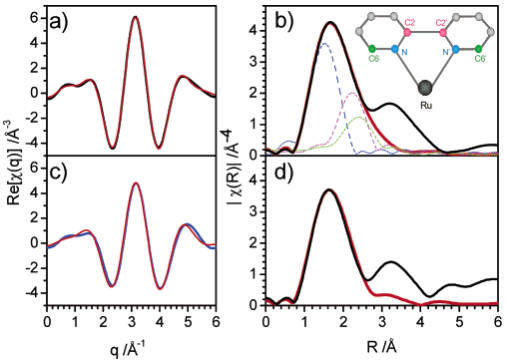

Figure 6. Wave vector spectra and pseudo-radial distribution functions (PRDF) of the ground state (a,b) and the excited state complex (c,d). The black lines represent the experimentally derived traces, while the red ones represent those simulated using the FEFF 8.20 code and the structural parameters from Table 3 (see also Table 2 of the Supporting Information). The PRDFs are decomposed in terms of the various single scattering contributions due to the N, C2, and C6 atoms as seen in the inset (colors correspond between atom and trace), which shows the Ru atom and one bpy ligand. Note that the PRDFs were not phase-corrected for the central atom phase shift, and therefore the actual peaks show up at *R* values shorter than those corresponding to nearest-neighbor atoms (the central atom phase shift can be included in the Fourier transform, and it results in a ca. 0.3−0.5 Å displacement of the radial distribution function).

Table 3. Results of the EXAFS Structural Analysis (Figure 6) for the Ground and the Excited Complex; the Former Is Compared to Crystallographic Data from the Literature

bond	ground state (crystallography)[a]	ground state (EXAFS)	bond change in excited state
Ru−N	2.05−2.064 Å	2.066 ± 0.017 Å	−0.037 ± 0.019 Å

[a] References 56 and 58.

effect[49]). Only the first peak of the PRDF was considered in the EXAFS analysis, as explained in the Supporting Information. Once again, the pseudo-radial distribution function for the excited complex reflects a small contraction with respect to the ground state. The simulated amplitudes of the three dominant single scattering (SS) shells in the 1−2.8 Å range of neighboring N and C atoms are shown, and their sum is compared with the experimental Fourier transform for the ground (Figure 6a) and excited complex (Figure 6d). We derive bond lengths for the ground state and the resulting bond contraction for the excited state that are given in Table 3. The agreement is good between the X-ray crystallography data and the EXAFS-extracted distances for the ground state (Table 3). The uncertainty (±0.019 Å) on the EXAFS data represents a limit for which we observe significant deviations from the measured spectrum. Our result (−0.037 ± 0.019 Å) for the Ru−N bond contraction agrees well with the estimates derived above from eq 5 (−0.02 Å) and eq 7 (−0.04 Å). We also find that all three shells (Ru−N, Ru−C2, and Ru−C6) exhibit a distance decrease from the central atom, compared to the ground-state structure (see Table SII), which shows the consistency of our EXAFS analysis.

To interpret these results, we need to identify the parameters that determine the structure and bonding of the Ru complex. The Ru d-orbitals undergo n-type bonding with the ligand σ-orbitals. In the ground state, the system adopts a nonoctahedral geometry due to the fact that the N−N distance of the bpy ligands is rigid. Under this constraint, the three bpy ligands arrange in a propeller-like geometry around the Ru atom. The coordination of the N atoms is close to octahedral but with deviations, consisting of a compression of the coordination octahedron along the trigonal axis by ∼0.5 Å and a trigonal twisting of ∼10° from the ideal octahedral geometry. In addition to this main bonding contribution, there exists an additional one due to π-back-bonding, resulting from the transfer of electron density from the t_{2g} orbitals to the empty π*-orbital of the ligand.

Our result of a weak bond contraction by ∼0.03 Å on the average (bearing in mind that we used a D_3 symmetry throughout our analysis), for the excited complex is quite close to earlier X-ray crystallography[22] and solution EXAFS[50] studies showing a bond contraction by ∼0.04 Å between $[Ru^{II}(NH_3)_6]^{2+}$ and $[Ru^{III}(NH_3)_6]^{3+}$. However, crystallographic studies on $[Ru^{II}(bpy)_3]^{2+}$ and $[Ru^{III}(bpy)_3]^{3+}$ [21] concluded to an indistinguishable Ru−N bond distance for the two species. In ref 22, the shortening of the Ru−N bond distances upon oxidation of the Ru−hexamine complex was attributed to polarization effects due to the increased charge on the Ru ion.

In the case of the ground-state complexes $[Ru^{II}(bpy)_3]^{2+}$ and $[Ru^{III}(bpy)_3]^{3+}$, the fact that no change of bond distances was reported upon oxidation of the Ru atom[21] suggests that, despite Ru becoming a stronger electron acceptor, either the reduced π-back-bonding contribution acts against it and/or the geometric constraints hinder the bpy ligand from moving inward. For the excited complex, however, quantum chemical calculations point to a near 100% transfer of charge from the metal to the ligand,[16,35] in agreement with Raman studies of the ^{3}MLCT state,[51] so considerations of donation and back-donation are not operative. A strong electrostatic interaction should occur between the metal atom and the reduced ligand with formation of a dipole and polarization of the uncharged ligands. This will tend to pull the ligands inward, but the fact that the bond contraction is not dramatic points to a steric effect due to straining of the bpy ligands. As mentioned above, these are already constrained in the ground-state geometry due to the rather rigid nature of the N−N distance (itself determined by the C2−C2′ bond distance). Further shortening of the Ru−N bond distances would necessitate a significant structural reorganization of the bpy ligands, which is energetically not possible. Therefore the ligands cannot undergo a significant inward rearrangement in the complex. Hence, we conclude that the mild bond contraction results from electrostatic and polarization forces, which tend to shorten the bond but are limited by steric effects.

One of the consequences of the weak structure rearrangement of the excited complex is on intermolecular electron-transfer processes, which play a role in the transport of excitation and charge in organized assemblies of metal polypyridine complexes[15] and in multicenter polypiridine complexes.[52] The rate of electron transfer between the ground and excited complex

(49) Stern, E. A. In *X-ray absorption principles, applications, techniques of exafs, sexafs and xanes*; Köningsberger, D. C., Prins, R., Eds.; Wiley: New York etc., 1988; pp XII, 673.

(50) Brunschwig, B. S.; Creutz, C.; McCartney, D. H.; Sham, T. K.; Sutin, N. *Faraday Discuss. Chem. Soc.* **1982**, *74*, 113−127.

(51) Webb, M. A.; Knorr, F. J.; McHale, J. L. *J. Raman Spectrosc.* **2001**, *32*, 481−485.

(52) Andersson, J.; Puntoriero, F.; Serroni, S.; Yartsev, A.; Pascher, T.; Polivka, T.; Campagna, S.; Sundstrom, V. *Chem. Phys. Lett.* **2004**, *386*, 336−341.

have, to our knowledge, not been measured, as the species are indistinguishable before and after the process. Our result of a small structural change suggests that electron-transfer processes will be very efficient between them and that, for contact pairs, it is difficult to distinguish from energy transfer. The high rates of 10^9-10^{10} M^{-1} s^{-1} [10,53−55] for energy transfer, leading to charge exchange, point in the same direction, implying a low barrier for electron transfer from one species to the other. This is to relate to the high rates of self-exchange between reduced and oxidized forms of Ru−polypiridine complexes,[5,8] which also suggest little structural reorganization, as pointed out by crystallographic[22,50,56−58] and EXAFS[50] studies.

4. Conclusions

We recorded the X-ray absorption spectra at the L-edges of Ru in the aqueous $[Ru^{II}(bpy)_3]^{2+}$ complex in the ground state and in the excited state, 50 ps up to nanoseconds after photoexcitation with an ultrashort 400 nm laser pulse. The XANES line shapes have been quantitatively simulated with excellent agreement with experiment, using an atomic multiplet code with octahedral and trigonal ligand field contributions, assuming a trigonal symmetry for the excited complex. The analysis of the XANES and of the EXAFS modulations point to a contraction of Ru−N bonds by ∼0.03 Å on the average. This weak bond contraction is discussed in terms of a dominant electrostatic and polarization interaction between the oxidized Ru atom and the neutral and reduced bpy ligands and by steric effects due to straining of the latter. Since the D_3 symmetry was used throughout the modelling of data, it cannot be excluded that the above bond contraction may be the average of several non-equivalent bond contractions. This is however unlikely on the ground of the above mentioned steric effects. The inability of the present data to distinguish between the more probable C_2 symmetry of the excited state and the D_3 symmetry is an inherent limitation of the system and not of the method, since the XANES signatures of the two are identical.

The remarkable quality of the data, in terms of energy resolution and sensitivity to photoinduced changes, and the quantitative spectral shape and structural analysis on the metal−polypyridine complex, show that picosecond and, hopefully soon, femtosecond XAS can be implemented for the study of a large class of photoinduced reactions in coordination chemistry and in biology.[23]

Acknowledgment. This work was supported by the Swiss NSF via Contracts 620-066145 and 2000-67912.02. The experiments were performed at beamline 5.3.1 of the Advanced Light Source. We are grateful to Drs. Alexander Tarnovsky, Maik Kaiser (Lausanne), and Daniel Grolimund (SLS, Villigen). We also thank Drs. S. L. Johnson, P. A. Heimann, and R. W. Schoenlein and Prof. R. Falcone (Berkeley) for their help and assistance during the measurements and Prof. P. Vogel (Lausanne) for useful discussions.

Supporting Information Available: Contains a description of the experimental methods and of the codes used to analyze the XANES line shapes and the EXAFS modulations, along with tables of parameters used in both cases. This material is available free of charge via the Internet at http://pubs.acs.org.

JA054932K

(53) Milosavljevic, B. H.; Thomas, J. K. *J. Phys. Chem.* **1983**, *87*, 616−621.
(54) Shaw, G. B.; Brown, C. L.; Papanikolas, J. M. *J. Phys. Chem. A* **2002**, *106*, 1483−1495.
(55) Ikeda, N.; Yoshimura, A.; Tsushima, M.; Ohno, T. *J. Phys. Chem. A* **2000**, *104*, 6158−6164.
(56) Rillema, D. P.; Jones, D. S.; Levy, H. A. *J. Chem. Soc., Chem. Commun.* **1979**, 849−851.
(57) Bernhard, P.; Bürgi, H. B.; Hauser, J.; Lehmann, H.; Lüdi, A. *Inorg. Chem.* **1982**, *21*, 3936−3941.
(58) Rillema, D. P.; Jones, D. S.; Woods, C.; Levy, H. A. *Inorg. Chem.* **1992**, *31*, 2935−2938.
(59) Desimone, R. E.; Drago, R. S. *J. Am. Chem. Soc.* **1970**, *92*, 2343−2352.

Supporting Information (SI):

I. Experimental Methods

The experimental strategy is based on the pump-probe scheme, using an ultrashort laser pulse to excite the system, and a hard x-ray pulse from a synchrotron to monitor the photoinduced changes in the system, at variable time delays after the pump pulse. Details of the setup including the data acquisition scheme, are given elsewhere [1-4]. Briefly, solutions with different concentrations (1-80 mM) of $[Ru^{II}(bpy)_3]^{2+}$ dissolved in deionised water, were circulated in a free-flowing jet of 0.1 mm thickness inside the sample chamber filled with helium gas at atmospheric pressure. The sample is excited with 400 nm, 150 fs pump pulses from the frequency-doubled output of an amplified Ti-sapphire femtosecond laser system at 1 kHz repetition rate and with varying intensities in the 100-550 J pulse energy range focused down to a 0.3 mm diameter spot on the liquid jet congruently overlapping with the probing x-ray beam (vertical x horizontal ~110 x 250 m^2 spot size). X-ray pulses with 70 ps FWHM width were used to probe the photoinduced changes in the sample. The jitter between both laser and x-ray pulses was measured by us to be $\leq$ 10 ps [1,2], though the limiting temporal jitter is expected to be ca. 1 ps, which defines the time resolution of our experiment.

The transient XAFS data is recorded at 2 kHz repetition rate with the laser exciting the sample at 1 kHz. Thus we record alternatively the transmitted x-ray pulse intensity for the unexcited and the laser-excited sample. These are then appropriately sorted and averaged for a given data (point) accumulation time and stored together with their in-situ measured standard deviation. This scheme permits us to record the transient absorption spectrum by step-scanning the x-ray monochromator at a fixed pump-probe time delay and subtracting adjacent data points.

By sorting the data according to the laser-excited and the dark sample, we obtain the static and photoexcited transient transmission spectra for a given photoexcitation yield. Alternatively, we can record the temporal evolution of the x-ray transmission by scanning the laser-x-ray time delay at a fixed energy. The recorded transmission spectra of the unexcited sample are transformed into absorption spectra via normalization with a transmission spectrum through the neat solvent, and the excited state spectrum is obtained from the measured transient absorption spectrum at each fixed time delay (see Section 2.2 of the article).

II. *Simulation of the XANES line shapes:*

The XANES line shapes were simulated using the TT (*Theo Thole*) - multiplet simulation code developed at the University of Utrecht[22]. The starting point is the calculation of the energy levels of the initial-state $2p^6 4d^N$ ($2p^6 4d^{N-1}$ for the excited state complex) multiplet and the final-state $2p^5 4d^{N+1}$ ($2p^5 4d^N$, excited state, respectively) multiplet in a spherical (atomic) symmetry. The crystal field effects are then stepwise included (Fig. 4 of the article), projecting the atomic multiplets onto the octahedral symmetry (O_h), then the trigonal (D_3) symmetry and including the spin-orbit interaction (ζLS). Finally, the dipole selection rules for the ground state of the initial-state multiplet to all final states in the x-ray absorption process are applied and convoluted with the lifetime and monochromator widths respectively.

The parameters, which enter the multiplet calculations of the XANES line shapes at the *L* edges, are: i) the spin-orbit splitting of the 2*p* core shell, ii) the spin-orbit splitting of the 4*d* electrons, iii) the correlations within the 4*d* valence band electrons (the correlations effects can be restated in the terminology of atomic physics as "multiplet effects" [5]), which are factorized via the F^2 and F^4 Slater integrals for the initial and final states,

iv) 2*p*-4*d* multipole Coulomb and exchange interactions, which are factorized via the F^2, G^1 and G^3 Slater integrals, v) crystal field splittings with their octahedral and trigonal (for the ground and the excited compound) contributions. Parameters i)-v) are obtained from a Hartree-Fock (H-F) calculation within the code and are summarized in Table S.I. As can be seen from this table, the 4*d*-4*d* correlations are dominant. The trigonal field constant for the ground state was taken as derived from the literature on magnetic resonance measurements [6]. Our measured 2*p* spin-orbit coupling of 85.7 eV was used rather than the value of 87.7 eV calculated by the code in order to reproduce the experimental L_3/L_2 energetic splitting.

In the case of $4d^N$ orbitals with $N>1$ (here: N=5,6 correspond to the excited and ground states respectively) strong intraband correlation effects occur [7]. The spectra have been calculated with reductions to 50% and 75% of the atomic values of the *dd* and *pd* Slater integrals, respectively. These reductions are introduced to account for the fact that the ground state is not purely $4d^N$. There will be admixtures of other configurations, in particular $4d^{N+1}\underline{L}$, where $\underline{L}$ denotes a hole on a ligand. In other words, some charge transfer from the valence electrons of the ligand partially populates the $4d^N$ states. In optical spectroscopy, these admixtures are known as the nephelauxatic effect [8].

The ground state line shapes were simulated with the (renormalized) atomic parameters plus the octahedral crystal field value as known from quantum chemical calculations. In the excited state, both the octahedral and the trigonal field splittings were

optimised according to the measurement. The values of the ligand field splittings are given in Table III of the Article. From the collection of calculated multiplet energy levels, together with their oscillator strengths, we have generated the simulated absorption spectrum via convolution with Lorentzian and Gaussian functions. The Lorentzian widths were set to 1.75 eV for the L_3 edge and have been determined between 1.9 and 2.1 eV for the L_2 edge [9,10] (for which we used 1.9 eV).

The Gaussian width was set to 1.2 eV (L_3 edge) and 1.3 eV (L_2 edge) corresponding to the Ge(111) double-crystal monochromator resolution at both absorption edges.

III. Analysis of the EXAFS:

The EXAFS analysis itself consists of several straightforward steps: the averaged L_3 edge XAS spectra of both states were reduced using the standard data reduction procedure [11], including pre-edge subtraction, determination of the ionization potential (IP) or edge energy E_0 (as described in the Article), normalization of the data to the measured (and fitted) edge step $\Delta\mu_0(E)$, and subtraction of the atomic background contribution $\mu_0(E)$. In this way, we isolate the oscillatory part of the EXAFS spectrum, $\mu(E)$, and obtain the EXAFS function $\chi(E)$ via:

$$\chi(E) = \frac{\mu(E) - \mu_0(E)}{\Delta\mu_0(E)} \qquad (1)$$

Subsequently, $\chi(E)$ is interpolated to achieve equidistant k-spacing using $k = \sqrt{\frac{2m_e}{\hbar^2}(E - E_0)}$, and multiplied by k^3 in order to obtain the k^3-weighted EXAFS, $k^3 \cdot \chi(k)$. Fourier transformation of the $\chi(k)$ data yields the Pseudo Radial Distribution Functions (PRDF) $\tilde{\chi}(R)$ of the nearest neighbour scatterers in R-space, from which we isolate the amplitudes and phases for different coordination shells by window-filtering of $\tilde{\chi}(R)$ and transforming it back into the k-space (actually the back Fourier-transformed k-space is called q-space) as can be seen in Fig. 6a,c of the article.

Special care was taken in order to keep the data reduction procedure identical for both ground and excited states including identical spline functions and normalization ranges. The only difference in treatment between both data sets is the edge energy shift ΔE_0 = 1.8 eV (Table I of the Article) imposed onto the product spectrum. For the EXAFS spectrum, the experimental k-spectrum was Fourier-transformed, and thus its PRDF was obtained (Fig. 6b,d of the Article).

Only the first (and most intense) peak of this function was fitted using the EXAFS equation as defined below. Later, the PRDF was back Fourier-transformed into q-space filtering out all other scattering contributions except those, which contribute to the first peak in the Fourier spectrum (R-space) (below 3.2 Å) of the data (these 3 backscatteres are shown in Fig. 6b,d in the Article). Finally, the back Fourier-transformed spectra were compared with their corresponding fit functions (also in q-space), as can be seen in Figs 6a and 6c.

The geometric structural information is extracted via the EXAFS formula, which was formulated by Sayers *et al* [12] as a quantitative method of parametrization of the EXAFS function in Eq. (1):

$$\chi(k) = \sum_i S_0^2 N_i \frac{|f_i(k)|}{kR_i^{\,2}} \cdot \sin(2kR_i + 2\delta_C + \Phi) \cdot e^{-\frac{2R_i}{\lambda(k)}} \cdot e^{-2\sigma_i^2 k^2} \qquad (2)$$

The structural parameters are indexed *i* to group them into shells of identical scatterers (having identical chemical properties and bond distances to the absorber), which are: the interatomic distances R_i, the coordination numbers N_i (number of equivalent scatterers at a distance R_i), and the temperature-dependent root-mean square fluctuations in bond length (or Debye-Waller factors) σ_i, which naturally include effects of structural disorder within the i[th] shell. The remaining parameters are the backscattering amplitudes $f_i(k) = |f_i(k)|\exp[\Phi_i(k)]$ including the phase shift of the backscattered photoelectron Φ_i, the central-atom partial-wave phase shift δ_C in the photoelectron's final state, and the energy-dependent photoelectron's mean-free path $\lambda(k)$. Finally, the amplitude reduction factor S_0^2 is added in order to account for intrinsic losses and many-body effects upon excitation of a core-level electron [13].

The main parameters used in the calculation are given in Table S.II. Curve fitting was performed with the Artemis code [14] in real space using the forward-Fourier-transformed (FFT) spectra $\tilde{\chi}(R)$ for both oxidation states of $[Ru(bpy)_3]^{2+}$. The theoretical backscattering amplitudes and phases used during the fit procedure were calculated by the FEFF 8.20 *ab-initio* EXAFS code [15,16]. The scattering potentials were calculated self-consistently based on the muffin-tin (MT) approximation, using as input the geometrical structure (in Cartesian atomic coordinates) of the $[Ru(bpy)_3]^{2+}$ single crystal, from crystallographic data [17-20]. Due to the intrinsically limited EXAFS energy range above the L_3 edge (see Fig. 2 of the Article) of the complex, the extracted EXAFS function $\chi(k)$ was limited to ca. 6 Å^{-1} only. In order to reduce the number of fitting parameters, we used the above described Fourier filtering and put rigid constraints on the available structural information in the data, using the available

crystallographic data [17-20]. We have neither varied the number of neighbouring atoms in the shells used in the fit nor the ionization potential shift, since these are not expected to change on a 50 ps timescale and have been measured experimentally, respectively. We have then obtained the variation of Debye-Waller factors and bond distances to change only within physically meaningful values. This and the precise determination of the IP (Table I of the Article), allowed us to limit the number of independent fit parameters and set the physically meaningful constraints.

TABLE S.I: Parameters used in the simulation of the XANES line shapes. The F and G Slater integrals are the Hartree-Fock values. In the multiplet simulation, the *d-d* integrals are reduced by 50%, while the *p-d* ones by 75 % (see text for details). The Lorentzian (L) linewidth corresponds to the core-hole lifetime, while the Gaussian (G) line widths represent the experimental resolution at the corresponding energy.

TT-Multiplet Parameters				
	$[Ru^{II}(bpy)_3]^{2+}$ $2p^6 4d^6$ initial state	$[Ru^{II}(bpy)_3]^{2+}$ $2p^5 4d^7$ final state	^{3}MLCT $2p^6 4d^5$ initial state	^{3}MLCT $2p^5 4d^6$ final state
Slater integrals				
F^2_{4d4d}	8.19	8.69	8.73	9.22
F^4_{4d4d}	5.35	5.68	5.74	6.06
F^2_{2p4d}		1.94		2.11
G^1_{2p4d}		1.60		1.75
G^3_{2p4d}		0.93		1.02
Spin-orbit coupling				
LS_{2p}		85.62		85.77
LS_{4d}	0.14	0.157	0.146	0.173
Linewidths				
L		1.70		1.70
G (L_3)		1.30		1.30
G (L_2)		1.20		1.20

TABLE S.II: EXAFS parameters used for the fit of the pseudo-radial distribution functions of Fig. 6. The σ^2's represent the Debye-Waller factors and the R's refer to bond distances of the first 3 single scattering shells used in the fit, i.e., Ru-N, Ru-C2 and Ru-C6 respectively. The estimated error bars for each of the parameters used in the fit are given in parentheses. The numbers in brackets represent the uncertainties,

Parameters	**Ground state**	**Excited state**
S_0^2	0.95478(0.074)	0.95478(0.074)
E_0	2847.1(1.7) eV	2849.2 (1.7) eV
R (Ru-N)	2.066(0.017) Å	2.029(0.019) Å
R (Ru-C2)	2.866(0.018) Å	2.787(0.021) Å
R (Ru-C6)	3.051(0.024) Å	3.025(0.024) Å
σ^2 (Ru-N)	$9(3.5) \times 10^{-3}$ Å^2	$10.3(4.5) \times 10^{-3}$ Å^2
σ^2 (Ru-C2)	$1.3(4) \times 10^{-3}$ Å^2	$6(4) \times 10^{-3}$ Å^2
σ^2 (Ru-C6)	$8.5(4) \times 10^{-3}$ Å^2	$9.9(5.4) \times 10^{-3}$ Å^2

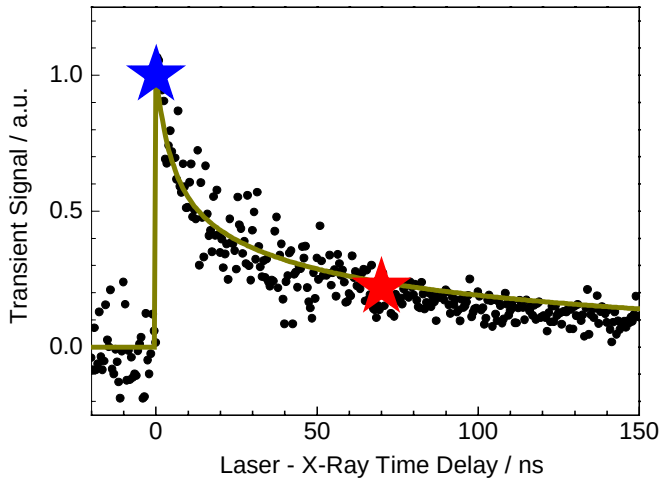

Figure S1: Kinetic decay of the transient XANES signal measured near the *B* feature (E_{probe} = 2840 eV). The ratio between the blue and the red star values equals 4.8, as used for rescaling the difference spectra in Fig. 3 of the main article. The yellow curve represents a simulation of the expected decay, when assuming that the signal arises due to decay of the ^{3}MLCT state only, i.e., assuming no contributions due to other product species, e.g., the ionized $[Ru^{III}(bpy)]^{3+}$ or the reduced $[Ru^{II}(bpy)_2bpy^{-}]^{1+}$ species.

References:

(1) Saes, M. G., W.; Kaiser, M.; Tarnovsky, A.; Bressler, Ch.; Chergui, M.; Johnson, S. L.; Grolimund, D.; Abela, R. *Synchrotron Radiation News* 2003, *16*, 12.

(2) Saes, M.; Bressler, C.; van Mourik, F.; Gawelda, W.; Kaiser, M.; Chergui, M.; Bressler, C.; Grolimund, D.; Abela, R.; Glover, T. E.; Heimann, P. A.; Schoenlein, R. W.; Johnson, S. L.; Lindenberg, A. M.; Falcone, R. W. *Rev Sci Instrum* 2004, *75*, 24-30.

(3) Bressler, C.; Chergui, M. *Chem Rev* 2004, *104*, 1781-1812.

(4) Gawelda, W.; Bressler, C.; Saes, M.; Kaiser, M.; Tarnovsky, A.; Grolimund, D.; Johnson, S. L.; Abela, R.; Chergui, M. *Physica Scripta* 2005, *T115*, 102.

(5) Sugano, S.; Tanabe, Y.; Kamimura, H. *Multiplets of transition-metal ions in crystals*; Academic Press: New York,, 1970.

(6) Desimone, R. E.; Drago, R. S. *J Am Chem Soc* 1970, *92*, 2343-+.

(7) Degroot, F. M. F. *J Electron Spectrosc* 1994, *67*, 529-622.

(8) J²rgensen, C. K. *Modern aspects of ligand field theory*; North-Holland Pub. Co.: Amsterdam,, 1971.

(9) de Siervo, A.; Landers, R.; de Castro, S. G. C.; Kleiman, G. G. *J Electron Spectrosc* 1998, *88*, 429-433.

(10) Ohno, M.; van Riessen, G. A. *J Electron Spectrosc* 2003, *128*, 1-31.

(11) Teo, B. K. *Exafs: Basic Principles and Data Analysis* Berlin ; New York, 1986.

(12) Sayers, D. E.; Stern, E. A.; Lytle, F. W. *Phys Rev Lett* 1971, *27*, 1204-&.

(13) Rehr, J. J.; Albers, R. C. *Rev Mod Phys* 2000, *72*, 621-654.

(14) Ravel, B.; Newville, M. *J Synchrotron Radiat* 2005, *12*, 537-541.

(15) Ankudinov, A. L.; Ravel, B.; Rehr, J. J.; Conradson, S. D. *Phys Rev B* 1998, *58*, 7565-7576.

(16) Ankudinov, A. L.; Bouldin, C. E.; Rehr, J. J.; Sims, J.; Hung, H. *Phys Rev B* 2002, *65*, -.

(17) Rillema, D. P.; Jones, D. S.; Levy, H. A. *J Chem Soc Chem Comm* 1979, 849-851.

(18) Rillema, D. P.; Jones, D. S.; Woods, C.; Levy, H. A. *Inorg Chem* 1992, *31*, 2935-2938.

(19) Biner, M.; Bürgi, H. B.; Ludi, A.; Röhr, C. *J Am Chem Soc* 1992, *114*, 5197-5203.

(20) Pinheiro, C. private communication.

Chapter 6

Spin Crossover Studied by Ultrafast Optical and X-ray Spectroscopies

In this Chapter, the results of the experimental studies of laser-induced spin transition in aqueous solutions of $[Fe^{II}(bpy)_3]^{2+}$ complex molecule are presented. In the first part (Section 6.1), we will present the femtosecond optical transient absorption results, which demonstrate the presence of both singlet and triplet MLCT states (^{1,3}MLCT) in the relaxation pathway to the HS state upon the light-induced SCO transition. These results demonstrate that the population leaves the charge transfer manifold in $\leq$120 fs before intersystem crossing to the lowest-lying quintet HS state. The analysis presented in Section 6.1.6 reveals that the arrival time to the quintet state, without involving the intermediate states as shown in Fig. 6.1), occurs in $\sim$960 fs. The high-intensity data shows an experimental evidence that the multiphoton absorption is involved in the excitation process and populates the higher-lying state, which decay to the HS state in ca. 3-4 ps. In agreement with earlier studies, our results confirm that the HS$\rightarrow$LS relaxation rate constant in aqueous solutions of $[Fe^{II}(bpy)_3]^{2+}$, at room temperature, is ca. 665 ps. Finally in Section 6.1.7, we propose a verified model for the relaxation dynamics, which involves different relaxation rate constants in a sequential reaction scheme involving both MLCT and LF states of singlet and triplet multiplicities. In the following part (Section 6.2), the picosecond XAS results of the same complex are presented. Here we capture for the first time the excited state molecular structure of the HS form of solvated aqueous $[Fe^{II}(bpy)_3]^{2+}$ at 50 ps after the photoexcitation. The laser-induced spin transition leads to a substantial Fe-N bond elongation of ca. 0.2 Å, which we extract by fitting directly the transient x-ray absorption spectra.

6.1 Ultrafast Optical Spectroscopy

6.1.1 Introduction

Similarly to most other SCO compounds, the steady-state optical absorption spectrum of $[Fe^{II}(bpy)_3]^{2+}$, also abbreviated with $Fe(bpy)_3$, exhibits the characteristic and intense broad band centered at 523 nm, which originates from singlet MLCT absorption, (^{1}MLCT). In Fig. 6.1a, we present the static optical absorption spectrum of aqueous $Fe(bpy)_3$ complex, which has already been discussed in Chapter 2, Section 2.4. Here, only the wavelength range of the spectrum covered by the spectral window of the probe pulse (i.e. λ_{probe}=350-650 nm) is shown, whereas the excitation wavelength (λ_{pump}=400 nm) is indicated by a vertical arrow in Fig. 6.1a.

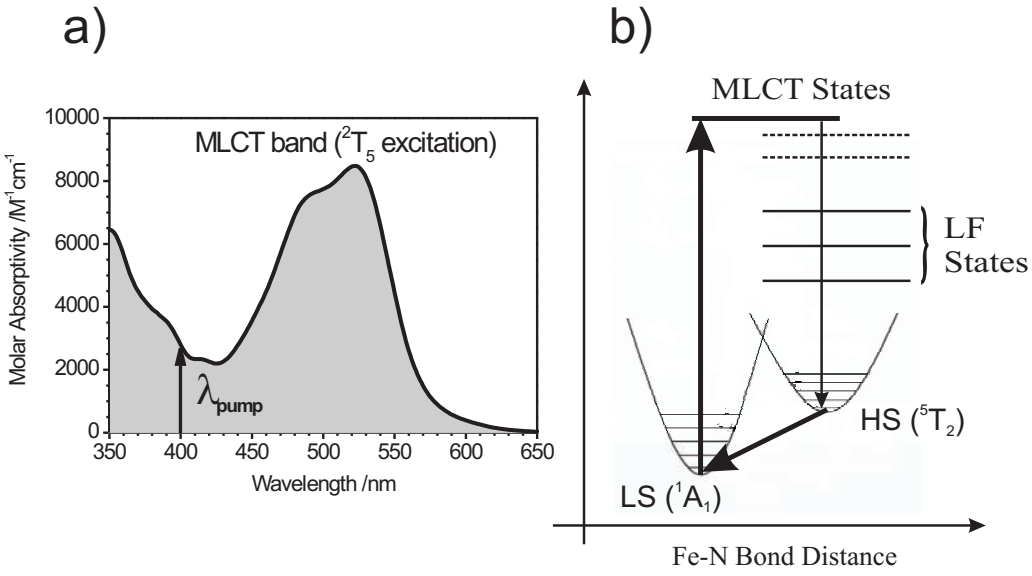

Figure 6.1: (a) Steady-state absorption spectrum of aqueous $[Fe^{II}(bpy)_3]^{2+}$ in the spectral window covered by the probe pulse (350-640 nm). The vertical arrow indicated the excitation wavelength at 400 nm. (b) The simplified energy level scheme of $[Fe^{II}(bpy)_3]^{2+}$ involving the ground state low-spin (LS) and the lowest-lying high-spin (HS) excited state. The intermediate states are of both MLCT and LF origin (their spin multiplicities were not included)

The photoexcitation into this band is followed by a cascade of intersystem crossing events involving both the MLCT and LF manifolds of different spin multiplicities. These are shown in a simplified picture in Fig. 6.1b (here again we refer to photochemical cycle of $Fe(bpy)_3$ as previously discussed in Chapter 2, Section 2.4). Here we explicitly omitted the spin multiplicities of the intermediate states. The vertical downward arrow indicates the intersystem crossing from the MLCT manifold via LF manifold down to the lowest-lying quintet HS state ($^5T_2$). The possible involvement of the lower-lying MLCT states was taken into account and is illustrated in Fig. 6.1b with the dashed lines at the bottom of the MLCT manifold.

The entire intersystem crossing process happens on the ultrafast timescale and it was reported to take no more than ca.1 ps [149] with an almost unit quantum efficiency [163] before the complex reaches the $^5T_2$ state (hereafter called the HS state). This state relaxes nonradiatively to the LS ground state ($^1A_1$ in Fig. 6.1b) in <700 ps in case of aqueous $Fe(bpy)_3$ at room temperature [93,357]. The ultrafast photochemistry of light-induced SCO has been characterized by conventional and ultrafast laser techniques over the past few years in a wide class of compounds (for more details and references see Section 2.13 of Chapter 2). In general, these studies delivered a consistent picture of the photochemical cycle, which describes the relaxation pathways in these complexes upon the MLCT photoexcitation in agreement with one shown in Fig. 6.1b. The initial Franck-Condon configuration is formed within the ^{1}MLCT manifold, which relaxes extremely fast into the lower-lying LF states before it finally thermalizes within the quintet HS state [149,357]. Whether or not, the triplet manifold ^{3}MLCT is involved in the initial relaxation pathway was never experimentally verified. Monat *et al.* [161] reported the ultrafast single-wavelength kinetics of a similar complex, where the ultrafast excited state absorption was measured prior to the HS relaxation. The authors assigned this feature to be the initial ^{1}MLCT absorption and obtained its lifetime of ca.80 fs, which could have been hindered by the temporal resolution of their apparatus. In their study, no existence of ^{3}MLCT, as a precursor state prior to subsequent relaxation to the LF manifold, was reported. Very recently, similar conclusions were reported by Juban and co-workers [93]. On the contrary to these hypotheses, femtosecond broadband fluorescence up-conversion studies by Cannizzo *et al.* [82] (with improved temporal resolution) have shown that the initial Frank-Condon configuration in aqueous $[Ru^{II}(bpy)_3]^{2+}$ is extremely short-lived, i.e. ∼15-20 fs, and it has ^{1}MLCT character. It was shown that the subsequent relaxation is followed within the ^{3}MLCT state before the thermalization occurs and the system decays back to the ground state. Similar ultrafast fluorescence studies on the aqueous $[Fe(bpy)_3$ [358] compound revealed that also in this case the initial excitation with 400 nm laser light forms the ^{1}MLCT state (as illustrated in Fig. 6.1a), which decays on a comparable timescale as in case of $[Ru^{II}(bpy)_3]^{2+}$. Yet, no ^{3}MLCT emission was observed in this study.

In the present work, we have performed a femtosecond broadband (350-650 nm) transient absorbtion study of the aqueous solutions of $[Fe(bpy)_3$ at room temperature upon different excitation intensities. The motivation for this study was two-fold: a) to verify experimentally the involvement of the ^{3}MLCT state in the initial relaxation pathway of $[Fe^{II}(bpy)_3]^{2+}$ (similar study for aqueous form of $[Ru^{II}(bpy)_3]^{2+}$ complex is presented in Chapter 5) and the subsequent relaxation dynamics within the LF manifold, including the lowest-lying quintet $^5T_2$ state; b) to perform comparative study of the picosecond excitation yields of $^5T_2$ state formation at varying pump intensities in order to disentangle the possible photoproducts, which may affect the structural analysis of the time-resolved XAS results of $[Fe(bpy)_3$ complex (these results are presented in Section 6.2 of this Chapter).

6.1.2 Transient Absorption Spectra

A representative set of transient absorption data, up to 20 ps, of 9 mM aqueous solution of $[Fe^{II}(bpy)_3]^{2+}$ photoexcited with 80 mJ/cm^2 is shown in Fig. 6.2. Our experimental apparatus (Section 4.10) allows recording simultaneously both the temporal and spectral evolution of the photoexcited complex and thus delivers a complete information about the excited state dynamics.

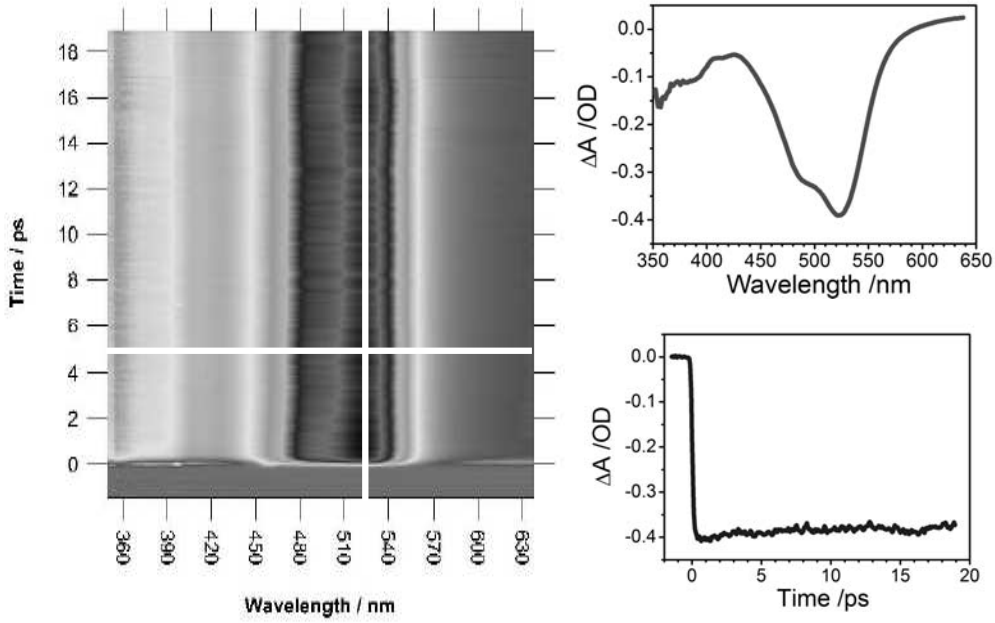

Figure 6.2: A representative set of 2D transient absorption data recorded in these measurements. The horizontal and vertical lines indicate the positions, at which the temporal and spectral (at a given time delay, i.e. 5 ps) slices (right-hand side of the figure) were taken, respectively.

They deliver the corresponding spectra and kinetics (at a given wavelength, i.e. 523 nm) respectively. In the present study, we have investigated the transient absorption spectra in 3 different time windows, defined by the recorded maximum time delay between the pump and probe pulses, namely up to $\leq$5 ps, 20 ps and 1.2 ns in order to disentangle the different relaxation pathways involved in the underlying SCO process.

6.1.3 Short-time Kinetics

In order to investigate the dynamical processes accompanying the photoinduced SCO transition, we have recorded the transient absorption spectra in both 5 ps and 20 ps time windows with the time step of 20 fs and 67 fs, respectively. In Fig. 6.3, the representative spectra recorded at various time delays within the first 1.5 ps following the photoexcitation are shown. The GVD correction was applied previously to all the data presented in the follow-

ing sections according to the procedure explained in Section 4.10. The strong negative absorption feature present in the early-time spectra shown in Fig. 6.3 (around time-zero) around 450-460 nm, is the aforementioned (see Fig. 4.32 in Section 4.10) impulsively-induced Raman signal of H_2O solvent, which delivered a cross-correlation signal between pump and probe pulses [300]. The additional peak observed around 400 nm is the residual scattered light contribution from the pump pulse.

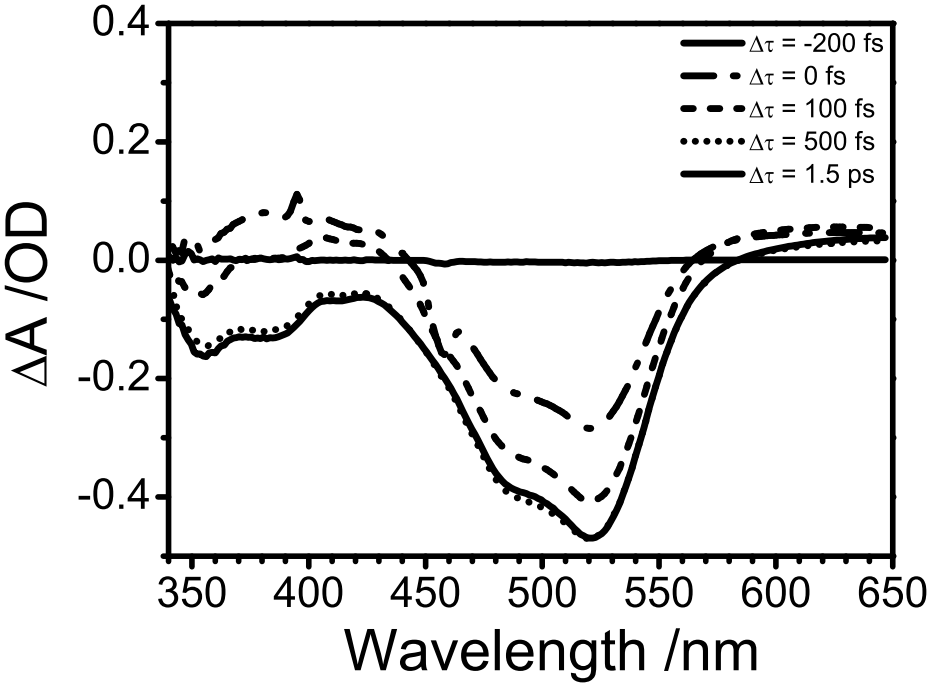

Figure 6.3: A set of representative spectra recorded for 9mM sample of aqueous $[Fe^{II}(bpy)_3]^{2+}$. The spectral evolution in the first 1.5 ps after the photoexcitation (t=0) is shown. The blue part of the spectrum shows a positive absorption in the first 200 fs after tie-zero, whereas the red side sustains the positive absorption at all times on this timescale

The spectral evolution on this timescale shows 2 dominant features; first we notice the simultaneous short-lived excited state absorption (ESA) positive signal in the 340-440 nm and 560-640 nm ranges, which is formed in the spectra instantaneously within the pump pulse duration. Within the first <200 fs, this transient ESA turns into a negative absorption in 340-440nm range, which we recognize as the ground state bleach (GSB) signal. Indeed the spectral features seen in Fig. 6.3 reflect the steady-state ground state absorption (Fig. 6.1). The GSB is persistent at all time delays after the very first hundreds of fs and for all concentrations and excitation intensities investigated here. On the red side of the spectrum (560-640 nm range), the initial ESA signal remains, however, now with significantly reduced intensity and with a long lifetime. In the subsequent Sections of this Chapter we will discuss the origin of both the short-live ESA

in the UV and of this long-lived absorption and identify its relaxation rate constant.

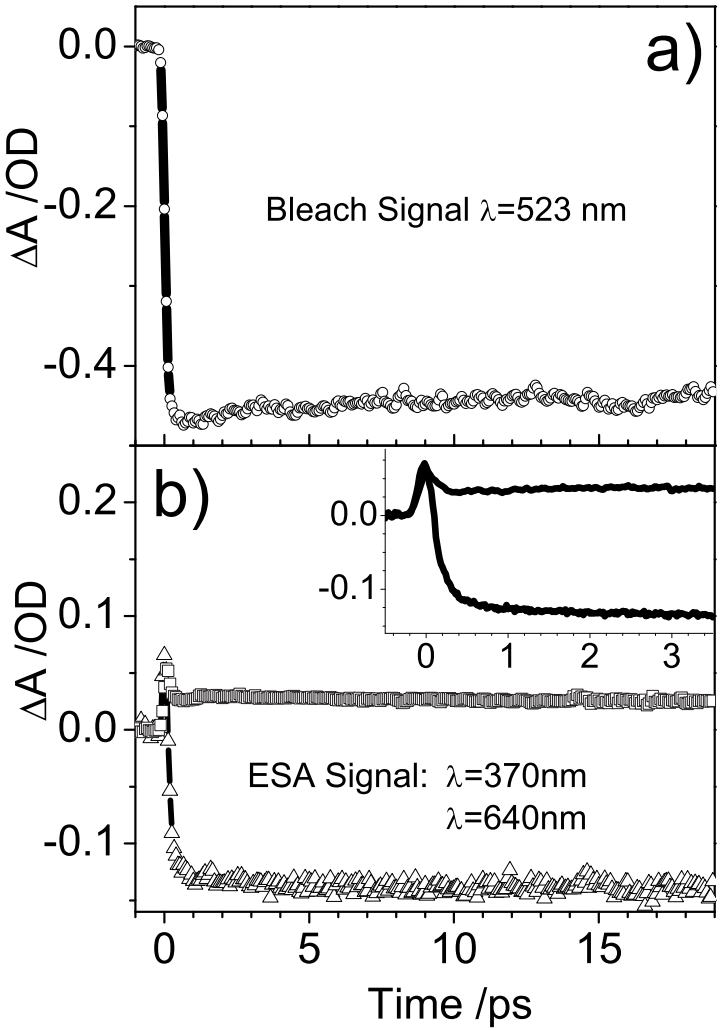

Figure 6.4: Representative kinetic traces recorded in 20 ps window are shown. In (a) the ground state bleach signal (523 nm) is displayed. In (b) two characteristic time slices in the blue-most (370 nm) and the red-most part (640 nm)of the spectra in Fig. 6.3 are shown. The inset figure zooms into the initial 3 ps time window to show that both excited state absorption signals occur simultaneously within the excitation pulse

The corresponding kinetics, recorded at characteristic wavelengths, are shown in Fig. 6.4. In a) we show the temporal evolution of the GSB signal (523 nm) in the 20 ps time window. It can be seen that this signal increases promptly and is followed by a faint recovery within the first <3 ps. At later time delays, the GSB decays according to the HS→LS relaxation rate constant, i.e. k=$1.5 \cdot 10^9$ s^{-1} (τ=665 ps) [148, 357], which will be discussed in details in the following Sections. In Fig. 6.4b, the kinetic traces at 370 nm and 640 nm are shown. These represent the typical temporal response encountered

in the spectral ranges, where the ultrafast ESA was detected. Although, the short-lived ESA signal cannot be directly detected on the spectra (Fig. 6.3), its existence is revealed by the kinetic traces at the red-most wavelengths of the spectra. We also observe that at later times it either turns into GSB or remains ESA with reduced intensity and different lifetime. The inset in Fig. 6.4b, zooms into the first 4 ps time window in order to show the details behavior of the discussed signals. We observe that no detectable time delay between the onset of both signals, in the blue-most and red-most parts of the spectrum (with respect to the GSB wavelength), was observed and both of them are present in the data shown in Figs. 6.3 and 6.4 within the cross-correlation time of the experiment (i.e. 145 fs as discussed in Section 4.10). This suggests that both ESA signals observed at 370 nm and 640 nm in Fig. 6.4b (and the inset) that appear instantaneously after (and within) the photoexcitation pulse can be attributed to the excited state species formed on these timescales as will be analyzed and discussed in the following Sections. The change in sign of the transient absorption signals at 370 nm and 640 nm on a longer timescale may already point towards an additional photoexcited species, whose kinetics affect the red part of the spectrum.

6.1.4 Long-time Kinetics

In Fig. 6.5a, we depict the long-time kinetics recorded in the 1 ns time window with 2 ps time steps at identical probe wavelengths as in Fig. 6.4. The signal at the blue-most wavelengths of the spectra (see Fig. 6.5b) resembles the one recorded in the vicinity of the GSB, which indicates that this spectral range (340-570 nm) is dominated by the signal originating from the depleted ground state species and thus can be associated with the fraction of ground state population that underwent the SCO transition into the HS state. In earlier works it was shown that upon the photoexcitation into the ^{1}MLCT band (see Fig. 6.1) leads, with nearly unity quantum yield, to population of the long-lived HS state [163,165,167,359]. The selective excitation into the lower-lying LF states has also shown no significant relaxation between these states and the ground state [360]. Therefore, we can directly link the observed GSB recovery signal with the lifetime decay of the HS state. However, as seen in Fig. 6.5b, the red-most part of the spectra shows a small, however, detectable, signal, which is present throughout the entire time window investigated. The decay rate of this signal is comparable with the GSB recovery time present at the bluer wavelengths (see the traces at representative wavelengths shown in Fig. 6.5a).

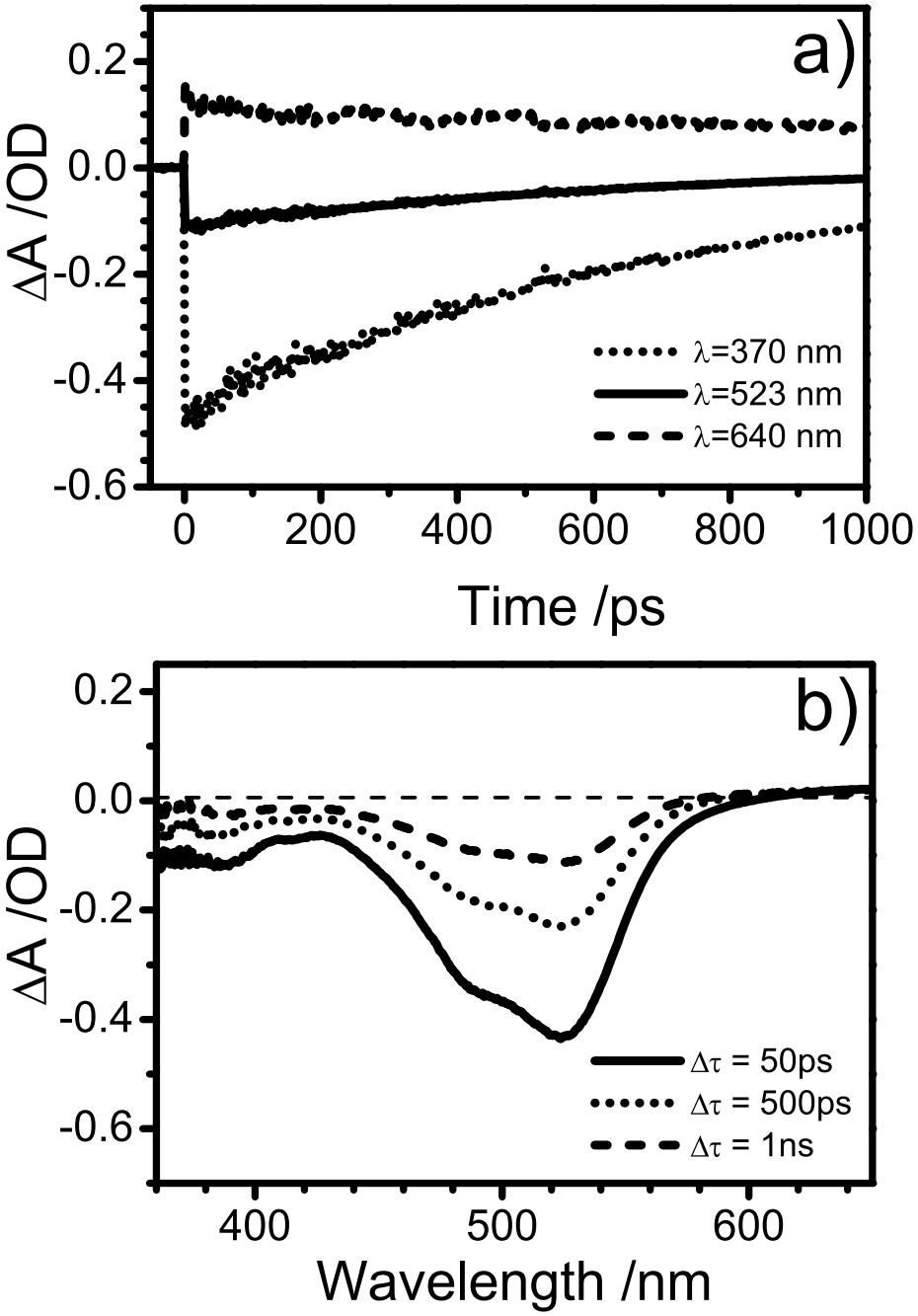

Figure 6.5: Long-time kinetics (a) and spectra (b) are shown here. The selected wavelengths of kinetic traces in (a) are the same as in Fig. 6.4. The long-time kinetics at all recorded wavelength show very similar behavior, with characteristic lifetime of the ground state bleach recover (see text for details). The long-time spectra show no significant deviation from the depleted ground state spectrum (Fig. 6.1)

Therefore we can identify this signal as a fractional ESA absorption of the long-lived HS state, which has a very small absorption cross section in the spectral range of interest. Indeed, the signal at 640 nm shown in Fig. 6.5a, is ca. 20 times weaker than the GSB signal at 523 nm. For the purpose of comparison, the kinetic trace in Fig. 6.5a was amplified by a factor of 5. The HS state of solvated $[Fe^{II}(bpy)_3]^{2+}$ at room temperature has never been reported in the literature before. Hauser *et al.* [360] reported the absorption spectra of this complex doped into several crystalline host lattices and measured at cryogenic temperature. In this case, the HS state spectrum was detected as a weak and broadband feature peaked around 820nm [360]. This leads us to the conclusion that the observed long-time (Fig. 6.5a) and spectral (Fig. 6.5b) evolution of the red part of the spectrum correspond to the GSB recovery and represents the decay of the HS state.

6.1.5 Analysis

In order to analyze the results presented in the preceding Section 6.1.2, we have employed the approach, discussed in Appendix D. In all cases (meaning at all different excitation fluences used in the experiment), the analysis consisted of the SVD decomposition of the time-resolved transient absorption data sets according to Eq. D.5. Next to it, it was followed by the global fitting of the kinetic V_k^T components retained after the transformation using the global fit function (defined in Eq. D.6) using Eq. D.7. Once all the SVD kinetic components are fitted, using the extracted pre-exponential fit coefficients $a_{i,k}$ we have constructed the decay-associated spectra (DAS) associated with the characteristic lifetimes τ_i used in the fit (see Eq. D.7). As already mentioned in Appendix D, we assume the absence of the spectral diffusion in our transient absorption data and the kinetic traces at different wavelengths will modeled by a sum of exponential function convoluted with the Gaussian-shaped IRF (for cross-correlation function refer to Fig. 4.32) of the experiment (in agreement with the Eq. D.6). This analysis approach will be applied to the results obtained in 3 different time windows, namely 5 ps, 20 ps and 1 ns for the aqueous solution of 9 mM $[Fe^{II}(bpy)_3]^{2+}$.

1 ns Time Window

We will start the analysis by applying the SVD transformation to the long-time kinetics (Fig. 6.5a) and spectra (Fig. 6.5b) recorded up to 1 ns time delay. The corresponding results are summarized in Fig. 6.6. In Figs. 6.6a and b, the SVD kinetics and spectral components are shown respectively. The criterion for the number of relevant singular values retained in the analysis is presented in Fig. 6.6c. Here we have plotted the singular values s_i obtained upon SVD transformation (see Eq. D.5) with their corresponding weights. Fig. 6.6 clearly justifies our choice only the first singular value s_1 to be retained in further analysis. Singular values of higher indices $s_i > s_1$ were excluded due to their insignificant weights and no physically meaningful spectro-temporal behavior.

In Fig. 6.6a, the analyzed V_1^T kinetic basis vector is shown together with the corresponding single exponential fit.

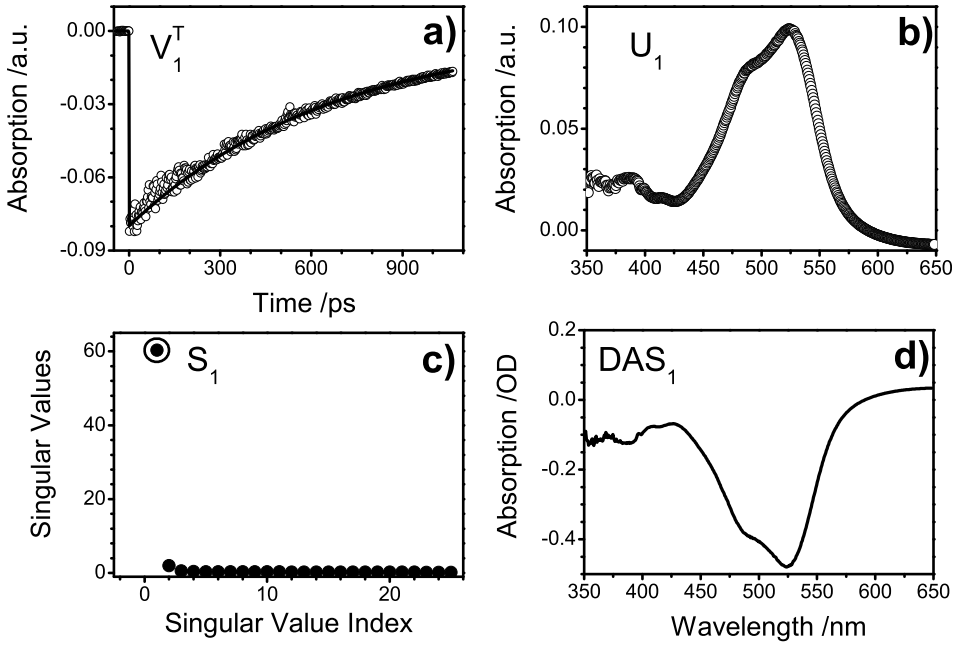

Figure 6.6: The SVD transformation of the 1-ns data is presented in panels (a)-(d). The kinetic and spectral basis vectors of the reduced data matrix are shown in (a) and (b), respectively. The singular values obtained during the decomposition are plotted in (c) and their weights select the singular values retained in the analysis (circle). In panel (d), the decay-associated spectrum, via Eq. D.8 in Appendix D, is presented.

The fitted lifetime was τ_1=665±45 ps. The obtained $a_{1,1}$ coefficients were used, via Eq. D.8, to extract the DAS corresponding to the fitted lifetime τ_1. The time decay-associated spectrum is presented in Fig. 6.6d. As it can seen, We can directly link the spectral shape of the obtained DAS to the ground state absorption spectrum of aqueous $[Fe^{II}(bpy)_3]^{2+}$ as previously shown in Fig. 6.1. This result suggests that on sub-ns ($>$ 20 ps) timescales the only relevant photoproduct present in the system is the photoexcited HS state associated with the GSB signal. This result provides a very important input to the photolysis yield analysis presented later in this Chapter and is highly relevant to the subsequent picosecond-resolved XAS studies where this parameter plays a crucial role in correct extraction of the excited state XAS spectrum via Eq. 6.1 (Section 6.2.3).

Short Time Windows: 5 ps

In the following, we have applied the SVD transformation to the short-time spectra and kinetics recorded in the 5 ps and 20 ps time windows (Figs. 6.3 and 6.4). In both cases, we have analyzed the transient absorption data of an aqueous 9 mM sample of $Fe(bpy)_3$ photoexcited with pump fluences in the range from 2.5 mJ/cm^2 to 160 mJ/cm^2. These results are summarized in Figs. 6.7, 6.8, 6.9 and 6.10.

First, we will discuss the outcome of the GA analysis applied to transient absorption results obtained within the initial < 5 ps following the photoexcitation. These are illustrated in Figs. 6.7 and 6.8.

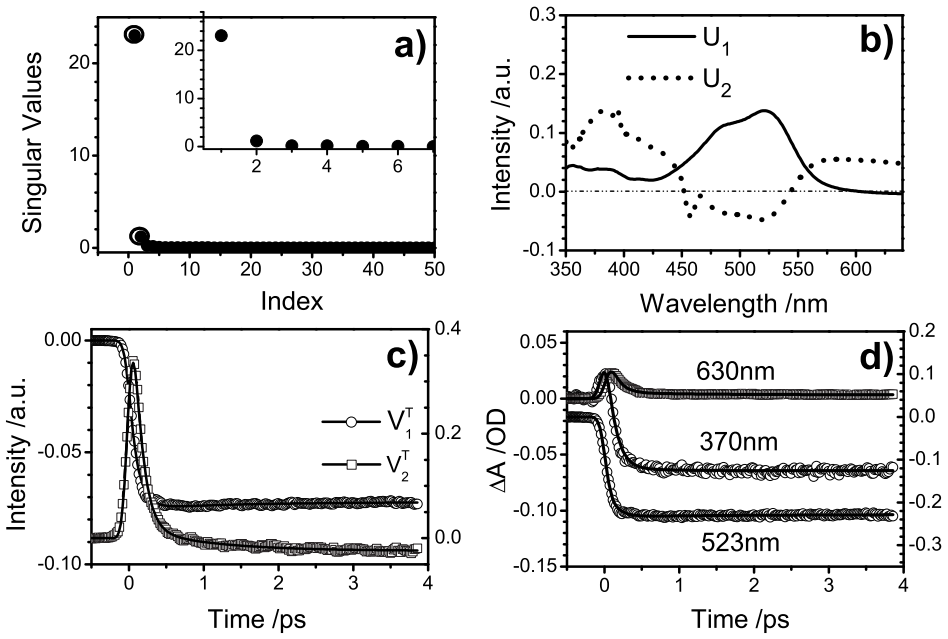

Figure 6.7: SVD results of the data recorded for 9mM aqueous solution of $[Fe^{II}(bpy)_3]^{2+}$ complex upon 35 mJ/cm^2 excitation fluence in 5 ps time window . Here panel (a) shows the singular values as obtained upon the decomposition (circles indicate the retained values), where the inset figure zooms into the initial 7 values to show better the noise cut-off of the singular values. Panel (b)-(c) show the spectral (U_i) and temporal (V_i^T) basis vectors used in the data reconstruction. In addition, panel (c) presents the global fit results of the SVD kinetics. In (d) the raw kinetics traces at 3 selected wavelengths are displayed together with their fit functions using a global fit model (further details in the text)

.

Panels a) through d) of Fig. 6.7 present the singular values retained in the analysis, their corresponding spectral U_i and temporal V_i^T basis sets together with the fit functions using the aforementioned kinetic model (refer to Appendix D, Eq. D.6) and the selected single-wavelength kinetic traces of the unreduced data set fitted using the same kinetic model.

The choice of the wavelengths is supported by the most relevant spectral regions, where significant ESA changes are observed on the very fast timescales (i.e. the ESA at 370 nm and 630 nm described in Figs. 6.3 and 6.4) and the very subtle rise time observed on the GSB signal (i.e. at 523 nm). The analysis of the data at fluences $\leq$35 mJ/cm^2 (Fig. 6.7) results in 2 dominant SVD components. The temporal components are depicted in Fig. 6.7c. We can clearly see that they account for the ESA absorption found at the blue-most and red-most parts of the transient absorption spectra (V_2^T) and the GSB signal (V_1^T) (see time traces in Fig. 6.7d). The spectral components U_1 and U_2 (Fig. 6.7b) can be associated with the ground state absorption spectrum (described above) and the reported spectrum of the reduced bipyridine (bpy^-) ligand. Indeed our U_2 spectrum resembles very much the steady-state spectrum of the reduced $[Fe^{II}(bpy)_3]^{1+}$ complex reported in Ref. [152]. In several similar transition-metal complexes, the reduced bpy^- absorption, obtained in the transient absorption measurements, was associated with the excited ^{3}MLCT state, which can be relatively long-lived in some compounds.

We have reported the ^{3}MLCT state spectrum in aqueous $[Ru^{II}(bpy)_3]^{2+}$ solution at high intensity photoexcitation in both Chapter 5 and Ref. [81]. Similarly to here, it is characterized by a strong absorption observed in the 340-425 nm range (compare the spectrum shown in Fig. 5.3 in Chapter 5). In the kinetic model used here, we assume the existence of three relaxation rate constants, which are linked to only two spectral components. Therefore we cannot directly link the U_2 spectrum (Fig. 6.7b) to the ^{3}MLCT species, although it contains a major fraction of its absorption band. On contrary, the U_1 component remains unchanged both in 5 ps and 1 ns time windows and thus we interpret its spectral components as directly linked to the *species-associated spectrum* (SAS) of the ground state LS species.

At higher excitation at fluences $\geq$35 mJ/cm^2 (see Fig. 6.8 for the case of 160 mJ/cm^2), the SVD results are best described by including an additional singular value component as shown in Fig. 6.8a. The corresponding U_i and V_i^T basis vectors are depicted in Figs. 6.8b and 6.8c. Clearly, the U_1 (solid line) spectrum is unchanged as compared to lower fluences, whereas the U_2 (full dots) component loses intensity in the red-most part of the spectrum (560-650nm). The blue-most and central parts of the U_2 spectrum are unchanged with respect to its low-intensity counterpart. The additional U_3 (dashed dots) component mainly accounts for the positive absorption in the red part of the spectral range, where it gains the intensity at the expense of the U_2 component.

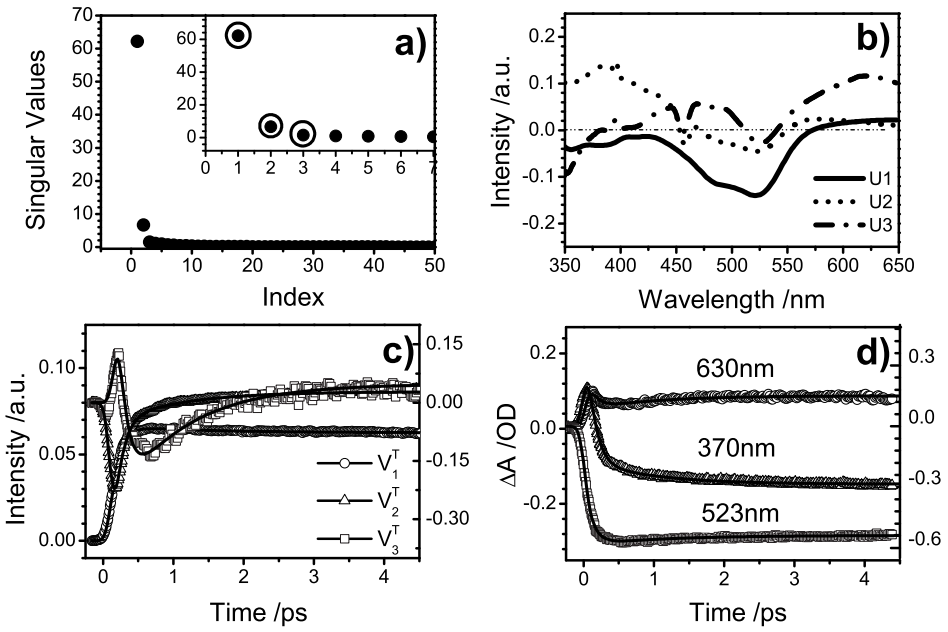

Figure 6.8: SVD results of the data recorded for 9mM aqueous solution of $[Fe^{II}(bpy)_3]^{2+}$ complex upon 160 mJ/cm^2 excitation fluence in the first 5 ps after the photoexcitation. Similarly to Fig. 6.7, panel (a) presents the singular values as obtained upon the decomposition (the circle indicate the retained values), where the inset figure zooms into the initial 7 values to show better the noise cut-off. Panel (b)-(c) show the spectral (U_i) and temporal (V_i^T) basis vectors used in the data reconstruction. In addition, panel (c) presents the global fit results of the SVD kinetics. In (d) the raw kinetics traces at 3 selected wavelengths are displayed together with their fit functions using a global fit model (further details in the text).

The weights of U_1 and U_2 components, given by the singular values factors s_i in Figs. 6.7a and 6.8a, are summarized below in Table 6.1. As we notice, at low fluences the ratio between the U_1 and U_2 components amounts to 19:1, which turns into 14:1:0.2 for U_1, U_2 and U_3 contributions at the higher fluences ($\geq$80 mJ/cm^2 in Table 6.1). This comparison shows that the inclusion of the U_3 components contributes by ca. 1.4% (as compared to the U_1) to the overall spectral weight. According to Table 6.1, the U_2 and U_3 components will increase nearly linear with increasing fluence, whereas the U_1 component, which we mainly assign to the GSB signal at very high fluences exhibits saturation.

Fluence	35 mJ/cm^2	80 mJ/cm^2	160 mJ/cm^2
s_1 (U_1)	23.1	48.6	62.2
s_2 (U_2)	1.2	3.4	6.7
s_3 (U_3)	0	0.7	1.5

Table 6.1: The weights of the singular values, corresponding to the spectral basis vectors U_1-U_3, obtained after the SVD decomposition of the data at different excitation fluences

Although the overall spectral weight of the U_3 component is minute compared to U_1 in Table 6.1, the SVD-reconstructed kinetics using two components deviated substantially from the raw kinetic traces at the wavelengths above 560-570 nm, showing the need of inclusion of the U_3 component. In Fig.6.8c, the kinetic components are shown together with their corresponding fit functions. The kinetic model used in the fit is identical to the one used at lower fluences (see Fig. 6.7) and in both cases the fit was obtained by simultaneous global adjustment of all V_i^T vectors. The kinetic model assumes 3 sequential relaxation processes governed by first-order kinetic law, which can be modeled by a sum of exponential decays as defined in Eq. D.6. The fit results consisting of the characteristic decay lifetimes τ_i, pre-exponential coefficients $a_{i,k}$, the cross-correlation pulse width and the time origin t_0 (denoted as μ parameter in Eq. D.6) of the experiment (time zero) are presented in Tables 6.2 and 6.3 in case of 35 mJ/cm^2 and 160 mJ/cm^2 pulse fluences respectively.

V_i^T	$a_{i,1}$	$a_{i,2}$	$a_{i,3}$	τ_1	τ_2	τ_3
V_1^T	0.05(0.002)	-0.003(0.001)	-0.07(0.001)	116(11) fs	960(100) fs	665 ps
V_2^T	0.7(0.003)	0.05(0.002)	-0.02(0.001)	116(11) fs	960(100) fs	665 ps
V_3^T	0	0	0	116(11) fs	960(100) fs	665 ps

Table 6.2: Global fit results, using the 3-exponential model (Eq. D.6), of the transient absorption data of aqueous 9mM sample of $[Fe^{II}(bpy)_3]^{2+}$ at 35 mJ/cm^2 pump fluence (Fig. 6.7)

V_i^T	$a_{i,1}$	$a_{i,2}$	$a_{i,3}$	τ_1	τ_2	τ_3
V_1^T	-0.05(0.02)	0.004(0.005)	0.06(0.002)	116(11) fs	960(100) fs	665 ps
V_2^T	-0.4(0.02)	-0.08(0.01)	0.03(0.002)	116(11) fs	960(100) fs	665 ps
V_3^T	0.6(0.03)	-0.3(0.01)	0.05(0.002)	116(11) fs	960(100) fs	665 ps

Table 6.3: Global fit results, using the 3-exponential model (Eq. D.6), of the transient absorption data of aqueous 9mM sample of $[Fe^{II}(bpy)_3]^{2+}$ at 160 mJ/cm^2 pump fluence (Fig. 6.8)

The FWHM was fixed globally to 145 fs and the time-zero was fixed globally for each data set at given fluence value. The pre-exponentials coefficients were free running parameters during the fit. The preliminary analysis was done by fitting the selected single-wavelength traces with the multiexponential function (as defined in Eq. D.6) and thus it confirmed that 3 lifetimes suffice to globally fit the raw data. In the latter analysis, these values were fixed and globally set for all data sets (at various fluences). The time-zero was fixed for each V_i^T component within each data set. The fit results shown in Table 6.2 had a single time-zero set to ca. 119 fs. On the contrary, the results in Table 6.3 required the time-zero of the V_3^T component to be slightly shifted with respect to V_1^T and V_2^T kinetics. This delay was about 70 fs, originates from the residual *cross-phase modulation* (CPM) [300] signal present in the V_3^T component very close to the nominal time-zero (small negative signal around time-zero in Fig. 6.8c.

This derivative-like spectral modulation was identified in earlier reports [361] and assigned to the CPM artifact and therefore it was left out of the fit. The 3 decay lifetimes used in the GA model are reported in Tables 6.2 and 6.3. The third lifetime, τ_3, accounts for the infinitely long-lived HS state (in this present time window) and it has the value determined by the SVD analysis of 1 ns data. The first two lifetimes, τ_1 and τ_2, are sufficient to fit the ESA absorption signal and the transient rise time observed in both the SVD kinetics and the unreduced data (Figs. 6.7c,d and 6.8c,d). The interpretation of these characteristic time constants accompanied with the extracted DAS will be presented in the following Sections and the spectral assignments of the involved species will be done.

Short Time Windows: 10 ps

In order to further verify the necessity of including an intermediate SVD component, V_3^T, we have analyzed the data recorded in 10 ps time window.The results for a very low excitation fluence (ca. 2.5 mJ/cm^2) are shown in Fig. 6.9.

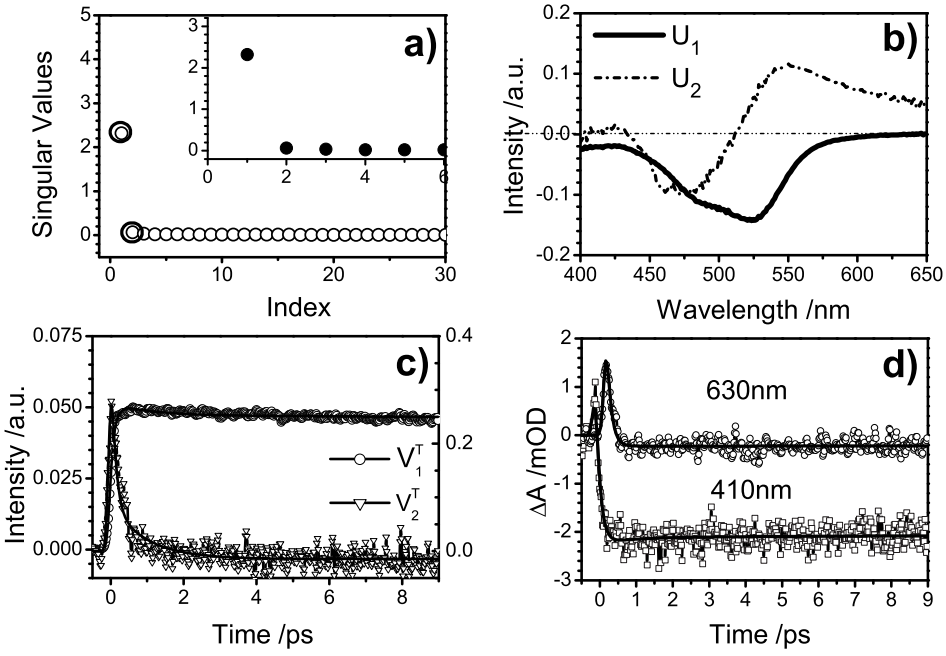

Figure 6.9: SVD results of the data recorded for 9mM aqueous solution of $[Fe^{II}(bpy)_3]^{2+}$ complex upon 2.5 mJ/cm^2 excitation fluence recorded in 10 ps time window. Panel (a) presents the singular values as obtained upon the decomposition (the circle indicate the retained values), where the inset figure zooms into the initial singular values. Panel (b)-(c) show the spectral (U_i) and temporal (V_i^T) basis vectors used in the data reconstruction. In addition, panel (c) presents the global fit results of the SVD kinetics. In (d) the raw kinetics traces at 2 selected wavelengths are displayed together with their fit functions using a global fit model (see text for further details).

In full agreement with our previous observation, at low intensities, the SVD decomposition yields 2 dominant principal kinetic components, which allow to globally fit the data with 3 decay lifetimes as mentioned before. It is worth noting in Fig. 6.9 that the second singular value is very close to the noise cut-off in the SVD analysis (Fig. 6.9a and the inset figure), but it can still be separated and it is indeed required to reconstruct the original data set and for the transient fits at 410 nm and 630 nm (Fig. 6.9d). The signal-to-noise (S/N) ratio in this experiment allows to detect very small signals down to $\leq$1 mOD change (less than 0.2% change in transmission).

At higher fluences above 80 mJ/cm^2, we can clearly observe the increasing weight of the third SVD component both in the spectral and temporal eigenvectors as illustrated in Figs. 6.10a-d. Otherwise the remaining SVD components and GA fits were obtained in a similar way as previously described for the 5ps-window data shown in Figs. 6.7 and 6.8.

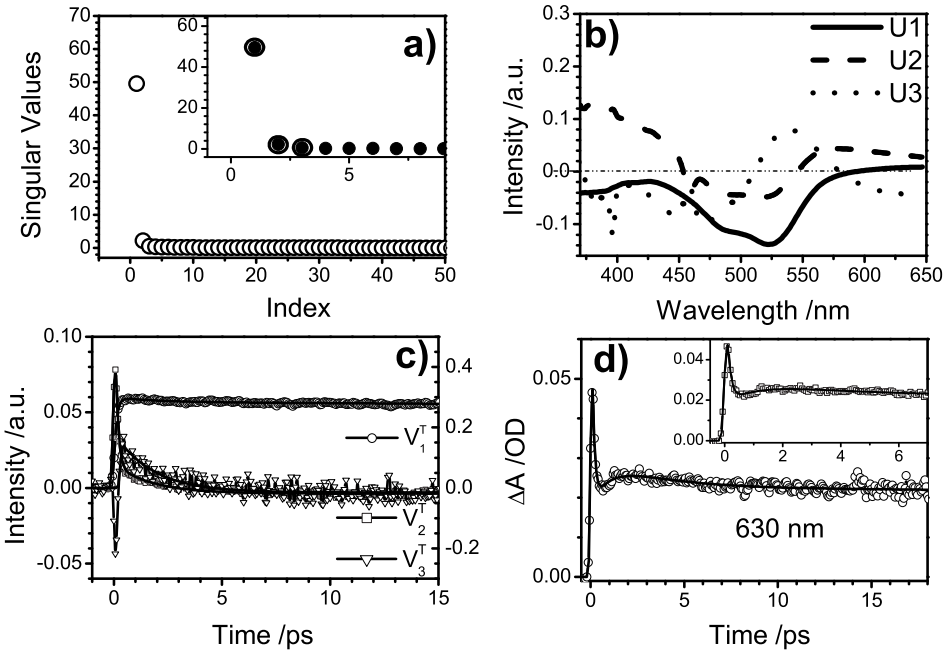

Figure 6.10: SVD results of the data recorded for 9mM aqueous solution of $[Fe^{II}(bpy)_3]^{2+}$ complex upon 80 mJ/cm^2 excitation fluence in the same time windows as in Fig. 6.9. Similarly, panel (a) presents the singular values as obtained upon the decomposition (the circle indicate the retained values), where the inset figure zooms into the initial values. Panel (b)-(c) show the spectral (U_i) and temporal (V_i^T) basis vectors used in the data reconstruction. In addition, panel (c) presents the global fit results of the SVD kinetics. We notice that at high intensities an additional V_i^T component has to be included (green trace). In (d) the raw kinetics at 630 nm is shown together with a corresponding fit, obtained via Eq. D.6 and D.7, using a global fit model (see text for more details).

Similarly to the analysis depicted in Fig. 6.8, the results shown in Fig. 6.10 were obtained via SVD decomposition retaining the dominant 3 SVD components (Fig. 6.10a), which are depicted in Figs. 6.10b and 6.10c. The V_3^T kinetics were fitted in the range from 300 fs-20 ps and thus neglecting the derivative-like part of the trace close to time-zero. The fit was performed assuming the 3 decay lifetime model presented before. However, the intermediate lifetime τ_2=960 fs could not reliably fit neither the V_2^T nor V_3^T kinetics. An increase of τ_2 up to ca.1.8 ps improved the fit to some extent. Yet, even with an increased value of τ_2, the unreduced kinetics in the red-most part of the spectrum (see the representative trace at 630 nm in Fig. 6.10d) could not be fitted with the 3-decay model. An inclusion of an additional lifetime τ_4 yielded the best match to the fitted data as shown in Fig. 6.10d. Here, we fitted globally the additional time constant τ_4, while preserving the (unchanged) values of τ_1-τ_3 as summarized in Tables 6.2 and 6.3, and obtained a value of 3.1±0.5 ps. At even higher fluences, a similar analysis was performed yielding again the same result using 4 decays. The fit results at 80 mJ/cm^2 excitation fluence are shown in Table 6.4. The preexponential coefficients are included for all four decays used in the fit, where only the additional lifetime value is given with its fit uncertainty. The preexponential component $a_{3,1}$ was kept zero during the fit given that the fit range for this kinetics was constrained to start 300 fs after time-zero, at which the contribution of τ_1 vanishes.

V_i^T	$a_{i,1}$	$a_{i,2}$	$a_{i,3}$	$a_{i,4}$
V_1^T	-0.06(0.04)	0.0014(0.002)	0.002(0.01)	0.06(0.002)
V_2^T	0.78(0.03)	0.04(0.02)	0.06(0.01)	-0.022(0.002)
V_3^T	0	0.03(0.01)	0.13(0.01)	-0.03(0.002)
τ_i	τ_1=116 fs	τ_2=960 fs	τ_3=3.14(0.8) ps	τ_4=665 ps

Table 6.4: Global fit results, using the 4-exponential model (Eqs D.6 and D.7), of the transient absorption data of aqueous 9mM sample of $[Fe^{II}(bpy)_3]^{2+}$ at 80 mJ/cm^2 pump fluence (Fig. 6.10)

6.1.6 Discussion

In the following Section, we will discuss and give the interpretation to the results presented previously. The decay-associated spectra (DAS), reconstructed, via Eq. D.8, using the global fit (Eqs D.6 and D.7) results of the SVD components will be presented and discussed. We will propose the major mechanism and/or identify the photochemical species contributing to the obtained DAS. In conclusion, we will propose a revised model describing the energy relaxation mechanism (see Fig. 6.1b) in aqueous $[Fe^{II}(bpy)_3]^{2+}$, which should in principle applicable to a larger class of solvated Fe(II) complexes undergoing the SCO transition upon light excitation at room temperature.

Initial Franck-Condon Configuration and Charge Transfer States

According to Fig. 6.1b and Refs [93, 149, 357] the initial excitation into the MLCT absorption band of the aqueous $[Fe^{II}(bpy)_3]^{2+}$ populates the ^{1}MLCT state, which was found to be extremely short-lived. We performed an ultrafast broadband fluorescence up-conversion study on aqueous samples of $[Fe^{II}(bpy)_3]^{2+}$ [358], which captured the initial ^{1}MLCT emission upon the photoexcitation with 400 nm light. Briefly, shown in Fig. 6.11 is the initial ^{1}MLCT emission recorded upon 400 nm excitation. The resulting luminescence band is symmetrically centered around 590 nm and decays, without neither prior shift nor broadening, within ca. 15±10 fs after the photoexcitation. The detailed analysis of these results can be found in [82,358]. The most relevant conclusion in the scope of the results presented here is that the initially formed ^{1}MLCT state departs from the F-C window in a very short time, again on comparable timescales as found in [82] in $[Ru^{II}(bpy)_3]^{2+}$, however, no presence of any residual ^{3}MLCT emission was detected, as in the latter case.

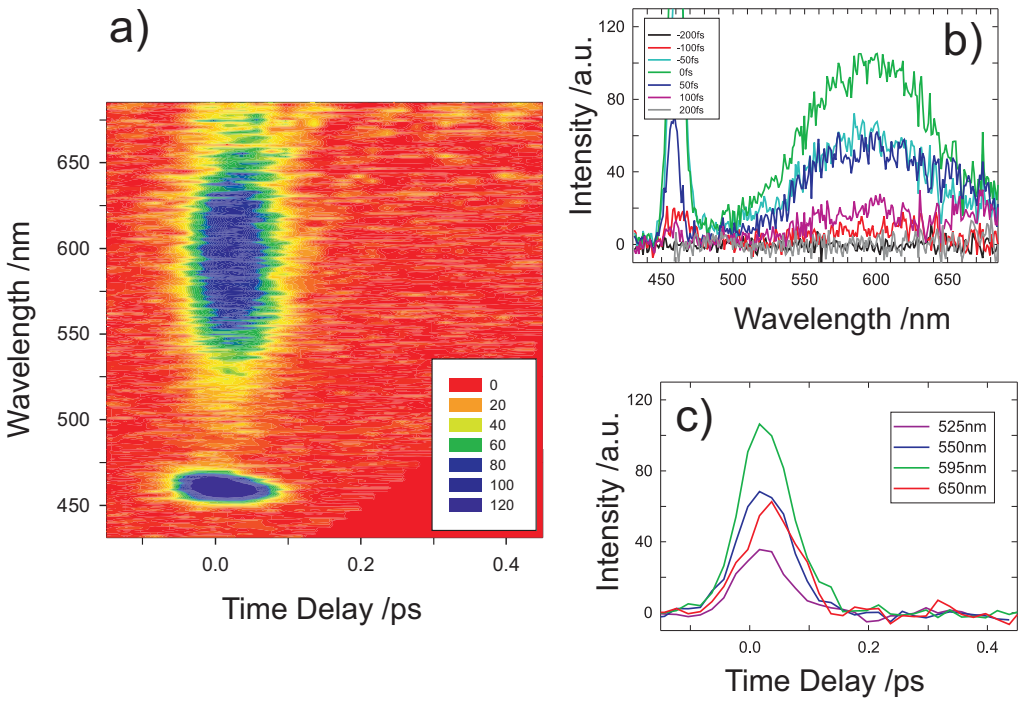

Figure 6.11: (a) 2D-plot of time resolved luminescence spectra of aqueous$[Fe^{II}(bpy)_3]^{2+}$ under excitation at 400 nm. The signal at 466 nm is the Raman line of water. (b) Luminescence spectra recorded at different time delays (obtained from (a) as horizontal traces) Arrows indicate wavelengths corresponding to the kinetic traces shown in (c).

Complementary to this study, our transient absorption data strongly suggests the presence of a short-lived ESA band, which can be assigned to the reduced bpy ligand (bpy^-) absorption. Similar to $[Ru^{II}(bpy)_3]^{2+}$ [81,305,306], this band is assigned to the presence of the ^{3}MLCT state, which is formed within the excitation and originates from the transition between the metal orbitals to the π-π^* orbital of the bpy ligand system [110].

The bpy^- absorption band peaks in the range between 350-370 nm in water [113, 319] and it can be clearly identified in our data within the first 200 fs after the excitation (Fig. 6.7b). Here, the second SVD component, U_2, shows the characteristic ESA in the blue-most part of the spectrum. The lifetime decay associated to this spectrum, which accounts for the initial ESA signal is ca. 120 fs (τ_1). This means, we can assume that the initial excitation to the ^{1}MLCT manifold is followed by an intersystem crossing into the ^{3}MLCT state. The kinetic component associated with U_2, namely V_2^T in Fig. 6.7c, does not purely reflect the ^{3}MLCT lifetime. Rather it is convoluted with the simultaneous GSB signal (negative part of the kinetics), which has a detectable rise-time of 960 fs (τ_2) and lasts for about 665 ps (τ_4). Therefore, neither the SVD spectra nor the DAS can be directly linked to one particular photochemical species although their spectral contributions can be estimated. However, we can conclude that the ^{1}MLCT$\rightarrow$^{3}MLCT intersystem crossings takes place within the first 15$\pm$10 fs and is followed by the departure from the ^{3}MLCT to either lower-lying LF states or higher-lying states in a multiphoton absorption process (or both simultaneously).

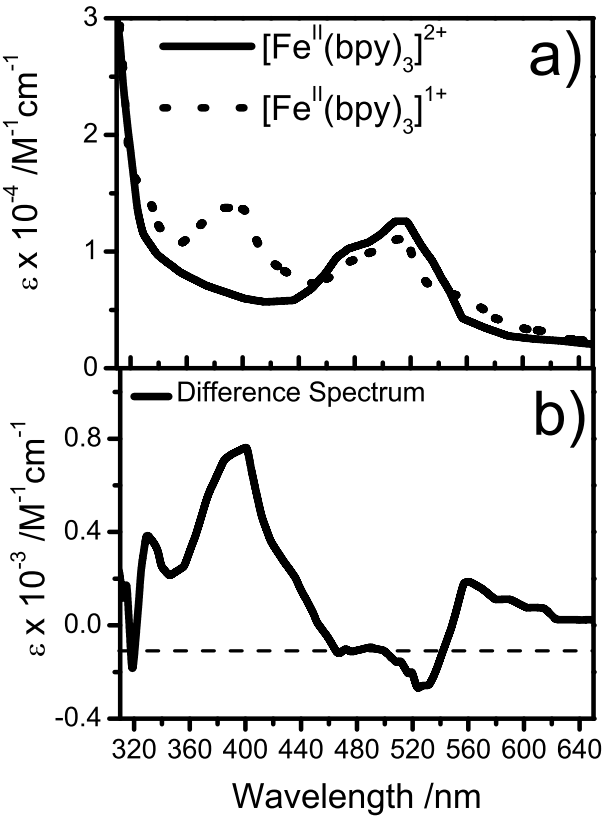

Figure 6.12: (a) Steady-state absorption spectra of parent $[Fe^{II}(bpy)_3]^{2+}$ and reduced $[Fe^{II}(bpy)_3]^{2+}$ complexes, taken from Ref. [152]. (b) The difference spectrum obtained by simple subtraction of $[Fe^{II}(bpy)_3]^{2+}$ species from $[Fe^{II}(bpy)_3]^{+}$ spectrum.

In any case, we can state that our data strongly suggest that ^{3}MLCT lives for no more than 200 fs. Indeed, the ^{3}MLCT absorption is the dominant process in the first 200 fs in the 350-450 nm and the red-most part of the spectrum. This argument can be strengthened by referring to Fig. 6.12. Here, in a) the steady-state absorption spectra of both the parent (2+ complex) and reduced (1+ complex) forms of $Fe(bpy)_3$ are shown [152] and in b) the difference spectrum dominated by the bpy^- spectral contribution is plotted. In Fig. 6.13, we have plotted the scaled difference spectrum from Fig. 6.12b on top of the DAS_1, which is the spectrum corresponding the dominant photochemical species associated with τ_1=120 fs lifetime. In this case the DAS_1 was obtained by using Eq. D.8 and the SVD components were taken from data recorded at 35 mJ/cm^2 as presented in Fig. 6.7b and c. In addition, we have subtracted the GSB contribution from the DAS_1 as the bleach signal is instantaneously present upon the photoexcitation.

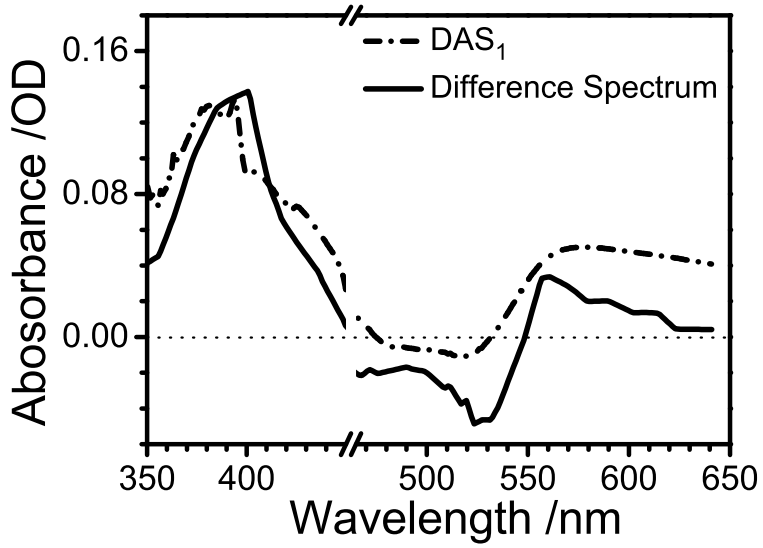

Figure 6.13: A comparison between the scaled difference spectrum from Fig. 6.12b and the DAS_1 (Fig. 6.7b and c),which is the spectrum associated with τ_1= 120 fs lifetime. Although the comparision is not quantitative, the resemblance of both spectra is striking and allows assigning the τ_1= 120 fs decay to the lifetime of the ^{3}MLCT state.

The summary of all extracted DAS at fluences $\leq$35 mJ/cm^2 (Fig. 6.7) is plotted in Fig. 6.14. As can be seen, the first time-associated spectrum has the characteristic band in the region between 350-450 nm (the negative absorption around 460 nm is the Raman band of H_2O discussed in Section 4.10). The central part of the spectrum is dominated by slightly red-shifted GSB signal in agreement the spectrum found in [152]. This leads us to conclude that the initial 200 fs time-window corresponds to the domain where the ^{3}MLCT absorption dominates the photochemical cycle of $[Fe^{II}(bpy)_3]^{2+}$.

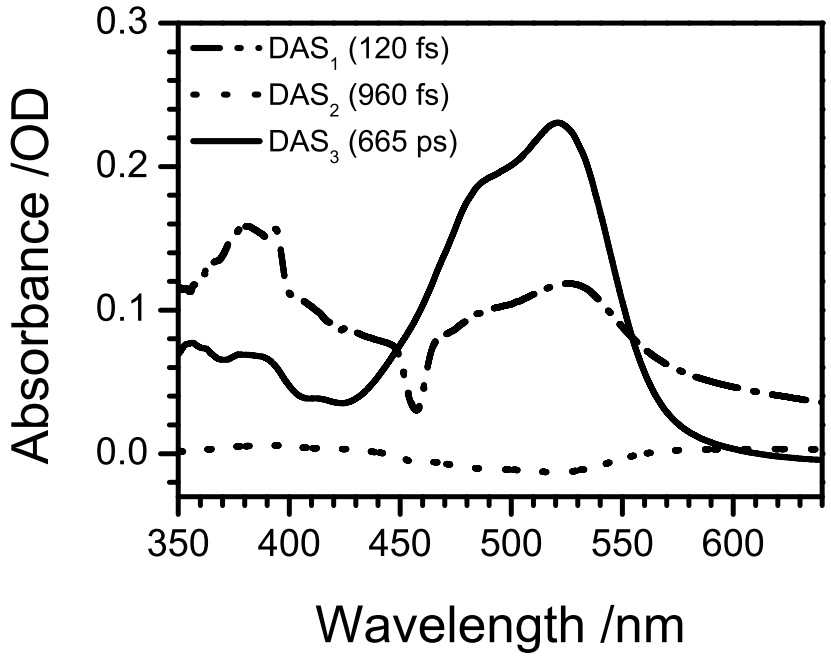

Figure 6.14: A summary of all extracted DAS at fluences $\leq$35 mJ/cm^2 (Fig. 6.7) is plotted.

Arrival Time to the $^5T_2$ (High-Spin) Manifold

At all excitation fluences examined in this study, the observable rise-time was detected (see Figs. 6.7-6.10). The decay time associated with it was determined during the GA to amount to ca. 960 fs. In previous works [93,149], it was suggested that the transit time from the initially excited charge-transfer manifold should be $\leq$ 1 ps, In these studies, it was concluded that the population of the $^5T_2$ state is directly linked to the ^{1}MLCT excitation, which has a lifetime of $\leq$ 100 fs (no intermediate absorption were observed in the initial 1 ps following the excitation). On the contrary, our data proves the existence of the ^{3}MLCT state and the subsequent arrival time to the HS manifold is measured to be <1 ps. In our experiment, we have detected broadband transient absorption spectra with improved temporal resolution as compared to Refs [93,149], which allowed to resolve the weak rise-time of the $^5T_2$ state. The DAS of the species linked to this time decay are shown in Figs. 6.14 and 6.15.

At lower fluences (Figs. 6.14 and 6.15 dotted spectrum), the associated spectrum is very weak (most of the time between 5-10% of the total weight in SVD analysis, see Table 6.1) and its SVD kinetics is merged into the V_2^T and V_3^T.

At higher fluences (Fig. 6.15 solid-line spectrum), the blue and red parts of the DAS increase nearly linearly with intensity (here a factor of ca. 4) but no observable change in the shape is detected.

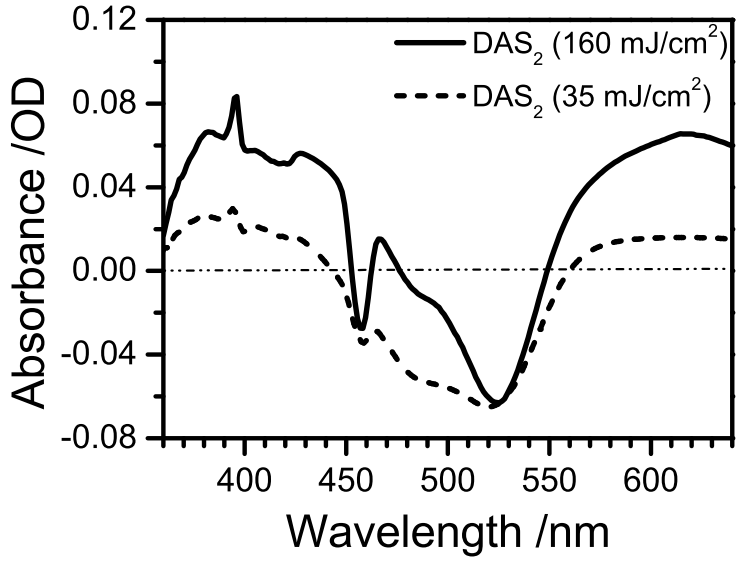

Figure 6.15: A comparison between DAS_2 at two different excitation fluences: 35 mJ/cm^2 (•) and 160 mJ/cm^2 (solid line). The increasing excitation power affects mostly the blue-most ($\leq$ 440 nm) and red-most ($\geq$ 550 nm) parts of the spectra. The observed increase of the signal shows a nearly linear behavior in the investigated fluence range.

We think that the existence of this component in both the ESA absorption $\geq$550 nm and within the GSB formation is the first evidence of the arrival time to the HS state. Furthermore, the analysis of long-time kinetics confirmed that the long-lived ESA in this range can be explained as the HS absorption and it has the same lifetime as the GSB recovery signal at 523 nm. The overall shape of the spectra in Fig. 6.15 resembles the residual ^{3}MLCT absorption, which could point towards the simultaneous population of the lower-lying MLCT states. The linear dependence upon the excitation fluence discards the multiphoton absorptions in these spectra. Most probably, we cannot link these spectra (Fig. 6.15) to any particular species as the system undergoes a cascade through several lower-lying MLCT and LF states on its way from the ^{3}MLCT to the $^5T_2$ state. (Fig. 6.1b). All these states are *d-d* metal-centered states with very weakly absorbing and strongly overlapping bands all over the spectral range considered here. Hauser *et al.* [360] have measured the absorption spectra of some of the intermediate LF states in a similar SCO complex in a low temperature crystal. The authors have estimated the corresponding cross-sections of the transitions to these bands to be 10^2-10^3 times weaker than the $^1A_1 \longrightarrow {}^1$MLCT transition. Yet, their conclusion was that no matter to which band the laser excitation was tuned the subsequent instantaneous formation of the $^5T_2$ state was observed.

Multiphoton Absorptions to Higher-lying States

In order to address in greater detail the nature of the third SVD kinetics and its associated spectrum we have analyzed the transient absorption data in an extended time domain up to ca. 10 ps. The SVD analysis results at 80 mJ/cm^2 excitation fluence are plotted in Fig. 6.10 and the GA results are summarized in Table 6.4. These results confirm that at elevated pump intensities the inclusion of the V_3^T component improves significantly the reconstructed data matrix and the analysis reveals the existence of a very weak 4^{th} time decay of ca. 3-4 ps, which contributes to the V_3^T kinetic component. The DAS extracted from results presented in Table 6.4 are plotted in Fig. 6.16. In Figs. 6.16a and 6.16c, the corresponding DAS of the 4 decay times are plotted. We can easily compare them to the results presented earlier and identify the reduced $[Fe^{II}(bpy)_3]^+$ spectrum (black curve) next to the ground state absorption spectrum of the $[Fe^{II}(bpy)_3]^{2+}$ LS state. The weak spectra underlying the region of the GSB are associated with the 0.96 ps (red curve) and 3.14 ps (green curve) components respectively. In Fig. 6.16b, we present a comparison of the bpy^- spectrum with GSB-corrected DAS of the 120 fs component. Again, as in previous discussion, we confirm the initial ^{3}MLCT absorption within the first hundreds of fs following the photoexcitation. The most intriguing observation is presented in Fig. 6.16c, where DAS_2 (black curve) and DAS_3 (red curve), corresponding to intermediate decay times, are shown. Clearly, their spectral intensity is about 20 times weaker in the GSB region than the remaining DAS and we identify a slight time-dependent blue shift of the spectrum on 1-4 ps time scale. This shift is even more pronounced around a very weak ESA detected in the region between 560-580 nm (see inset of Fig. 6.16c).

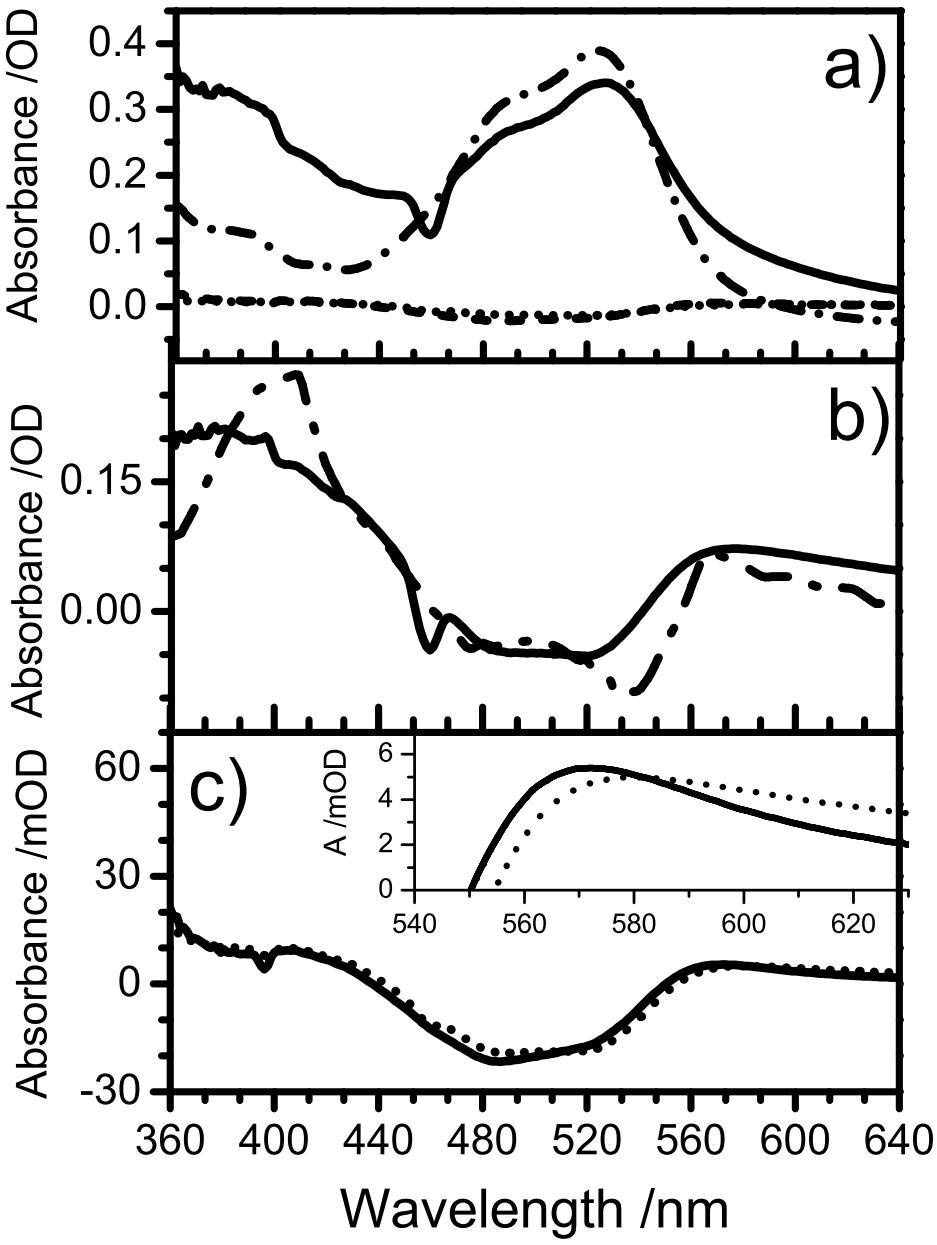

Figure 6.16: The DAS, obtained via Eq. D.8, from results presented in Table 6.4 are plotted in (a). The early spectrum (solid line), associated with τ_1=120 fs, is plotted in (b) together with the bpy^- spectrum ($\cdot - \cdot$). The GSB spectrum, τ_1=665 ps, ($\cdot - \cdot$) is displayed in (a). The intermediate time constants, τ_2=0.96 ps and τ_3=3.14 p), have their corresponding DAS shown in (a) ($- - -$ and $\cdots$, respectively). In (c) DAS_2 (solid line) and DAS_3 ($- - -$) are plotted and the inset zooms into the spectral region from 540-630 nm in order to amplify a slight energy shift, which occurs on 3 ps time scale between the DAS_2 and DAS_3.

Apparently, these spectra shift towards higher energies by ∼4-5 nm and slightly narrow down on a few ps timescale. It is worth noting again, that the intensities of this ESA bands lies in a few mOD range (4-6 mOD), which is about a factor of 100 weaker than the GSB and ^{3}MLCT spectra, as expected for intermediate *d*-*d* bands underlying the MLCT manifolds. However, although the inclusion the additional lifetime improves the fit results, we cannot assign it to the vibrational relaxation within the vibrational manifold of quintet state. The counterargument is presented in Fig. 6.17. Here the raw data kinetics at 620 nm (only the red-most part of the spectrum contains significant contribution of the SVD spectral component associated with this lifetime).

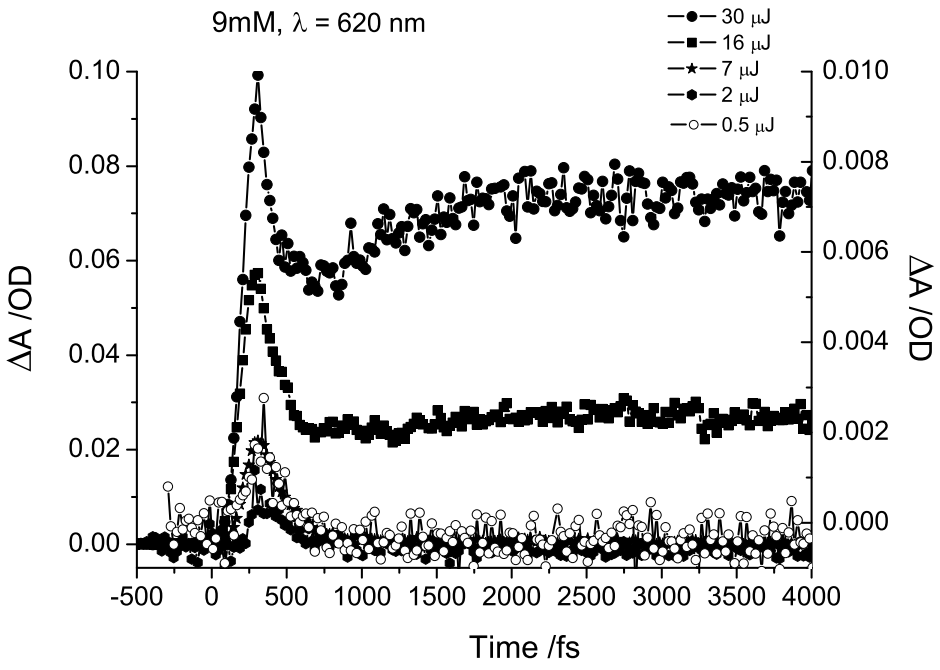

Figure 6.17: The power dependence of the transient kinetic traces at the red-most part of the transient absorption spectra (here at 620 nm) is shown here. The selected kinetic traces were measured in a broad pump fluence range. Here the excitation fluence was varied from 2.5 mJ/cm^2 (0.5 μJ pump energy) up to 150 mJ/cm^2 (30 μJ pump energy).

We clearly observe the appearance of the additional component, with 3-4 ps rise time, at increasing excitation fluences (2.5-150 mJ/cm^2). Clearly, at F $>$ 35 mJ/cm^2 (above 7 μJ pulse energy in Fig. 6.17), this component grows in intensity. Fig. 6.18a presents the log-log plots of the extracted signal intensities in a broad range of excitation fluences (2.5-480 mJ/cm^2), and Fig. 6.18b shows some of the representative kinetic traces used to generate log-log plots are shown.

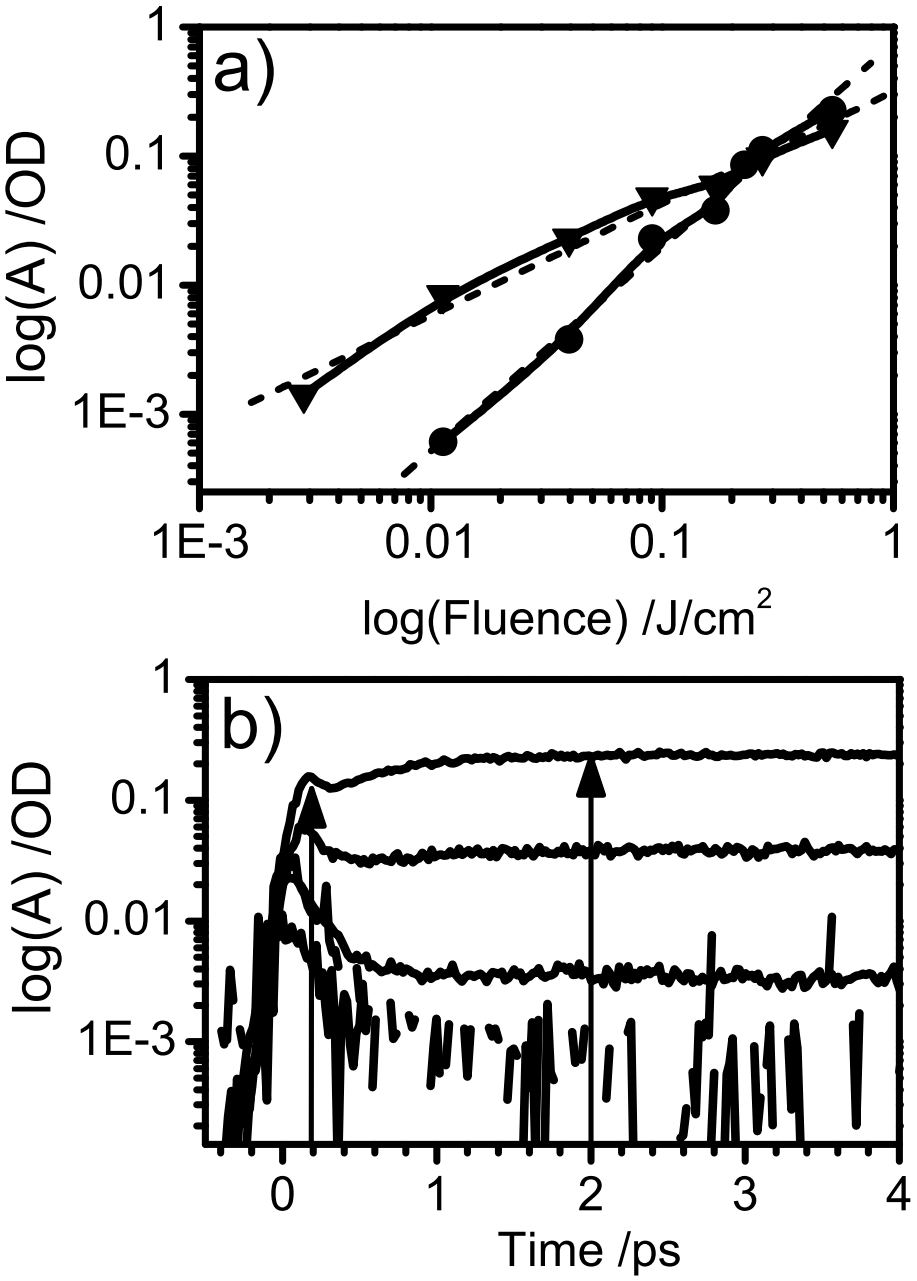

Figure 6.18: (a) The power dependence of the transient ESA signal at 640 nm is plotted on log-log scale. The signal intensities at two time delays are displayed: the MLCT absorption at ca. 200 fs. time delay (▼) and the additional ESA signal at ca. 2 ps time delay (•). The time delays are indicated by the vertical arrows in (b). Similarly to Fig. 6.17, the kinetic traces at various excitation fluences ranging from 2.5-480 mJ/cm^2 are shown in (b). The signals plotted in (b) were analyzed in (a).

The vertical arrows indicate the two time-delays, at which the signal intensities were compared. The first short-live ESA peak corresponds to ^{3}MLCT absorption as discussed previously. The second peak arises due to the intermediate 3-4 ps lifetime as obtained in the SVD analysis. The power dependence of the later (•) deviates significantly from linearity. A fit, using a function of a general form $\alpha \cdot F^{\beta}$ (where α and *beta* are adjustable fit parameters and F denotes the excitation fluence), delivers the values given in Table 6.5 for the fit curves shown in Fig. 6.18a.

DAS	α	β
120 fs	0.9±0.05	-0.5±0.08
3.14 ps	1.6±0.07	-0.12±0.08

Table 6.5: The fit parameters α and β used to fit the *log-log* plots shown in Fig. 6.18, via $\alpha \cdot F^{\beta}$

Clearly, the signal at 2-3 ps has a nearly quadratic dependence, while at $\leq$ 200 fs (assigned to ^{3}MLCT absorption), the nonlinearity is minuscule and thus we assume it is linear within the fit uncertainty. Therefore, in conclusion we discard the hypothesis of the vibrational relaxation (as suggested in [93, 158, 161], and attribute the signal at loner times to the HS population from multiphoton absorptions to higher-lying states from initial MLCT manifold (either singlet or triplet).

Ground State Bleach Recovery Kinetics

In agreement with the relaxation mechanism proposed in the preceding Sections, we can draw a conclusion that after the initial 5-10 ps, the system finds itself in a thermalized $^5T_2$ state, which relaxes back to the ground state within ca. 665±40 ps (see Figs. 6.5a, and 6.6). This implies that the 1ns time window is dominated by the GSB recovery signal in the blue-most and central part of the spectral window investigated here, while a residual HS state absorption is present in the red-most part of the spectrum (above 560-570 nm in Figs. 6.5a and 6.6). The long-time kinetics and spectra also confirm that the dominant photoproduct present on these timescales at all excitation fluences is the HS state, which relaxes back to the ground state in 665 ps. On these timescales, the involved dynamics is purely intramolecular leaving no time for higher-order reactions, i.e. second-order bimolecular reactions. Although the fluence range investigated here was rather high, we have not observed any significant contribution from either the solvated electron or the oxidized species, $[Fe^{II,III}(bpy)_3]^{1+}$, signal in the data (in Fig. 6.6c the noise cut-off in the SVD analysis was around <3% of the GSB component), contrary to $[Ru^{II}(bpy)_3]^{2+}$ [358]. The ^{3}MLCT states of $[Fe^{II}(bpy)_3]^{2+}$ complex are extremely short-lived and less likely to interact with the solvated electron and the surrounding solvent and/or ground and excited state molecules. The LF *d-d* states are known to be far less reactive than MLCT ones, and their cross-sections are orders of magnitude weaker then those of the charge transfer states.

This conclusion has some important implications for the photolysis yield estimates extracted from the data measured by the optical spectroscopy. These values form an essential input into the HS excited state x-ray spectrum analysis presented and discussed in detail in the following Sections of this Chapter. The presence of only one dominant photoproduct ensures that the retrieved excited state structure corresponds to the $^5T_2$ state of aqueous $[Fe^{II}(bpy)_3]^{2+}$ and the relative excitation yield can be simply estimated by monitoring the GSB magnitude at certain time-delay after the photoexcitation. In the case of the x-ray experiments presented here, the 50 ps laser-x-ray time delay fall into the timescales where the only contributing photoproduct is the thermalized HS state.

6.1.7 Conclusions

To summarize, we propose a complete photochemical cycle of the solvated $[Fe^{II}(bpy)_3]^{2+}$ complex and identify the characteristic timescales for various relaxation mechanisms identified in these studies. In analogy to Fig. 6.1b, the revised and simplified energy level scheme is depicted in Fig. 6.19. Here, we presented the data supporting the photochemical cycle depicted in Fig. 6.19, where the initial photoexcitation of the ^{1}MLCT state is followed by the intersystem crossing into the ^{3}MLCT state on the 15(10) fs timescale. Subsequent relaxation over the timescales up to 1 ns reveals that the triplet charge-transfer state lives for $\leq$ 120 fs before relaxing into the manifold of singlet and triplet LF *d*-*d* states. In addition, given the close resemblance of the 1ps DAS (Figure 6.15) and the early 120 fs spectra (Figure 6.13), we cannot completely discard the existence of lower-energy MLCT states underlying the ^{3}MLCT state (see dashed lines in Fig. 6.19). The weak rise-time on the GSB signal suggests the population time of the $^5T_2$ state to be of the order of 960 fs.

Nevertheless, contrary to the relaxation model proposed by McCusker *et al.* [149] and recently reviewed by Brady et al. [148], we detect directly the existence of the ^{3}MLCT and determine precisely the arrival time to the quintet $^5T_2$ state, which relaxes back to the ground state in ca. 665 ps in room temperature solution, in agreement with earlier works. The data presented here showed no detectable excitation fluence dependence of the HS relaxation rate constant. Although not shown here, we have examined, upon identical experimental conditions, various solute concentrations in the range from 1-20 mM and as expected we do not observe concentration dependence of the relaxation mechanisms and their characteristic time decays involved in the photochemical cycle proposed here.

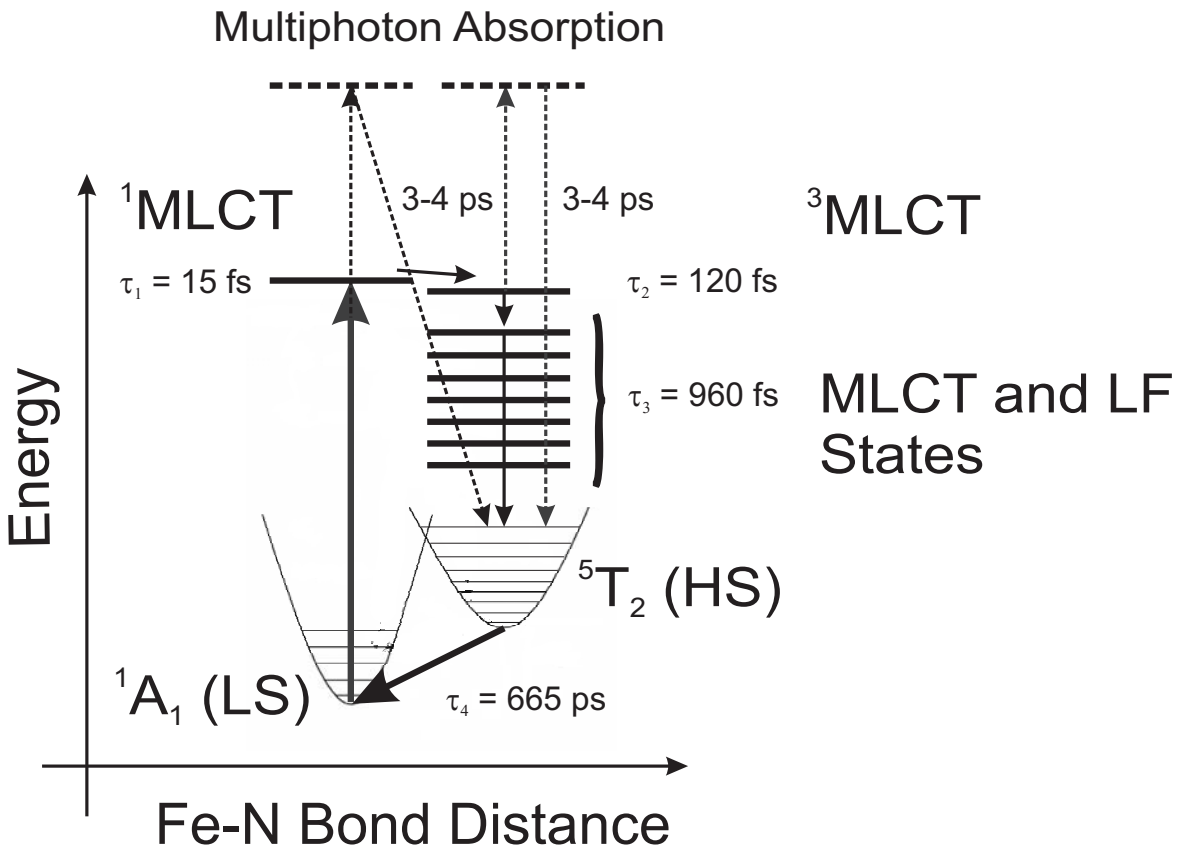

Figure 6.19: The revised photochemical cycle of $[Fe^{II}(bpy)_3]^{2+}$ (compare with Fig. 2.13). The characteristic lifetime obtained during the above presented analysis are displayed and the inclusion of 3MLCT is confirmed. At higher fluences, the possibility of multiphoton absorptions originating from either ^{1}MLCT or ^{3}MLCT are included.

6.2 Picosecond Transient XAS Results

6.2.1 Introduction

The results presented here are the first picosecond-resolved study of the Fe K-edge absorption of $[Fe^{II}(bpy)_3]^{2+}$ in water solution at room temperature. Compared to previous x-ray studies on SCO complexes, both static and time-resolved (see Section 2.4.5 and 2.4.6 for references), this contribution presents new developments in several aspects that are: a) we record the transient structure of a short lived photoinduced HS intermediate in "on-the-fly" (no LIESST effect involved), with 100 ps hard x-ray pulses; b) we extract the structural parameters of the HS state directly from a fit of the experimental transient absorption spectra, without prior assumptions about its structure, as previously done; c) we retrieve structural and electronic parameters from the transient difference X-ray Absorption Near Edge Structure (XANES) features and the consistency of our results is supported by fitting of the Extended X-ray Absorption Fine Structure (EXAFS) features.

6.2.2 Low-Spin XAS of Fe(II)-tris-bipyridine

A representative K-edge absorption spectrum of 25 mM aqueous solution of $[Fe^{II}(bpy)_3]^{2+}$ LS (ground state) complex is shown in Fig. 6.20. It shows the entire extended energy range covered in our experiments in both raw (Fig. 6.20a) and normalized (Fig. 6.20b) spectra. The solid lines plotted in Fig. 6.20a together with the spectrum are used in the following normalization of the spectrum (e.g. Fig. 6.20b). As previously discussed in Section 3.1.3, the normalization of XAS spectra involves the accurate *pre-edge* (blue line in Fig. 6.20a) and *post-edge* (red line Fig. 6.20b) subtraction, which accounts for the background absorption both below (pre-edge) and above (post-edge) the absorption edge. Here these two contributions were fitted using so called *spline* function [249] (polynomial function), which was subsequently subtracted from the data to yield normalized spectrum (with respect to the absorption edge jump, see Eq. 3.3 in Section 3.1)

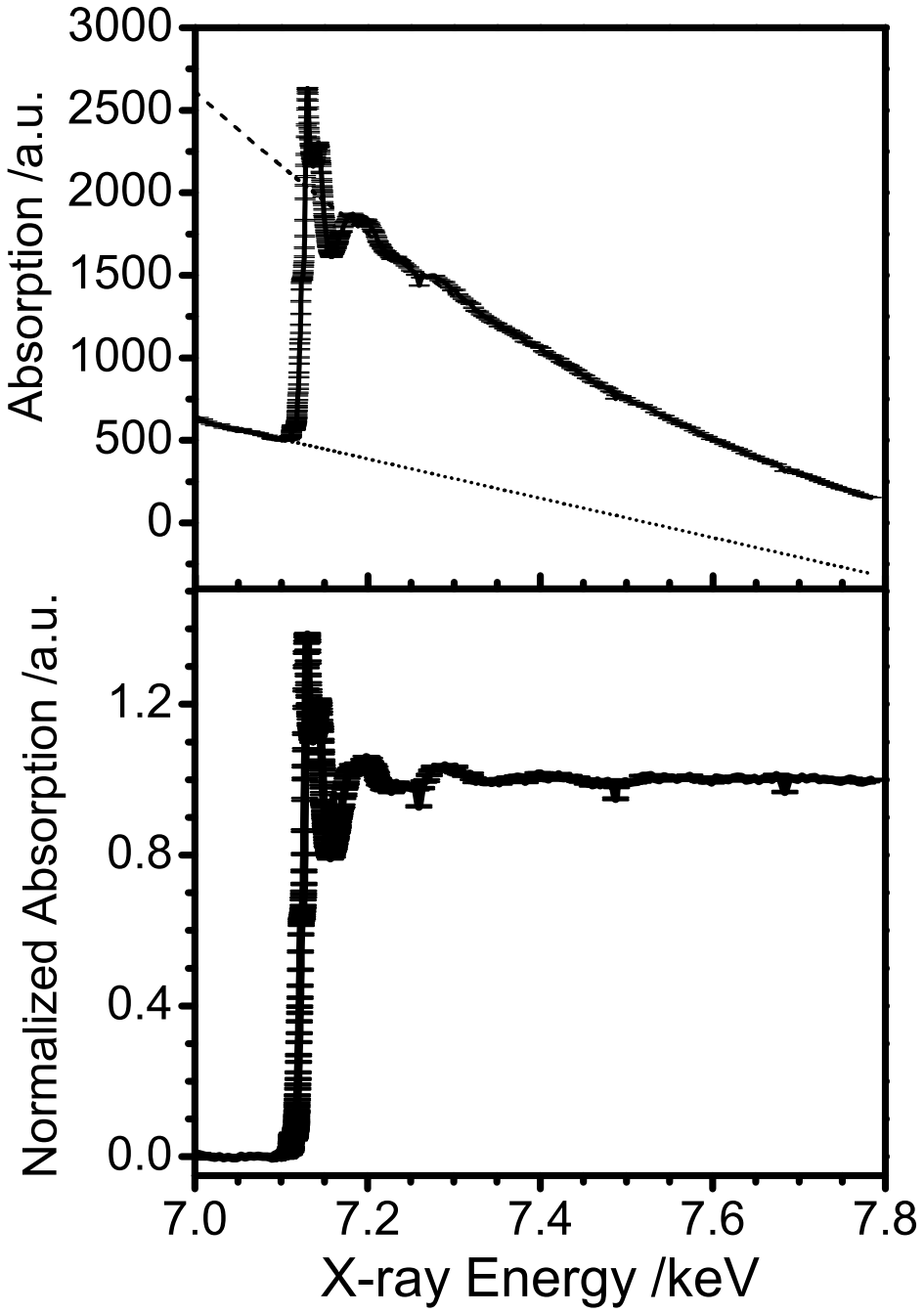

Figure 6.20: (a) The K-edge XAS of the ground state (LS) 25 mM aqueous $[Fe^{II}(bpy)_3]^{2+}$ complex. The data is shown in the entire range recorded during the experiments. The spline functions of the pre-edge $(\cdots)$ and post-edge $(- - -)$ are used to normalize the spectrum, as shown in (b). The normalization is done, so that the edge jump is unity.

The sudden singularities observed at 3 different energies in the normalized spectrum are the monochromator glitches originating from the Si(111) crystals of the x-ray monochromator, which can be further removed before the analysis by fitting them with another set of spline functions in a limited energy range around the glitch. The spectrum shown in Fig. 6.20b, is characterized by a number of intense XANES resonances within the first 50 eV above the absorption edge and less pronounced EXAFS oscillations in the high energy side of the spectrum. Fig. 6.21, zooms into the first 150 eV above the absorption edge where the most pronounced XANES transitions and the onset of EXAFS are found. In the following, we will label and assign some of these resonances to either bound-bound transitions or multiple scattering (MS) resonances. In the low-energy region, at ca. 7115 eV in Fig. 6.21, we find the only pronounced pre-edge feature, A, originating from $1s \rightarrow 3d$ transition.

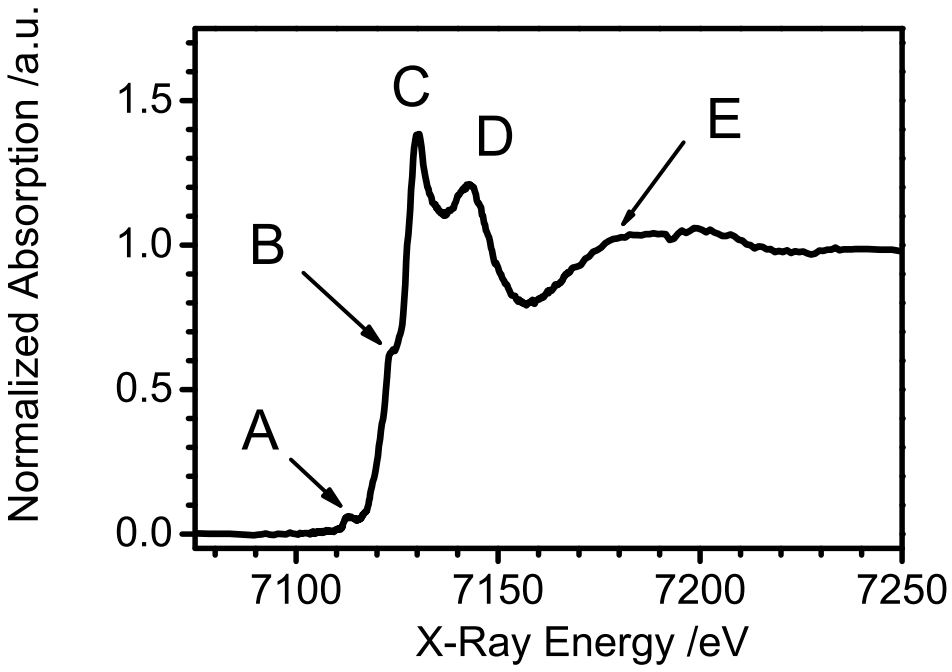

Figure 6.21: The XANES part of the spectrum shown in Fig. 6.20b is displayed and the main spectra features are labeled (see the text for details on the assignments).

As it was discussed in Section 2.4.3, the electronic configuration of the ground state complex among the crystal field-split Fe $3d$ states is t_{2g}^6. The e_g states remain unfilled in the LS state, however, the $1s \rightarrow 3d(e_g)$ transition is formally symmetry-forbidden in octahedral crystal field and becomes partially allowed due to trigonal distortion of the ground state D_3 symmetry. In addition, the intensity of this feature reflects the possible mixing of $3d$ orbitals with other symmetry-allowed orbitals (e.g. $4p$ metal orbitals and $2p$ ligand orbitals) due to vibronic interactions and quadrupole transitions [362]. This

mixing greatly enhances the oscillator strength and in consequence it enhances the transition intensity as seen in Fig. 6.21.

Approximately 3-4 eV above the inflection point of the absorption edge, $E_0 = 7122.5$ eV, we find the next clearly distinguishable feature labeled B. The origin of this resonance is still a subject to debate. In earlier works [139, 362], the origin of this feature was assigned, within the molecular orbital theory, to the $1s \rightarrow 4p$ transition, containing an admixture with the Fe($4s$) and N($2p$) orbitals. An alternative assignment was proposed by Briois *et al.* [226, 227], in which the authors used the full multiple scattering (FMS) theory in order to simulate both the LS and HS XANES spectra of ferrous SCO compound. In their study, it was shown that by spatially enlarging the molecular cluster taken into consideration in subsequent XANES simulations, they could reliably reproduce all main XANES features, including B feature, by changing the MS conditions as function of the cluster size. In the FMS approach, the electronic spin plays no part in constituting the scattering potentials and thus the resulting changes in the XANES spectra were solely attributed to the structural changes occurring between LS and HS complexes.

Next to B feature, we find another resonance labeled C in Fig. 6.21. Here again the interpretations are divided between the bound-bound and MS scattering origin . Some of earlier works [362] attributed it to the next bound-bound transition to higher-lying 4s states (and thus it would reflect the $1s \rightarrow 4s$ transition), although this one should be formally symmetry-forbidden, however, the orbital mixing with lower lying $4p$ states was proposed as the origin of the intensity enhancement. On the other hand, recent progress of the computational codes using the FMS theory and their application to calculate the XANES spectra of various transition metal complexes including Fe SCO compounds, has shown that most probably C feature stems from the MS resonances [227], similarly to aforementioned B feature. In similar way, the following band D found in Fig. 6.21 is interpreted in the vast majority of Fe SCO K-edge absorption spectra [48, 134, 135, 138, 139, 185, 226, 227]

The onset of the EXAFS region in Fig. 6.21 starts at approximately 40-50 eV above the inflection point E_0 (around 7160-7170 eV), where we identify the first broad EXAFS oscillations denoted as E. This feature is most commonly interpreted as dominated by the single-scattering of the photoelectron with the nearest N atom coordination shell [226, 227]. Above 7200 eV (see Fig. 6.20b), we can still clearly distinguish a few broad EXAFS oscillations, which significantly diminish in intensity above 7400 eV.

6.2.3 Transient Picosecond XAS

As described in preceding Chapters, the main outcome of the picosecond XAS experiment is the transient difference spectrum (hereafter called transient spectrum $\Delta A(E,t)$) recorded at a certain time delay between the laser pump and x-ray probe pulses (i.e. at 50 ps time delay). This spectrum is displayed in Fig. 6.22.

Here we show an average of 53 scans recorded in both transmission and fluorescence yield modes. Prior to averaging, the transmission and fluorescence scans had to be properly normalized with respect to the absorption edge jump as the LS spectrum in Fig. 6.20.

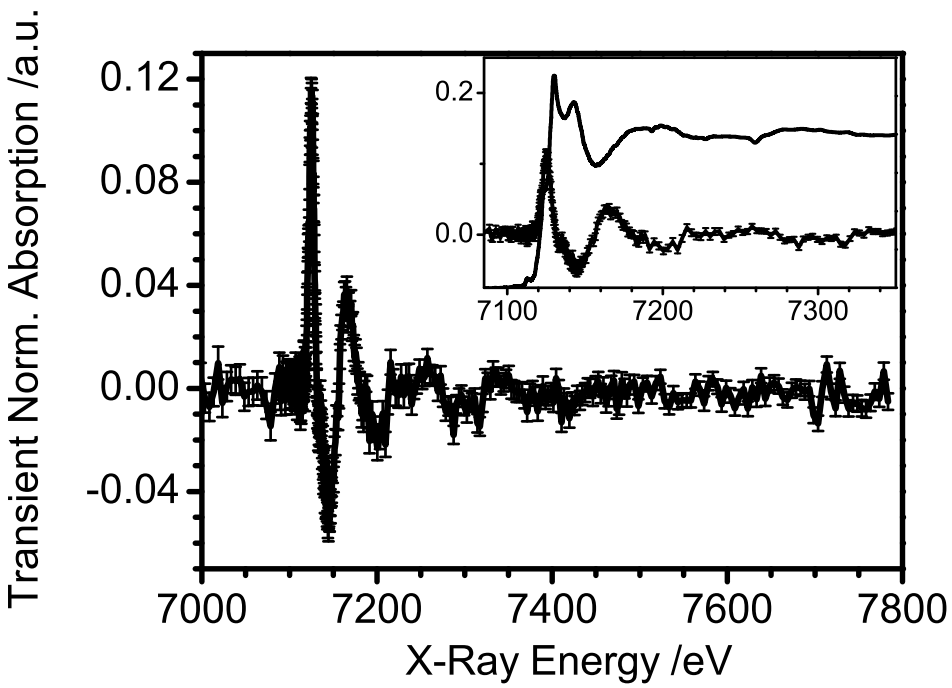

Figure 6.22: Transient XAS of the 25 mM aqueous $[Fe^{II}(bpy)_3]^{2+}$ is shown in the extended energy range together with its error bars. The inset displays the XANES part of the transient in comparison to the same energy range of the LS spectrum frm Fig. 6.21. The comparison helps in assigning the photoinduced changes to the particular resonances depicted and labeled in Fig. 6.21.

The inset in Fig. 6.22 shows the average normalized ΔA(E,t) spectrum plotted next to a rescaled LS (ground state) normalized spectrum. The ordinate axis in the both the main plot and the inset plot of Fig. 6.22 indicate the transient absorbtion intensity of ΔA(E,t) with respect to the absorption edge jump. The most intense changes in the transient spectrum (around the B feature at 7126 eV) reach almost 12% of the absorption edge increase. Translating the magnitude of the observed changes in the inset of Fig. 6.22 into transmission units, we observe a change of 0.24% with respect to the transmission edge change, which is equivalent to 1mOD (in absorbance units, OD=log(1/T)). It means our current detection sensitivity allows to record transient x-ray signals of ca. 1 mOD magnitudes, with only $\leq 1 \cdot 10^4$ incident photons/pulse, which is already a very challenging task in time-resolved optical experiments. The normalization was performed similarly as in case o the LS spectrum in Fig. 6.20. The same spline functions of both the pre- and post-edges of the LS spectrum were used in order to normalize the transient fluorescence data [249].

Analogous procedure was applied to transmission data, although in this case, due to relatively small transmission change at the absorption edge (only ca. 1.6% at 25 mM), the normalization was more ambiguous. Finally, we were able to use a single spline function to normalize both the averaged transmission difference spectra and their corresponding error bars. Once both sets of data were properly normalized to the edge jump (together with their uncertainties), we could average them together and obtain the spectrum presented in Fig. 6.22.

In order to keep the S/N ratio constant over the entire scan range, we have been gradually increasing the integration time (number of incident photons per data point) towards higher energies of the spectrum. Also, the energy step was varied (to as much as 5 eV at 7500-7800 eV range) during the scans as the EXAFS features tend to broaden significantly at high energies. The XANES part was recorded with 1-2 s integration times that increased up to 9 s in the EXAFS region. The number of incident photons per data point can be estimated as ca. $1\text{-}2{\cdot}10^8$ photons/data point (assuming 1-2 s integration time and ca. 6000 photons/pulse at 1 kHz repletion rate) in Fig. 6.22 (53 scans) and approximately $3{\cdot}10^9$ photons/data point in the region around 7500-7800 eV (9 s acquisition time).

The photoinduced changes captured in the ΔA(E,t) spectrum will affect some of the near-edge resonances as discussed above. A careful insight at the inset of Fig. 6.22, shows that the most pronounces changes are expected in the vicinity of the B feature (7126 eV), which gains intensity and slightly red-shifts, C and D features also loose intensity and clearly the E band undergoes a significant shift towards lower energies. A detailed discussion and interpretation of the observed transient changes will follow in Section 6.3 of this Chapter. In order to extract the excited state HS spectrum from the ΔA(E,t) spectrum (Fig. 6.22) and the ground state LS spectrum (see Figs. 6.20 and 6.21), we define the transient difference absorption spectrum ΔA(E,t) as follows [27]:

$$\Delta A(E,t) = f(t)\Delta[A_{HS}(E,t) - A_{LS}(E)] \tag{6.1}$$

where $f(t)$ is the fractional population of the HS complex at time delay t after the photoexcitation, $A_{LS}(E)$ refers to the absorption spectrum of the LS complex (Figs. 6.20 and 6.21), and $A_{HS}(E,t)$ describes the HS excited state spectrum (see Fig. 6.24 in further text), at the time delay t (i.e. 50 ps in Fig. 6.22).

6.2.4 High-Spin Excited XAS

According to Eq. 6.1, in order to extract the excited state HS absorption spectrum (hereafter called HS spectrum) correctly, $f(t)$ must be known. This parameter determines the excited state fraction present in the sample after the photoexcitation and actively contributing to the measured ΔA(E,t). We have estimated the value of f(t) in two independent ways; a) we have performed separate laser-only transient absorption measurements [358] at identical experimental conditions (excitation intensity, time delay and similar concentration)

presented in preceding part of this Chapter (see Section 6.1.6), and b) we have estimated the lower limit of $f(t)$ by the comparison of simultaneously detected transmission and fluorescence yield signals with shot-noise limited distributions. By correlating the number of absorbed x-ray photons with those that were detected in x-ray fluorescence process, this approach allowed us to estimate within a factor of 2 the lowest concentration of the photoexcited HS state fraction contributing to the detected transient x-ray signal at a given energy. In order to extract the excitation yield unambiguously, we have performed concentration-dependent studies in 1-100 mM range of the transient XANES spectra and analyzed both the transmission and fluorescence yield data. These results are presented in Appendix C.

The summary of the above mentioned results is included in Fig. 6.23. It captures the variation of the excited state concentration $[c]_{HS}$ and the corresponding photolysis yield $f(t)$ as a function of the investigated sample concentrations in the range between 1-100 mM of aqueous solutions of $[Fe^{II}(bpy)_3]^{2+}$.

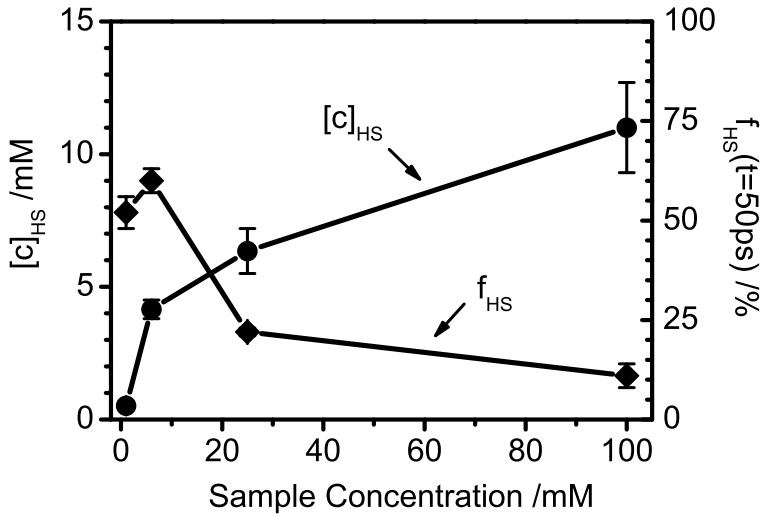

Figure 6.23: The variation of the excited state concentration ($[c]_{HS}$) and the photolysis yield (f(t=50 ps)) is plotted as the function of the sample concentration. These results were obtained from independent all-optical transient absorption measurements discussed in Section 6.1.6 , and compared to the excited state yield measurements presented in Appendix C

The first thing we observe is the gradual increase of the excited state concentration ($[c]_{HS}$) as a function of the sample concentration (black curve). Next to it, the relative excitation yield $f(t)$ decreases for more concentrated samples as displayed y the blue curve in Fig. 6.23. As the result of the photolysis yield analysis, we have obtained the f_{HS}(t=50 ps)=22(2)% in case of the analyzed 25 mM aqueous solution of $[Fe^{II}(bpy)_3]^{2+}$ complex (Figs. 6.22), which is necessary in order to extract the excited state spectrum properly (Eq. 6.1).

In Fig. 6.24, the reconstructed HS excited state spectrum is plotted (blue curve) with its error bars and the corresponding LS spectrum (black curve), used in Eq. 6.1, is shown.

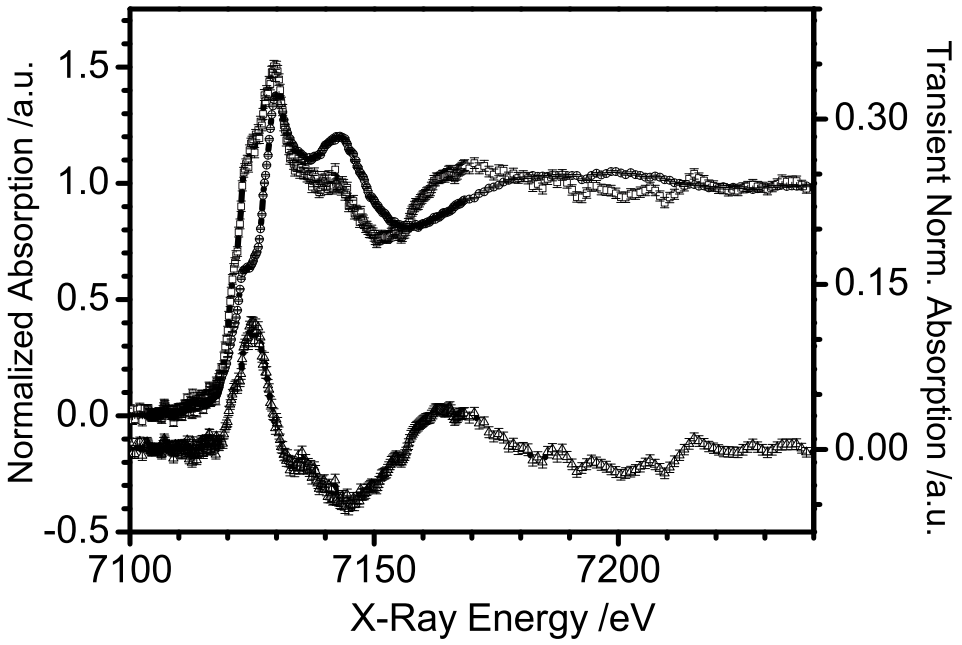

Figure 6.24: XAS spectrum of the LS state of $[Fe^{II}(bpy)_3]^{2+}$ (•) is plotted next to the transient difference XAS recorded 50 ps after laser excitation (△). The excited state HS XAS (□) was obtained from LS and transient spectra, via Eq. 6.1, with f(t=50 ps)= 22 %.

The underlying transient spectrum (red curve) is plotted on a separate ordinate axis (see the right axis)in order to highlight the photoinduced spectral changes of the HS state with respect to the ground state spectrum. As briefly mentioned above, we see a substantial intensity variation in the vicinity of B feature and a small shift towards the lower energies accompanied by increased intensity of the C feature. The D band looses intensity, whereas the E feature shifts to the red with respect to its LS energy position. All three spectra presented in Fig. 6.24 were used in the structural analysis presented in the Section 6.3 of this Chapter.

6.2.5 X-ray Kinetics of the HS State Lifetime Decay

At Δt=50 ps, the appearance of the transient x-ray absorption signal measured in Fig. 6.22 can be solely attributed the presence of the HS complex. The optical measurements confirmed this statement by showing that the only dominant photoproduct, present upon a wide range of excitation intensities (including the intensity used in the present study), on ps-ns timescales is the excited HS state formed with 22% excitation efficiency (Appendix C).

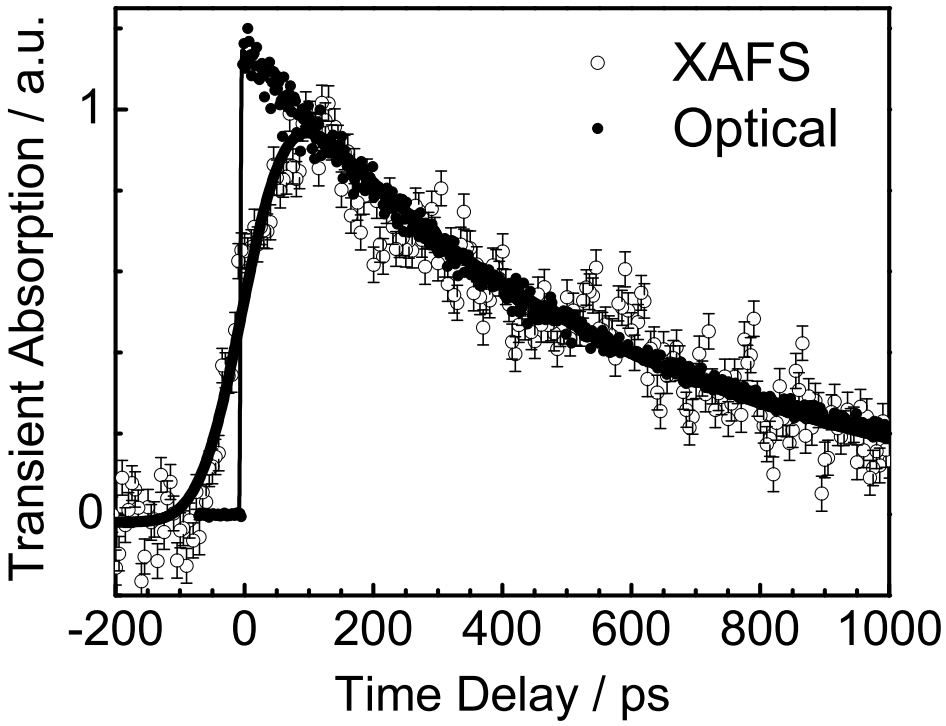

Figure 6.25: Kinetics of the transient XAS signal of aqueous $[Fe^{II}(bpy)_3]^{2+}$ recorded at 7126 eV (○) upon 400 nm excitation, and that of the optical signal (◇) recorded in transmission at 523 nm, and reflecting the repopulation of the ground state together with fit curves. The solid lines represent the fit curves, which in the case of the x-ray signal is a single-exponential convoluted with the 100 ps width of the x-ray pulse.

In order to further verify these findings, we have recorded the decay kinetics of ΔA(E,t) signal at the energy, which corresponds to B feature in Fig. 6.21 ($\sim$7126 eV), where the most pronounced spectral changes in the difference spectrum were observed. The trace shown in Fig. 6.25 (○) was fitted with an instrument response function having a 100 ps rise time, corresponding to the x-ray pulse width, and a monoexponential decay of ca.600 ps, which is the lifetime of the HS state known from laser experiments (•) as presented in Sections 6.1.4 and 6.1.6.

The resulted decay curve shown in Fig. 6.25 and is compared with the ground state bleach recovery curve measured in the time-resolved optical pump-probe experiments [148,357] (Section 6.1.6). The very good agreement of both decay curves confirms that the observed transient decay of the x-ray signal at 7126 eV can be attributed to the lifetime decay the photoexcited state HS state of the complex. This result confirms unambiguously that the origin of the structural changes obtained in further analysis can be directly linked to the HS form of the aqueous $Fe(bpy)_3$ complex.

6.3 Analysis and Discussion

The quantitative structural analysis of the x-ray spectra presented in Fig. 6.24 was performed with the aim of deriving structural information, using two independent approaches.

In the first, we implemented the MXAN code [253, 254] described in greater detail in Section 3.2.2 and Appendix A. This method is based on the iterative comparison between experimental difference spectra and several theoretical calculations performed by varying selected structural and electronic parameters starting from a well defined initial (that of the LS ground state) geometrical configuration around the absorber. The optimization in parameter space is achieved by minimization of the square residual function R^2 (see Refs). We recall that MXAN code uses the FMS theory in order calculate the x-ray absorption cross-sections of the electron scattering processes without any a priori selection of the relevant MS paths. The electronic structure of the molecular cluster is build based on the muffin-tin (MT) approximation for the shape of the atomic potentials of individual atoms, which are later overlapped between each other using the Norman criterion and the potential is recalculated at each step of the minimization procedure, keeping the overlap factor fixed. During the initial steps of the calculation, this electronic structure is recalculated and optimized at each step of the minimization procedure. MXAN code can be used in its standard form to calculate the static x-ray absorption spectra and subsequently fit them with an input structure defined in terms of atomic coordinates of all constituent atoms. A novel extension of MXAN was recently developed by Benfatto *et al.* [256], which allows fitting the transient difference absorption spectra directly. This is a more sensitive way of extracting structural parameters than by fitting full spectra, as it was demonstrated in case of minute structural changed obtained using this approach for an aqueous $[Ru^{II}(bpy)_3]^{2+}$ complex. This reference is attached to Appendix A. In both approaches, MXAN limits its energy range to the first 200 eV, where the MS processes are mostly pronounced (because the backscattering amplitude decreases drastically with increasing energy) and the quantitative structural information can be retrieved even from very limited energy range in the XANES region. Another advantage stems from the fact that MXAN analysis is performed in energy space and thus allows avoiding systematic errors associated with, e.g., a limited k-range and truncation errors due to the Fourier transformations. In this study, we have applied MXAN analysis to both the $\Delta A(E,t)$ and HS spectra, as plotted in Fig. 6.24.

In the second approach, we fitted the EXAFS region of the HS XAS spectrum, which we retrieve from the LS and the picosecond $\Delta A(E,t)$ spectra using Eq. 6.1, with the FEFF8.2 code [251, 252], after converting into photoelectron wave vector space (k-space). Here we have used the entire extended XAS energy region of both the transient and excited state HS spectra. The results obtained in this analysis are fully consistent with those obtained with MXAN approach, however, the retrieved bond length change uncertainties are smaller and thus narrow down the measured structural changes with more precision.

6.3.1 MXAN Analysis

The results of MXAN analysis of both the LS ground state spectrum and the transient difference spectrum are plotted in Fig. 6.26a and 6.26b, respectively. The inset in Fig. 6.26a zooms into the absorption edge region of the LS spectrum to show the excellent agreement of the fit with the experimental data. The MXAN results reproduce nearly all of the above mentioned characteristic features in the LS XANES region, including the B feature (7126 eV), which lies only 3-4 eV above E_0, except for the A feature, which lies ∼9-10 eV below the inflection point. The reason MXAN fits poorly the bound-bound transitions stems from the FMS theory it is based on. Simply, the electronic spin of the LS and HS states does not play any role in the scattering MT potential formalism used by FMS and thus the calculation of these potentials does not take into account the difference in electron occupancy of t_{2g} and e_g states of Fe $3d$-orbitals underlying this low-energy resonance.In Fig. 6.26b, the corresponding ΔA(E,t=50 ps) spectrum is plotted together with the fit. It contains all the photoinduced spectral changes, which occur upon the spin crossover transition.

In Fig. 6.26a, the LS ground state spectrum (same spectrum as shown in Fig. 6.21 together with its MXAN fit is displayed in the energy range up to 200 eV above the inflection point (7122 eV). In addition, the inset presents a zoomed absorption edge region accompanied with the labels A-D assigned to all visible spectra features as previously discussed. In both Fig. 6.26a and the inset, the energy axis is given in energy units relative to E_0=7122 eV. The ordinate axes in both Figs. 6.26a and b are normalized to the absorbtion edge jump. In aforementioned discussion, we have already mentioned certain spectral changes (features A-E), which occur in the photoexcited transient spectrum. The analysis (fit curves) presented in Fig. 6.26 was performed in two independent steps; we started off with the simulation of the ground state (LS) complex, using the input structural parameters as delivered by x-ray crystallography. The fit agreement is very good as can be seen in Fig. 6.26a, and the anticipated Fe-N bond length of the LS ground state, R_{Fe-N}=2.0±0.02Å, agrees within the error bars with both x-ray crystallographic data (R_{Fe-N}=1.98Å) [150] and the theoretical predictions derived from the time-dependent DFT calculations (R_{Fe-N}=1.985Å) [151].

In the following step, we have used the best-fitted LS structure (fit results in 6.26a) and the ΔA(E,t=50 ps) spectrum in the transient difference spectrum fit (data and the fit curve in Fig. 6.26b). The LS spectrum serves as the fixed reference spectrum, which is subtracted from the fitted spectrum at each iteration step, multiplied by the excitation yield f(t=50 ps), in agreement with Eq. 6.1, and compared to the experimental difference spectrum. During the transient difference spectrum fit, we can obtain an independent measure of the excitation yield optimized during the procedure, which can be compared to the value obtained in all-optical measurements (Section 6.1.6 and Fig. 6.23) estimated from concentration-dependent x-ray measurements as presented in Appendix C.

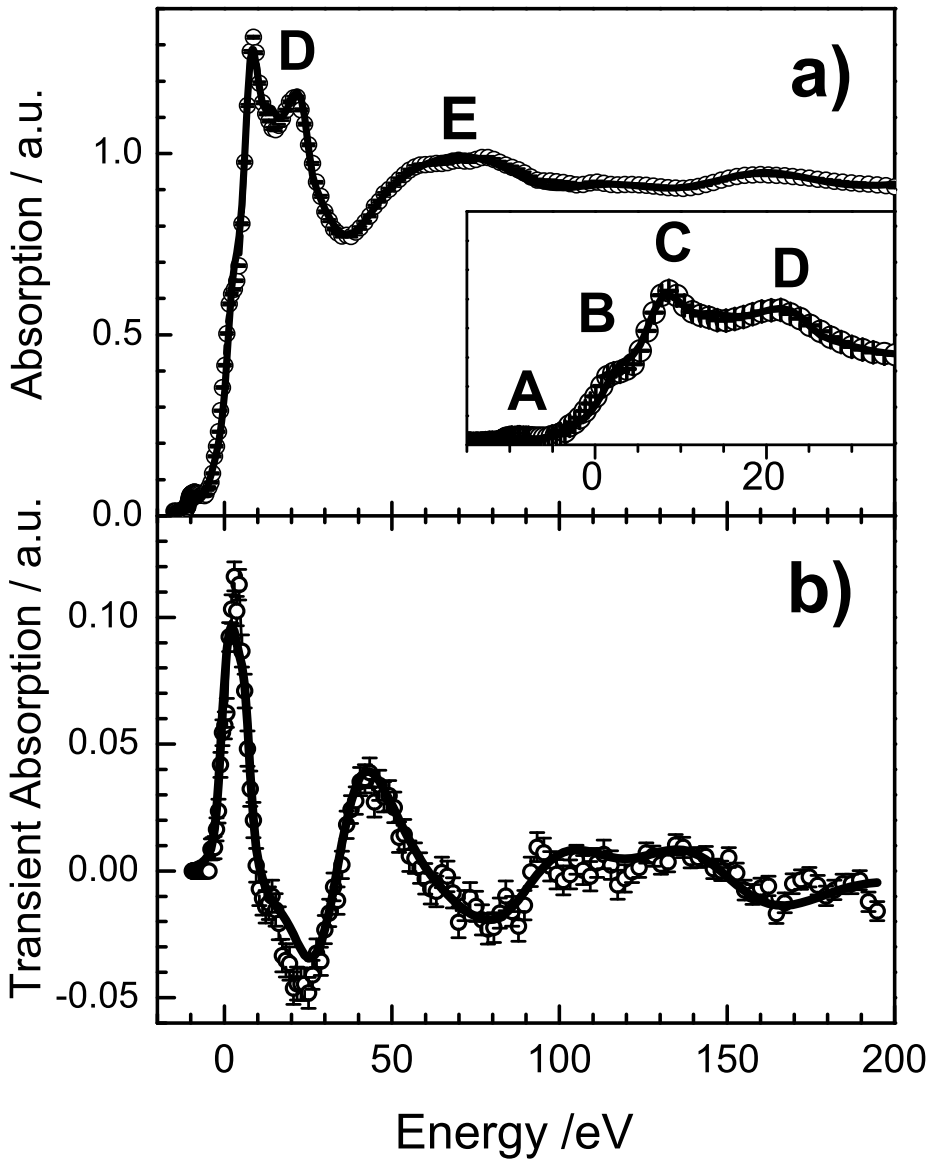

Figure 6.26: a) LS ground state XAS spectrum of $[Fe^{II}(bpy)_3]^{2+}$ (Fig. 6.24) is plotted together with the fit obtained during the MXAN analysis. The inset figure zooms into the edge region to show the fit agreement with the low energy resonances observed in the XANES region. b) Transient XAS spectrum from Fig. 6.24 is presented with its corresponding MXAN fit.

In addition, we can detect whether there is any significant energy shift between both spectra. Both of these aspects were explored during the fit procedure and will be discussed in further details below.

The fit results, shown in Figs. 6.26a and b, reproduce very well the all recorded changes with regards to spectral bands B-E, however, as rationalized before, it fails to account for the A-band intensity. Most of the observed changes in our spectra can be attributed to the bond length change [226, 227], inferred via the change in MS conditions in both spin states of the complex, in between the Fe atom and the ligand, rather than to electronic structure changes, except for the B-feature, whose intensity increase is can be related to both the bonding change and the decrease in $4s$-$4p$ hybridization and in metal-ligand orbital mixing upon Fe-N bond elongation [135, 226, 362]. In addition, upon the SCO transition one expects changes in the electron occupation numbers of the ligand-field split $3d$ states (denoted as t_{2g} and e_g states in Fig. 2.12 in Section 2.4.3) and the energy splitting between them [219] (according to Eq. 2.4) and therefore a spectral modulation around the A band in the XAS spectrum of the HS state. Note that detecting the anticipated changes (due to a change of the ligand-field splitting upon spin crossover transition) of the A-band is beyond the sensitivity and energy resolution of our set-up. The anticipated changes at all other features show up in the ΔA(E,t=50 ps) spectrum as can be seen in Fig. 6.26b. It worth remarking here that the detected changes in the EXAFS region (shown in Fig. 6.22) are also clearly observed, spanning an energy range of >650 eV above the edge, which clearly point to a significant Fe-N bond change in both spin state (further analysis of the extended energy region will be presented in following Sections). In MXAN analysis the FMS approach limits the energy range regarded in the fitting procedure due to a) extended computational cost of these calculations and b) rapidly decaying MS probability at higher energies above XANES region (where SS events are more probable and dominate the EXAFS part of the spectrum).

Concerning the HS complex, one would expect not only bond distances, but also the ionization threshold IP (which is related to the E_0) and underlying bound-bound transitions to be affected upon the spin crossover. Obviously, the bond distance change will induce spectral shifts of certain spectral resonances in the XAS spectrum, especially those that are very sensitive to the Fe-N bond length (i.e. all features in Fig. 6.26a, if regarded as MS resonances will shift due to the bonding and IP change). According to Natoli's rule [9, 250, 257, 363, 364], the increase of the HS state metal-ligand bonds will induce a corresponding red shift of EXAFS peaks in agreement with $\Delta E \cdot R^2$=const, where $\Delta E = E_{res} - E_0$ denotes the energy splitting of a given MS resonance feature E_{res} (i.e. features B-E in Fig. 6.26a) with respect to the threshold energy (inflection point) E_0. Using Natoli's rule and the red-shift of the E feature (E^E_{res}) observed in Fig. 6.24 with respect to the energy reference pre-edge feature A (E^A_{res}), we obtained the following results summarized in Table 6.6.

Spin State	E_0	E^A_{res}	E^E_{res}	Constant	R_{Fe-N}
Low-Spin (S=0)	7122.5 eV	7184 eV	7113 eV	284 eV^2	2.0
High-Spin (S=2)	7120 eV	7171 eV	7113 eV	284 eV^2	2.21

Table 6.6: The results of Natoli's rule applied to the data from Fig. 6.26. The observed energy shifts of the selected XANES features were quantified and the estimated bond distance changes were derived via $\Delta E \cdot R^2$=const

During the analysis we have noticed that the threshold energy E_0 changes upon the SCO transition (-2.5 eV shift), which reflects the underlying IP shift and therefore it should not be used as the reference energy in Natoli's rule. On the other hand, no spectral changes were observed around the A feature. In case of the low-spin complex, assuming the $\Delta E_{LS} \equiv E^E_{res}(LS) - E^A_{res}(LS)$=71 eV (see Table 6.6) and the ground state Fe-N bond length R^{LS}_{Fe-N}=2.0 Å, we get the const= 284 eV·Å^2. According to the rule, this constant should remain unchanged in both spin states and thus taking $\Delta E_{HS} \equiv E^E_{res}(HS) - E^A_{res}(HS)$=58 eV and keeping const= 284 eV·Å^2, we derive R^{HS}_{Fe-N}= 2.21 Å.

Furthermore, the FMS theory predicts that also the resonances in the close vicinity to the absorption edge will be affected by the Fe-N bond distance change as long as the resonance conditions of the scattering operator change at a particular energy (see features C and D in Fig. 6.26a). Concerning the absorption threshold energy (and its relation to the ionization potential) and lower-lying bound-bound transitions (features A and B in Fig. 6.26a), we expect them to change their relative energies and intensities as a function of the Fe-N bond length as well. This can be rationalized by the *chemical shift* of XAS spectra (refer also to Section 3.1.1 of Chapter 3), which responds to the change in the local chemical environment around the absorber atom [224]. In the case of SCO complexes, the chemical shift originates from a severe perturbation of the local chemical bonding around the transition metal ion , which affects the ionization potential and the energies of the lower-lying bound-bound transitions. As it was mentioned in Section 3.1.1, the chemical shift may arise also from different valencies of the transition metal ion (oxidation state shift) as in case of Ru^{2+} and Ru^{3+} in $Ru(bpy)_3$ [35] (Section 5.2 of Chapter 5. On contrary to this case, the oxidation state of Fe ion in $Fe(bpy)_3$ remains unchanged (i.e. Fe^{2+}) in both LS and HS states. Nevertheless, the anticipated Fe-N bond length elongation results in detectable chemical shift observed in the XANES region of Fig. 6.21 and above. The most pronounced changes observed there occur in the vicinity of B-band (Fig. 6.26. This feature can be assigned to one of the transitions to higher-lying states, eg. $4p$ and $4s$ metal orbitals, will experience an elongated Fe-N bond distances, which change the mixing between metal and $2p$ ligand orbitals of the N atoms (hybridization and covalency change) and increases the available number of unoccupied density of states of metallic character (increases the oscillator strength of $1s \rightarrow 4p$ transition and hence its intensity). The ionization potential (reflected qualitatively by E_0 shift) follows these changes as well and its energy should decrease in the HS state due to the aforementioned rationale. In principle, the SCO transition also affects the electronic structure, which may demonstrate in the XAS spec-

tra. The most dramatic (from electronic point of view) consequence of the spin transition is the electron redistribution among t_{2g} and e_g states of the metal orbitals, which in turn decreases the ligand-field splitting 10Dq between them and affects the energies of these states. This change should manifest itself at the pre-edge resonance A [219, 228] (see Fig. 6.21) is not observed in our experiments. In general, $1s \rightarrow 3d$ transition (feature A in Fig. 6.21) is formally symmetry-forbidden in centrosymmetric molecular symmetries, like O_h, yet its intensity is often enhanced due to small distortions from the perfect centrosymmetric geometry, like trigonal distortion in D_3 symmetry (i.e. $Fe(bpy)_3$), which allow orbital mixing of $3d$ orbital with other symmetry-allowed ones, like $4p$ metal orbital in Fe complexes. This is the main reason we can actually detect the A-band in Fe XANES spectra as displayed in Fig. 6.21, although our experimental setup does not allow to capture any photoinduced changes within this transition.

As already mentioned above, the observed energetic red-shift of E_0 turned out to be critical to the structural determination. Since this shift is not *a priori* known, we first carried out a Monte-Carlo optimization of the fit that minimizes the square residual function, assuming a excitation yield of 22-23% (as shown in Fig. 6.27). We thus found that the chemical shift lies at -2.5±0.5 eV, yielding an Fe-N bond elongation between HS and LS complexes of ΔR_{HL}=0.2±0.05 Å (R_{HS}=2.2±0.05 Å). By changing the chemical shift, we are affecting the resulting Fe-N bond lengths optimized during the fit because these two parameters are highly correlated during the calculation.

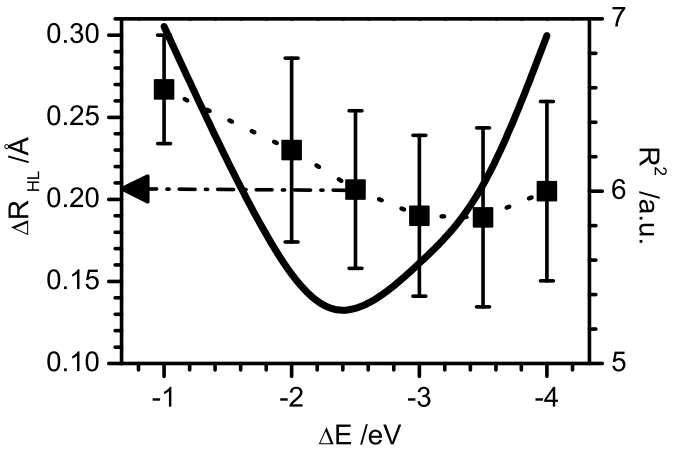

Figure 6.27: The correlation plot of ΔR_{HL} as a function of various chemical shift ΔE_{cs} values. The minimum value is found by analyzing the square residuals R^2, which describe the fit goodness.

The results of several MXAN transient difference fits using various values of the chemical shift are plotted in Fig. 6.27. The results of MXAN fits assuming different values of the chemical shift ΔE_{cs} in the range between -1 and -4 eV (■) and their corresponding error bars are shown in Fig. 6.27.

The left ordinate axis shows the variation of the Fe-N bond length difference (between LS and HS states) ΔR_{HL} (solid line). Additional right ordinate axis indicates the square residuals R^2 corresponding to each ΔR_{HL}, and thus ΔE_{cs}. Clearly, there is a well-defined minimum of R^2 around ΔE_{cs}=-2.5±0.5 eV, which corresponds to the ΔR_{HL}=0.21±0.05 Å. Alternatively, assuming a chemical shift of ΔE_{cs}=-2.5 eV, we repeated the optimization of the excitation yield $f(t)$ in the range from 10-26%, and arrived to another minimum value of $f(t)$= 22(1)% corresponding to ΔR_{HL}=0.19±0.03 Å for the minimized R^2 as displayed in Fig. 6.28.

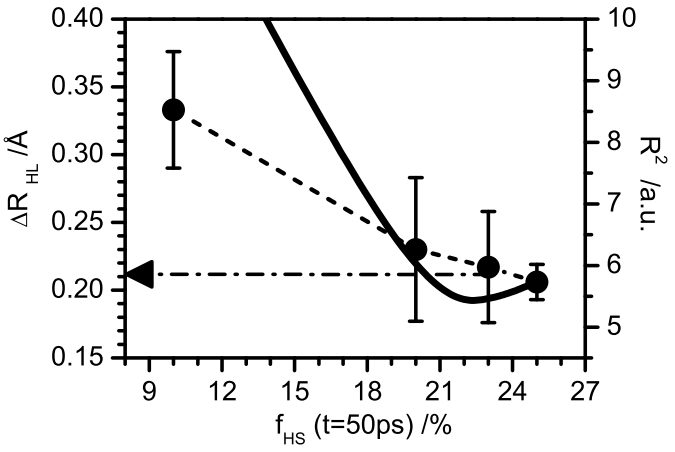

Figure 6.28: The correlation plot of ΔR_{HL} as a function of varying fractional population f(t) of the HS state. Similarly to Fig. 6.27, a minimum is reached and quantified by comparing the corresponding R^2 of each fit.

It should be remarked here that the MXAN fit curves of the transient ΔA(E,t=50 ps) spectrum, shown previously in Fig. 6.26b, were obtained including the minimized chemical shift value of ΔE_{cs}=-2.5 eV and the optimized value of $f(t)$= 22(1)%. We should also comment that the retrieved fractional population of the excited state from MXAN optimization agrees remarkably well with the yield measurements presented in Section 6.1.6 (and Fig. 6.23) and Appendix C. The final MXAN fit results of both LS and transient spectra from Fig. 6.26a and b can be summarized in Table 6.7.

Spectrum	ΔE_{cs}	$f(t)$	R_{Fe-N}
Low-Spin	0eV	100% eV	2.0±0.02 Å
ΔA(E,t=50 ps)	-2.5 eV	22±1 %	2.20±0.04 Å

Table 6.7: The best fit values of the MXAN analysis are summarized. The fit curve shown in Fig. 6.26 was obtained with fit parameters given here.

These values are in very good agreement with the LS-to-HS bond elongation of ca. 0.2 Å calculated by DFT for the same compound [151], and with those derived for similar Fe(II)-based SCO compounds [170, 171].

Finally, we have also performed a MXAN fit for the HS complex spectrum, as shown in Fig 6.24, as defined in Eq. 6.1. A priori, the $f(t)$ value is unknown and thus the HS spectrum is not straightforwardly obtained. Here, we have determined $f(t)$ with high precision (see results presented in Appendix C) and delivered high-spin excited state spectrum scaling factor (i.e. $f(t)$). In Fig. 6.29, the HS spectrum (identical to the one in Fig. 6.24) with its fit curve is shown.

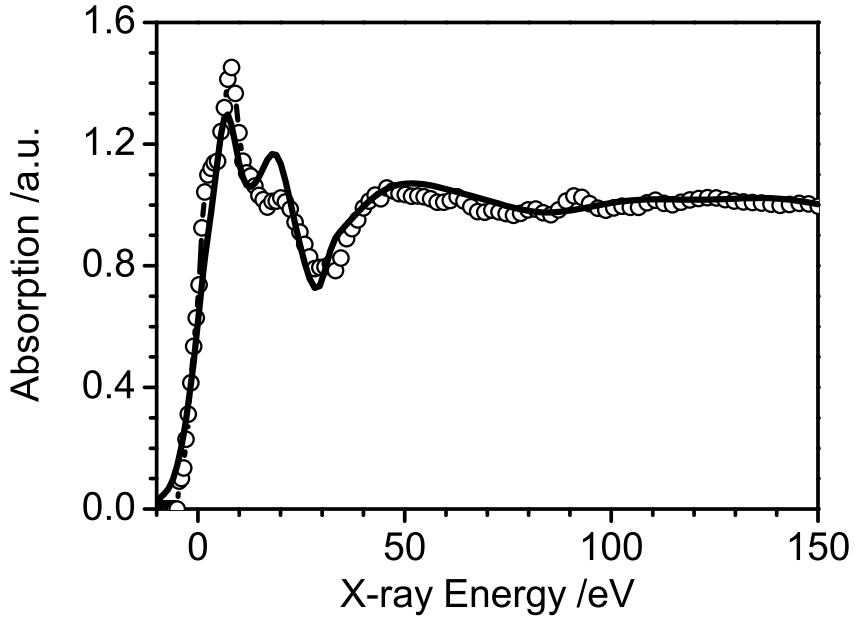

Figure 6.29: XAS spectrum of the HS state of $[Fe^{II}(bpy)_3]^{2+}$ is plotted with its MXAN fit, yielding the Fe-N bond distance change of 0.2 Å (see text for more details)

The fitting procedure was the same as in case of LS data shown in Fig. 6.26a. The HS spectrum plotted here was obtained assuming 22% of the fractional population of the HS state. The fit agreement is rather poor, especially in the vicinity of C and D features. The B intensity is also not completely reproduced in comparison to LS spectrum from Fig. 6.26a. Only the E feature is relatively the well-matched by the fit curve out of all resonances in this energy range. The fit results deliver the Fe-N bond length of R^{HS}_{Fe-N}=2.18±0.03 Å, with rather poor R^2 value of 72 (compare the typical values of R^2 in transient fit results reported in Figs 6.27 and 6.28). Although, the obtained bond distance agrees with the value refined in transient MXAN fits, the overall fit quality using the extracted excited state spectrum discourages this approach. The statistical residuals also significantly decrease, more than 1 order of magnitude, when fitting the transient spectra. Recently, we have demonstrated a similar trend (MXAN fit goodness of the excited state spectra as compared to transient difference spectra) in case of $Ru(bpy)_3$ complex and these results can be found in [256] attached to Appendix A.

6.3.2 EXAFS Analysis-FEFF

The following Section describes the structural analysis of the high-energy part of the spectrum, the EXAFS part, using the FEFF 8.20 code. In the first part, the standard curve-fitting procedure used in the EXAFS analysis will be presented involving the Fourier-transformed EXAFS spectra of both spin states of $Fe(bpy)_3$ complex. Next, an attempt of an alternative approach will be presented, where the transient EXAFS spectra are simulated directly and compared them with those derived from the transient XAS measurements over the entire energy range.

Curve Fitting of EXAFS Spectra

The curve-fitting procedure applied to EXAFS spectra has been extensively described in the literature [4, 236, 239, 240, 365, 366]. In Section 3.1.3 (see Fig. 3.7) of Chapter 3, we have already laid out some of the principle steps preceding the actual fitting of the considered spectra. Also the time-resolved L_3-edge XAS results on aqueous samples of $Ru(bpy)_3$ have been analyzed in a similar way (see Section 5.2 in Chapter 5).

The purpose of the analysis presented here was to extract the geometrical changes in both spin states of $Fe(bpy)_3$. Prior to the fitting, the K-edge XAS spectra of both the LS and HS states (as shown in Fig. 6.24) were reduced using *Athena* [249] and IFEFFIT [367] codes. The data reduction procedure, similarly to the data presented and discussed in Fig. 6.20 and Section 6.2.2, included:

1. Pre-edge and post-edge subtraction (spline functions as in Fig. 6.20)
2. Determination of the absorption threshold energy E_0
3. Normalization of the data to a measured and simulated edge step (using Eq. 3.3)
4. Interpolation of the spectra from energy space to k-space using Eq. 3.1
5. Atomic background removal by fitting a cubic spline to the data using AUTOBK algorithm [368].
6. Weighting of the EXAFS $\chi(k)$ function by n^{th} power of k ,i.e. $k^n \times \chi(k)$ (typically n=1-3)
7. Fourier-transforming the $\chi(k)$ data into R-space
8. Isolation of the backscattering amplitudes and phases of different coordination shells by the so called windowing (here we used Kaiser-Bessel window function)

9. Backward Fourier Transform of the χ(R) spectra into k-space (often called q-space to distinguish between the raw EXAFS function χ(k) and the backtransformed χ(q) function, which contains only the isolated scattering contributions used during the fitting of the Fourier-transformed spectra χ(R)

10. Comparison of the back-transformed EXAFS function χ(q) with raw χ(k) data.

All the above enumerated steps of the data reduction procedure, applied to the case of $Fe(bpy)_3$ in both spin states, are summarized in Fig. 6.30.

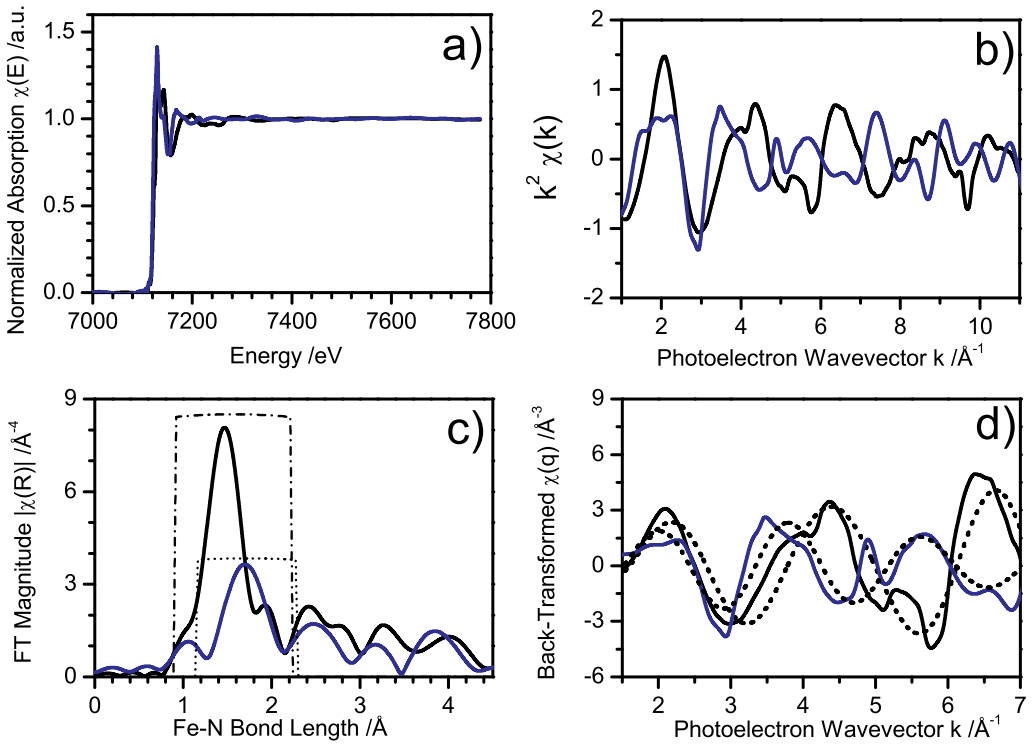

Figure 6.30: Panels (a)-(d) display the consecutive steps of the data reduction procedure applied to the LS (black line) and HS (blue line) spectra prior to the fitting. In (a)the normaized XAS spectra in energy space are shown. These are converted in to k-space, via Eq. 3.1 and weighted by k^2, as displayed in (b). In next step (c),$k^2\chi$(k) spectra are Fourier-transformed and the special window function (Hanning-Bessel) are applied in the selected R range (dashed and dotted windows). The χ(R) spectra (c) are then fitted, as presented in Fig. 6.31. The windowed χ(R) spectra can be back Fourier-transformed into k-space and are often referred to as the so called filtered χ(k) (often the backtransformed k-space is denoted and q-space in roder to distinguish between the raw and filtered EXAFS spectra)

In Fig. 6.30a, the normalized spectra in energy space of both the LS (black) and HS (blue) species are shown. These were transformed into the photoelectron's wavevector space (Eq. 3.1), k-space, and weighted by k^3 (Fig. 6.30b) after background subtraction as described above. Next, the Fourier transformation of the χ(k) EXAFS spectra was performed in order to obtain the characteristic frequencies hidden in the periodic oscillations there. These frequencies are directly linked to the interatomic bond distances of the constituent atoms, i.e. Fe-N, Fe-C etc. The Fourier spectra of both the LS and HS states, χ_{LS}(R) and χ_{HS}(R), are depicted in Fig. 6.30c. Finally, in Fig. 6.30d, we plotted the Fourier back-transformed spectra χ(q) (dashed lines) corresponding to the selected window ranges in Fig. 6.30c. These include only these frequencies, which find themselves in the selected ranges. As a matter of comparison, we have included the raw χ(k) data (solid lines) of both spin states (Fig. 6.30b). This comparison shows that the most dominant frequencies present in χ(k) stem from the photoelectron scattering of the nearest neighbor shell of N atoms (as retained by windowing in the analysis, Fig. 6.30c). The χ_{LS}(R) and χ_{HS}(R) Fourier-transformed spectra in Fig. 6.30 were not phase-corrected [4], which means that the interatomic distance they present appear to be at smaller values [236]. This phase-shift arises from the central-atom phase shift $2\delta_c$ contribution in the argument of the sine function in the EXAFS equation [3] (see Eq. 3.4 in Section 3.1). The factor 2 accounts for the fact that the photoelectron experiences this phase shift twice; first, when its propagating outwards the central atom and second time, when it is back-scattered off the neighboring atoms towards the absorber (central atom). The usual central-atom phase shift correction yields a constant factor, which shifts χ(R) spectra by ca. 0.3-0.5 Å towards higher R values. Yet, the fitting of χ(R) spectra always yields correct bond lengths, which are accounted for during the fitting procedure.

During the analysis, special care was taken in order to keep the data reduction procedure unchanged for both ground and excited states including identical spline functions and normalization ranges. The only difference between both data sets was the E_0 energy shift imposed onto the product spectrum, which equaled to ΔE_{cs} = -2.5 eV, as determined during the MXAN analysis (Fig. 6.27). The structural information present in XAS spectra shown in Fig. 6.30 can be derived using the so called EXAFS equation, which was proposed by Sayers *et al.* [3], who developed a quantitative method of parametrization of EXAFS data and since then, it has become a standard for much of the current work in this field. Here we are going to recall the Eq. 3.4 from Section 3.1:

$$\chi(k) = \sum_i S_0^2 N_i \frac{|f_i(k)|}{kR_i^2} \sin(2kR_i + 2\delta_c + \phi) e^{-2\sigma_i^2 k^2} e^{-2R_i/\lambda(k)}, \qquad (6.2)$$

Here the structural parameters, which enter Eq. 6.2 has already been discussed in details in Section 3.1.2 of Chapter 3. Historically, the original EXAFS formula referred only to single-scattering (SS) contributions coming from neighboring atomic shells in the high-energy part EXAFS part of the XAS spectrum.

Recent developments in theory brought a unified and accurate treatment (see Eqs. 3.11-3.13 in Section 3.2.2) of both single-scattering and multiple scattering effects, thus allowing very precise predictions to be made both in XANES, and EXAFS regions [11, 244]. The analysis of reduced data was handled using *Artemis*, code which serves as a very convenient GUI (Graphical User Interface) shell for aforementioned *IFEFFIT* code [367]. The fitting was performed on Fourier-transformed spectra χ(R) of both spin states of $[Fe^{II}(bpy)_3]^{2+}$ using theoretical backscattering amplitudes and phases calculated by FEFF8.20 *ab-initio* EXAFS code [251, 252]. The scattering potentials were calculated self-consistently based on muffin-tin approximation [257] using as the input geometrical structure the atomic coordinates of $[Fe^{II}(bpy)_3]^{2+}\times(PF_6)_2$ crystal as determined by x-ray diffraction experiments [150]. The magnitudes of Fourier-transformed spectra of both the ground and excited states are plotted in Fig. 6.31.

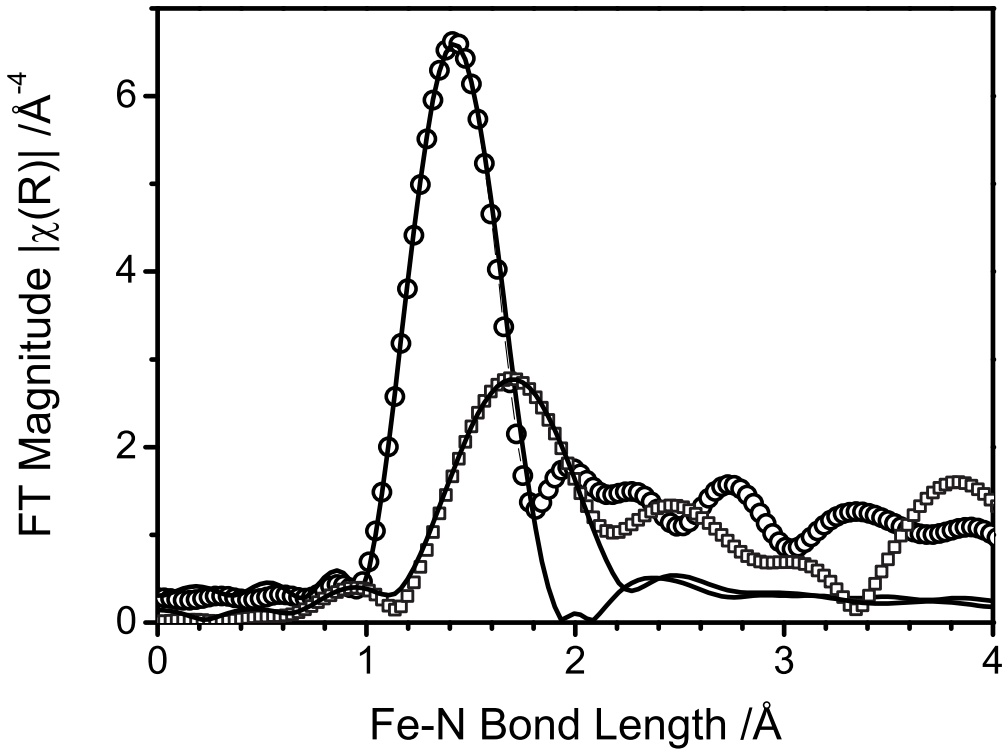

Figure 6.31: Fourier Transforms (FT) of k^3-weighted EXAFS spectra of the LS (∘) and HS (□) complexes together with their fits (solid lines) using a first-shell model with 6 nearest neighbor N-atoms (FT magnitudes are not phase-corrected therefore they appear at shorter bond lengths).

In Fig. 6.31, both χ_{LS}(R) (∘) and χ_{HS}(R) (□) were not phase-corrected, which is the reason the interatomic bond distances indicated by Fourier peaks are shifted towards lower R values [4, 236]. In present fit, only the single-scattering paths of Fe-N atoms were taken into account. The fit curves corresponding the LS and HS are plotted with solid lines in Fig. 6.31. We can see that the fit agreement with the isolated Fourier components in the range between 1-2.2 Å is excellent in both spin states of the complex. The extracted physical parameters, as defined in Eq. 6.2 are summarized in Table 6.8.

Spectrum	S_0^2	ΔE_0	R_{Fe-N}	σ^2_{Fe-N}
Low-Spin	0.75±0.2	0 eV	1.98±0.02 Å	$6{\cdot}10^{-3}{\pm}1{\cdot}10^{-3}$ Å^2
High-Spin	0.75±0.2	-2.8±0.5 eV	2.17±0.03 Å	$7.5{\cdot}10^{-3}{\pm}2{\cdot}10^{-3}$ Å^2

Table 6.8: The summary of EXAFS fit results shown in Fig. 6.31.

Here we have included the fit parameters, which were optimized during the fitting procedure, which yielded both fit curves displayed in Fig. 6.31. As we can see, the results obtained here, in terms of derived Fe-N bond lengths, are in full agreement with previously derived in MXAN analysis (6.7). As expected, ΔE_0 shift between the HS and LS states reflects the previously estimated chemical shift ΔE_{cs} and the the derived value of -2.8±0.5 eV agrees very well with MXAN-fitted -2.5±0.5 eV. The last column of Table 6.8 shows the slightly increased Debye-Waller factors of the excited state structure as compared to the ground state one. In both cases, the fitted σ^2_{Fe-N} factors of both LS and HS data agree well with values found in the literature for similar SCO complexes [170, 171]. The amplitude reduction factors S_0^2 were fixed to the literature valued optimized for similar Fe(II) complexes [48, 369].

Simulation of Transient EXAFS Spectra

As a complementary extension of this analysis, we have tried to simulate the transient ΔA(E,t) spectrum directly. To this purpose, the LS spectrum was fitted first in the k^2-weighted space in the range from 1-11 Å^{-1}. The fit result is shown in Fig. 6.32a. Here, the static χ_{LS}(k) EXAFS has been plotted with the corresponding it curve, obtained by using the scattering amplitudes and phases from the the EXAFS calculation performed with the FEFF8.20 code over a large energy range (ca. 650 eV above the edge). The results yield an excellent agreement with the LS structure as determined by static x-ray crystallography. The fit was done by taking into account all MS contributions (37 atoms excluding hydrogens) and by varying their Debye-Waller factors to best match the experimental data. In addition, we have refined the Fe-N bond distance by setting it as a free running parameter and the obtained result agrees very well with the published value of 1.97 Å within its uncertainty of 0.01 Å. In the next step, we have used the fitted values in a simulation of the transient EXAFS spectrum shown in Fig. 6.32b.

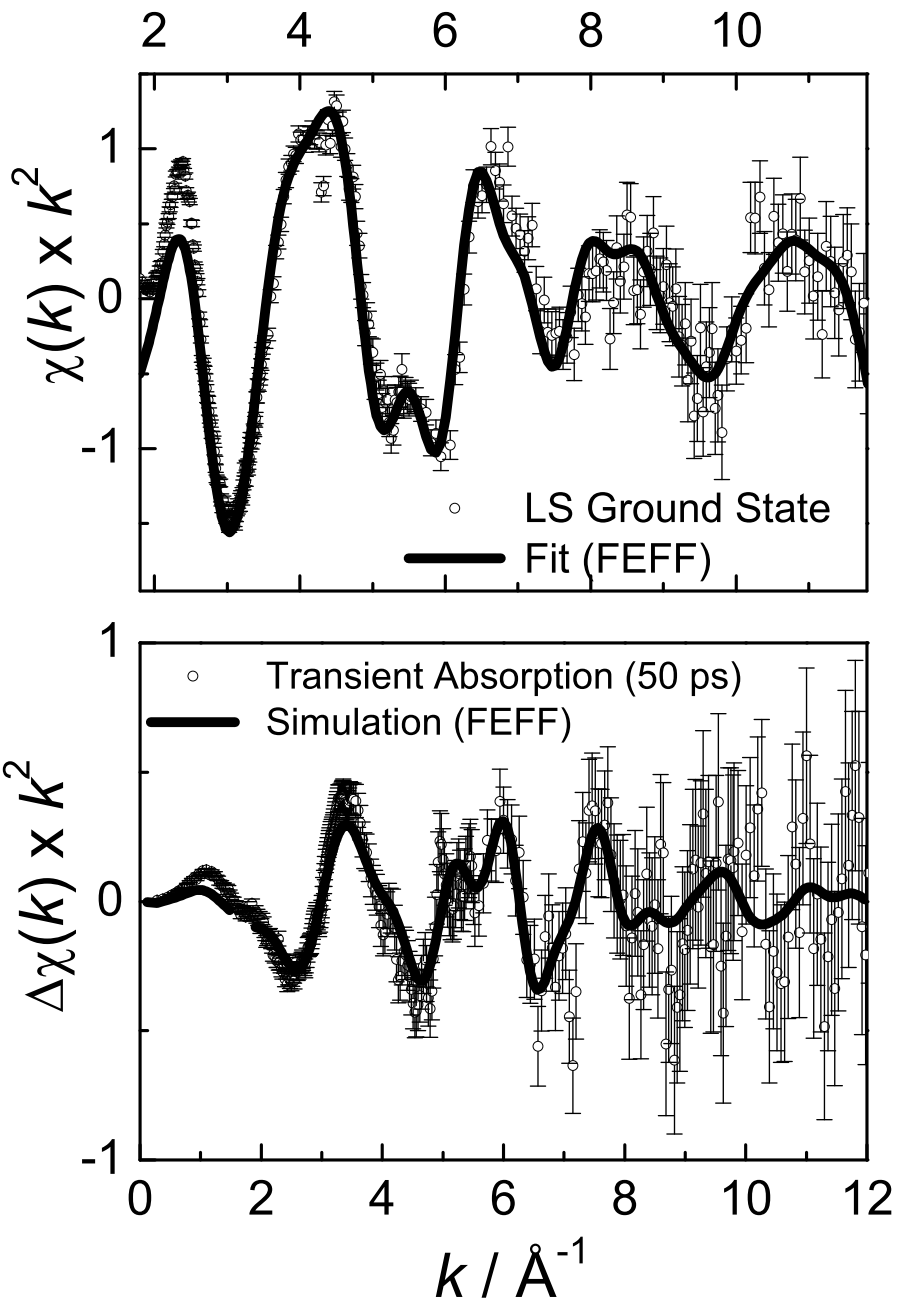

Figure 6.32: (a) LS state EXAFS spectrum together with the fit curve yielding R_{Fe-N}=1.97±0.01 Å. (b) Transient EXAFS after 50 ps together with a transient simulation for ΔR_{Fe-N}=0.18 Å

.

Here we have converted the measured ΔA(E,t=50 ps) spectrum (Fig. 6.22 in to k-space (using Eq. 3.1) and used k^2 to amplify the EXAFS oscillations at higher k-values. The corresponding error bars were also converted into k-space and equally weighted. The comparison of the ΔA(E,t=50 ps) spectrum and the simulation results is plotted in Fig. 6.32b. These results were obtained by performing several EXAFS calculations for various structural models with different Fe-N distances (the actual models were obtained by moving all 3 bpy ligands symmetrically outwards the Fe atom and thus modifying the bond lengths of all constituent atoms with respect to the absorber) in steps ranging from 0.03 to 0.005 Å. The input ground state structure of all these models was the crystallographic data taken from [150]. The molecular modelling software, *Cerius II*, was used in order to generate the structural models for transient EXAFS simulations, as described above. To each model, we have calculated its corresponding EXAFS spectrum, keeping all the parameters identical, so that the spectra differences can be solely attributed to structural modifications. In all FEFF simulations we have kept $f(t)$=22%. The fit was carried out by calculation of the x-ray absorption cross-section ($\chi(k)$) using the EXAFS formula (Eq. 6.2), first for the LS, assuming E_0=7122.5 eV, and then for HS compound. However, in the latter case the E_0 value was shifted by the amount of chemical shift ΔE_{cp}=-2.50±0.5 eV, as derived from MXAN fits of the XANES features (and confirmed during the EXAFS fits with ΔE_0). The sole adjustable parameter was the Fe-N bond distance, which was varied in increments of 0.03 Å (as determined by the structural models). A remarkable fit agreement was obtained for a ΔR_{Fe-N}=0.18±0.025 Å, shown in Fig. 6.32b. Although not shown here, we have carried out square residual analysis in order to determine the model, which best-fit the experimental data and the best-fit result is the one presented above.

The novel analysis (although still in progress) fully confirms previously retrieved values from the MXAN fitting (Table 6.7) and curve-fitting of χ_{LS}(R) and χ_{HS}(R) (see Table 6.7, while simultaneously narrowing down the bond length uncertainty (here 0.025 Å). We are currently implementing a fit procedure to reliably quantify the actual bond length increase, as measured in the transient absorption spectra ΔA(E,t). This novel approach may yield uncertainties on the order of conventional state-of-the-art EXAFS studies, i.e., in the 0.01-0.001 Å range [370]. This is because transient structural changes are rather small compared to the ground state structure. With the precise knowledge of the ground state structure (e.g., from crystallographic measurements), the fit procedure for determining the excited state becomes less ambiguous. Using the transient XAFS instead of the excited state XAFS spectrum can then deliver much more precise values for the structural changes.

6.4 Conclusions

In summary, we have detected the transient structural and electronic changes of the short-lived high spin state of $[Fe^{II}(bpy)_3]^{2+}$ by x-ray absorption spectroscopy with 100 ps time resolution. A full multiple scattering analysis of the photoinduced changes in the XANES and of the EXAFS region point to a bond elongation by $\sim$0.2 Å in the HS state.

Our results stand in contrast to previous XAS studies of SCO systems, which used the LIESST phenomenon to gain information about the structural characteristics of the HS state. The LIESST effect involves "trapping" of the HS population at low temperatures due to the decrease in temperature-dependent HS LS relaxation rate constant and thus upon continuous irradiation with light, it yields an almost complete conversion of the solid sample into its HS form. In Ref. [48], the detected HS complex in solution was relatively long-lived (60 ns) compared to the experimental resolution (50-100 ps). Here, we impulsively photoinduce a spin crossover transition at room temperature and then directly probe the electronic and structural properties of the short-lived population of the HS state.

In addition, the HS$\rightarrow$LS relaxation rate in $[Fe^{II}(bpy)_3]^{2+}$ complex remains too fast, even at cryogenic temperature, due to unusually large ΔE^0_{HL} (as discussed in detail in Section 2.4.5 of Chapter 2) and thus no LIESST effect was observed for this compound in its liquid or pure solid phase. Hauser *et al.* [360] has reported the LIESST effect in similar solid compounds where $[Fe^{II}(bpy)_3]^{2+}$ molecules were doped into several host lattices in order to increase the chemical pressure of the lattice environment and destabilize the HS state, which led to effective decrease in ΔE^0_{HL} and slowed down the spin relaxation rate constant.

Our experimental results are the first to report the photogenerated HS structure of $[Fe^{II}(bpy)_3]^{2+}$ compound recorded in "real-time" at room temperature solution. The relaxation from the singlet ^{1}MLCT to the HS state is considered to occur in < 1 ps (see Section 2.13), via several intermediate singlet and triplet states, implying structural changes. Optical spectroscopy has so far not been able to resolve these steps, but x-ray absorption spectroscopy has the full capability to "freeze" their corresponding structures, provided sufficiently short pulses of x-rays are produced, which is not far from now given the implementation of the femtosecond slicing scheme at synchrotrons [55–57]. Future extension of these experiments using femtosecond x-ray pulses may soon provide better insight into this relaxation process.

Chapter 7

Conclusions and Perspectives

7.1 General Conclusions

Ultrafast X-ray Absorption Spectroscopy is a young and still developing technique [27], which permits the investigation of photoinduced processes on a large variety of systems and on time scales down to the cross-correlation time between the laser and the x-ray pulses (i.e. 50-100 ps using synchrotron-based x-ray pulses). In this thesis, the high potential and the present state-of-the-art of research exploiting this method, have been presented on two examples of solvated transition metal complexes. In both cases, no optical spectroscopic method was so far capable of probing the influence of the charge transfer reaction on the metal-ligand bond distance directly. These limitations are suppressed with the advent of ultrafast XAS. Therefore the results presented and discussed in Chapters 5 and 6 are not only model systems for this new and nascent methodology, but also bring in new chemically- and physically-relevant observations and open up new venues for the structural studies in this class of complexes.

Our findings in case of $[Ru^{II}(bpy)_3]^{2+}$ has delivered, for the first time, the structural distortion of the Ru-N bond length by only $\sim$-0.04$\pm$0.02 Å, which occurs on picosecond time scale upon the photoinduced electron transfer reaction. As mentioned before, this class of reactions is paramount to Chemistry, Biology and Material Sciences, and so far no experimental technique was capable of delivering structural details on these time scales. To go beyond the present status of ultrafast XAS, one could envision that by using even shorter x-ray pulses (e.g. 50-100 fs as in case of standard femtosecond lasers), one could disentangle the eternal problem in describing the photochemical events by means of the so called configuration coordinate models.

This thesis shows some examples that prove the validity of ultrafast XAS as the powerful alternative to overcome these limitations of optical experiments (see Chapter 5). Chapter 5 proves that indeed the additional charge on the bpy ligand has a detectable, although minute, effect on the metal-ligand bond length. Another important detail, concerning these results, stems from the electronic structural details one may access simultaneously by means of ultrafast XAS. The XANES spectra, in the vicinity of the absorption edge, contain a great deal of both structural and electronic information about the chemically-relevant ground and excited state energy levels. One of the key parameter is the ligand-field splitting, which determines the energetics of the chemically-active orbitals and reflect the molecular symmetry of the system. Although paramount to Chemistry, it is not accessible by means of optical spectroscopy due to the forbidden character of *d-d* transitions between t_{2g} and e_g bands (Section 2.3.2). In case of $[Ru^{II}(bpy)_3]^{2+}$, the time-resolved XANES spectra has delivered the ligand-field splitting directly as the energetic splitting of A and B bands as seen in the excited state XAS spectrum (Section 5.2).

The studies of the light-induced spin crossover transition in $[Fe^{II}(bpy)_3]^{2+}$, Chapter 6, has also delivered several novel and exciting results, both in terms of the new chemical information and the technical improvements of the detection setup (Chapter 4). The later aspect has been especially successful in using the dual-detection mode, where both x-ray transmission and fluorescence signals can be detected simultaneously. The transient EXAFS spectra in an extended energy range up ca. 700 eV above the absorption edge were recorded (Fig 6.22) with excellent S/N ratio, allowing to extract the excited state HS state geometric structure (Section 6.3.2, Fig. 6.31). In addition, the correlation between the florescence and transmission photons could be established due to the shot-noise limited quality of the recorded data. These correlations were paramount in estimating the fractional population of the excited state species as discussed in appendix C.

Our results can be applied to any SCO compound, given its excited state lifetime is longer than the x-ray pulse-limited temporal resolution of the method. The key point of our studies was to demonstrate the possibility of characterizing the SCO complexes with short-lived HS states at any temperature, without the necessity of either cooling or chemical tailoring of the excited state properties. Although, the Fe-N bond distance elongation, by ca. 0.2 ± 0.03 Å, determined by ultrafast XAS agrees with previously calculated and structurally-derived values, it is a pioneering work on this class of compounds, where the excited state geometry has been established in "real time".

In addition, an extensive ultrafast optical studies of $[Fe^{II}(bpy)_3]^{2+}$ were undertaken. The motivation was naturally set by the requirements of the XAS experiments, where an independent measure of the HS fractional population is required. Nevertheless, our results are contributing significantly to the overall picture of the relaxation pathways involved in their photochemical cycle (see Fig. 6.19 in Section 6.1.7).

The systemic characterization of the excited state dynamics of $[Fe^{II}(bpy)_3]^{2+}$ has revealed several new aspects concerning the involved charge transfer state upon the photoexcited with 400 nm light. The femtosecond broadband fluorescence up-conversion studies (Fig. 6.11) have delivered, for the first time , the ultrashort lifetime of the initially excited ^{1}MLCT state $\sim$15 fs. Next to it, we found an experimental evidence, also never reported before, that the intersystem crossing between the ^{1}MLCT and lower-lying MLCT states (most probably ^{3}MLCT), indeed, takes place in $\leq$200 fs(similarly to $[Fe^{II}(bpy)_3]^{2+}$, Section 5.1). The population time of the HS state was also measured for the first to time to be $\leq$1 ps. The systematic investigation in a wide excitation fluence range, has revealed additional high-energy excitations to most probably higher lying charge transfer states, which all relax to the HS states in $\leq$ 3-4 ps. Therefore a complete picture of the energy and structural relaxation has been established (Fig. 6.19) on timescales from 15 fs upon to 1 ns, accompanied by the geometrical characterization of the HS state on 50 ps time scale. It is therefore an unique example, where combined ultrafast optical and x-ray probes deliver a complete picture of the relaxation dynamics, upon the spin transition, including the temporal (and spectral in the VIS) and structural characteristics of the process.

7.2 Perspectives

In this thesis, the boundary conditions of the state-of-the-art picosecond XAS technique has been extensively discussed and strengthened by the experimental demonstration that these studies can be now almost routinely implemented with reasonable data accumulation times on relatively dilute chemical and biological samples (down to $\geq$1 mM concentrations). However, time-resolved XAS is not limited by the time scale and it is due to technical limitations of the present synchrotron storage rings, which prevents us from reaching the femtosecond domain. In the scope of the emerging alternative schemes, such as femtosecond electron bunch slicing [56], ultrafast x-ray streak cameras [38, 371–373], electron bunch compression [374], etc. As a near-term perspective, I would envision several follow-up experiments, of both molecules presented here, using the hard x-ray fs x-ray pulse, as provided by the FEMTO add-on option currently being commissioned at the microXAS beamline of the SLS. It would be of high scientific and technological importance to carry out these experiments. On hand, the demonstration of the applicability of such low-flux ultrashort x-ray pulses could be provided. More interestingly, the structural dynamics in both $[Fe^{II}(bpy)_3]^{2+}$ and $[Ru^{II}(bpy)_3]^{2+}$ complexes is completely unknown on these time scales. The numerical example of our model calculations (Appendix E) on $[Fe^{II}(bpy)_3]^{2+}$ have shown an excellent agreement between the measured and calculated S/N ratios, thus confirming the applicability of the shot-noise limited treatment of our data. If so, we could easily estimate the required number of photons to repeat the experiments from Chapter 6, but now using low-flux fs x-ray pulses.

The total number of photons per data point in Figs E.2 and E.3 was $1{\cdot}10^8$ photons/s in order to achieve S/N≈10. In the most unfavorable case, assuming S/N≈1 in a femtosecond experiment, this requirement will decrease by a factor of 100 (using Eq. E.1), so that we would have to accumulate ca.$1{\cdot}10^6$ photons/s. The recently measured fs x-ray photo flux at microXAS beamline amounts to ca. 100 photons/pulse (at 1 kHz repetition rate) [375], which means $1{\cdot}10^5$ photons/s. Clearly, with only 10 s accumulation times we could achieve S/N=1, and in a more favorable case of S/N=3, this would increase to 1.5 min/point. Given the shot-noise limited characteristics of the microXAS beamline, this range of acquisition times do not sound too unreasonable. Similar cases of other transition metal complexes could be envisioned as summarized in Figs 7.1a. Here the results of numerical calculations of the required number of incident x-ray photons, in case of either the K-edge or L_3-edge absorption edges, for various elements are plotted [27]. Fig. 7.1b draws the feasibility bands, where typical time-resolved XANES and EXAFS experiments could be classified (in terms of the S/N ratios at a given excitation yield. Again, we can clearly assume that provided the x-ray photon fluxes in range between $1{\cdot}10^6$ photons/s/data point and $1{\cdot}10^9$ photons/s/data point, many potentially interesting and exciting systems could be studied. In order to extrapolate the results from Fig. 7.1 to femtosecond domain, it suffices to assume an overall flux reduction of ca.$1{\cdot}10^2$-$1{\cdot}10^4$, which takes into account the flux reduction when decreasing the electron bunch length from 100 ps to 100 fs ($1{\cdot}10^3$) plus some additional inefficiencies, which should not exceed another factor of 10. It is clear that this class of experiments is very challenging, yet I believe that given the excellent detection sensitivity, they will shortly become possible.

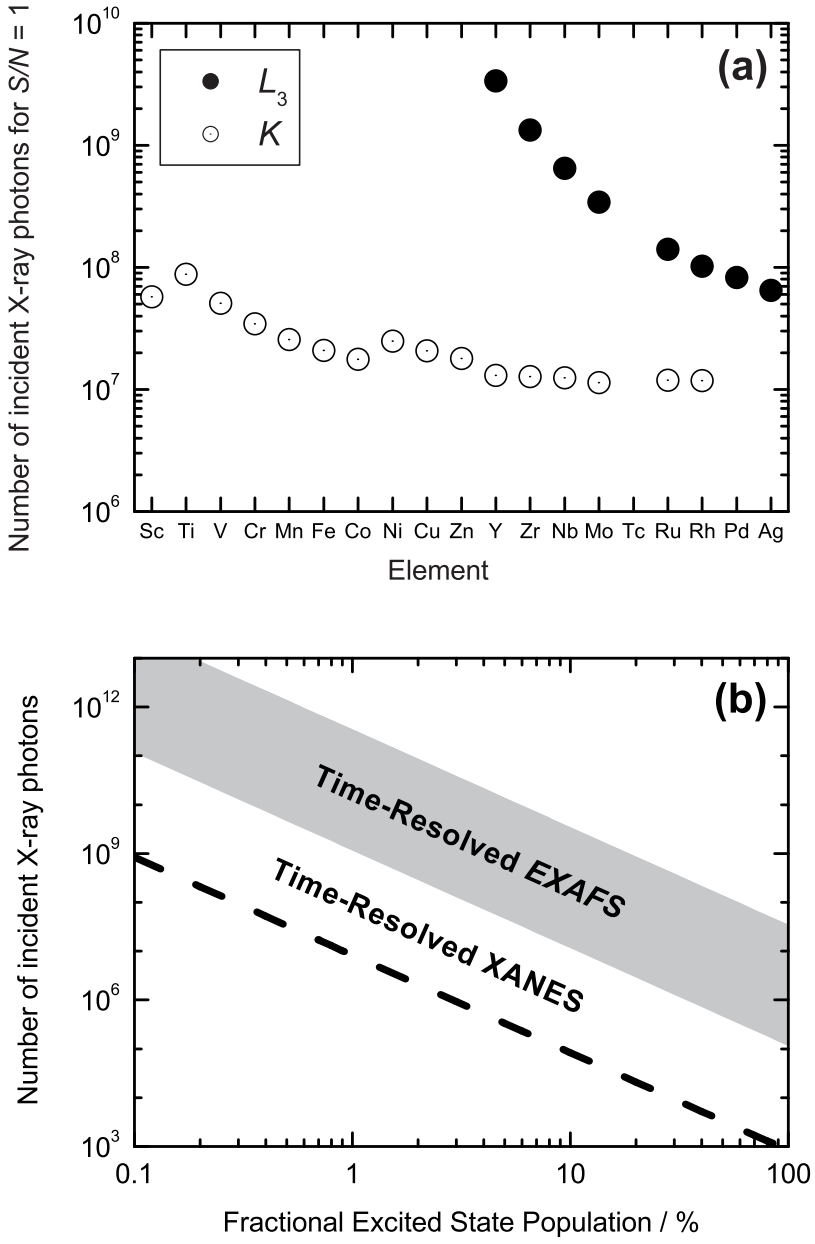

Figure 7.1: (a) The numerical feasibility studies of the required incident x-ray fluxes in order to observe time-resolved EXAFS of transition metal compounds in H_2O solution with a signal-to-noise ratio S/N = 1. No ligand or counterion contributions were included. The input parameters assumed: f=10 %, and χ= 1 % (relative to the absorption edge jump of the selected element, see Appendix E for details). (b) The results from (a) can be translated into both XANES and EXAFS ranges of the time-resolved XAS. The shaded region indicates the required incoming x-ray flux (photons/s/data point) as a function of the fractional excited state population f(t). Here we assumed that typically the signals observed in XANES region are 10-50 times larger than the corresponding EXAFS signals.

Like in any other field of science, many advances in ultrafast XAS are driven by technological breakthroughs. Indeed, new schemes are being proposed and developed, especially when large-scale installations are concerned. On one hand, linac-based sources of electrons, called *energy-recovery linacs* (ERLs), are being proposed [376–378] that offer the best performance as a dedicated user facility for producing ultrashort x-ray pulses, at moderate repetition rates in the 1-10 kHz range. In such a facility, electrons are accelerated in a linac to several GeV energies and subsequently forced to radiate x-rays in a series of conventional insertion devices. After that, the decelerated electron beam is circulated in the same linac again, in order to recover the energy. The striking advantage of this concept is that the electron bunch passes through the undulators only once, which frees it from several instability issues, present in the storage rings, such as scattering losses, bunch instabilities and emittance, which contribute to the overall intensity and pulse width degradation [379]. The photon fluxes expected to be available from these machines are depicted in Fig. 7.2.

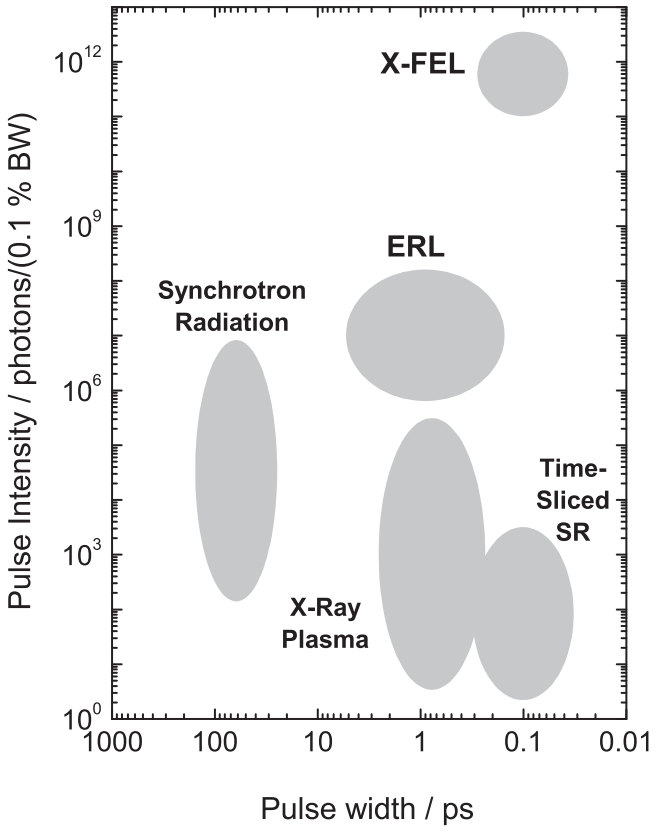

Figure 7.2: Comparison of photon fluxes (pulse intensity per 0.1% BW) and time resolutions of present and future sources of picosecond pulsed x-rays. The pulse intensity here does not account for the repetition rate and the brightness of these sources, which may be completely different.

On the other hand, a completely new type of machine, the *X-ray Free Electron Laser* (X-FEL), are currently being developed in Hamburg (TESLA) [380] and Stanford (LCLS) [381]. These are linac-based machines, which will exploit self-amplified spontaneous emission (SASE) [382, 383] within a long undulator and generate ultra intense monochromatic hard x-radiation with pulse durations of $\leq$100 fs. The idea underlying an X-FEL assumes that the electron beam is sent down a very long undulator behind the linac in order to create a tunable, $<$ 200 fs x-ray pulse. By manipulating the energy levels of the electrons in the linac with the magnetic field of the undulator, one can tune the x-ray wavelength. The extremely long undulator allows x-ray photons, emitted by the electron bunches, to interact coherently (just as in case of an optical laser), stimulating the emission of more x-ray photons. The long undulator is essential because this laser "cavity" is has no end mirrors, thus giving rise to SASE processes. When this beam is seeded into a second long undulator, the monochromatic output radiation intensity grows to unprecedented values, comparable to those of optical lasers, ca.10^{11}-10^{12} per pulse, but with 3-4 orders of magnitude larger pulse energies, as shown in Fig. 7.2.

Obviously, the new era of ultrafast structural dynamics is yet to come in the next decade. The availability of X-FELs, and even ERLs, will certainly open up entirely new horizons to this research field. Although remote in time, several innovative experiments have already been suggested, such as single protein diffraction [384]. Another area, which has been envisioned with these machines, embraces all kinds of nonlinear x-ray phenomena, in analogy to nonlinear optical processes. Extending the formalisms and techniques of nonlinear optical methods to the x-ray domain [385], has been proposed already been proposed [386–391], although at present, their experimental verification remains impossible.

In the scope of the aforementioned possibilities, the state-of-the-art time-resolved XAS is just the necessary first and pioneering step towards these unexplored and revolutionary fields of Science.

Appendix A

The FMS Interpretation of Time-Resolved XAS Spectra

This Appendix includes a copy of an article published in the *Journal of Physical Chemistry B*. A color reprint of the paper can be obtained from the electronic edition of the journal using the reference: M. Benfatto, S. Della Longa, K. Hatada, K. Hayakawa, W. Gawelda, C. Bressler and M. Chergui, *J. Phys. Chem. B*, **110**(2006) 14035-39.

THE JOURNAL OF PHYSICAL CHEMISTRY B LETTERS

14035

2006, *110,* 14035−14039
Published on Web 06/30/2006

A Full Multiple Scattering Model for the Analysis of Time-Resolved X-ray Difference Absorption Spectra

Maurizio Benfatto,[†] Stefano Della Longa,[†,‡] Keisuke Hatada,[†] Kuniko Hayakawa,[†] Wojciech Gawelda,[§] Christian Bressler,[§] and Majed Chergui*[,§]

Laboratori Nazionali di Frascati, INFN, CP13, I-00044 Frascati, Italy, Dipartimento di Medicina Sperimentale, Universitá dell'Aquila, 67100 L'Aquila, Italy, and Laboratoire de Spectroscopie Ultrarapide (LSU), ISIC-FSB, BSP, Ecole Polytechnique Fédérale de Lausanne (EPFL), CH-1015 Lausanne-Dorigny, Switzerland

Received: May 30, 2006; In Final Form: June 16, 2006

A full multiple theoretical model (MXAN) is applied to fit picosecond difference X-ray absorption spectra at the ruthenium L_3 edge upon photoexcitation of aqueous $[Ru^{II}(bpy)_3]^{2+}$. We show that fitting difference spectra allows an increase in sensitivity, such that slight structural changes can be retrieved, which are not detected in fitting full spectra. The Ru−N bond distances of the excited complex in the ^{3}MLCT state are in good agreement with recently published values. The implementation of the present approach to L-edge spectra and its high sensitivity opens opportunities for its extension to a large class of experiments where difference X-ray absorption spectra are recorded.

I. Introduction

X-ray Absorption spectroscopy (XAS) delivers details about the electronic structure of an atom of interest, i.e., orbital occupancy, degree of oxidation, and ligand field strength of its valence states, which are those driving chemical reactions, via X-ray absorption near-edge structure (XANES) spectroscopy. Simultaneously, coordination numbers and bond distances around a specific atom can be determined from the extended X-ray absorption fine structure (EXAFS) spectroscopy.

In recent years, there has been growing activity using XAS in a pump−probe scheme to detect photoinduced electronic and structural changes in real time. In these experiments, the system is excited by an ultrashort pump laser pulse and is probed by a short X-ray probe pulse, whose time delay with respect to the laser pump pulse can be continuously varied.[1] Bressler, Chergui, and co-workers[2−5] pioneered the differential transient absorption spectroscopy (XANES and EXAFS), which consists of recording the difference between the transmission spectra of the unexcited and laser-excited sample. This increases greatly the sensitivity of the experiment (differential signals below 10^{-4} optical density (OD) can be identified, thanks also to the high stability of synchrotron sources), while largely reducing systematic errors such as intensity fluctuations or deterioration of the sample during the experiment.[4,5] Recently, a variant of this approach was used in a dispersive XAS setup, to retrieve by EXAFS very small structural changes induced by magnetostriction on an iron−cobalt film.[6] These studies show the potential of differential X-ray absorption spectroscopy, not only in the case of light-induced or magnetic-field induced changes, but also when the changes are induced by temperature,[7,8] pressure,[9,10] pH changes (important in biology),[11−13] and so forth.

The importance of differential XAS for theoretical modeling can only be emphasized, as fitting difference spectra has the important advantage of increasing the sensitivity of the fit and decreasing the influence of possible systematic errors in the calculations, which come from the approximations used in the theoretical approach. In the above study by Pettifer et al.,[6] the simulations were limited solely to the differential EXAFS spectra of the Fe K edge, and there has so far not been a theoretical study of differential XANES spectra. In recent years, Benfatto and co-workers[14] have developed a fitting procedure (called MXAN) based on a full multiple scattering analysis of X-ray absorption features.[15] However, this approach has not been implemented in the case of differential spectra, let alone at L edges.

This contribution presents new extensions of MXAN, to the case of the recently published[2,16] picosecond L_3-edge XANES and EXAFS difference spectra of a coordination compound, $[Ru^{II}(bpy)_3]^{2+}$ in a water solution, excited by a 400 nm ultrashort laser pulse. This excitation brings the molecule to the singlet metal-to-ligand charge-transfer (MLCT) state, which then undergoes ultrafast (<100 fs) intersystem crossing to the low-lying ^{3}MLCT state,[17] whose radiative lifetime is on the order of several hundreds of nanoseconds. In the process, the central Ru atom is oxidized because an electron is transferred to the bpy ligands. Gawelda et al.[16] recorded the differential XAS spectra between the ground state and the excited complex in its ^{3}MLCT state, from which the excited state XAS can be reliably constructed.

The analysis of the XANES line shapes using an atomic multiplet code,[18] with both octahedral and trigonal ligand fields superimposed to describe the excited-state complex and of the EXAFS region of the excited states, pointed to a contraction of Ru−N bonds by ∼0.035 Å in the excited-state complex. However, this treatment handled the bound−bound and bound−

[†] INFN.
[‡] Universitá dell'Aquila.
[§] Ecole Polytechnique Fédérale de Lausanne.

10.1021/jp063326o CCC: $33.50

continuum transitions with different theoretical approaches. It also left an above-ionization resonance (the so-called C-feature, see below) unassigned, and the structural analysis was limited to the first shells of N and C atoms surrounding the Ru atom. Finally, it assumed a trigonal symmetry for the excited complex. While this last assumption seems justified, in part because of the excellent agreement between the simulated and experimental XANES line shapes,[16] strictly speaking, the excited complex has a C_2 symmetry.

This present contribution introduces a number of novel aspects: (i) Using MXAN, we provide a global approach for the description, in a consistent way, of the bound−bound and bound−continuum features of the spectra. (ii) We implement for the first time MXAN, to analyze L-edge spectra of metals and demonstrate its applicability to coordination chemistry compounds. (iii) We apply it to the simulation of differential spectra and show that this improves the sensitivity and thus delivers structural information about transient species, that the simulation and fit of full spectra cannot retrieve. These points underscore the importance of the present procedure to a very broad range of systems and phenomena, where XAS is used to monitor weak changes, caused by an external perturbation.

II. Theoretical Details

The quantitative analysis of the energy region around the L_3 edge of Ru was performed using the MXAN code, with the aim of deriving structural information, using the same procedure described in refs 14 and 19. The method is based on the comparison between experimental data and several theoretical calculations performed by varying selected structural parameters starting from a well-defined initial geometrical configuration around the absorber. The optimization in parameter space is achieved by minimization of the square residual function

$$R_{\mathrm{aq}} = n \frac{\sum_{i=1}^{m} w_i[(y_i^{\mathrm{th}} - y_i^{\mathrm{exp}})\epsilon_i^{-1}]^2}{\sum_{i=1}^{m} w_{\mathrm{i}}}$$

where n is the number of independent parameters, m is the number of data points, y_i^{th} and y_i^{exp} are the theoretical and experimental values of absorption, respectively, ϵ_i is the individual error in the experimental data set, and w_i is a statistical weight. For $w_i = 1$, the square residual function R_{sq} becomes the statistical χ^2 function. In this paper, we assume a constant experimental error ϵ equal to 0.6% of the main jump for the whole experimental data set.

Theoretical calculations are performed within the so-called full multiple scattering (FMS) approach, i.e., the inverse of the scattering path operator is computed exactly, avoiding any "a priori" selection of the relevant MS paths, and using the muffin-tin (MT) approximation for the shape of the potential.[15] The MT radii are chosen according to the Norman criterion with specified percentage of overlap, and the potential is recalculated at each step of the minimization procedure, keeping the overlap factor fixed.

The exchange and correlation part of the potential is calculated in the framework of the Hedin−Lundqvist (HL) scheme. To avoid overdamping of the spectrum at low energies, caused by the use of the full complex HL potential, MXAN uses a phenomenological approach to calculate the inelastic losses.[20,21] It is based on the convolution of the theoretical spectrum, calculated using only the real part of the HL potential, with a suitable Lorentzian function with an energy-dependent width given by $\Gamma = \Gamma_c + \Gamma(E)$. The constant part Γ_c accounts for contributions of the core hole lifetime and the experimental resolution, while the energy-dependent term $\Gamma(E)$ represents both intrinsic and extrinsic inelastic processes. $\Gamma(E)$ is zero below an onset energy E_s and begins to increase from a value A_s, following the universal functional form of the mean free path in a solid. This method introduces three nonstructural parameters that are derived during the fit on the basis of a Monte Carlo search, at each step of the computation. Application of this procedure to different systems confirmed the reliability of this approach.[22,23]

The fits of the XANES difference absorption spectra between excited- and ground-state Ru compounds ($Ru^{es} - Ru^{gs}$) have been obtained by a modification of the MXAN program, using the following procedure: First, the theoretical XANES spectrum of Ru^{gs} is calculated as a reference using the structural coordinates obtained by the direct fit of the ground state. This structure is equal, within the statistical errors, to the crystallographic determination. Then, MXAN calculates various theoretical spectra, one at each step of the fit, for all the different structures obtained by varying the selected coordinate parameters starting from the spectrum. All these XANES spectra have been calculated using only the real part of the HL potential, i.e., without including any damping factor. Finally, using the procedure previously described, the real theoretical difference spectrum is convoluted in order to compare with the experimental data and to reach the best-fit condition. This procedure assumes that the damping parameters are not correlated to the structural parameters and are identical for both ground and excited states. The number of nonstructural parameters used by this new procedure is equal to that fitting the full spectra.

The non-MT corrections are normally very weak and confined to the first 10−20 eV from the edge, with a very small influence on the structural determination as demonstrated in several test cases.[15−18] However, they can provide some additional details on the potential-energy landscape around the absorbing atom, due to the lifting of the muffin-tin averaging approximations. Indeed, in the MT approximation, the potential is spherically symmetric in nonoverlapping spheres defined around each atom and is assumed constant in the interatomic region. This is a drawback, in particular, in the region at very low energy, where the fine details of the potential are important, because the photoelectron energy is low and on the order of the error in the value of the potential. To assess the relevance of these non-MT corrections, we have also performed full potential calculations. These are based on the finite difference method (FDM), which is a method to solve the Schrödinger equation (SE) for a potential of general shape.[24] Essentially, it writes the SE equation over a three-dimensional grid, obtaining a very large system of linear equations connecting the value of the wave function on all of the grid points. We have used the FDMSE program developed by Joly.[25] The exchange and correlation part of the potential is again calculated by the HL scheme, using only the real part.

III. Results and Discussion

Figure 1 shows the X-ray absorption spectrum of $[Ru^{II}(bpy)_3]^{2+}$ in the region of the L_3 and L_2 edges (a), the differential absorption spectrum obtained 50 ps after laser excitation (b), and the X-ray absorption spectrum of the excited compound in the ^{3}MLCT (c) retrieved from spectra (a) and (b), using a photolysis yield of 10%, measured in laser pump−probe

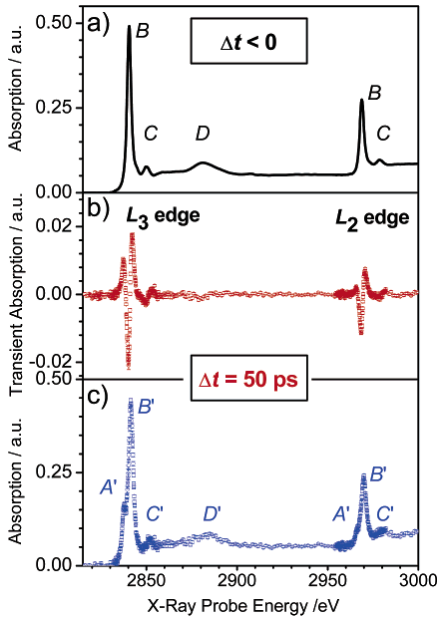

Figure 1. (a) Static absorption spectrum of aqueous $[Ru(bpy)_3]^{2+}$ in the region of the Ru L_3 and L_2 edges. (b) Transient difference absorption spectrum measured 50 ps after photoexcitation. (c) Excited-state XAS spectrum extracted from spectra a and b (see ref 16 for details). Note that, in comparison with spectrum a, an additional band (A′) shows up.

experiments (see ref 16 for details). The ground-state spectrum exhibit bands labeled B, C, and D. The B-band is assigned to transition from the 2p core shell to the ligand field split empty 4d(e_g) level (all 6 electrons of Ru^{II} are in the lowest 4d(t_{2g}) level). In ref 16, we tentatively assigned band C to an above-ionization resonance. This interpretation is confirmed by the present simulations (see below). Finally, band D is clearly an above-ionization scattering feature.[16]

In the excited complex (Figure 2), the analogues of the B, C, and D bands are all recovered (primes are used for the excited state), along with an additional one (A′), which appears below the B′ band, because we have created a hole in the previously filled t_{2g} level, as a result of the photoexcitation that transfers an electron from the Ru atom to one of the bpy ligands.

In the following analysis, we will only concentrate on the L_3 edge[16] and first fit its full spectra in the ground and excited states (Figure 1a,c). The known crystallographic data of the ground state is taken as initial structure.[26,27] This choice is reasonable, as it was found that the EXAFS spectra are well-reproduced with these input parameters.[16] The entire cluster of 37 atoms (1 Ru, 6 N, and 30 C atoms of the bpy ligands, disregarding the outermost 30 H atoms) has been used in the present analysis. The structural parameters allowed to change during the fitting procedure are as follows: (i) two distances between the absorber and the nitrogen atoms of the three rings up and down the plane perpendicular to the C_3 axis and (ii) the angle of one triplet with respect to the other two. The atoms of each ring are linked to the corresponding nitrogen and move with it during the fit. Rings up and down are linked during the movement; in this way, only three independent structural parameters are used in the fit procedure.

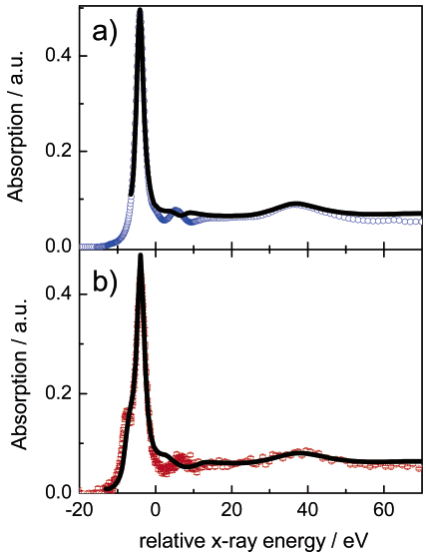

Figure 2. Fit using the muffin-tin (MT) approximation (back trace) of the ground (a) and excited (b) states experimental L_3-edge spectra (points) of aqueous $[Ru^{II}(bpy)_3]^{2+}$, taking a cluster of 37 atoms.

TABLE 1: Fit Parameters of the Full Spectra for the Ground and Excited States of the Complex[a]

	Ru−N_{up} (Å)	Ru−N_{down} (Å)	$\Delta\phi$	Γ_c (eV)	R_{sq}
ground state	2.06 (0.03)	2.06 (0.03)	1.91° (7°)	2.09	1.12
excited state	2.06 (0.04)	2.06 (0.04)	−7.89° (7.4°)	2.20	5.52

[a] Up (down) refers to the N atoms in the pyridine rings up (down) the plane perpendicular to the C_3 axis. $\Delta\phi$ represents the angle between one triplet of pyridines with respect to the other. Γ_c is the core hole lifetime and R_{sq} is the square residual function defined in the text.

Figure 2 shows the best fits for the ground- and excited-state experimental L_3-edge XAS spectra. The agreement is satisfactory over the entire energy region, apart for band C, that is missing in the calculation (this is discussed below), and the offset between simulated and experimental spectra at high energies. Nevertheless, for the ground state, the relatively good agreement confirms the quality of the method, given the available crystallographic data.[26,27] For the excited-state spectrum (Figure 2b), the calculation reproduces the new A′ band, although the A′−B′ energy splitting is smaller than in the experimental spectrum. This is due to a limitation of the MT approximation, which is less suitable for low-lying states.[14,28−30]

The fit results for both ground and excited states are given in Table 1. Within statistical error, the quality of fits is unable to retrieve a structural difference between the ground- and excited-state spectra.[16] In Table 1, we also report the value of the core hole lifetime coming from the Monte Carlo search in the nonstructural parameter space, and it is in good agreement with the literature value (the core hole lifetime of L_3 or Ru has been reported in the 1.7−2.0 eV range[31]). The main conclusion from Figure 2 and Table 1 is that fitting full spectra with MXAN is not sufficient to retrieve the subtle structural changes between ground and excited complex.

To identify the origin of band C, we performed several calculations using the FDM method. In this way, we can check the effect of the MT approximation. Figure 3 shows a comparison between the experimental excited-state spectrum and

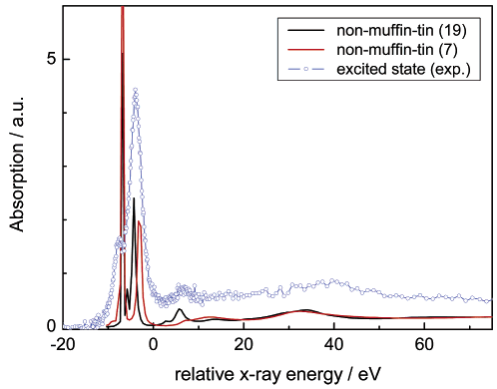

Figure 3. Non-MT calculations of the excited-state spectra for two clusters of 7 (red trace) and 19 (black trace) atoms, compared to the experimental spectrum (points).

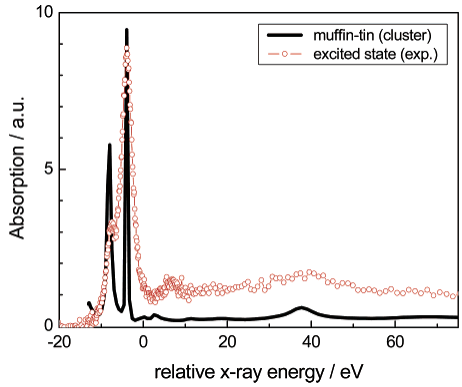

Figure 4. Simulation of the excited-state spectrum using MT without damping of the photoelectron wave, for a cluster of 37 atoms (i.e., the entire molecule, without the H atoms).

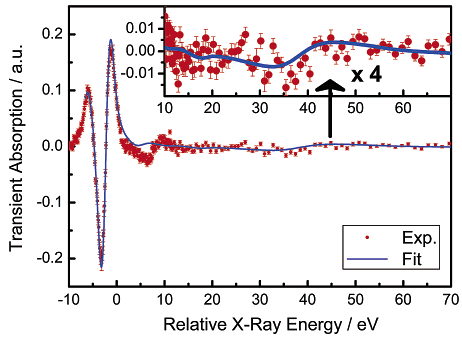

Figure 5. Fits of the difference XAS spectra using MT and a 37-atom cluster for a chemical shift of 1 eV. The inset shows a zoom of the D-band region.

two simulations, one using a small cluster of 7 atoms, i.e., only the neighboring nitrogen atoms around the absorber, and another one using the nearest 19 atoms (thus with 2 more carbon shells included). The theoretical calculations are made using only the real HL potential to put in evidence the effect of the cluster size. The computer time needed for this non-MT calculation makes it prohibitive to use a larger cluster, e.g., the entire molecule. However, the comparison between both sets gives insight into the overall trend. Peaks A′ and B′ are present in both calculations, confirming their bound−bound transition character, while peak C′ appears only when the cluster size is large enough to generate a multiple scattering (MS) resonance of sufficient amplitude. This confirms our previous tentative assignment[16] that band C is a true MS resonance, based on the fact that it lies 3.2 eV above the ionization limit, which corresponds to a photoelectron wavelength of ∼6.3 Å, i.e., on the order of the spatial extension of the molecule. It contradicts an earlier one,[32] which assigned band C to the 2p−5s bound−bound transition. Note also that the 19-atom case exhibits additional weak lines between the two main low-lying lines, compared to the 7-atom case, because the second shell of atoms provides an additional ligand field that is superimposed onto the main one, due to first-shell coordination.

We now return to the MT calculations, which allow a more detailed look into the geometric structural changes. In Figure 4, we show the comparison between the experimental data and the MT MXAN calculation performed using the entire 37-atom cluster and the real part of the HL potential. Peaks A′, B′, and D′ are located at the right relative energy position with a reasonable intensity ratio, while peak C′, though present, deviates strongly in intensity and energy position, because (discussed above) it is located in the energy range, where details of the potential can be important. Nevertheless, the non-MT corrections do not affect the extraction of structural information, because the later essentially involves the relative position of peaks B (B′) and D (D′) and their intensities, and because these corrections are essentially confined to the first 10 eV or so of the spectrum.

Since the fits of full spectra cannot reveal structural differences between the ground- and excited-state compounds, we fitted the difference spectra using the procedure described in section II. Figure 5 shows the fit taking the chemical shift of 1 eV determined in ref 16 and a core hole lifetime of 2.17 eV. Here, the sole adjustable structural parameter is the Ru−N distance. The result is satisfactory in the entire energy range, except in the region of band C, as expected. Note that the fit captures well, both in energy and in amplitude, the details of spectral changes in both the region of the edge (A,B-band region) and that of the D-band, well above (>20 eV) the edge. The latter is important, since the fit of the difference spectra is capable of capturing the small but noticeable spectral change at the D-band, which reflects a weak contraction of the Ru−N distance in the excited state. This clearly shows that fitting difference spectra is much more sensitive than fitting full spectra. In addition, the statistical quality of the fit is improved, as can be seen from the value of the square residual function R_{sq}= 1.89, to be compared with the value of 5.52 (Table 1) resulting from the fit of the full spectrum. Finally, the Ru−N bond contraction we obtain from the fit (0.045 Å) is in good agreement with the value derived in ref 16 (0.037 ± 0.0135 Å) using the FEFF8.2 code. As discussed then,[16] $[Ru^{II}(bpy)_3]^{2+}$ does not lend itself easily to a fit of the EXAFS features, as the energy range of the latter is rather limited (<130 eV). The present approach using MXAN does not suffer from this limitation, and it shows that the present fit under D_3 symmetry agrees with the results of ref 16.

As mentioned in the Introduction, from an electronic point of view, the system adopts a C_2 symmetry in the excited state, rather than a D_3 symmetry. Therefore, we also carried out fits of the difference spectra, assuming that two neutral bpy's remain

at fixed positions, while the Ru−N distance to the reduced bpy is used as an adjustable parameter. A reasonably good fit was obtained for a Ru−N bond contraction by ∼0.07 Å. However, given the quality of the data and the arbitrary assumptions (e.g., the two unmoved bpy ligands) made for this simulation, it is difficult to draw conclusions about the validity of the Ru−N bond contractions under one or the other symmetries. Nevertheless, this shows that MXAN can fit data reasonably well in the case of nontotally symmetric structural changes.

In conclusion, as far as $[Ru^{II}(bpy)_3]^{2+}$ is concerned, the present simulation allowed us to demonstrate the following: (i) that band C is a feature resulting from multiple scattering over the entire molecule, (ii) that the Ru−N bond contractions in the excited-state complex are in very good agreement with those derived in ref 16 when using a trigonal symmetry for the excited state, and (iii) that bond changes for nontotally symmetric distortions can be extracted from the fit.

On a more general perspective, the present methodology based on fitting difference absorption spectra introduces many novel advantages: (i) It increases the sensitivity and the statistical quality of the fit. In particular, the statistical error bars using transient difference spectra allow us to increase the sensitivity by a factor of ∼3 for the present data (based on the R_{sq} factors). (ii) There is no data reduction, as the fits are done in energy space, contrary to other methods where, e.g., Fourier transformation-related errors can occur due to truncation. (iii) The present work represents the first application of the MXAN code to L absorption edges. This point is of importance due to the role of transition-metal complexes in coordination chemistry and biology (protein binding sites). (iv) The methodology presented here is not limited to time-resolved light-induced difference spectra, but can be applied to any situation, where changes in XAS spectra are generated by temperature, pressure, pH, magnetic fields, and so forth.

Acknowledgment. This work was partly supported by the Swiss National Science Foundation via grants 620-066145 and 200021-105239/1, by the Swiss Light Source (Villigen), and by the DYNA program of the European Science Foundation.

References and Notes

(1) Bressler, C.; Chergui, M. *Chem. Rev.* **2004**, *104*, 1781−1812.
(2) Saes, M.; Bressler, C.; Abela, R.; Grolimund, D.; Johnson, S. L.; Heimann, P. A.; Chergui, M. *Phys. Rev. Lett.* **2003**, *90*, 047403−047401.
(3) Saes, M.; Bressler, C.; van Mourik, F.; Gawelda, W.; Kaiser, M.; Chergui, M.; Bressler, C.; Grolimund, D.; Abela, R.; Glover, T. E.; Heimann, P. A.; Schoenlein, R. W.; Johnson, S. L.; Lindenberg, A. M.; Falcone, R. W. *Rev. Sci. Instrum.* **2004**, *75*, 24−30.
(4) Saes, M. G. W.; Kaiser, M.; Tarnovsky, A.; Bressler, Ch.; Chergui, M.; Johnson, S. L.; Grolimund, D.; Abela, R. *Synchrotron Radiat. News* **2003**, *16*, 12.
(5) Gawelda, W.; Bressler, C.; Saes, M.; Kaiser, M.; Tarnovsky, A.; Grolimund, D.; Johnson, S. L.; Abela, R.; Chergui, M. *Phys. Scr.* **2005**, *T115*, 102.
(6) Pettifer, R. F.; Mathon, O.; Pascarelli, S.; Cooke, M. D.; Gibbs, M. R. J. *Nature (London)* **2005**, *435*, 78−81.
(7) Yokoyama, T.; Murakami, Y.; Kiguchi, M.; Komatsu, T.; Kojima, N. *Phys. Rev. B* **1998**, *58*, 14238−14244.
(8) Boca, R.; Vrbova, M.; Werner, R.; Haase, W. *Chem. Phys. Lett.* **2000**, *328*, 188−196.
(9) Baudelet, F.; Pascarelli, S.; Mathon, O.; Itie, J. P.; Polian, A.; d'Astuto, M.; Chervin, J. C. *J. Phys.: Condens. Matter* **2005**, *17*, S957−S966.
(10) Itie, J. P.; Baudelet, F.; Congeduti, A.; Couzinet, B.; Farges, F.; Polian, A. *J. Phys.: Condens. Matter* **2005**, *17*, S883−S888.
(11) Frank, P.; Carlson, R. M. K.; Carlson, E. J.; Hodgson, K. O. *Coord. Chem. Rev.* **2003**, *237*, 31−39.
(12) Flogeac, K.; Guillon, E.; Aplincourt, M. *Eur. J. Inorg. Chem.* **2005**, 1552−1558.
(13) Jezowska-Bojczuk, M.; Szczepanik, W.; Mangani, S.; Gaggelli, E.; Gaggelli, N.; Valensin, G. *Eur. J. Inorg. Chem.* **2005**, 3063−3071.
(14) Benfatto, M.; Congiu-Castellano, A.; Daniele, A.; Longa, S. D. *J Synchrotron Radiat.* **2001**, *8*, 267−269.
(15) Tyson, T. A.; Hodgson, K. O.; Natoli, C. R.; Benfatto, M. *Phys. Rev. B* **1992**, *46*, 5997−6019.
(16) Gawelda, W.; Johnson, M.; de Groot, F. M. F.; Abela, R.; Bressler, C.; Chergui, M. *J. Am. Chem. Soc.* **2006**, *128*, 5001−5009.
(17) Cannizzo, A.; van Mourik, F.; Gawelda, W.; Zgrablic, G.; Bressler, C.; Chergui, M. *Angew. Chem., Int. Ed.* **2006**, *45*, 3174−3176.
(18) de Groot, F. *Coord. Chem. Rev.* **2005**, *249*, 31−63.
(19) Benfatto, M.; D'Angelo, P.; Della Longa, S.; Pavel, N. V. *Phys. Rev. B* **2002**, *65*, 174205.
(20) Della Longa, S.; Arcovito, A.; Girasole, M.; Hazemann, J. L.; Benfatto, M. *Phys. Rev. Lett.* **2001**, *8715*, 155501.
(21) Benfatto, M.; Della Longa, S.; D'Angelo, P. *Phys. Scr.* **2005**, *T115*, 28.
(22) D'Angelo, P.; Benfatto, M.; Della Longa, S.; Pavel, N. V. *Phys. Rev. B* **2002**, *66*, 064209.
(23) Hayakawa, K.; Hatada, K.; D'Angelo, P.; Della Longa, S.; Natoli, C. R.; Benfatto, M. *J. Am. Chem. Soc.* **2004**, *126*, 15618−15623.
(24) Kimball, G. E.; Shortley, G. H. *Phys. Rev.* **1934**, *45*, 815.
(25) Joly, Y. *Phys. Rev. B* **2001**, *63*, article no. 125120.
(26) Rillema, D. P.; Jones, D. S.; Levy, H. A. *J. Chem. Soc., Chem. Comm.* **1979**, 849−851.
(27) Biner, M.; Bürgi, H. B.; Ludi, A.; Röhr, C. *J. Am. Chem. Soc.* **1992**, *114*, 5197−5203.
(28) Natoli, C. R.; Benfatto, M.; Doniach, S. *Phys. Rev. A* **1986**, *34*, 4682−4694.
(29) Foulis, D. L.; Pettifer, R. F.; Sherwood, P. *Europhys. Lett.* **1995**, *29*, 647−652.
(30) Cabaret, D.; Joly, Y.; Renevier, H.; Natoli, C. R. *J. Synchrotron Radiat.* **1999**, *6*, 258−260.
(31) Krause, M. O.; Oliver, J. H. *J. Phys. Chem. Ref. Data* **1979**, *8*, 329−338.
(32) Sham, T. K. *J. Am. Chem. Soc.* **1983**, *105*, 2269−2273.

Appendix B

Experimental Setup for Time-Resolved XAS at the ALS

This appendix includes a copy of an article published in the *Review of Scientific Instruments*, which describes the experimental details of our detection setup, used at beamline BL 5.3.1. at the ALS, Berkeley, USA. A reprint of this publication can be obtained from the electronic edition of the journal using the reference: M. Saes, F. van Mourik, W. Gawelda, M. Kaiser, M. Chergui, C. Bressler, D. Grolimund, R. Abela, T. E. Glover, P. A. Heimann, R. W. Schoenlein, S. L. Johnson, A. M. Lindenberg and R. W. Falcone, *Rev. Sci. Instrum.*, **75**(2004) 24-30.

REVIEW OF SCIENTIFIC INSTRUMENTS VOLUME 75, NUMBER 1 JANUARY 2004

A setup for ultrafast time-resolved x-ray absorption spectroscopy

Melanie Saes,[a] Frank van Mourik, Wojciech Gawelda, Maik Kaiser, Majed Chergui, and Christian Bressler[b]
Université de Lausanne, IPMC-BSP, CH-1015 Lausanne-Dorigny, Switzerland

Daniel Grolimund
Nuclear Energy and Safety Research Department, Paul Scherrer Institut, CH-5232 Villigen-PSI, Switzerland

Rafael Abela
Swiss Light Source, CH-5232 Villigen-PSI, Switzerland

Thornton E. Glover, Philip A. Heimann, and Robert W. Schoenlein
Material Science Division, Advanced Light Source, Lawrence Berkeley National Laboratories, 1 Cyclotron Road, Berkeley, California 94720

Steven L. Johnson,[c] Aaron M. Lindenberg, and Roger W. Falcone
Department of Physics, 366 LeConte Hall, University of California, Berkeley, California 94720

(Received 17 July 2003; accepted 14 October 2003)

We present a setup which allows the measurement of time-resolved x-ray absorption spectra with picosecond temporal resolution on liquid samples at the Advanced Light Source at Lawrence Berkeley National Laboratories. The temporal resolution is limited by the pulse width of the synchrotron source. We characterize the different sources of noise that limit the experiment and present a single-pulse detection scheme. © *2004 American Institute of Physics.*
[DOI: 10.1063/1.1633003]

I. INTRODUCTION

Ultrafast (femtosecond to picosecond) spectroscopy allows a better understanding of the possible pathways/mechanisms of chemical reactions.[1] In a pump–probe experiment, which is a typical scheme for ultrafast spectroscopy, the pump pulse triggers a chemical reaction and the probe pulse takes a snapshot of the ongoing reaction at a fixed time delay. By changing the time delay between pump and probe pulse, one can observe the development of the photoinduced reaction. A complete description of chemical dynamics ideally requires, besides ultrafast temporal resolution, a spatial resolution on the atomic scale. Furthermore, since many elementary reactions in chemistry and biology take place in a solvent environment, structural techniques, which can be implemented on solvated samples, are very desirable.

One method, which provides temporal resolution in the picosecond/femtosecond domain with atomic scale spatial resolution, is ultrafast time-resolved x-ray absorption spectroscopy (XAS). In this type of pump–probe experiment, the probe pulse consists of an x-ray pulse, while an ultrashort laser pulse triggers the reaction. The x-ray probe yields information on the oxidation state of an atom of interest and on the unoccupied valence states via x-ray absorption near-edge structure spectroscopy and information on the local molecular structure around an atom of interest via extended x-ray absorption fine structure (EXAFS).[2]

Only a few fast and ultrafast time-resolved XAS measurements have been carried out so far.[3–7] The x-ray sources used in these studies were either laser driven plasma sources[3] or synchrotrons.[4–7] These experiments generally suffer from the small signals typical of laser-induced changes to x-ray absorption spectra.[8] Moreover, the photon flux of the x-ray source is a major limiting factor for the signal-to-noise ratio of the experiment. In the following, we limit our considerations to synchrotron radiation, which is currently the brightest and most stable and reliable source of tuneable hard x rays.

We report on a setup realized at beamline 5.3.1 at the Advanced Light Source (ALS) at Lawrence Berkeley National Laboratories. The focus will be on the single-pulse detection scheme that we use in our x-ray transmission measurements, which makes it possible to isolate and characterize the different noise sources that potentially limit the experiment. The data obtained allow us to evaluate the feasibility of future experiments.

II. INSTRUMENTS AND METHOD

Figure 1 displays the main elements required for a picosecond (ps) time-resolved x-ray absorption experiment at a synchrotron. The different components consisting of x-ray source, beamline, laser system, and data acquisition will be described in the following.

A. X-ray source

Synchrotrons sources provide typically 50–100 ps long pulses of polychromatic radiation. The repetition rate of the pulses depends on the filling pattern of the storage ring and its revolution frequency. At the ALS storage ring, which has a revolution frequency of 1.52 MHz, we make use of the

[a]Also at: Swiss Light Source, CH-5232 Villigen-PSI, Switzerland.
[b]Author to whom correspondence should be addressed; electronic mail: christian.bressler@ipmc.unil.ch
[c]Current address: Swiss Light Source, CH-5232 Villigen-PSI, Switzerland.

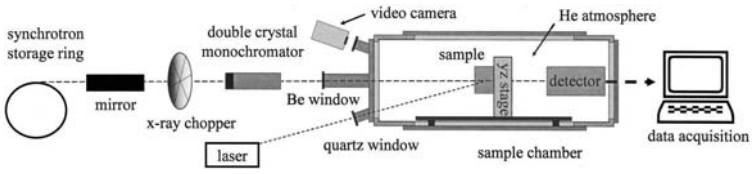

FIG. 1. Schematic setup for a laser-pump x-ray-probe experiment. X rays from a synchrotron are guided through a beamline into the sample chamber where they overlap with synchronized laser pulses at the sample position. The laser pulses excite the sample, while the x xrays probe pulses the photoinduced changes. A detection scheme in transmission mode records the x-ray pulse intensities.

''camshaft mode'' operation, shown in Fig. 2. In this mode, the ring is filled with 276 electron bunches separated by 2 ns, each contributing 1.4 mA to the overall ring current. One isolated bunch, which contributes 10 mA, is placed within the 100 ns empty section of the ring. We will refer to the 276 closely packed bunches as ''multibunch'' and the isolated bunch as the ''camshaft pulse.'' A modestly fast x-ray detector (e.g., large area avalanche photodiode) can single out the radiation from the camshaft pulse (Fig. 3), which is therefore a suitable probe pulse for the time-resolved experiment. Note that the time-resolved experiment uses only a fraction of the available flux. The multibunch is completely ignored and, in addition, the repetition rate of the experiment depends on the usually lower repetition rate of the laser system. We use an amplified femtosecond laser system which delivers intense and ultrashort pump pulses at a repetition rate of 1 kHz. Thus, the useful flux of the synchrotron is reduced by a factor of 10^5, which makes it, compared to the laser pump pulse (10^{15} photons), a weak probe pulse (10^4 photons).

B. Advanced Light Source beamline 5.3.1

Beamline 5.3.1 is a bend magnet beamline designed for various time-resolved experiments. The radiation is collected under a 5 mrad grazing incidence angle by a toroidal platinum-coated mirror, which provides a 1:1 double focus 24 m from the source. The focus images the electron-beam source, approximately 50 μm (vertical)$\times$250 μm (horizontal). A Ge(111) double monochromator with fixed output beam height (which is located 2 m upstream from the focus) selects monochromatic x rays from 2.2 keV to 12 keV with an energy resolution of $\Delta E/E=3\times10^{-4}$ to 1×10^{-3} bandwidth, respectively (with E being photon energy). A mechanical chopper placed before the monochromator cuts out an average of 95% of the x-ray flux to reduce the overall heatload on the first monochromator crystal. Details of the beamline setup are given in Ref. 9.

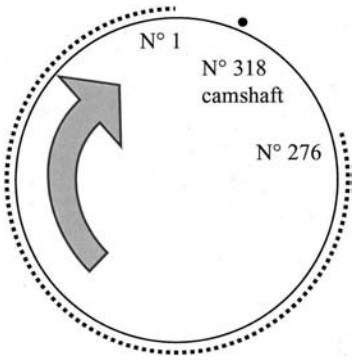

FIG. 2. Electron filling pattern used in our experiments at the ALS. In total, there are 328 possible electron buckets. In the camshaft mode at the ALS buckets 1 to 276 are filled and a single pulse, the camshaft pulse, is placed in the gap between the empty buckets 277 and 328 (typically bucket No. 318).

C. Sample chamber

The x rays enter the sample chamber (Fig. 1) through a 50 μm thick beryllium window. The window separates the ultrahigh vacuum of the beamline from the chamber, which is purged with helium at atmospheric pressure. The laser enters through a quartz window on the beamline side of the chamber. Another window allows the monitoring of the sample with a video camera. The sample (see below) is mounted on a motorized yz translation stage for adjusting its position within the x-ray beam. The x-ray detector is placed about 20 cm behind the sample for transmission signal measurements.

D. Sample

Our samples are liquid solutions. A sapphire nozzle creates a thin, flat jet at the point where x ray and laser beams overlap, as indicated in Fig. 4. We typically choose a nozzle so as to obtain a thickness of the jet of 100–500 μm, depending on the experiment.[8] The liquid jet has a velocity of $\sim$5 m/s, which is fast enough to ensure the renewal of the sample at the repetition rate of the measurement. The liquid from the jet is caught and recycled by passing through a reservoir, also kept under a helium atmosphere.

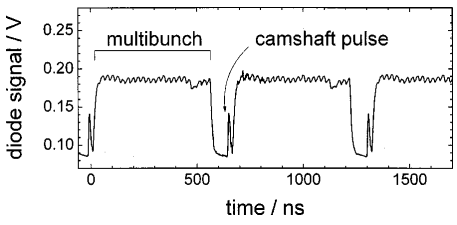

FIG. 3. Oscilloscope trace of the x-ray train recorded by a large area avalanche photodiode. Due to its slower response its signal on the multibunch train accumulates for $\sim$ ten bunches, which in return lets the much more intense single-camshaft pulse appear smaller in the figure.

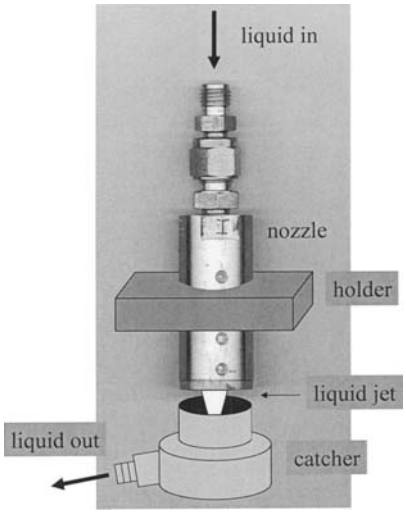

FIG. 4. Sapphire nozzle creating a thin liquid jet of the sample. The displacement of the sample is possible in the plane perpendicular to the incident x rays.

E. Laser source

High intensity laser pulses are needed to excite a significant fraction of the sample.[8,10] The laser pulse length should be similar to the x-ray probe length or shorter in order to keep the temporal resolution as high as possible. We use a Ti–sapphire-based amplified femtosecond laser system (Spectra-Physics) producing 150 fs pulses at 800 nm with a pulse energy of ~2 mJ at a repetition rate of 1 kHz. By second-harmonic generation in a BBO crystal ($12\times12\times0.5$ mm, type 1, $\theta=29°$, $\varphi=90°$), we typically obtain 500 μJ/pulse at 400 nm.

A pump–probe experiment relies on the reproducibility of the time delay between pump and probe pulses. Therefore, the laser has to be accurately synchronized to the x-ray source. The laser oscillator is synchronized to the 500 MHz radio frequency (rf) of the storage ring by adjusting the oscillator cavity length (and thus its frequency) proportionally to the phase error between the rf and the sixth-harmonic of the oscillator output.[11,12] The laser amplifier is synchronized to the revolution frequency of the storage ring and the opening window of the x-ray chopper. Thus, a seed pulse from the oscillator will be selected and amplified every millisecond, which coincides with a particular x-ray pulse (the camshaft pulse) on the sample.

The delay between x-ray and laser pulses can be adjusted in coarse steps of 12 ns by selecting different seed pulses from the laser oscillator. For finer tuning, a computer-controlled phase shifter (I.F. Engineering, model QPMX-499) is used to adjust the phase of the reference rf signal, which synchronizes the laser oscillator.[13] The jitter between laser and x-ray pulses was estimated to be less than 10 ps.[14] Typical values reported for the jitter between a laser oscillator and a synchrotron or free electron laser source are on the order of 1 ps or less.[11,12]

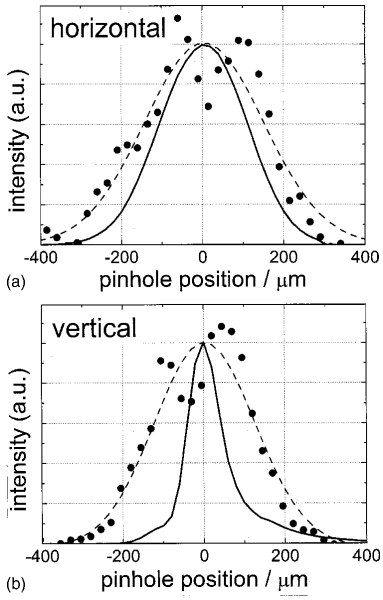

FIG. 5. X-ray (solid line) and laser beam profiles (dotted and dashed curves as fit) scanned through a 50 μm diameter pinhole.

F. Spatial overlap

The spatial overlap between x-ray and laser pulses is obtained by replacing the sample with a 50 μm diameter pinhole on a 25 μm thick tungsten substrate that is placed at the exact position of the jet. A two-dimensional translation stage (Fig. 1) moves the pinhole across the x-ray beam, while an x-ray transmission measurement maps out the beam profile. The pinhole is centered on the x-ray beam and the laser is then guided through the pinhole. The angle between laser and x-ray beam is about 15°. Figure 5 shows the vertical and horizontal beam profiles of the x-ray and the laser beams at the sample position. The x-ray beam size is vertically 100 μm and horizontally 260 μm. The laser spot has a circular shape and was adjusted in size to the horizontal diameter of the x-ray spot.

G. Temporal overlap

For setting the temporal overlap, we place a fast windowless photodiode (rise time ~0.7 ns) at the sample position and record both the laser and the x-ray pulses. Using a 1 GHz oscilloscope, we adjust the timing to within a few hundred picoseconds. During the experiment, the relative timing of camshaft and laser pulses is monitored constantly by simultaneously measuring the laser pulses and visible synchrotron pulses from another beamline at the same bend magnet.

For defining the temporal overlap more precisely, a pump–probe signal of a sample is used. A suitable sample to achieve this is $[Ru(bpy)_3]^{2+}$ in water. In this case, a signal is generated by a 400 nm pulse in a 0.1 mm thick free flow-

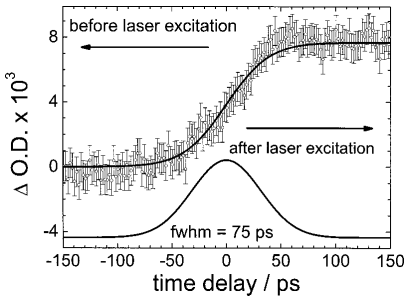

FIG. 6. Pump–probe signal of aqueous $[Ru^{II}(bpy)_3]^{2+}$ together with a fit as a function of pump–probe time delay. The onset of the photoinduced signal (<300 fs) is comparable to a step function; thus, the rise we measure is a convolution of the pump–probe effect with the width of the synchrotron pulse. The lower curve is the derivative of the fit curve (which yields a Gaussian) whose width corresponds to the cross-correlation signal, which is governed by the indicated x-ray pulse width.

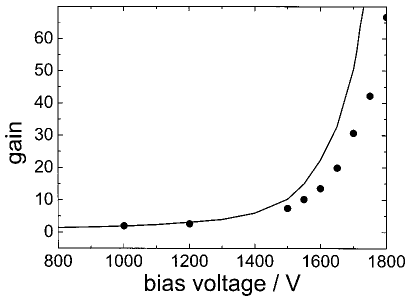

FIG. 7. APD gain curve for visible (line) and x-ray (dots) pulses. The lower gain for x-ray pulses is attributed to space-charge effects and local heating in the avalanche region of the detector.

ing water jet of 80 mM $[Ru(bpy)_3]^{2+}$. Upon excitation, the central ion of the compound changes its oxidation state according to

$$[Ru^{II}(bpy)_3]^{2+} + 400 \text{ nm} \rightarrow [Ru^{III}(bpy)_2(bpy)^-]^{2+}.$$

This product is created on a sub-ps time scale, and decays on a time scale of a few hundred ns.[15] On a ps time scale, the onset of the photoinduced reaction is comparable to a step function. Setting the monochromator to 2840 eV and monitoring the valence shift of the Ru L_3 edge as a function of pump–probe delay,[7] we obtain a pump–probe signal, which shows this step function convoluted with the x-ray probe pulse length. The scan, as shown in Fig. 6, yields a cross correlation time of 75 ± 10 ps, which includes the actual x-ray pulse width and the synchronization jitter. The accuracy of fitting the slope of the signal onset in Fig. 6 defines an upper limit for the synchronization jitter. The error bars represent the sum of all noise sources including the synchronization jitter in the region of the signal onset. Since the error bars on the plateaus before and after time zero have the same magnitude as the error bars in the signal onset, we conclude that the noise introduced by the jitter is not dominant. Therefore, with the given error bars, we can make an upper estimate for the synchronization jitter, which is ± 10 ps. Higher accumulation times should narrow down the error bars and allow a better estimate.

H. Detection/data acquisition

The detector is a windowless APD (Advanced Photonix, model 394-70-72-500). The Avalanche photodiode (APD) is mounted in a sealed metal box with a 15 μm thick beryllium window over the active area, which protects the diode from the intense scatter of the laser pulse. In addition, a 10 μm foil of mylar protects the beryllium window from the humidity created by the aqueous sample upon laser excitation. The rise time of the APD is 12 ns, which is sufficiently fast to measure the isolated camshaft pulse (Fig. 3).

In order to estimate the gain of the detector, we measured the output of the APD as a function of bias voltage under two different conditions:

(1) 80 fs pulses of 1.5 eV visible photons at 1 kHz pulse repetition rate, and
(2) 3000 eV x-ray photons from the camshaft pulse.

The curves are plotted in Fig. 7. They were normalized to the signal at low bias, corresponding to unit gain. The signals obtained with laser light are in excellent agreement with the curve provided by the manufacturer, over the whole range of bias settings.

The deviation at higher bias voltages between visible light and x-ray measurements has been reported before,[16,17] and was attributed to space-charge effects decreasing the electrical field in the avalanche region and local heating by the high-energy x-ray pulses. Whereas a visible photon produces only a single electron, an x-ray photon produces on the order of 1000 electrons in a very confined volume, which could locally cause a reduced gain. Note that due to the local nature of the effect, this need not give rise to an overall nonlinear response. As long as the x-ray photons are spread over a sufficiently large area of the detector, the electron pulses produced by different x-ray absorption events are independent of each other and only affect their own local gain. Therefore, the measured signal should still be proportional to the number of x-ray photons on the detector.

Indeed, the linear response of the APD (bias voltage 1750 V) was verified by measuring the signal from the camshaft pulse as a function of the camshaft current (data provided by the ALS), and both were found to be proportional (see Fig. 8). According to our measurements, the linearity of the detector is given to at least 13 000 photons per pulse detected within an estimated area of $150\ \mu m \times 600\ \mu m$. When carrying out this experiment at an undulator beamline, which has about 10–100 times larger pulse intensities, it may be necessary to move the detector further away from the x-ray focus, so as to make use of a bigger spot size on the detector.

Figure 9 introduces the detection scheme used at beamline 5.3.1. In the experiment, the detector signal was amplified by a factor of 5 in a fast preamplifier (Stanford Research

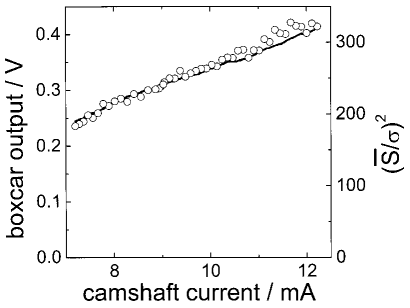

FIG. 8. The x-ray transmission signal (at 2840 eV) as given by the gated integrator output is plotted vs the camshaft current (line). The linearity between camshaft intensity and detector signal is apparent. The squared signal-to-noise ratio $(\overline{S}/\sigma)^2$ (dots) follows the same trend and indicates that the detection scheme is mainly limited by the shot noise of the x-ray source.

Systems, SR445). The amplified signal from the camshaft pulse was picked out using a gated integrator (Stanford Research Systems, SR250), and digitized using an analog-to-digital converter (National Instruments, PCI-6035E). In our experiment, the difference spectra are more important than the actual x-ray absorption spectra; therefore, we used the most simple detection scheme, using a single-x-ray detector without a reference detector before the sample. To get a difference signal, we detect the camshaft pulse at twice the repetition rate of the laser, so the detector alternately measures the excited and unexcited samples once. Because both signals are subtracted to give the difference signal, slow drifts in the detector or electronics are effectively eliminated. Simultaneously, with the APD signal, a reference signal from the laser trigger is digitized. This allows sorting out the laser-excited and unexcited transmission signals. An interesting side effect of this detection technique is its insensitivity to slow (minutes to hours) sample degradation. Because reference spectra are taken within short intervals of 500 μs, the difference signal induced by the photoexcitation will be unaffected, provided that the photodissociation products exhibit no additional photoinduced x-ray absorption changes.

There is an advantage in further increasing the repetition rate of the measurement to 4 kHz. There is no baseline drift on the difference spectra, but there is one for the individual excited and unexcited spectra. So, when we want to compare the height of the pump–probe effect to the absolute transmission signal to estimate the overall effect, it would be profitable to actually measure the magnitude of the baseline drift on a shot-to-shot basis. When measuring at four times the laser frequency (4 kHz), the 2 kHz x-ray chopper cuts out the x-ray flux for every second data point allowing the measurement of the zero offset. Thus, we measure the pump–probe signal with high precision as

$$\log \frac{I_{\text{unexcited}} - I^0_{\text{unexcited}}}{I_{\text{excited}} - I^0_{\text{excited}}}, \tag{1}$$

where I_{excited} and $I_{\text{unexcited}}$ are the transmission signals through the laser-illuminated and dark samples, respectively; I^0_{excited} and $I^0_{\text{unexcited}}$ are the corresponding zero offsets (without x rays). The transformation of the static transmission spectra into absorption spectra via

$$\log \frac{I_0}{I_{\text{unexcited}}} \tag{2}$$

is carried out more roughly by scanning the x-ray energy once with ($I_{\text{unexcited}}$) and once without (I_0) the sample in the beam.

During an energy or a time-delay scan, the data acquisition process is set to a halt until the new experimental conditions have settled, i.e., while the monochromator is moving or the laser timing is adjusted, no data are recorded.

In order to discriminate between electronic noise in our detection scheme and true fluctuations in the x-ray flux, we measured the pulse–height distribution of the APD output with and without x rays on the detector. The left-hand side curve in Fig. 10 shows the pulse–height distribution with the x-ray shutter closed, which gives a measure for the total electronic noise in our detection system. In this example, the distribution measured with a typical flux of x rays on the detector is about 20 times higher. If we make the reasonable assumption that the electronic noise is independent of the photon statistics, then the electronic noise in the x-ray mea-

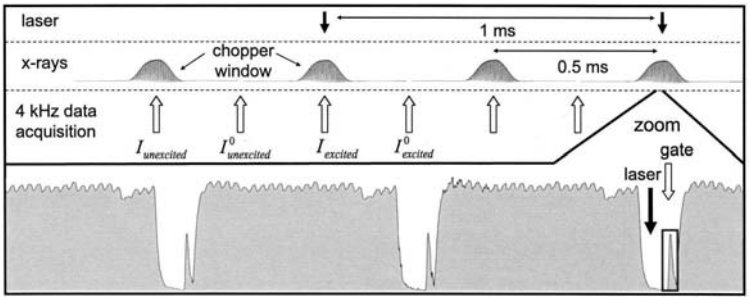

FIG. 9. 4 kHz-based setup for the data acquisition. The black arrows represent the 1 kHz repetition rate laser pump pulse. A 2 kHz chopper window (black, Gaussian features) allows x rays on the sample for every second detection gate. The white arrows represent the detection gate synchronized to the camshaft pulse. By reading out data within and without the chopper window, the absolute zero offset (I^0_{excited} and $I^0_{\text{unexcited}}$) can be measured. Every second chopper window coincides with a laser pulse (I_{excited}), while the other serves as a reference ($I_{\text{unexcited}}$). In this way, slow noise components on the data can be eliminated. In the lower part of the figure, we show a close-up view of the detection gate on the camshaft pulse with a preceding laser-pump pulse.

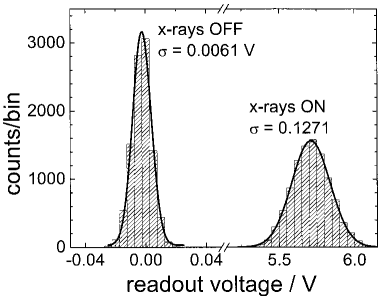

FIG. 10. Camshaft pulse–height distribution with x rays ON and OFF. The noise contribution from the setup (x-ray OFF) is negligible compared to the noise in the photon flux.

surement is negligible since the total noise is calculated from the square root of the sum of the squared standard deviations. In the case of the example in Fig. 10, reducing the electronic noise to zero would only reduce the overall noise from 0.1271 V to 0.1270 V. Note that the pulse–height distribution is very well described by a Gaussian distribution.

By measuring the noise in the photon flux as a function of the flux (Fig. 8), we find a square law dependence of the noise, which is characteristic for shot noise. For other sources of noise, e.g., noise entering through variations in the throughput of the beamline optics (due to vibrations), we would expect a deviation from the square law dependence. Therefore, we conclude that no other significant noise sources play a role, and that, consequently, our noise measurement should be a precise measure for the absolute photon flux.

We calculate the photon flux via the measurement of the pulse–height distribution and application of the equation:

$$\left(\frac{\overline{S}}{\sigma}\right)^2 = \text{photons/pulse}, \tag{3}$$

where $\overline{S}$ is the average signal of the pulse–height distribution and σ is the corresponding standard deviation. With a camshaft current of 4.6 mA at an x-ray energy of 2850 eV, we measured a standard deviation of 0.0374 V on a signal of 2.0209 V. For the shot-noise limited case, this corresponds to 2915 photons per pulse on the detector. Correction for the transmission of beryllium windows (total of 65 μm, $T=74\%$), helium (50 cm, $T=98\%$), and mylar (10 μm, $T=81\%$) and the normalization to 10 mA camshaft current yields 1.1×10^4 photons at the end of the beamline. This compares to 9×10^3 photons/pulse, which are the specifications of the beamline.[18] Thus, we can conclude that the absolute photon flux can be measured with our setup and that the measurements are indeed shot-noise limited.

With this arrangement, we can record the x-ray absorption spectrum of the transient species of $[Ru(bpy)_3]^{2+}$ in a pump–probe scheme (see Fig. 11 and Ref. 7). Figure 11(a) shows the static absorption spectrum around the ruthenium L_3 edge. Figure 11(b) presents the laser-induced absorption changes recorded at a fixed time delay of 60 ($\pm$10) ps. The detailed interpretation of the chemical processes, which are

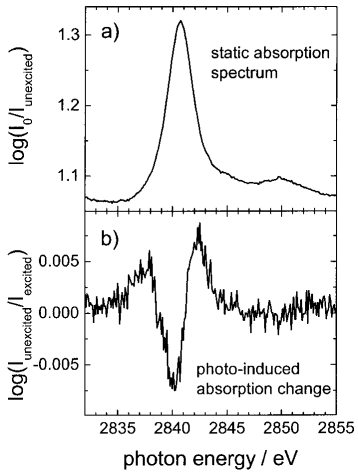

FIG. 11. (a) Static absorption spectrum of aqueous $[Ru(bpy)_3]^{2+}$ showing the Ru L_3 edge. (b) Laser-induced absorption changes recorded at a fixed delay of 60 ps (see Ref. 7 for details).

mirrored in the spectral changes, is given elsewhere.[7,10] Here, we focus on the evaluation of the detection sensitivity of our setup. The noise level on the difference spectrum corresponds to a detection sensitivity of 1 mOD, which allows the detection of the transient changes in the ruthenium sample with a signal-to-noise ratio of 10. The number of incident photons is 5×10^6 photons/data point, which corresponds to an integration over 2000 camshaft pulses per data point. The overall energy scan takes 15 min. This is a reasonable integration time over which the experimental parameters (e.g., synchronization and laser power) can easily be stabilized. The excitation yield of the sample is on the order of 10%.[7] By increasing the integration time, the sensitivity of the setup can be pushed down into the sub-mOD regime, which would allow the study of smaller pump–probe effects like measurements on dilute samples[10] or the study of molecular structural changes via EXAFS, as proposed earlier.[8]

III. DISCUSSION

We have developed a setup at a synchrotron radiation source, which is capable of monitoring laser-induced transient x-ray absorption with ps temporal resolution, and a sensitivity that allows the measurement of changes in x-ray absorption on the order of 1 mOD. The statistical analysis reveals that the noise in the x-ray probe signal is fully governed by the shot noise of the x-ray photon source.

The limiting factor of the temporal resolution of this setup is the duration of the synchrotron pulse. By exploiting the femtosecond-slicing technique,[19] which is now in commission at the ALS, and under construction at the Swiss Light Source (SLS), we could descend to the hundreds of femtosecond time domain. This way, the temporal resolution of our laser pump–x-ray probe experiment would improve by three orders of magnitude. The available flux from the slicing technique, as employed by the SLS, has been esti-

mated to deliver about 100–1000 photons/pulse to the beamline. Therefore, we envisage the possibility of performing our experiments with this source with a large gain in temporal resolution, at the expense of a moderate reduction in the signal-to-noise ratio.

ACKNOWLEDGMENTS

The authors would like to thank Dr. Alexander Tarnovsky, Dr. Bernhard Lang, Dr. Jan Helbing, Dr. Philip Pattison, Dr. Marc Hertlein, Dr. Ali Belkacem, Dr. Inuk Kang, and Dr. Thomas Missalla for their help in this project. This work was financed by the FNRS via Contract Nos. 620-66145.01 and 2000-067912-02/1, by the *Swiss Light Source*, by the *Advanced Light Source* via DOE Contract No. DE-AC03-76SF00098, and by the University of Lausanne.

[1] *Femtochemistry and Femtobiology: Ultrafast Dynamics in Molecular Science*, edited by A. Douhal and J. Santamaria (World Scientific, Singapore, 2002).
[2] *X-ray Absorption Spectroscopy*, edited by D. C. Koeningsberger and R. Prins (Wiley, New York, 1988).
[3] F. R. Raksi, K. R. Wilson, Z. Jiang, A. Ikhlef, C. Y. Cote, and J.-C. Kieffer, J. Chem. Phys. **104**, 6066 (1996).
[4] L. X. Chen, W. J. H. Jäger, G. Jennings, D. J. Gosztola, A. Munkholm, and J. P. Hessler, Science **292**, 262 (2001).
[5] L. X. Chen, G. B. Shaw, I. Novozhilova, T. Liu, G. Jennings, K. Attenkofer, G. J. Meyer, and P. Coppens, J. Am. Chem. Soc. **125**, 7022 (2003).
[6] B. W. Adams, M. F. DeCamp, E. M. Dufresne, and D. A. Reis, Rev. Sci. Instrum. **73**, 4150 (2002).
[7] M. Saes, C. Bressler, R. Abela, D. Grolimund, S. L. Johnson, P. A. Heimann, and M. Chergui, Phys. Rev. Lett. **90**, 047403 (2003).
[8] C. Bressler, M. Saes, M. Chergui, D. Grolimund, R. Abela, and P. Pattison, J. Chem. Phys. **116**, 2955 (2002).
[9] P. A. Heimann, A. M. Lindenberg, I. Kang, S. L. Johnson, T. Missalla, Z. Chang, R. W. Falcone, R. W. Schoenlein, T. E. Glover, and H. A. Padmore, Nucl. Instrum. Methods Phys. Res. A **467**, 986 (2001).
[10] M. Saes, W. Gawelda, M. Kaiser, A. N. Tarnovsky, C. Bressler, M. Chergui, S. L. Johnson, D. Grolimund, and R. Abela, Synchrotron Radiat. News **16**, 12 (2003).
[11] M. J. W. Rodwell, D. M. Bloom, and K. J. Weingarten, IEEE J. Quantum Electron. **25**, 817 (1989).
[12] G. M. H. Knippels, M. J. van de Pol, H. P. M. Pellemans, P. C. M. Planken, and A. F. G. van der Meer, Opt. Lett. **23**, 1754 (1998).
[13] S. L. Johnson, Ph.D. thesis, University of California, Berkeley, 2002.
[14] A. M. Lindenberg, Ph.D. thesis, University of California, Berkeley, 2001.
[15] N. H. Damrauer, G. Cerullo, A. Yeh, T. R. Boussie, C. V. Shank, and J. K. McCusker, Science **275**, 54 (1997).
[16] M. Moszynski, M. Szawlowski, M. Kapusta, M. Balcerzyk, and D. Wolski, IEEE Trans. Nucl. Sci. **47**, 1297 (2000).
[17] E. M. Gullikson, E. Gramsch, and M. Szawlowski, Appl. Opt. **34**, 4662 (1995).
[18] T. E. Glover, P. A. Heimann, and R. W. Schoenlein, Advanced Light Source, Lawrence Berkeley National Laboratories, Berkeley, California Internal Report, ''Beamline 5.3.1 Spectrally-Resolved Flux'' (March 2002).
[19] R. W. Schoenlein, S. Chattopadhyay, H. H. W. Chong, T. E. Glover, P. A. Heimann, C. V. Shank, A. A. Zholents, and M. S. Zolotorev, Science **287**, 2237 (2000).

Appendix C

High-Spin Fractional Population Measurements

C.1 Introduction

According to Eq. 6.1 (Chapter 6), the correct extraction of the excited state HS absorption spectrum necessitates an accurate estimation of photolysis yield value $f(t)$ [27,36]. This parameter determines the excited state fraction present in the sample after the photoexcitation and allows correct superposition of ground and transient spectra. As shown in Section 6.2.3, in case of $[Fe^{II}(bpy)_3]^{2+}$, we have estimated this in two independent ways: a) in separate laser-only transient absorption experiments under identical experimental conditions as at the synchrotron (Section 6.1.6) and b) by comparing and analyzing simultaneously detected transmission and fluorescence yield signals assuming their pulse height distributions are shot-noise limited (Section 4.9.2). This novel approach allowed estimating the lower limit of $f(t)$. The derived quantitative correlations, in terms of the number of absorbed x-ray photons with those that were detected in x-ray fluorescence process, between transmission and fluorescence signals agreed very well within a factor of two (the strongest deviation in the case of the highest concentration). The results delivered the lowest concentration of the photoexcited HS state fraction contributing to the detected transient x-ray signal at a given energy. In the present study, we have investigated the aqueous samples of $[Fe^{II}(bpy)_3]^{2+}$ in a wide range of concentrations of 1-100 mM, for which we have recorded absorption edge spectra (only the first 50 eV around the inflection point) in order to examine the concentration dependence and estimate the experimental sensitivity of our fluorescence detection. The x-ray results will be compared to the results obtain in all-optical transient absorption measurements at the corresponding time delay $\Delta\tau$=50 ps in a broad range of excitation fluences up to 1 J/cm^2.

C.2 Low Concentration Samples

In Fig. C.1, we present the results of the optical measurements of the LS state photolysis yield in 1mM solution of $[Fe^{II}(bpy)_3]^{2+}$ upon the excitation fluence up to 0.7 J/cm^2. As mentioned earlier (Section 6.1.6), at the time delay of 50 ps following photoexcitation, the observed dynamics in a laser-only transient absorption experiment can be solely attributed to the disappearance of the ground state LS complex and its ultrafast conversion into the HS excited state complex.

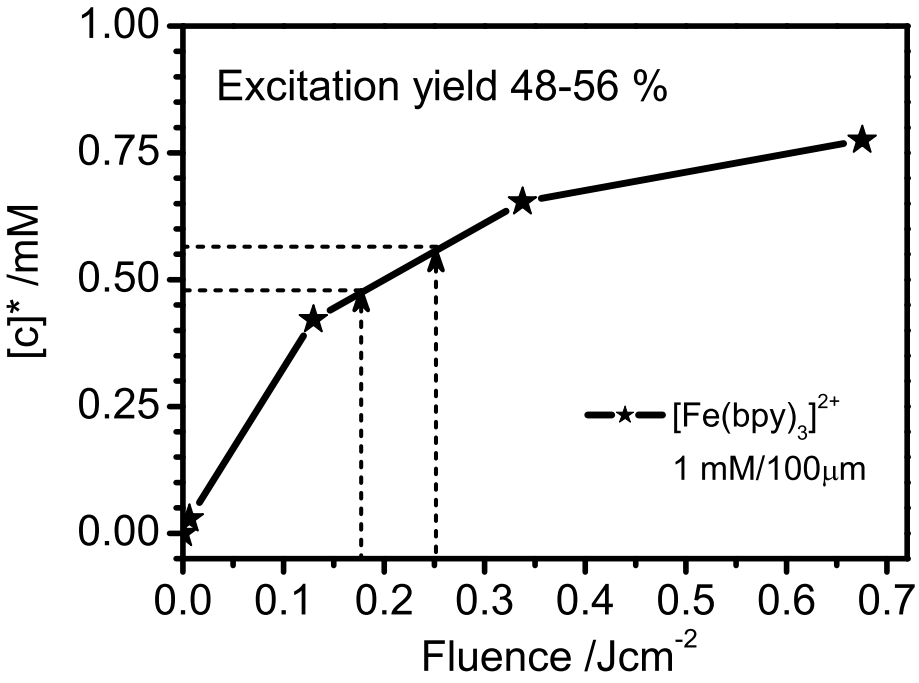

Figure C.1: Power dependence studies of a 1 mM aqueous solution of $[Fe^{II}(bpy)_3]^{2+}$ by means of femtosecond optical transient absorption spectroscopy. The excitation wavelength equals to λ_{pump}=400 nm and the probe wavelength covers a broad spectral range from 350-640 nm. In agreement with the conclusions of Section 6.1.6, the GSB magnitude (523 nm) at 50 ps time delay, reflects the decay of the HS state (and thus repopulation of the ground state). Give the unit quantum yield of the HS photoexcitation, the plotted GSB magnitude at different fluences can be directly linked to the excited state population of the HS state.

Therefore, at this time delay, we can follow the GSB magnitude as a function of incident pump fluence (as shows Fig. C.1) and link directly the bleached concentration to the newly formed excited state species (assuming unit quantum yield as reported in Ref. [162]. The vertical dashed arrows in Fig. C.1 indicate the excitation fluence region used in the x-ray studies. We deduce that upon 0.18-0.25 J/cm2 excitation we obtain ca. 0.5-0.6 mM of the excited state HS species, which corresponds to ca. 52(4)% photolysis yield.

The corresponding x-ray measurement is depicted in Fig. C.2.

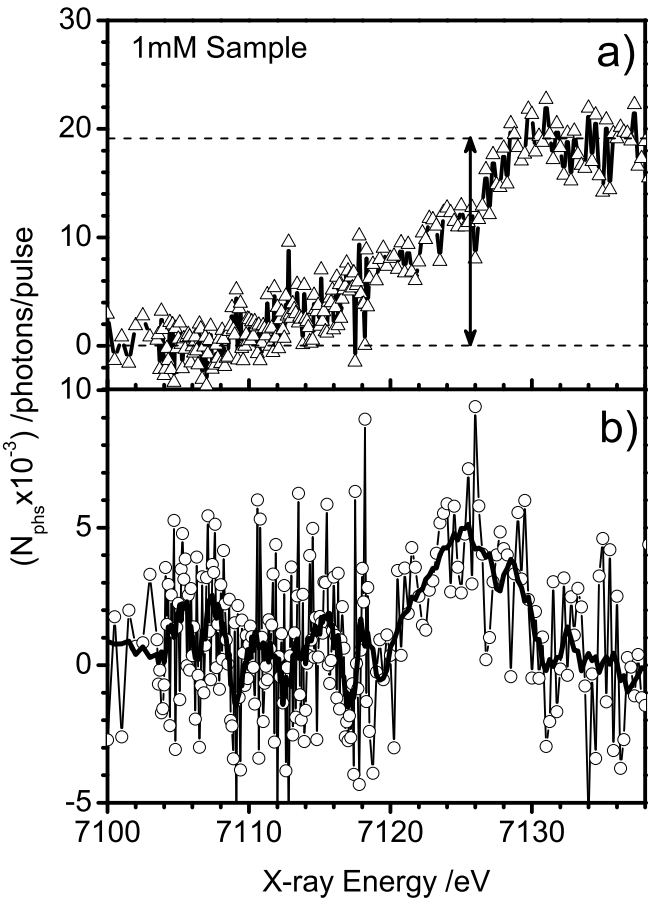

Figure C.2: (a) Static XAS signal of the K-edge of 1 mM aqueous sample of$[Fe^{II}(bpy)_3]^{2+}$, measured in fluorescence mode. The energy region was limited to the first 50 eV in the vicinity of the absorption edge (7122.5 eV). The absorption intensity is expressed in photons/pulse, via Eq. 4.6. The vertical arrow indicates the total sinal increase above the absorption edge (7130 eV). In (b) the corresponding transient XAS spectrum is plotted in the same energy range and the ordinate axis, similarly to (a), displayed the number of photons, which contributed to the transient difference spectrum.

In panel (a), the K-edge absorption spectrum of 1mM sample of $[Fe^{II}(bpy)_3]^{2+}$ is plotted in the 7100-7140 eV range. The lower panel shows the corresponding transient ΔA(E,t=50 ps) spectrum recorded in the same energy range. Note that the ordinate axis of both plots indicates the recorded intensity in a number of photons N_{phs} per single x-ray pulse. As explained in Chapter 4 (Section 4.9.2), our detection sensitivity allows us extracting with a high accuracy the number of detected photons due to the absence of any additional noise sources in our measurements, except the shot-noise of the x-ray photon beam. The dashed lines in Fig. C.2a indicate the absorption jump between 7100-7130 eV. Note that the most pronounced changes in the transient spectrum occur around ∼7126 eV (B resonance), so at nearly half of the absorption jump. In Table C.1, the summary of the most relevant parameters used in the further analysis is found.

Energy /eV	N_{phs}^{LS} /photons/pulse	$N_{phs}^{\Delta A}$ /photons/pulse	f(t)($[c]_{HS}$) /%(/mM)
7125-7126	0.01	0.004-0.005	≥40-50(≥0.4-0.5)
7131	0.02	-	-

Table C.1: The summary of the parameters obtained from Fig. C.2 at selected x-ray energies.

Using these values we can estimate that we have excited at least 40-50% of the LS molecules meaning we have photoexcited 0.4-0.5 mM of the excited state. The excitation yield estimated in this short energy range represents only the lower limit of the accessed photolysis yield and need to be correlated with the optical measurement (see Fig. C.1). From these we have estimated the excited state concentration $[c]_{HS}$=0.5-0.6 mM, which, ≥ 0.4-0.5 mM, as included in Table C.1. Unfortunately, at such low concentrations, the transmitted beam intensity is basically unchanged with respect to the incident intensity. According to Lambert-Beer law (Eq. 3.16 in Section 3.10), we can calculate the theoretical value of the expected absorption edge jump in a 1mM sample, which amounts to 0.064% ($6.4{\cdot}10^{-4}$). Assuming the incident intensity to vary between 3000 photons/pulse, it would imply that ca. 1.9 photons/pulse would contribute to the absorption edge jump and thus would stimulate the x-ray fluorescence process. Therefore, including the fluorescence quantum yield and solid angle losses ($1{\cdot}10^{-2}$ in total), we would expect to detect 0.019 photons/pulse contributing to the absorption edge in fluorescence yield signal. We detect ca. 0.02 photons/pulse at 7130 eV, which is in excellent agreement with the theoretically estimated value.

Similar analysis was applied to a more concentrated sample of $[Fe^{II}(bpy)_3]^{2+}$. Still in the low-concentration limit, we have investigated a 6mM solution and the corresponding results are summarized in Figs. C.3 and C.4. In Fig. C.3, a photolysis yield study in the excitation fluence range between up to 0.95 J/cm^2 is shown for a 10.5 mM sample flown in 200 μm jet, which implies identical optical densities (OD=0.584) of both sample at the excitation wavelength.

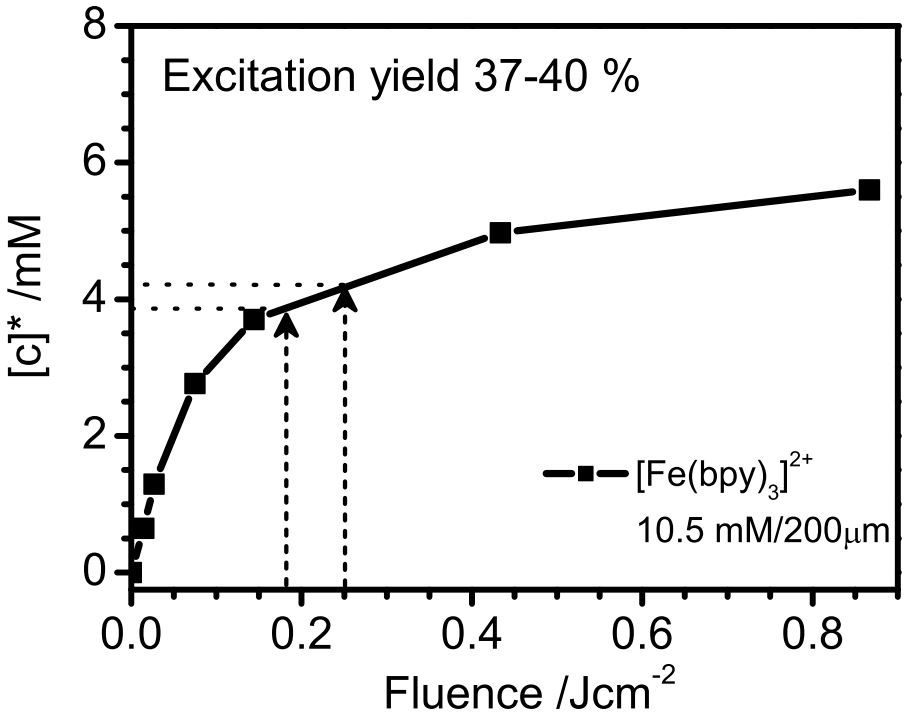

Figure C.3: Power dependence studies of a 10 mM aqueous solution of $[Fe^{II}(bpy)_3]^{2+}$ by means of femtosecond optical transient absorption spectroscopy, analogously to the results shown in Fig. C.1. The excitation and probe conditions in the experiment were identical to the previous case (1 mM sample). Similarly, the plot shows the GSB magnitude (523 nm) at 50 ps time delay as a function of the excitation fluence, which is directly related to the excited state concentration $[c_{HS}]$ of the HS state.

Figure C.4 illustrates the x-ray results in the absorption edge region of the same sample. Here, panel (a) shows he transient transmission signal recorded in the 7100-7140 eV range, whereas panel (b) shows both the static XAS and the corresponding transient XAS signals, both recorded in fluorescence mode and normalized to the edge jump (see dashed lines in Fig. C.4b).In Fig. C.4a, the ordinate axis indicates the transmission changes in 10^{-2} %. The signal intensity in Fig C.4b is expressed again in N_{phs}/pulse. In Table C.2, the resulted parameters are shown. In a similar way, the estimated excitation yield is $\geq$60%, which translates into ca. 3.6 mM of the HS excited state complex.

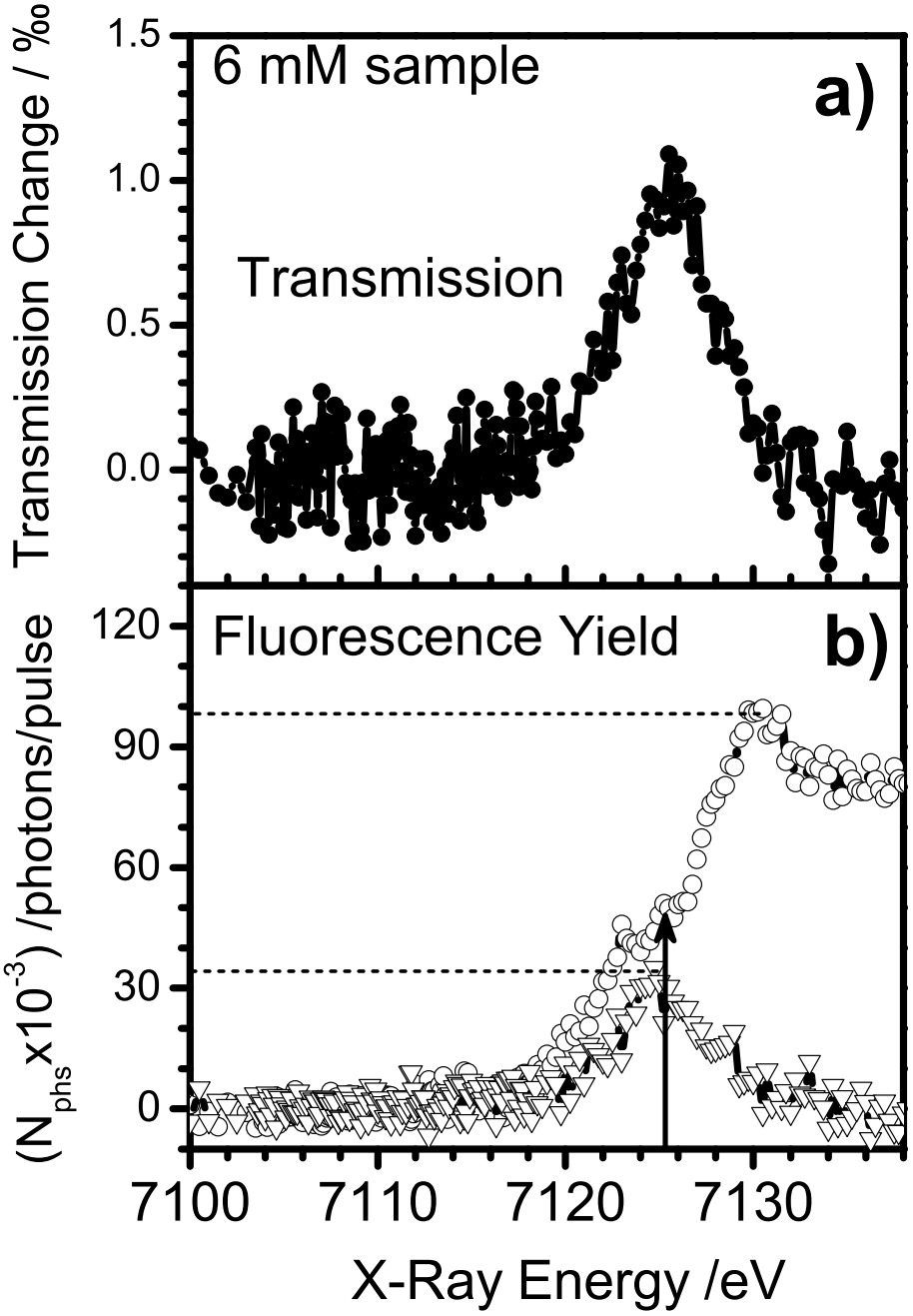

Figure C.4: (a) Transient transmission XAS signal of the K-edge of 6 mM aqueous sample of$[Fe^{II}(bpy)_3]^{2+}$. (b) Static (∘) and transient (▽) XAS signals of the same sample (6 mM) measured in fluorescence mode. In both (a) and (b), the energy region was identical as in Fig. C.2. Similarly, the signal magnitude is given in photons/pulse (Eq. 4.6). The vertical arrow indicates the energy, at which the most pronounce change in the transient XAS signal is observed (7126 eV). The parameters obtained from both (a) and (b) and used in the analysis are quoted in Table C.2

From optical spectroscopy (Fig. C.3) we derive the same concentration to lie in 3.8-4.5 mM range, which show again very good agreement ($f(t)^{optical} \geq f(t)^{x-ray}$) Here, an additional column includes the measured amplitude of

Energy /eV	N_{phs}^{LS} /photons/pulse	$N_{phs}^{\Delta A}$ /photons/pulse	f(t)($[c]_{HS}$) /%(/mM)	ΔT /10^{-2} %
7125-7126	0.05	0.03	$\geq$60($\geq$3.6)	1-1.1
7131	0.1	-	-	-

Table C.2: The summary of the parameters obtained from Fig. C.4 at selected x-ray energies.

transmission changes ΔT (Fig. C.4a) at 7125 eV (Fig. 28a). The calculated transmission change at the absorption edge amounts to ca. 0.384%, which translates into 0.115 photons/pulse assuming identical incident flux as in 1mM case. As can be seen in Fig. C.4b, the measured value at 7130 eV agrees with the theoretical value within 15%. On the hand, the transient transmission change recorded for 6mM sample is equal to 10^{-2} %. Assuming the lower limit for f(t)$\geq$60 %, we can calculate back the absorption edge change. The results yield $1.83 \cdot 10^{-2}$ % and $3.67 \cdot 10^{-2}$ % at 7125 eV and 7130 eV, respectively, which agrees within 5% with the change estimated from the Lambert-Beer law ($3.84 \cdot 10^{-2}$ %).

C.3 High Concentration Samples

We also carried out the same analysis as before on high concentrated samples of 25 mM and 100 mM. The optical and x-ray results for 25mM sample of $[Fe^{II}(bpy)_3]^{2+}$ are shown in Figs. C.5 and C.6. The optical spectroscopy in the 0.18-0.25 J/cm^2 fluence range delivered the excited state concentration $[c]_{HS}$=6-7.5 mM at 50 ps time delay following photoexcitation. This number corresponds to ca. 33$\pm$3.5 % for the photolysis yield in the investigated fluence range.

The x-ray fluorescence results are presented in Fig. C.6. At this sample concentration, all of the experimental results presented so far in Section 6.2 were recorded. Here, similarly to Fig. C.4, we will compare both the transmission and fluorescence signals recorded simultaneously in the 7100-7140 eV energy range. According to Fig. C.6, the fluorescence measurement at this concentration delivered ca. 0.51 photons/pulse at 7130 eV and 0.25 photons/pulse at 7125 eV, respectively. Analogously, the transmission signal, presented in Fig. C.6, delivered ca. $1.6 \cdot 10^{-2}$ % transmission change.

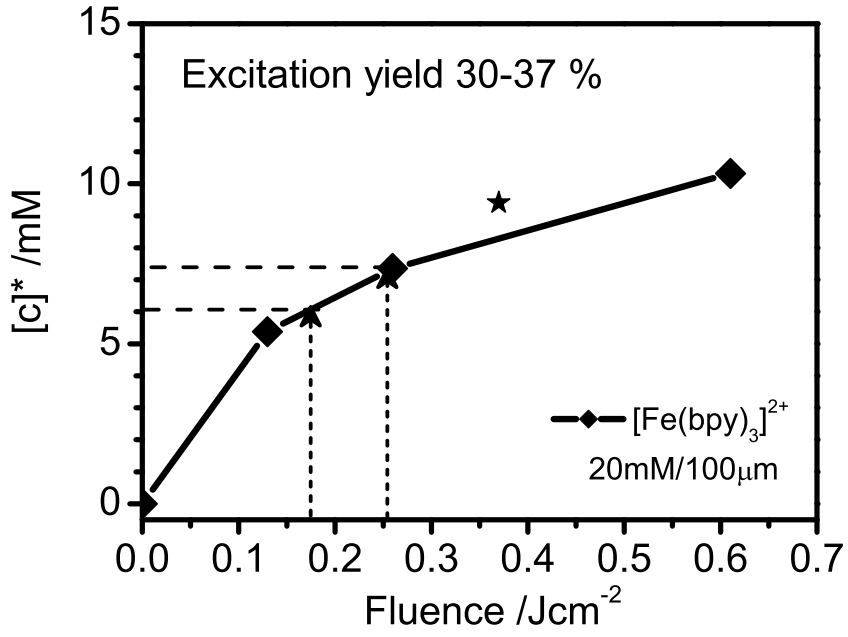

Figure C.5: Power dependence studies of a 20 mM aqueous solution of $[Fe^{II}(bpy)_3]^{2+}$ by means of femtosecond optical transient absorption spectroscopy (compare to Figs. C.1 and C.3). The plot shows the GSB magnitude (523 nm) at 50 ps time delay as a function of the excitation fluence, which is directly related to the excited state concentration $[c_{HS}]$ of the HS state.

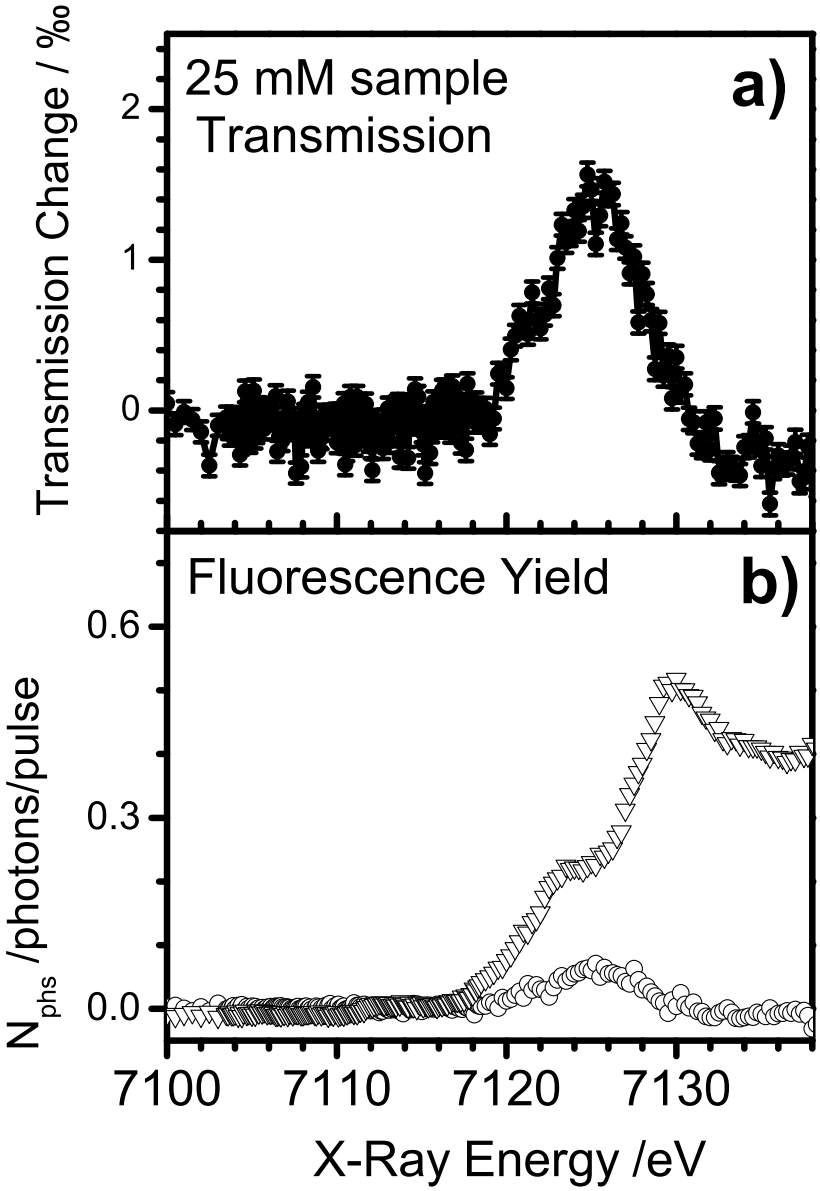

Figure C.6: (a) Transient transmission XAS signal of the K-edge of 25 mM aqueous sample of$[Fe^{II}(bpy)_3]^{2+}$ (see Figs 6.20 and 6.22). (b) Static (∘) and transient (▽) XAS signals of the same sample (25 mM) measured in fluorescence mode. In both (a) and (b), the energy region was identical as in Fig. C.2. Similarly, the signal magnitude is given in photons/pulse (Eq. 4.6). The signal magnitudes obtained from both (a) and (b) and used in the analysis are quoted in Table C.3

These numbers, compared to the transient change value (0.055-0.06 photons/pulse), deliver the lower limit for the f(t)≥22-24 % and are summarized in Table C.3.

Energy /eV	N_{phs}^{LS} /photons/pulse	$N_{phs}^{\Delta A}$ /photons/pulse	f(t)($[c]_{HS}$) /%(/mM)	ΔT $/10^{-2}$ %
7125-7126	0.25	0.055-0.06	≥22-24(≥5.5-6)	1.6-1.7
7131	0.5	-	-	-

Table C.3: The summary of the parameters obtained from Fig. C.6 at selected x-ray energies.

Similarly to previous cases (1-6 mM), we note a very close agreement between the x-ray-derived and optically-derived concentrations. For the x-ray measurements (Fig. C.6a and C.6b), we noticed the uncertainty in the initial concentration of the sample (between 25-30 mM). Therefore we can assume it to be 27.5±2.5 mM. In this case, the average excited state concentration is equal to 6.35±0.85 mM, which corresponds to 23< pm1%. Even at concentrations above 25 mM, the transmission signal originating from the absorption edge remained invisible. The expected transmission change in the case of 25 mM sample amounts to only 1.5-1.9 % (25-30 mM). Assuming 1.7% to be the average signal due to the absorption edge and 22-24% the excitation yield, we would estimate the transient transmission signal to ca. 0.19-0.2 %. In Fig. C.6a, we can confirm that the measured transmission signal amounted to 0.16-0.17 %, which remarkably agrees with the theoretical value within 15 %. Assuming the estimated photolysis yield, we would expect that only about 50 photons out of incident 3000 photons would contribute to the measured absorption edge. This in turn delivers ca. 0.5 photons/pulse measured at 7130 eV (Fig. C.6b) According to these estimates, we have retained a value of 22-23 % as the photolysis yield f(t=50 ps) used in Eq. 6.1 in order to extract the corresponding high-spin state spectrum of aqueous [Fe(bpy)3]2+ complex (see Fig. 6.24 in Section 6.2.4).

The highest concentration investigated in this study was ca. 0.1 M. The corresponding fluorescence yield and transmission change results are depicted in Figs. C.7a and C.7b, respectively. The corresponding values read off of these graphs are summarized in Table C.4.

Energy /eV	N_{phs}^{LS} /photons/pulse	$N_{phs}^{\Delta A}$ /photons/pulse	f(t)($[c]_{HS}$) /%(/mM)	ΔT $/10^{-2}$ %
7125-7126	1	0.12	≥11(≥11)	1.0-1.1
7131	2.15	-	-	-

Table C.4: The summary of the parameters obtained from Fig. C.7 (see below) at selected x-ray energies.

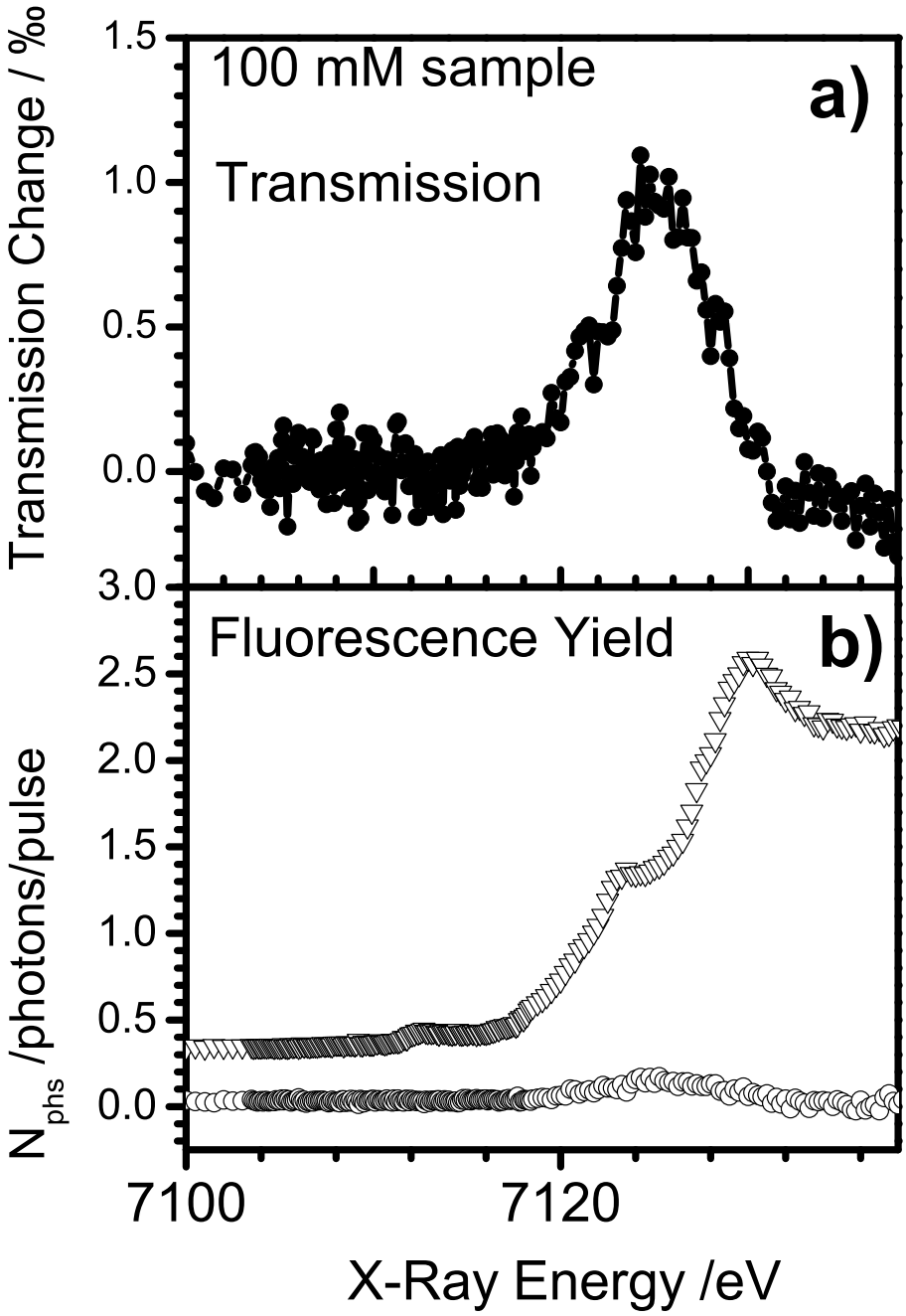

Figure C.7: (a) Transient transmission XAS signal of the K-edge of 0.1 M aqueous sample of$[Fe^{II}(bpy)_3]^{2+}$. (b) Static (○) and transient (▽) XAS signals of the same sample (0.1 M) measured in fluorescence mode. In both (a) and (b), the energy region was identical as in Fig. C.2. Similarly, the signal magnitude is given in photons/pulse (Eq. 4.6). The signal magnitudes obtained from both (a) and (b) and used in the analysis are summarized above in Table C.4

At 100 mM concentration, a considerable deviation between the estimated and measured results is found. In this case, the static transmission signal becomes visible due to ca. 5.5-6 % transmission change, which is expected in the vicinity of the absorption edge. In Fig. C.8, we can clearly see that out of ca. incident 3100 photons/pulse, only about 325 photons contribute to the absorption change at 7130 eV and nearly a factor of 2 less at 7125 eV. Assuming the 5.5-6% transmission change at the edge, we would expect rather 180 photons/pulse measured at 7130 eV.

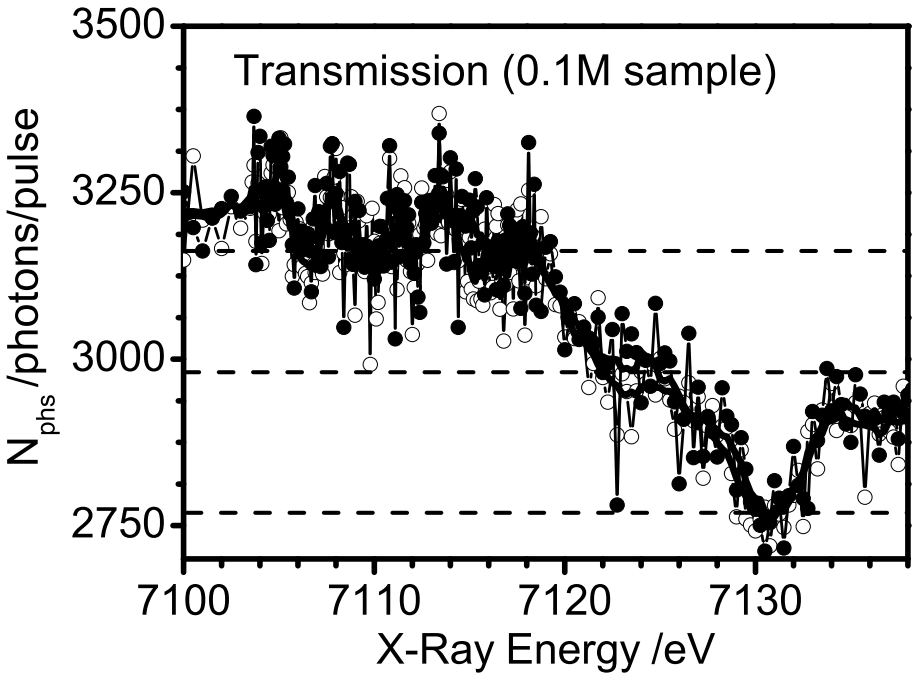

Figure C.8: Unpumped (○) and pumped (●) transmission XAS spectra of of 100 mM aqueous sample of $[Fe^{II}(bpy)_3]^{2+}$. As a "guide-to-the-eye", the smoothed unpumped and pumped spectra (solid lines) are overlaid on top of the raw data. The horizontal dashed lines indicated the transmitted number of photons below the edge, at half-edge energy (ca. 7126 eV) and above the edge (ca. 7130 eV). The edge jump can be estimated to ca. 325 photons/pulse. For the details of the analysis, see the text below.

At this point, one could think that the real concentration of the sample was twice larger, but the fluorescence photons (Fig. C.7b) indicate consistently that the concentration increased 4 times as compared to 25 mM sample (2.1 photons/pulse vs. 0.5 photons/pulse at 7130 eV in Figs. C.7b and C.6b respectively). Assuming the fluorescence yield measurements deliver correct result, one would expect ca. 11 mM of the excited state molecules, which means ca. 11% excitation yield.

In order to cross-check our results at 25 mM and 100 mM, the expected fluorescence yields at both concentrations were calculated using the following Eq. 3.24 (see Chapter 3, Section 3.3.2):

$$I_f = \frac{I_0 \mu_A(E) \epsilon_A}{\mu_T + \mu_f} \{1 - exp[-(\mu_T + \mu_f) d']\} \tag{C.1}$$

where I_0 is the incident x-ray intensity in photons/pulse, Φ= 0.3 is the quantum efficiency of the x-ray fluorescence process at Fe K-edge, $\Omega/4\pi$ is the solid angle fraction covered by the detector (in Chapter 4 we have estimated the loss factor $\Phi_f \cdot \frac{\Omega}{4\pi}$= 1%), μ_a is the mass absorption coefficient of a give core excitation (it accounts for the absorption change due to the Fe K-edge jump), μ_T is the total absorption coefficient at a given energy (here 7130 eV) and μ_f is the total absorption coefficient at the fluorescence photon energy (here the dominant x-ray emission originates from $K_{\alpha 1}$ and $K_{\alpha 2}$ lines, which correspond to recombination process from L_3 ($2p_{3/2} \rightarrow 1s$) and L_2 ($2p_{1/2} \rightarrow 1s$) edges). The cross-sections at $K_{\alpha 1}$ (6405 eV) and $K_{\alpha 2}$ (6392 eV) lines are nearly identical and given the fact that 60 % of the detected fluorescence originates from the $K_{\alpha 1}$ emission line, we will assume μ_f at 6405 eV. Here we also assume that the incident and outcoming photon trajectories are at 45° and thus we can assume that $\sin\alpha \equiv \sin\beta = sin(45°) = 0.707$. The tabulated values of all required absorption coefficient are summarized in Table C.5. The jet thickness was assumed 0.03 cm (300 μm) in both cases. Mass coefficients were calculated for 100 mM concentration, assuming 0.65 g/cm^3 density of $[Fe^{II}(bpy)_3]^{2+}$ complex at nominal concentration of 0.92 M in the crystal form.

Sample Concentration /mM	μ_T (7130 eV)	μ_f (6405 eV)	μ_a (Edge jump)
25	0.63 cm^{-1}	0.96 cm^{-1}	0.5 cm^{-1}
100	3.83 cm^{-1}	2.5 cm^{-1}	2 cm^{-1}

Table C.5: The calculated absorption coefficients, for two different concentrations of 25 mM and 100 mM, at three different energies, as imposed by the Eq. C.1, used to estimate the expected integrated x-ray fluorescence signal. All absorption coefficients were calculated using the software described in Ref. [249]

Using Eq. C.1 and Table C.5, we obtained the following results: I_f^{25mM}=$I_0 \cdot 2 \cdot 10^{-4}$ and I_f^{100mM}=$I_0 \cdot 7.5 \cdot 10^{-4}$, respectively. Assuming I_0=3000 photons/pulse in both cases, we should expect to detect at 7130 eV approximately 0.61 photons/pulse and 2.25 photons/pulse for 25 mM and 100 mM samples respectively. These values agree very well with the measured fluorescence yields reported in Tables C.3 and C.4. For both measurements the agreement is met within 5-13%, which again confirms our assumption about the shot-noise limited detection sensitivity. It also confirms that the x-ray fluorescence yield delivers correct results and we can confirm the investigated sample was indeed of 100 mM concentration.

What still remains unsolved (and puzzling), is the factor of 2 discrepancy between the measured fluorescence and transmission photons. The reabsorption of the x-ray fluorescence within the escape depth of the sample would not account for such a large deviation and the reported distortions of the EXAFS data due to self-absorption are usually smaller than 20-30%. In any case, we think it is the transmission measurement, which delivered erroneous photon flux. One possible explanation could assume that at the increased bias voltage of the transmission APD detector, we have actually reached a region where the response is not longer linear. At lower concentrations, this effect would not be seen due to insignificant edge absorption. At 100 mM, we count with 6% signal change due to the edge, which can be clearly detected in transmission measurement.

Appendix D

Optical Transient Absorption Data Analysis

This appendix includes a detailed description of the data analysis applied to the femtosecond optical transient absorption results presented in Section 5.1 (Chapter 5) and Section 6.1 (Chapter 6). In the first case, the data on aqueous samples of $[Ru^{II}(bpy)_3]^{2+}$ was obtained at several selected time delays and the transient absorption spectra and kinetics were analyzed, via Eq. D.3, as a linear combination of all photoexcited photoproduct concentration. In case of $[Fe^{II}(bpy)_3]^{2+}$, the entire spectral and temporal information was analyzed globally. Prior to the global fit, via Eq. D.6, the raw data was decomposed using the singular value decomposition procedure (Eq. D.5). The SVD-reconstructed data was subsequently fit at all wavelengths simultaneously and the *decay-associated spectra* (DAS) were obtained from Eq. D.8.

D.1 Transient Spectra Analysis

In these experiments, the transient absorption spectra were recorded at several time delays for a wide range of excitation fluences. In the analysis and discussion of the results presented in Section 5.1 (Chapter 5) the peak irradiance I_0 and the fluence E_0 of the 400 nm excitation pulses were obtained from the expressions for Gaussian-shaped pulses in both time and space:

$$I_0 = E \cdot \frac{8(\pi^{-1}\ln 2)^{3/2}}{(\hbar\omega_{400nm} d^2 \tau_p)} \tag{D.1}$$

$$E_0 = E \cdot \frac{4(\ln 2)}{\pi d^2} \tag{D.2}$$

where E is the total pulse energy, and $\hbar\omega_{400nm}$ is the energy of a 400-nm photon (=3.1 eV). The largest E_0 in this study was 0.31 Jcm^{-2} (I_0=4.35·10^{30} photons/cm^2/s), corresponding to a power of 2.15 TW/cm^2.

The transient absorption spectra acquired at delay times t≥10 ps were fitted to the absorption spectra of the reactant ($[Ru^{II}(bpy)_3]^{2+}$) and of the formed product species, with their concentrations being the only fit parameters via:

$$\Delta A^t_\lambda = \frac{10^{-3} N_A l}{\ln 10} \cdot \sum_{i=1}^{5} \Delta c^t(i) \cdot \sigma_\lambda(i) \tag{D.3}$$

Here, N_A=6.022×10^{23} mol^{-1} is Avogadro's constant, l is the sample thickness (in cm), and $\sigma_\lambda(i)$ are the absorption cross-sections of the photoproducts involved in the involved photochemical cycle. The fit parameters $\Delta c^t(i)$ are defined as $\Delta c^t(i) = c^t(i) - c^{t<0}(i)$, where $c^{t<0}(i)$ and $c^t(i)$ are the concentration of the reactant, and of the products at time t after photoexcitation, respectively. The initial reactant concentration ($[Ru^{II}(bpy)_3]^{2+}$) is equal to that of the prepared solution (no products prior to photoexcitation).

D.2 Global Analysis and SVD Decomposition

The transient absorption results presented and discussed in Section 6.1 (Chapter 6) were analyzed by means of the global analysis (GA) approach [392]. The GA term refers to simultaneous analysis of all measurements contained in a multivariable data set [393]. The time-resolved transient absorption spectra recorded in these experiments are a typical example of 2-variable measurements, where the independently measured variables are the wavelengths and time (or more precisely the time delay between the pump and the probe pulses). A representative set of transient absorption data measured with our setup is shown in Fig. 6.2. The data is sorted into M × N matrix, where M defines the wavelength dimension (in this case there are 512 discrete wavelength measurements each corresponding to a diode pixel) and N corresponds to discrete time steps over the entire time delay measured in the experiments (In Fig. 6.2 the time step was ca. 67 fs and the total time delay measured was 20 ps, which means we have measured this delay with 299 time steps). In case a data set, as shown in Fig. 6.2, the GA allows simultaneous analysis of the dynamical information across the entire spectral and temporal range by fitting the data with just one model scenario. In addition, the global techniques permit to separate the physically-relevant information from the stochastically-distributed additive noise present in the data set (by means of *Singular Value Decomposition*, SVD [394]).

In principle, SVD procedure allows determining the rank of an arbitrary matrix corrupted by random noise. In data analysis, it translates into a powerful technique of data reduction and noise suppression [392]. It allows reducing the data dimensionality and permits performing a nonlinear least square global fit on the reduced data, without losing any relevant information contained in the data. If we assume that the data matrix we measure during the transient absorption experiment is defined as follows:

$$\Delta A(\lambda_i, t_k) \equiv A = \widetilde{A} + \Xi \tag{D.4}$$

where $\Delta A(\lambda_i, t_k)$ is M × N matrix composed of discrete sets of wavelengths λ_i and time delay t_k. Assuming the noise Ξ contribution, present in the data is additive, the matrix $\widetilde{A}$ is the one, which contains all the information about the spectral evolution of the system, where as the matrix Ξ represents the normally-distributed noise with zero mean value. The SVD procedure allows decomposing the A matrix into a product of 3 components according via:

$$A = USV^T \tag{D.5}$$

where U and V^T stand for the orthogonal matrices of M × M and N × N dimensions, respectively. Their columns contain the left and right singular vectors. In case of transient absorption data absorption data, the SVD approach yields U and V^T matrices, which we can identify as basis spectra and basis kinetics of the data matrix A [361, 395]. The diagonal elements of S matrix yield the singular values S_{ii}=s_i [396]. The outcome of the SVD transformation

reduces significantly the number of relevant kinetic and spectral components required to describe the entire spectral and temporal evolution of the system. Nevertheless, the SVD analysis, a priori, does not yield any specific physical information. It only reduces the rank of the data matrix A (and thus reduces the amount of data, which has to be included in the global fit), which then has to be verified according to a physically meaningful kinetic model. In our case, we assume a sequential kinetic scheme [392], in which the temporal evolution of the system can be described by a sequence of events with specific first-order decay rates k_i and the corresponding lifetimes τ_i, so that the kinetic response can be modeled by a sum of N model functions. We also assume no significant spectra diffusion present in the transient absorption spectra (see the results presented in Section 6.1.2). All the kinetics presented in Section 6.1.2 were modeled with a sum of exponential functions convoluted with the temporal *instrument response function* (IRF), which was approximated with a Gaussian function of FWHM equal to the cross-correlation function of the experiment (i.e. 145(15) fs as in Fig. 4.32). The analytical function is given by [392]:

$$\begin{aligned}\Delta A(t) &= e^{-k_i t} \otimes IRF(t) = \\ &= \tfrac{1}{2}\sum_{i=1}^{N} a_i exp\Big[k_i(\mu - t) + \tfrac{(k_i\sigma)^2}{2}\Big] \times \\ &\quad \times \Big[1 + erf\Big(\tfrac{t-(\mu+k_i\sigma^2)}{\sqrt{2}\sigma}\Big)\Big]\end{aligned} \tag{D.6}$$

where a_i is the amplitude of i^{th} decay, μ describes the time origin of the IRF function (time-zero) and σ its width. FWHM is then defined as FWHM=$2\sigma\sqrt{2\ln 2}$. The GA consists of simultaneous fitting of all significant V_i^T traces with a number of $\Delta A_k(t)$ functions [392]:

$$V_i^T = \sum_{k=1}^{K} a_{i,k}\Delta A_k(t) \tag{D.7}$$

The coefficients $a_{i,k}$ obtained in the fit can be used to calculate the corresponding decay-associated spectra (DAS) of the involved kinetics by using the set of properly weighted U_i spectral SVD components via [392]:

$$DAS_k = \sum_{i=1}^{N} a_{i,k} s_i U_i \tag{D.8}$$

The obtained DAS present the spectral contributions of the photochemical species involved in different processes, which occur within the time window defined by the corresponding decay τ_i. In some case, the decay-associated spectra can be directly attributed to the so called species-associated spectra (SAS), which deliver the true absorption spectra of the transient species. A representative example of the SVD analysis applied to the transient absorption results discussed in Section 6.1 are illustrated in Figs 6.6, 6.7, 6.8 ,6.9 and 6.10.

Appendix E

Numerical Example-Aqueous $Fe^{II}(bpy)_3]^{2+}$

The theoretical model laid out in Section 3.4.2 can be applied to optimize the sample concentration prior to the actual experiment [27, 75, 76]. In the following, the numerical results of such optimization calculations will be illustrated in case of $[Fe^{II}(bpy)_3]^{2+}$ in H_2O. These results are summarized in Figs. E.1a and b, where the outcome of the numerical calculations is displayed in a broad range of concentrations (0.01-10 M in Fig. E.1a). Fig, E.1b zooms into the low concentration part (10-100 mM)of the plot in Fig. E.1a and the calculated S/N ratio for a 25 mM sample (as analyzed in Chapter 6.2) is indicated with arrows.

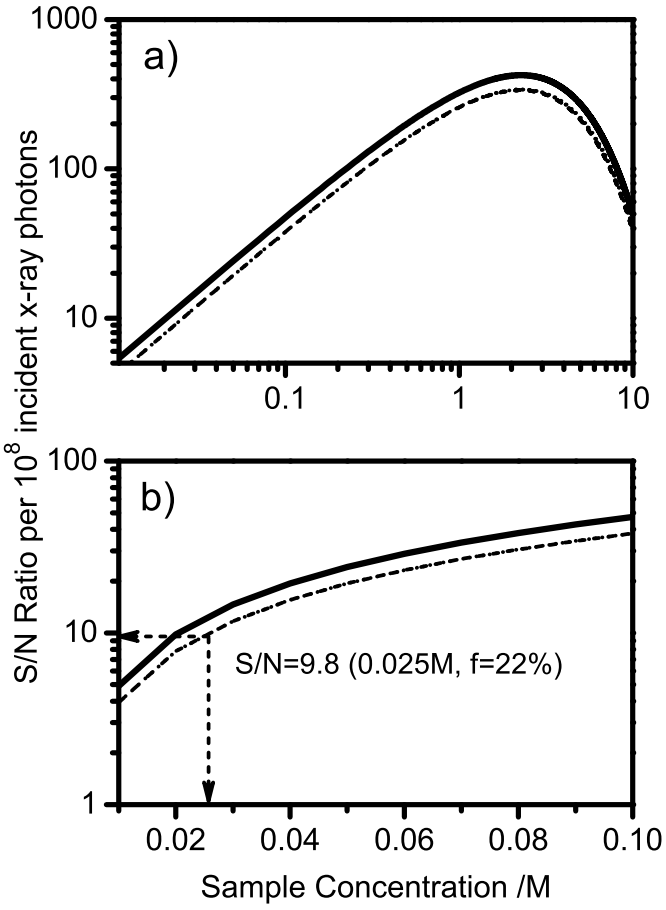

Figure E.1: Calculated S/N ratio as a function of the sample concentration in case of a room temperature $[Fe^{II}(bpy)_3]^{2+}$ in H_2O solution. In (a) the full concentration range is shown from 0.01-10 M, whereas (b) zooms in to the low concentration region between 10-100 mM. The solid line describes a bare transition metal ion (gas-phase) case in the absence of both the solvent and ligand molecules. The dashed curve illustrates the case the transition metal ion in an aqueous solution, whereas the dotted curve accounts for ligand, solvent and counterion molecules. The dashed arrows in (b) indicate the actual sample concentration and the experimentally verified photolysis yield of the experiments presented in Chapter 6, to which the optimized S/N ratio will be compared (see Fig. E.2).

Here the S/N ratio is plotted as a function of sample concentration. Figs E.1a and b shows the three calculated cases: (1) displays the concentration dependence for an isolated transition metal atom (solid line), (2) shows the case of the central atom only in H_2O environment, and (3) shows the full calculation including the H_2O solvent and the three bipyridine ligands. The sample optimization shown in Fig. E.1 was performed in relation with the x-ray experiments presented in Chapter 6.

Several assumptions were taken into account in the numerical calculations. First of all, it was assumed that the typical EXAFS oscillations represent typically 1 to 20% modulations of the edge height [27] (compare in Fig. 3.3). Another assumption concerns the excitation yield $f(t)$, where we have set the requirement to a reasonable value of $f(t)$=22% for the amount of excited state species (as determined in Chapter 6 and Appendix C). With these assumptions, and setting the desired S/N=1, the calculation yields the required number of incident x-ray photons in order to measure the EXAFS signal. The results will then deliver a reasonable estimate for the feasibility of such an experiment the available x-ray photon flux at the aforementioned beamlines (see Chapter 4). Here, we also note that the optimized x-ray intensity I_0 (expressed in terms of number of incident x-ray photons) for such an experiment obeys the following dependence [27]:

$$I_0 \propto \left(\frac{S/N}{f \cdot \Delta\chi}\right)^2 \tag{E.1}$$

which implies that we can either modify the results according to previously measured excitation yield f or scale the results assuming different magnitude of EXAFS oscillations. The summary of the chosen values of several parameters (not all of them were mentioned above) is included in Table E.1. The

Optimization Parameter	Value
Absorption Edge	K(Fe)
I_0	$1{\cdot}10^8$ phs/sec/data point
EXAFS Magnitude $\Delta\chi$	55%
Photolysis Yield f	22%
Jet Thickness	0.3 mm
Concentration	25 mM

Table E.1: Parameter values of the sample optimization calculation yielding the results plotted in Figs. E.1(a) and (b)

values from Table E.1 were chosen in agreement with the experimental conditions (Chapter 6). Additional sample restrictions, e.g., solubility limits, may require even more dilute concentrations. The concentration used here, 25 mM, was also the actual concentration of the experiment (Chapter 6). Concerning the solvent, we have restricted our considerations to H_2O solvent only. In case of other solvents, the results may be change due to differences in hard x-ray absorption cross sections, although considering the first-row solvents (e.g., acetonitrile, hexane, etc.), the results presented here will not be significantly

affected. This may change for heavier solvents, like CCl_4, where our results are not applicable anymore [27]. In case of Fe molecule (Fig. E.1, the solvent effects (background absorption) using 0.3 mm are negligible, since the solvent transmission is quite high at this x-ray energy. Introducing the entire $[Fe^{II}(bpy)_3]^{2+}$ molecule including two Cl^- counterions delivers nearly the same result as without the ligand, since the difference in absorption between H_2O and the sample ligands and counterions is also very small.

In order to verify the applicability of our model and the numerical optimization, the comparison of the calculated number of incident x-ray photons required in time-resolved EXAFS transmission measurement with the experimental data will be presented.

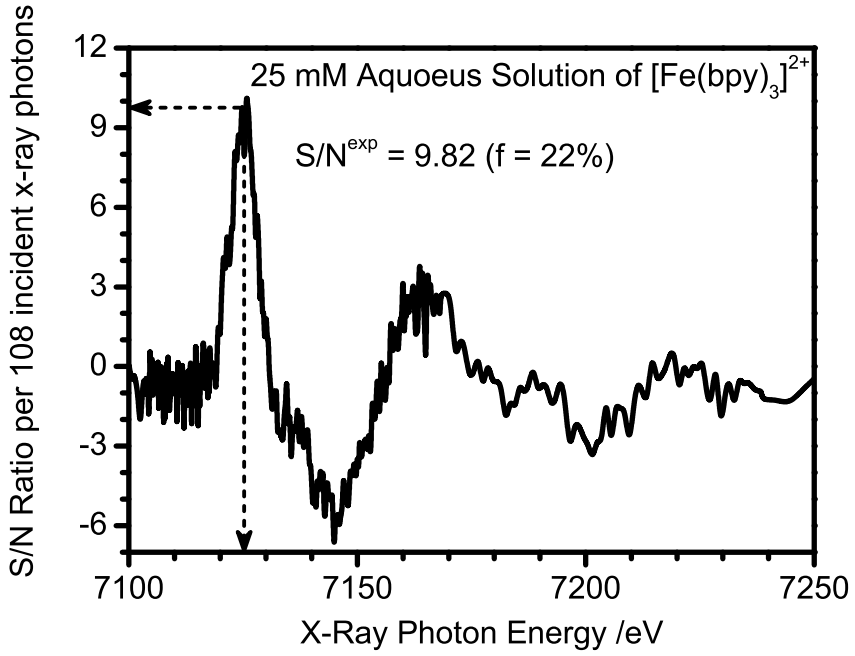

Figure E.2: Transient absorption EXAFS spectrum of 25 mM aqueous sample of $[Fe^{II}(bpy)_3]^{2+}$ measured in transmission mode. Here the intensity changes are plotted in terms of the S/N ratio as a function of the incident x-ray energy. The dashed arrow indicate the maximum S/N ratio at 7126 eV, which agrees very well with the numerically optimized value in Fig. E.1

The data plotted in Fig. E.2 shows the transient K-edge absorption spectrum of the identical sample as the one considered in Fig. E.1a. However, here we have used a concentration of 25 mM and the S/N ratio in the EXAFS range was around 1-3, whereas it is almost 10 in the XANES region. The results presented in Fig. E.2 were normalized to the absorption edge jump and at 7130 eV it amounts to ca. 12% of the absorption edge change. The incident x-ray photon flux was $\sim 1 \times 10^8$ photons/s/data point.

In order to link the measured S/N ratio and the numerically optimized value, we had to change on of the parameters listed in Table E.1, namely the EXAFS magnitude $\Delta\chi$. The reason for that is illustrated in Fig. E.3.

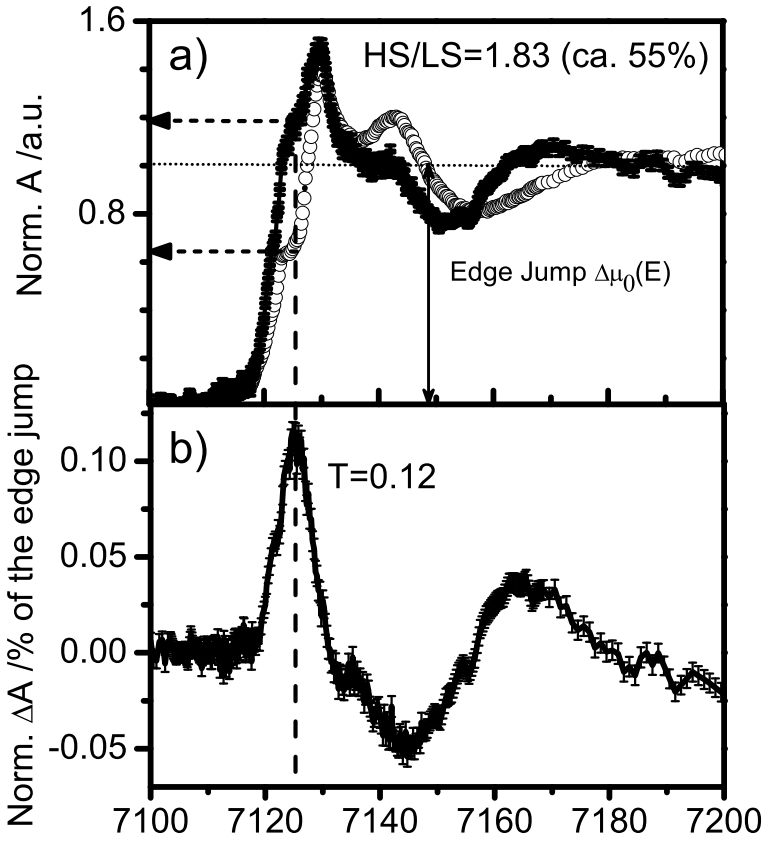

Figure E.3: (a) The ground (LS) and excited state (HS) spectra of $[Fe^{II}(bpy)_3]^{2+}$ (Chapter 6) are shown and the relative increase of the absorption cross section, at 7126 eV , is indicated with dashed arrows. The edge jump, $\Delta\mu_0$(E) used in the normalization of both spectra is shown using a horizontal dotted line. (b) the transient absorption spectrum, normalized with respect to $\Delta\mu_0$(E), in the same energy region as the spectra in (a) is displayed. The maximum changes at 7126 eV reach ca. 12% of $\Delta\mu_0$(E) of the LS spectrum.

Here we see that the absorption cross section of the excited state (HS state) increases by nearly 55% in the region around 7126 eV. In previous calculations (not shown here), the assumption of $\Delta\chi$=1% was done, which underestimated the measured changes and increased the required x-ray photon flux I_0, via Eq. E.1, $2.5{\cdot}10^4$! Using the correct value of $\Delta\chi$=55% and the other parameters from Table E.1, we have obtained an excellent agreement between the measured and simulated S/N ratios as verified by comparing the indicated values in Figs. E.1b and E.2.

Acknowledgements

Many people have contributed to this research project over the past four and half years, and therefore I would like to acknowledge all of them for their contributions, even if they were not always solely scientific.

First of all, I would like to express my deepest gratitude to Prof. Majed Chergui. Since July 2002, when Majed has given me the opportunity to carry out my doctoral studies in his group, he has been a continuous inspiration and motivation, not only on a scientific, but also on a human level. His openness has created great atmosphere within the group, which helped enormously during the hard times and made the thesis supervision outstanding.

I am also very thankful to Prof. Christian Bressler, who has been leading the x-ray project in Lausanne together with Prof. Majed Chergui and co-directing this thesis. It is hard to express how much I owe to Christian, since the very first day I have met him. Working with him was a true pleasure and a constant inspiration and his world-wide expertise in the ultrafast x-ray science has made a tremendous impact on the outcome of my research. However, most importantly, Christian has become a dear friend with whom I could always share all my problems and hesitations, either scientific or personal.

I would also like to acknowledge all the members of my Ph.D. committee. I am very grateful to Prof. Villy Sundström and Dr. Maurizio Benfatto, who agreed to travel from abroad, despite their busy time schedules. I would also like to thank Prof. Robert Schaller and Prof. Friso van der Veen for their acceptance to become the part of the jury and their interest in my work.

As mentioned above, this thesis is a result of a collective effort of many people, who have been involved in the time-resolved x-ray project over the past years. I would like to thank Dr. Melanie Johnson, who was the first graduate student in Lausanne involved in this research and with whom I shared more than 2 years of common work. Her thoughtful guidance during the initial

steps helped me to become more independent in a relatively short time. My big thanks goes to Prof. Alexander Tarnovsky, with whom I shared many great moments in Switzerland, both scientific and personal. I would also like to acknowledge Dr. Maik Kaiser and Dr. Yuri Zaushitsyn, former post-docs in our group, and my successors: Van-Thai Pham and Amal El Nahhas, the next generation of graduate students, who are involved in this project and with whom I had a pleasure to work together and share my experiences.

In addition to the Lausanne team, there are many other collaborators with whom I had a great pleasure to work and interact over the past years. The experiments presented in this thesis were carried out at synchrotron facilities around the world involving the outstanding teams of people working there. Chronologically, I would like to express my gratitude to the entire beamline 5.3.1. *Femtosecond Phenomena* team at the Advanced Light Source in Berkeley, USA. I want to especially thank Dr. Phil A. Heimann, Dr. Donnacha Lowney, Dr. Marc Hertlein, Dr. Robert W. Schoenlein and Prof. Roger Falcone for their expertise, constant help and support during the beamtimes. One very special person I would like to acknowledge here is Dr. Steven L. Johnson. I must truly express my gratitude to him for all the contributions he has made to this research project. He has been a constant source of knowledge about the electronics, programming, ultrafast x-ray science and synchrotrons and I have enjoyed a lot the possibility to work with him and learn from him over the past years. Furthermore, I would like to acknowledge all the microXAS beamline team at the Swiss Light Source in Villigen, Switzerland. Especially, Dr. Daniel Grolimund, who taught me about the x-ray absorption spectroscopy and synchrotron technology, Dr. Messaoud Harfouche, Markus Willimann and Beat Meyer. My great thanks to FEMTO project team: Dr. Gerhard Ingold, Dr. Paul Beaud and Dr. Steven L. Johnson (this time in Switzerland). In addition, I would like to acknowledge Dr. Rafael Abela for his constant support and active involvement in the ultrafast x-ray project, since the very beginning of this project and for his help in providing me with the financial support from the SLS during my Ph.D. studies.

I am grateful to all the colleagues with whom I shared my time in Lausanne. I owe to them many unforgettable moments that I have lived here and I have benefitted enormously from their scientific expertise and skills in laser spectroscopy and physical chemistry. My special thanks go to Dr. Frank van

Mourik (including our squash games!), Dr. Andrea Cannizzo (special thanks for fluorescence up-conversion figure), Dr. Andrea Callegari, Prof. Stefan Haacke, Dr. Selma Schenkl, Dr. Andrea Tortschanoff, Dr. Dino Tonti, Dr. Erwin Portuondo Campa, Dr. Goran Zgrablič, Dr. Pascal Larregaray, Alejandro Gonzalez, Jinquan Liu, Dr. Gerard Giraud, Bartosz Sobanek and many others! My special thanks to all my office colleagues: Awos Al Salman, Camilla Bonatti and Dr. Luigi Bonacina. Thanks to Michel Kessous for his computer support and kindness, Mr. Moser and Mr. Rittner for their help and support with mechanical and electronic equipment at all times.

The extensive international collaborations that has been established during my Ph.D. studies has given me the chance to meet and interact with many world-wide experts in the field of both laser and x-ray spectroscopies. I would like to express my special acknowledgements to Dr. F. M. F. de Groot for teaching me how to use the multiplet code, Dr. Maurizio Benfatto for his powerful MXAN code, Dr. Bruce Ravel for many useful tips on EXAFS analysis, Prof. John J. Rehr for his FEFF code and Prof. Andreas Hauser for introducing me into spin crossover world.

Last but not least, I am grateful to my family and friends: kochanym Rodzicom i siostrze Asi za Wasze nieustanne wsparcie, wiarę i zaufanie, kochanym Dziadkom, którzy niestety nie doczekali zakończenia tej pracy doktorskiej, wszystkim najdroższym przyjaciołom z Poznania (i nie tylko!). Enormes agradecimientos y gracias a toda mi familia española, por vuestro apoyo y confianza! Y por supuesto, un enorme agradecimiento a mi mujer, amiga y compañera de este viaje, Ana Belén. Sin ti nunca hubiera llegado a donde estoy hoy en día. Gracias por todo lo que hiciste por mi!

Curriculum Vitae

Name:	Wojciech GAWELDA
Date, place of birth:	30-01-1978, Poznan, Poland
Nationality:	Polish
Address:	Laboratoire de Spectroscopie Ultrarapide
	ISIC-SB
	Swiss Federal Institute of Technology Lausanne
	BSP, CH-1015
	Tel: +41-21-6930452
	Fax: +41-21-6930422
	E-mail: Wojciech.Gawelda@epfl.ch

Current Research Interest and Experience

Molecular Physics, Condensed Phase Dynamics, Physical Chemistry, Phase Transitions, Chemical Reaction Dynamics, Experimental Laser Physics, X-ray Absorption Spectroscopy, Synchrotron Radiation, Ultrashort X-rays, Ultrafast Time-Resolved Optical and X-ray Techniques, Femtosecond Pulses, Pump-Probe Spectroscopy, Generation and Application of Ultrashort Laser and X-ray Pulses, XFEL.

Employment

2002-Present

Assistant Diplômé Laboratoire de Spectroscopie Ultrarapide,
École Polytechnique Fédérale de Lausanne
(until 09/2003 at Université de Lausanne)

2001-2002

Junior (Graduate) Research Assistant, Instituto de Óptica "Daza de Valdés", CSIC, Madrid, Spain

Education

2002-2006

Ph.D thesis on "Time-Resolved X-Ray Absorption Spectroscopy of Transition Metal Complexes" under the supervision of Prof. M. Chergui and Prof. C. Bressler

June 2001

M.Sc. in Experimental Physics (Magister Fizyki),
Best Student (Cum Laude) Award
M.Sc. Thesis Title: "Noncollinear Optical Parametric Amplifier",
Uniwersytet im. Adama Mickiewicza, Poznań, Poland,

1996-2001

Undergraduate Studies in Physics at the Department of Physics,
Uniwersytet im. Adama Mickiewicza, Poznań, Poland

June 1996

High School Degree (Matura), Poznań, Poland

Teaching Experience

2003-2005

- *Tutorials and assistantship to "Atomes et Rayonnement" course for undergraduate physics students lectured by Prof. Dr Christian Bressler at EPF-Lausanne*

1996-2001

- *Private tuition of physics for high school and undergraduate students*

Professional Memberships

- *American Physical Society, Swiss Physical Society, Swiss Chemical Society*

Publications

- **W. Gawelda**, V-T. Pham, M. Benfatto, Y. Zaushitsyn, M. Kaiser, D. Grolimund, S. L. Johnson, R. Abela, A. Hauser, M. Chergui and Ch. Bressler, **Structural Determination of a Short-lived Iron(II) Complex by Picosecond X-ray Absorption Spectroscopy**, *Physical Review Letters*, In press 2006

- **W. Gawelda**, A. Cannizzo, V-T. Pham, F. van Mourik, A. Hauser, C. Bressler and M. Chergui, **Femtosecond Transient Absorption and Fluorescence Up-Conversion Studies of Fe(bpy)$_3$**, *Journal of the American Chemical Society*, In preprint 2006

- **W. Gawelda**, M. Johnson, F. M. F. de Groot , Ch. Bressler and M. Chergui, **Electronic and Molecular Structure of Photoexcited [Ru^{II}(bpy)$_3$]$^{2+}$ Probed by Picosecond X-ray Absorption Spectroscopy**, *Journal of the American Chemical Society*, **126**, (2006) 5001

- M. Benfatto, S. Della Longa, K. Hatada, K. Hayakawa, **W. Gawelda**, Ch. Bressler and M. Chergui, **A Full Multiple Scattering Model for the Analysis of Time-Resolved *L*-Edge X-Ray Difference Absorption Spectra**, *Journal of Physical Chemistry B*, **110**, (2006) 14035-39

- A.Cannizzo, F. v. Mourik, **W. Gawelda**, Ch. Bressler and M. Chergui, **Broadband Femtosecond Fluorescence Spectroscopy of [Ru(bpy)$_3$]$^{2+}$**, *Angewandte Chemie-International Edition*, **45**, (2006) 3174

- A.N. Tarnovsky, **W. Gawelda**, M. Saes, Ch. Bressler and M. Chergui, **Photolysis of Aqueous Ruthenium(II) tris(2,2'-bipyridine) under High Excitation and High Density Conditions**, *Journal of Physical Chemistry B*, In press, 2006

- **W. Gawelda**, C. Bressler, M. Saes, M. Kaiser, A. Tarnovsky, D. Grolimund, S.L. Johnson, R. Abela, M. Chergui, **Picosecond Time-Resolved X-Ray Absorption Spectroscopy of Solvated Organometallic Complexes**, *Physica Scripta*, **T115**, (2005) 102

- M. Saes, **W. Gawelda**, F. van Mourik, M. Kaiser, M. Chergui, C. Bressler, D. Grolimund, R. Abela, T.E. Glover, P.A. Heimann, R.W. Schoenlein, S.L. Johnson, A.M. Lindenberg, R.W. Falcone, **A Setup for Ultrafast Time-Resolved X-ray Absorption Spectroscopy**, *Review of Scientific Instruments*, **75**, (2004) 24-30

- **W. Gawelda**, M. Saes, M. Kaiser, A.N. Tarnovsky, S.L. Johnson, D. Grolimund, R. Abela, M. Chergui, C. Bressler, **Structural dynamics and electronic structure changes probed with lasers and x-rays**, *Ultrafast Molecular Events in Chemistry and Biology*, Ed. by M. Martin, J. T. Hynes, Eds., Elsevier Science Publishers (2004), p.353

- M. Saes, **W. Gawelda**, M. Kaiser, A.Tarnovsky, D. Grolimund, S.L. Johnson, R. Abela, C. Bressler, M. Chergui, **Ultrafast Time-Resolved X-Ray Absorption Spectroscopy of Chemical Systems**, *Synch. Rad. News* (**Invited**), **16**(4), (2003) 12-20

- S.M. Wiggins, **W. Gawelda**, J. Solis, R. Serna and C.N. Afonso, **Time-resolved Dynamics of Rapid Melting and Resolidification of Sb Thin Films under ns and ps Laser Pulse Irradiation**, *Journal of Applied Physics*, **94**, (2003) 4961-4966

- A. Cannizzo, **W. Gawelda**, M. Leone, E. Portuondo-Campa, F. van Mourik, A. Callegari, M. Chergui, **Ultrafast relaxation processes in excited states of point defect in vitreous silica**, In preprint, Physical Review B 2006

Oral Presentations

Invited Talks

- 04/2005 *Local Molecular Structure of Photoexcited Coordination Chemistry Compounds* COST D14 Working Group Workshop "Functional Transition Metal, Hyères les Palmiers, France

- 11/2004 *Local Structure of Solvated Transition-Metal Complexes Probed by Picosecond Time-Resolved XAFS*, Department of Inorganic Chemistry, University of Utrecht, The Netherlands

- 10/2004 *Ultrafast X-Ray Absorption Spectroscopy* 5^{th} SLS Users' Meeting, Swiss Light Source, PSI, Villigen, Switzerland

- 09/2004 *Structural Dynamics with Current and Future X-Ray Sources* Instituto de Óptica, CSIC, Madrid, Spain

- 03/2002 *Ultrafast Reversible Phase Transitions in Amorphous Sb-rich GeSb Thin Films in Application for Optical Recording* Institut de Physique de la Matière Condensée, Université de Lausanne, Lausanne, Switzerland

- 02/2001 *The Characterization and Diagnostics of fs Two-Stage NOPA and its Application in Spectroscopy*, Instituto de Óptica, CSIC, Madrid, Spain

Contributed Talks

- 02/2006 *Light-Induced Spin Transition Probed by Picosecond Time-Resolved XAFS* Swiss Physical Society Annual Meeting, EPFL, Lausanne, Switzerland
- 10/2005 *Transient Molecular and Electronic Structure of Photoexcited Coordination Chemistry Compounds* Swiss Chemical Society Annual Meeting, EPFL, Lausanne, Switzerland
- 03/2004 *The Photocycle of the Aqueous Ruthenium(II)tris-bipyridine Complex Studied by Time-Resolved X-ray Absorption Spectroscopy* Swiss Physical Society Annual Meeting, University of Neuchâtel, Switzerland
- 07/2003 *Picosecond Time-Resolved X-Ray Absorption Spectroscopy of Solvated Organometallics* Summer School on Ultrafast X-ray Science, Institut D'Ètudes Scientifiques de Cargèse, Corsica, France
- 06/2003 *Time-Resolved X-Ray Absorption Spectroscopy at Synchrotrons with Picosecond Temporal Resolution*, XAFS 12 International Conference, Malmö, Sweden
- 03/2003 *Time-Resolved X-Ray Absorption Spectroscopy with Sub-100 ps Temporal Resolution* Swiss Physical Society Annual Meeting, University of Basel, Switzerland
- 07/2002 *Determination of Optical Properties of Thermal Liquid Antimony* 2^{nd} Annual XPOSE Research Training Network Meeting, Paris, France

Poster Presentations

- 07/2006 *Picosecond Structural Dynamics of Condensed Phase Systems Observed via Time-Resolved XAFS* XAFS 13, Stanford University, Stanford, USA
- 07/2006 07/2006 *Energy and Structural Relaxation of Metal Bisbipyridine Complexes Investigated by Ultrafast Optical and X-ray Spectroscopies* IPS 16, University of Uppsala, Sweden
- 02/2006 *Direct Observation of I0 upon Photoionization of Aqueous I^- using Ultrafast X-Ray Absorption Spectroscopy* Swiss Physical Society Annual Meeting, EPFL, Lausanne, Switzerland
- 10/2005 *Ultrafast Structural Dynamics Research at the Swiss Light Source* 5^{th} Swiss Light Source User's Meeting, SLS, PSI, Villigen, Switzerland

- 04/2005 *Transient Local Structure of Solvated Transition-Metal Complexes probed by Picosecond Time-Resolved XAFS* BESSY Ultrafast X-Ray Science Workshop, Berlin-Zeuthen, Germany

- 10/2003 *Picosecond Time-Resolved X-Ray Absorption Spectroscopy of Laser-Excited* $[Ru(bpy)_3]^{2+}$ 4^{th} Swiss Light Source User's Meeting, SLS, PSI, Villigen, Switzerland

- 07/2003 *An Experimental Setup for Ultrafast X-Ray Absorption Spectroscopy" "Picosecond Time-Resolved X-Ray Spectroscopy of Solvated Organometallics* Femtochemistry VI, Paris, France

- 07/2003 *An Experimental Setup for Ultrafast X-Ray Absorption Spectroscopy* Summer School on Ultrafast X-ray Science, Institut D'Ètudes Scientifiques de Cargèse, Corsica, France

- 06/2003 *Picosecond Time-Resolved X-Ray Absorption Spectroscopy of Laser-Excited* $[Ru(bpy)_3]^{2+}$ XAFS 12 International Conference, Malmö, Sweden

- 04/2003 *Picosecond Time-Resolved X-Ray Absorption Spectroscopy of Laser-Excited Aqueous* $[Ru(bpy)_3]^{2+}$ Ultrafast Science with X-Rays and Electrons-Workshop, Montreux, Switzerland

- 04/2003 *Time-Resolved X-Ray Absorption Spectroscopy at Synchrotrons with Picosecond Temporal Resolution* Ultrafast Science with X-Rays and Electrons-Workshop, Montreux, Switzerland

- 10/2002 *Picosecond Time-Resolved X-Ray Spectroscopy of Laser-Excited Organometallics in Solution "Ultrafast Phenomena by Synchrotron Radiation*" Workshop, Elettra, Trieste, Italy

- 10/2002 *Picosecond Time-Resolved X-Ray Spectroscopy of Laser-Excited Organometallics in Solution* The Advanced Light Source Users' Meeting, LBNL, Berkeley, USA

- 09/2002 *Picosecond Time-Resolved X-Ray Spectroscopy of Aqueous Organometallic Complexes* Late Summer CEAC Workshop, Swiss Light Source, PSI, Villigen, Switzerland

Scientific Highlights

- **Research Highlights of the Swiss Light Source, Paul Scherrer Institut, Villigen, Switzerland**
  Transient Molecular Structures Observed by Picosecond X-ray Absorption Spectroscopy,

  W. Gawelda, V-T. Pham, S. L. Johnson, D. Grolimund, R. Abela, M. Kaiser, Y. Zaushitsyn, B. Verbrugge, M. Cascella, I. Tavernelli, A. Hauser, M. Chergui, C. Bressler, *PSI Scientific Reports 2005*, **Vol.1**, (2006) 12-13

- **Scientific Highlights of the Advanced Light Source, Berkeley, USA**,
  Ultrafast XANES Technique Reveals Photochemical Transients,

  M. Saes, W. Gawelda, D. Grolimund, R. Abela, S.L. Johnson, P.A. Heimann, C. Bressler, M. Chergui, Scientific Highlights, *ALS News* **227**, August 6, 2003

Bibliography

[1] http://nobelprize.org/.

[2] F. Crick, Physics Today **March**, 19 (2000).

[3] D. E. Sayers, E. A. Stern, and F. W. Lytle, Physical Review Letters **27**, 1204 (1971).

[4] D. C. Koningsberger, *X-ray Absorption Principles, Applications, Techniques of EXAFS, SEXAFS and XANES*, Wiley, New York, 1988.

[5] E. A. Stern, Physical Review B **10**, 3027 (1974).

[6] E. A. Stern and S. M. Heald, Basic Principles and Applications of EXAFS, in *Handbook on Synchrotron Radiation*, edited by D. E. Eastman and E. E. Koch, volume 1, pages 955–1014, North-Holland, Amsterdam, 1983.

[7] E. A. Stern, Theory of EXAFS, in *X-ray Absorption Principles, Applications, Techniques of EXAFS, SEXAFS and XANES*, edited by D. C. Königsberger and R. Prins, page 3, Wiley, New York, 1988.

[8] A. Bianconi, *EXAFS and Near-Edge structure. Proceedings of the International Conference Frascati, September 13-17, 1982*, Springer, Berlin etc., 1983.

[9] A. Bianconi, E. Fritsch, G. Calas, and J. Petiau, Physical Review B **32**, 4292 (1985).

[10] A. Bianconi, XANES spectroscopy, in *X-ray Absorption Principles, Applications, Techniques of EXAFS, SEXAFS and XANES*, edited by R. Koningsberger, D. C.: Prins, pages XII, 673, Wiley, New York, 1988.

[11] J. J. Rehr and R. C. Albers, Reviews of Modern Physics **72**, 621 (2000).

[12] A. H. Zewail, Journal of Physical Chemistry A **104**, 5660 (2000).

[13] M. Chergui, *Femtochemistry: Ultrafast Chemical and Physical Processes in Molecular Systems. Lausanne, Switzerland, September 4-8, 1995*, World Scientific, Singapore etc., 1996.

[14] M. Chergui, ChemPhysChem **8**, 713 (2002).

[15] T. Baumert, M. Grosser, R. Thalweiser, and G. Gerber, Physical Review Letters **67**, 3753 (1991).

[16] T. Baumert, V. Engel, C. Rottgermann, W. T. Strunz, and G. Gerber, Chemical Physics Letters **191**, 639 (1992).

[17] R. M. Bowman, M. Dantus, and A. H. Zewail, Chemical Physics Letters **161**, 297 (1989).

[18] M. Gruebele, G. Roberts, M. Dantus, R. M. Bowman, and A. H. Zewail, Chemical Physics Letters **166**, 459 (1990).

[19] T. S. Rose, M. J. Rosker, and A. H. Zewail, Journal of Chemical Physics **91**, 7415 (1989).

[20] J. C. Williamson and A. H. Zewail, Proceedings of the National Academy of Sciences of the United States of America **88**, 5021 (1991).

[21] J. C. Williamson, M. Dantus, S. B. Kim, and A. H. Zewail, Chemical Physics Letters **196**, 529 (1992).

[22] J. C. Williamson and A. H. Zewail, Journal of Physical Chemistry **98**, 2766 (1994).

[23] M. Dantus, S. B. Kim, J. C. Williamson, and A. H. Zewail, Journal of Physical Chemistry **98**, 2782 (1994).

[24] H. Ihee, J. S. Feenstra, J. M. Cao, and A. H. Zewail, Chemical Physics Letters **353**, 325 (2002).

[25] H. Ihee, B. M. Goodson, R. Srinivasan, V. A. Lobastov, and A. H. Zewail, Journal of Physical Chemistry A **106**, 4087 (2002).

[26] J. M. Cao, H. Ihee, and A. H. Zewail, Proceedings of the National Academy of Sciences of the United States of America **96**, 338 (1999).

[27] C. Bressler and M. Chergui, Chemical Reviews **104**, 1781 (2004).

[28] F. L. H. Brown, K. R. Wilson, and J. S. Cao, Journal of Chemical Physics **111**, 6238 (1999).

[29] J. P. Bergsma et al., Journal of Chemical Physics **84**, 6151 (1986).

[30] P. Chen, I. V. Tomov, and P. M. Rentzepis, Journal of Chemical Physics **104**, 10001 (1996).

[31] P. Chen, I. V. Tomov, and P. M. Rentzepis, Journal of Applied Crystallography **32**, 82 (1999).

[32] P. L. Chen, I. V. Tomov, and P. M. Rentzepis, Journal of Physical Chemistry A **103**, 2359 (1999).

[33] A. Cavalleri et al., Physical Review B **6319**, 193306 (2001).

[34] A. Cavalleri et al., Physical Review Letters **8723**, 237401 (2001).

[35] W. Gawelda et al., Journal of the American Chemical Society **128**, 5001 (2006).

[36] W. Gawelda et al., Physica Scripta **T115**, 102 (2005).

[37] J. Larsson et al., Applied Physics A-Materials Science and Processing **66**, 587 (1998).

[38] A. M. Lindenberg et al., Optics Letters **27**, 869 (2002).

[39] A. M. Lindenberg et al., Physical Review Letters **84**, 111 (2000).

[40] C. Rose-Petruck et al., Nature **398**, 310 (1999).

[41] K. Sokolowski-Tinten et al., Nature **422**, 287 (2003).

[42] A. Rousse et al., Journal of Applied Crystallography **32**, 977 (1999).

[43] L. X. Chen et al., Science **292**, 262 (2001).

[44] L. X. Chen et al., Journal of the American Chemical Society **124**, 10861 (2002).

[45] L. X. Chen et al., Journal of the American Chemical Society **125**, 7022 (2003).

[46] L. X. Chen, Journal of Electron Spectroscopy and Related Phenomena **119**, 161 (2001).

[47] L. X. Chen et al., Journal of Physical Chemistry B **103**, 3270 (1999).

[48] M. Khalil et al., Journal of Physical Chemistry A **110**, 38 (2006).

[49] M. Saes et al., Synchrotron Radiation News **16**, 12 (2003).

[50] M. Saes et al., Physical Review Letters **90**, 047403 (2003).

[51] S. L. Johnson et al., Physical Review Letters **91**, 157403 (2003).

[52] L. X. Chen, Angewandte Chemie-International Edition **43**, 2886 (2004).

[53] B. W. Adams, M. F. DeCamp, E. M. Dufresne, and D. A. Reis, Review of Scientific Instruments **73**, 4150 (2002).

[54] S. L. Johnson et al., Physical Review Letters **94**, 057407 (2005).

[55] R. W. Schoenlein et al., Applied Physics B-Lasers and Optics **71**, 1 (2000).

[56] R. W. Schoenlein et al., Science **287**, 2237 (2000).

[57] R. W. Schoenlein et al., Comptes Rendus de l'Academie Des Sciences, Serie IV: Physique Astrophysique **2**, 1373 (2001).

[58] M. M. Murnane, H. C. Kapteyn, and R. W. Falcone, Physics of Fluids B-Plasma Physics **3**, 2409 (1991).

[59] M. M. Murnane, H. C. Kapteyn, M. D. Rosen, and R. W. Falcone, Science **251**, 531 (1991).

[60] J. C. Kieffer et al., Physics of Fluids B-Plasma Physics **5**, 2676 (1993).

[61] J. C. Kieffer et al., Laser Physics **11**, 1201 (2001).

[62] J. C. Kieffer et al., Comptes Rendus de l'Academie des Sciences, Serie IV: Physique Astrophysique **1**, 297 (2000).

[63] K. Hatanaka, T. Miura, and H. Fukumura, Applied Physics Letters **80**, 3925 (2002).

[64] K. Hatanaka, T. Miura, H. Odaka, H. Ono, and H. Fukumura, Bunseki Kagaku **52**, 373 (2003).

[65] D. Von der Linde et al., Laser and Particle Beams **19**, 15 (2001).

[66] A. Rousse, C. Rischel, and J. C. Gauthier, Comptes Rendus de l'Academie des Sciences, Serie IV: Physique Astrophysique **1**, 305 (2000).

[67] D. M. Mills, A. Lewis, A. Harootunian, J. Huang, and B. Smith, Science **223**, 811 (1984).

[68] D. J. Thiel, P. Livins, E. A. Stern, and A. Lewis, Nature **363**, 565 (1993).

[69] A. Clozza, A. C. Castellano, S. Dellalonga, A. Giovannelli, and A. Bianconi, Review of Scientific Instruments **60**, 2519 (1989).

[70] M. R. Chance et al., Review of Scientific Instruments **64**, 2035 (1993).

[71] T. Ohyanagi, A. Miyashita, K. Murakami, and O. Yoda, Japanese Journal of Applied Physics Part 1-Regular Papers Short Notes and Review Papers **33**, 2586 (1994).

[72] J. M. Lee, M. A. Paesler, D. E. Sayers, and A. Fontaine, Physica B **158**, 52 (1989).

[73] M. E. Kassner, X. Li, and H. J. Mcqueen, Materials Science and Engineering A-Structural Materials Properties Microstructure and Processing **169**, 9 (1993).

[74] C. Bressler, M. Saes, M. Chergui, R. Abela, and P. Pattison, Nuclear Instruments and Methods in Physics Research Section A-Accelerators Spectrometers Detectors and Associated Equipment **467**, 1444 (2001).

[75] C. Bressler et al., Journal of Chemical Physics **116**, 2955 (2002).

[76] C. Bressler, M. Saes, M. Chergui, D. Grolimund, and R. Abela, Towards Structural Dynamics Research with Ultrashort Pulse Lasers and Synchrotron Radiation, in *Femtochemistry and Femtobiology: Ultrafast Dynamics in Molecular Science*, edited by A. Douhal, page 834, World Scientific, New Jersey, 2002.

[77] R. A. Marcus, Angewandte Chemie-International Edition in English **32**, 1111 (1993).

[78] R. A. Marcus, Journal of Electroanalytical Chemistry **438**, 251 (1997).

[79] R. A. Marcus, Pure and Applied Chemistry **69**, 13 (1997).

[80] R. A. Marcus, Electron Transfer-from Isolated Molecules to Biomolecules, Pt 1 **106**, 1 (1999).

[81] A. Tarnovsky, Journal of Physical Chemistry B **In press** (2006).

[82] A. Cannizzo et al., Angewandte Chemie International Edition **45**, 3174 (2006).

[83] J. S. Griffiths, *The Theory of Transition Metal Ions*, Cambridge University Press, New York, 1961.

[84] S. F. A. Kettle, *Physical Inorganic Chemistry. A Coordintion Chemistry Approach*, Oxford University Press, Oxford, England, 1996.

[85] A. Vlcek, Coordination Chemistry Reviews **177**, 1 (1998).

[86] A. Vlcek, Coordination Chemistry Reviews **200**, 933 (2000).

[87] J. Ferguson, F. Herren, E. R. Krausz, M. Maeder, and J. Vrbancich, Coordination Chemistry Reviews **64**, 21 (1985).

[88] J. K. McCusker, Accounts of Chemical Research **36**, 876 (2003).

[89] N. Serpone and M. A. Jamieson, Coordination Chemistry Reviews **93**, 87 (1989).

[90] V. Balzani, A. Juris, M. Venturi, S. Campagna, and S. Serroni, Chemical Reviews **96**, 759 (1996).

[91] A. Juris et al., Coordination Chemistry Reviews **84**, 85 (1988).

[92] V. Balzani, *Electron Transfer in Chemistry*, Wiley-VCH, Weinheim ; New York, 2001.

[93] E. A. Juban, A. L. Smeigh, J. E. Monat, and J. K. McCusker, Coordination Chemistry Reviews **250**, 1783 (2006).

[94] M. Gerloch, Coordination Chemistry Reviews **99**, 117 (1990).

[95] R. D. Cowan, *The Theory of Atomic Structure and Spectra*, The University of California, Berkeley, Berkeley, 1981.

[96] G. A. Crosby, R. J. Watts, and D. H. Carstens, Science **170**, 1195 (1970).

[97] A. Hauser, Spin Crossover in Transition Metal Compounds I **233**, 49 (2004).

[98] J. P. Paris and W. W. Brandt, Journal of the American Chemical Society **81**, 5001 (1959).

[99] L. Hammarstrom, L. C. Sun, B. Akermark, and S. Styring, Spectrochimica Acta Part A-Molecular and Biomolecular Spectroscopy **57**, 2145 (2001).

[100] A. Hagfeldt and M. Gratzel, Chemical Reviews **95**, 49 (1995).

[101] M. Gratzel, Nature **414**, 338 (2001).

[102] K. Kalyanasundaram and M. Gratzel, Coordination Chemistry Reviews **177**, 347 (1998).

[103] D. P. Rillema, D. S. Jones, and H. A. Levy, Journal of the Chemical Society-Chemical Communications , 849 (1979).

[104] D. P. Rillema, D. S. Jones, C. Woods, and H. A. Levy, Inorganic Chemistry **31**, 2935 (1992).

[105] C. Pinheiro, Private Communication .

[106] K. W. Hipps and G. A. Crosby, Journal of the American Chemical Society **97**, 7042 (1975).

[107] D. C. Harris and M. D. Bertolucci, *Symmetry and Spectroscopy: An Introduction to Vibrational and Electronic Spectroscopy*, Dover Publications, New York, 1989.

[108] S. Sugano, Y. Tanabe, and H. Kamimura, *Multiplets of Transition Metal Ions in Crystals*, Pure and applied physics, vol. 33, Academic Press, New York, 1970.

[109] H. Watanabe, *Operator Methods in Ligand Field Theory*, Prentice-Hall International Series in Chemistry, Prentice-Hall, Inc., Englewood Cliffs, New Jersey, 1966.

[110] G. Calzaferri and R. Rytz, Journal of Physical Chemistry **99**, 12141 (1995).

[111] N. H. Damrauer et al., Science **275**, 54 (1997).

[112] A. T. Yeh, C. V. Shank, and J. K. McCusker, Science **289**, 935 (2000).

[113] C. Creutz, M. Chou, T. L. Netzel, M. Okumura, and N. Sutin, Journal of the American Chemical Society **102**, 1309 (1980).

[114] H. C. Stynes and I. J. A., Inorganic Chemistry **10**, 2304 (1971).

[115] P. K. Mallick, D. P. Strommen, and J. R. Kincaid, Journal of the American Chemical Society **112**, 1686 (1990).

[116] V. I. Baranovski, O. O. Lubimova, A. A. Makarov, and O. V. Sizova, Chemical Physics Letters **361**, 196 (2002).

[117] M. A. Webb, F. J. Knorr, and J. L. McHale, Journal of Raman Spectroscopy **32**, 481 (2001).

[118] C. N. Fleming, K. A. Maxwell, J. M. DeSimone, T. J. Meyer, and J. M. Papanikolas, Journal of the American Chemical Society **123**, 10336 (2001).

[119] G. B. Shaw and J. M. Papanikolas, Journal of Physical Chemistry B **106**, 6156 (2002).

[120] V. Balzani, N. Sabbatini, and F. Scandola, Chemical Reviews **86**, 319 (1986).

[121] K. Kalyanasundaram, S. M. Zakeeruddin, and M. K. Nazeeruddin, Coordination Chemistry Reviews **132**, 259 (1994).

[122] S. K. Doorn and J. T. Hupp, Journal of the American Chemical Society **111**, 4704 (1989).

[123] D. P. Strommen, P. K. Mallick, G. D. Danzer, R. S. Lumpkin, and J. R. Kincaid, Journal of Physical Chemistry **94**, 1357 (1990).

[124] M. Biner, H. B. Bürgi, A. Ludi, and C. Röhr, Journal of the American Chemical Society **114**, 5197 (1992).

[125] J. K. Beattie, Advances in Inorganic Chemistry **32**, 1 (1988).

[126] J. F. Letard, P. Guionneau, and L. Goux-Capes, Topics in Current Chemistry: Spin Crossover in Transition Metal Compounds III **235**, 221 (2004).

[127] J. N. Harvey, Faraday Discussions **127**, 165 (2004).

[128] P. Gutlich, Y. Garcia, and H. A. Goodwin, Chemical Society Reviews **29**, 419 (2000).

[129] P. Gutlich and H. A. Goodwin, Topics in Current Chemistry: Spin Crossover in Transition Metal Compounds I **233**, 1 (2004).

[130] A. Hauser, Spin Crossover in Transition Metal Compounds II **234**, 155 (2004).

[131] P. Gutlich and A. Hauser, Pure and Applied Chemistry **61**, 849 (1989).

[132] P. Gutlich and A. Hauser, Coordination Chemistry Reviews **97**, 1 (1990).

[133] P. Gutlich, A. Hauser, and H. Spiering, Angewandte Chemie-International Edition in English **33**, 2024 (1994).

[134] H. Oyanagi, T. Tayagaki, and K. Tanaka, Journal of Physics and Chemistry of Solids **65**, 1485 (2004).

[135] H. Oyanagi, T. Tayagaki, and K. Tanaka, Journal of Luminescence **119**, 361 (2006).

[136] H. Oyanagi, X-ray absorption fine structure, in *Applications of Synchrotron Radiation to Material Science*, edited by Y. Saisho, H; Gohshi, Elsevier Science B. V., 1996.

[137] K. Okamoto et al., Journal of Synchrotron Radiation **10**, 242 (2003).

[138] K. Okamoto, K. Nagai, J. Miyawaki, H. Kondoh, and T. Ohta, Chemical Physics Letters **371**, 707 (2003).

[139] L. X. Chen, Z. Y. Wang, J. K. Burdett, P. A. Montano, and J. R. Norris, Journal of Physical Chemistry **99**, 7958 (1995).

[140] H. Toftlund, Monatshefte Für Chemie **132**, 1269 (2001).

[141] M. L. Boillot et al., New Journal of Chemistry **26**, 313 (2002).

[142] Y. Garcia, V. Ksenofontov, G. Levchenko, and P. Gutlich, Journal of Materials Chemistry **10**, 2274 (2000).

[143] Y. Garcia, V. Ksenofontov, G. Levchenko, G. Schmitt, and P. Gutlich, Journal of Physical Chemistry B **104**, 5045 (2000).

[144] C. Roux et al., Inorganic Chemistry **35**, 2846 (1996).

[145] C. Roux, J. Zarembowitch, J. P. Itie, A. Polian, and M. Verdaguer, Inorganic Chemistry **35**, 574 (1996).

[146] V. Ksenofontov, A. B. Gaspar, and P. Gutlich, Topics in Current Chemistry: Spin Crossover in Transition Metal Compounds III **235**, 23 (2004).

[147] V. Ksenofontov, A. B. Gaspar, G. Levchenko, B. Fitzsimmons, and P. Gutlich, Journal of Physical Chemistry B **108**, 7723 (2004).

[148] C. Brady, J. J. McGarvey, J. K. McCusker, H. Toftlund, and D. N. Hendrickson, Topics in Current Chemistry: Spin Crossover in Transition Metal Compounds III **235**, 1 (2004).

[149] J. K. McCusker et al., Journal of the American Chemical Society **115**, 298 (1993).

[150] S. Dick, Zeitschrift Für Kristallographie-New Crystal Structures **213**, 356 (1998).

[151] L. M. L. Daku, A. Vargas, A. Hauser, A. Fouqueau, and M. E. Casida, ChemPhysChem **6**, 1393 (2005).

[152] P. S. Braterman, J. I. Song, and R. D. Peacock, Inorganic Chemistry **31**, 555 (1992).

[153] R. M. Berger and D. R. McMillin, Inorganica Chimica Acta **177**, 65 (1990).

[154] E. M. Kober and T. J. Meyer, Inorganic Chemistry **21**, 3967 (1982).

[155] A. Thorne, U. Litzén, and S. Johansson, *Spectrophysics*, Springer-Verlag, Heidelberg, Germany, 1999.

[156] R. H. Green, Chemistry in Britain **4**, 518 (1968).

[157] E. König and K. J. Watson, Chemical Physics Letters **6**, 457 (1970).

[158] C. Brady et al., Inorganic Chemistry **43**, 4289 (2004).

[159] J. K. Mccusker, H. Toftlund, A. L. Rheingold, and D. N. Hendrickson, Journal of the American Chemical Society **115**, 1797 (1993).

[160] J. K. McCusker, A. L. Rheingold, and D. N. Hendrickson, Inorganic Chemistry **35**, 2100 (1996).

[161] J. E. Monat and J. K. McCusker, Journal of the American Chemical Society **122**, 4092 (2000).

[162] M. A. Bergkamp, B. S. Brunschwig, P. Gutlich, T. L. Netzel, and N. Sutin, Chemical Physics Letters **81**, 147 (1981).

[163] M. A. Bergkamp, C. K. Chang, and T. L. Netzel, Journal of Physical Chemistry **87**, 4441 (1983).

[164] A. J. Conti, C. L. Xie, and D. N. Hendrickson, Abstracts of Papers of the American Chemical Society **194**, 207 (1987).

[165] A. D. Kirk, P. E. Hoggard, G. B. Porter, M. G. Rockley, and M. W. Windsor, Chemical Physics Letters **37**, 199 (1976).

[166] C. L. Xie and D. N. Hendrickson, Journal of the American Chemical Society **109**, 6981 (1987).

[167] A. J. Street, D. M. Goodall, and R. C. Greenhow, Chemical Physics Letters **56**, 326 (1978).

[168] A. Hauser, C. Enachescu, M. L. Daku, A. Vargas, and N. Amstutz, Coordination Chemistry Reviews **250**, 1642 (2006).

[169] E. Buhks, G. Navon, M. Bixon, and J. Jortner, Journal of the American Chemical Society **102**, 2918 (1980).

[170] P. Guionneau et al., Journal of Materials Chemistry **9**, 985 (1999).

[171] P. Guionneau, M. Marchivie, G. Bravic, J. F. Letard, and D. Chasseau, Spin Crossover in Transition Metal Compounds II **234**, 97 (2004).

[172] J. F. Letard et al., Inorganic Chemistry **37**, 4432 (1998).

[173] R. Shankar, *Principles of Quantum Mechanics*, Plenum Press, New York, USA, 1994.

[174] A. Messiah, *Quantum Mechanics*, North-Holland, Amsterdam, 9^{th} edition, 1976.

[175] C. J. Donnelly and G. F. Imbusch, in *Advances in Noradiative Processes in Solids*, edited by B. di Bartolo, Plenum Press, New York, 1991.

[176] T. C. Brunold and H. U. Guedel, in *Inorganic Electronic Structure and Spectroscopy Vol. I*, edited by E. I. Solomon and A. B. P. Lever, Wiley, New York, 1999.

[177] P. Suppan, Topics in Current Chemistry **163**, 95 (1992).

[178] P. Suppan, *Chemistry and Light*, The Royal Society of Chemistry, London, England, 1994.

[179] A. Hauser, Comments on Inorganic Chemistry **17**, 17 (1995).

[180] A. L. Thompson, A. E. Goeta, J. A. Real, A. Galet, and M. C. Munoz, Chemical Communications , 1390 (2004).

[181] P. Guionneau, J. S. Costa, and J. F. Letard, Acta Crystallographica Section C-Crystal Structure Communications **60**, M587 (2004).

[182] M. Hostettler, K. W. Tornroos, D. Chernyshov, B. Vangdal, and H. B. Burgi, Angewandte Chemie-International Edition **43**, 4589 (2004).

[183] C. Hannay et al., Inorganic Chemistry **36**, 5580 (1997).

[184] T. Yokoyama, Y. Murakami, M. Kiguchi, T. Komatsu, and N. Kojima, Physical Review B **58**, 14238 (1998).

[185] J. J. Lee et al., Journal of the American Chemical Society **122**, 5742 (2000).

[186] B. S. Brunschwig, C. Creutz, D. H. McCartney, T. K. Sham, and N. Sutin, Faraday Discuss. Chem. Soc. **74**, 113 (1982).

[187] H. Paulsen et al., European Physical Journal B **23**, 463 (2001).

[188] G. P. Zhang, W. Hubner, E. Beaurepaire, and J. Y. Bigot, Spin Dynamics in Confined Magnetic Structures I **83**, 245 (2002).

[189] M. Dantus, M. J. Rosker, and A. H. Zewail, Journal of Chemical Physics **89**, 6128 (1988).

[190] M. J. Rosker, M. Dantus, and A. H. Zewail, Journal of Chemical Physics **89**, 6113 (1988).

[191] M. Chergui, C. Bressler, and R. Abela, Synchrotron radiation News (2004).

[192] B. M. Garraway and K. A. Suominen, Reports on Progress in Physics **58**, 365 (1995).

[193] G. A. Voth and R. M. Hochstrasser, Journal of Physical Chemistry **100**, 13034 (1996).

[194] G. R. Fleming, T. Joo, and M. Cho, Femtosecond chemical dynamics in condensed phases, in *Chemical Reactions and their Control on the Femtosecond Time Scale, XXth Solvay Conference on Chemistry*, edited by P. Gaspard and I. S. (Bruxelles), volume 101, pages 141–184, Wiley, New York, 1997.

[195] M. Chergui, Comptes Rendus de l'Academie des Sciences, Serie IV: Physique Astrophysique **2**, 1453 (2001).

[196] C. Jeannin et al., Chemical Physics Letters **316**, 51 (2000).

[197] F. Vigliotti, L. Bonacina, and M. Chergui, Journal of Chemical Physics **116**, 4553 (2002).

[198] F. Vigliotti, L. Bonacina, and M. Chergui, Physical Review B **67**, Art. No. 115118 (2003).

[199] C. C. Moser, J. M. Keske, K. Warncke, R. S. Farid, and P. L. Dutton, Nature **355**, 796 (1992).

[200] R. van Grondelle, J. P. Dekker, T. Gillbro, and V. Sundstrom, Biochimica Et Biophysica Acta-Bioenergetics **1187**, 1 (1994).

[201] S. Schenkl, F. van Mourik, G. van der Zwan, S. Haacke, and M. Chergui, Science **309**, 917 (2005).

[202] S. Schenkl et al., Proceedings of the National Academy of Sciences **103**, 4101 (2006).

[203] L. X. Chen et al., Science **292**, 262 (2001).

[204] J. Larsson et al., X-ray Lasers , 367 (1996).

[205] J. Larsson et al., Applied Physics A-Materials Science and Processing **75**, 467 (2002).

[206] E. Collet et al., Science **300**, 612 (2003).

[207] E. Collet, M. Buron-Le Cointe, and H. Cailleau, Journal of the Physical Society of Japan **75** (2006).

[208] L. Guerin et al., Journal De Physique IV **114**, 99 (2004).

[209] L. Guerin et al., Chemical Physics **299**, 163 (2004).

[210] M. Wulff et al., Journal De Chimie Physique Et De Physico-Chimie Biologique **93**, 1915 (1996).

[211] D. M. Mills, Acta Crystallographica Section A **40**, C393 (1984).

[212] D. M. Mills, Nuclear Instruments and Methods in Physics Research Section A-Accelerators Spectrometers Detectors and Associated Equipment **222**, 159 (1984).

[213] M. Saes, Ph.D. Thesis, Ecole Polytechnique Fédérale de Lausanne, 2004.

[214] P. A. Lee and J. B. Pendry, Physical Review B **11**, 2795 (1975).

[215] P. A. Lee, P. H. Citrin, P. Eisenberger, and B. M. Kincaid, Reviews of Modern Physics **53**, 769 (1981).

[216] A. Bianconi, S. Doniach, and D. Lublin, Chemical Physics Letters **59**, 121 (1978).

[217] A. Bianconi, Surface Science **99**, 76 (1980).

[218] M. Belli et al., Solid State Communications **35**, 355 (1980).

[219] T. E. Westre et al., Journal of the American Chemical Society **119**, 6297 (1997).

[220] A. H. de Vries, L. Hozoi, and R. Broer, International Journal of Quantum Chemistry **91**, 57 (2003).

[221] J. Wong, F. W. Lytle, R. P. Messmer, and D. H. Maylotte, Physical Review B **30**, 5596 (1984).

[222] C. Mande and V. B. Sapre, Chemical Shifts in X-Ray Absorption Spectra, in *Advances in X-Ray Spectroscopy*, edited by C. Bonnelle and C. Mande, pages 287–301, Pergamon Press, New York, 1982.

[223] V. Kunzl, Collect. Czech. Chem. Comm. **4**, 213 (1932).

[224] I. Lindgren, Journal of Electron Spectroscopy and Related Phenomena **137-40**, 59 (2004).

[225] A. Meisel, Chemical Shifts and Changes in Shape of X-Ray Emission Lines in Solids, in *Advances in X-Ray Spectroscopy*, edited by C. Bonnelle and C. Mande, pages 302–337, Pergamon Press, New York, 1982.

[226] V. Briois, C. C. D. Moulin, P. Sainctavit, C. Brouder, and A. M. Flank, Journal of the American Chemical Society **117**, 1019 (1995).

[227] V. Briois, P. Sainctavit, G. J. Long, and F. Grandjean, Inorganic Chemistry **40**, 912 (2001).

[228] M. Wilke, F. Farges, P. E. Petit, G. E. Brown, and F. Martin, American Mineralogist **86**, 714 (2001).

[229] M. Benfatto, P. D'Angelo, S. Della Longa, and N. V. Pavel, Physical Review B **65**, (2002).

[230] T. A. Ferrett et al., Physical Review A **34**, 1916 (1986).

[231] H. Nakamatsu, T. Mukoyama, and H. Adachi, Journal of Chemical Physics **95**, 3167 (1991).

[232] F. Sette, J. Stohr, and A. P. Hitchcock, Chemical Physics Letters **110**, 517 (1984).

[233] F. Sette, J. Stohr, and A. P. Hitchcock, Journal of Chemical Physics **81**, 4906 (1984).

[234] J. Stöhr, *NEXAFS Spectroscopy*, Springer, Berlin etc., 1992.

[235] M. Newville, *Fundamentals of XAFS*, http://xafs.org/Tutorials.

[236] E. A. Stern, D. E. Sayers, and F. W. Lytle, Physical Review B **11**, 4836 (1975).

[237] F. W. Lytle, D. E. Sayers, and E. A. Stern, Physical Review B **11**, 4825 (1975).

[238] L. Campbell, L. Hedin, J. J. Rehr, and W. Bardyszewski, Physical Review B **65** (2002).

[239] B. K. Teo, *EXAFS: Basic Principles and Data Analysis*, Berlin ; New York, 1986.

[240] E. A. Stern, Y. J. Ma, O. Hanskepetitpierre, and C. E. Bouldin, Physical Review B **46**, 687 (1992).

[241] S. I. Zabinsky, J. J. Rehr, A. Ankudinov, R. C. Albers, and M. J. Eller, Physical Review B **52**, 2995 (1995).

[242] J. Mustre, Y. Yacoby, E. A. Stern, and J. J. Rehr, Physical Review B **42**, 10843 (1990).

[243] B. Ravel, Journal of Alloys and Compounds **401**, 118 (2005).

[244] J. J. Rehr and R. C. Albers, Physical Review B **41**, 8139 (1990).

[245] J. L. Beeby, Proceedings of the Royal Society of London Series A-Mathematical and Physical Sciences **302**, 113 (1967).

[246] P. Lloyd and P. V. Smith, Advances in Physics **21**, 69 (1972).

[247] J. J. Rehr and A. L. Ankudinov, Journal of Synchrotron Radiation **8**, 61 (2001).

[248] M. O. Krause and J. H. Oliver, Journal of Physical and Chemical Reference Data **8**, 329 (1979).

[249] B. Ravel and M. Newville, Journal of Synchrotron Radiation **12**, 537 (2005).

[250] C. R. Natoli, M. Benfatto, and S. Doniach, Physical Review A **34**, 4682 (1986).

[251] A. L. Ankudinov, B. Ravel, J. J. Rehr, and S. D. Conradson, Physical Review B **58**, 7565 (1998).

[252] A. L. Ankudinov, C. E. Bouldin, J. J. Rehr, J. Sims, and H. Hung, Physical Review B **65**, 104107 (2002).

[253] M. Benfatto, A. Congiu-Castellano, A. Daniele, and S. D. Longa, Journal of Synchrotron Radiation **8**, 267 (2001).

[254] M. Benfatto and S. Della Longa, Journal of Synchrotron Radiation **8**, 1087 (2001).

[255] M. Benfatto, S. Della Longa, and P. D'Angelo, Physica Scripta **T115**, 28 (2005).

[256] M. Benfatto et al., Journal of physical Chemistry B **110**, 14035 (2006).

[257] T. A. Tyson, K. O. Hodgson, C. R. Natoli, and M. Benfatto, Physical Review B **46**, 5997 (1992).

[258] S. Della Longa, A. Arcovito, M. Girasole, J. L. Hazemann, and M. Benfatto, Physical Review Letters **8715**, (2001).

[259] J. J. Rehr, Foundations of Physics **33**, 1735 (2003).

[260] F. M. F. de Groot et al., Journal of Chemical Physics **101**, 6570 (1994).

[261] F. M. F. de Groot, Journal of Electron Spectroscopy and Related Phenomena **67**, 529 (1994).

[262] F. de Groot, Coordination Chemistry Reviews **249**, 31 (2005).

[263] F. M. F. de Groot and J. Vogel, Fundamentals of X-ray Absorption and Dichroism, Oxford University Press, Oxford, 2004.

[264] http://www.anorg.chem.uu.nl/people/staff/index.html.

[265] C. H. Booth and F. Bridges, Physica Scripta **T115**, 202 (2005).

[266] S. Eisebitt, T. Boske, J. E. Rubensson, and W. Eberhardt, Physical Review B **47**, 14103 (1993).

[267] D. M. Pease, D. L. Brewe, Z. Tan, J. I. Budnick, and C. C. Law, Physics Letters A **138**, 230 (1989).

[268] P. Pfalzer et al., Physical Review B **60**, 9335 (1999).

[269] Z. Q. Tan, J. I. Budnick, and S. M. Heald, Review of Scientific Instruments **60**, 1021 (1989).

[270] L. Troger et al., Physical Review B **46**, 3283 (1992).

[271] J. Jaklevic et al., Solid State Communications **23**, 679 (1977).

[272] M. O. Krause, Journal of Physical and Chemical Reference Data **8**, 307 (1979).

[273] D. L. Brewe, D. M. Pease, and J. I. Budnick, Physical Review B **50**, 9025 (1994).

[274] P. Kirkpatrick and A. V. Baez, Journal of the Optical Society of America **38**, 766 (1948).

[275] J. R. Taylor, *Introduction to Error Analysis. The Study of uncertainties in physical measurements*, University Science Books, Sausalito, CA USA, 1997.

[276] M. Saes et al., Review of Scientific Instruments **75**, 24 (2004).

[277] G. Margaritondo, *Introduction to Synchrotron Radiation*, Oxford University Press, Oxford, England, 1988.

[278] http://www.synchrotron soleil.fr.

[279] S. Krinsky, Fundamentals of Hard X-Ray Synchrotron Radiation Sources, in *Third-Generation Hard X-ray Synchrotron Radiation Sources*, edited by D. M. Mills, pages 1–40, John Wiley and Sons, Inc., New York, 2002.

[280] http://www.als.lbl.gov/als/quickguide/vugraph.html.

[281] http://www.synchrotron.vic.gov.au.

[282] http://sb3.epfl.ch/gm perso.data/margaritondo4.pdf.

[283] http://sls.web.psi.ch/view.php/beamlines/mxas/layout/index.html.

[284] http://sls.web.psi.ch/view.php/science/lsy/femto/facility/index.html.

[285] S. Johnson, P. Beaud, G. Ingold, and A. Tarnovsky, PSI Scientific Reports **VII** (2003).

[286] G. Ingold et al., PSI Scientific Reports **VII** (2002).

[287] A. A. Zholents and M. S. Zolotorev, Nuclear Instruments and Methods in Physics Research Section A-Accelerators Spectrometers Detectors and Associated Equipment **358**, 455 (1995).

[288] D. Grolimund, A. M. Scheidegger, J. F. van der Veen, and R. Abela, PSI Scientific Reports **VII**, 56 (2001).

[289] D. Grolimund, Private Communication .

[290] M. Moszynski, M. Kapusta, M. Balcerzyk, M. Szawlowski, and D. Wolski, Nuclear Instruments and Methods in Physics Research Section A-Accelerators Spectrometers Detectors and Associated Equipment **442**, 230 (2000).

[291] M. Moszynski, M. Szawlowski, M. Kapusta, and M. Balcerzyk, Nuclear Instruments and Methods in Physics Research Section A-Accelerators Spectrometers Detectors and Associated Equipment **485**, 504 (2002).

[292] M. Moszynski, M. Szawlowski, M. Kapusta, and M. Balcerzyk, Nuclear Instruments and Methods in Physics Research Section A-Accelerators Spectrometers Detectors and Associated Equipment **497**, 226 (2003).

[293] A. Q. R. Baron, Hyperfine Interactions **125**, 29 (2000).

[294] A. Thorne, U. Litzén, and S. Johansson, *Ultrashort Laser Pulse Phenomena. Fundamentals, Techniques and Applications on a Femtosecond Time Scale*, Academic Press, Inc., San Diego, USA, 1996.

[295] A. Brodeur and S. L. Chin, Journal of the Optical Society of America B-Optical Physics **16**, 637 (1999).

[296] D. Bebelaar, Chemical Physics **3**, 205 (1974).

[297] H. E. Lessing, A. Vonjena, and M. Reichert, Chemical Physics Letters **36**, 517 (1975).

[298] H. E. Lessing and A. V. Jena, Chemical Physics Letters **42**, 213 (1976).

[299] M. Rasmusson, A. N. Tarnovsky, E. Akesson, and V. Sundstrom, Chemical Physics Letters **335**, 201 (2001).

[300] M. Lorenc et al., Applied Physics B-Lasers and Optics **74**, 19 (2002).

[301] M. Ziolek, M. Lorenc, and R. Naskrecki, Applied Physics B-Lasers and Optics **72**, 843 (2001).

[302] K. Kalyanasundaram, Coordination Chemistry Reviews **46**, 159 (1982).

[303] B. H. Milosavljevic and J. K. Thomas, Journal of Physical Chemistry **87**, 616 (1983).

[304] G. B. Shaw, C. L. Brown, and J. M. Papanikolas, Journal of Physical Chemistry A **106**, 1483 (2002).

[305] S. Wallin, J. Davidsson, J. Modin, and L. Hammarstrom, Journal of Physical Chemistry A **109**, 4697 (2005).

[306] S. Wallin, J. Davidsson, J. Modin, and L. Hammarstrom, Journal of Physical Chemistry A **109**, 9378 (2005).

[307] A. C. Bhasikuttan, M. Suzuki, S. Nakashima, and T. Okada, Journal of the American Chemical Society **124**, 8398 (2002).

[308] J. N. Demas and G. A. Crosby, Journal of the American Chemical Society **93**, 2841 (1971).

[309] J. Vanhouten and R. J. Watts, Journal of the American Chemical Society **97**, 3843 (1975).

[310] H. B. Gray, Electron Transfer in Metalloproteins, in *Electron Transfer in Chemistry*, edited by V. Balzani, Wiley-VCH, Weinheim, 2001.

[311] J. P. Sauvage et al., Chemical Reviews **94**, 993 (1994).

[312] M. Goez, M. Schiewek, and M. H. O. Musa, Angewandte Chemie-International Edition **41**, 1535 (2002).

[313] M. Goez, D. von Ramin-Marro, M. H. O. Musa, and M. Schiewek, Journal of Physical Chemistry A **108**, 1090 (2004).

[314] J. N. Demas and G. A. Crosby, Journal of the American Chemical Society **92**, 7262 (1970).

[315] N. Ikeda, A. Yoshimura, M. Tsushima, and T. Ohno, Journal of Physical Chemistry A **104**, 6158 (2000).

[316] G. Ferraudi and G. A. Arguello, Inorganica Chimica Acta **144**, 53 (1988).

[317] D. W. Thompson, J. F. Wishart, B. S. Brunschwig, and N. Sutin, Journal of Physical Chemistry A **105**, 8117 (2001).

[318] C. D. Jonah, M. S. Matheson, and D. Meisel, Journal of the American Chemical Society **100**, 1449 (1978).

[319] U. Lachish, P. P. Infelta, and M. Gratzel, Chemical Physics Letters **62** (1979).

[320] Q. G. Mulazzani, S. Emmi, P. G. Fuochi, M. Z. Hoffman, and M. Venturi, Journal of the American Chemical Society **100**, 981 (1978).

[321] M. Assel, R. Laenen, and A. Laubereau, Journal of Chemical Physics **111**, 6869 (1999).

[322] R. Bonneau, I. Carmichael, and G. L. Hug, Pure and Applied Chemistry **63**, 290 (1991).

[323] R. Bensasson, C. Salet, and V. Balzani, Journal of the American Chemical Society **98**, 3722 (1976).

[324] K. Kalyanasundaram and M. Neumannspallart, Chemical Physics Letters **88**, 7 (1982).

[325] K. Miedlar and P. K. Das, Journal of the American Chemical Society **104**, 7462 (1982).

[326] T. Ohno, A. Yoshimura, and N. Mataga, Journal of Physical Chemistry **94**, 4871 (1990).

[327] P. S. Braterman, A. Harriman, G. A. Heath, and L. J. Yellowlees, Journal of the Chemical Society-Dalton Transactions , 1801 (1983).

[328] A. Hauser and E. Krausz, Chemical Physics Letters **138**, 355 (1987).

[329] M. Rougee, T. Ebbesen, F. Ghetti, and R. V. Bensasson, Journal of Physical Chemistry **86**, 4404 (1982).

[330] A. Yoshimura, M. Z. Hoffman, and H. Sun, Journal of Photochemistry and Photobiology a-Chemistry **70**, 29 (1993).

[331] T. Ohno, A. Yoshimura, D. R. Prasad, and M. Z. Hoffman, Journal of Physical Chemistry **95**, 4723 (1991).

[332] R. A. Crowell et al., Journal of Physical Chemistry A **108**, 9105 (2004).

[333] J. L. McGowen, H. M. Ajo, J. Z. Zhang, and B. J. Schwartz, Chemical Physics Letters **231**, 504 (1994).

[334] K. Yokoyama, C. Silva, D. H. Son, P. K. Walhout, and P. F. Barbara, Journal of Physical Chemistry A **102**, 6957 (1998).

[335] A. Henseler and E. Vauthey, Chemical Physics Letters **228**, 66 (1994).

[336] J. P. Cushing, C. Butoi, and D. F. Kelley, Journal of Physical Chemistry A **101**, 7222 (1997).

[337] L. F. Cooley, P. Bergquist, and D. F. Kelley, Journal of the American Chemical Society **112**, 2612 (1990).

[338] Y. Masuda and H. Yamatera, Journal of Physical Chemistry **88**, 3425 (1984).

[339] A. C. Albrecht, Journal of Molecular Spectroscopy **6**, 84 (1961).

[340] R. A. Crowell and D. M. Bartels, Journal of Physical Chemistry **100**, 17940 (1996).

[341] D. Meisel, M. S. Matheson, W. A. Mulac, and J. Rabani, Journal of Physical Chemistry **81**, 1449 (1977).

[342] S. J. Atherton, Journal of Physical Chemistry **88**, 2840 (1984).

[343] D. B. Naik and W. Schnabel, Chemical Physics Letters **228**, 616 (1994).

[344] D. B. Naik and W. Schnabel, Chemical Physics Letters **315**, 416 (1999).

[345] J. A. Kloepfer, V. H. Vilchiz, V. A. Lenchenkov, A. C. Germaine, and S. E. Bradforth, Journal of Chemical Physics **113**, 6288 (2000).

[346] L. L. Miller, E. A. Mayeda, and G. D. Nordblom, Journal of Organic Chemistry **37**, 916 (1972).

[347] D. Lide, editor, *CRC Handbook of Chemistry and Physics*, CRC Press, Boca Raton, 80^{th} edition, 1999.

[348] P. Kambhampati, D. H. Son, T. W. Kee, and P. F. Barbara, Journal of Physical Chemistry A **106**, 2374 (2002).

[349] V. H. Vilchiz, J. A. Kloepfer, A. C. Germaine, V. A. Lenchenkov, and S. E. Bradforth, Journal of Physical Chemistry A **105**, 1711 (2001).

[350] J. A. Kloepfer, V. H. Vilchiz, V. A. Lenchenkov, and S. E. Bradforth, Liquid Dynamics: Experiment, Simulation, and Theory **820**, 108 (2002).

[351] D. H. Son, P. Kambhampati, T. W. Kee, and P. F. Barbara, Chemical Physics Letters **342**, 571 (2001).

[352] J. V. Coe et al., Journal of Chemical Physics **107**, 6023 (1997).

[353] G. V. Buxton, C. L. Greenstock, W. P. Helman, and A. B. Ross, Journal of Physical and Chemical Reference Data **17**, 513 (1988).

[354] J. Baxendal and M. Fiti, Journal of the Chemical Society-Dalton Transactions , 1995 (1972).

[355] R. M. Whitnell, K. R. Wilson, and J. T. Hynes, Journal of Physical Chemistry **94**, 8625 (1990).

[356] R. M. Whitnell, K. R. Wilson, and J. T. Hynes, Journal of Chemical Physics **96**, 5354 (1992).

[357] J. K. Mccusker et al., Journal of the American Chemical Society **114**, 6919 (1992).

[358] W. Gawelda et al., **In preprint** (2006).

[359] A. Hauser, Chemical Physics Letters **173**, 507 (1990).

[360] A. Hauser, Journal of Chemical Physics **94**, 2741 (1991).

[361] S. Franzen, L. Kiger, C. Poyart, and J. L. Martin, Biophysical Journal **80**, 2372 (2001).

[362] R. G. Shulman, Y. Yafet, P. Eisenberger, and W. E. Blumberg, Proceedings of the National Academy of Sciences of the United States of America **73**, 1384 (1976).

[363] T. A. Tyson, M. Benfatto, C. R. Natoli, B. Hedman, and K. O. Hodgson, Physica B **158**, 425 (1989).

[364] K. O. Hodgson, B. Hedman, and J. E. Penner-Hahn, *EXAFS and Near Edge Structure III : Proceedings of an International Conference, Stanford, CA, July 16-20, 1984*, Springer Proceedings in Physics ; v. 2, Springer-Verlag, Berlin ; New York, 1984.

[365] B. K. Agarwal, *X-ray Spectroscopy. An Introduction*, Springer-Verlag, Heidelberg, Germany, 2^{nd} edition, 1991.

[366] E. A. Stern, Physical Review B **48**, 9825 (1993).

[367] M. Newville, Journal of Synchrotron Radiation **8**, 322 (2001).

[368] M. Newville, P. Livins, Y. Yacoby, J. J. Rehr, and E. A. Stern, Japanese Journal of Applied Physics Part 1-Regular Papers Short Notes and Review Papers **32**, 125 (1993).

[369] G. Sankar, J. M. Thomas, V. Varma, G. U. Kulkarni, and C. N. R. Rao, Chemical Physics Letters **251**, 79 (1996).

[370] R. F. Pettifer, O. Mathon, S. Pascarelli, M. D. Cooke, and M. R. J. Gibbs, Nature **435**, 78 (2005).

[371] J. Larsson et al., Optics Letters **22**, 1012 (1997).

[372] P. A. Heimann et al., Nuclear Instruments and Methods in Physics Research Section A-Accelerators Spectrometers Detectors and Associated Equipment **467**, 986 (2001).

[373] M. M. Murnane, H. C. Kapteyn, and R. W. Falcone, Applied Physics Letters **56**, 1948 (1990).

[374] A. Zholents, P. Heimann, M. Zolotorev, and J. Byrd, Nuclear Instruments and Methods in Physics Research Section A-Accelerators Spectrometers Detectors and Associated Equipment **425**, 385 (1999).

[375] S. L. Johnson, (2006).

[376] S. M. Gruner et al., Review of Scientific Instruments **73**, 1402 (2002).

[377] S. M. Gruner and D. H. Bilderback, Nuclear Instruments and Methods in Physics Research Section A-Accelerators Spectrometers Detectors and Associated Equipment **500**, 25 (2003).

[378] J. Corlett et al., A Recirculating Linac-Based Facility for Ultrafast X-ray Science, in *Particle Accelerator Conference*, Portland, Oregon, 2003.

[379] http://erl.chess.cornell.edu/.

[380] http://xfel.desy.de/.

[381] http://www ssrl.slac.stanford.edu/lcls/.

[382] J. Pfluger and M. Tischer, Nuclear Instruments and Methods in Physics Research Section A-Accelerators Spectrometers Detectors and Associated Equipment **483**, 388 (2002).

[383] B. Sonntag, Nuclear Instruments and Methods in Physics Research Section A-Accelerators Spectrometers Detectors and Associated Equipment **467**, 8 (2001).

[384] R. Neutze, R. Wouts, D. van der Spoel, E. Weckert, and J. Hajdu, Nature **406**, 752 (2000).

[385] S. Mukamel, *Principles of Nonlinear Optical Spectroscopy*, Oxford University Press, New York, 1995.

[386] S. Tanaka, V. Chernyak, and S. Mukamel, Physical Review A **6306**, Art. No. 063405 (2001).

[387] S. Tanaka and S. Mukamel, Physical Review A **6403**, Art. No. 032503 (2001).

[388] S. Tanaka and S. Mukamel, Physical Review Letters **89**, Art. No. 043001 (2002).

[389] S. Tanaka and S. Mukamel, Journal of Chemical Physics **116**, 1877 (2002).

[390] S. Tanaka and S. Mukamel, Physical Review A **67**, Art. No. 033818 (2003).

[391] S. Tanaka, S. Volkov, and S. Mukamel, Journal of Chemical Physics **118**, 3065 (2003).

[392] I. H. M. van Stokkum, D. S. Larsen, and R. van Grondelle, Biochimica Et Biophysica Acta-Bioenergetics **1657**, 82 (2004).

[393] R. Bonneau, J. Wirz, and A. D. Zuberbuhler, Pure and Applied Chemistry **69**, 979 (1997).

[394] S. Brandt, *Data Analysis. Statistical and Computational Methods for Scientists and Engineers*, Springer-Verlag, New York, USA, 1999.

[395] J. Helbing et al., Biophysical Journal **87**, 1881 (2004).

[396] H. Gampp, M. Maeder, C. J. Meyer, and A. D. Zuberbuhler, Talanta **32**, 95 (1985).